Structural and Photophysical Properties of Internal Charge Transfer 2-Arylidene and 2,5-Diarylidene Cyclopentanones

By

Christopher A. Zoto

A Dissertation

Submitted to the Faculty

of the

WORCESTER POLYTECHNIC INSTITUTE

in partial fulfillment of the requirements for the

Degree of Doctor of Philosophy

in

Chemistry

_____

July, 2012

APPROVED:

_____   _____
Dr. Robert E. Connors   Dr. John C. MacDonald
Research Advisor   Committee Member

_____   _____
Dr. James P. Dittami   Dr. John Lombardi
Committee Member   External Examiner

ABSTRACT

A series of symmetric and asymmetric 2-arylidene and 2,5-diarylidene cyclopentanone dyes have been synthesized. Their electronic absorption and fluorescence spectra have been measured in a wide variety of nonpolar and polar, aprotic and protic solvents. Absorption and fluorescence spectral maxima have been correlated with the $E_T(30)$ empirical solvent polarity scale. Lippert-Mataga analysis (in aprotic solvents) demonstrates the increase in the electronic dipole moment from the ground singlet to excited singlet states, consistent with the internal charge transfer (ICT) nature of the $S_0 \rightarrow S_1$ excitation. TD-DFT spectral calculations support the ICT natures of these compounds.

Photophysical properties of these compounds involved measuring both fluorescence quantum yields and lifetimes in various solvents. Investigation of the deactivation kinetics involved determining the first-order radiative and nonradiative rates of decay upon knowledge of the quantum yield and lifetime data. Fluorescence quantum yields and lifetimes of the compounds studied varied depending on the nature of the solvent environments. Excited state protonation in acetic acid was observed for several 2,5-diarylidene cyclopentanones and ΔpKa's have been determined via the Forster Cycle. Thorough work on the photochemistry of (2E,5E)-2,5-bis(p-dimethylaminobenzylidene)-cyclopentanone (bis-dmab) was carried out, consisting of testing bis-dmab as a singlet oxygen photosensitizer, and examination of both the chemical reactivity of bis-dmab with singlet state oxygen (self-sensitized photooxidation) and (E,E) $\rightarrow$ (E,Z) photoisomerization.

ACKNOWLEDGEMENTS

In my feelings about graduate school, I have found that pursuing an advanced degree in research requires not only a lot of hard work, persistence, and long hours/days in the lab, but also patience and understanding. You need to be patient and understanding with yourself, your research advisor, your graduate work, and your family and friends. Science, like anything else in life, comes with time and you need to take everything one step at a time. My mom and Professor Connors have always been very supportive and encouraging, especially during the last stage of my graduate career. They would sometimes remind me to take it one step at a time.

This PhD dissertation on the "Structural and Photophysical Properties of Internal Charge Transfer 2-Arylidene and 2,5-Diarylidene Cyclopentanones" is dedicated to my family, friends, and committee members.

TABLE OF CONTENTS

iv

LIST OF FIGURES

x

LIST OF TABLES

1   INTRODUCTION

1.1   Introduction

Substituted and unsubstituted 2,5-diarylidene cyclopentanones have received attention for their applications in a wide variety of areas. For instance, potential applications of these functionalized ketocyanine dyes include their use as photosensitizers for electronic energy transfer processes [1], fluorescent solvent polarity probes [2,3], fluoroionophores [4], and nonlinear optical materials [5-10]. Connors and Ucak-Astarlioglu [11] previously reported on the electronic structure and spectroscopic properties for a series of unsubstituted 2,5-diarylidene cyclopentanones in a variety of solvents, whose generic chemical structure is shown in Figure 1 ($R_1 = R_2 = H$, $n_1 = n_2 = 1, 2, 3$).
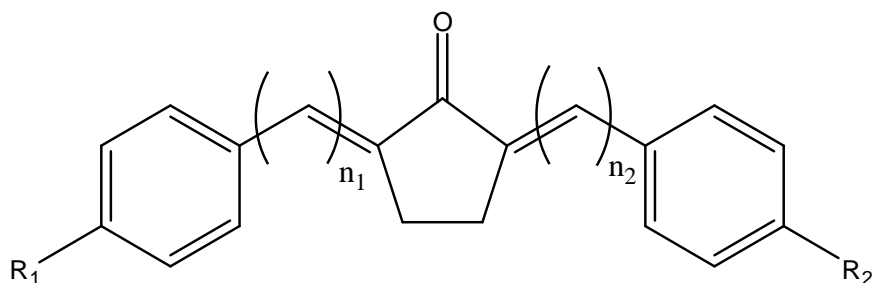
Figure 1. General structure of 2,5-diarylidene cyclopentanones.

The research reported in this dissertation serves as an extension to the work of Ucak-Astarlioglu on the electronic absorption and fluorescence properties of C_{2v} unsubstituted 2,5-diarylidene cyclopentanones [12]. Research reported in this dissertation includes thorough studies of the spectroscopic and photophysical analyses of a series of alkylamino substituted 2-arylidene and 2,5-diarylidene cyclopentanone compounds. Figure 2 shows the chemical

1

structures of the compounds studied. These include (E)-2-(p-dimethylaminobenzylidene)-cyclopentanone (dmab), (E)-2-(p-dimethylaminocinnamylidene)-cyclopentanone (dmac), (2E,5E)-2,5-bis(p-dimethylaminobenzylidene)-cyclopentanone (bis-dmab), (2E,5E)-2-(p-dimethylaminobenzylidene)-5-(p-dimethylaminocinnamylidene)-cyclopentanone (Ashrbor), (2E,5E)-2,5-bis(p-dimethylaminocinnamylidene)-cyclopentanone (bis-dmac) and its spatially restricted julolidinic analogue (2E,5E)-2,5-bis((E)-3-(1,2,3,5,6,7-hexahydropyrido[3,2,1-ij]quinolin-9-yl)allylidene)-cyclopentanone (bis-juldmac). These compounds are of interest due to their electron "push-pull" structures. Both dmab and dmac are categorized as D-A molecules and bis-dmab, Ashrbor, bis-dmac, and bis-juldmac are D-A-D systems (where D is an electron donor group and A is an electron acceptor group).

A unique feature of these types of electron "push-pull" polyene compounds are their photoinduced internal charge transfer (ICT) properties. The ICT state is an excited state characterized by the transfer of electron density from the electron donor end of the molecule to the electron acceptor end of the molecule upon photoexcitation. A special type of ICT state is termed the twisted internal charge transfer (TICT) state, where the plane of a dimethylamino group is at a twisted angle with respect to the rest of the molecule due to rotation about the C-N bond. A section of this dissertation involves comparing the spectroscopic and photophysical properties of bis-dmac and its spatially-restricted julolidine analogue (bis-juldmac). Contrary to bis-dmac, which contains dimethylamino groups substituted on the aryl moieties, bis-juldmac is spatially restricted on the aryl moieties due to the presence of closed, saturated ring systems that structurally prevent it from having a TICT state. Comparisons of the spectroscopic and photophysical properties of these two molecules will lead to determining whether or not bis-dmac undergoes formation of a TICT excited state.
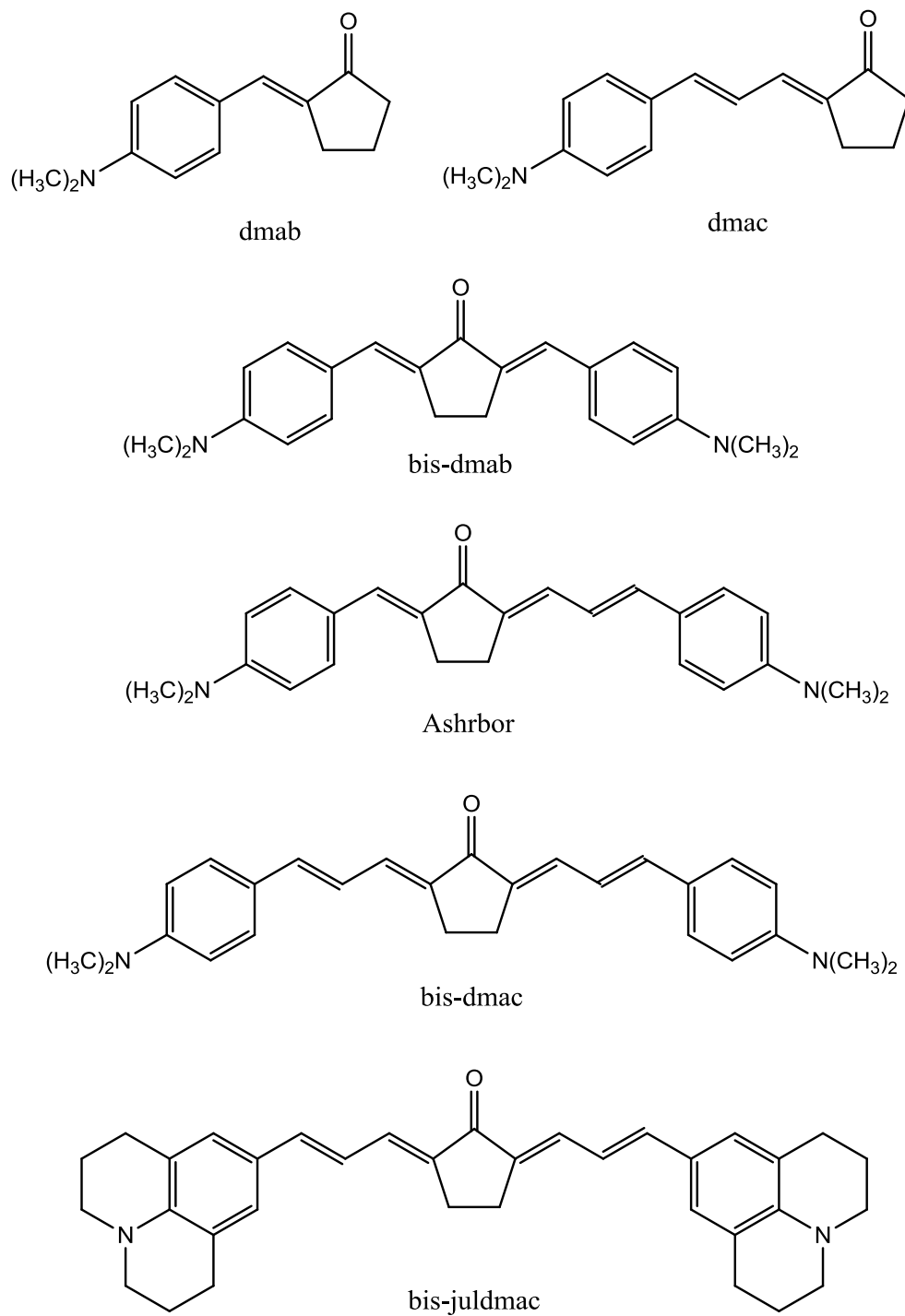
Figure 2. Structures of dmab, dmac, bis-dmab, Ashrbor, bis-dmac, and bis-juldmac.

An extension to the series of alkylamino substituted 2-arylidene and 2,5-diarylidene cyclopentanones involves the spectroscopic and photophysical studies of an asymmetrically substituted 2,5-diarylidene cyclopentanone compound belonging to the class of D-A-A systems. Figure 3 shows the structure of (2E,5E)-2-(p-cyanobenzylidene)-5-(p-dimethylaminobenzylidene)-cyclopentanone (Asdimcy1), which is known to have potential for applications utilizing two-photon absorption (TPA) and has already been shown to exhibit significant TPA when dissolved in chloroform [10]. Results reported here on the spectroscopic and photophysical properties of Asdimcy1 in a variety of solvent systems have been published and will be presented in chapter 4 of this thesis [13].
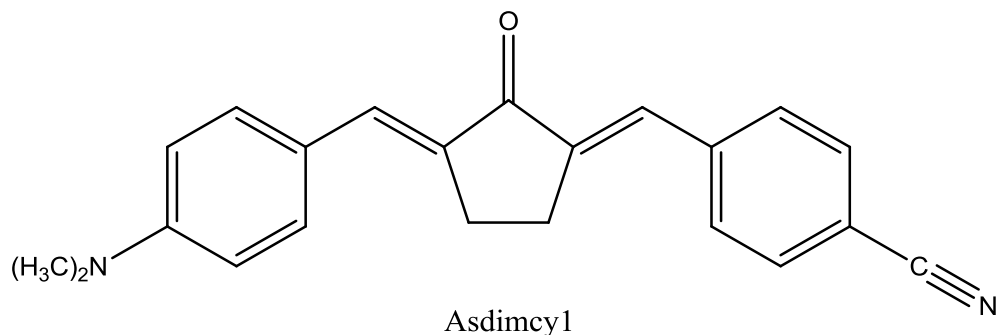
Asdimcy1

Figure 3. Structure of Asdimcy1.

A series of additional symmetric and asymmetric 2,5-diarylidene-cyclopentanones have been synthesized and studied, some to a minor extent and others more completely. Shown in Figure 4 are the structures of (2E,5E)-2,5-bis(p-methoxybenzylidene)-cyclopentanone (1dbmxcp), (2E,5E)-2,5-bis(p-methoxycinnamylidene)-cyclopentanone (2dbmxcp), (2E,5E)-2,5-bis(benzofuran-2-ylmethylene)-cyclopentanone (1dbzfcp), and (2E,5E)-2-benzylidene-5-cinnamylidene-cyclopentanone (Asunsub).
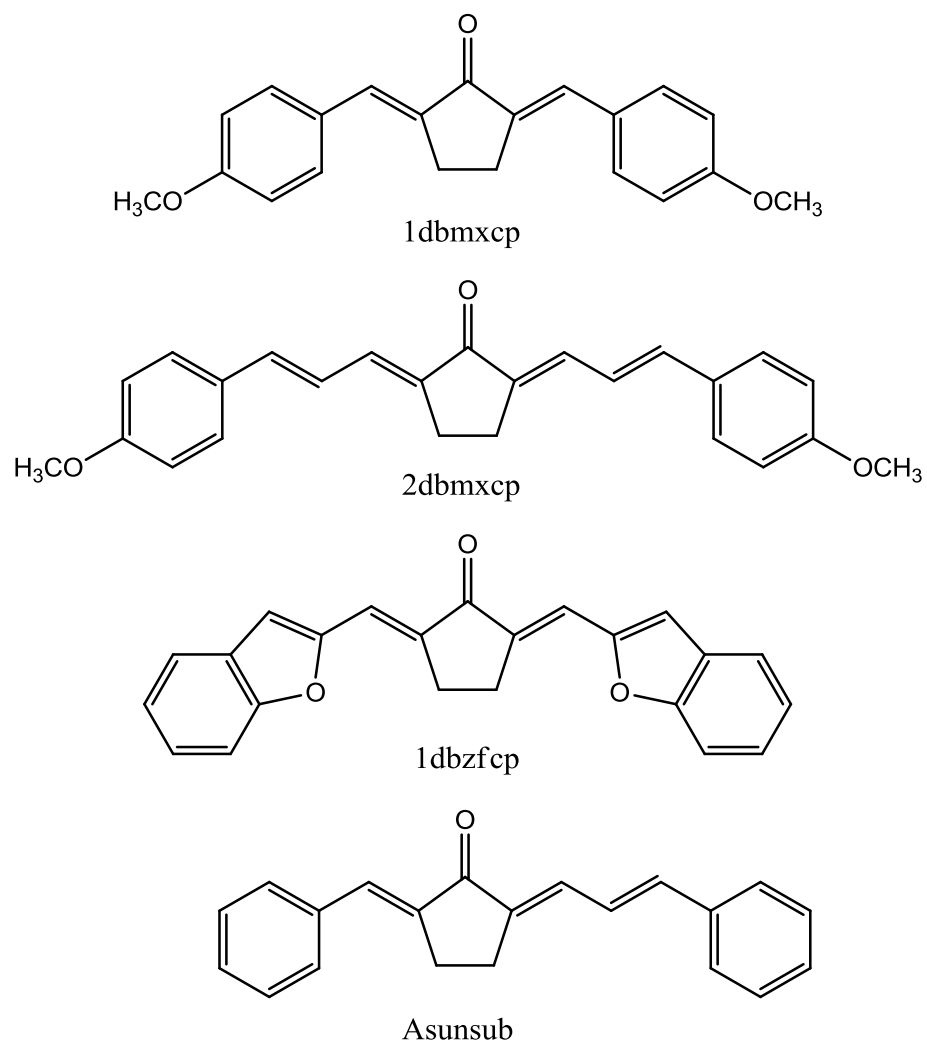
Figure 4. Structures of 1dbmxcp, 2dbmxcp, 1dbzfcp, and Asunsub.

1.2   Objective and Scope

The research presented in this dissertation serves as an extension to the work reported by Ucak-Astarlioglu on the electronic structure and spectroscopy of symmetrically unsubstituted 2,5-diarylidene cyclopentanones [12]. Specifically, the new work includes thorough studies on the electronic spectroscopy and photophysics of a series of substituted 2-arylidene cyclopentanones, symmetrically substituted 2,5-diarylidene cyclopentanones, and asymmetrically unsubstituted and substituted 2,5-diarylidene cyclopentanones, several of which are novel. The studies carried out in this thesis provide insight on the electronic structure, spectroscopic, and photophysical properties of this class of compounds. The objectives fall within the following scope.

1. Determination of the electronic structure, spectroscopic, and photophysical properties of a series of 2-arylidene and 2,5-diarylidene cyclopentanone compounds.

2. Investigation of the effect of polyene chain length on the electronic structure and spectroscopic properties of these compounds.

3. Investigation of the effect of electron donor and/or electron acceptor groups covalently bound to the aromatic ring system on the spectroscopic and photophysical properties of these compounds.

4. Investigation of the effect of solvent polarity on the spectroscopic, photophysical and excited state decay properties of these compounds.

5. Investigation of dual fluorescence emission from the excited states of members of this class of compounds that exhibit excited state proton transfer in acetic acid.

6. Investigation of the photochemistry of this class of compounds by thorough examination of the photochemistry of bis-dmab, testing (i) bis-dmab as a photosensitizer of singlet

oxygen, (ii) chemical reactivity of bis-dmab with singlet oxygen (self-sensitized photooxidation), and (iii) *trans-cis* photoisomerization of bis-dmab.

1.3 Thesis Layout

This dissertation on the "Structural and Photophysical Properties of Internal Charge Transfer 2-Arylidene and 2,5-Diarylidene Cyclopentanones" is subdivided into five sections. The introduction, objective, and scope of the research are discussed in this chapter (Chapter 1). A literature review of previous work for this class of compounds along with chemical theory and background are discussed in Chapter 2.

Chapter 3 (experimental) first begins with the synthetic procedures and purification workup of all intermediate and target compounds along with tabulated spectral characterization data, then delves into discussing the methodology that was employed for measuring fluorescence quantum yields (Φ_f) and fluorescence lifetimes (τ_f). A brief account of the photochemical study of bis-dmab is also discussed in this section, which includes the testing of bis-dmab as a photosensitizer of singlet oxygen, self-sensitized photooxidation, and photoisomerization experiments. In addition, a brief description of X-ray diffraction studies is also reported. Furthermore, identification of all instruments and computational software used is presented in chapter 3.

Chapter 4 presents the results and discussion for all the compounds studied. This chapter is subdivided into the following sections: (1) spectroscopic and photophysical properties of Asdimcy1; (2) spectroscopic and photophysical properties of alkylamino substituted 2-arylidene and 2,5-diarylidene-cyclopentanone compounds (dmab, dmac, bis-dmab, bis-dmac, bis-juldmac, and Ashrbor); (3) spectroscopic and photophysical properties of 2dbmxcp (in comparison to

bis-dmac), along with the structural and spectroscopic properties of Asunsub; (4) excited state protonation studies of various 2,5-diarylidene-cyclopentanone compounds in acetic acid; and (5) photochemistry of bis-dmab, consisting of testing bis-dmab as a photosensitizer of singlet state oxygen, self-sensitized photooxidation, and photoisomerization studies. Lastly, chapter 5 provides a summary and recommendations for future research.

2 LITERATURE REVIEW

2.1 Introduction

Ketocyanine dyes have been widely known for their expressed solvatochromic properties and have been noted in their functional use as photosensitizers for electronic energy transfer processes, fluoroionophores, solvent polarity probes and nonlinear optical materials (references provided in chapter 1). This chapter is divided into five sections. (1) A review will be presented on research that has been reported on the spectroscopic and photophysical properties of conjugated polyene systems. (2) A section on the influence of solvent polarity on both the ground and excited state electronic properties is discussed, subdivided into three parts: (a) general solvent effects, (b) electronic state dipole moment calculation (Lippert-Mataga method) and (c) excited state proton transfer effect (Forster Cycle). (3) A review of spin-orbit coupling, vibronic coupling, and vibronic spin-orbit coupling will be discussed. (4) An overview on the process of two-photon absorption (TPA), different applications of TPA and experimental and theoretical calculations involved in determining the TPA cross-section are discussed. (5) A review of the chemistry of singlet state oxygen and a literature survey of reactions involving singlet oxygen as a substrate are discussed.

2.2 Review on the Spectroscopic and Photophysical Properties of Polyene Ketones

Conjugated organic compounds containing carbon-carbon double or triple bonds oriented in a 1,3-relationship can exhibit a variety of conformations enabling differing degrees of p orbital overlap. Unlike linearly conjugated polyenes (i.e. 1,3-butadiene and 1,3,5-hexatriene), it is possible for two systems to also be in cross conjugation with each other (see Figure 5). Aryl- and diarylpolyene ketones are such examples of cross conjugated compounds, where two double

bonds are conjugated to a third one, but not in a linear arrangement. The π electronic system thus

forms a bifurcation [14].

1,3-butadiene

1,3,5-hexatriene

(a)

1,4-pentadien-3-one

p-quinone

benzophenone

(b)
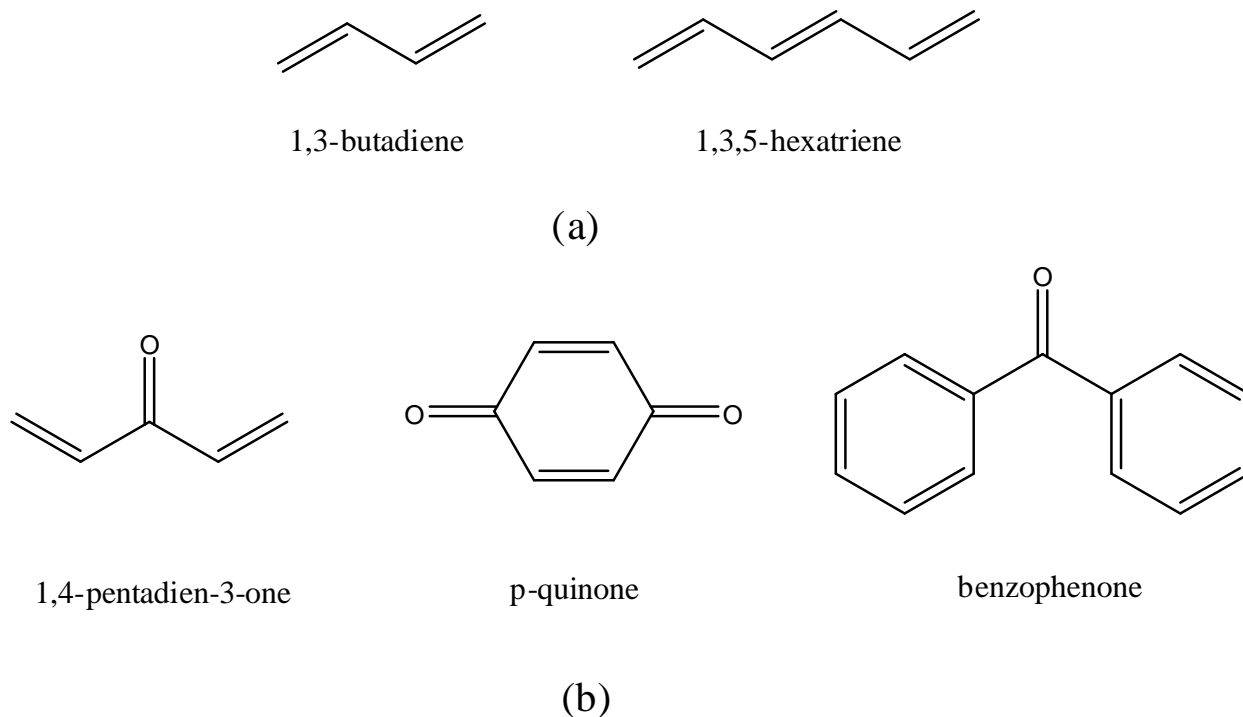
Figure 5. (a) Linearly conjugated and (b) cross conjugated molecules.

Of particular note is work published by Connors *et al.* regarding the electronic structure

and spectroscopy of C_{2v} symmetrically unsubstituted 2,5-diarylidene cyclopentanone dyes,

which include (2E,5E)-2,5-dibenzylidene cyclopentanone (1dbcp), (2E,5E)-2,5-dicinnamylidene

cyclopentanone (2dbcp) and (2E,5E)-2,5-bis((2E,4E)-5-phenyl-penta-2,4-dienylidene)

cyclopentanone (3dbcp), shown in Figure 6 [11, 15]. Spectroscopic studies indicated that 1dbcp

did not fluoresce in any solvents, while 2dbcp fluoresced only in alcohols and 3dbcp fluoresced

within both protic and aprotic solvents. Solvents that induced fluorescence were believed to

invert the order of the $^1(n, \pi^*)$ and $^1(\pi, \pi^*)$ electronic states [11]. Because compound 3dbcp was

found to fluoresce in a number of aprotic solvents as well as protic solvents, a more extensive

study of solvent effects on both absorption and fluorescence characteristics was conducted. It was found that both absorption and fluorescence spectral maxima red shifted to lower energies as solvent polarity increased, and that the difference between the absorption and fluorescence spectral maxima (Stokes shift) increased in energy as solvent polarity increased.
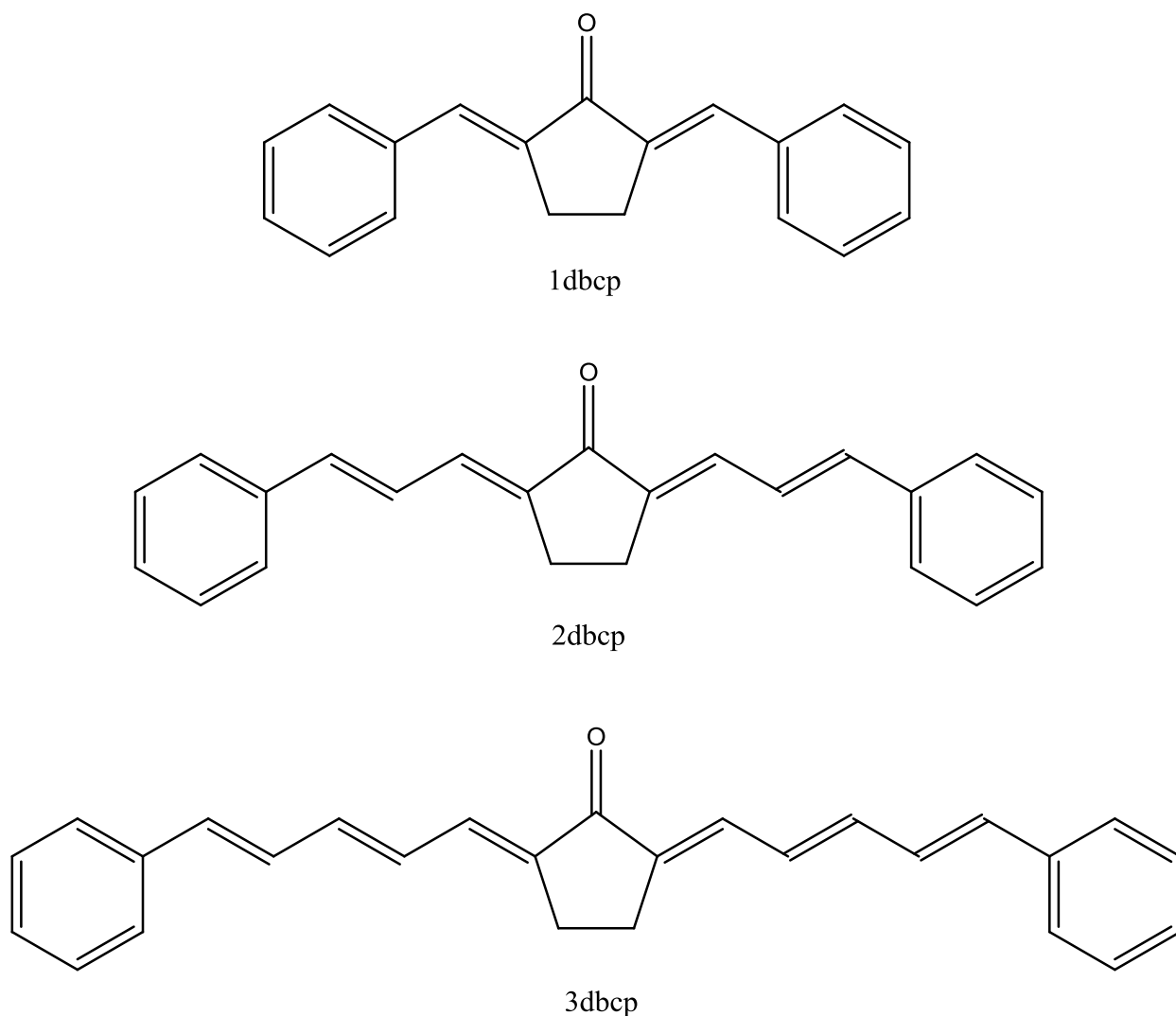
1dbcp

2dbcp

3dbcp

Figure 6. Structures of 1dbcp, 2dbcp, and 3dbcp.

Nad and Pal [16] investigated the spectral and photophysical properties of coumarin-151 (7-amino-4-trifluoromethyl-1,2-benzopyrone) in various solvents. Coumarin-151, being an electron donor-acceptor charge transfer compound, showed strong solvent dependence, with maximum absorption and fluorescent energies shifted to the red with respect to solvent polarity increase. They observed that the spectral shifts, both in absorbance and fluorescence, to smaller energy and the rise in Stokes shift with increased solvent polarity are consistent with the internal charge transfer nature of coumarin-151.

In addition, Pal has co-authored a paper discussing the effect of solvent polarity on the photophysical properties of two aminostyryl-thiazoloquinoxaline dyes, one structurally composed of a flexible diphenylamino group and the other with a spatially restricted julolidinyl group [17]. It was found in their studies that both dyes undergo bathochromic shifts in their absorbance and fluorescence spectra, with variations in fluorescence quantum yields and lifetimes (both Φ_f and τ_f being the largest in the intermediate solvent polarity region). From the absorption and fluorescence spectral studies, it was concluded that the excited states of these dyes were of intramolecular charge transfer character.

Chudomel, *et al.* [18] have reported the photophysical characteristics of three triarylamine compounds composed of a dianisylamino substituent (acting as the electron donor) covalently bound to an anthracene ring (acting as the electron acceptor). It was found from their studies that all three triarylamine compounds, namely 9-(N,N-dianisylamino)-anthracene, 9,10-bis(N,N-dianisylamino)-anthracene, and 9-(N,N-dianisylamino)-dinaphth([1,2-a:2'-1'-j])-anthracene, show strong positive solvatofluorochromism and solvent induced changes in photophysical properties, making them suitable materials for photoinduced intramolecular charge transfer.

Pivovarenko, *et al.* [4, 19-22] have done extensive work on the solvatochromic and photophysical properties of various types of electron donor-acceptor charge transfer systems belonging to the class of diarylpolyene ketones. To exemplify, the solvent sensitivity of a series of 3-hydroxychromone compounds, varying in the degree of electron donating behavior [19] and a novel diethylaminobenzofuran substituted 2,5-diarylidene cyclopentanone dye of increased solvatochromic behavior [20] make them suitable charge transfer candidates.

Related research on ketocyanine dyes has been reported by Doroshenko and Pivovarenko [22]. A series of six alkylamino substituted 2,5-diarylidene cyclopentanone dyes (structures shown in Figure 7) were synthesized and its absorption and fluorescent properties were studied in solvents of differing polarities. They found that solvent polarity had an influence on (i) absorption and fluorescence spectral characteristics (induced quenching of fluorescence in polar solvents) and (ii) fluorescence quantum yields (Φ_f) and lifetimes (τ_f). Similar to the observation of Connors and Ucak-Astarlioglu [11], it was argued for the symmetric alkylamino substituted 2,5-diarylidene cyclopentanones that the increase in Φ_f from nonpolar to moderately polar, aprotic solvents is attributed to the decreasing rate of $S_1(\pi, \pi^*) \rightarrow T_m(n, \pi^*)$ intersystem crossing and further increase in polarity to alcohols results in the decrease in Φ_f due to the increasing rate of internal conversion. A mechanism was suggested by Doroshenko and Pivovarenko that in cases where the energy of the $T_m(n, \pi^*)$ state lies above the energy of the $S_1(\pi, \pi^*)$ state, the occurrence of thermally activated $S_1(\pi, \pi^*) \rightarrow T_m(n, \pi^*)$ intersystem crossing is possible. As will be discussed in this dissertation, vibronic spin-orbit coupling is considered to be an alternative mechanism that is less restrictive than the thermally activated intersystem crossing mechanism in its requirement for the magnitude of the $S_1(\pi, \pi^*)$-$T_m(n, \pi^*)$ energy gap relative to k_BT.

13

R = -H (I), -CH$_3$ (II), -CH(CH$_3$)$_2$ (III), -C$_6$H$_5$ (VI)

V

IV
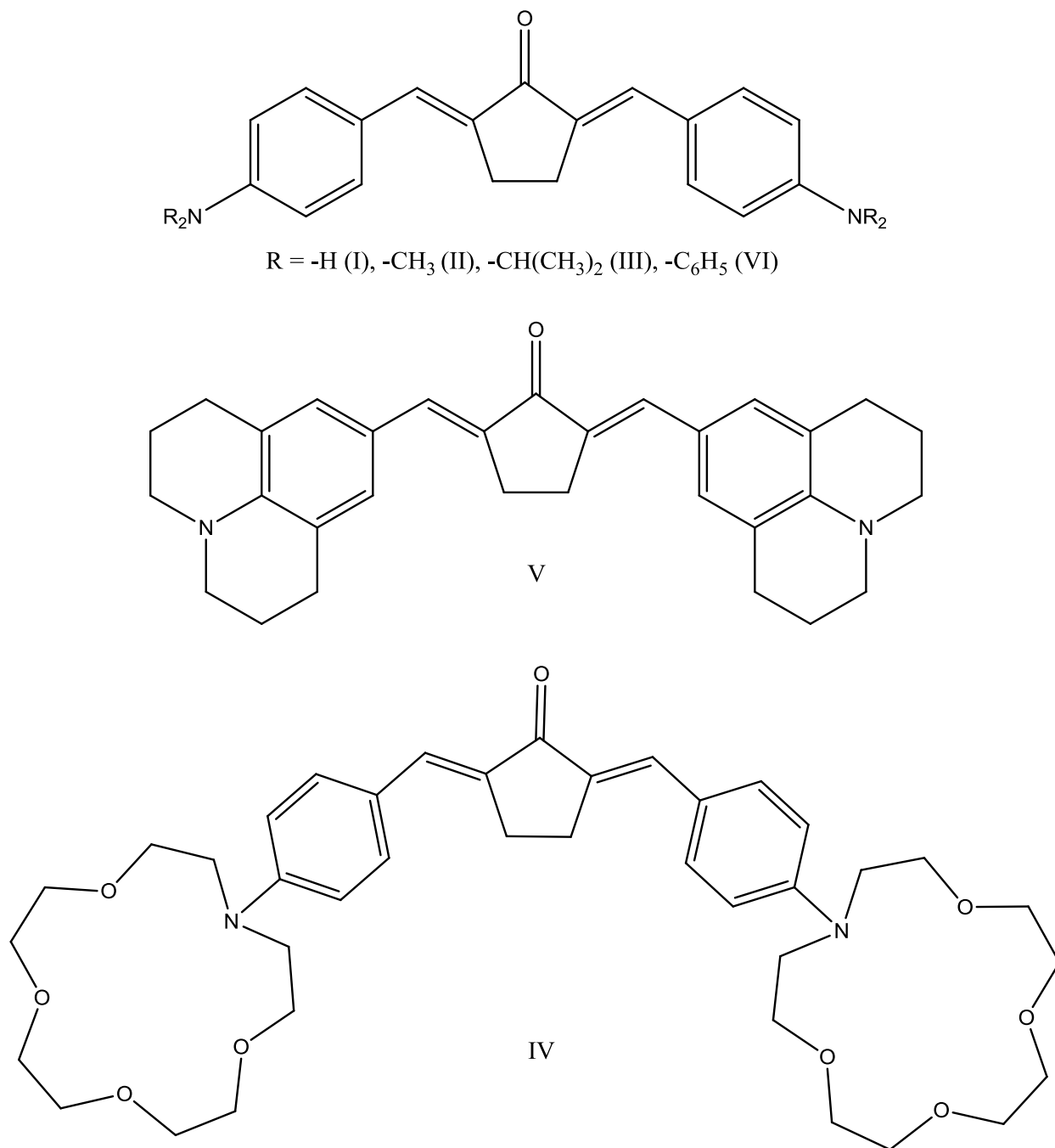
Figure 7. Structures of compounds I-VI studied by Doroshenko and Pivovarenko [22].

The photoisomerization of 1dbcp in tetrahydrofuran has been studied by George and Roth [23] and Ucak-Astarlioglu [12]. Ucak-Astarlioglu found (E,E) → (E,Z) photoisomerization with established photoequilibrium at 45 minutes of irradiation. Photochemistry studies of Doroshenko's compound V were carried out with emphasis placed on studying the (E,E) → (E,Z) photoisomerization in toluene and methanol [22]. Three separate experiments on the photoisomerization study of V were carried out, each solution irradiated with a high pressure lamp at various intervals and monitored by UV-visible absorption spectroscopy: (i) V in toluene with filter (total irradiation time = 60 mins); (ii) V in toluene without filter (total irradiation time = 20 mins); (iii) V in methanol with filter (total irradiation time = 90 mins). They found spectral changes for the irradiation studies in toluene, reporting significant acceleration in the photochemistry of V in the absence of filter (hence, the smaller cumulative time). However, no change in the absorption spectrum of V was observed in methanol.

For observed photochemistry of V in toluene, the dominant absorption band with λ_{max} = 479 nm was reduced and the spectral band centered at λ ~345 nm increased with prolonged irradiation. The emerged spectral band was assigned to represent absorption of the (E,Z)-photoisomer of V. An isosbestic point was found at λ ~390 nm, which is a characteristic feature in *trans-cis* photoisomerization, in that the molar extinction coefficients of both isomers are equivalent [24]. It was asserted in their studies that the rate of photoisomerization is strongly dependent on the probability of the molecule's triplet state population. An extension of the *trans-cis* photoisomerization of V presented in this dissertation involved studying the photochemistry of its dimethylamino analogue (bis-dmab). This provides further insight for the *trans-cis* photoisomerization of this class of compounds.

2.3   Solvent Effects on Ground and Excited State Properties of Molecules

2.3.1   General Solvent Effects

Solvatochromism is the ability of a chemical substance to change color in different solvents [25]. Depending upon the nature of the solvent environment, solvatochromic molecules undergo either hypsochromic (blue) or bathochromic (red) shifts in their optical absorption and fluorescence spectra. A singlet energy state level diagram is shown in Figure 8, illustrating the radiative processes of absorption and fluorescence with nonradiative solvent relaxation. Irradiation of a ground state chemical species, with an electronic dipole moment of μ_g, results in promoting the ground state species to the first excited singlet state having a dipole moment μ_e, followed by nonradiative vibrational relaxation to the lowest vibrational energy level. The excited state molecule relaxes on the order of 10^{-10} s (0.1 ns). Solvent relaxation involves forming a solvent cage that is appropriate for the distribution of charge in the excited molecule. The initial solvent cage is appropriate for the ground state distribution of charge in the molecule. The reorientation of solvent results in a net stabilization of the molecule-solvent ensemble, which is demonstrated by a red shift in the fluorescence relative to the absorption band (Stokes shift). The Stokes shift for a molecule that has undergone a charge transfer transition upon excitation is greater in polar solvents than in nonpolar solvents (see Figure 8).

The two low energy excited states spectroscopists are primarily concerned with are (π, π^*) and (n, π^*) states. A (π, π^*) excited state arises in the transition of an electron from a π orbital (bonding) to a π^* orbital (antibonding), and a (n, π^*) excited state arises in the transition of an electron from a nonbonding (n) orbital to a π^* orbital. The positions of (n, π^*) and (π, π^*) states behave differently under the influence of a change of solvent polarity. As depicted in the generalized energy level diagram in Figure 9, whereas (n, π^*) states undergo a hypsochromic

16

shift with increased solvent polarity, (π, π^*) states undergo a bathochromic shift [25]. In the case

shown, the shift results in an inversion in the order of states. Whether there is or is not an

inversion of states depends on the specific solute and/or solvent system.
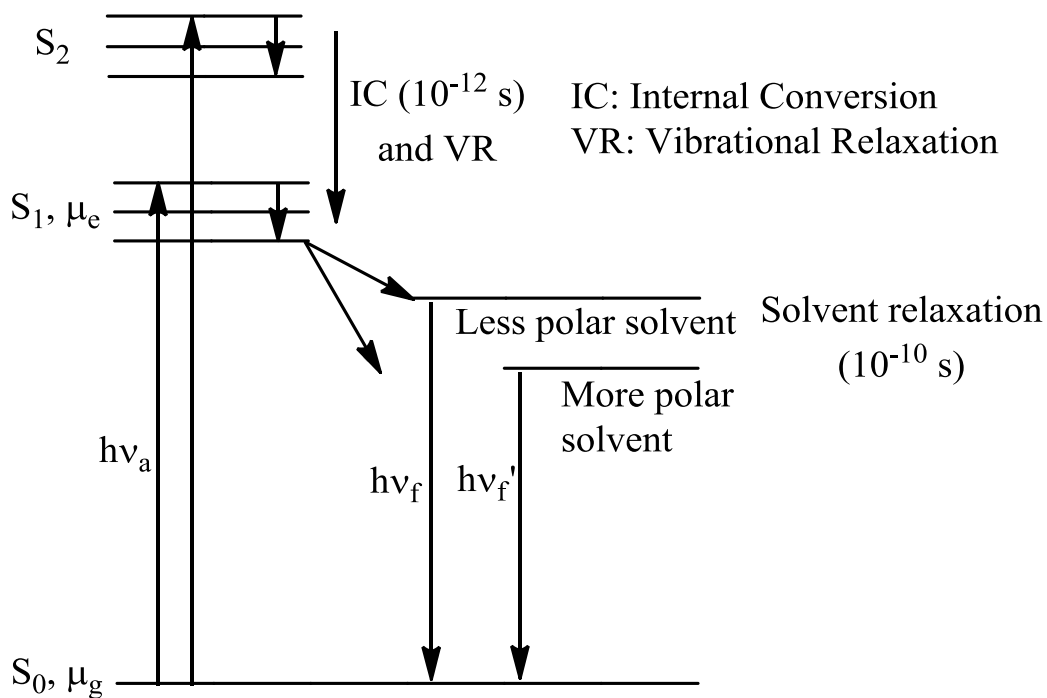
Figure 8. Singlet energy state level diagram showing fluorescence with solvent relaxation.
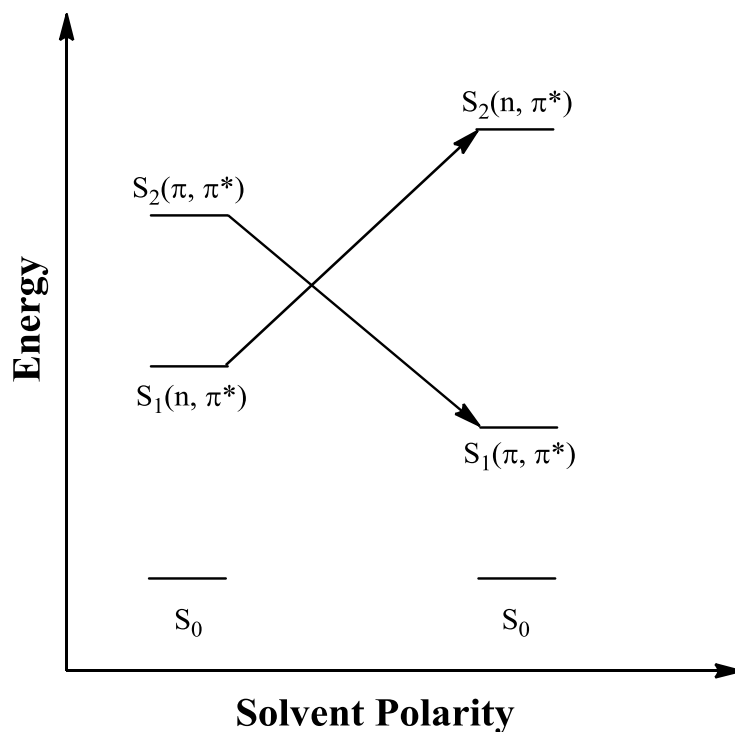
Figure 9. Effect of solvent polarity on the order of (π, π*) and (n, π*) states [25].

Both the Dimroth-Reichardt empirical scale of solvent polarity ($E_T(30)$) and the solvent polarity function (Δf) are parameters whose magnitudes are used to measure solvent polarity. The $E_T(30)$ empirical solvent polarity scale is a measure of the ionizing strength (polarity) of a solvent, based on the wavelength of the first absorption maximum of an indicator dye, namely 2,6-diphenyl-4-(2,4,6-triphenyl-1-pyridino)-phenolate (shown in Figure 10), calculated from the relationship expressed in equation 2-1 [3].
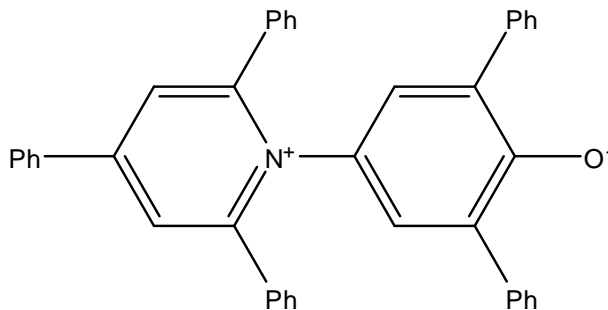
Figure 10. Structure of 2,6-diphenyl-4-(2,4,6-triphenyl-1-pyridino)-phenolate.

$$E_T(30)(\text{kcal mol}^{-1}) = \frac{28590}{\lambda_{max}^{abs}\ (\text{nm})} \qquad (2\text{-}1)$$

The solvent polarity function (Δf) is dependent upon both the dielectric constant (ε) and the refractive index (n) of the solvent, defined by the equation:

$$\Delta f = \frac{\varepsilon - 1}{2\varepsilon + 1} - \frac{n^2 - 1}{2n^2 + 1} \qquad (2\text{-}2)$$

From equation 2-2, the solvent polarity function is a measure of only the orientation polarization of the solvent, since the electronic polarization part $((n^2 - 1)/(2n^2 + 1))$ is subtracted from the total polarization $((\varepsilon - 1)/(2\varepsilon + 1))$ of the solvent [17]. Hence, Δf is also referred to as the solvent's orientation polarization function.

2.3.2 Electronic State Dipole Moment Calculation (Lippert-Mataga Method)

The Lippert-Mataga method is used to experimentally calculate the change in the electronic dipole moment of a compound when it is excited from the ground state to the lowest excited singlet state. Lippert-Mataga plots directly relate the Stokes shift $(\Delta\tilde{\upsilon})$ of a molecule in different solvents to the solvent polarity function (Δf). The Stokes shift is related linearly to Δf by the Lippert-Mataga equation [26]

$$\Delta\tilde{\upsilon} = \frac{2\Delta\mu^2}{hca^3}\Delta f + constant \qquad (2\text{-}3)$$

where $\Delta\mu = \mu_e - \mu_g$ is the difference between the excited state and the ground state electronic dipole moments, h is Planck's constant (6.626×10^{-34} J s = 6.626×10^{-27} erg s), c is the speed of light in a vacuum (2.998×10^8 m s^{-1} = 2.998×10^{10} cm s^{-1}) and a is the Onsager cavity radius for the spherical interaction of the dipole in a solvent [cm], respectively. Thus, a plot of $\Delta\tilde{\upsilon}$ as a function of Δf yields a straight line with a slope equal to $2\Delta\mu^2/hca^3$, which can be used to calculate the change in dipole moment of the compound. If a and μ_g are known, μ_e can be determined. Usually, these two parameters are computed using molecular modeling software. Ultimately, the quality of the determination of μ_e depends on the quality of the quantum mechanical modeling. The computational method used in these studies is state of the art and generally considered to provide good results for ground state molecular dimensions and dipole moments.

2.3.3 Excited State Proton Transfer (Forster Cycle)

In acidic environments, a hydrogen bonding chromophore changes ground state solvation equilibrium and protonation or deprotonation may take place to reach an excited state equilibrium [27]. The excited state protonation of a series of 2,5-diarylidene cyclopentanone dyes (which are presented in chapter 4) and its effects on absorption and fluorescence emission spectra can be examined through the Forster cycle. As illustrated in Figure 11, the Forster cycle is based on the thermally equilibrated states existing between the ground state of the base (A) and the lowest excited singlet state of its conjugate acid (HA^+) [28].

The pK_a of a base chromophore (A) changes in going from the ground electronic state to the excited singlet state and may become protonated to form HA^+. The emission energy changes in going from unprotonated to protonated, often with experimentally observed dual fluorescence emission. The difference in pK_a of a chromophore between the ground and excited singlet states (ΔpK_a) can be directly calculated in knowing the emission energies from S_1 of both the unprotonated (base) and protonated (conjugate acid) forms, using equation 2-4.

$$\Delta pK_a = pK_a^* - pK_a = \frac{N_A hc(\tilde{\upsilon}_A^f - \tilde{\upsilon}_{HA^+}^f)}{2.303RT} \tag{2-4}$$

In the above equation, pK_a and pK_a* are the pKa values of the molecule in the ground and excited electronic states, $\tilde{\upsilon}_A^f$ and $\tilde{\upsilon}_{HA^+}^f$ are the emission wavenumbers for both the unprotonated (A) and protonated (HA^+) forms [cm^{-1}], h is Planck's constant, c is the speed of light in a vacuum, N_A is Avogadro's number (6.022×10^{23} mol^{-1}), R is the universal gas constant

(8.3145 J mol^{-1}K^{-1}) and T is the temperature (K). The following discussion shows the derivation of equation 2-4.

The changes in Gibbs free energy for the HA$^+$/A system both in the ground state and the excited state (denoted by the asterisk) at constant absolute temperature are defined as follows:

$$\Delta G = \Delta H - T\Delta S = -RT \ln K_a$$
$$\Delta G^* = \Delta H^* - T\Delta S^* = -RT \ln K_a^*$$

where ΔH is the change in enthalpy, ΔS is the change in entropy, and K$_a$ is the acid dissociation equilibrium constant (K$_a$ = [A][H$^+$]/[HA$^+$]). Assuming that ΔS does not change in going from the ground state to the excited state ($\Delta S = \Delta S^*$),

$$\Delta H - \Delta H^* = -RT \ln\left(\frac{K_a}{K_a^*}\right)$$

Accounting for energy balance,

$$\Delta H - \Delta H^* = N_A h v_{HA^+}^f - N_A h v_A^f = N_A h\left(v_{HA^+}^f - v_A^f\right) =$$
$$-RT \ln\left(\frac{K_a}{K_a^*}\right) = -RT\left(\ln K_a - \ln K_a^*\right)$$

Since pKa = -2.303lnK$_a$, the above expression can be rewritten as

$$N_A h\left(v_{HA^+}^f - v_A^f\right) = 2.303RT\left(pK_a - pK_a^*\right)$$

Further simplification gives equation 2-4.

$^1(HA^+)*$ $\Delta H*$ $^1A* + H^+$

ν_{HA+} ν_A

$^1(HA^+)$ ΔH $^1A + H^+$
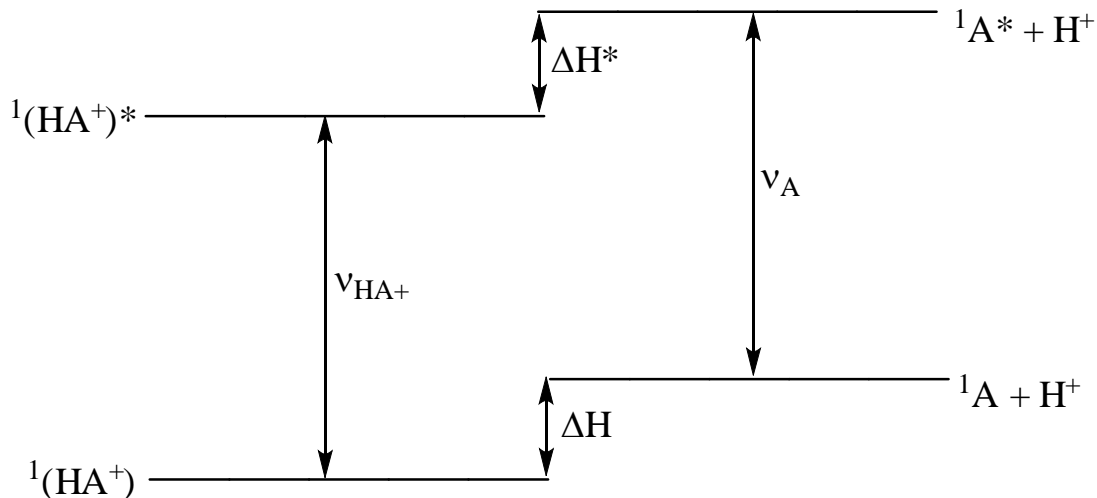
Figure 11. Electronic energy levels of a base chromophore (A) and its conjugate acid (HA^+) in both the ground and excited singlet states (Forster cycle) [29].

It was previously demonstrated by Ucak-Astarlioglu and Connors that both 2dbcp and 3dbcp exhibit excited state protonation when dissolved in concentrated acetic acid [15]. Two spectral bands were observed in the fluorescence emission spectra for both compounds. From the fluorescence emission spectra, the change in pK_a between the ground state and first excited singlet state was calculated. The ΔpK_a values for 2dbcp and 3dbcp were found to be 5.2 and 4.1, respectively [15]. The ΔpK_a values for 2dbcp and 3dbcp are included with the ΔpK_a's, along with semi-empirically computed atomic charges of the carbonyl oxygen atom at both the ground and lowest lying $^1(\pi, \pi*)$ excited states, for additional compounds presented in this dissertation that exhibited excited state protonation.

2.4 Spin-Orbit Coupling, Vibronic Coupling, and Vibronic Spin-Orbit Coupling

The rate of radiationless singlet → triplet intersystem crossing is expressed by Fermi's Golden Rule as [30]

$$k_{isc} = \frac{2\pi}{\hbar} \left| \left\langle \Psi_S \left| \hat{H}' \right| \Psi_T \right\rangle \right|^2 \rho(E) \tag{2-5}$$

where $\hat{H}'$ is the perturbation that drives the radiationless transition from the singlet state to isoenergetic vibrational levels of the triplet state. The energy density of the final states is $\rho(E)$. Without going into details, theoretical and experimental data support the assignment of the perturbation to contributions from spin-orbit ($\hat{H}_{SO}$) and vibronic spin-orbit ($\hat{H}_{VSO}$) coupling terms. The matrix element for the spin-orbit coupling between the electronic wavefunctions $^1\Psi_n$ and $^3\Psi_m$ for states n and m, is expressed by the Dirac notation

$$\left\langle {}^1\Psi_n \left| \hat{H}_{so} \right| {}^3\Psi_m \right\rangle \tag{2-6}$$

where $\hat{H}_{SO}$ is the spin-orbit coupling Hamiltonian operator that mixes the electronic states of different spin multiplicities.

In spin-orbit coupling, it is the total angular momentum of the electrons that is conserved, not the individual spin and orbital angular momenta. For a many electron system with a central field where the coupling between the spin angular momentum of one electron and the orbital angular momentum of another is neglected,

$$\hat{H}_{so} = \sum_i \xi_{SO,i} \, \hat{L}_i \cdot \hat{S}_i \tag{2-7}$$

where ξ_{SO} is the spin-orbit coupling constant, related to the nuclear charge that the electron sees as it orbits the atoms in the molecule. The magnitude of ξ_{SO} is directly proportional to the fourth power of the atomic number (Z^4). Hence, the magnitude of ξ_{SO} for organic molecules containing only light-sized atoms (e.g. H, C, O, N, and F) is typically much smaller (~0.01-0.1 kcal mol^{-1}) than vibrational energies (~5-0.5 kcal mol^{-1}), but the magnitude for heavy atoms (e.g. Br and Pb) can be large and even exceed the values of vibrational energies. $\hat{L}$ and $\hat{S}$ are the operators for an electron's orbital angular momentum and spin angular momentum, respectively [31].

According to the zero-order approximation, if a molecule is in an initial singlet state, it will remain in a singlet state, or if it is in an initial triplet state, it will remain in a triplet state [32]. In the first order approximation, a singlet state has some triplet character and conversely, a triplet state has some singlet character. The singlet and triplet state wavefunctions showing mixing of states of different spin multiplicities, can be expressed by perturbation theory as

$$^1\Psi_n = \,^1\varphi_n + \sum_m \frac{\langle \,^3\varphi_m | \hat{H}_{SO} | \,^1\varphi_n \rangle}{E_{Sn} - E_{Tm}} \,^3\varphi_m \qquad (2\text{-}8)$$

$$^3\Psi_n = \,^3\varphi_n + \sum_k \frac{\langle \,^1\varphi_k | \hat{H}_{SO} | \,^3\varphi_n \rangle}{E_{Tn} - E_{Sk}} \,^1\varphi_k \qquad (2\text{-}9)$$

where $^1\phi_n$ and $^3\phi_n$ are the zeroth-order (unperturbed) singlet and triplet state wavefunctions, and E is the energy of the respective electronic state.

For a heteroaromatic molecule, the types of singlet → triplet intersystem crossing that are most important are

$$^1(\pi, \pi^*) \rightarrow {}^3(\pi, \pi^*)$$

$$^1(\pi, \pi^*) \rightarrow {}^3(n, \pi^*)$$

$$^1(n, \pi^*) \rightarrow {}^3(\pi, \pi^*)$$

$$^1(n, \pi^*) \rightarrow {}^3(n, \pi^*)$$
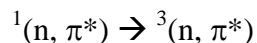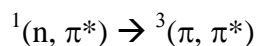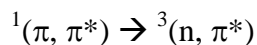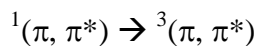
In his original paper on spin-orbit coupling and radiationless processes in nitrogen heterocyclic compounds, M. A. El-Sayed [33] observed nitrogen heterocyclic compounds (e.g. pyrazine) that have their lowest excited singlet state of the (n, π^*) type exhibit strong phosphorescence, but no fluorescence. The reason for no observable fluorescence in nitrogen heterocyclics is due to highly efficient $^1(n, \pi^*) \rightarrow {}^3(\pi, \pi^*)$ intersystem crossing. It was proposed by El-Sayed that the nonradiative rate of intersystem crossing between two electronically excited states of different orbital configurations is greater than that between two states of the same orbital configuration. Therefore, the following selection rules were established:

$$k_{isc} \left\{ {}^1(\pi, \pi^*) \rightsquigarrow {}^3(n, \pi^*) \right\} \text{ and } \left(k_{isc} \left\{ {}^1(n, \pi^*) \rightsquigarrow {}^3(\pi, \pi^*) \right\} \right)$$

are much greater than

$$k_{isc} \left\{ {}^1(\pi, \pi^*) \rightsquigarrow {}^3(\pi, \pi^*) \right\} \text{ and } \left(k_{isc} \left\{ {}^1(n, \pi^*) \rightsquigarrow {}^3(n, \pi^*) \right\} \right)$$

The reason for efficient intersystem crossing between two electronic states of different configurations is due to a one-center spin-orbit coupling term surviving the expansion of molecular orbitals over atomic orbitals; in other words, one of the three one-center matrix

elements for the spin-orbit coupling between a nonbonding orbital and an out of plane p orbital

localized on the same atom is nonzero. This is contrary to the matrix elements for the spin-orbit

coupling of states with identical configuration, in which neither one- nor two-center matrix

elements survive, but only three-center terms survive. When evaluated, multicenter terms are

smaller than one-center terms. Hence, it is found that there is strong spin-orbit coupling between

two states of different orbital configurations and weak coupling between two states of the same

orbital configuration. Calculations suggest a difference of approximately 10^3. Refer to Appendix

A to see in detail the basis of El-Sayed's rules for the relationship between orbital configurations

and spin-orbit coupling.

For a number of the dyes in this study, both S_1 and T_1 are of (π, π^*) orbital configuration.

Hence, direct spin-orbit coupling between these states is weak. However, (n, π^*) states are

expected to be nearby in energy above S_1 and T_1. For molecules such as these, vibronic spin-

orbit coupling has been shown to be the dominant mechanism in promoting singlet → triplet

intersystem crossing. Vibronic coupling mixes states of the same spin multiplicity. Before

discussing vibronic spin-orbit coupling, more detail will be given for vibronic coupling.

The Herzberg-Teller treatment of vibronic coupling is another perturbation theory

approximation, in which nuclear displacements (vibrations) have an effect on the mixing of

electronic states of the same spin multiplicity. For an unperturbed (zero order) system, the

Schrödinger equation consisting of the electronic Hamiltonian operator for the electrons in the

field of fixed nuclei Q_0 is given by

$$\hat{H}^0(Q_0)\Phi_i^0(q,Q_0)=E_i^0\Phi_i^0(q,Q_0) \qquad (2\text{-}10)$$

where $\Phi_i^0(q,Q_0)$ represents the zeroth-order wavefunction at electronic energy state i, and E_i^0 is the corresponding electronic energy of state i. For a small change in nuclear configuration, the total Hamiltonian operator becomes

$$\hat{H} = H^0(\hat{Q}_0) + H^1(\hat{Q}_0) = H^0(\hat{Q}_0) + \left(\frac{\partial \hat{H}}{\partial Q}\right)_{Q_0} Q \qquad (2\text{-}11)$$

In general, the first-order (perturbation) Hamiltonian operator for a 'N' atom molecular system is equal to

$$H^1(\hat{Q}_0) = \sum_{i=1}^{3N-6} \left(\frac{\partial \hat{H}}{\partial Q_i}\right)_{Q_0} Q_i \qquad (2\text{-}12)$$

This perturbation term can mix two zeroth-order electronic states of the same spin multiplicity. For instance, the mixing of electronic state 'k' with state 'm' results in a perturbed wavefunction expression of the form

$$\Phi_m = \Phi_m^0 + \sum_k \sum_i^{3N-6} \frac{\left\langle \Phi_k^0 \left| \left(\frac{\partial \hat{H}}{\partial Q}\right)_{Q_0} \right| \Phi_m^0 \right\rangle Q_i \Phi_k^0}{E_m^0 - E_k^0} \qquad (2\text{-}13)$$

This equation demonstrates that the vibronic coupling between electronic states k and m is inversely dependent on the energy difference between both states. Therefore, the closer state k is to state m, the stronger the vibronic coupling between both states, and conversely, the larger the spacing between these two states, the weaker the vibronic coupling. Factors that can shift the

28

location of excited states, such as solvent effects, will change the extent of state mixing by vibronic coupling.

Vibronic spin-orbit coupling combines the effects of vibronic coupling and spin-orbit coupling. Given El-Sayed's rules, $S_1(\pi, \pi*) \rightarrow T_1(\pi, \pi*)$ intersystem crossing is not promoted by direct spin-orbit coupling between these two states. However, vibronic spin-orbit coupling is a second order mechanism that is effective in mixing S_1 character into T_1, thus supporting intersystem crossing between these two states.

Vibronic coupling may occur in the singlet manifold of states

$$S_1(\pi, \pi*) \leftarrow VC \rightarrow S_m(n, \pi*) \leftarrow SOC \rightarrow T_1(\pi, \pi*)$$
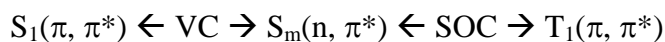
or in the triplet manifold of states

$$S_1(\pi, \pi*) \leftarrow SOC \rightarrow T_m(n, \pi*) \leftarrow VC \rightarrow T_1(\pi, \pi*)$$
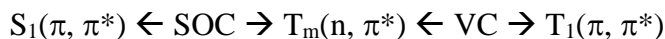
Both of these mechanisms are more effective in mixing S_1 and T_1 than the direct spin-orbit coupling mechanism $S_1(\pi, \pi*) \leftarrow SOC \rightarrow T_1(\pi, \pi*)$.

2.5   Two-Photon Absorption (TPA) and TPA Cross Section

Two-photon absorption (TPA) is a process that involves the excitation of a molecular species by the simultaneous absorption of two photons of either the same or different frequencies, unlike in one-photon absorption, where excitation involves absorption of a single photon (see Figure 12) [34]. In TPA, the sum of the absorption frequencies of both photons matches well to the energy gap between a singly excited state and the ground singlet state. One important characteristic of TPA is that absorption depends on the square of the photon intensity. TPA was theoretically predicted by Göeppert-Mayer in 1931 [35] and wasn't experimentally observed until the 1960's when lasers were developed [36]. Since then, TPA has attracted great attention due to its applications in two-photon up-converted laser [37], two-photon optical limiting [38], two-photon photopolymerization (TPP) [39, 40], two-photon photodynamic therapy [41], and two-photon microscopy [42].

The two-photon photopolymerization (TPP) technique is used in three dimensional microfabrication. In two-photon photopolymerization, the sample of interest in monomeric form, either as a liquid or as a block of gel, is mixed with a photoinitiator and irradiated with a focused laser, which sketches the three dimensional image of the object to be created. Two commercially available photoinitiators that are commonly used in TPP are o-chlorohexaarylbisimidazole (HABI) and 4,4'-dimethyldiphenyliodinium hexafluorophosphate (Omnicat 820). The laser beam initiates the polymerization, but only at the focal point due to the nonlinear nature of the excitation. After the sketching is completed, the three-dimensionally structured object may be recovered by washing away the unpolymerized gel with appropriate organic solvents.

S_1 ——

$h\nu_A$

S_0 ——

OPA

S_1 ——

$h\nu_{A2}$

——

$h\nu_{A1}$

S_0 ——

TPA
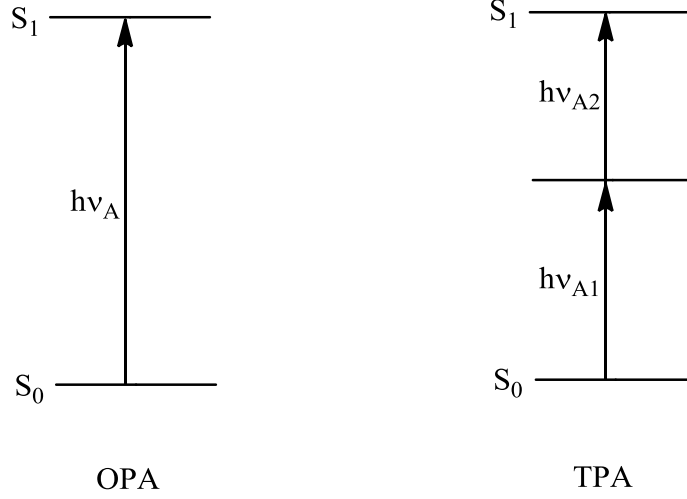
Figure 12. Excitation from $S_0 \rightarrow S_1$ for one-photon absorption (OPA) and two-photon absorption (TPA).

The TPA cross section (δ) is an absorption coefficient for TPA and can be calculated from the following equation [34]:

$$\delta_{GM} = \frac{(2\pi)^3 \alpha\, a_0^5\, \omega^2}{c\,\pi\,\Gamma}\,\delta_{a.u.},$$
(2-14)

where α is the fine structure constant (7.29735×10^{-3}), a_0 is the radius of the first Bohr orbit (5.29177×10^{-9} cm), c is the speed of light (2.9979×10^{10} cm s^{-1}), $\pi\Gamma$ is the normalization factor coming from the Lorentzian-shape broadening of the excited state ($\Gamma = 0.1$ eV $= 3.6749 \times 10^{-3}$ Hartree), ω is the energy of the incoming photons in Hartree, and $\delta_{a.u.}$ is referred to as the two-photon transition probability, defined as follows:

$$\delta_{a.u.} = \frac{1}{30}\sum_{ij}\left(F T_{ii}^{2\omega,f} T_{jj}^{2\omega,f*} + G T_{ij}^{2\omega,f} T_{ij}^{2\omega,f*} + H T_{ij}^{2\omega,f} T_{ji}^{2\omega,f*}\right),$$
(2-15)

31

where F = G = H = 2 are the appropriate coefficients for a linearly polarized light beam and T is referred to as the two-photon absorption transition amplitude tensor of the respective excitation from the ground electronic state to an excited electronic state. Quantum mechanical programs can compute TPA cross sections of allowed and forbidden excited states for molecules, which can be compared to experimental values.

2.6   Review on Singlet State Oxygen and Singlet Oxygen Reactions

2.6.1   Chemistry of Singlet Oxygen

Singlet oxygen is a very strong oxidant finding widespread application as a cytotoxic agent in photodynamic therapy in destroying targeted tumor and cancerous cells in living organisms [43]. Photodynamic therapy (PDT), also referred to as photochemotherapy, has become a clinical treatment option for ophthalmic and cancer-related diseases [44]. In the process of PDT, diseased regions of the body are treated with the introduction of a photosensitizer followed by intense light irradiation onto a target area. Irradiation causes the photosensitizer to generate singlet oxygen from ambient triplet state oxygen that destroys cells through either apoptosis or necrosis [45].

Molecular oxygen is an important participant in photochemical processes because of its high chemical energy content, its low lying excited states, and its ubiquity as an "impurity" in reaction systems [32]. A neutral oxygen molecule is composed of a total of 16 electrons. Ground state (ambient) oxygen is a member of a triplet spin manifold ($^3\Sigma_g^-$), in that the doubly degenerate π_{2p}^* molecular orbitals, designated as π_x^* and π_y^*, contain two spin unpaired electrons, as depicted in Figure 13. First excited singlet state oxygen ($^1\Delta_g$), lying 22.4 kcal mol^{-1} (93.7 kJ mol^{-1}) above the ground state triplet, contains two spin paired electrons in the π_x^* orbital, whereas second excited singlet state oxygen ($^1\Sigma_g^+$), lying 37 kcal mol^{-1} (154.8 kJ mol^{-1}) above the ground state triplet, contains two spin paired electrons, each in the π_x^* and π_y^* orbitals. The second excited singlet state of O_2 is relatively short lived (1 ps) in solution due to a rapid spin-allowed transition to the longer lived (1 μs-1 ms) first excited state [46].

33
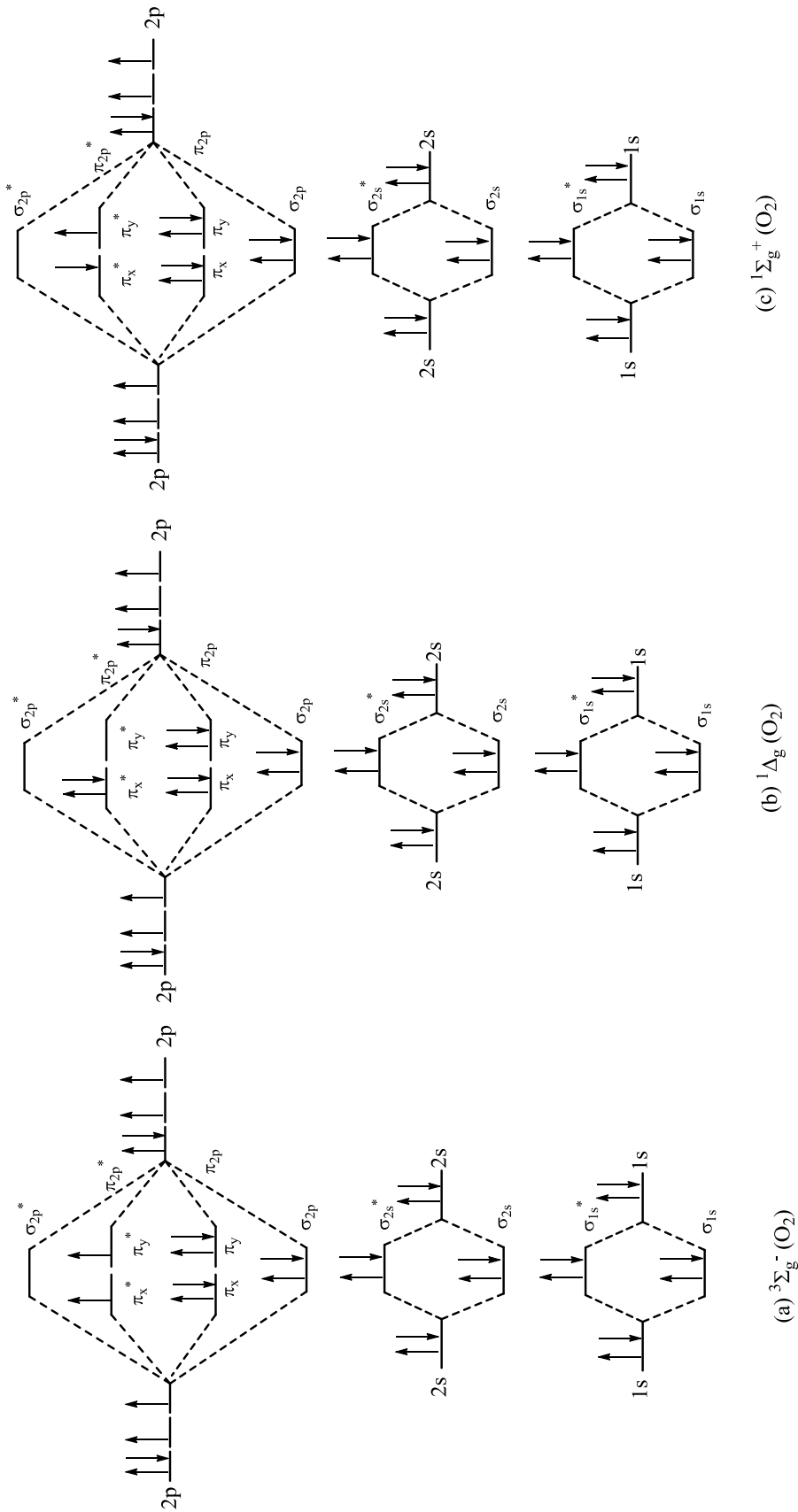
Figure 13. Molecular orbital diagrams of (a) triplet (ground) state O_2 ($^3\Sigma_g^-$), (b) first excited singlet state O_2 ($^1\Delta_g$), and (c) second excited singlet state O_2 ($^1\Sigma_g^+$).

34

The triplet photosensitized production of singlet oxygen is the general and synthetically useful method for producing singlet oxygen [32]. As depicted in Figure 14, the reaction pathway for the photosensitized production of singlet oxygen consists of (i) photoexcitation of a ground state photosensitizer (^1PS) to a higher energy excited singlet state ($^1PS^*$), followed by (ii) rapid intersystem crossing from the singlet to triplet excited state manifold ($^3PS^*$), whereupon (iii) collisional interaction of the lowest triplet state ($^3PS^*$) with triplet (ground) state oxygen results in energy transfer, yielding $^1O_2^*$.

$$^1PS \xrightarrow{h\nu} {}^1PS^* \qquad \text{(i) Excitation}$$

$$^1PS^* \longrightarrow {}^3PS^* \qquad \text{(ii) Intersystem Crossing}$$

$$^3PS^* + {}^3O_2 \longrightarrow {}^1PS + {}^1O_2^* \qquad \text{(iii) Energy Transfer}$$
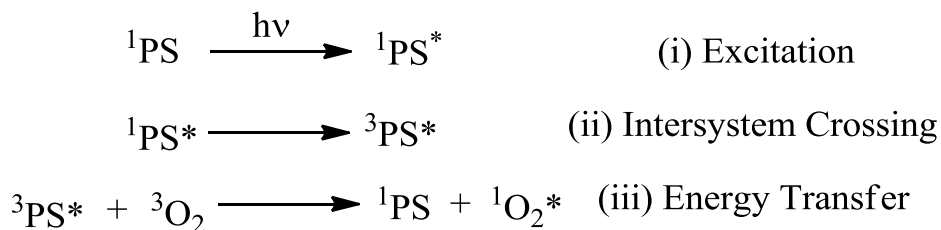
Figure 14. Reaction pathway for the photosensitized production of singlet state oxygen ($^1O_2$).

2.6.2 Reactions Involving Singlet Oxygen

Singlet oxygen is considered to be a reactive intermediate in the photooxidation of organic compounds in solution [46]. For example, the Schenck reaction, notably named after Günther Schenck, is a concerted reaction between an olefinic (ene) system and $^1O_2$, resulting in the formation of an allylic hydroperoxide [47]. Figure 15(a) shows the Schenck reaction between 2,3-dimethyl-2-butene (tetramethylethylene, TME) and $^1O_2$, giving 3-hydroperoxy-2,3-dimethyl-1-butene [48]. Polycyclic aromatic hydrocarbons have been well studied for their photoswitchable properties in trapping and releasing singlet oxygen. As exemplified in Figures 15(b) and 15(c), polynuclear aromatic hydrocarbons, such as naphthalenic and anthracenic systems, have been shown to react with $^1O_2$ in a $[4\pi + 2\pi]$ cycloaddition reaction, giving

35

endoperoxides, which, under thermal conditions, release $^1O_2$ and revert back to starting

naphthalene and anthracene parental hydrocarbons [49]. N-substituted 2-pyridones also exhibit

the same reversible photoswitchable property, as depicted in Figure 15(d). Light-activated

oxidation gives exclusively the corresponding 1,4-endoperoxide cycloadduct, whereby heat

results in endoperoxide decomposition, reversibly regenerating starting pyridones while

liberating $^1O_2$ in high yields [48(a)]. Lastly, depicted in Figure 15(e), the $[2\pi + 2\pi]$

cycloaddition reaction of (E)-stilbene with $^1O_2$ in the presence of 9,10-dicyanoanthracene (DCA)

in acetonitrile to give (1) benzaldehyde, (2) (Z)-stilbene (photoisomer), (3) *trans*-2,3-

diphenyloxirane, and (4) benzil as the observed photoproducts [50].
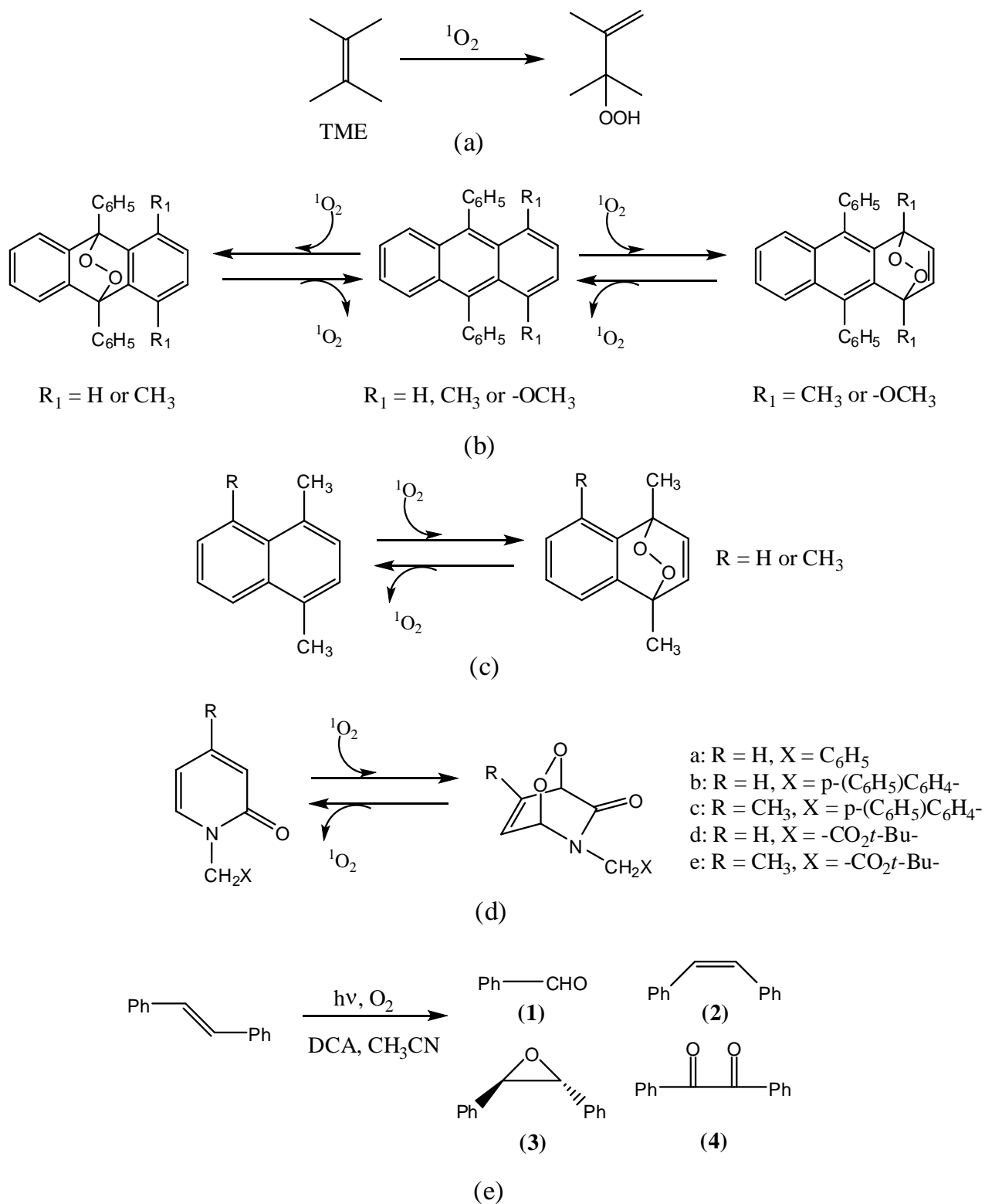
Figure 15. Reactions of organic compounds with $^1O_2$ [47-50].

3   EXPERIMENTAL

3.1   Syntheses of Compounds

This section discusses the chemical reactions for the syntheses of all intermediate and target compounds, along with the ^{1}H NMR, ^{13}C NMR and IR characterization data in tabulated format that were employed for the compounds. NMR and IR spectra are provided in Appendices B and C, respectively. This section is subdivided and presented in the order below:

3.1.1   Symmetrical 2,5-Diarylidene Cyclopentanones

3.1.2   (E)-2-Arylidene Cyclopentanones

3.1.3   Asymmetrical 2,5-Diarylidene Cyclopentanones

3.1.1 Symmetrical 2,5-Diarylidene Cyclopentanones

3.1.1.1 (2E,5E)-2,5-bis(p-dimethylaminobenzylidene)-cyclopentanone (bis-dmab)

Compound bis-dmab was synthesized via an intermolecular base-catalyzed mixed aldol condensation reaction between cyclopentanone (1 mol eq) and 4-dimethylaminobenzaldehyde (2 mol eq) at room temperature, followed by recrystallization from toluene. Figure 16 shows the reaction scheme for the synthesis of bis-dmab. ^{1}H NMR, ^{13}C NMR in CDCl$_3$, and IR data for bis-dmab are presented in Table 1.
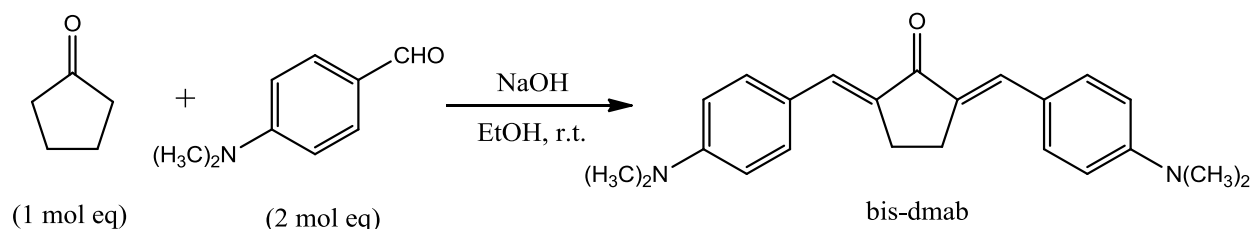
Figure 16. Reaction scheme for the synthesis of bis-dmab.

3.1.1.2 (2E,5E)-2,5-bis(p-dimethylaminocinnamylidene)-cyclopentanone (bis-dmac)

The synthesis of bis-dmac involved an intermolecular base-catalyzed crossed aldol condensation between cyclopentanone (1 mol eq) with (E)-4-dimethylaminocinnamaldehyde (2 mol eq) at room temperature, followed by recrystallization from benzene. Figure 17 shows the reaction scheme for the synthesis of bis-dmac. The melting point of bis-dmac was found to be 265°C. ^{1}H NMR, ^{13}C NMR in CDCl$_3$, and IR data for bis-dmac are presented in Table 1.

39
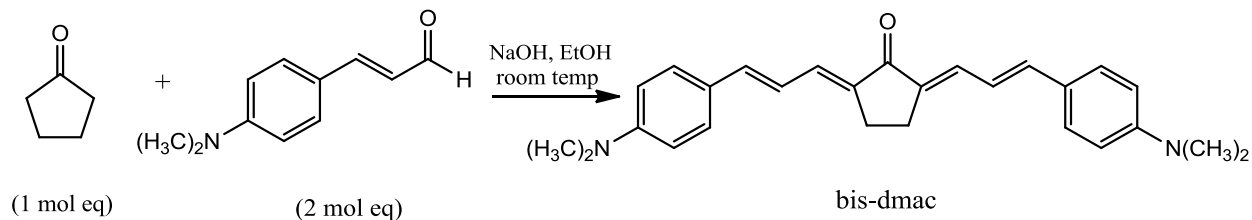
Figure 17. Reaction scheme for the synthesis of bis-dmac.

3.1.1.3 (2E,5E)-2,5-bis((E)-3-(1,2,3,5,6,7-hexahydropyrido[3,2,1-ij]quinolin-9-yl)allylidene)-cyclopentanone (bis-juldmac)

The julolidinic analog of bis-dmac, bis-juldmac, was synthesized via a three-step synthesis scheme, as displayed in Figure 18. First, a solution of commercially available julolidine (Alfa Aesar®) and N,N-dimethylformamide (DMF) was added to a solution of phosphorous oxychloride (POCl₃) in DMF to yield 9-julolidinylcarbaldehyde [51]. Two carbon homologation of the aldehyde using silver perchlorate (AgClO₄) catalyzed addition of the zirconocene complex derived from the hydrozirconation of 1-ethoxyethyne (Alfa Aesar®) with bis(cyclopentadienyl) zirconium hydridochloride (Strem®) followed by acid-catalyzed dehydration was then performed yielding the (E)-α,β-unsaturated aldehyde, namely (E)-3-(9-julolidinyl)-prop-2-en-1-al [52]. Finally, an intermolecular base-catalyzed crossed-aldol condensation reaction between cyclopentanone (1 mole eq) and (E)-3-(9-julolidinyl)-prop-2-en-1-al (2 mole eq) yielded the target bis-juldmac. The crude product was purified by column chromatography using 30 % ethyl acetate in hexanes. Both ¹H NMR in CDCl₃ and IR data for bis-juldmac are presented in Table 1.
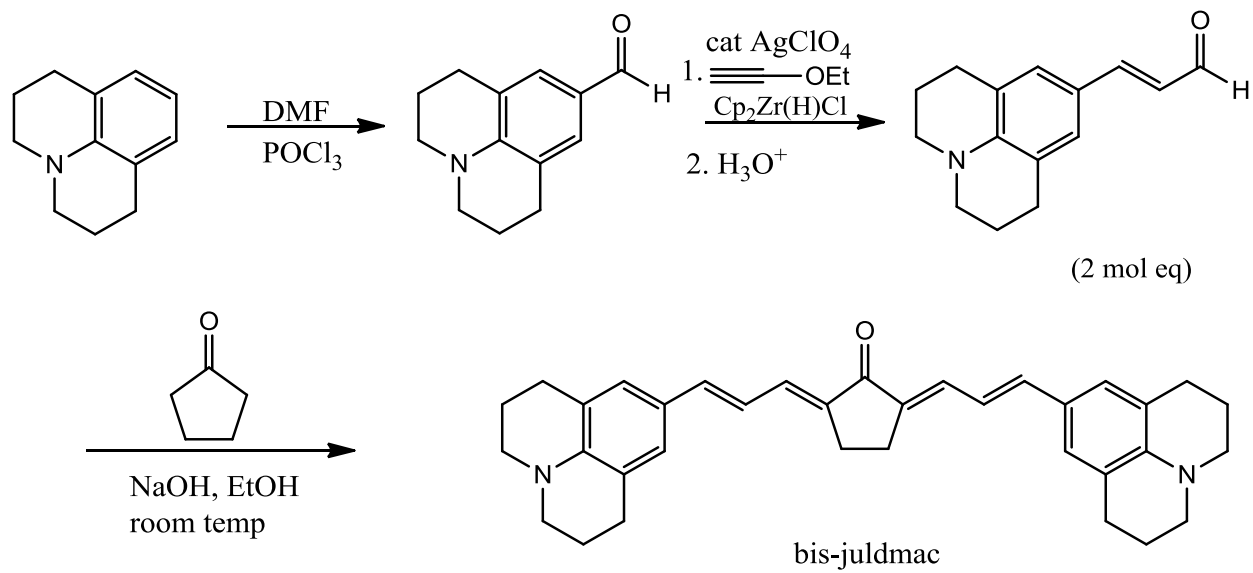
Figure 18. Reaction scheme for the synthesis of bis-juldmac.

Table 1. ^{1}H NMR, ^{13}C NMR, and IR data for bis-dmab*, bis-dmac**, and bis-juldmac***.

Compound	^{1}H NMR	^{13}C NMR	IR (cm^{-1})
	δ (ppm)	δ (ppm)	
bis-dmab	7.62-7.55 (m, 6H), 6.80 (d, 4H), 3.15 (s, 4H), 3.11 (s, 12H)	196.0, 150.6, 133.4, 132.5, 124.1, 111.8, 40.1, 26.6	3141, 3094, 2897, 2803, 1672, 1579, 1569, 1518, 1427, 1361, 1285, 1222, 1159, 1123, 980, 813
bis-dmac	7.5-7.2 (m, 6H), 6.9-6.5 (m, 8H), 3.0 (s, 12H), 2.8 (s, 4H),	195.1, 151.3, 142.1, 138.3, 133.8, 129.1, 125.3, 121.0, 112.4, 40.7, 24.4	3446, 2347, 1579, 1525, 1368, 1282, 1212, 1151, 949, 807
bis-juldmac	7.2-7.0 (m, 4H), 6.9-6.6 (m, 6H), 3.2-3.1 (t, 8H), 2.8 (s, 4H), 2.7-2.6 (t, 8H), 2.0-1.8 (m, 8H)	-	2961, 2926, 2360, 1661, 1259, 1204, 1146, 1083, 1015, 796

*^{13}C NMR data of bis-dmab taken from M. Duff, Jr. (MQP, 2002) [53]

**^{1}H and ^{13}C NMR data of bis-dmac taken from Ucak-Astarlioglu (Ph. D., 2003) [12]

***^{13}C NMR data of bis-juldmac could not be obtained

3.1.1.4 (2E,5E)-2,5-bis(p-methoxycinnamylidene)-cyclopentanone (2dbmxcp)

Compound 2dbmxcp was synthesized via a crossed aldol condensation reaction between cyclopentanone (1 mol eq) with (E)-4-methoxycinnamaldehyde (2 mol eq) in the presence of NaOH (see Figure 19). Orange solid precipitated from solution. The crude material was collected by vacuum filtration and recrystallized from toluene, yielding lustrous orange crystals. ^{1}H NMR spectroscopy was used for structural identification of 2dbmxcp. Both ^{1}H NMR in CDCl$_3$ and IR spectral data are presented in Table 2. Purity was confirmed by TLC (showing one spot upon development).
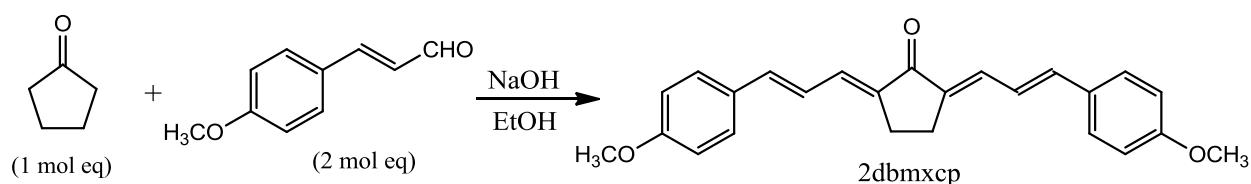
Figure 19. Reaction scheme for the synthesis of 2dbmxcp.

3.1.1.5 (2E,5E)-2,5-bis(benzofuran-2-ylmethylene)-cyclopentanone (1dbzfcp)

Compound 1dbzfcp was synthesized via an intermolecular base-catalyzed crossed aldol condensation reaction between cyclopentanone (1 mol eq) with 2-benzofurancarboxaldehyde (2 mol eq) at room temperature, yielding a yellow precipitate. The reaction (see Figure 20) was allowed to run overnight with continuous stirring at room temperature. The crude solid material was collected and dried via vacuum filtration and purified by recrystallization from ethanol. ^{1}H, ^{13}C NMR, and IR spectroscopy were used to structurally identify 1dbzfcp. ^{1}H, ^{13}C NMR and IR spectral data are presented in Table 2. Purity was confirmed by TLC (showing one spot upon development).
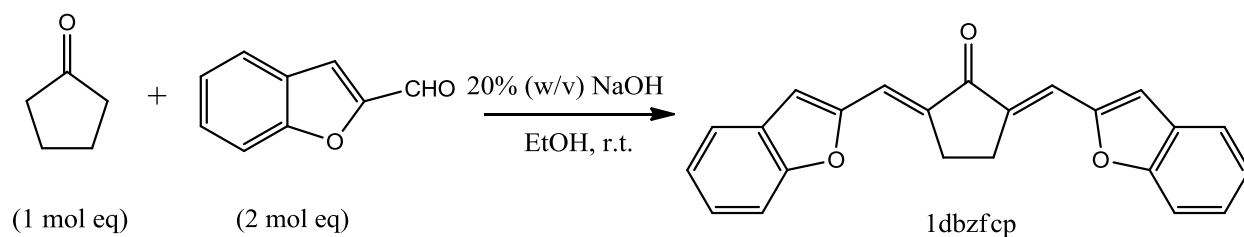
Figure 20. Reaction scheme for the synthesis of 1dbzfcp.

Table 2. ^{1}H NMR, ^{13}C NMR, and IR data for 2dbmxcp* and 1dbzfcp.

Compound	^{1}H NMR	^{13}C NMR	IR (cm^{-1})
	δ (ppm)	δ (ppm)	
2dbmxcp	7.38 (d, 4H), 7.16 (s, 1H), 6.89-6.74 (m, 9H), 3.77 (s, 6H), 2.82 (s, 4H)	-	3090, 3072, 3030, 3009, 2959, 2909, 2835, 1738, 1669, 1615, 1575, 1568, 1507, 1464, 1456, 1438, 1420, 1363, 1306, 1277, 1245, 1205, 1174, 1151, 1105, 1027, 971
1dbzfcp	7.64 (d, 2H), 7.55 (d, 2H), 7.49 (s, 2H), 7.39 (td, 2H, 7.28 (t, 2H), 7.06 (s, 2H), 3.32 (s, 4H)	195.2, 155.9, 154.2, 138.8, 128.5, 126.3, 123.4, 121.8, 120.5, 112.5, 111.5, 26.2	3110, 3083, 3033, 2919, 1682, 1620, 1595, 1555, 1474, 1444, 1434, 1357, 1346, 1305, 1281, 1271, 1259, 1221, 1195, 1174, 1153, 1139, 1124, 1107, 997

*^{13}C NMR data for 2dbmxcp could not be obtained.

3.1.2 (E)-2-Arylidene Cyclopentanones

A convenient approach towards synthesizing monoarylidene derivatives of aldehydes and enolizable ketones involves the use of DIMCARB, namely N,N-dimethylammonium-N',N'-dimethylcarbamate (chemical structure displayed in Figure 21), acting as both a recyclable medium and as a catalyst [54, 55]. DIMCARB is synthesized by introducing gaseous dimethylamine into a flask with dry ice (solid CO_2) and warming it up to ambient temperature, resulting in its formation, recognized as a 2:1 adduct and a colourless viscous oil [56]. A series of organic reactions leading to the syntheses of trans-configured monoarylidene α,β-unsaturated ketones have been achieved via the DIMCARB approach, resulting in moderate to excellent yields [54]. Although the DIMCARB reaction could be recognized as a mono Claisen-Schmidt crossed aldol condensation, the mechanistic pathway involves Mannich reactions and elimination.
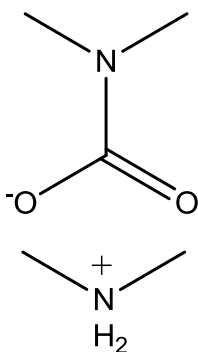
Figure 21. Structure of N,N-dimethylammonium-N',N'-dimethylcarbamate (DIMCARB).

The generalized reaction scheme for the DIMCARB mediated approach towards the synthesis of various trans-configured 2-arylidene-cyclopentanones is illustrated in Figure 22. Procedurewise, DIMCARB (27.5 mmol, 3.3 mL) was added to a suspension of the aldehyde of interest (5 mmol) in dichloromethane (5.5 mL) at ambient temperature. Cyclopentanone (5 mmol) was then added in a single portion to the mixture [54].
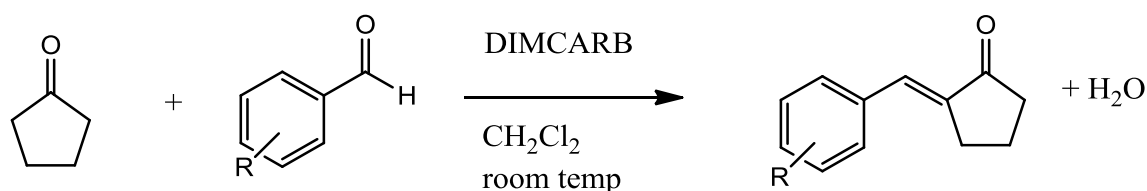
Figure 22. Generalized reaction scheme for the selective synthesis of (E)-2-aryl-α,β-unsaturated cyclopentanones via the DIMCARB-mediated route.

3.1.2.1 (E)-2-benzylidene-cyclopentanone (1pdbun)

(E)-2-benzylidene-cyclopentanone (1pdbun) was synthesized via an overnight DIMCARB-catalyzed reaction between cyclopentanone (5.0 mmol, 0.44 mL) and benzaldehyde (5.0 mmol, 0.51 mL) in CH_2Cl_2 (see Figure 23). The solvent was removed *in vacuo*. To the residue was added 0.5 M H_2SO_4 (10 mL) and the solvent was extracted with ethyl acetate. The combined organic layer extracts were dried over Na_2SO_4, filtered and concentrated *in vacuo*. Purification consisted of running silica gel column chromatography, employing a gradient approach with a hexanes/ethyl acetate binary solvent system, yielding pure 1pdbun as a yellow solid, characterized by ^{1}H and ^{13}C NMR spectroscopy. Purity was confirmed by TLC (showing one spot upon development).
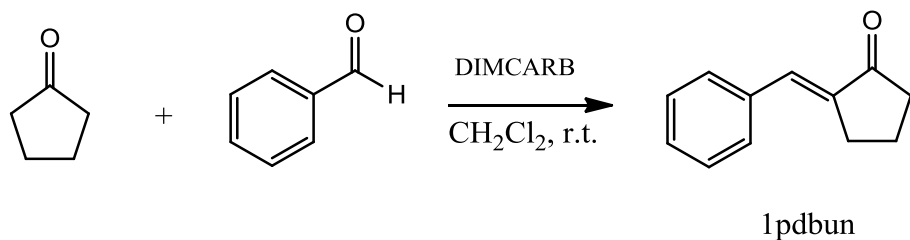
Figure 23. Reaction scheme for the synthesis of 1pdbun.

3.1.2.2 (E)-2-(p-dimethylaminobenzylidene)-cyclopentanone (dmab)

   (E)-2-(p-dimethylaminobenzylidene)-cyclopentanone (dmab) was synthesized via an overnight DIMCARB-catalyzed reaction between cyclopentanone (5.0 mmol, 0.44 mL) and 4-dimethylaminobenzaldehyde (5.0 mmol, 0.75 g) in CH_2Cl_2 (see Figure 24). The reaction was continuously stirred at room temperature overnight. The solvent was removed *in vacuo*. The organic layer was extracted with CH_2Cl_2 and the combined organic extracts were dried over Na_2SO_4, filtered and concentrated *in vacuo*. Purification consisted of running silica gel column chromatography, employing a gradient approach with a hexanes/ethyl acetate binary solvent system, yielding pure dmab as a yellow solid, characterized by ^1H and ^{13}C NMR spectroscopy. Purity was confirmed by TLC (showing one spot upon development).
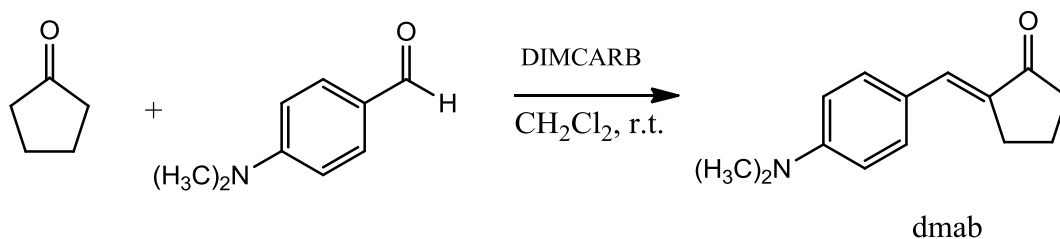
Figure 24. Reaction scheme for the synthesis of dmab.

47

3.1.2.3 (E)-2-(p-cyanobenzylidene)-cyclopentanone (1pdbcy)

(E)-2-(p-cyanobenzylidene)-cyclopentanone (1pdbcy) was synthesized via a DIMCARB-catalyzed reaction between cyclopentanone (5.0 mmol, 0.44 mL) and 4-cyanobenzaldehyde (5.0 mmol, 0.66 g) in CH_2Cl_2 (see Figure 25). Reaction time was approximately 60 hours. The solvent was removed *in vacuo*. To the residue was added 0.5 M H_2SO_4 (10 mL) and the organic layer was extracted with dichloromethane. The combined organic layer extracts were dried over Na_2SO_4, filtered, and concentrated *in vacuo*. Purification consisted of running silica gel column chromatography, employing a gradient approach with a hexanes/ethyl acetate binary solvent system, yielding pure 1pdbcy as a green solid, characterized by ^{1}H and ^{13}C NMR spectroscopy. Purity was confirmed by TLC (showing one spot upon development).
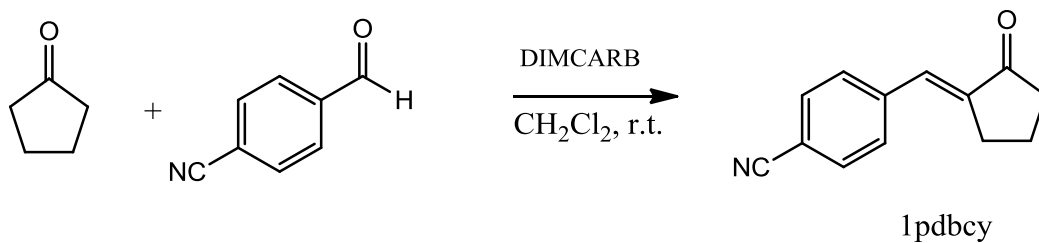
Figure 25. Reaction scheme for the synthesis of 1pdbcy.

3.1.2.4 (E)-2-(p-methoxybenzylidene)-cyclopentanone (1pdbmx)

(E)-2-(p-methoxybenzylidene)-cyclopentanone (1pdbmx) was synthesized via an overnight DIMCARB-catalyzed reaction between cyclopentanone (5.0 mmol, 0.44 mL) and 4-methoxybenzaldehyde (5.0 mmol, 0.61 mL) in CH_2Cl_2 (see Figure 26). The reaction was continuously stirred at room temperature overnight. The solvent was removed *in vacuo*. To the

residue was added 0.5 M H_2SO_4 (10 mL) and the organic layer was extracted with ethyl acetate. The combined organic extracts were dried over Na_2SO_4, filtered, and concentrated *in vacuo* to afford 1pdbmx as an orange solid, characterized by ^1H and ^{13}C NMR spectroscopy. No further purification was run for 1pdbmx.
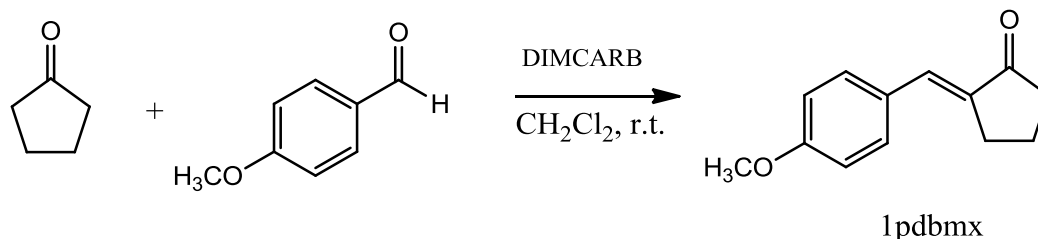
Figure 26. Reaction scheme for the synthesis of 1pdbmx.

3.1.2.5 (E)-2-(benzofuran-2-ylmethylene)-cyclopentanone (1pdbzf)

(E)-2-(benzofuran-2-ylmethylene)-cyclopentanone (1pdbzf) was synthesized via a DIMCARB-catalyzed reaction between cyclopentanone (5.0 mmol, 0.44 mL) and 2-benzofurancarboxaldehyde (5.0 mmol, 0.61 mL) in CH_2Cl_2 (see Figure 27). Reaction time was approximately 2 hours. The solvent was removed *in vacuo*. To the residue was added 0.5 M H_2SO_4 (10 mL) and the organic layer was extracted with dichloromethane. The combined organic layer extracts were dried over Na_2SO_4, filtered, and concentrated *in vacuo*. Purification consisted of running silica gel column chromatography, employing a gradient approach with a hexanes/ethyl acetate binary solvent system yielding pure 1pdbzf as a yellow/orange solid, characterized by ^1H and ^{13}C NMR spectroscopy. Purity was confirmed by TLC (showing one spot upon development).
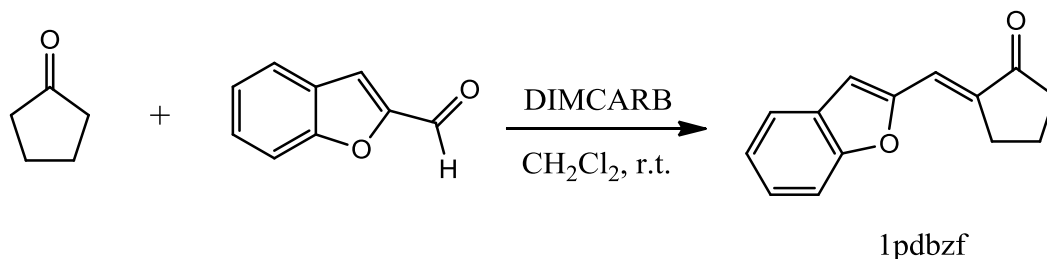
Figure 27. Reaction scheme for the synthesis of 1pdbzf.

3.1.2.6 (E)-2-(p-dimethylaminocinnamylidene)-cyclopentanone (dmac)

The two carbon homologue of dmab, namely (E)-2-(p-dimethylaminocinnamylidene)-cyclopentanone (dmac), was synthesized, however, not by the DIMCARB approach. Instead, powdered NaOH (~0.1 g) was added to cyclopentanone, in excess (283 mmol, 25 mL), noticing a change in color to orange, indicating enolate formation. Afterwards, a solution of (E)-4-dimethylaminocinnamaldehyde (1 mmol, 0.175 g) in EtOH was added to the enolate solution over a period of approximately 30 minutes. The reaction scheme is shown in Figure 28. The reaction was continuously stirred at room temperature overnight. The product mixture was concentrated *in vacuo*, washed with dIH_2O, extracted with CH_2Cl_2 and dried over anhydrous Na_2SO_4. Purification by silica gel column chromatography followed by washing with cold hexanes to remove remaining cyclopentanone residue yielded pure dmac as an orange solid, characterized by both ^1H and and ^{13}C NMR spectroscopy. Purity was confirmed by TLC (showing one spot upon development).
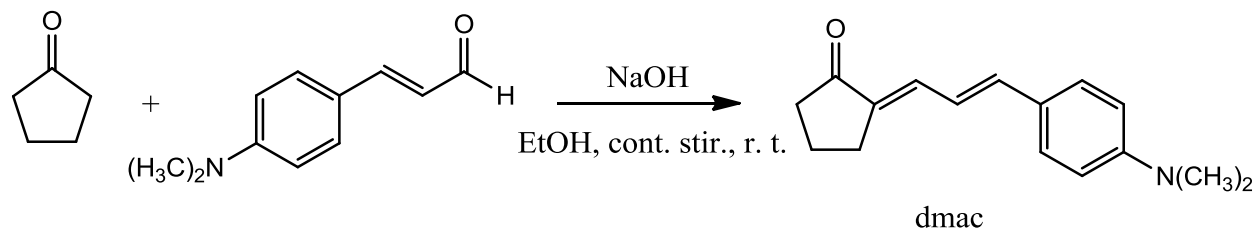
Figure 28. Reaction scheme for the synthesis of dmac.

Table 3. ^{1}H NMR and ^{13}C NMR data for all (E)-2-aryl-α,β-unsaturated cyclopentanones.

Compound	^{1}H NMR	^{13}C NMR
	δ (ppm)	δ (ppm)
1pdbun	7.46 (d, 2H), 7.36-7.29 (m, 4H) 2.91 (td, 2H), 2.34 (t, 2H) 1.96 (p, 2H)	208.1, 136.1, 135.5, 132.3, 130.5, 129.3, 128.7, 37.8, 29.4, 20.2
dmab	7.38 (d, 2H), 7.28 (s, 1H) 6.62 (d, 2H), 2.95 (s, 6H), 2.87 (td, 2H), 2.30 (t, 2H), 1.94 (p, 2H)	207.1, 149.9, 132.3, 131.5, 130.0, 122.3, 110.8, 39.1, 36.8, 28.7, 28.4, 19.1
1pdbcy	7.62 (d, 2H), 7.53 (d, 2H), 7.27 (s, 1H), 2.91 (t, 2H), 2.37 (t, 2H), 2.00 (p, 2H)	206.4, 139.0, 138.3, 131.3, 129.6, 128.8, 117.5, 111.3, 36.6, 28.4, 19.1
1pdbmx	7.44 (d, 2H), 7.29 (t, 1H), 6.88 (d, 2H), 3.78 (s, 3H), 2.88 (td, 2H), 2.33 (t, 2H), 1.96 (p, 2H)	208.2, 160.5, 133.7, 132.3, 132.2, 128.3, 114.2, 55.4, 37.8, 29.3, 20.2
1pdbzf	7.52 (d, 1H), 7.41 (d, 1H), 7.27 (t, 1H), 7.18-7.16 (m, 2H) 6.91 (s, 1H), 3.09 (t, 2H), 2.36 (t, 2H), 2.00 (p, 2H)	206.7, 154.7, 152.7, 135.7, 127.3, 125.0, 122.3, 120.6, 117.9, 111.1, 110.4, 37.0, 28.3, 18.7
dmac	7.35 (d, 2H), 7.09 (d, 1H), 6.86 (d, 1H), 6.69-6.62 (m, 3H), 2.98 (s, 6H), 2.76 (td, 2H), 2.35 (t, 2H), 1.96 (p, 2H)	205.1, 148.4, 140.0, 131.7, 130.6, 126.2, 122.1, 117.7, 109.5, 37.7, 36.2, 24.9, 17.4

3.1.3 Asymmetrical 2,5-Diarylidene Cyclopentanones

3.1.3.1 (2E,5E)-2-(p-cyanobenzylidene)-5-(p-dimethylaminobenzylidene)-cyclopentanone

(Asdimcy1)

As displayed in Figure 29, Asdimcy1 was synthesized via an intermolecular base-catalyzed crossed aldol condensation reaction between dmab (2.1 mmol, 0.45 g) and 4-cyanobenzaldehyde (2.1 mmol, 0.27 g) in MeOH in the presence of 2.5 % (w/v) NaOH (0.6 mL). A light red precipitate emerged immediately from the reaction mixture, which was allowed to react overnight. The precipitate was collected by vacuum filtration, washed with cold MeOH and dried. Silica gel column chromatography afforded pure Asdimcy1, characterized by ^{1}H, ^{13}C NMR and IR spectroscopy (see Table 4). Purity was also confirmed by TLC, showing 1 spot upon development. Melting point measurements were attempted several times; however, Asdimcy1 decomposed at ~260°C.
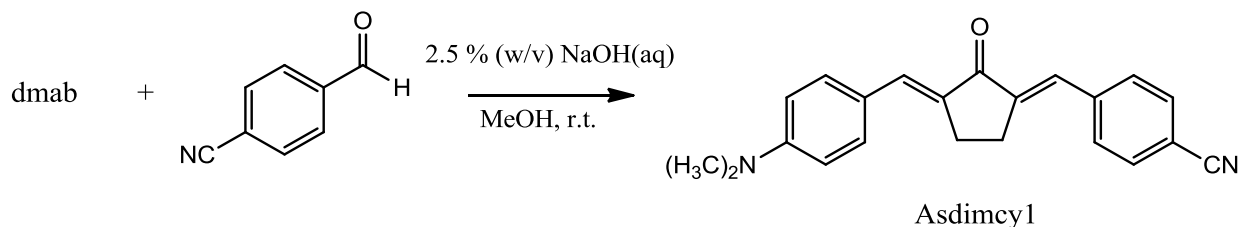
Figure 29. Reaction scheme for the synthesis of Asdimcy1.

3.1.3.2 (2E,5E)-2-(p-dimethylaminobenzylidene)-5-(p-dimethylaminocinnamylidene)-

cyclopentanone (Ashrbor)

As shown in Figure 30, Ashrbor was synthesized via an intermolecular base-catalyzed

crossed aldol condensation reaction between dmab (1.86 mmol, 0.40 g) and (E)-4-

dimethylaminocinnamaldehyde (1.86 mmol, 0.33 g) in MeOH in the presence of 2.5 % (w/v)

NaOH (1.0 mL). The reaction was allowed to run for 24 hours. The product mixture was

concentrated *in vacuo*, washed with dIH$_2$O and extracted with dichloromethane. The combined

organic layers were dried over Na$_2$SO$_4$, filtered, and concentrated *in vacuo*. Silica gel column

chromatography yielded pure Ashrbor, characterized by ^{1}H, ^{13}C NMR and IR spectroscopy (see

Table 4). Purity was also confirmed by TLC (showing 1 spot upon development). Melting point

measurements were attempted several times; however, Ashrbor decomposed at ~250°C.
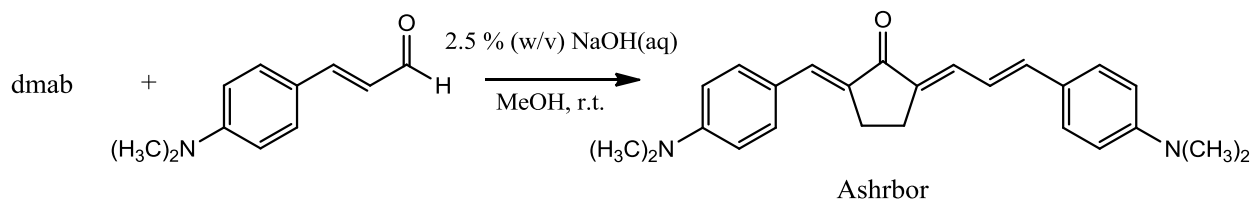
Figure 30. Reaction scheme for the synthesis of Ashrbor.

3.1.3.3 (2E,5E)-2-benzylidene-5-cinnamylidene-cyclopentanone (Asunsub)

As shown in Figure 31, Asunsub was synthesized via an intermolecular base-catalyzed crossed aldol condensation reaction between 1pdbun (4.3 mmol, 0.75 g) and (E)-cinnamaldehyde (4.3 mmol, 0.54 mL) in EtOH in the presence of 2.5 % (w/v) NaOH (2.0 mL). A yellow solid precipitated from solution and the reaction was stirred for an additional 14 hours. The solid product was collected via vacuum filtration, washed with cold EtOH and dried. Recrystallization from EtOH (2 x) yielded pure Asunsub in the form of yellow crystals, characterized by ^{1}H, ^{13}C NMR and IR spectroscopy (see Table 4). Purity was confirmed by TLC (showing 1 spot upon development). The melting point is 192°C.
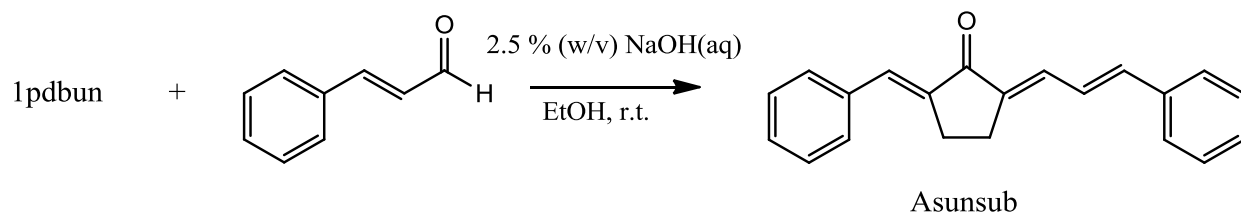
Figure 31. Reaction scheme for the synthesis of Asunsub.

Table 4. ^{1}H NMR, ^{13}C NMR, and IR data for Asdimcy1, Ashrbor, and Asunsub.

Compound	^{1}H NMR	^{13}C NMR	IR (cm^{-1})
	δ (ppm)	δ (ppm)	
Asdimcy1	7.62 (d, 2H), 7.60 (d, 2H), 7.55 (s, 1H), 7.47 (d, 2H), 7.42 (s, 1H), 6.66 (d, 2H), 3.03 (s, 4H), 2.99 (s, 6H), 2.99 (s, 6H)	194.3, 150.3, 140.9, 139.7, 135.4, 132.1, 131.3, 130.5, 129.6, 128.6, 122.4, 117.7, 110.9, 110.7, 39.1, 25.61, 25.56	2907, 2224, 1682, 1612, 1574, 1528, 1444, 1414, 1372, 1321, 1285, 1254, 1231, 1180, 1165, 1119, 1059, 988, 944, 828, 812
Ashrbor	7.44-7.40 (m, 3H), 7.31 (d, 2H), 7.21-7.18 (m, 1H), 6.82 (d, 1H), 6.73-6.70 (m, 1H), 6.65 (d, 2H), 6.58 (d, 2H), 2.94-2.79 (m, 16H)	194.3, 149.8, 149.7, 140.5, 135.8, 133.5, 132.5, 132.4, 131.6, 127.7, 124.0, 123.1, 119.6, 111.0, 110.9, 39.2, 39.1, 28.7, 28.3, 25.2, 23.3	2922, 1670, 1580, 1520, 1429, 1359, 1279, 1260, 1224, 1183, 1091, 1015, 965, 861
Asunsub	7.52 (d, 2H), 7.46-7.44 (m, 3H), 7.37 (t, 3H), 7.30 (t, 3H), 7.24 (d, 2H), 6.94-6.92 (m, 2H), 3.05-3.00 (m, 2H), 2.92-2.85 (m, 2H)	195.7, 141.6, 138.6, 138.5, 136.5, 135.9, 133.3, 130.7, 129.3, 129.1, 128.8, 127.3, 124.7, 26.2, 24.4	3059, 1682, 1624, 1590, 1514, 1491, 1465, 1447, 1338, 1281, 1240, 1181, 1154, 1104, 969, 919, 894, 837

3.2 Spectroscopic Instrumentation

All solutions were freshly prepared prior to spectroscopic measurements. Room temperature absorption spectra were measured using a Shimadzu® UV2100 UV-Visible spectrophotometer and a Perkin Elmer® Lambda 35 UV/VIS spectrometer. Fluorescence spectra at room temperature were measured using a Perkin Elmer® LS-50B luminescence spectrophotometer equipped with a red-sensitive R928 phototube detector. Both ^{1}H NMR and ^{13}C NMR spectra were obtained using a Bruker® AVANCE 400 MHz NMR spectrometer and a Bruker® AVANCE III 500 (500 MHz) NMR spectrometer (Appendix B). Infrared spectra were obtained using a Bruker® Vertex 70 spectrometer and a Perkin Elmer® Spectrum One IR spectrometer (Appendix C). For LC/MS testing, an Agilent® Technologies 1200 Series equipped with a C-18 nonpolar reverse phase column, and an Agilent® Technologies 6130 Quadrupole were used. Ammonium formate (NH_4COO) was used as the buffer for both the organic and aqueous eluting solvents (organic solvent system: 5 mM NH_4COO in 95% acetonitrile/5% deionized water; aqueous solvent system: 5 mM NH_4COO in 100 % deionized water). All solutions were filtered prior to running LC/MS measurements.

3.2.1 Fluorescence Quantum Yield Determination

The fluorescence quantum yield (Φ_f) is defined as the ratio of the number of photons emitted to the original number of photons absorbed by an analyte, and can be determined using the equation

$$\Phi_f = \Phi_{std} \frac{A_{std}}{A} \frac{n^2}{n_{std}^2} \frac{D}{D_{std}}, \tag{3-1}$$

where Φ_{std} is the fluorescence quantum yield of a known standard (obtained from literature), A is the absorbance value at a fixed excitation wavelength, n is the refractive index of the solvents employed and D is the area under the corrected emission spectrum. In order to correct the fluorescence emission spectra for instrument response, the literature emission spectrum of N,N-dimethylamino-3-nitrobenzene (N,N-DMANB) [29] was compared to the experimental emission spectrum of N,N-DMANB measured using the LS-50B status. A set of scale factors were determined every 50 cm^{-1} between 12,500 cm^{-1} (800 nm) and 22,200 cm^{-1} (450 nm). For quantum yield measurements of dmab and dmac, the fluorescence emission spectrum of a 10^{-3} M solution of quinine sulfate in 0.1 N H$_2$SO$_4$ was compared to the literature emission spectrum measured using the LS-50B status [29]. A set of scale factors were determined every 50 cm^{-1} between 15,750 cm^{-1} (635 nm) and 26,000 cm^{-1} (385 nm). The correction factor calculations for the fluorescence emission spectra can be viewed in Appendix E.

The fluorescence quantum yields for bis-dmab, bis-dmac (in several solvents), bis-juldmac, Asdimcy1, Ashrbor, and 2dbmxcp were calculated by the comparative method, using fluorescein in 0.1 N NaOH as the standard, $\Phi_f = 0.95$ [29]. A stock solution of fluorescein in 0.1 N NaOH was prepared (maximum absorbance of approximately 0.5). The stock solution was accurately diluted tenfold to give an absorbance maximum of approximately 0.05. Optical absorption spectra were generated for both the stock and diluted solutions. A fluorescence emission spectrum of the diluted standard solution was obtained. The same procedures were followed for samples of interest. Experimental fluorescence emission data were imported into Microsoft Excel to convert the data from wavelength to wavenumbers. Data was imported into Mathcad, which corrected the fluorescence emission spectra of both the standard and the analyte

and computed the fluorescence quantum yields. A sample Φ_f calculation is provided in Appendix F.

The same experimental procedures were followed for measuring the fluorescence quantum yields of dmab and dmac using coumarin-481 (7-N,N-diethylamino-4-trifluoromethyl-1,2-benzopyrone) in acetonitrile ($\Phi_f = 0.11$) as the standard [57].

3.2.2 Fluorescence Lifetime Determination

The fluorescence lifetime (τ_f) is the inverse of the sum of the first-order radiative and nonradiative rates of decay ($\tau_f = 1/(k_f + k_{nr})$). All fluorescence lifetimes were measured using a Photon Technology International® TM-3 time-resolved spectrofluorometer equipped with a GL-3300 nitrogen laser and GL-302 dye laser. In order to prevent quenching of excited state molecules by oxygen, solutions were properly degassed by purging with nitrogen gas prior to measuring fluorescence lifetimes. FeliX32 analysis module was the computer software employed for analyzing fluorescence decay curves. Data analysis involved utilizing a curve fitting procedure and best fit curves were selectively chosen on the basis of how well the field fit curves fit to the sample decay curve by statistical analysis. In addition, the fluorescence decay profile of an instrument response function (IRF) was generated. The IRF is the response of the instrument to a zero lifetime sample. In other words, the IRF represents the shortest time pulse which can be measured by the instrument. An aqueous non-dairy creamer solution served as the IRF for the majority of fluorescence lifetime measurements. Ludox®, purchased from Aldrich® as a 30 wt% suspension of colloidal silica in water, was used as the IRF for several lifetime measurements. A sample τ_f calculation is provided in Appendix G.

3.2.3 Molar Extinction Coefficient Calculations

Molar extinction coefficients were measured for Asdimcy1 in chloroform and bis-dmac in toluene and dichloromethane. The weighed amount of desired compound was dissolved in a known volume of solvent to prepare the stock solution. A series of diluted solutions were prepared from the stock solution and UV/VIS absorption measurements of both the stock and diluted solutions were taken. The calibration curve consisted of plotting the absorbance (A) values at λ_{max} against molar concentrations (c) of the analyte and the molar extinction coefficients (ε) were taken from the slope of the plot in accordance to Beer's law of absorption

$$A = \varepsilon lc, \tag{3-2}$$

where l is the path length of the cuvette (l = 1.00 cm).

3.2.4 Photochemistry Studies

Photochemistry studies of bis-dmab were carried out using a 150 W Xe arc lamp in the presence of either a green glass filter (Newport®, model # FSQ-GG400, cut-on 400 nm) or a yellow glass filter (Newport®, model # FSQ-OG515, cut-on 515 nm). Photochemistry studies consisted of first testing bis-dmab as a photosensitizer for singlet state oxygen in toluene-d_8, methanol-d_4, and chloroform-d, using 2,3-dimethyl-2-butene (tetramethylethylene, TME) as the singlet oxygen indicator, which was monitored at various irradiation intervals by ^{1}H NMR spectroscopy. Further photochemistry experiments involved irradiating solutions of bis-dmab in chloroform, toluene, acetonitrile, methanol, and methanol-d_4 (i) while bubbling O_2 through the solutions and (ii) under N_2 in a septum equipped quartz UV-Vis cuvette with monitoring of the

absorption spectrum at various irradiation/bubbling intervals. Further analytical testing of the photooxidation of bis-dmab involved conducting ^{1}H NMR and LC/MS experiments.

3.3   X-Ray Diffractometry Studies

Single crystals of Asdimcy1, bis-dmab, and Asunsub were grown in organic solvents at ambient room temperature. Crystals were mounted on a Bruker-AXS Kappa APEX CCD diffractometer that collected diffraction data at room temperature (296 K – 299 K) using graphite monochromated Mo-K$_\alpha$ radiation ($\lambda = 0.71073$ Å). The unit cells and space groups were determined using the SAINT+ program [58]. Structures were solved by direct methods and refined by full matrix least-squares using the SHELXTL program [59]. Mercury 2.4 software was used to examine the molecular structures and crystal packing arrangements in the solved X-ray crystal structures [60]. Single crystal X-ray structures of all compounds were refined to give overall refinement values of $< 5\%$.

3.4   Quantum Chemical Calculations

Gaussian 09® [61] was used to perform all DFT and TD-DFT spectral calculations. Solvent effects were computed using the Self-Consistent Reaction Field (SCRF) Polarizable Continuum Model (PCM) options. Minimum energy structures were confirmed by obtaining all positive vibrational frequencies for the calculated normal modes of vibration. The DFT gas phase geometry was used in all solvent calculations without further optimization. Molecular Orbital Package for Spectroscopy-Fujitsu (MOSF) was the molecular orbital program used for carrying out atomic charge calculations for several molecules both in the ground and excited states [62].

4   RESULTS AND DISCUSSION

4.1   Spectroscopic and Photophysical Properties of an Asymmetrically Substituted 2,5-Diarylidene Cyclopentanone Dye Possessing Electron Donor and Acceptor Substituents

4.1.1   Introduction

This section presents the spectroscopic and photophysical properties of an asymmetrical 2,5-diarylidene-cyclopentanone dye, (2E,5E)-2-(p-cyanobenzylidene)-5-(p-dimethylaminobenzylidene)-cyclopentanone (Asdimcy1), in a variety of solvent systems. Recently, it has been reported that this novel asymmetric push-pull cyclopentanone dye exhibits efficient two-photon absorption (TPA) when dissolved in chloroform [10]. The TPA cross-section was determined by comparing the two-photon up-converted fluorescence of Asdimcy1 to that of a reference compound. These measurements require knowledge of the one-photon absorption and fluorescence properties of the target molecule in the solvent used for the two-photon experiment. Chloroform was the only solvent used in this previous study. This section of the dissertation reports the photophysical properties of Asdimcy1 in a wide variety of solvent environments. The results demonstrate that these properties vary significantly with solvent. Current theories for the radiationless deactivation of S_1 are employed to explain the nearly parabolic dependence of k_{nr} on the S_0-S_1 energy gap. The work presented here is expected to be of importance to those interested in solvent effects on TPA and other fundamental properties of dyes. It will also be of interest to those interested in practical applications of dyes similar to Asdimcy1. For example, it has been noted that Asdimcy1 is likely to be useful as a fluorescence probe in two-photon microscopy because of the desirable qualities of high quantum yields, strong two-photon up-converted fluorescence, broad absorption wavelength range, and solubility in a wide variety of solvents [10].

4.1.2 Molecular Structure of Asdimcy1

Asdimcy1 crystallizes in a triclinic system, belonging to the P-1 space group. Crystallographic data and refinement parameters are listed in Table 5 and the X-ray geometry of Asdimcy1, in two views, is shown in Figure 32. As depicted, the single crystal structure of Asdimcy1 is essentially planar, with ~3° rotations both in the inner cyclopentanone ring system and of the phenyl rings on each end relative to the central ring. Direct comparison between the X-ray geometry and its predicted gas phase geometry at the B3LYP/6-311+G(d,p) level of theory shows excellent agreement in both bond lengths and bond angles (see Table 6). Absolute differences between experimental and calculated bond lengths varied between 0.001 Å – 0.023 Å and bond angles between 0.01° – 3.5°. The predicted DFT geometry is nearly planar as well, with ~6° rotation of the substituted phenyl rings.

Table 5. Crystallographic data and refinement parameters of Asdimcy1.

Crystal Form	
Formula	$C_{22}H_{20}N_2O$
Formula weight (g mol^{-1})	328.40
Crystal system	triclinic
Space group	P-1
Color and habit	Red, needles
Crystal size	0.05 mm $\times$ 0.20 mm $\times$ 0.50 mm
a (Å)	6.8743(2)
b (Å)	8.8115(2)
c (Å)	14.9664(4)
α (deg)	77.135(2)
β (deg)	81.351(2)
γ (deg)	80.975(2)
Volume (Å^3)	866.56(4)
Z	2
λ (Å)	0.71073
ρ_{calc} (g cm^{-3})	1.259
Temperature (K)	296(2)
F(000)	348
θ range for data collection (deg)	2.39 – 28.47
Ranges of miller indices	$-9 \leq h \leq 9$ $-11 \leq k \leq 11$ $-20 \leq l \leq 19$
Absorption coefficient (mm^{-1})	0.078
Reflections collected	16663
Independent reflections	4370 [R_{int} = 0.0279]
Reflections [$I > 2\sigma(I)$]	2395
Data/restraints/parameters	4370/0/228
Goodness of fit on F^2	1.004
R (all data)	R_1 = 0.0496 wR_2 = 0.1460
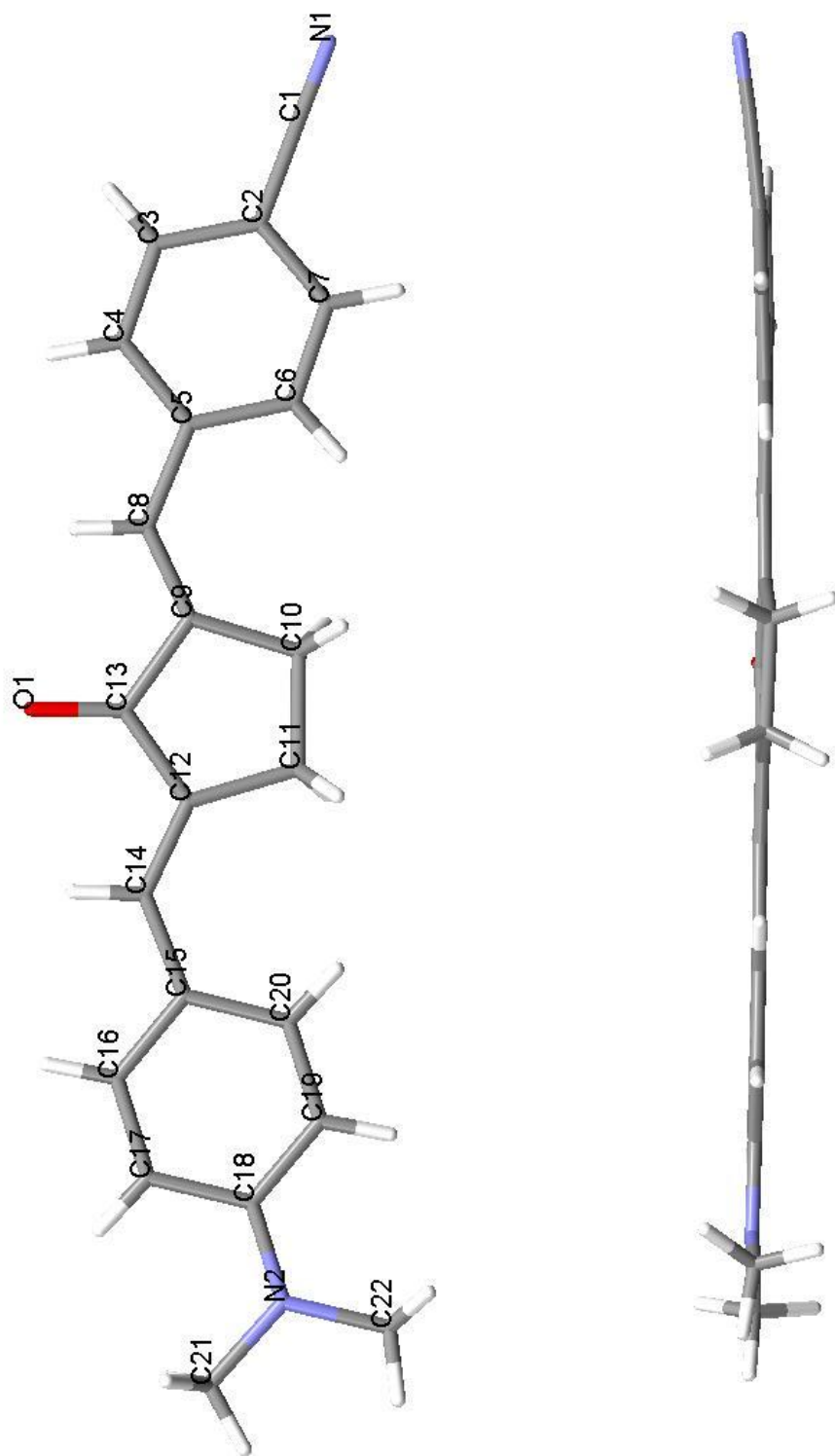
Figure 32. Single crystal X-ray structure of Asdimcy1.

Table 6. Single crystal geometry of Asdimcy1 by X-ray diffractometry and its predicted gas phase geometry at the DFT B3LYP/6-311+G(d,p) level of theory. Δ = X-ray-DFT

Bond Lengths (Å)			
	X-ray	DFT	Δ
C_1-C_2	1.440(3)	1.429	0.011
C_1-N_1	1.131(3)	1.156	-0.025
C_2-C_3	1.383(3)	1.403	-0.020
C_2-C_7	1.383(3)	1.403	-0.020
C_3-C_4	1.363(3)	1.385	-0.022
C_4-C_5	1.396(3)	1.410	-0.014
C_5-C_6	1.394(3)	1.410	-0.016
C_5-C_8	1.453(2)	1.459	-0.006
C_6-C_7	1.374(3)	1.386	-0.012
C_8-C_9	1.336(2)	1.347	-0.011
C_9-C_{10}	1.498(2)	1.507	-0.009
C_9-C_{13}	1.485(2)	1.500	-0.015
C_{10}-C_{11}	1.545(2)	1.557	-0.012
C_{11}-C_{12}	1.500(2)	1.508	-0.008
C_{12}-C_{13}	1.467(3)	1.480	-0.013
C_{12}-C_{14}	1.343(2)	1.355	-0.012
C_{13}-O_1	1.227(2)	1.222	0.005
C_{14}-C_{15}	1.441(2)	1.447	-0.006
C_{15}-C_{16}	1.398(2)	1.411	-0.013
C_{15}-C_{20}	1.399(3)	1.411	-0.012
C_{16}-C_{17}	1.371(3)	1.382	-0.011
C_{17}-C_{18}	1.401(3)	1.416	-0.015
C_{18}-C_{19}	1.397(3)	1.416	-0.019
C_{18}-N_2	1.372(3)	1.377	-0.005
C_{19}-C_{20}	1.374(3)	1.383	-0.009
C_{21}-N_2	1.453(3)	1.455	-0.002
C_{22}-N_2	1.436(4)	1.455	-0.019

Dihedral Angles (°)		
	X-ray	DFT
C_{10}-C_9-C_5-C_6	-3.8	7.1
C_{11}-C_{12}-C_{15}-C_{20}	1.2	4.6

Bond Angles (°)			
	X-ray	DFT	Δ
C_1-C_2-C_3	121.0(2)	120.4	0.6
C_1-C_2-C_7	119.8(2)	120.2	-0.4
C_2-C_1-N_1	178.0(3)	179.9	-1.9
C_2-C_3-C_4	119.8(2)	119.8	-0.01
C_2-C_7-C_6	120.8(2)	120.3	0.5
C_3-C_2-C_7	119.2(2)	119.4	-0.2
C_3-C_4-C_5	122.1(2)	121.7	0.4
C_4-C_5-C_6	117.4(2)	117.6	-0.2
C_4-C_5-C_8	118.5(1)	117.8	0.7
C_5-C_6-C_7	120.6(2)	121.2	-0.6
C_5-C_8-C_9	132.1(1)	130.9	1.2
C_6-C_5-C_8	124.2(1)	124.6	-0.4
C_8-C_9-C_{10}	132.4(1)	131.6	0.8
C_8-C_9-C_{13}	118.8(1)	119.3	-0.5
C_9-C_{10}-C_{11}	106.5(1)	106.3	0.2
C_9-C_{13}-C_{12}	108.9(1)	107.9	1.0
C_9-C_{13}-O_1	124.7(1)	125.2	-0.5
C_{10}-C_9-C_{13}	108.8(1)	109.1	-0.3
C_{10}-C_{11}-C_{12}	106.6(1)	106.1	0.5
C_{11}-C_{12}-C_{13}	109.1(1)	109.7	-0.6
C_{11}-C_{12}-C_{14}	131.8(1)	130.7	1.1
C_{12}-C_{13}-O_1	126.5(1)	126.9	-0.4
C_{12}-C_{14}-C_{15}	132.7(1)	131.6	1.1
C_{13}-C_{12}-C_{14}	119.1(1)	119.5	-0.4
C_{14}-C_{15}-C_{16}	118.4(1)	118.3	0.1
C_{14}-C_{15}-C_{20}	125.7(1)	125.4	0.3
C_{15}-C_{16}-C_{17}	122.7(2)	122.6	0.1
C_{15}-C_{20}-C_{19}	122.0(2)	122.0	0.01
C_{16}-C_{15}-C_{20}	115.9(2)	116.2	-0.3
C_{16}-C_{17}-C_{18}	121.0(2)	120.8	0.2
C_{17}-C_{18}-C_{19}	116.8(2)	117.0	-0.2
C_{17}-C_{18}-N_2	121.0(2)	121.5	-0.5
C_{18}-C_{19}-C_{20}	121.7(2)	121.4	0.3
C_{18}-N_2-C_{21}	120.6(2)	120.0	0.6
C_{18}-N_2-C_{22}	120.9(2)	120.2	0.7
C_{19}-C_{18}-N_2	122.2(2)	121.5	0.7
C_{21}-N_2-C_{22}	118.2(2)	118.8	-0.6

4.1.3   Spectroscopic Properties of Asdimcy1

TD-DFT B3LYP/6-311+G(d,p) spectral calculations were performed using the optimized ground state geometry. Presented in Table 7 are the excitation energies for the first four excited singlet and triplet states in the gas phase. Also presented are the theoretical oscillator strengths for each electronic transition.

Table 7. Gas phase TD-DFT spectral calculations of Asdimcy1 at the B3LYP/6-311+G(d,p) level of theory.

State	Transition Energy			f	MO	CI Coef.
	eV	cm^{-1}	nm			
T$_1$ (π, π*)	1.89	15244	656	0.00	84→88	0.16428
					84→89	-0.10005
					87→88	0.69172
					87→89	-0.27280
T$_2$ (π, π*)	2.29	18450	542	0.00	81→93	-0.11477
					82→90	-0.12722
					84→88	0.12570
					85→88	0.11486
					86→88	0.73324
					86→89	0.15207
					87→89	-0.13782
T$_3$ (n, π*)	2.60	20921	478	0.00	85→88	0.69270
					85→89	-0.13138
					86→88	-0.11247
S$_1$ (π, π*)	2.62	21142	473	0.73	87→88	0.65820
S$_2$ (n, π*)	2.91	23474	426	0.01	85→88	0.64708
					86→88	-0.20127
T$_4$ (π, π*)	3.09	24938	401	0.00	83→91	-0.12132
					84→88	-0.11370
					84→89	0.13730
					86→88	0.13511
					87→88	0.25800
					87→89	0.60274
					87→93	-0.20254
S$_3$ (π, π*)	3.38	27248	367	0.84	85→88	0.15449
					86→88	0.48318
					87→89	0.40901
S$_4$ (π, π*)	3.59	28986	345	0.05	85→88	-0.11136
					86→88	-0.32689
					87→89	0.48727

The room temperature absorption spectrum of Asdimcy1 in chloroform along with the results of the TD-DFT spectral calculations (PCM = chloroform) are shown in Figure 33. Results for the first three computed singlet excitations along with experimental data are summarized in Table 8. Examination of the orbitals that make the major contribution to the configuration interaction (CI) description of the excited state provides insight to the nature of these excitations. The $S_0 \rightarrow S_1$ transition is experimentally observed at 468 nm in chloroform and is predicted by TD-DFT to be a strong transition appearing at 473 nm in the gas phase and 515 nm in chloroform, arising from the HOMO $\rightarrow$ LUMO orbital configuration. Figure 34 depicts the computed HOMO, LUMO and nonbonding orbitals of Asdimcy1. Examination of the HOMO and LUMO reveals the internal charge transfer (ICT) (π, π^*) nature of this excitation, in that π electron density is transferred from the electron donor side of the molecule in the HOMO to the electron acceptor end of the molecule in the LUMO.

The $S_0 \rightarrow S_2$ transition is computed to be a forbidden (n, π^*) excitation arising from HOMO-2 $\rightarrow$ LUMO, where HOMO-2 is a nonbonding orbital localized on the carbonyl oxygen (Figure 34). The calculated wavelengths are 426 nm in the gas phase and 403 nm in chloroform. Absorption to this state has not been observed owing to its forbidden nature. Excitation to S_3 is predicted to occur at 367 nm in the gas phase and 376 nm in chloroform with major CI configurations HOMO-1 $\rightarrow$ LUMO and HOMO $\rightarrow$ LUMO+1, corresponding to a (π, π^*) transition delocalized over the entire molecule. The band observed at $\lambda_{max} = 322$ nm is assigned to this computed excitation.
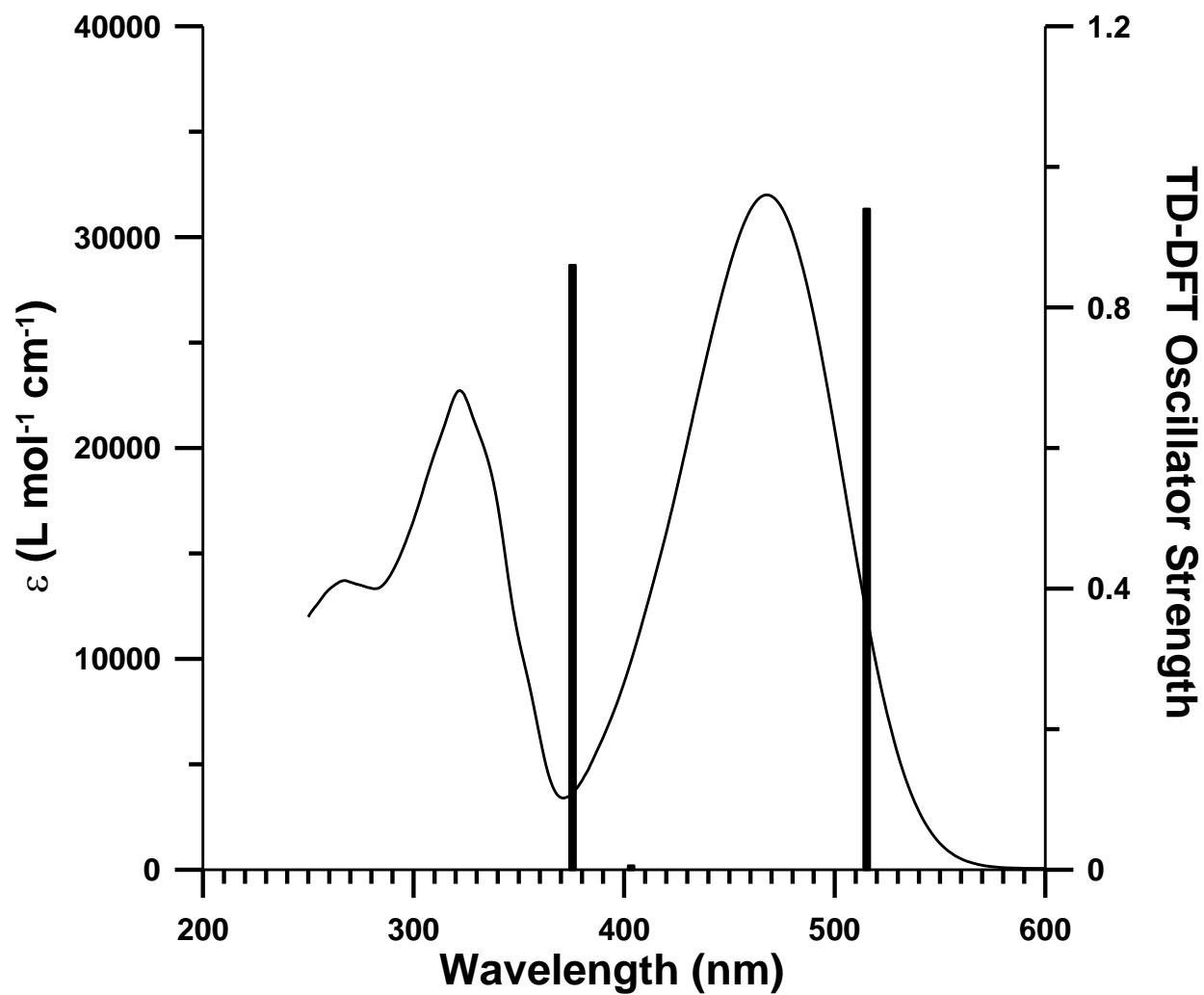
Figure 33. Absorption spectrum and TD-DFT oscillator strength results for Asdimcy1 in chloroform.

Table 8. Experimental spectral data and B3LYP/6-311+G(d,p) TD-DFT calculated results for Asdimcy1.

State		Gas phase (calc.)	CHCl$_3$ (calc.)	CHCl$_3$ (expt.)
S$_1$ (ICT, π, π^*)	λ_{max}	473 nm	515 nm	468 nm
	f	0.73	0.94	0.61
	ε_{max}	-	-	3.20×10^4 (M^{-1} cm^{-1})
S$_2$ (n, π^*)	λ_{max}	426 nm	403 nm	Not observed
	f	0.00	0.00	
	ε_{max}	-	-	
S$_3$ (π, π^*)	λ_{max}	367 nm	376 nm	322 nm
	f	0.84	0.86	0.8 ± 0.2
	ε_{max}	-	-	2.27×10^4 (M^{-1} cm^{-1})

LUMO (π_A*) (MO 88)
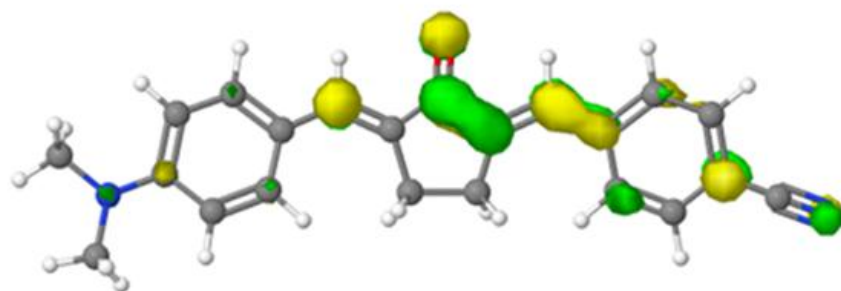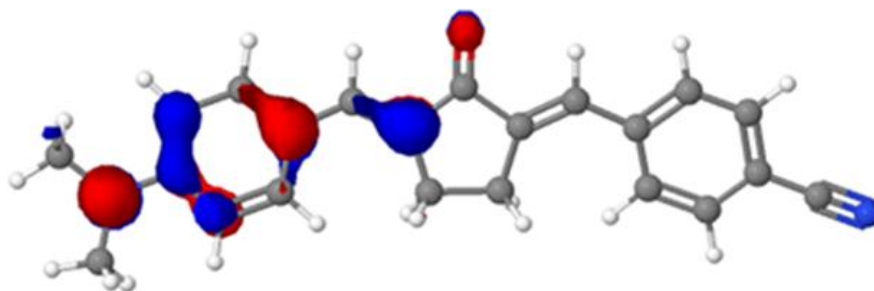
HOMO (π_D) (MO 87)
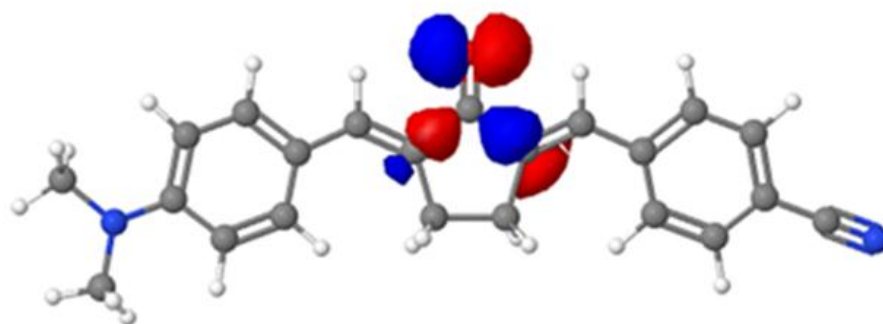
HOMO-2 (n_O) (MO 85)

Figure 34. Computed molecular orbitals of Asdimcy1.

Absorption and fluorescence properties of Asdimcy1 were examined in twenty three solvents and the results are presented in Table 9. A survey of absorption and fluorescence emission spectra of Asdimcy1 in six of these solvents which differ in polarity and hydrogen bonding strength (nonpolar, polar aprotic, and protic) is shown in Figure 35. The absorption and fluorescence spectral maxima, in units of wavenumbers, are plotted against the $E_T(30)$ empirical solvent polarity scale in Figure 36. It is seen that with respect to increasing solvent polarity, there is a small shift towards the red (bathochromic shift) in the absorption spectra and a much larger shift in the fluorescence spectra. Furthermore, protic solvents do not appear to be anomalous in the absorption plot, but they clearly fall on a separate line in the fluorescence plot. Previous studies of molecules similar to Asdimcy1 have noted that there is a transfer of electron charge to the carbonyl oxygen atom following excitation from S_0 to S_1 causing the molecule to become a stronger base in the excited state. The increased basicity in S_1 results in a stronger hydrogen bond with protic solvents which is manifested in Figure 36 by a shift of the fluorescence trend line for alcohols relative to other solvents [15, 63].

Table 9. Spectroscopic properties of Asdimcy1 in various solvents.

Solvent	λ_{abs} (nm)	λ_f (nm)	ν_{abs} (cm^{-1})	ν_f (cm^{-1})	$E_T(30)$* (kcal mol^{-1})	Δf*	$\Delta\nu$ (cm^{-1})
Carbon tetrachloride	446	513	22,422	19,487	32.4	0.0119	2935
Carbon disulfide	464	535	21,552	18,688	32.8	-0.0007	2864
Toluene	455	558	21,978	17,923	33.9	0.0131	4055
Benzene	457	569	21,882	17,583	34.3	0.0031	4299
Diethyl ether	438	580	22,831	17,234	34.5	0.1669	5597
Tetrahydrofuran	458	651	21,834	15,360	37.4	0.2104	6474
o-Dichlorobenzene	465	625	21,505	16,000	38.0	0.1867	5505
Ethyl acetate	446	643	22,422	15,550	38.1	0.1996	6872
Ethyl benzoate	459	641	21,786	15,600	38.1	0.1581	6186
n-Butyl acetate	442	631	22,624	15,850	38.5	0.1709	6774
Chloroform	469	603	21,322	16,597	39.1	0.1491	4725
Cyclopentanone	460	678	21,739	14,760	39.4	0.2391	6979
Pyridine	467	673	21,413	14,863	40.5	0.2124	6550
Dichloromethane	464	643	21,552	15,560	40.7	0.2171	5992
Acetone	454	718	22,026	13,930	42.2	0.2843	8096
Dimethylformamide	464	740	21,552	13,520	43.2	0.2752	8032
Dimethyl sulfoxide	471	731	21,231	13,673	45.1	0.2637	7558
Acetonitrile	456	721	21,930	13,868	45.6	0.3054	8062
Isopropanol	471	647	21,231	15,450	48.4	0.2769	5781
n-Butanol	473	648	21,142	15,432	50.2	0.2642	5710
n-Propanol	473	644	21,142	15,530	50.7	0.2746	5612
Ethanol	472	659	21,186	15,177	51.9	0.2887	6009
Methanol	473	693	21,142	14,420	55.4	0.3093	6722

*Both Δf and $E_T(30)$ values are taken from Suppan, P. and Ghonheim, N., in *Solvatochromism*, The Royal Society of Chemistry, Cambridge, 1997; and Lide, D. R., *CRC Handbook of Chemistry and Physics*, 89th ed., 2008.
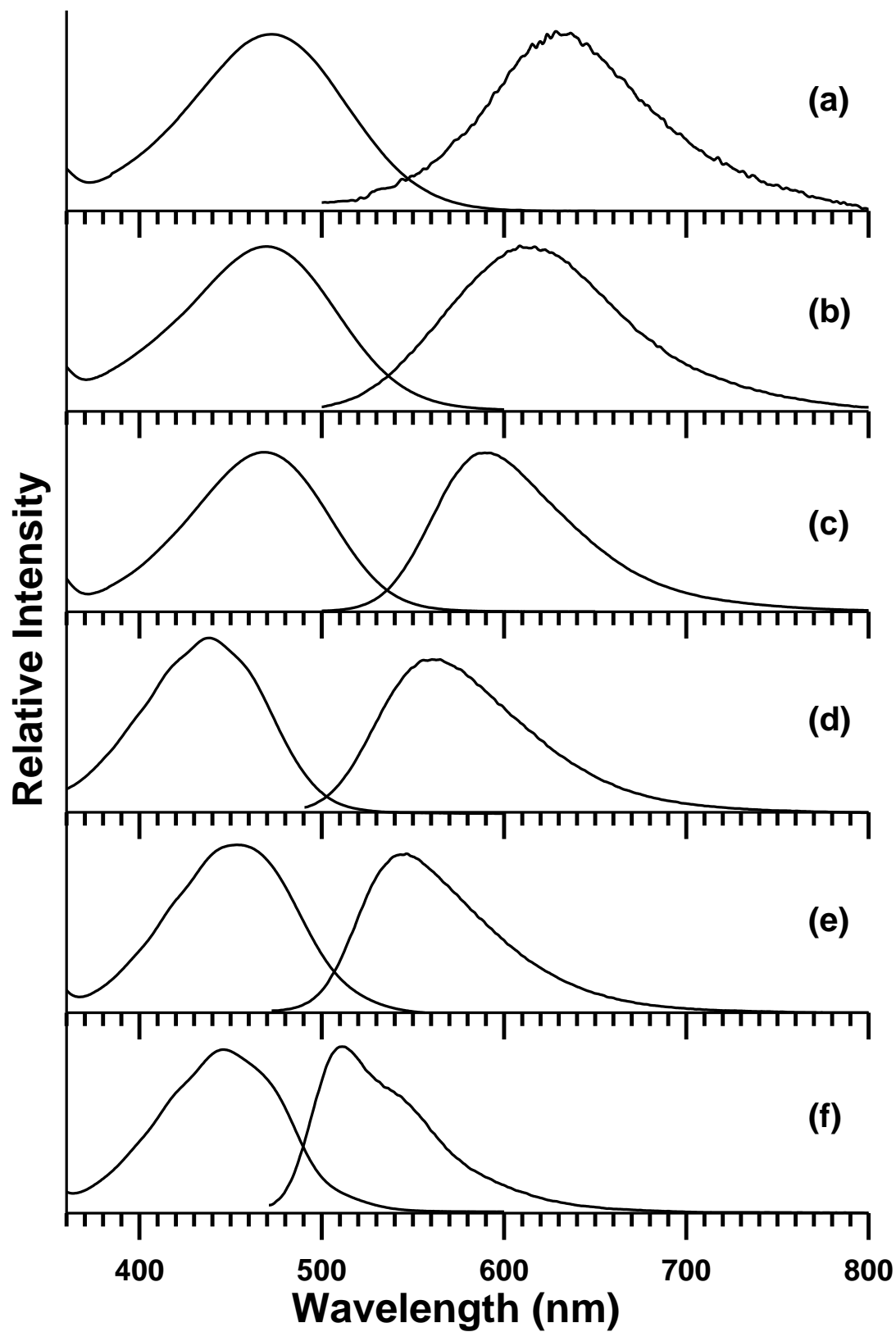
Figure 35. Absorption and fluorescence emission spectra of Asdimcy1 in (a) methanol, (b) 2-propanol, (c) chloroform, (d) diethyl ether, (e) toluene, and (f) carbon tetrachloride.
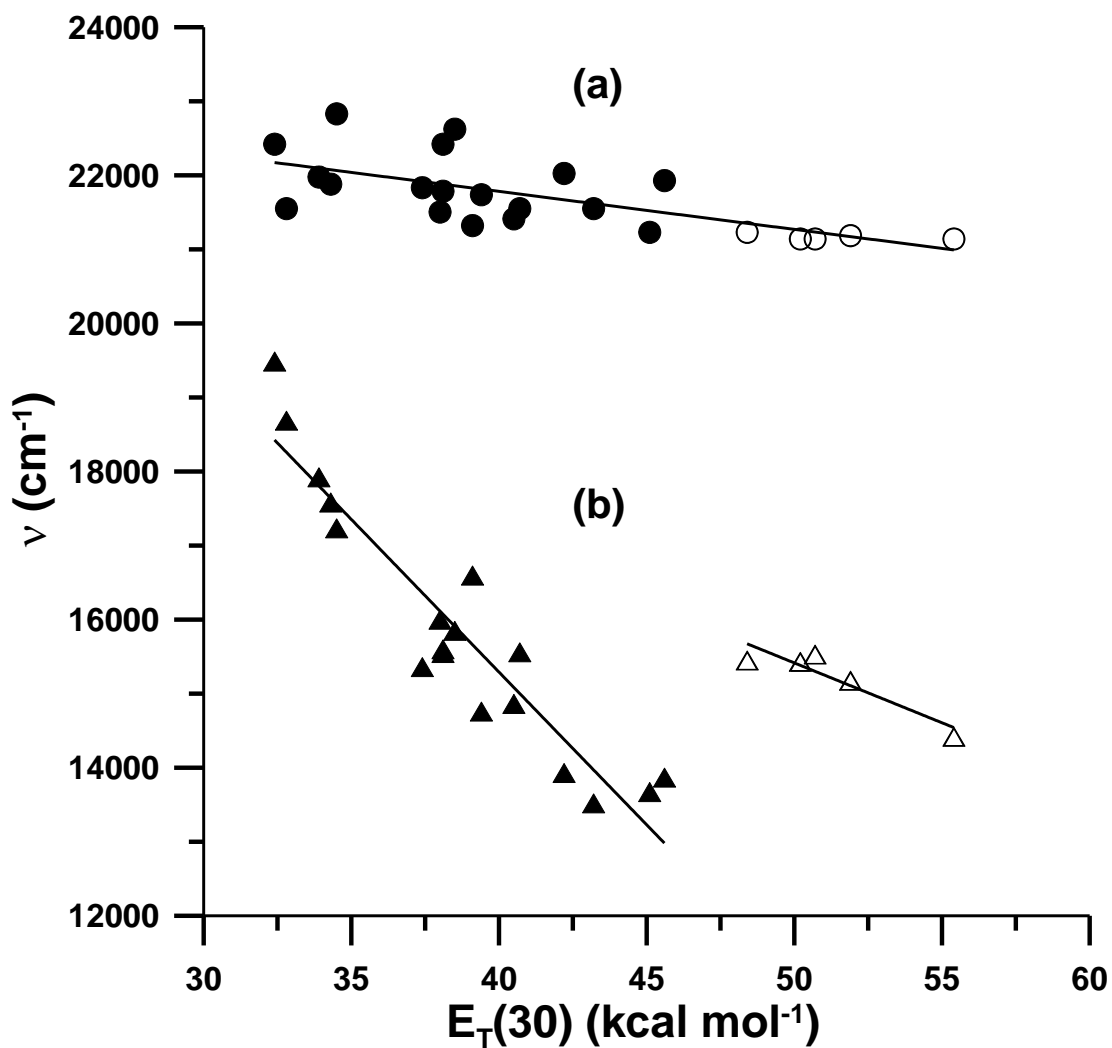
Figure 36. Plot of (a) absorption and (b) fluorescence spectral maxima of Asdimcy1 in various

solvents against the $E_T(30)$ scale. Solid symbols represent aprotic solvents; open symbols

represent protic solvents.

Figure 37 shows a Lippert-Mataga plot of the Stokes shift (Δv), the difference in wavenumbers between the absorption and fluorescence spectral maxima, plotted against the solvent's orientation polarization function (Δf). Similar to the plots in Figure 36, separate lines are drawn for alcohols and nonalcohols. The positive slope is evidence that the dipole moment is larger in the excited electronic state than in the ground state. Application of the Lippert-Mataga equation (discussed in the literature review section) to the data for non-alcohols in Figure 37 yields a $\Delta\mu = 16.0$ D (using an Onsager cavity radius of 5.50 Å, computed by B3LYP/6-311+G(d,p)). Using the ground state dipole moment $\mu_g = 11.0$ D, calculated by B3LYP/6-311+G(d,p), an excited state dipole moment $\mu_e = 27.0$ D is obtained. The large increase in dipole moment supports the ICT assignment for the $S_0 \rightarrow S_1$ electronic transition.
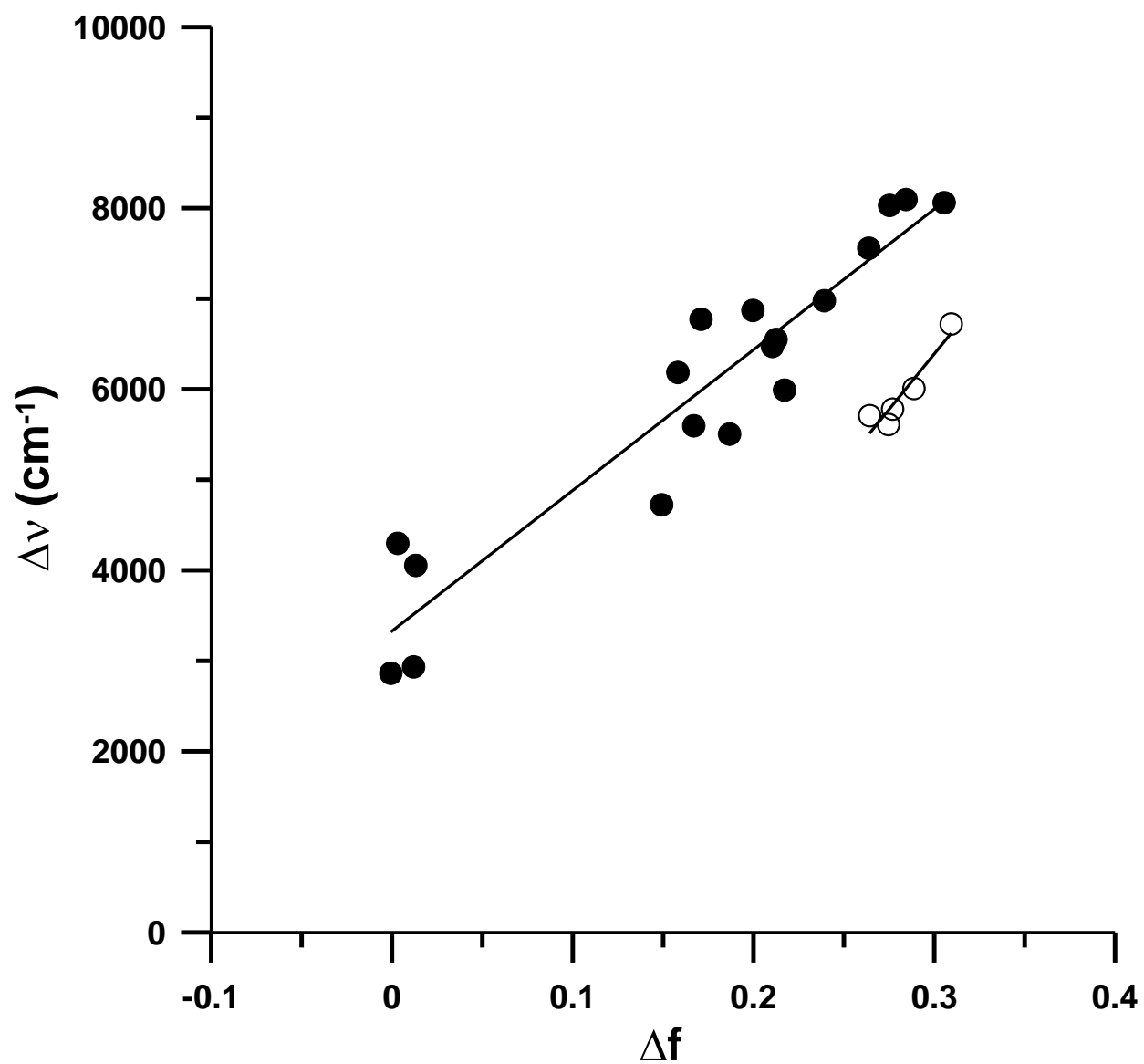
Figure 37. Lippert-Mataga plot of Asdimcy1 in various solvents. Solid symbols represent aprotic solvents; open symbols represent protic solvents.

4.1.4 Fluorescence Quantum Yields, Lifetimes, and Decay Constants

Investigation of the deactivation kinetics of the excited molecule back to the ground electronic state involved determining both the first-order radiative (k_f) and nonradiative (k_{nr}) rates of decay from knowledge of Φ_f and τ_f. The decay constants were determined from the following equations:

$$k_f = \frac{\Phi_f}{\tau_f}$$

$$(4\text{-}1)$$

$$k_{nr} = \left(\frac{1}{\Phi_f} - 1\right)k_f$$

$$(4\text{-}2)$$

Listed in Table 10 are Φ_f, τ_f, k_f, and k_{nr} values for Asdimcy1. A plot of Φ_f against the corrected maximum frequency of fluorescence for Asdimcy1 in various solvents is shown in Figure 38. The appearance of the plot is reminiscent of Figure 11 of previous work from this lab [11], where a similar plot is shown for an unsubstituted 2,5-diarylidene-cyclopentanone [(2E,5E)-2,5-bis-(5-phenyl-penta-2,4-dienylidene)-cyclopentanone]. It is seen that Φ_f reaches a maximum (CHCl$_3$, $\Phi_f = 0.33$), approximately in the middle (16,597 cm^{-1}) of the frequency range plotted (13,000-20,000 cm^{-1}), then falls off towards higher frequencies (nonpolar: CCl$_4$, $\Phi_f = 0.021$) and towards lower frequencies (polar protic: MeOH, $\Phi_f = 0.003$ and aprotic solvents: ACN, $\Phi_f = 0.004$).

Table 10. Photophysical properties of Asdimcy1 in various solvents.

	Solvent	Φ_f	τ_f (ns)	k_f (s^{-1})	k_{nr} (s^{-1})
1	Carbon tetrachloride	0.021	0.17	1.24×10^8	5.76×10^9
2	Carbon disulfide	0.038	0.28	1.36×10^8	3.44×10^9
3	Toluene	0.056	0.56	1.00×10^8	1.69×10^9
4	Benzene	0.074	0.76	9.74×10^7	1.22×10^9
5	Diethyl ether	0.083	0.89	9.33×10^7	1.03×10^9
6	Tetrahydrofuran	0.030	0.18	1.67×10^8	5.39×10^9
7	o-Dichlorobenzene	0.32	2.18	1.47×10^8	3.12×10^8
8	Ethyl acetate	0.10	0.90	1.11×10^8	1.00×10^9
9	Ethyl benzoate	0.20	1.24	1.61×10^8	6.45×10^8
10	n-Butyl acetate	0.16	1.01	1.58×10^8	8.32×10^8
11	Chloroform	0.33	2.08	1.59×10^8	3.22×10^8
12	Cyclopentanone	0.038	0.31	1.23×10^8	3.10×10^9
13	Pyridine	0.057	0.41	1.39×10^8	2.30×10^9
14	Dichloromethane	0.19	1.29	1.47×10^8	6.28×10^8
15	Acetone	0.011	0.23	4.78×10^7	4.30×10^9
16	Dimethylformamide	0.0073	0.18	4.06×10^7	5.52×10^9
17	Dimethyl sulfoxide	0.0082	0.19	4.32×10^7	5.22×10^9
18	Acetonitrile	0.0039	0.17	2.29×10^7	5.86×10^9
19	Isopropanol	0.029	0.21	1.38×10^8	4.62×10^9
20	n-Butanol	0.019	0.22	8.64×10^7	4.46×10^9
21	n-Propanol	0.015	0.18	8.33×10^7	5.47×10^9
22	Ethanol	0.0068	0.14	4.86×10^7	7.09×10^9
23	Methanol	0.0030	0.13	2.31×10^7	7.67×10^9
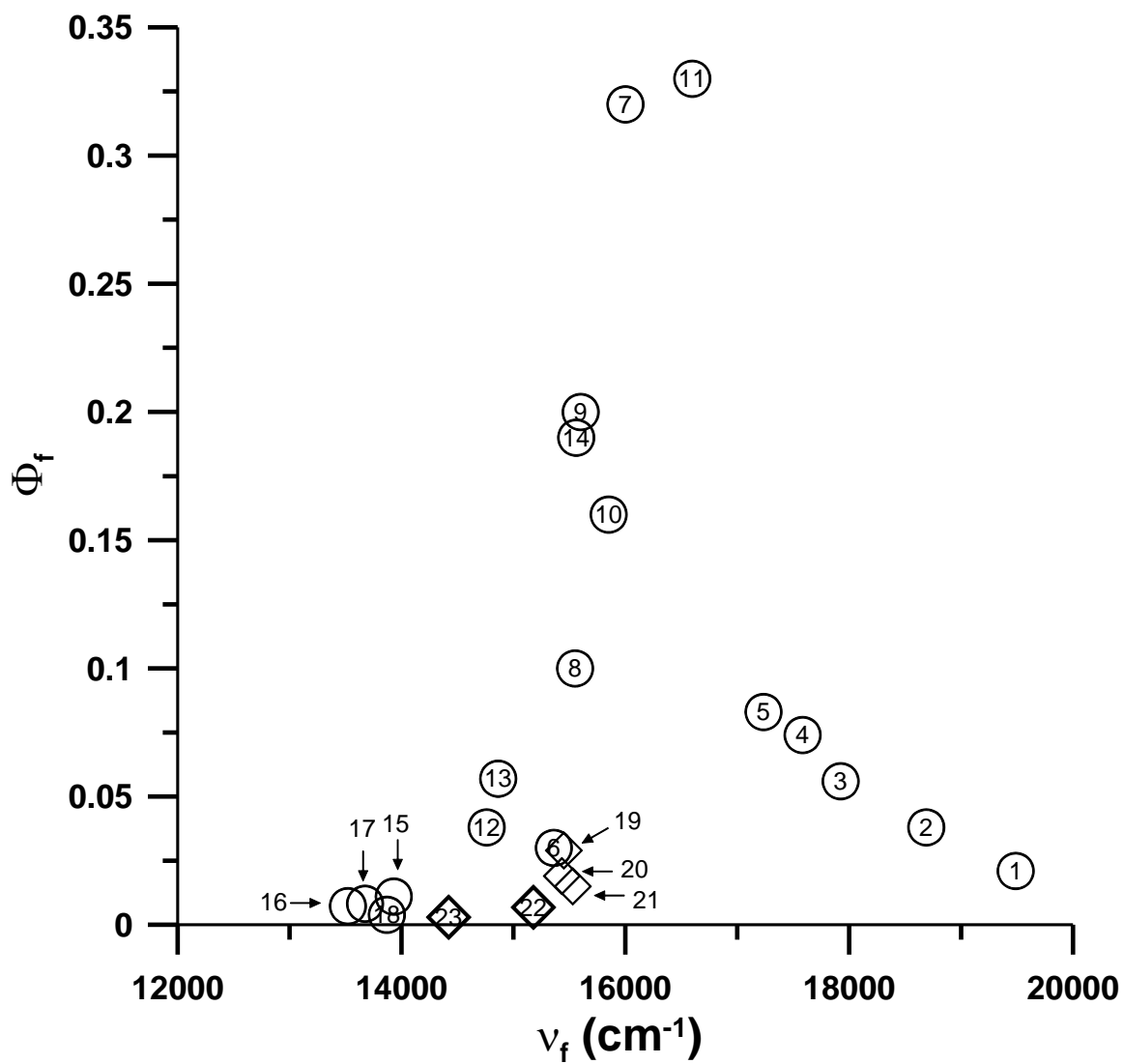
Figure 38. Fluorescence quantum yields (Φ_f) plotted against the fluorescence spectral maxima of Asdimcy1 in various solvents. Circles represent aprotic solvents; diamonds represent protic solvents.

Related to the quantum yield plot in Figure 38 is the plot shown in Figure 39 of k_{nr} against the frequency of fluorescence. Here a minimum is observed for k_{nr} in the mid frequency range with an increase in k_{nr} towards higher and lower frequencies. The data for the aprotic solvents describes a trend in k_{nr} that is nearly parabolic over the frequency range of fluorescence emission. The k_{nr} rates for Asdimcy1 in alcohols are higher than the rates for Asdimcy1 in aprotic solvents that have similar positions for their fluorescence spectral maxima, suggesting a hydrogen bonding influence on the nonradiative decay of Asdimcy1. In discussing the major routes for nonradiative decay in aprotic solvents, Figure 39 can be partitioned into two regions: the region from the minimum to the low frequency side (region 1) and the region from the minimum to the high frequency side (region 2). In region 1, k_{nr} increases from 3.1×10^8 s^{-1} (o-dichlorobenzene, $\nu_f = 16,000$ cm^{-1}) to 5.9×10^9 s^{-1} (polar aprotic: acetonitrile, $\nu_f = 13,868$ cm^{-1}). In region 2, k_{nr} decreases from 5.8×10^9 s^{-1} (CCl$_4$, $\nu_f = 19,487$ cm^{-1}) to 3.2×10^8 s^{-1} (chloroform, $\nu_f = 16,597$ cm^{-1}).

Noting that $k_{nr} = k_{ic} + k_{isc}$, where k_{ic} is the rate of internal conversion and k_{isc} is the rate of intersystem crossing from the singlet to the triplet manifold of states, it is believed that the variation in k_{nr} shown in Figure 39 can be attributed to opposing behavior for these two rates with respect to solvent polarity. In shifting from nonpolar (high ν_f) to polar solvents (low ν_f), k_{ic} increases while k_{isc} decreases. In region 1, where k_{nr} increases with a decrease in ν_f, the increase in k_{ic} dominates the decrease in k_{isc}; whereas in region 2, where k_{nr} decreases with a decrease in ν_f, the decrease in k_{isc} dominates the increase in k_{ic}.

The order of magnitude increase in k_{nr} found in region 1 is attributed to the energy gap law for internal conversion, which predicts an exponential dependence of k_{ic} on the S_0-S_1 energy gap (ΔE) [64]:

$$k_{ic} = \alpha \exp(-\beta \Delta E) \qquad (4\text{-}3)$$

According to the energy gap law of internal conversion for excited states, the first order nonradiative decay constant, k_{nr}, is expected to increase as the energy gap between S_0 and S_1 decreases due to greater vibrational overlap (Franck-Condon factor) between the S_0 and S_1 states. Expressed in Dirac notation of integrals, the Franck-Condon factor is given by $\langle \chi_{S_1}^{n=0} | \chi_{S_0}^{n=a} \rangle$, where $\chi_{S_1}^{n=0}$ represents the wavefunction for the lowest vibrational energy level of the first excited singlet state and $\chi_{S_0}^{n=a}$ represents the wavefunction for the vibrational energy level of the ground singlet state at $n = a$ (isoenergetic with S_1, $n=0$ vibrational level). As the S_0-S_1 energy gap decreases, the overlap of vibrational wavefunctions between isoenergetic energy levels of S_0 and S_1 increases (fewer number of nodes in the S_0 vibrational wavefunction), thereby resulting in an increase in the nonradiative rate of internal conversion.

In region 2, where intersystem crossing is the major nonradiative decay channel, it is believed that the solvent modulated location of (n, π^*) states relative to the S_1(π, π^*) and T_1(π, π^*) states influences the rate of S $\rightarrow$ T intersystem crossing. The positions of (n, π^*) states and (π, π^*) states behave differently under the influence of a change in solvent polarity. Whereas (n, π^*) states undergo a hypsochromic shift with increased solvent polarity, (π, π^*) states undergo a bathochromic shift [25]. Experimental data presented in Figure 35 and Table 9 confirm the bathochromic shift expected for S_1(π, π^*).

A mechanism involving thermally activated intersystem crossing from $S_1(\pi, \pi^*)$ to a higher lying $^3(n, \pi^*)$ state has been offered to explain solvent effects on the intersystem crossing for molecules related to Asdimcy1 [22]. Vibronic spin-orbit coupling [65] is presented here as an alternative mechanism that is less restrictive than the thermally activated intersystem crossing mechanism in its requirement for the magnitude of the $S_1(\pi, \pi^*)$-$T(n, \pi^*)$ energy gap relative to $k_B T$. This mechanism is expected to apply to other dyes of similar electronic structure.

As described in section 2.4, for the vibronic spin-orbit coupling mechanism, spin-orbit coupling between (π, π^*) and (n, π^*) states in different spin manifolds and vibronic coupling within the same spin manifold are operative in promoting intersystem crossing.

$$S_1(\pi, \pi^*) \leftarrow SOC \rightarrow T_m(n, \pi^*) \leftarrow VC \rightarrow T_1(\pi, \pi^*)$$
$$S_1(\pi, \pi^*) \leftarrow VC \rightarrow S_m(n, \pi^*) \leftarrow SOC \rightarrow T_1(\pi, \pi^*)$$
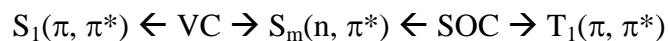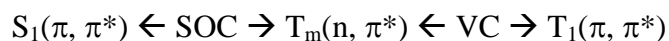
As depicted in Figure 40, as solvent polarity increases, the (n, π^*)-(π, π^*) energy spacing also increases, which in turn reduces the vibronic coupling between two states of the same spin multiplicity in reference to equation 2-13. Therefore, the reduction of vibronic coupling attenuates the degree of state mixing between two states of different spin manifolds, which in turn reduces the rate of $S \rightarrow T$ intersystem crossing [30].

Both the thermally activated mechanism and the vibronic spin-orbit coupling mechanism are favored over direct spin-orbit coupling between $S_1(\pi, \pi^*)$ and $T_1(\pi, \pi^*)$ because of the well-established understanding that the matrix element for spin-orbit coupling between states of different orbital configurations is greater than the matrix element for spin-orbit coupling between states of the same orbital configuration, as discussed in section 2.4. The smooth decrease in k_{nr}

shown in Figure 39 is consistent with a gradual solvent induced increase in the spacing between S_1/T_1 (π, π*) and higher energy (n, π*) states. Table 11 provides theoretical support for this interpretation with the results of TD-DFT calculations modeled in carbon tetrachloride, toluene, and chloroform solvent environments. It is clearly seen that there is an inverse relationship between the magnitude of the computed energy gaps of the lowest lying (n, π*) and (π, π*) states and the experimental k_{nr} values. At this level of theory, the qualitative trend calculated is expected to be more meaningful than the numeric values calculated for the (n, π*)-(π, π*) energy gaps. It is possible that a combination of thermally activated and vibronic spin-orbit coupling mechanisms contribute to solvent dependent S → T intersystem crossing observed for Asdimcy1 at room temperature.
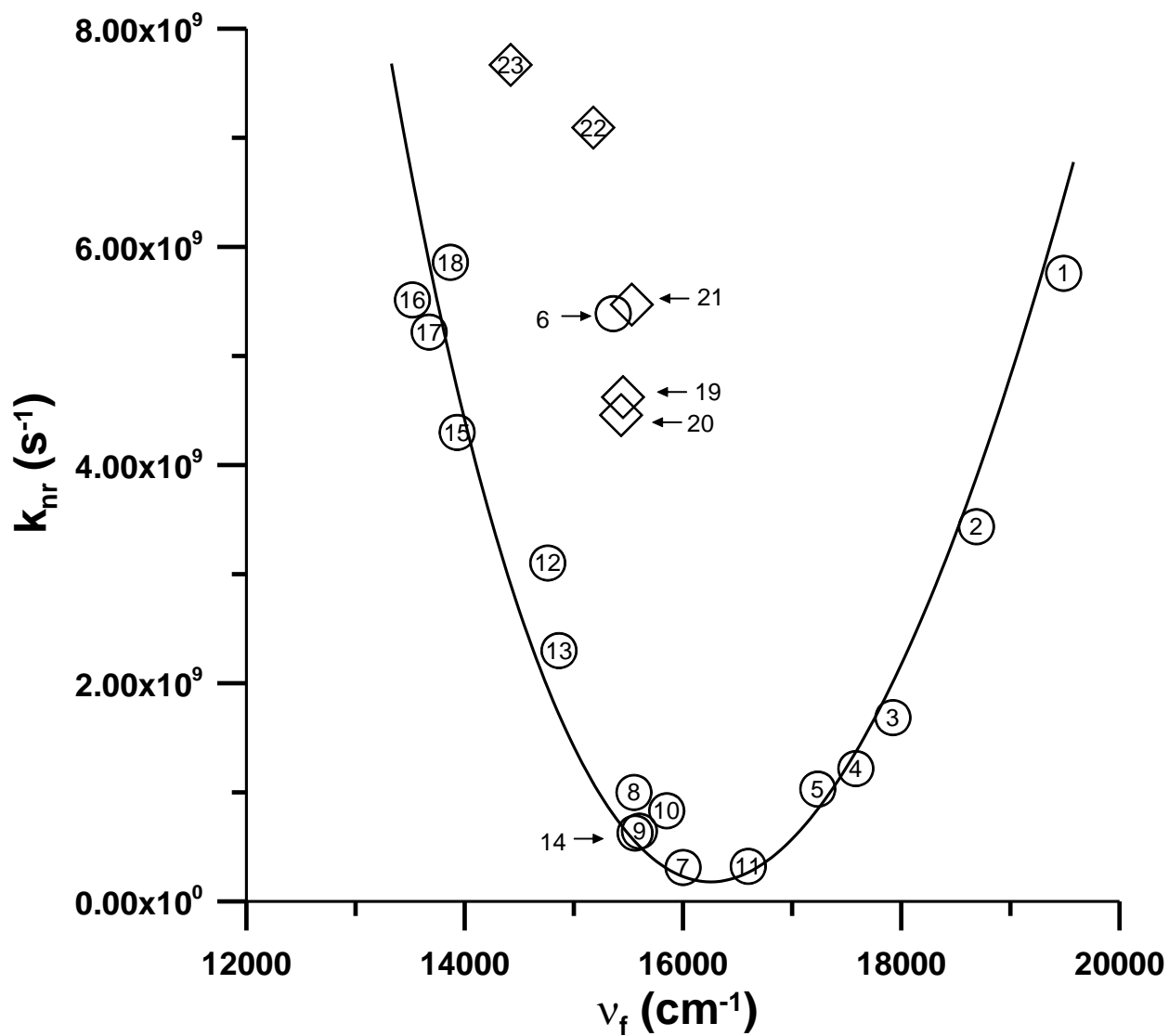
Figure 39. Nonradiative decay constants (k_{nr}) plotted against the fluorescence spectral maxima of Asdimcy1 in various solvents. Circles represent aprotic solvents; diamonds represent protic solvents.

Energy

$S_m(n, \pi^*)$ ———

$S_1(\pi, \pi^*)$ ———

$T_m(n, \pi^*)$

$T_1(\pi, \pi^*)$

S_0 ———
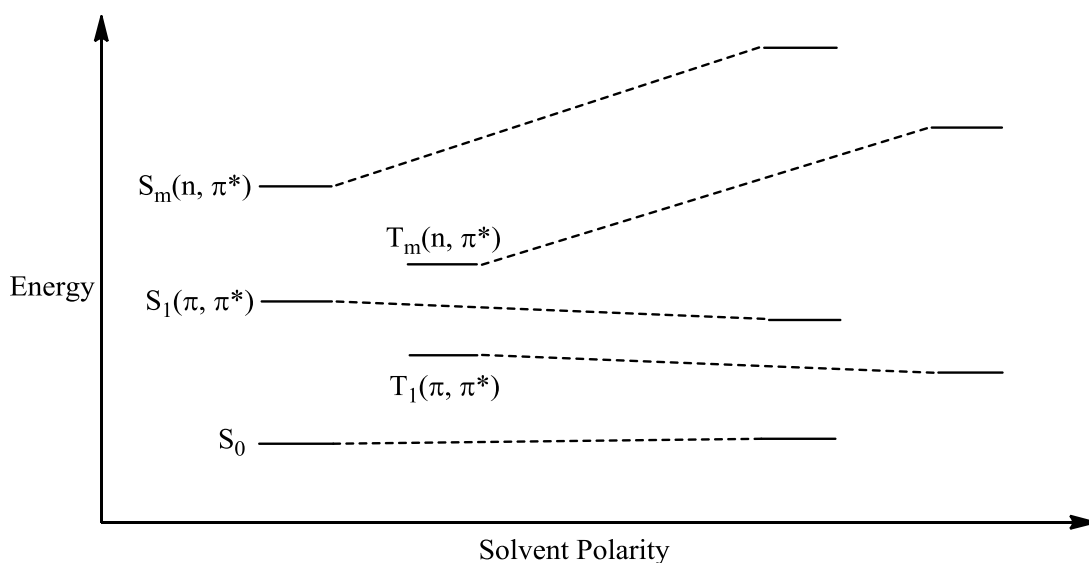
Solvent Polarity

Figure 40. Solvent polarity effect on the states mixed by spin-orbit coupling and vibronic coupling. The increase in the (n, π^*)-(π, π^*) energy gap reduces the effectiveness of mixing singlet and triplet states.

Table 11. TD-DFT computed energy gaps between the lowest lying (n, π^*) and (π, π^*) states and experimental k_{nr} values for Asdimcy1.

	Carbon Tetrachloride	Toluene	Chloroform
$T_3(n, \pi^*)$-$T_1(\pi, \pi^*)$	7138 cm^{-1}	7234 cm^{-1}	8112 cm^{-1}
$S_2(n, \pi^*)$-$S_1(\pi, \pi^*)$	4465 cm^{-1}	4592 cm^{-1}	5384 cm^{-1}
$k_{nr} \times 10^{-8}$ (s^{-1})	57.6	16.9	3.22

The radiative rates of decay (k_f) vary less with solvent and have been plotted against the maximum frequency of fluorescence, as shown in Figure 41. Although somewhat scattered, the experimental k_f values show a general trend towards lower values with smaller ν_f, as predicted by Einstein's treatment of electronic transitions [64c].
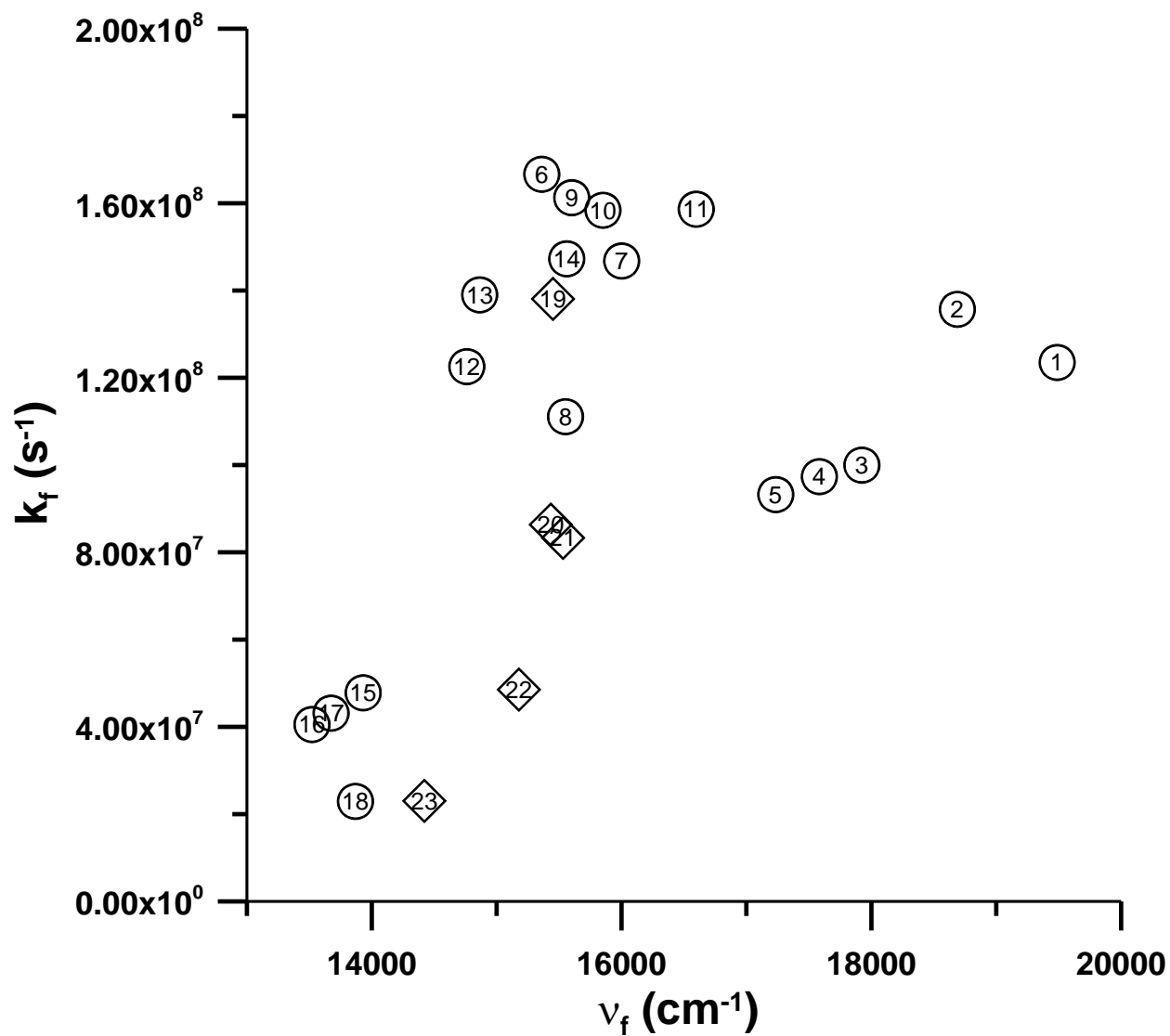
Figure 41. Radiative decay constants (k_f) plotted against the fluorescence spectral maxima of Asdimcy1 in various solvents. Circles represent aprotic solvents; diamonds represent protic solvents.

4.1.5 Two-Photon Absorption (TPA) Cross Sections

It was recently reported that Asdimcy1 exhibits efficient two-photon absorption (TPA) when dissolved in chloroform [10]. The TPA cross section was determined by comparing the two-photon up-converted fluorescence of Asdimcy1 to that of a reference compound. The Dalton$^{©}$ computer program was used to theoretically determine the S_1-S_3 excitation energies for Asdimcy1, which were then used to calculate the TPA cross sections in the gas phase for the first three excited singlet states using equation 2-14. *Ab initio* cc-pVDZ was the level of theory employed for the TPA cross section calculations. The excitation energies computed by cc-pVDZ and presented in Table 12 are close to the TD-DFT results presented earlier in Table 8. The TPA cross sections for $S_0 \rightarrow S_1$ and $S_0 \rightarrow S_3$ excited states were calculated to be 484 GM and 785 GM. These computed values are significantly greater than the experimental value, 17.2 GM, measured in chloroform [10]. Further investigation is necessary to evaluate the relationship between calculated gas phase results and experimental data measured in solution. The data do agree with the experimental finding that Asdimcy1 exhibits significant TPA.

Table 12. Calculated TPA cross sections for Asdimcy1 in the gas phase.

Excited State	Excitation Energy (eV)	δ (cm^4 s $photon^{-1}$)	δ (GM)*
S_1	2.67	4.84×10^{-48}	484
S_2	2.89	2.44×10^{-50}	2.44
S_3	3.65	7.85×10^{-48}	785

*GM stands for [Maria] Göeppert-Mayer, named after the physicist who first proposed two-photon absorption. 1 GM = 10^{-50} cm^4 s $photon^{-1}$.

4.1.6 Conclusions

The computed molecular structure and X-ray results are in excellent agreement for Asdimcy1. The spectroscopic and photophysical properties have been found to vary considerably with solvent. The natures of the low lying excited states have been assigned with the assistance of experimental and theoretical data. The significant internal charge transfer property of this compound is clearly supported by the solvatochromic plots, computed molecular orbitals, and large electronic dipole moment in the excited state. The behavior of k_{nr} with respect to fluorescence wavelength and solvent polarity can be divided into two regions. In region 1, the increase in the rate of internal conversion dominates the competitive decrease in the rate of intersystem crossing; whereas, in region 2, intersystem crossing is the dominant channel of decay from S_1. The variation in the rates of internal conversion and intersystem crossing are interpreted to be related to solvent induced changes in energy gaps on the singlet and triplet spin manifolds.

4.2 Spectroscopic and Photophysical Properties of Alkylamino Substituted 2-Arylidene and 2,5-Diarylidene Cyclopentanone Dyes

4.2.1 Introduction

This section is subdivided into presenting and discussing experimentally observed absorption and fluorescence spectral data of dmab, dmac, bis-dmab, Ashrbor, bis-dmac, and its julolidine analogue, bis-juldmac (for structures, see Figure 2). Section 4.2.2 presents and discusses results of both dmab and dmac and section 4.2.3 presents and discusses the results of bis-dmab, bis-dmac, bis-juldmac, and Ashrbor. Comparative studies of the spectral properties of dmab vs. bis-dmab and dmac vs. bis-dmac, in addition to other alkylamino substituted 2,5-diarylidene cyclopentanone dyes are also discussed.

Photophysical properties involved measuring fluorescence quantum yields (Φ_f) and lifetimes (τ_f) in various solvent systems. Only fluorescence quantum yields are presented for dmab and dmac. First-order radiative (k_f) and nonradiative (k_{nr}) rates of decay have been determined from the Φ_f and τ_f data.

Ground state geometry optimizations at the DFT B3LYP/6-31G(d) level of theory were carried out for all compounds. Minimum energy structures were confirmed by obtaining all positive frequencies for the calculated normal modes of vibration. TD-DFT spectral calculations were also carried out at the B3LYP/6-31G(d) level of theory both in the gas phase and in solvent environment. For solvent calculations, the self-consistent reaction field polarizable continuum model (SCRF PCM) was employed.

4.2.2 Spectroscopic and Photophysical Properties of Alkylamino Substituted (E)-2-Arylidene Cyclopentanones: dmab and dmac

4.2.2.1 dmab

Figure 42 shows the DFT B3LYP/6-31G(d) optimized geometry of dmab along with its computed gas phase dipole moment (6.33 D). As depicted in the side view, dmab exhibits ~11° rotation of the substituted phenyl ring and ~30° rotation in the inner cyclopentanone ring (atoms 1-5-4-3). Using the optimized structure, TD-DFT spectral calculations were carried out in the gas phase and also in four solvent environments (n-hexane, toluene, chloroform, and methanol).
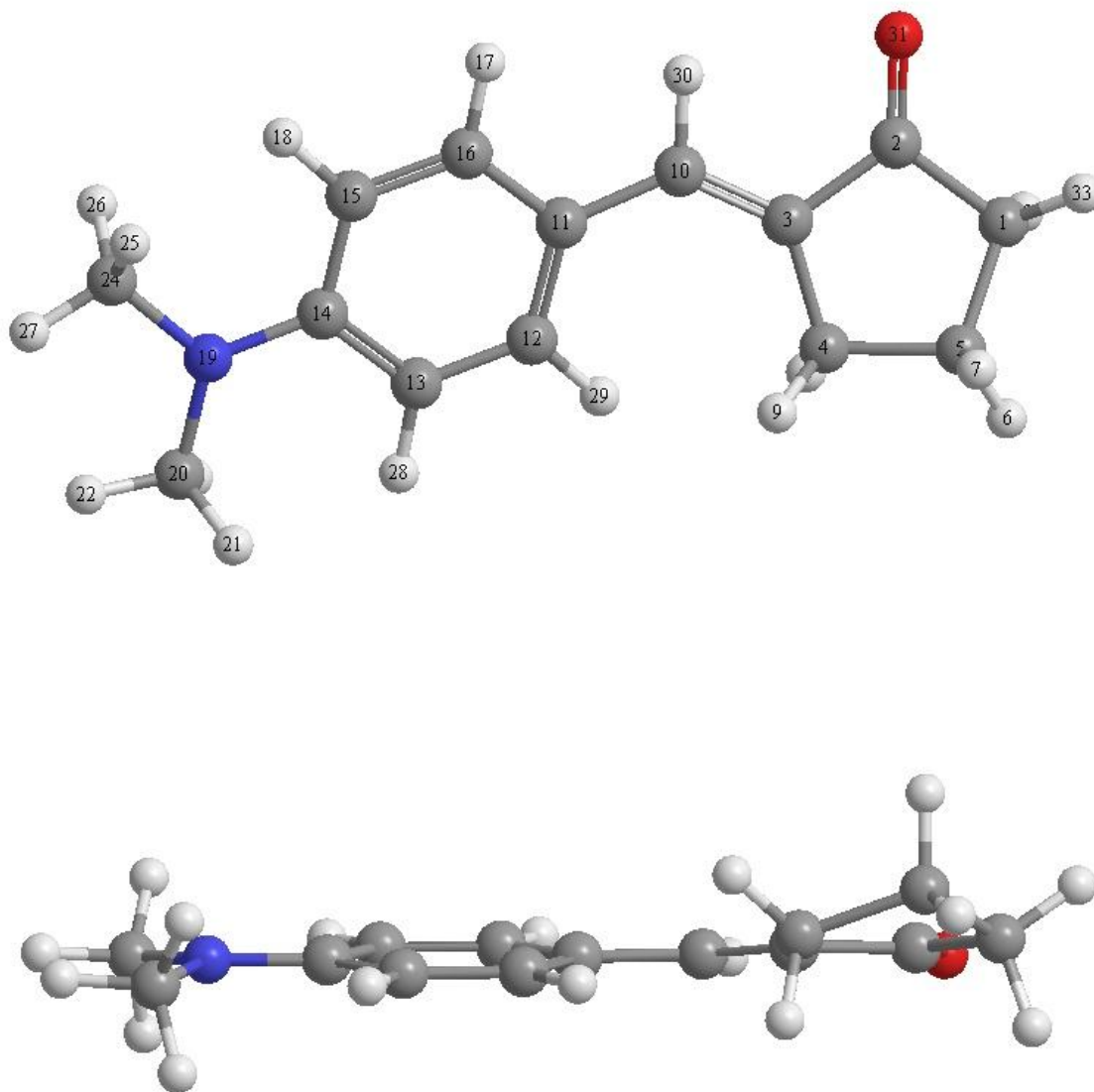
Figure 42. Optimized geometry of dmab at the B3LYP/6-31G(d) level of theory. Gas phase

dipole moment = 6.33 D.

Table 13. B3LYP/6-31G(d) calculated ground state optimized geometry of dmab.

Bond Lengths (Å)	
C_1-C_2	1.53
C_1-C_5	1.54
C_2-C_3	1.49
C_2-O_{31}	1.22
C_3-C_4	1.51
C_3-C_{10}	1.35
C_4-C_5	1.55
C_{10}-C_{11}	1.45
C_{11}-C_{12}	1.41
C_{11}-C_{16}	1.41
C_{12}-C_{13}	1.39
C_{13}-C_{14}	1.42
C_{14}-C_{15}	1.42
C_{14}-N_{19}	1.38
C_{15}-C_{16}	1.39
N_{19}-C_{20}	1.45
N_{19}-C_{24}	1.45

Bond Angles (°)	
C_1-C_2-C_3	107.94
C_1-C_2-O_{31}	125.45
C_1-C_5-C_4	105.04
C_2-C_1-C_5	104.37
C_2-C_3-C_4	108.96
C_2-C_3-C_{10}	119.39
C_3-C_2-O_{31}	126.61
C_3-C_4-C_5	104.45
C_3-C_{10}-C_{11}	131.27
C_4-C_3-C_{10}	131.64
C_{10}-C_{11}-C_{12}	125.05
C_{10}-C_{11}-C_{16}	118.63
C_{11}-C_{12}-C_{13}	121.96
C_{11}-C_{16}-C_{15}	122.52
C_{12}-C_{11}-C_{16}	116.31
C_{12}-C_{13}-C_{14}	121.30
C_{13}-C_{14}-C_{15}	117.07
C_{13}-C_{14}-N_{19}	121.43
C_{14}-C_{15}-C_{16}	120.81
C_{14}-N_{19}-C_{20}	119.94
C_{14}-N_{19}-C_{24}	119.87
C_{15}-C_{14}-N_{19}	121.49
C_{20}-N_{19}-C_{24}	119.11

Atomic Charges	
C_1	-0.357
C_2	0.396
C_3	0.0935
C_4	-0.354
C_5	-0.290
C_{10}	-0.252
C_{11}	0.182
C_{12}	-0.192
C_{13}	-0.196
C_{14}	0.375
C_{15}	-0.197
C_{16}	-0.196
N_{19}	-0.472
C_{24}	-0.313
O_{31}	-0.484

Dihedral Angles (°)	
C_1-C_2-C_{11}-C_{12}	-10.65
C_1-C_5-C_4-C_3	-29.03
C_1-C_5-C_{11}-C_{12}	29.56
C_4-C_3-C_{11}-C_{12}	-11.07
C_4-C_3-C_{11}-C_{16}	16.07

Both the absorption and fluorescence spectral properties of dmab were examined in nineteen solvents of differing polarities, presented in Table 14. Experimental absorption and fluorescence spectra in seven of the solvents studied are shown in Figure 43. Although hardly any solvatochromic shifting was observed in the absorption spectra, a noticeable bathochromic shift was observed in the fluorescence spectra in going from n-hexane to methanol. The larger degree of solvatochromism in the fluorescence compared to absorption are seen in Figure 44 where the frequencies of absorbance and fluorescence spectral maxima are plotted against the $E_T(30)$ scale. Examination of both tabulated spectral data (Table 14) and Figure 44 show that minor solvatochromic behavior is observed in absorption, with the band maximum varying from 28,043 cm^{-1} (357 nm) in n-hexane to 25,374 cm^{-1} (394 nm) in 1-propanol. A steeper slope is observed in the fluorescence plot with corrected emission energies ranging from 24,667 cm^{-1} (405 nm) in n-hexane to 19,860 cm^{-1} (504 nm) in N,N-dimethylformamide. Fluorescence quantum yields of dmab ranged between 0.0006 (in several solvents) to 0.01 (in DMF). Fluorescence lifetimes of dmab were not measured because of weak fluorescence.

Also noteworthy to consider is that although the protic solvents do not appear to be anomalous in the absorption plot, it appears that they fall on a distinct trendline in the fluorescence plot. As previously asserted in the discussion on the asymmetric dye, Asdimcy1, a transfer of internal electron charge to the carbonyl oxygen following photoexcitation from S_0 to S_1 causes the molecule to become a stronger base in the excited state, thereby resulting in stronger hydrogen bonding with protic solvents [15, 63].

Table 14. Spectroscopic and photophysical properties of dmab in various solvents.

Solvent	ν_{flu} (cm^{-1})	ν_{abs} (cm^{-1})	$\Delta\nu$ (cm^{-1})	Δf^*	$E_T(30)^*$ (kcal mol^{-1})	Φ_f
Methanol	20,495 (488 nm)	25,556 (391 nm)	5061	0.3093	55.4	0.002
Ethanol	20,844 (480 nm)	25,641 (390 nm)	4797	0.2887	51.9	0.003
1-Propanol	20,864 (479 nm)	25,374 (394 nm)	4510	0.2746	50.7	0.003
1-Butanol	20,864 (479 nm)	25,504 (392 nm)	4640	0.2642	50.2	0.003
2-Propanol	21,203 (472 nm)	25,615 (390 nm)	4412	0.2769	48.4	0.002
Acetonitrile	20,495 (488 nm)	26,323 (380 nm)	5828	0.3054	45.6	0.005
DMSO	20,290 (493 nm)	26,082 (383 nm)	5792	0.2637	45.1	-
N,N-DMF	19,860 (504 nm)	26,082 (383 nm)	6222	0.2752	43.2	0.01
Acetone	21,100 (474 nm)	26,392 (379 nm)	5292	0.2843	42.2	0.004
DCM	21,192 (472 nm)	26,089 (383 nm)	4897	0.2171	40.7	0.003
Pyridine	20,813 (480 nm)	26,076 (384 nm)	5263	0.2124	40.5	0.008
Chloroform	21,326 (469 nm)	26,082 (383 nm)	4756	0.1491	39.1	0.003
EtOAc	22,320 (448 nm)	26,998 (370 nm)	4678	0.1996	38.1	0.002
Diethyl ether	23,806 (420 nm)	27,397 (365 nm)	3591	0.1669	34.5	0.0006
Benzene	23,007 (435 nm)	26,309 (380 nm)	3302	0.0031	34.3	0.003
Toluene	23,611 (424 nm)	26,824 (373 nm)	3213	0.0131	33.9	0.0009
CS$_2$	23,724 (422 nm)	25,840 (387 nm)	2116	-0.0007	32.8	0.0006
CCl$_4$	23,201 (431 nm)	27,005 (370 nm)	3804	0.0119	32.4	0.0006
n-Hexane	24,667 (405 nm)	28,043 (357 nm)	3376	-0.0004	31.0	-

*Both Δf and $E_T(30)$ values are taken from Suppan, P. and Ghonheim, N., in *Solvatochromism*, The Royal Society of Chemistry, Cambridge, 1997.
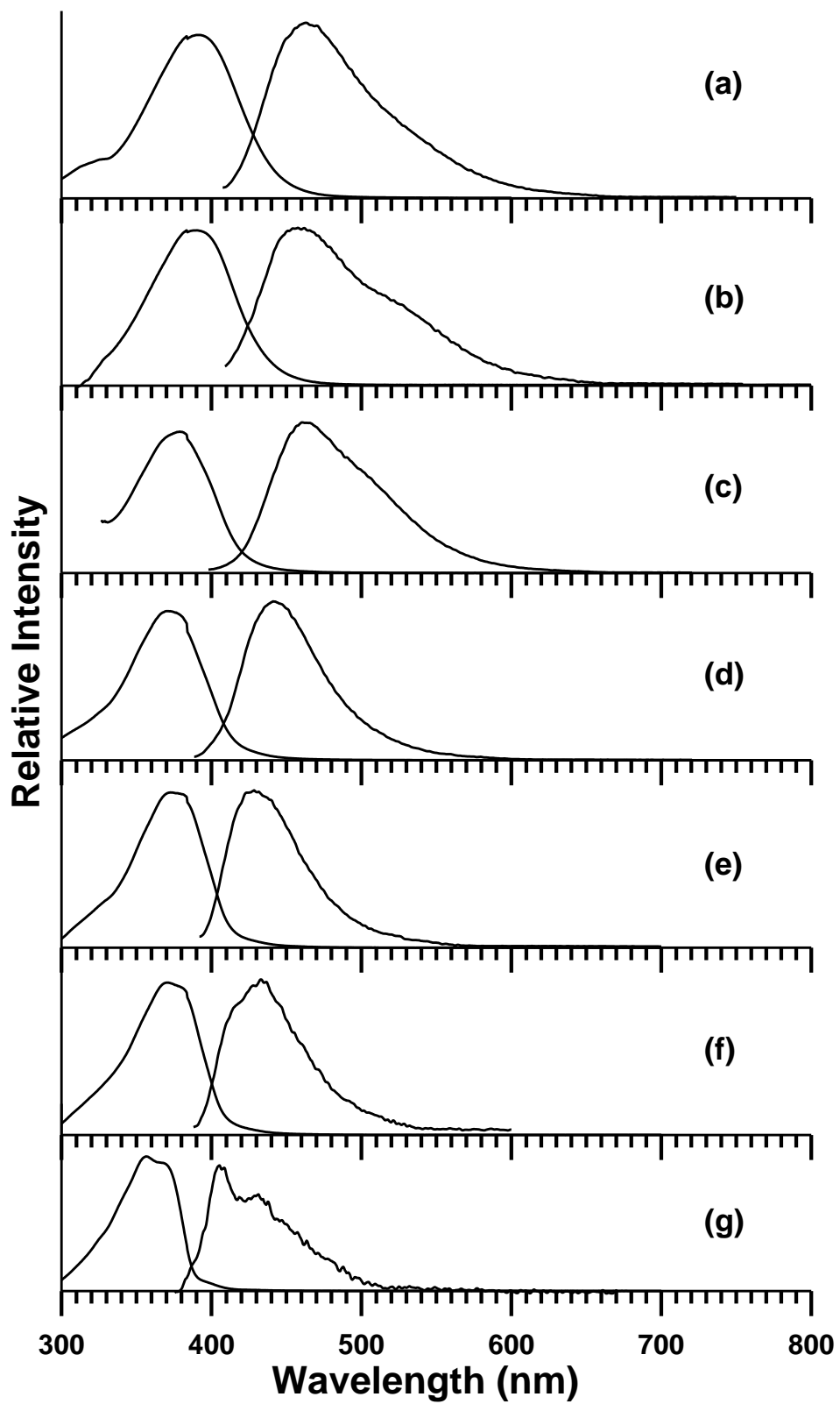
Figure 43. Absorption and fluorescence emission spectra of dmab in (a) methanol, (b) 2-propanol, (c) acetone, (d) ethyl acetate, (e) toluene, (f) carbon tetrachloride, and (g) n-hexane.
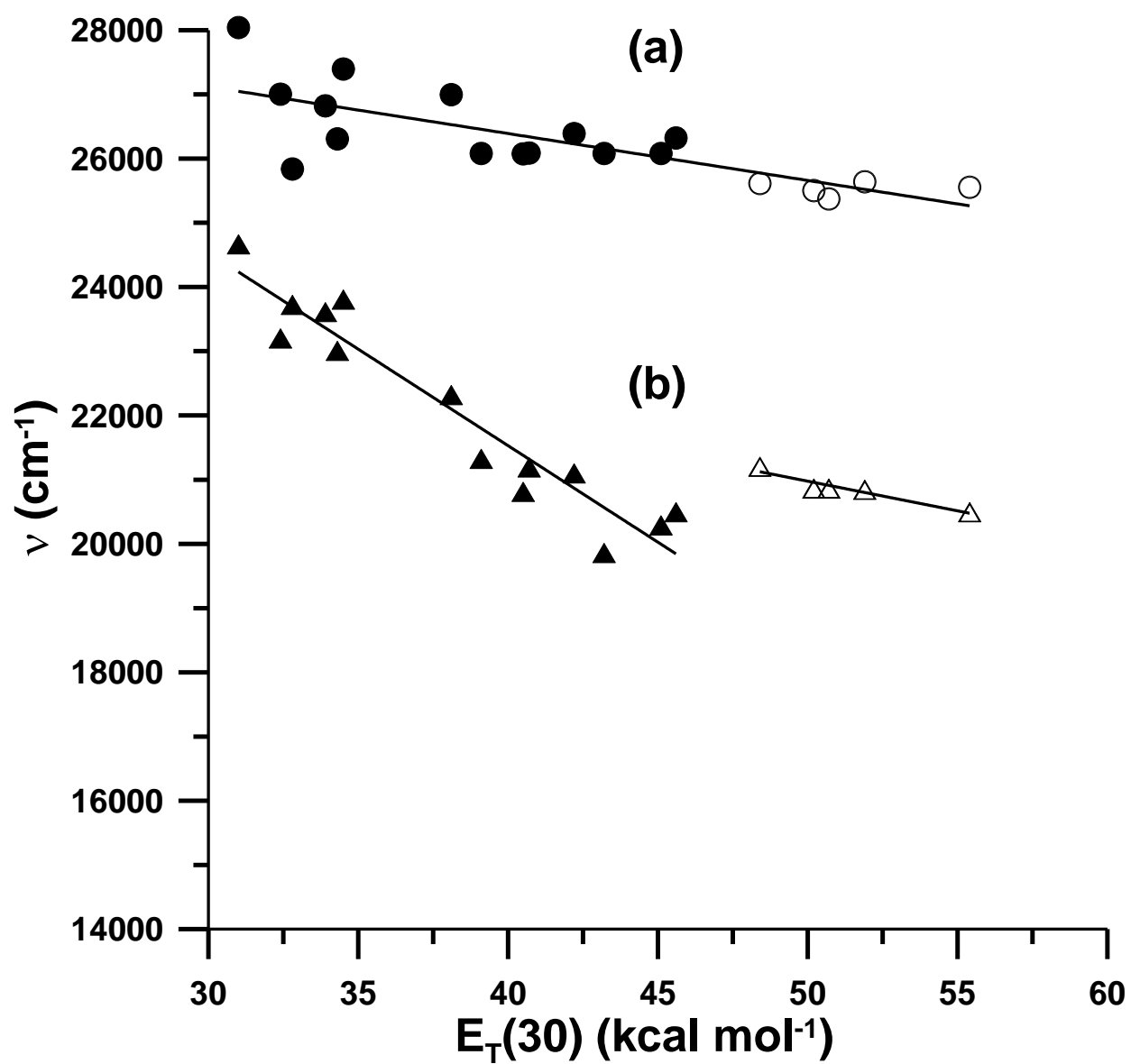
Figure 44. Plot of (a) absorption and (b) fluorescence spectral maxima of dmab in various solvents against the $E_T(30)$ scale. Solid symbols represent aprotic solvents; open symbols represent protic solvents.

The excited state dipole moment of dmab was calculated using the Lippert-Mataga approach. A Lippert-Mataga plot of Stokes shift (Δv) for dmab against the solvent's orientation polarization function (Δf) in various solvents is shown in Figure 45. Similar to the fluorescence plot in Figure 44, it appears that the protic solvents lie on a separate line than the aprotic solvents. Application of the Lippert-Mataga method to the data in nonalcohols and using the ground state dipole moment and Onsager cavity radius of dmab computed to be 6.33 D and 4.88 Å by B3LYP/6-31G(d), the excited state dipole moment is found to be 16.6 D ($\Delta\mu = 10.3$ D).
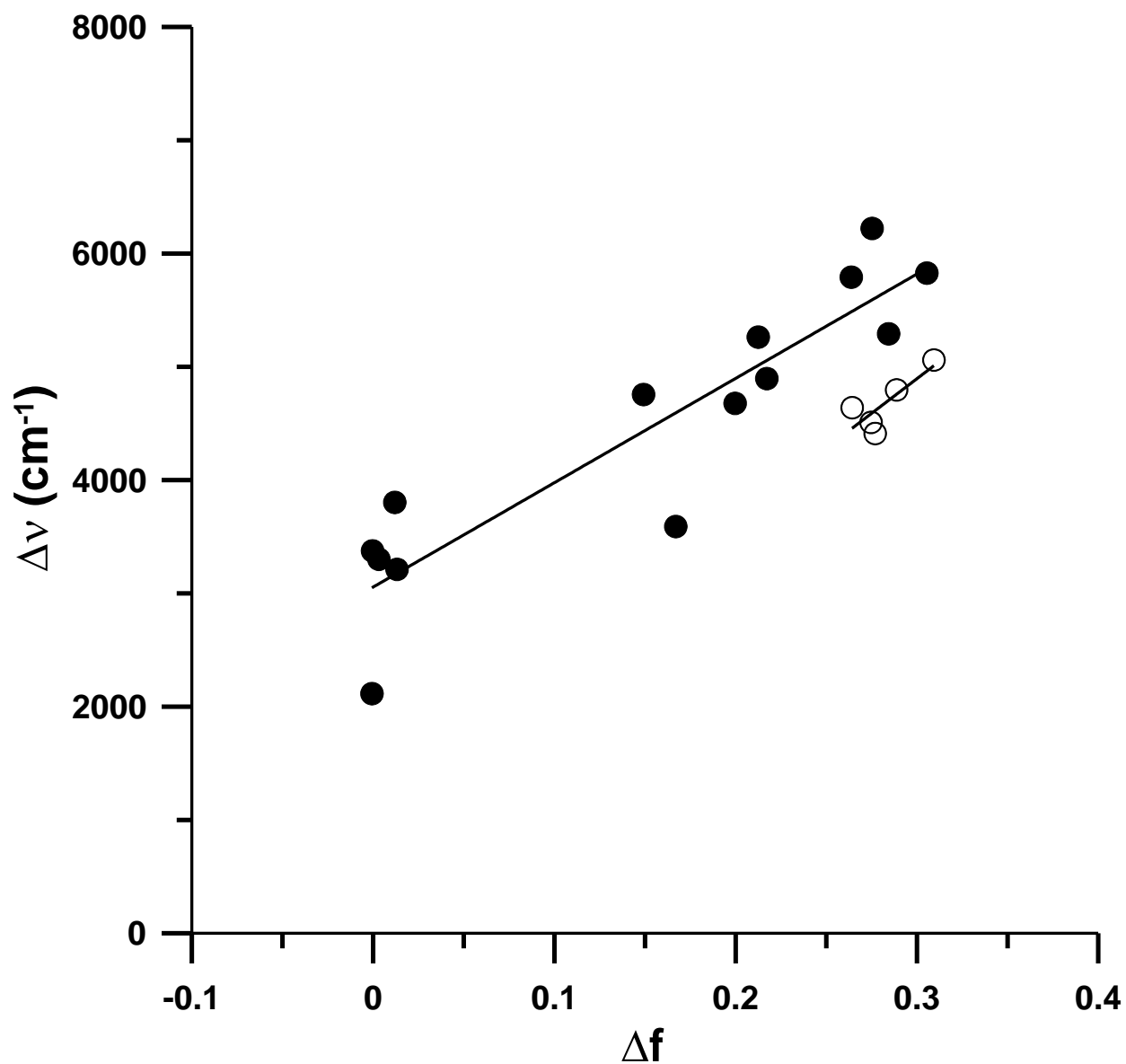
Figure 45. Lippert-Mataga plot of dmab in various solvents. Solid symbols represent aprotic

solvents; open symbols represent protic solvents.

TD-DFT spectral calculations of dmab for the first three excited singlet and triplet states both in the gas phase and in solvent environments are presented in Table 15 and computed molecular orbitals are shown in Figure 46. In the gas phase, excitation to S_1 is predicted to be a weak transition localized at 368 nm (f = 0.014) with HOMO-1 (n) → LUMO (π^*) as the orbital configuration. Excitation to the S_2 state is predicted to be a strong transition occurring at 344 nm (f = 0.80) with major CI configuration of HOMO → LUMO, corresponding to a (π, π^*) transition.

SCRF PCM solvent calculations show that in going from the gas phase to solvent environment, the energy of the $^1(\pi, \pi^*)$ state falls below the $^1(n, \pi^*)$ state, regardless of solvent polarity. In the gas phase, the $^1(\pi, \pi^*)$ state, predicted to be S_2, is localized at 3.60 eV (344 nm). In solvent, S_1 is assigned an orbital configuration of (π, π^*) and the energy of this state continuously decreases with respect to an increase in solvent polarity. The energy of the $S_1(\pi, \pi^*)$ state decreases in the following order: 3.40 eV (365 nm, n-hexane), 3.36 eV (369 nm, toluene), 3.34 eV (372 nm, chloroform), and 3.32 eV (374 nm, methanol). This is characteristic of the typical bathochromic shifting observed with respect to an increase in solvent polarity. The inversion of the $^1(\pi, \pi^*)$ state from S_2 in the gas phase to S_1 in solvent provides a reasonable argument as to why fluorescence was observed experimentally in all solvents.

The $^1(n, \pi^*)$ state inverts from being S_1 in the gas phase to S_2 in solvent. In the gas phase, the $^1(n, \pi^*)$ state is computed to be located at 3.37 eV (368 nm). In solvent, the $^1(n, \pi^*)$ state undergoes a characteristic hypsochromic shift, increasing in the following order: 3.46 eV (358 nm, n-hexane), 3.47 eV (358 nm, toluene), 3.50 eV (354 nm, chloroform), and 3.54 eV (350 nm, methanol). As depicted in Figure 47, good agreement is established between the experimental

absorption spectra of dmab and the TD-DFT calculations in each of the four solvents with excitation to $S_1(\pi, \pi^*)$ being the strongest electronic transition. It is also shown in Figure 47 that from the TD-DFT data, with respect to an increase in solvent polarity, (i) the $S_2(n, \pi^*)$-$S_1(\pi, \pi^*)$ energy gap becomes larger, and (ii) the ratio of the oscillator strengths of $S_2(n, \pi^*)$ to $S_1(\pi, \pi^*)$ becomes smaller. The increase in the S_2-S_1 energy gap is attributed to the hypsochromic shift of (n, π^*) and the bathochromic shift of (π, π^*).

The unusually large oscillator strength predicted for the lowest $n \rightarrow \pi^*$ transition of dmab in n-hexane (f = 0.32) appears to be a manifestation of a well-known limitation with the TD-DFT method, where nearly degenerate excited states undergo strong configuration mixing [66]. This mixing causes a blending of the properties of the nearly degenerate excited states. The energy separation of $S_1(\pi, \pi^*)$ and $S_2(n, \pi^*)$ is only 536 cm^{-1}, hence the blending of $^1(\pi, \pi^*)$ and $^1(n, \pi^*)$ properties, including the oscillator strength. As seen from Table 16, the larger the $^1(n, \pi^*)$-$^1(\pi, \pi^*)$ energy gap, the smaller the $^1(n, \pi^*)$ oscillator strength. For large gaps, e.g. methanol, the low oscillator strength expected to be computed for an $n \rightarrow \pi^*$ transition is observed (f = 0.015).

Table 15. TD-DFT spectral calculations of dmab both in the gas phase and in solvent environments at the B3LYP/6-31G(d) level of theory.

Solvent	State	Transition Energy			f	MO	CI Coef.
		eV	cm^{-1}	nm			
Gas (μ = 6.33 D)	T_1 (π, π^*)	2.23	17986	556	0.00	56$\rightarrow$59	-0.21201
						58$\rightarrow$59	0.66492
	T_2 (n, π^*)	2.97	23923	418	0.00	57$\rightarrow$59	0.67952
						57$\rightarrow$61	-0.17224
	S_1 (n, π^*)	3.37	27174	368	0.014	57$\rightarrow$59	0.68352
						57$\rightarrow$61	-0.12868
						58$\rightarrow$59	-0.11341
	S_2 (π, π^*)	3.60	29070	344	0.80	57$\rightarrow$59	0.11439
						58$\rightarrow$59	0.69446
	T_3 (π, π^*)	3.65	29499	339	0.00	54$\rightarrow$59	-0.15933
						56$\rightarrow$59	0.59462
						58$\rightarrow$59	0.18001
						58$\rightarrow$61	0.24499
	S_3 (π, π^*)	4.29	34602	289	0.013	55$\rightarrow$59	-0.35110
						58$\rightarrow$60	0.59785
n-Hexane (μ = 7.06 D)	T_1 (π, π^*)	2.21	17825	561	0.00	56$\rightarrow$59	-0.20730
						58$\rightarrow$59	0.66657
	T_2 (n, π^*)	3.04	24510	408	0.00	57$\rightarrow$59	0.68076
						57$\rightarrow$61	-0.16828
	S_1 (π, π^*)	3.40	27397	365	0.61	57$\rightarrow$59	-0.38874
						58$\rightarrow$59	0.58301
	S_2 (n, π^*)	3.46	27933	358	0.32	57$\rightarrow$59	0.57424
						58$\rightarrow$59	0.39733
	T_3 (π, π^*)	3.62	29155	343	0.00	54$\rightarrow$59	-0.15586
						55$\rightarrow$59	-0.11207
						56$\rightarrow$59	0.60376
						58$\rightarrow$59	0.18408
						58$\rightarrow$61	0.21836
	S_3 (π, π^*)	4.24	34247	292	0.016	55$\rightarrow$59	-0.34956
						56$\rightarrow$59	-0.10331
						58$\rightarrow$60	0.59845

Toluene (μ = 7.28 D)	T_1 (π, π*)	2.20	17762	563	0.00	56→59	-0.20555
						58→59	0.66720
	T_2 (n, π*)	3.06	24691	405	0.00	57→59	0.68110
						57→61	-0.16711
	S_1 (π, π*)	3.36	27100	369	0.86	57→59	-0.19696
						58→59	0.67614
	S_2 (n, π*)	3.47	27933	358	0.091	57→59	0.66502
						57→61	-0.11772
						58→59	0.20239
	T_3 (π, π*)	3.61	29070	344	0.00	54→59	-0.15485
						55→59	-0.11650
						56→59	0.60605
						58→59	0.18456
						58→61	0.21063
	S_3 (π, π*)	4.23	34130	293	0.016	55→59	-0.34946
						56→59	-0.10439
						58→60	0.59848
Chloroform (μ = 7.77 D)	T_1 (π, π*)	2.18	17606	568	0.00	56→59	-0.20125
						58→59	0.66882
	T_2 (n, π*)	3.11	25063	399	0.00	57→59	0.68182
						57→61	-0.16455
	S_1 (π, π*)	3.34	26882	372	0.91	57→59	-0.10821
						58→59	0.69694
	S_2 (n, π*)	3.50	28249	354	0.030	57→59	0.68535
						57→61	-0.12084
						58→59	0.11213
	T_3 (π, π*)	3.58	28902	346	0.00	54→59	-0.15267
						55→59	-0.12329
						56→59	0.61084
						58→59	0.18447
						58→61	0.19416
	S_3 (π, π*)	4.20	33898	295	0.014	55→59	-0.35707
						56→59	-0.10785
						58→60	0.59350

						56→59	-0.19620
	T_1 (π, π*)	2.16	17422	574	0.00	58→59	0.67082
						57→59	0.68251
	T_2 (n, π*)	3.15	25445	393	0.00	57→61	-0.16181
	S_1 (π, π*)	3.32	26738	374	0.89	58→59	0.70158
						57→59	0.69001
Methanol	S_2 (n, π*)	3.54	28571	350	0.015	57→61	-0.12013
(μ = 8.30 D)						54→59	-0.15030
						55→59	-0.12441
	T_3 (π, π*)	3.55	28653	349	0.00	56→59	0.61610
						58→59	0.18270
						58→61	0.17783
						55→59	-0.36708
	S_3 (π, π*)	4.17	33670	297	0.012	56→59	-0.10784
						58→60	0.58750

LUMO (π^*, #59)
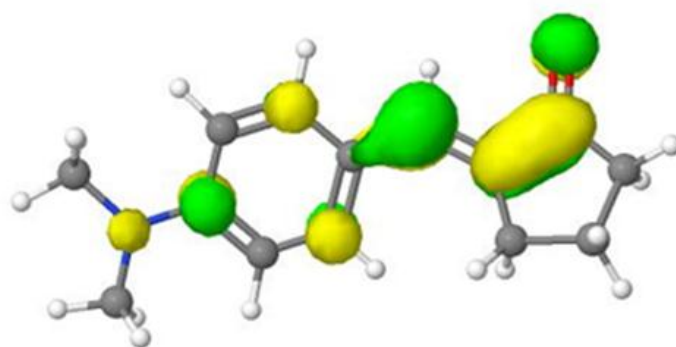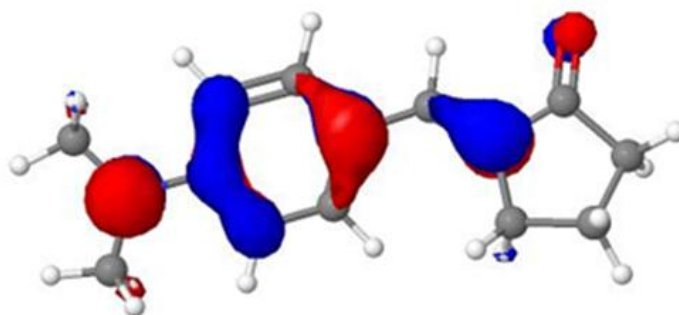
HOMO (π, #58)
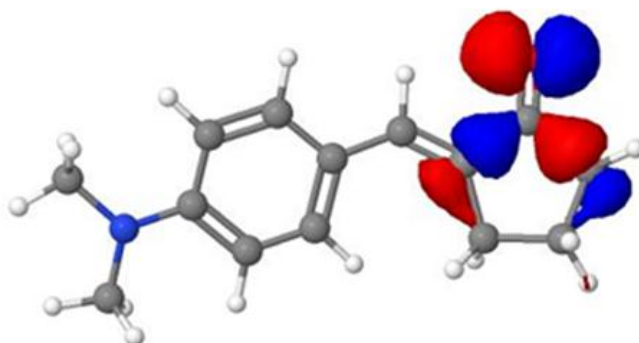
HOMO-1 (n, #57)

Figure 46. Computed molecular orbitals of dmab in the gas phase.
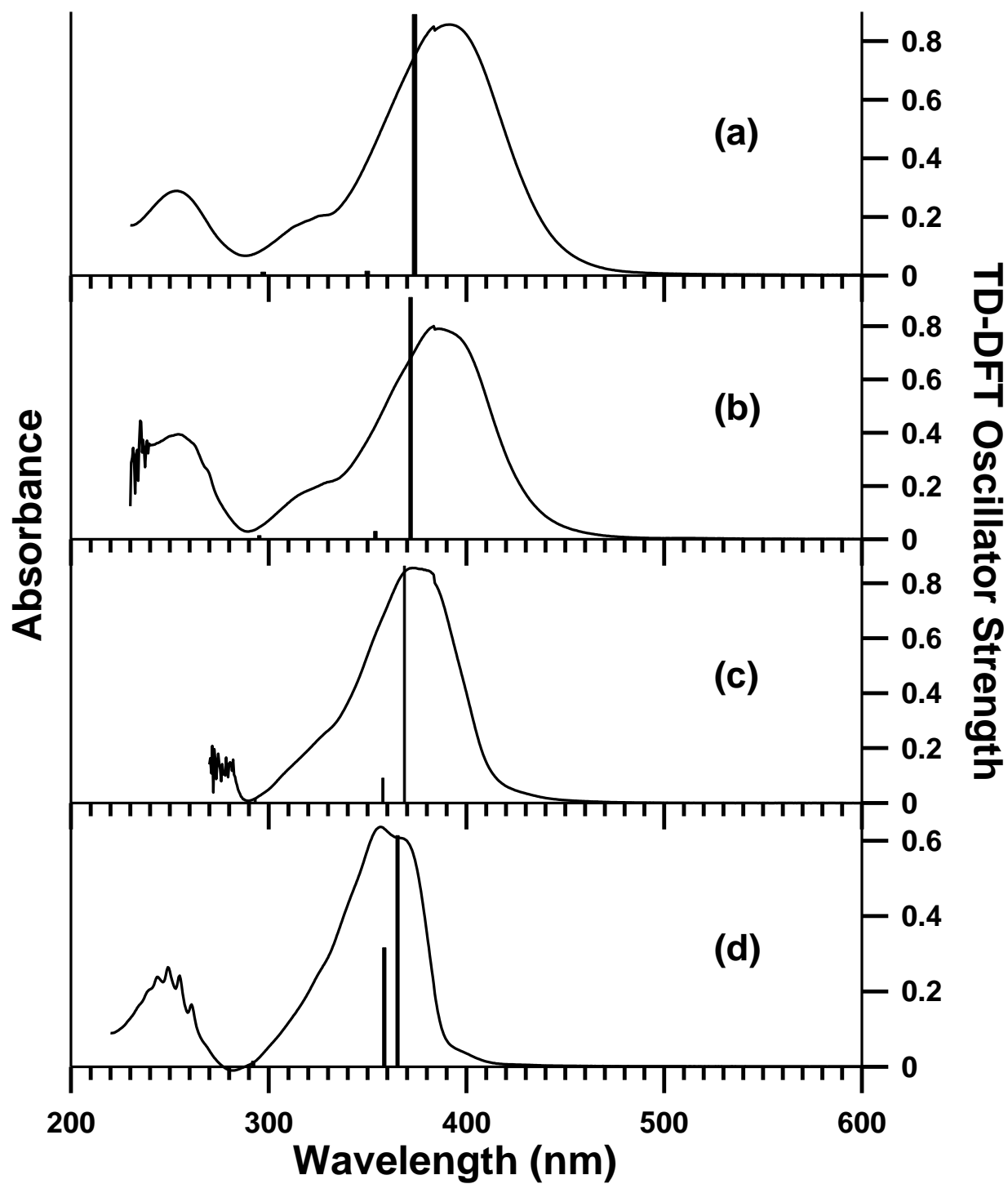
Figure 47. Experimental absorption spectra of dmab in (a) methanol, (b) chloroform, (c) toluene, and (d) n-hexane and their corresponding TD-DFT oscillator strengths at the B3LYP/6-31G(d) level of theory.

Table 16. TD-DFT energy gaps of the lowest lying $^1(\pi, \pi^*)$ and $^1(n, \pi^*)$ states and f values for the $^1(n, \pi^*)$ states of dmab.

Solvent	$\left| \Delta E[^1(n, \pi^*)-^1(\pi, \pi^*)] \right|$ (cm^{-1})	$f[^1(n, \pi^*)]$
n-Hexane	536	0.32
Toluene	833	0.091
Chloroform	1367	0.030
Methanol	1833	0.015
Gas	1896	0.014

4.2.2.2 dmac

Figure 48 shows the gas phase optimized geometry of dmac (the two carbon homologue of dmab) at the DFT B3LYP/6-31G(d) level of theory. As shown in the side view, contrary to dmab, the molecule is planar except for nonplanarity in the inner cyclopentanone ring with ~30° torsional angle (atoms 1-5-4-3).
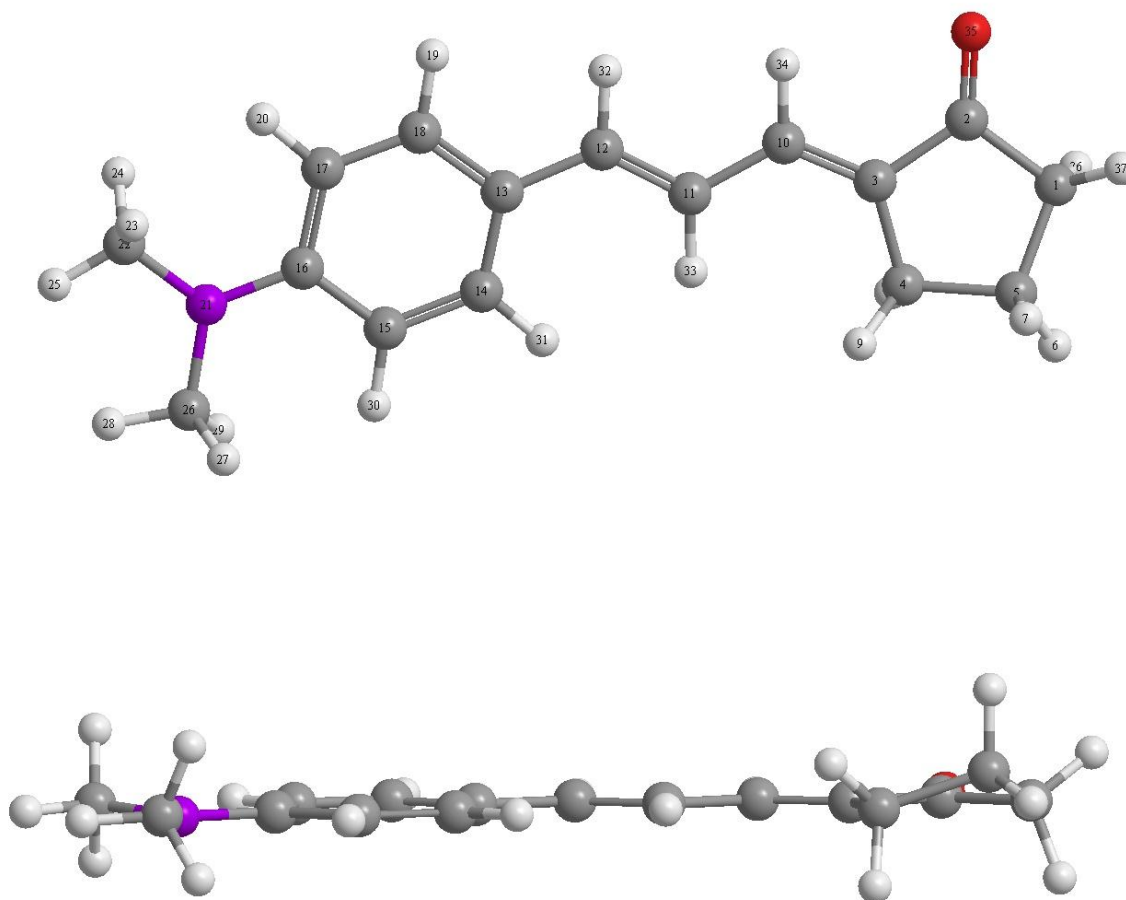
Figure 48. Optimized geometry of dmac at the B3LYP/6-31G(d) level of theory. Gas phase dipole moment = 7.39 D.

Table 17. B3LYP/6-31G(d) calculated ground state optimized geometry of dmac.

Bond Lengths (Å)	
C_1-C_2	1.53
C_1-C_5	1.54
C_2-C_3	1.48
C_2-O_{35}	1.22
C_3-C_4	1.51
C_3-C_{10}	1.36
C_4-C_5	1.55
C_{10}-C_{11}	1.44
C_{11}-C_{12}	1.36
C_{12}-C_{13}	1.45
C_{13}-C_{14}	1.41
C_{13}-C_{18}	1.41
C_{14}-C_{15}	1.38
C_{16}-C_{17}	1.42
C_{17}-C_{18}	1.39
N_{21}-C_{22}	1.45
N_{21}-C_{26}	1.45

Bond Angles (°)	
C_1-C_2-C_3	107.76
C_1-C_2-O_{35}	125.62
C_1-C_5-C_4	104.85
C_2-C_1-C_5	104.36
C_2-C_3-C_4	109.23
C_2-C_3-C_{10}	121.19
C_3-C_2-O_{35}	126.61
C_3-C_4-C_5	104.07
C_3-C_{10}-C_{11}	126.70
C_4-C_3-C_{10}	129.58
C_{10}-C_{11}-C_{12}	122.55
C_{11}-C_{12}-C_{13}	128.21
C_{12}-C_{13}-C_{14}	124.00
C_{12}-C_{13}-C_{18}	119.57
C_{13}-C_{14}-C_{15}	122.00
C_{13}-C_{18}-C_{17}	122.42
C_{14}-C_{13}-C_{18}	116.44
C_{14}-C_{15}-C_{16}	121.23
C_{15}-C_{16}-C_{17}	117.08
C_{15}-C_{16}-N_{21}	121.36
C_{16}-C_{17}-C_{18}	120.83
C_{16}-N_{21}-C_{22}	119.85
C_{16}-N_{21}-C_{26}	119.96
C_{17}-C_{16}-N_{21}	121.56
C_{22}-N_{21}-C_{26}	119.17

Atomic Charges	
C_1	-0.357
C_2	0.394
C_3	0.0734
C_4	-0.345
C_5	-0.287
C_{10}	-0.161
C_{11}	-0.124
C_{12}	-0.185
C_{13}	0.175
C_{14}	-0.188
C_{15}	-0.193
C_{16}	0.374
C_{17}	-0.195
C_{18}	-0.203
N_{21}	-0.472
C_{22}	-0.314
C_{26}	-0.313
O_{35}	-0.483

Dihedral Angles (°)	
C_1-C_5-C_4-C_3	-30.05
C_1-C_5-C_{13}-C_{14}	19.55
C_1-C_5-C_{13}-C_{18}	-27.99
C_4-C_3-C_{13}-C_{14}	-0.25
C_4-C_3-C_{13}-C_{18}	0.47

Both the absorption and fluorescence spectral properties of dmac were examined in eighteen solvents of differing polarities (Table 18). Experimental absorption and fluorescence spectra in seven of the solvents studied are shown in Figure 49. Similar to dmab, although little solvatochromic shifting is observed in the absorption spectra, a significant bathochromic shift is observed in the fluorescence spectra in going from n-hexane to methanol. The solvatochromism in absorption and fluorescence are shown in Figure 50 where frequencies of spectral maxima are plotted against the $E_T(30)$ scale. Compound dmac undergoes a small bathochromic shift in absorption in going from n-hexane (25,381 cm^{-1}, 394 nm) to 1-butanol (23,529 cm^{-1}, 425 nm). More pronounced red shifting is observed in fluorescence, with corrected emission energies ranging from 21,315 cm^{-1} (469 nm) in n-hexane to 16,280 cm^{-1} (614 nm) in methanol. In comparing dmac with dmab, the overall solvatochromic shift in fluorescence to the red was 228 cm^{-1} larger, which is consistent with a higher degree of internal charge transfer for dmac. Furthermore, the fluorescence quantum yields of dmac are also very low, ranging between 0.001 (in n-hexane) to 0.01 (in dimethylformamide, pyridine, and methanol). Fluorescence lifetimes were not measured due to weak fluorescence.

Table 18. Spectroscopic and photophysical properties of dmac in various solvents.

Solvent	ν_{fl} (cm^{-1})	ν_{abs} (cm^{-1})	$\Delta\nu$ (cm^{-1})	Δf*	$E_T(30)$* (kcal mol^{-1})	Φ_f
Methanol	16,280 (614 nm)	23,810 (420 nm)	7530	0.3093	55.4	0.01
Ethanol	16,620 (602 nm)	23,697 (422 nm)	7077	0.2887	51.9	0.009
1-Propanol	16,825 (594 nm)	23,697 (422 nm)	6872	0.2746	50.7	0.007
1-Butanol	16,945 (590 nm)	23,529 (425 nm)	6584	0.2642	50.2	0.008
2-Propanol	17,080 (585 nm)	23,810 (420 nm)	6730	0.2769	48.4	0.007
Acetonitrile	17,350 (576 nm)	24,450 (409 nm)	7100	0.3054	45.6	0.008
N,N-DMF	17,370 (576 nm)	24,038 (416 nm)	6668	0.2752	43.2	0.01
Acetone	17,900 (559 nm)	24,510 (408 nm)	6610	0.2843	42.2	0.007
Dichloromethane	18,065 (554 nm)	24,038 (416 nm)	5973	0.2171	40.7	0.007
Pyridine	17,700 (565 nm)	23,810 (420 nm)	6110	0.2124	40.5	0.01
Chloroform	18,435 (542 nm)	23,866 (419 nm)	5431	0.1491	39.1	0.005
Ethyl Acetate	18,875 (530 nm)	24,752 (404 nm)	5877	0.1996	38.1	0.004
Tetrahydrofuran	17,890 (559 nm)	24,510 (408 nm)	6620	0.2104	37.4	0.004
Diethyl Ether	20,000 (500 nm)	25,063 (399 nm)	5063	0.1669	34.5	0.002
Benzene	19,450 (514 nm)	24,331 (411 nm)	4881	0.0031	34.3	0.004
Toluene	19,750 (506 nm)	24,450 (409 nm)	4700	0.0131	33.9	0.003
CCl$_4$	20,065 (498 nm)	24,570 (407 nm)	4505	0.0119	32.4	0.003
n-Hexane	21,315 (469 nm)	25,381 (394 nm)	4066	-0.0004	31.0	0.001

*Both Δf and $E_T(30)$ values are taken from Suppan, P. and Ghonheim, N., in *Solvatochromism*, The Royal Society of Chemistry, Cambridge, 1997; and Lide, D. R., *CRC Handbook of Chemistry and Physics*, 89th ed., 2008.
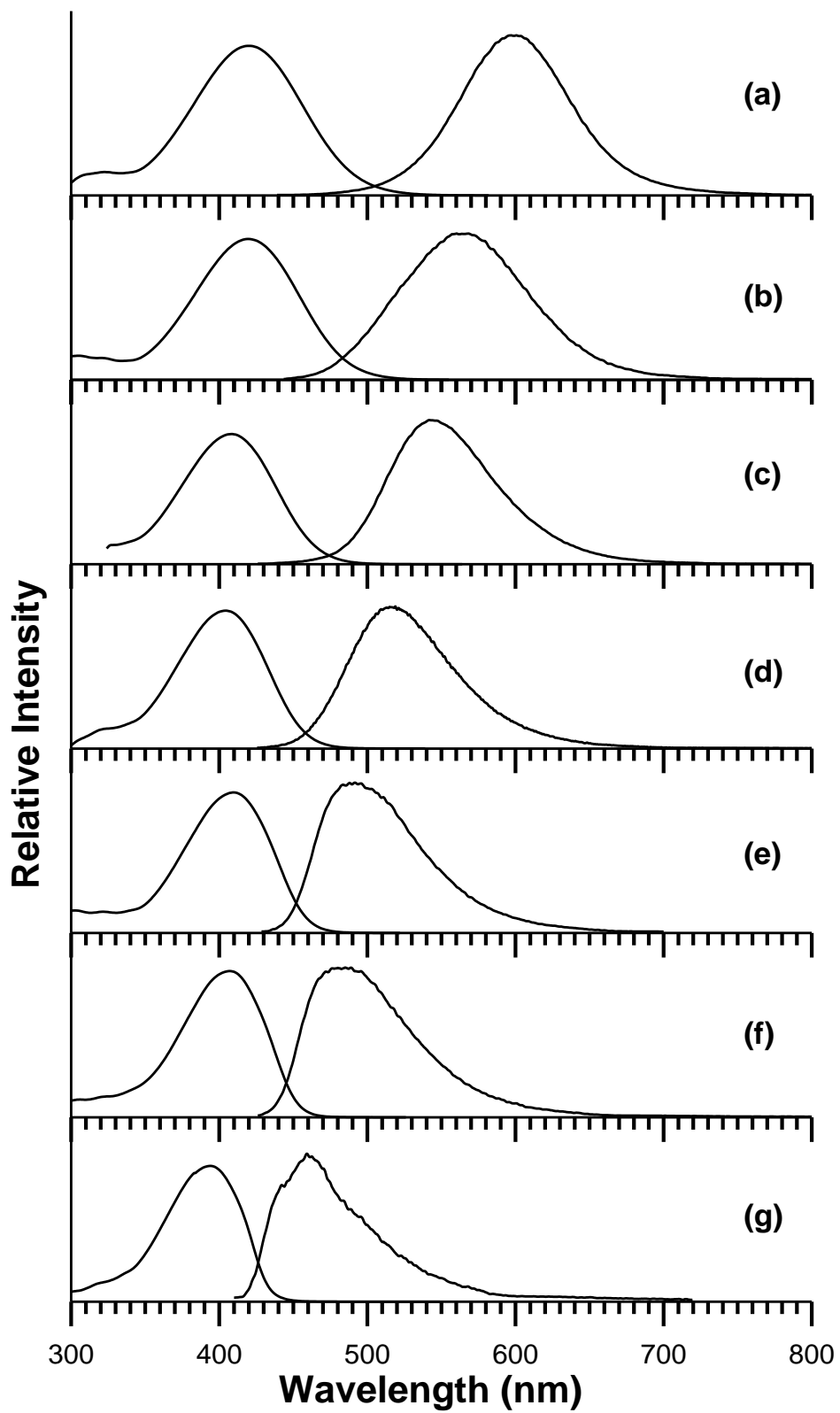
Figure 49. Absorption and fluorescence emission spectra of dmac in (a) methanol, (b) 2-propanol, (c) acetone, (d) ethyl acetate, (e) toluene, (f) carbon tetrachloride, and (g) n-hexane.
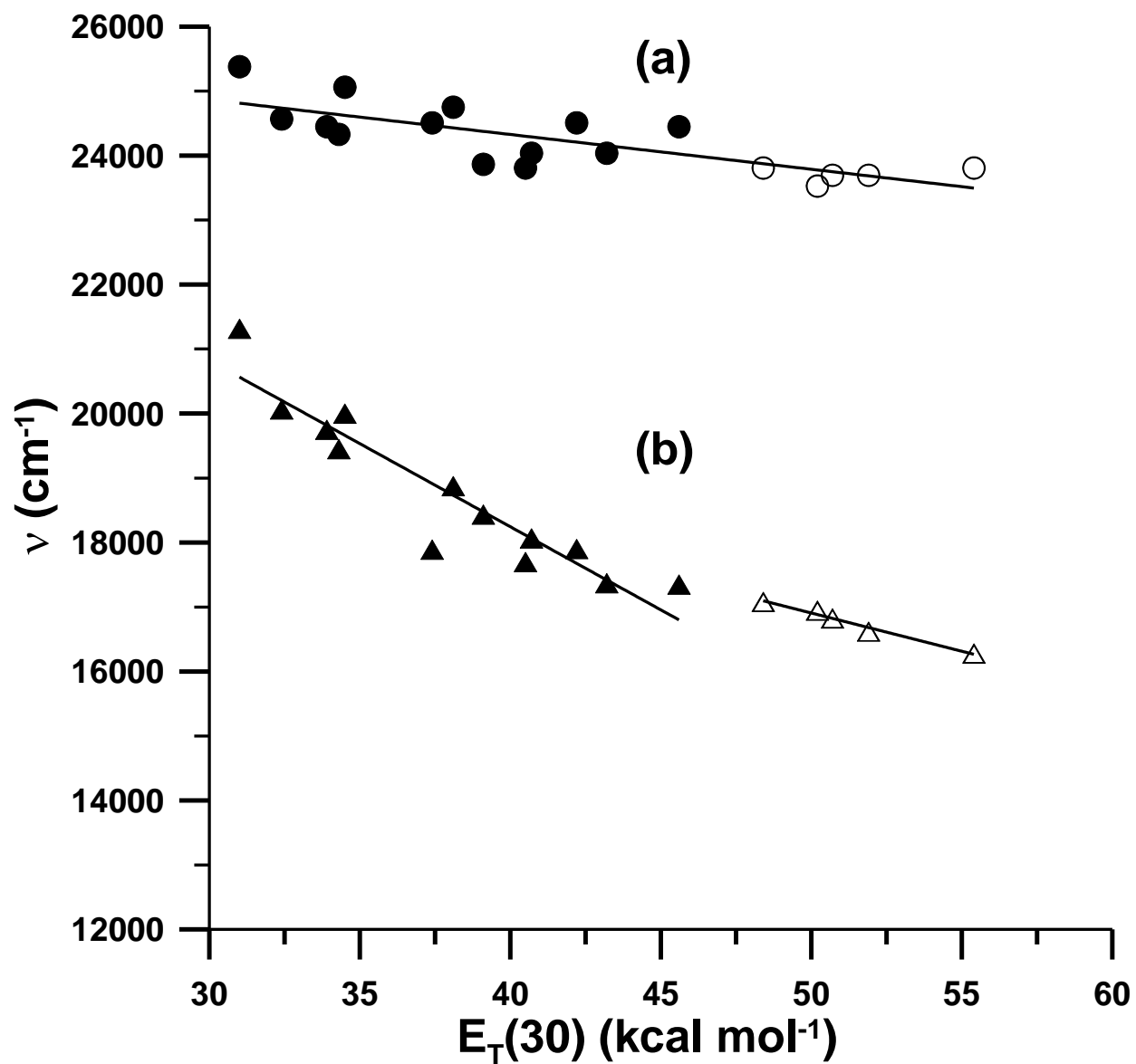
Figure 50. Plot of (a) absorption and (b) fluorescence spectral maxima of dmac in various solvents against the $E_T(30)$ scale. Solid symbols represent aprotic solvents; open symbols represent protic solvents.

The Lippert-Mataga plot of dmac is shown in Figure 51. Similar to dmab, the protic solvents appear to fall on a different trendline compared to the nonalcohols. Application of the Lippert-Mataga method to the aprotic solvents and knowing that the computed ground state dipole moment and Onsager cavity radius of dmac at the B3LYP/6-31G(d) level of theory are 7.39 D and 5.19 Å, the excited state dipole moment is found to be 17.9 D ($\Delta\mu = 10.5$ D). The larger μ_e observed for dmac, compared to dmab ($\mu_e = 16.6$ D), is attributed to a higher degree of internal charge transfer in the longer π-conjugated framework. It is reported that 4.8 D is the dipole moment resulting from a charge separation of one unit charge by 1 Å [29]. In applying this conversion to both dmab and dmac, μ_e values of 16.6 D and 17.9 D are the result of unit-charge separations of 3.5 Å and 3.7 Å, respectively. Therefore, the larger unit-charge separation for dmac also suggests its greater ICT nature.
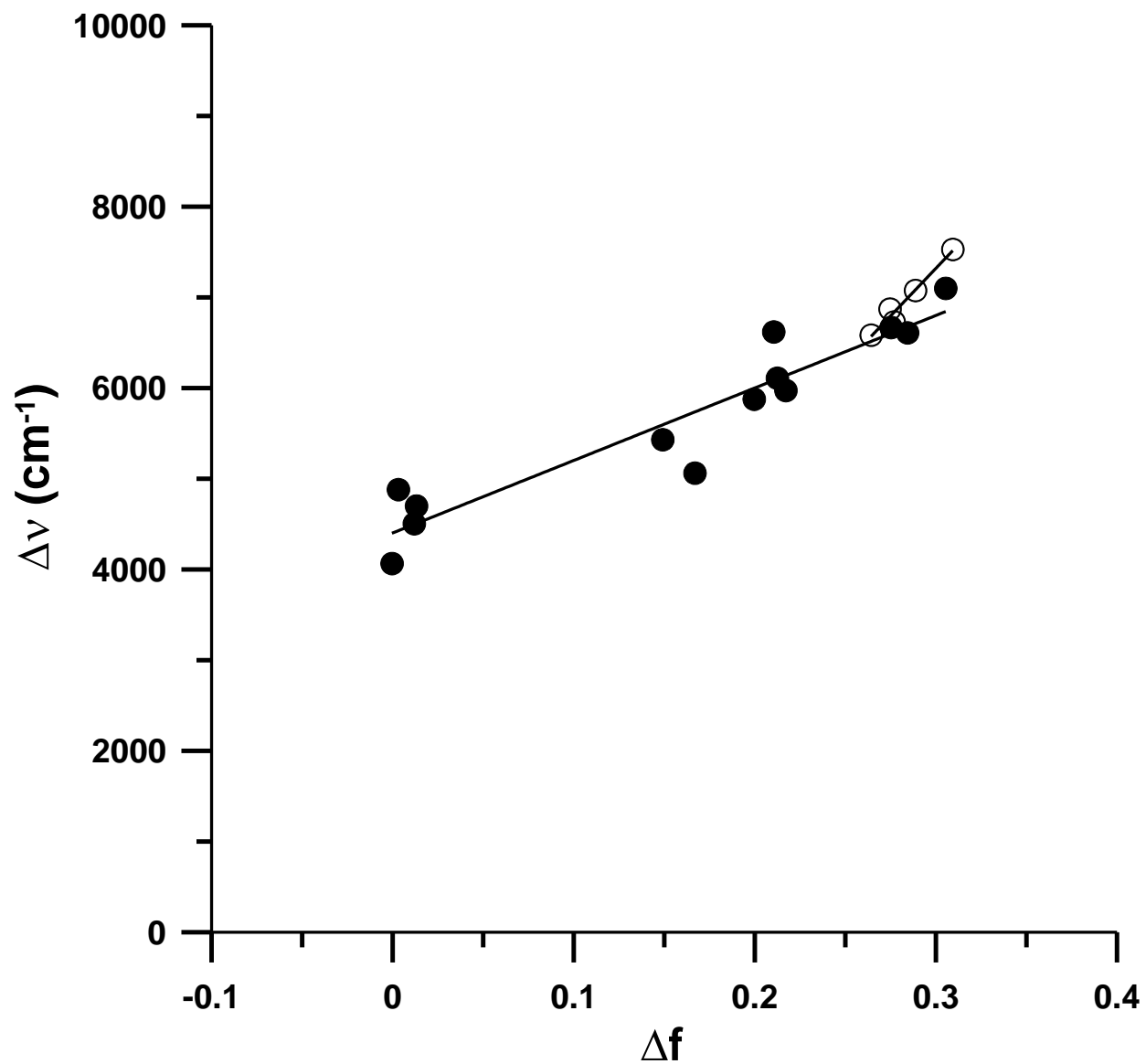
Figure 51. Lippert-Mataga plot of dmac in various solvents. Solid symbols represent aprotic

solvents; open symbols represent protic solvents.

Figure 52 and Table 19 show the computed molecular orbitals of dmac and the TD-DFT spectral calculations in the gas phase and in solvents. Similar to dmab, S_1 is predicted to be (n, π^*) in the gas phase and (π, π^*) in solvent. In the gas phase, the S_1 state is computed to be a transition localized at 394 nm (f = 0.23) with HOMO-1 (n) → LUMO (π^*) as the primary CI configuration. Excitation to the S_2 state is predicted to be a strong electronic transition at 389 nm (f = 0.97) with a major CI configuration of HOMO (π) → LUMO (π^*). As with dmab, the unusually large oscillator strength computed for the n → π^* transition in the gas phase is a result of configuration mixing of nearly degenerate states ($\Delta E = 326$ cm^{-1}) (see Table 20).

In solvent, S_1 is computed to be (π, π^*), arising from a HOMO → LUMO transition, and the energy of S_1 is calculated to continuously decrease with respect to an increase in solvent polarity. The energy of the S_1(π, π^*) state decreases in the following order: 2.98 eV (416 nm, n-hexane), 2.93 eV (423 nm, toluene), 2.91 eV (427 nm, chloroform), and 2.90 eV (428 nm, methanol). This is typical bathochromic shifting observed for (π, π^*) excitations with respect to an increase in solvent polarity. Similar to dmab, the inversion of the ^{1}(π, π^*) state from S_2 in the gas phase to S_1 in solvent provides a reasonable argument as to why fluorescence is observed experimentally in all solvents. As shown in Figure 53, good agreement is observed between the absorption spectra of dmac and the TD-DFT calculated spectra in the four solvents.

Table 19. TD-DFT spectral calculations of dmac both in the gas phase and in solvent environments at the B3LYP/6-31G(d) level of theory.

Solvent	State	Transition Energy			f	MO	CI Coef.
		eV	cm^{-1}	nm			
Gas (μ = 7.38 D)	T$_1$ (π, π*)	1.72	13908	719	0.00	63→66	-0.24376
						65→66	0.66070
						65←66	0.10818
	T$_2$ (n, π*)	2.78	22472	445	0.00	64→66	0.66672
						64→68	-0.19042
	T$_3$ (π, π*)	3.08	24814	403	0.00	61→66	-0.15163
						63→66	0.58548
						65→66	0.19535
						65→67	-0.13337
						65→68	0.25103
	S$_1$ (n, π*)	3.15	25381	394	0.23	64→66	0.60911
						64→68	-0.13145
						65→66	0.31427
	S$_2$ (π, π*)	3.19	25707	389	0.97	64→66	-0.31262
						65→66	0.62907
	S$_3$ (π, π*)	4.18	33670	297	0.025	62→66	0.30500
						63→66	0.26145
						65→67	0.57094
n-Hexane (μ = 8.27 D)	T$_1$ (π, π*)	1.72	13850	722	0.00	63→66	-0.24348
						65→66	0.65842
						65←66	0.10251
	T$_2$ (n, π*)	2.86	23095	433	0.00	64→66	0.66334
						64→68	0.17581
	S$_1$ (π, π*)	2.98	24038	416	1.32	65→66	0.70533
	T$_3$ (π, π*)	3.04	24510	408	0.00	61→66	-0.14612
						63→66	0.59556
						65→66	0.20538
						65→67	-0.13671
						65→68	-0.21475
	S$_2$ (n, π*)	3.23	26042	384	0.0042	63→66	0.13147
						64→66	0.67373
						64→68	0.13294
	S$_3$ (π, π*)	4.12	33223	301	0.091	62→66	0.23920
						63→66	0.44802
						65→67	0.47220

	T$_1$ (π, π^*)	1.72	13831	723	0.00	63→66	-0.23685
						65→66	0.65800
						65←66	0.10094
	T$_2$ (n, π^*)	2.89	23256	430	0.00	63→66	0.13157
						64→66	0.65528
						64→68	0.16667
Toluene (μ = 8.53 D)	S$_1$ (π, π^*)	2.93	23641	423	1.35	65→66	0.70602
	T$_3$ (π, π^*)	3.02	24390	410	0.00	61→66	-0.14414
						63→66	0.59397
						65→66	0.20709
						65→67	-0.13729
						65→68	-0.20308
	S$_2$ (n, π^*)	3.25	26247	381	0.0026	63→66	0.20068
						64→66	0.65697
						64→68	0.12674
	S$_3$ (π, π^*)	4.10	33113	302	0.12	62→66	0.20429
						63→66	0.49425
						64→66	-0.15362
						65→67	0.42279
	T$_1$ (π, π^*)	1.71	13793	725	0.00	63→66	-0.14080
						64→66	0.20934
						65→66	0.65750
	S$_1$ (π, π^*)	2.91	23419	427	1.32	65→66	0.70638
	T$_2$	2.93	23641	423	0.00	63→66	0.41094
						63→68	0.12993
						64→66	0.52187
Chloroform* (μ = 9.10 D)	T$_3$	3.00	24155	414	0.00	61→66	-0.13536
						63→66	0.50539
						64→66	-0.34919
						65→66	0.20213
						65→67	-0.13323
						65→68	-0.17089
	S$_2$	3.30	26596	376	0.0014	63→66	0.55150
						63→68	0.10508
						64→66	0.41053
	S$_3$	4.07	32787	305	0.16	62→66	-0.17813
						63→66	-0.33140
						64→66	0.44865
						65→67	-0.38209

					64→66	-0.24629
	T_1 (π, π^*)	1.70	13717	729	0.00	65→66	0.65758
	S_1 (π, π^*)	2.90	23364	428	1.28	65→66	0.70652
						61→66	-0.12278
						63→66	-0.18300
	T_2 (π, π^*)	2.95	23753	421	0.00	64→66	0.59852
Methanol (μ = 9.71 D)						65→66	0.19522
						65→67	-0.12861
						65→68	-0.14158
						63→66	0.64395
	T_3 (n, π^*)	3.00	24213	413	0.00	63→67	0.10453
						63→68	0.13513
						64→66	0.14597
						63→66	0.66532
	S_2 (n, π^*)	3.35	27027	370	0.0008	63→68	0.11611
						64→66	-0.17535
						62→66	0.16641
	S_3 (π, π^*)	4.03	32468	308	0.20	63→66	0.14443
						64→66	0.55450
						65→67	0.36648

*The orbital natures of T_2, T_3, S_2, and S_3 in chloroform are not assigned because both MOs 63 and 64 are a mixture of both nonbonding and π-bonding characters.

LUMO (π*, #66)

HOMO (π, #65)

HOMO-1 (n, #64)
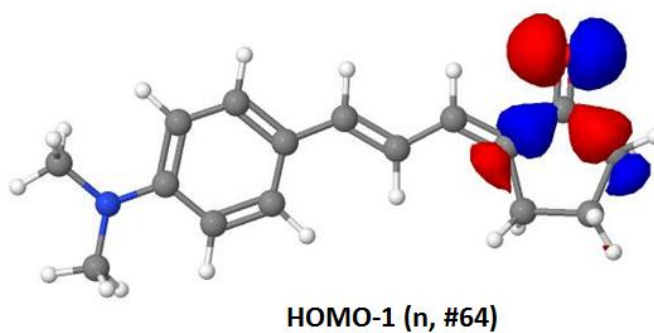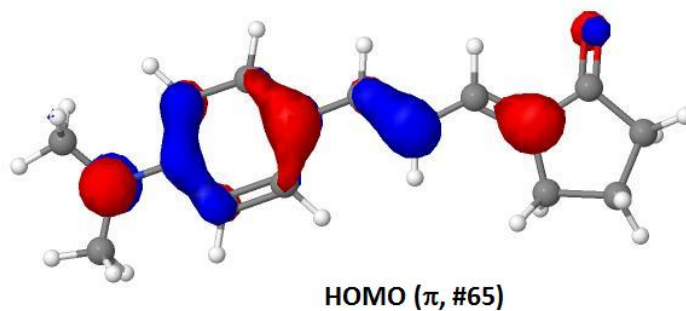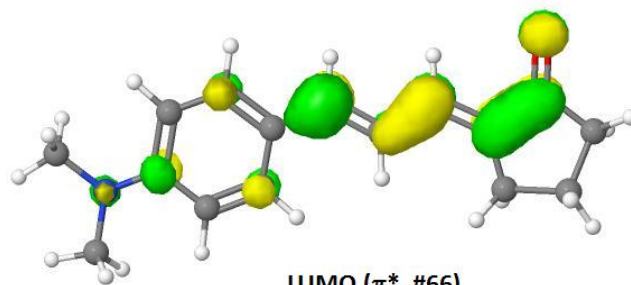
Figure 52. Computed molecular orbitals of dmac in the gas phase.

Table 20. TD-DFT energy gaps of the lowest lying $^1(\pi, \pi^*)$ and $^1(n, \pi^*)$ states and f values for the $^1(n, \pi^*)$ states of dmac.

Solvent	$\left| \Delta E[^1(n, \pi^*)-^1(\pi, \pi^*)] \right|$ (cm^{-1})	f[$^1(n, \pi^*)$]
Gas	326	0.23
n-Hexane	2004	0.0042
Toluene	2606	0.0026
Chloroform	3177	0.0014
Methanol	3663	0.0008
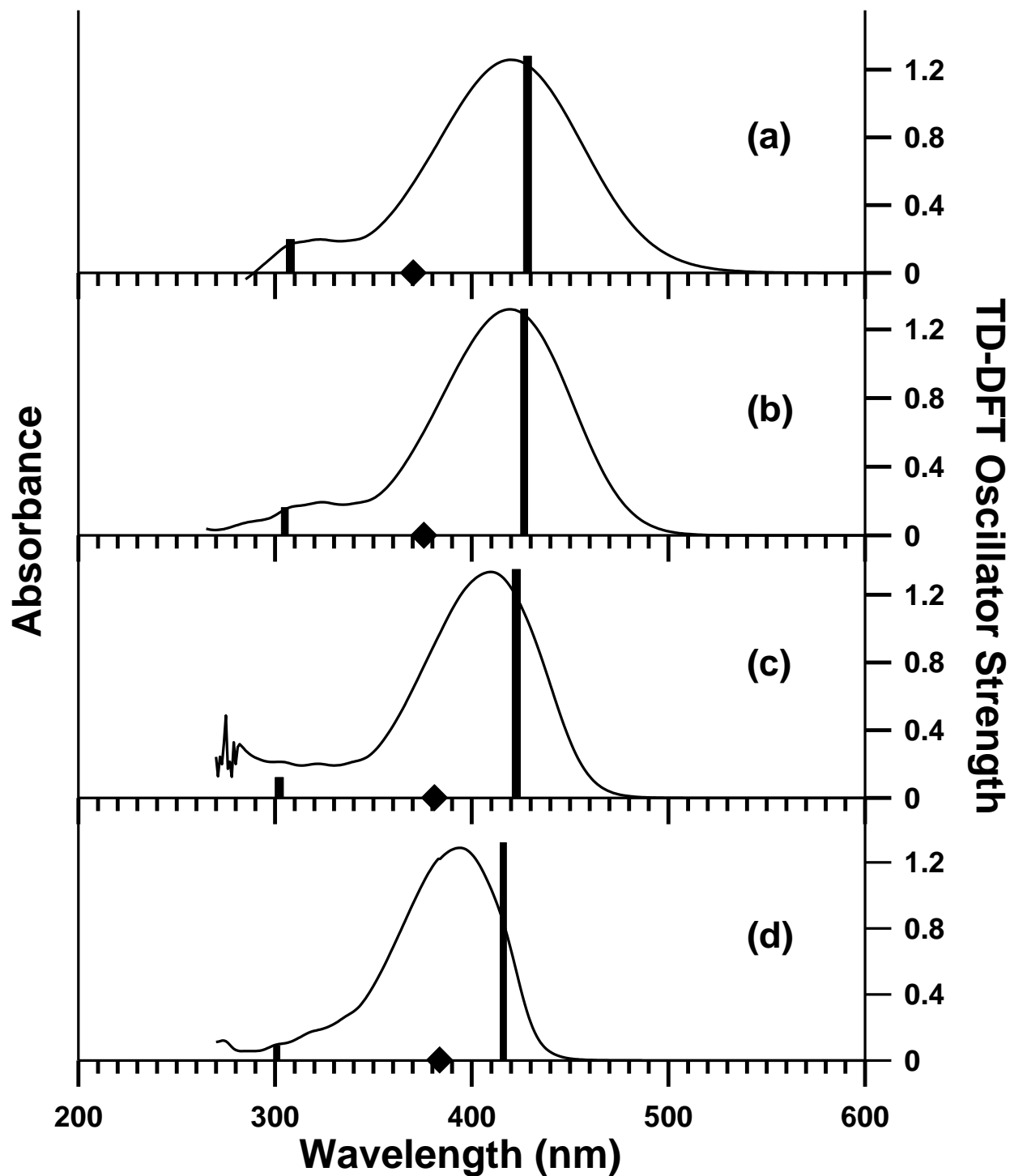
Figure 53. Experimental absorption spectra of dmac in (a) methanol, (b) chloroform, (c) toluene, and (d) n-hexane and their corresponding TD-DFT oscillator strengths at the B3LYP/6-31G(d) level of theory. The forbidden $S_2(n, \pi^*)$ excited states are represented by the filled diamonds.

The low Φ_f values observed in all of the studied solvents for dmab and dmac can be attributed to the fast rate of intersystem crossing from the singlet to the triplet state manifolds of different orbital configurations, as stated by El-Sayed's rule of intersystem crossing. TD-DFT spectral calculations provide theoretical rationale for the low Φ_f's of both compounds. Figure 54 shows Jablonski diagrams for the TD-DFT calculations of dmab and dmac, along with experimental Φ_f values, in toluene and methanol. For dmab, TD-DFT predicts the energy levels of $S_1(\pi, \pi^*)$ and $T_2(n, \pi^*)$ to be equal to 3.36 eV (27,100 cm^{-1}) and 3.06 eV (24,691 cm^{-1}) (in toluene) and 3.32 eV (26,738 cm^{-1}) and 3.15 eV (25,445 cm^{-1}) (in methanol). In both cases, since the energy of T_2 falls below that of S_1, strong SOC and fast S $\rightarrow$ T intersystem crossing is expected.

For the case of dmac in toluene, TD-DFT predicts the energy levels of $S_1(\pi, \pi^*)$ and $T_2(n, \pi^*)$ to be equal to 2.93 eV (23,641 cm^{-1}) and 2.89 eV (23,256 cm^{-1}). The mechanism of direct strong SOC between S_1 and T_2 still holds for dmac in toluene, since the predicted energy of T_2 is below that of S_1. However, in methanol, the predicted energy of now the $T_3(n, \pi^*)$ state (3.00 eV, 24,213 cm^{-1}) is above that of $S_1(\pi, \pi^*)$ (2.90 eV, 23,364 cm^{-1}), suggesting that fast intersystem crossing is not possible. Thermally activated population of $^3(n, \pi^*)$ from $^1(\pi, \pi^*)$ could occur (Boltzmann distribution). However, vibronic spin-orbit coupling is considered to be a more likely mechanism of intersystem crossing, where the vibronic coupling between two states of the same spin multiplicity and spin-orbit coupling between two states of different multiplicities are operative in promoting intersystem crossing. Also noteworthy to consider is that Φ_f of dmac is higher in methanol than in toluene. This is consistent with the predicted energy level of $T_3(n, \pi^*)$ lying above that of $S_1(\pi, \pi^*)$ (slower rate of intersystem crossing).

3.47 eV S_2 (n, π^*)————

3.36 eV S_1 (π, π^*)—— *fast*

T_2 (n, π^*) 3.06 eV

T_1 (π, π^*) 2.20 eV

S_0

Toluene, Φ_f = 0.0009

3.54 eV S_2 (n, π^*)————

3.32 eV S_1 (π, π^*)—— *fast*

T_2 (n, π^*) 3.15 eV

T_1 (π, π^*) 2.16 eV

S_0

Methanol, Φ_f = 0.002

dmab

3.25 eV S_2 (n, π^*)————

2.93 eV S_1 (π, π^*)—— *fast*

T_2 (n, π^*) 2.89 eV

T_1 (π, π^*) 1.72 eV

S_0

Toluene, Φ_f = 0.003

3.35 eV S_2 (n, π^*)————

VC   SOC

T_3 (n, π^*) 3.00 eV

T_2 (π, π^*) 2.95 eV

2.90 eV S_1 (π, π^*)——

VC

T_1 (π, π^*) 1.70 eV

S_0

Methanol, Φ_f = 0.01
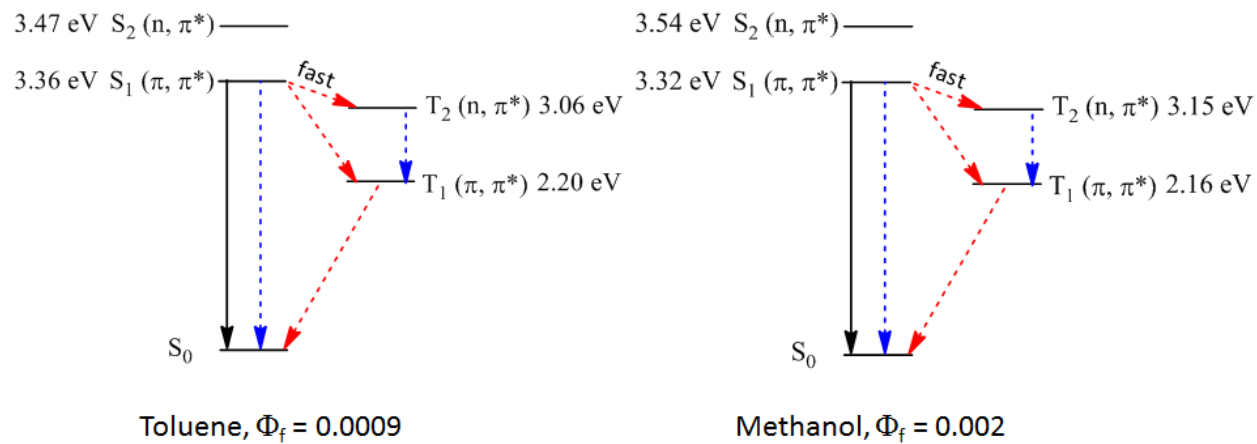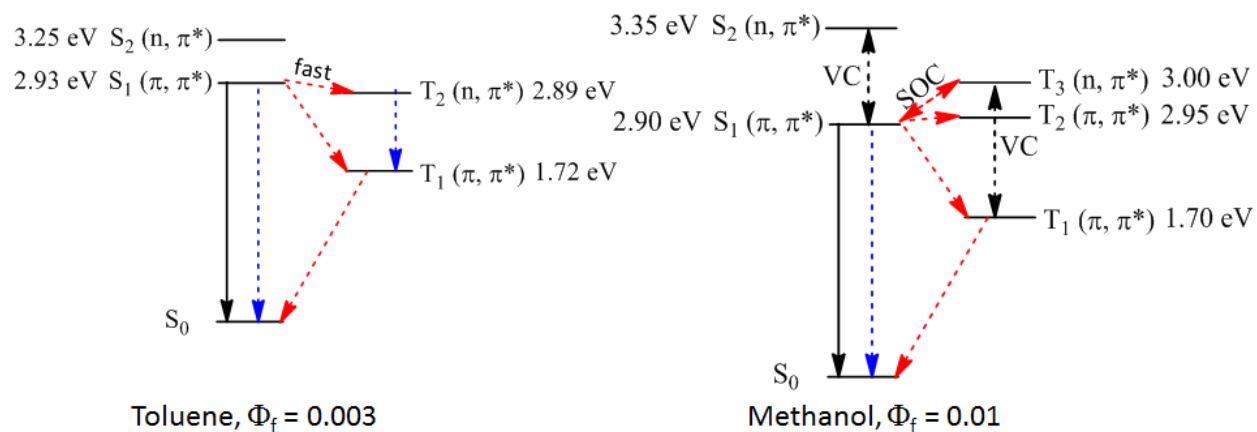
dmac

Figure 54. Jablonski diagrams for the TD-DFT spectral calculations of dmab and dmac in toluene and methanol along with experimentally measured fluorescence quantum yields. The black solid arrow represents fluorescence, and the dashed arrows represent internal conversion (blue) and intersystem crossing (red).

125

In summary, both alkylamino substituted 2-arylidene cyclopentanones, dmab and dmac, behave similarly in their spectroscopic and photophysical properties. Consistent with the extended π-conjugation, compound dmac is slightly more red shifted in its absorption and fluorescence energies than dmab, and it exhibits larger $\Delta\mu$ and μ_e values. This argues to support its higher degree of ICT. The fluorescence is observed to be very weak for both compounds in all solvents studied, consistent with highly efficient singlet $\rightarrow$ triplet intersystem crossing between excited states of different orbital configurations in accordance to El-Sayed's rule. TD-DFT spectral calculations provide theoretical support for this argument.

4.2.3 Spectroscopic and Photophysical Properties of Alkylamino Substituted 2,5-Diarylidene Cyclopentanones: bis-dmac, bis-juldmac, bis-dmab, and Ashrbor

This section presents and discusses the spectroscopic and photophysical properties of all alkylamino substituted 2,5-diarylidene cyclopentanone dyes investigated in this thesis (names provided in the introductory section of this chapter). Firstly, the spectroscopic and photophysical data on bis-dmac and its spatially restricted julolidine analogue bis-juldmac will be discussed. This will be followed by presenting and discussing the spectroscopic and photophysical data of compound bis-dmab. Finally, spectroscopic and photophysical data for the asymmetric alkylamino compound Ashrbor, considered to be a hybrid of both bis-dmab and bis-dmac, will be discussed.

4.2.3.1   bis-dmac and bis-juldmac

4.2.3.1.1 Introduction

This section consists of a presentation and discussion of the spectroscopic and photophysical properties of bis-dmac and its spatially-restricted julolidine analogue (bis-juldmac). Contrary to bis-dmac, which contains dimethylamino groups substituted on the aryl moieties, bis-juldmac is spatially restricted on the aryl moieties due to the presence of closed, saturated ring systems that structurally prevent it from twisting about the aryl-N bond. Comparisons of the spectroscopic and photophysical properties of these two molecules will determine whether or not bis-dmac undergoes formation of a twisted internal charge transfer (TICT) excited state.

Recall that in a TICT excited state, the plane of a dimethylamino group is at a twisted angle with respect to the rest of the molecule due to rotation about the C-N bond. Fluorescence emission of a polar TICT state is red shifted relative to the locally excited state and its fluorescence is quenched. Previous workers have argued that the fluorescence quenching of ketocyanine dyes in polar solvents is due to the formation of a TICT state in these solvents [22].

4.2.3.1.2 Computed Structures of bis-dmac and bis-juldmac

        The gas phase optimized geometries of bis-dmac and its julolidine analogue bis-juldmac are shown in Figures 55 and 56. As seen, both compounds are essentially planar with ~10° torsional angles within the inner cyclopentanone rings. Additional nonplanarity is seen in bis-juldmac, with ~50° calculated torsional angles in the saturated heterocyclic rings of the julolidine moiety (e.g. atoms 15-18-19-20).
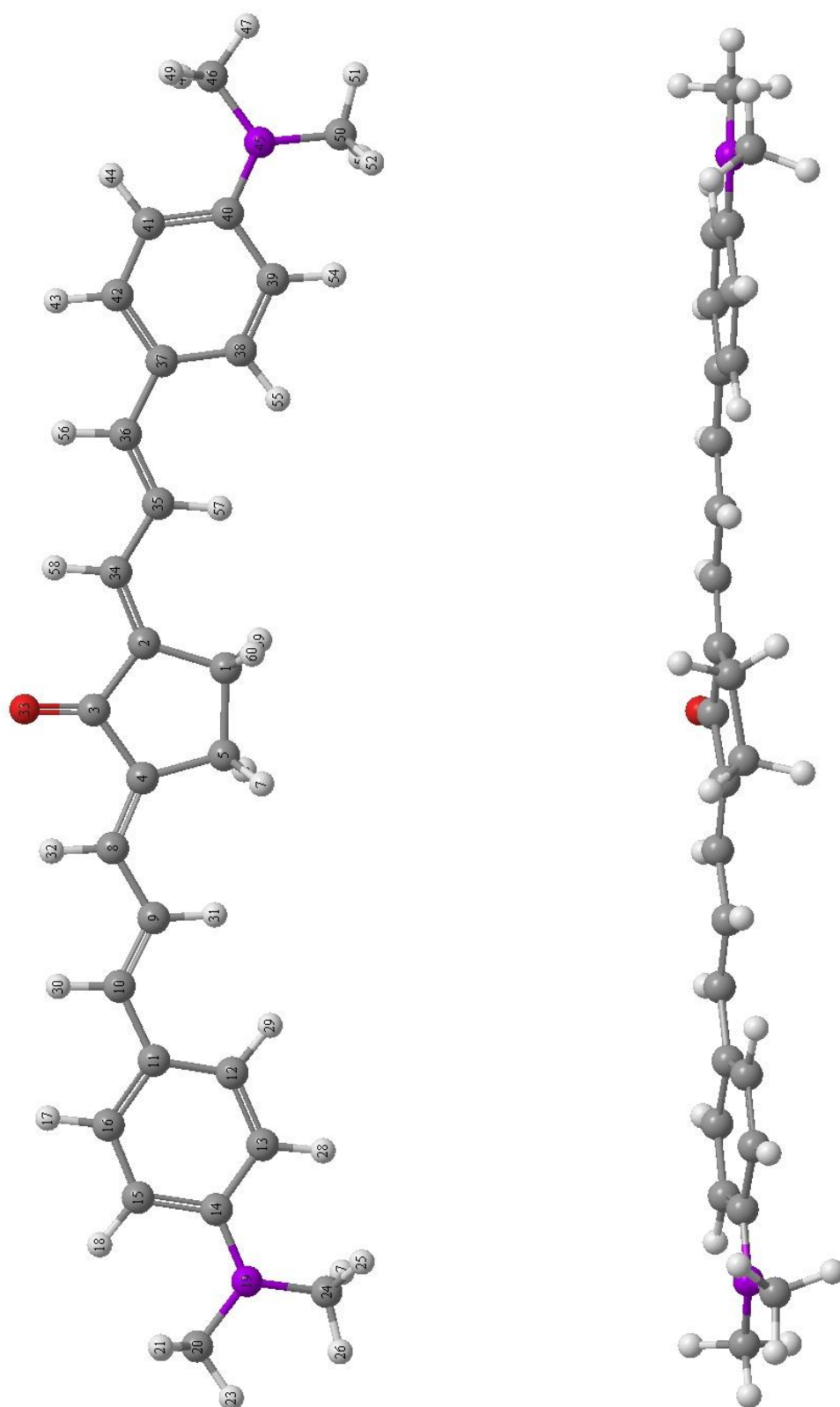
Figure 55. Optimized geometry of bis-dmac at the B3LYP/6-31G(d) level of theory. Gas phase

dipole moment = 5.84 D.

Table 21. B3LYP/6-31G(d) calculated ground state optimized geometry of bis-dmac.

Bond Lengths (Å)	
C_1-C_2	1.51
C_1-C_5	1.56
C_2-C_3	1.48
C_3-O_{33}	1.23
C_4-C_8	1.36
C_8-C_9	1.44
C_9-C_{10}	1.36
C_{10}-C_{11}	1.45
C_{11}-C_{12}	1.41
C_{11}-C_{16}	1.41
C_{12}-C_{13}	1.38
C_{13}-C_{14}	1.42
C_{14}-C_{15}	1.41
C_{14}-N_{19}	1.38
C_{15}-C_{16}	1.39
N_{19}-C_{20}	1.45
N_{19}-C_{24}	1.45

Bond Angles (°)	
C_1-C_2-C_3	109.86
C_1-C_5-C_4	105.64
C_2-C_3-C_4	107.60
C_2-C_3-O_{33}	126.20
C_3-C_4-C_8	121.35
C_4-C_8-C_9	126.46
C_5-C_4-C_8	128.79
C_8-C_9-C_{10}	122.80
C_9-C_{10}-C_{11}	128.17
C_{10}-C_{11}-C_{12}	124.05
C_{10}-C_{11}-C_{16}	119.59
C_{11}-C_{12}-C_{13}	122.04
C_{11}-C_{16}-C_{15}	122.44
C_{12}-C_{11}-C_{16}	116.37
C_{12}-C_{13}-C_{14}	121.24
C_{13}-C_{14}-C_{15}	117.03
C_{13}-C_{14}-N_{19}	121.38
C_{14}-C_{15}-C_{16}	120.87
C_{14}-N_{19}-C_{20}	119.73
C_{14}-N_{19}-C_{24}	119.84
C_{15}-C_{14}-N_{19}	121.58
C_{20}-N_{19}-C_{24}	118.97

Atomic Charges	
C_1	-0.359
C_2	0.0756
C_3	0.350
C_8	-0.169
C_9	-0.120
C_{10}	-0.189
C_{11}	0.177
C_{12}	-0.190
C_{13}	-0.193
C_{14}	0.372
C_{15}	-0.195
C_{16}	-0.204
N_{19}	-0.472
C_{20}	-0.313
C_{24}	-0.312
O_{33}	-0.521

Dihedral Angles (°)	
C_1-C_2-C_{37}-C_{38}	1.34
C_2-C_1-C_5-C_4	-11.87
C_5-C_1-C_2-C_3	9.86
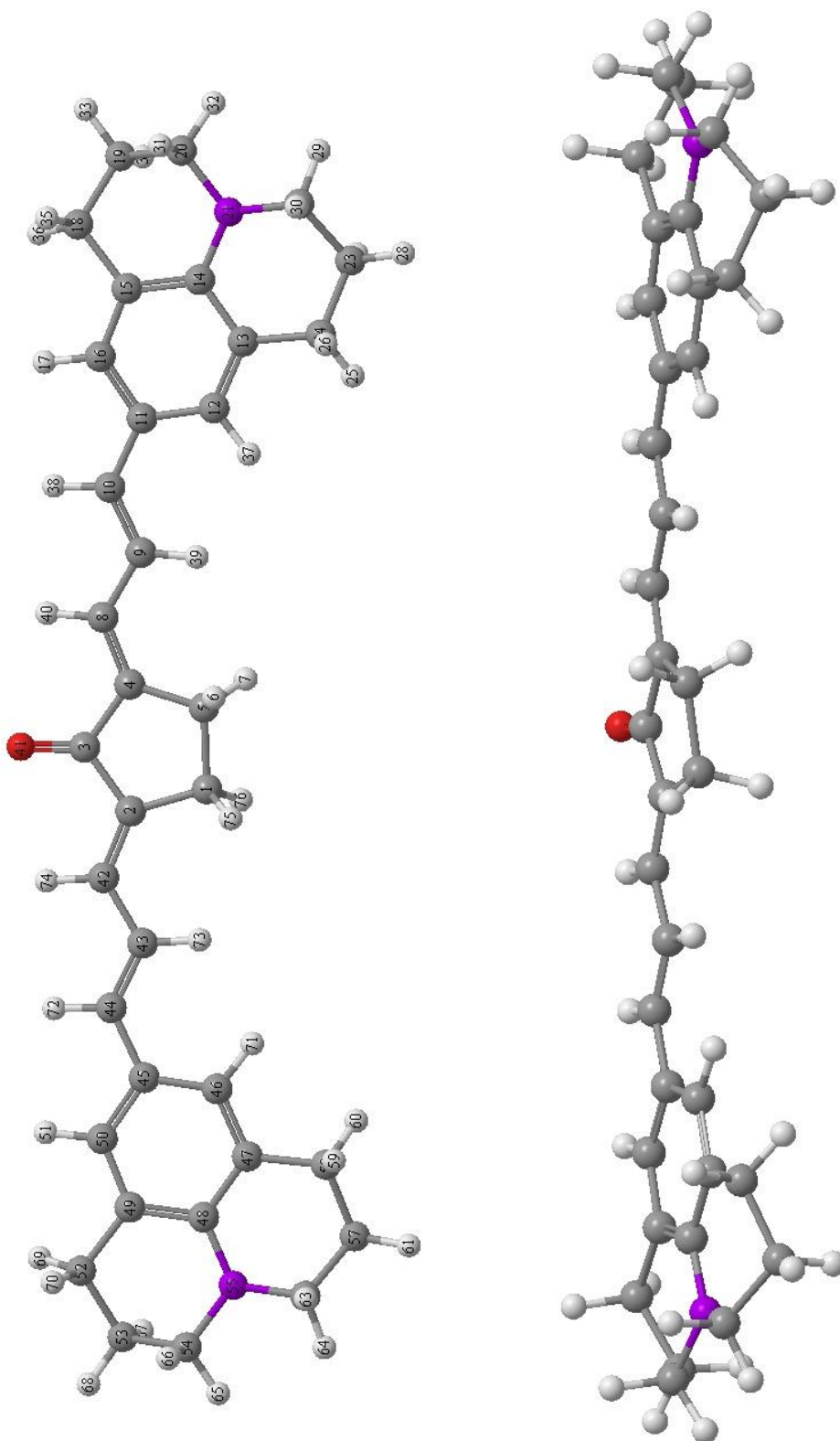
Figure 56. Optimized geometry of bis-juldmac at the B3LYP/6-31G(d) level of theory. Gas phase dipole moment = 5.76 D.

Table 22. B3LYP/6-31G(d) calculated ground state optimized geometry of bis-juldmac.

Bond Lengths (Å)	
C_1-C_2	1.51
C_1-C_5	1.56
C_2-C_3	1.48
C_3-O_{41}	1.23
C_4-C_8	1.36
C_8-C_9	1.44
C_9-C_{10}	1.36
C_{10}-C_{11}	1.45
C_{11}-C_{12}	1.41
C_{11}-C_{16}	1.41
C_{12}-C_{13}	1.39
C_{13}-C_{14}	1.42
C_{13}-C_{24}	1.52
C_{14}-C_{15}	1.42
C_{14}-N_{21}	1.40
C_{15}-C_{16}	1.39
C_{15}-C_{18}	1.52
C_{18}-C_{19}	1.53
C_{19}-C_{20}	1.53
C_{20}-N_{21}	1.46
N_{21}-C_{22}	1.46
C_{22}-C_{23}	1.53
C_{23}-C_{24}	1.53

Bond Angles (°)	
C_1-C_2-C_3	109.90
C_1-C_5-C_4	105.69
C_2-C_3-C_4	107.61
C_2-C_3-O_{41}	126.19
C_3-C_4-C_8	121.37
C_4-C_8-C_9	126.48
C_5-C_4-C_8	128.71
C_8-C_9-C_{10}	122.80
C_9-C_{10}-C_{11}	128.22
C_{10}-C_{11}-C_{12}	123.99
C_{10}-C_{11}-C_{16}	119.49
C_{11}-C_{12}-C_{13}	122.63
C_{11}-C_{16}-C_{15}	123.01
C_{12}-C_{11}-C_{16}	116.52
C_{12}-C_{13}-C_{14}	119.71
C_{12}-C_{13}-C_{24}	119.86
C_{13}-C_{14}-C_{15}	118.76
C_{13}-C_{14}-N_{21}	120.55
C_{13}-C_{24}-C_{23}	111.61
C_{14}-C_{13}-C_{24}	120.43
C_{14}-C_{15}-C_{16}	119.37
C_{14}-C_{15}-C_{18}	120.62
C_{14}-N_{21}-C_{20}	119.57
C_{14}-N_{21}-C_{22}	119.78
C_{15}-C_{14}-N_{21}	120.65
C_{15}-C_{18}-C_{19}	111.56
C_{16}-C_{15}-C_{18}	120.00
C_{18}-C_{19}-C_{20}	109.62
C_{19}-C_{20}-N_{21}	110.87
C_{20}-N_{21}-C_{22}	116.00
N_{21}-C_{22}-C_{23}	110.84
C_{22}-C_{23}-C_{24}	109.53

Atomic Charges	
C_1	-0.359
C_2	0.0752
C_3	0.350
C_8	-0.169
C_9	-0.121
C_{10}	-0.192
C_{11}	0.200
C_{12}	-0.277
C_{13}	0.134
C_{14}	0.278
C_{15}	0.130
C_{16}	-0.290
C_{18}	-0.340
C_{19}	-0.281
C_{20}	-0.125
N_{21}	-0.514
C_{22}	-0.125
C_{23}	-0.281
C_{24}	-0.341
O_{41}	-0.523

Dihedral Angles (°)	
C_1-C_2-C_{46}-C_{45}	0.92
C_2-C_1-C_5-C_4	-11.02
C_{15}-C_{18}-C_{19}-C_{20}	49.21

4.2.3.1.3 Spectroscopic Properties of bis-dmac and bis-juldmac

Absorption and fluorescence properties of bis-dmac were investigated in twenty solvents (see Table 23). Experimental absorption and fluorescence spectra in six solvents of differing polarities are shown in Figure 57. This compound exhibits a high degree of solvatochromism, in that it undergoes bathochromic shifts in going from nonpolar to polar, aprotic and protic solvents. The shifts are more pronounced in the fluorescence spectra than in absorption. In addition to the significant red shift to lower energies, the spectral broadening becomes greater with respect to the increase in solvent polarity. Both solvatochromic shifts and spectral broadening effects are attributed to an internal charge transfer transition from the nitrogen atom of the alkylamino group to the carbonyl oxygen atom. Because of its high solvatochromic nature, bis-dmac undergoes spectral energy shifts of 2778 cm^{-1} (from CCl$_4$ to TFE) in absorbance and 7072 cm^{-1} (from n-hexane to TFE) in fluorescence. The molar extinction coefficients (ε_{max}) of bis-dmac in toluene and dichloromethane were measured to be 66,800 M^{-1}cm^{-1} and 72,600 M^{-1}cm^{-1}, which are in agreement with the extinction coefficients of similar alkylamino substituted 2,5-diarylidene-cyclopentanone dyes [67].

The spectral characteristics of bis-dmac have been compared to its one-sided analogue (dmac) by plotting both the absorption spectral maxima of both molecules (Figure 58) and the fluorescence spectral maxima of both molecules (Figure 59) on the same plot. As with dmac, a small bathochromic shift in absorption maxima is observed for bis-dmac and the protic solvents appear to fall on the same line as for the aprotic solvents. However, the alcohols appear to be anomalous in the fluorescence plot, falling on a different trendline. Comparative analysis among the trendline slopes in fluorescence in aprotic solvents provides further conclusive evidence to the larger solvatochromic and charge transfer character exhibited by bis-dmac compared to

dmac. In Figure 59 for aprotic solvents, the slope of bis-dmac is approximately 1.6-fold greater in magnitude than that for dmac.

Table 23. Spectroscopic properties of bis-dmac in various solvents.

Solvent	λ_{abs} (nm)	λ_f (nm)	ν_{abs} (cm^{-1})	ν_f (cm^{-1})	$E_T(30)$* (kcal mol^{-1})	Δf*	$\Delta\nu$ (cm^{-1})
Trifluoroethanol	534	764	18,727	13,089	59.4	0.3159	5638
Methanol	523	735	19,139	13,605	55.4	0.3093	5534
Ethanol	510	744	19,608	13,445	51.9	0.2887	6163
1-Propanol	515	740	19,417	13,520	50.7	0.2746	5897
1-Butanol	524	739	19,084	13,530	50.2	0.2642	5554
2-Propanol	515	718	19,417	13,925	48.4	0.2769	5492
Acetonitrile	490	717	20,408	13,950	45.6	0.3054	6458
Dimethyl sulfoxide	512	727	19,531	13,750	45.1	0.2637	5781
Dimethylformamide	507	715	19,724	13,980	43.2	0.2752	5744
Acetone	493	694	20,284	14,400	42.2	0.2843	5884
Dichloromethane	503	672	19,901	14,880	40.7	0.2171	5020
Pyridine	507	681	19,743	14,680	40.5	0.2124	5063
Ethyl acetate	480	644	20,833	15,520	38.1	0.1996	5313
Diethyl ether	475	586	21,053	17,075	34.5	0.1669	3978
Benzene	475	567	21,053	17,650	34.3	0.0031	3403
Toluene	495	553	20,202	18,090	33.9	0.0131	2112
Carbon disulfide	480	568	20,833	17,610	32.8	-0.0007	3223
Carbon tetrachloride	465	537	21,505	18,622	32.4	0.0119	2883
n-Hexane	478	496	20,921	20,161	31.0	-0.0004	760
Cyclohexane	480	500	20,833	20,000	30.9	-0.0004	833

*Both Δf and $E_T(30)$ values are taken from Suppan, P. and Ghonheim, N., in *Solvatochromism*, The Royal Society of Chemistry, Cambridge, 1997; and Lide, D. R., *CRC Handbook of Chemistry and Physics*, 89th ed., 2008.
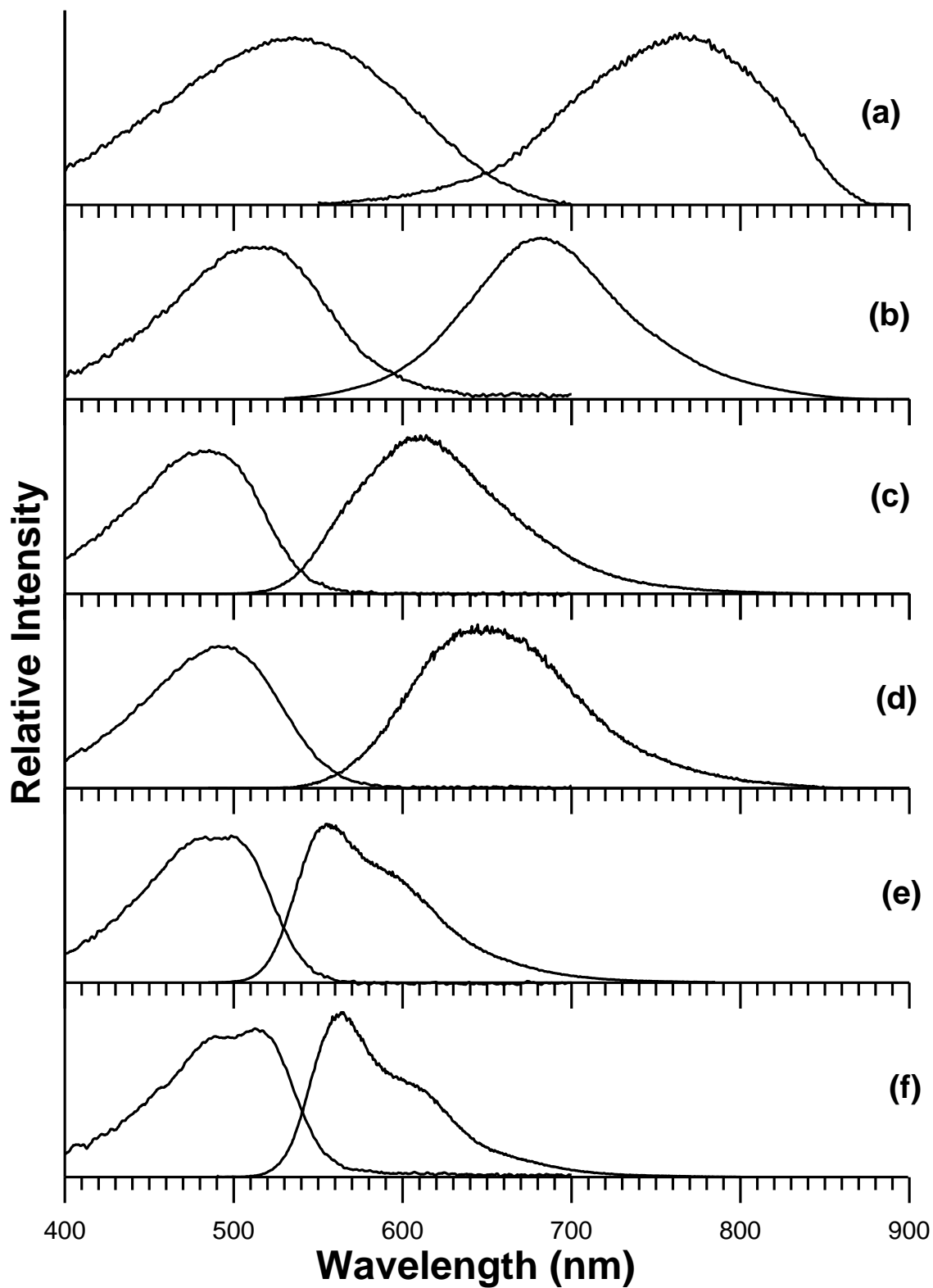
Figure 57. Absorption and fluorescence emission spectra of bis-dmac in (a) 2,2,2-trifluoroethanol (TFE), (b) 2-propanol, (c) ethyl acetate, (d) acetone, (e) benzene, and (f) carbon disulfide.

137
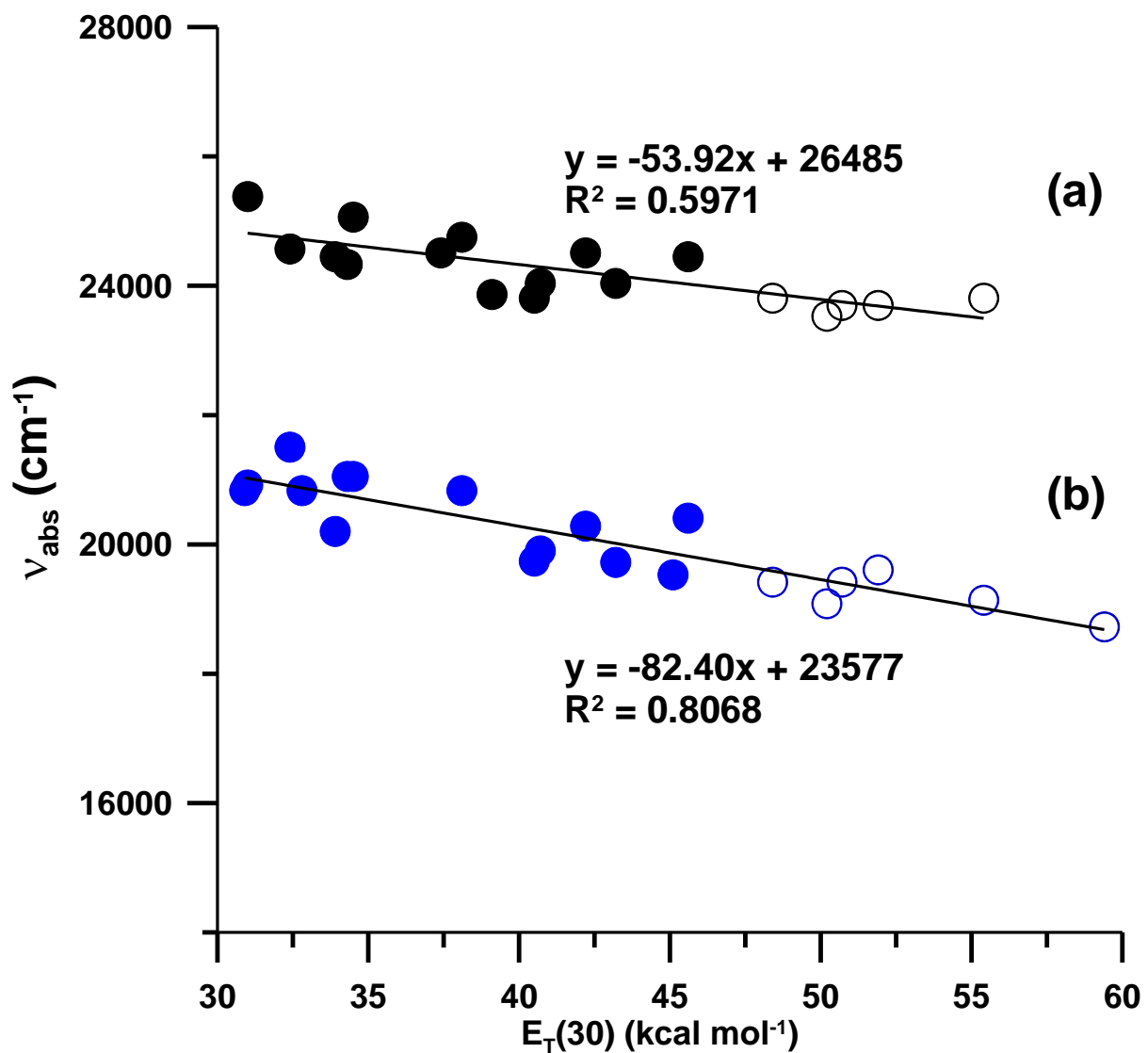
Figure 58. Plot of absorption spectral maxima of (a) dmac and (b) bis-dmac in various solvents against the $E_T(30)$ scale. Solid symbols represent aprotic solvents; open symbols represent protic solvents.
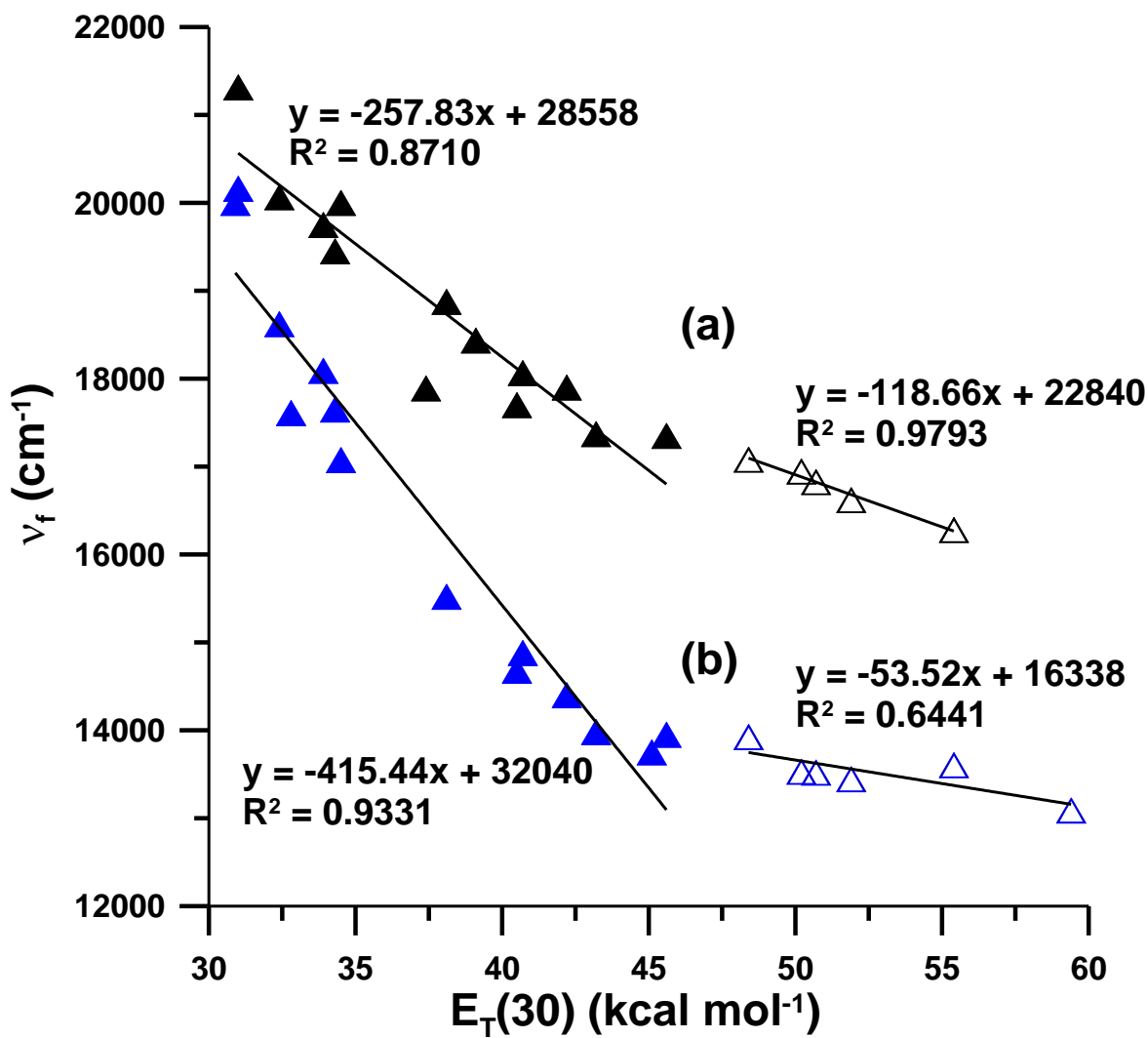
Figure 59. Plot of fluorescence spectral maxima of (a) dmac and (b) bis-dmac in various

solvents against the $E_T(30)$ scale. Solid symbols represent aprotic solvents; open symbols

represent protic solvents.

Similar behavior is observed for the solvatochromism of the julolidine analogue bis-juldmac. Both the absorption and fluorescence properties of bis-juldmac were examined in eighteen solvents, presented in Table 24. Experimental absorption and fluorescence spectra in seven of the solvents are shown in Figure 60. As was observed with bis-dmac, both red shifts and spectral broadening (far more pronounced in fluorescence) are seen with respect to increased solvent polarity. Maximum absorption and fluorescence energies have been plotted against the $E_T(30)$ scale (Figure 61); this plot is similar to the solvatochromic plots for bis-dmac.

Table 24. Spectroscopic properties of bis-juldmac in various solvents.

Solvent	λ_{abs} (nm)	λ_f (nm)	ν_{abs} (cm^{-1})	ν_f (cm^{-1})	$E_T(30)$* (kcal mol^{-1})	Δf*	$\Delta\nu$ (cm^{-1})
Trifluoroethanol	584	745	17,123	13,426	59.4	0.3159	3697
Methanol	523	750	19,120	13,333	55.4	0.3093	5787
Ethanol	538	748	18,587	13,375	51.9	0.2887	5212
1-Propanol	541	747	18,484	13,392	50.7	0.2746	5092
1-Butanol	543	744	18,416	13,435	50.2	0.2642	4981
2-Propanol	535	740	18,692	13,510	48.4	0.2769	5182
Dimethyl sulfoxide	539	740	18,553	13,520	45.1	0.2637	5033
Acetonitrile	510	736	19,608	13,579	45.6	0.3054	6029
Dimethylformamide	532	736	18,797	13,590	43.2	0.2752	5207
Acetone	515	732	19,417	13,670	42.2	0.2843	5747
Pyridine	534	720	18,727	13,885	40.5	0.2124	4842
Dichloromethane	529	723	18,904	13,830	40.7	0.2171	5074
Ethyl acetate	495	660	20,202	15,152	38.1	0.1996	5050
Carbon disulfide	530	616	18,868	16,230	32.8	-0.0007	2638
Diethyl ether	494	632	20,243	15,820	34.5	0.1669	4423
Benzene	510	593	19,608	16,860	34.3	0.0031	2748
Toluene	505	588	19,802	17,020	33.9	0.0131	2782
n-Hexane	457	524	21,882	19,070	31.0	-0.0004	2812

*Both Δf and $E_T(30)$ values are taken from Suppan, P. and Ghonheim, N., in *Solvatochromism*, The Royal Society of Chemistry, Cambridge, 1997; and Lide, D. R., *CRC Handbook of Chemistry and Physics*, 89th ed., 2008.
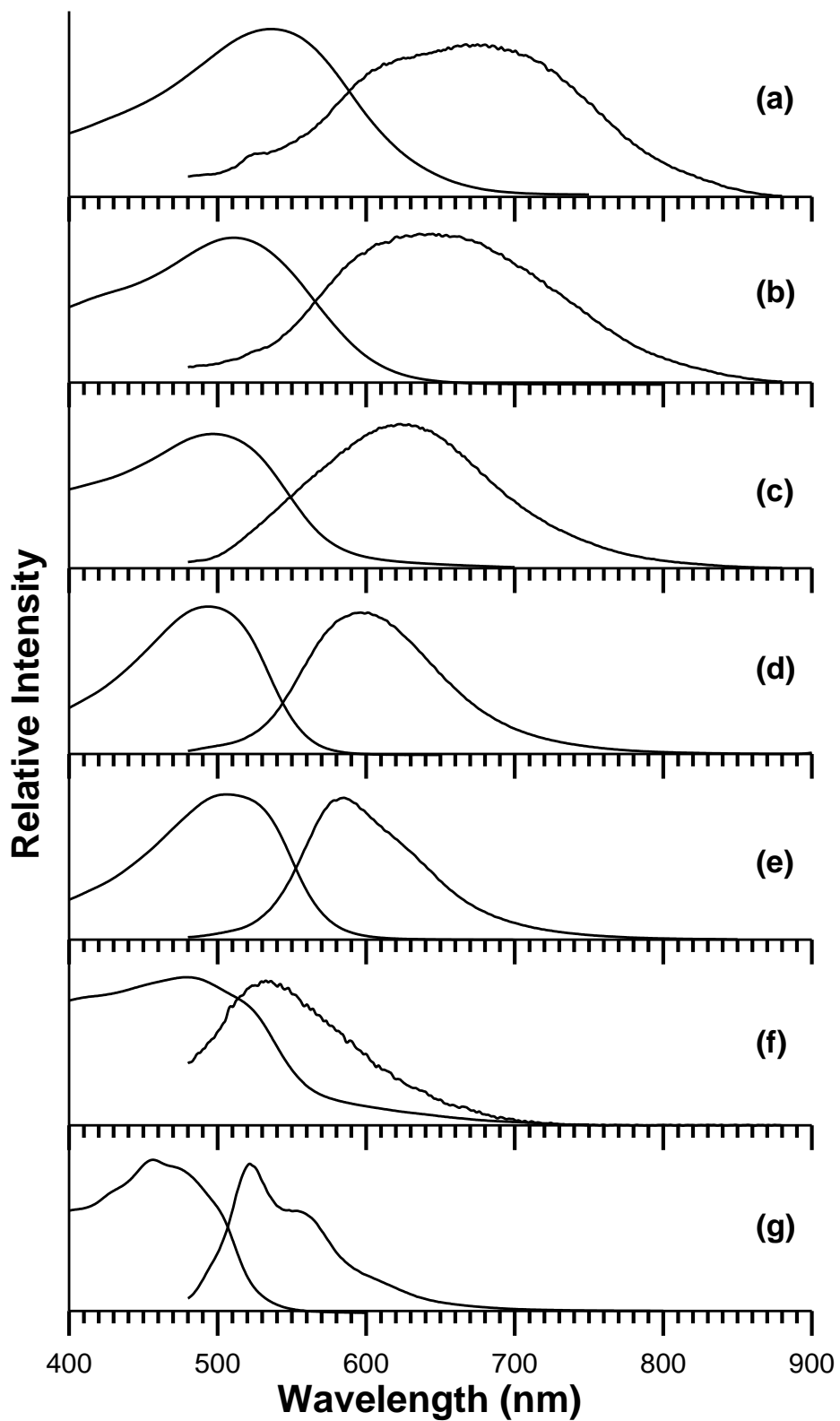
Figure 60. Absorption and fluorescence emission spectra of bis-juldmac in (a) 2-propanol, (b) acetonitrile, (c) ethyl acetate, (d) diethyl ether, (e) toluene, (f) carbon tetrachloride, and (g) n-hexane.

142
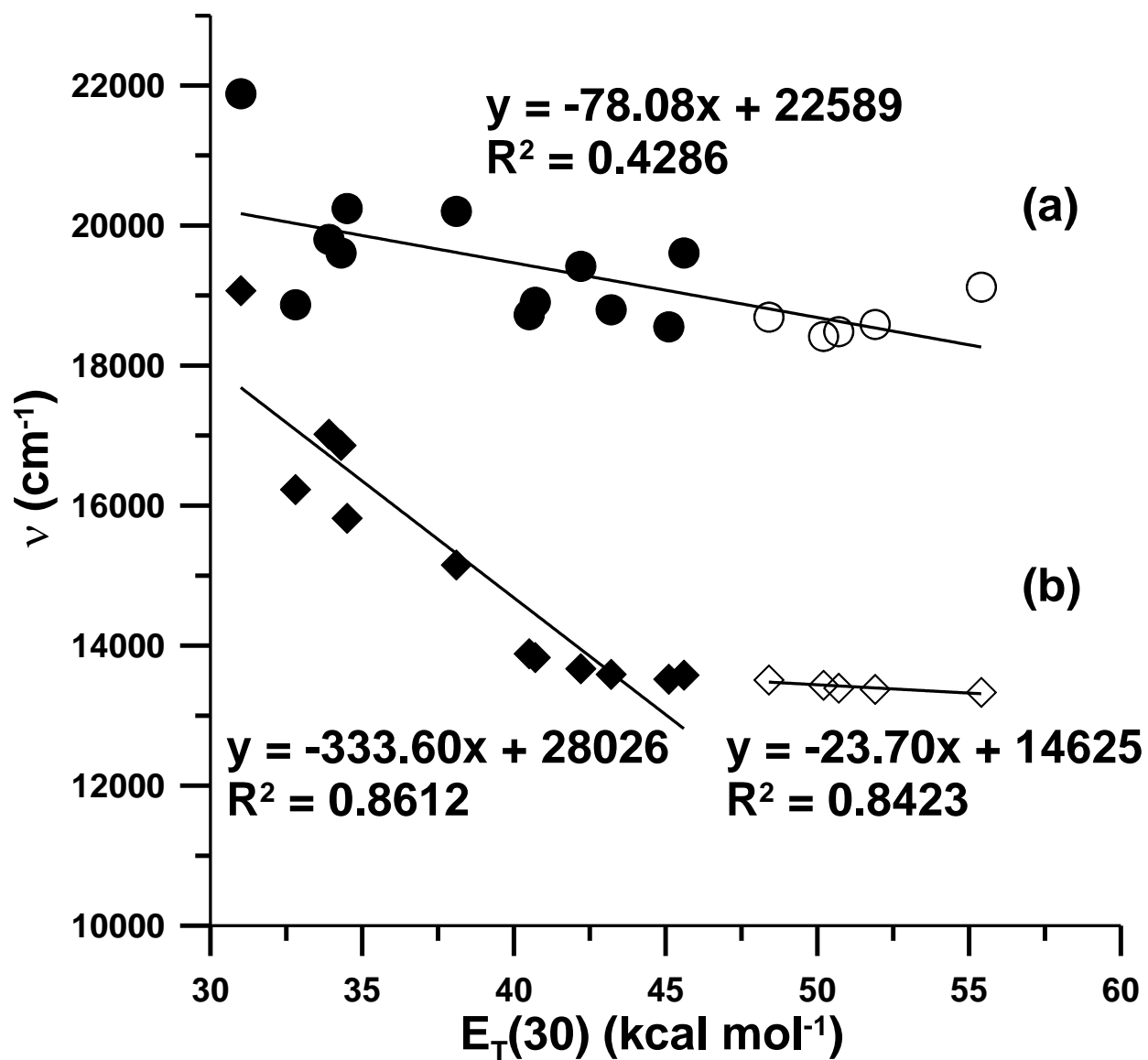
Figure 61. Plot of (a) absorption and (b) fluorescence spectral maxima of bis-juldmac in various solvents against the $E_T(30)$ scale. Solid symbols represent aprotic solvents; open symbols represent protic solvents.

The excited state dipole moments of bis-dmac and bis-juldmac were determined via the Lippert-Mataga approach (plots shown in Figure 62). At the DFT B3LYP/6-31G(d) level of theory, the Onsager cavity radii of bis-dmac and bis-juldmac were computed to be 5.95 Å and 6.34 Å and ground state dipole moments to be 5.84 D and 5.76 D, respectively. Application of the Lippert-Mataga method to the data for aprotic solvents yields excited state dipole moments for bis-dmac and bis-juldmac of 21.0 D ($\Delta\mu$ = 15.2 D) and 21.8 D ($\Delta\mu$ = 16.0 D). The ~4-fold increase in the dipole moments going from the ground to excited state is attributed to the internal charge transfer natures of these two compounds.

The computed molecular orbitals of bis-dmac and bis-juldmac (Figures 63 and 64) also show the internal charge transfer properties of these compounds. In the π-bonding HOMO, electron density is evenly distributed along the conjugated framework, with significant density centered on the nitrogen atoms of the alkylamino groups. In the π^*-antibonding LUMO, electron density is transferred from the electron donor ends of the molecule to the electron acceptor end (carbonyl oxygen atom), signifying a significant charge transfer process.
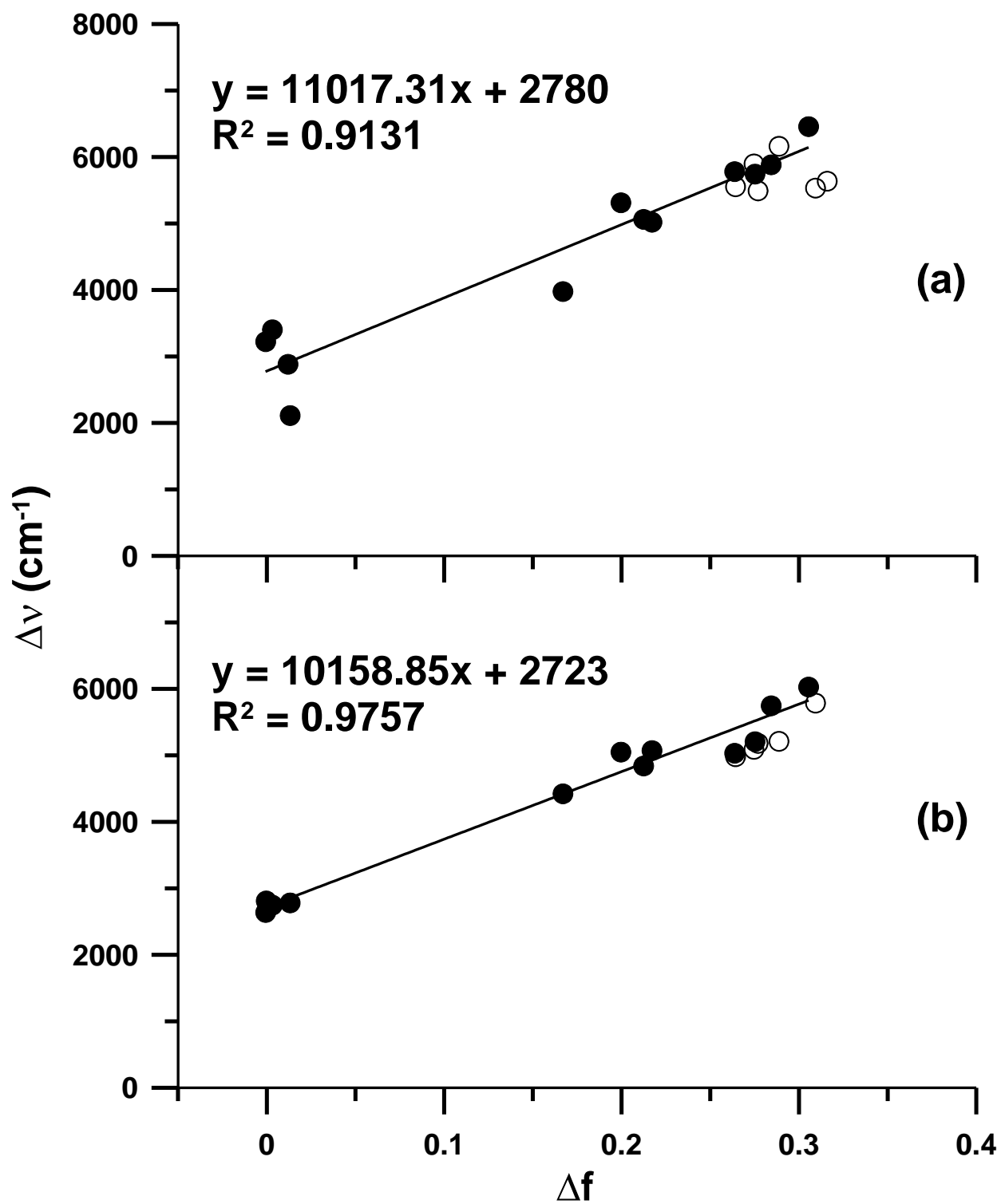
Figure 62. Lippert-Mataga plots of (a) bis-dmac and (b) bis-juldmac in various solvents. Solid symbols represent aprotic solvents; open symbols represent protic solvents.

LUMO (π*, b₁)
MO 108
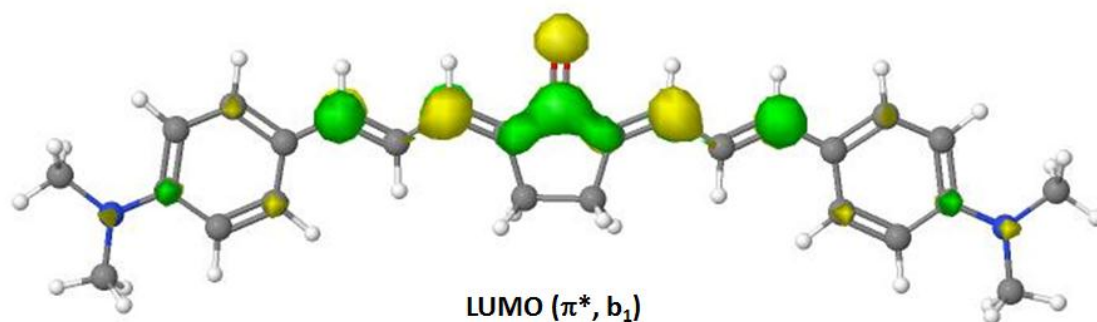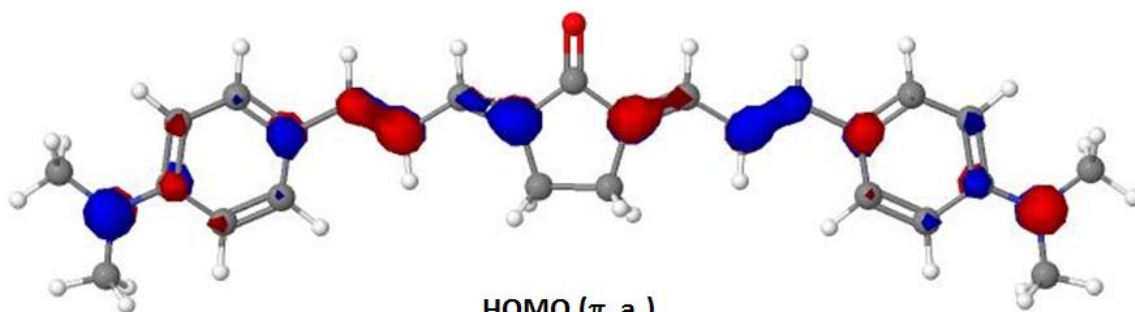
HOMO (π, a₂)
MO 107
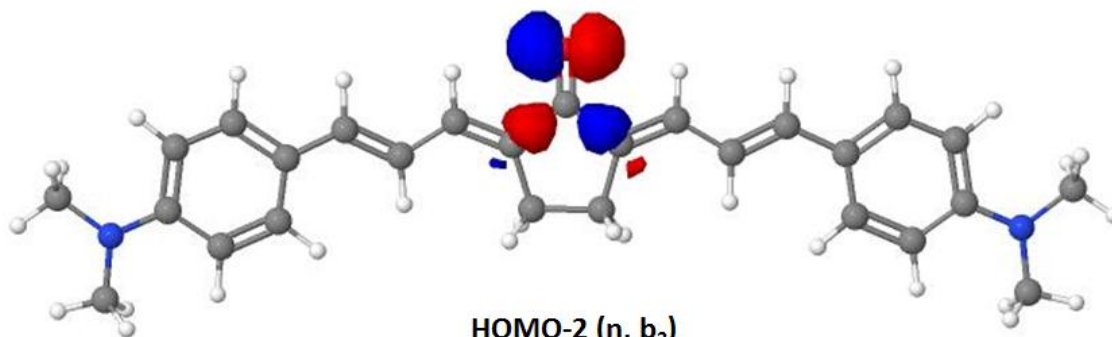
HOMO-2 (n, b₂)
MO 105

Figure 63. Computed molecular orbitals of bis-dmac in the gas phase.

LUMO (π*, b₁)
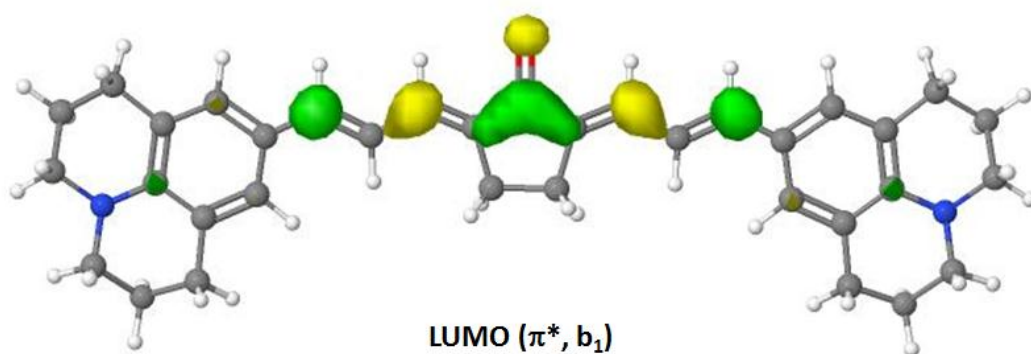
MO 136
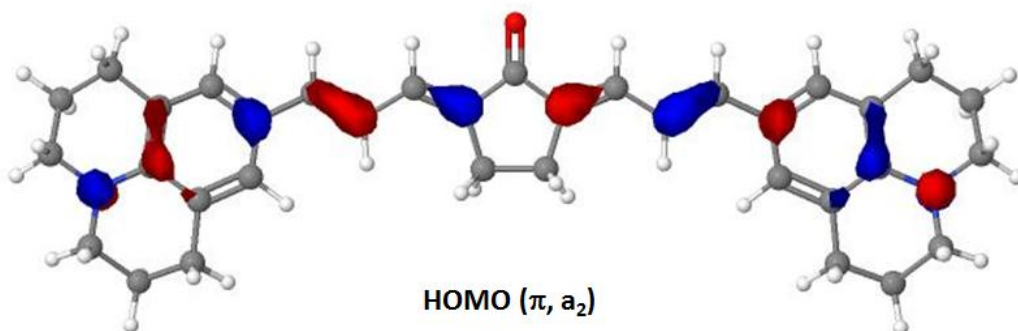
HOMO (π, a₂)

MO 135
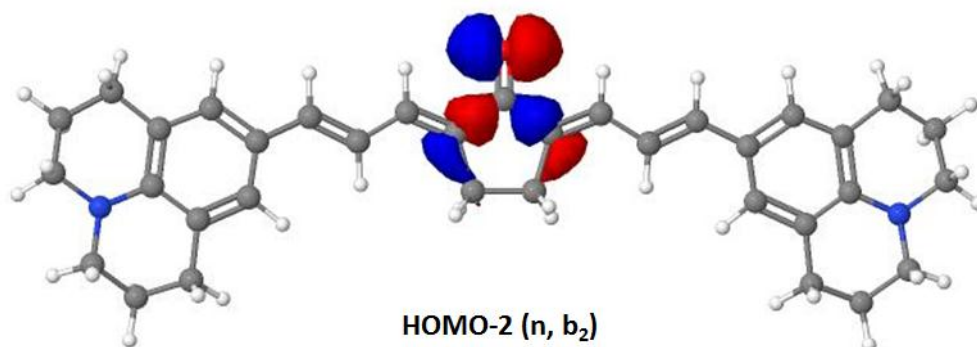
HOMO-2 (n, b₂)

MO 133

Figure 64. Computed molecular orbitals of bis-juldmac in the gas phase.

Tables 25 and 26 present the TD-DFT spectral calculations in the gas phase and in

solvent environments for bis-dmac and bis-juldmac. Figure 65 shows a direct comparison of the

predicted excited state energies for bis-dmac and bis-juldmac in the gas phase. Tables 27 and 28

present the molecular orbitals (with their corresponding symmetries) that are important in the

configuration interactions for both compounds. For purposes of classification, C_{2V} symmetry is

assumed. For bis-dmac, in the gas phase, TD-DFT computes S_1 as a strong symmetry allowed

$B_2 \leftarrow A_1$ transition of the (π, π^*) type localized at 2.54 eV (λ 488 nm, f = 2.02), arising from the

orbital excitation $a_2(\pi) \rightarrow b_1(\pi^*)$, where $a_2(\pi)$ is the HOMO and $b_1(\pi^*)$ is the LUMO. The S_2

state is computed to be a symmetry forbidden $A_2 \leftarrow A_1$ transition of the (n, π^*) type localized at

2.80 eV (λ 444 nm, f = 0.0009), arising from the orbital excitation $b_2(n) \rightarrow b_1(\pi^*)$, where $b_2(n)$ is

the HOMO-2 nonbonding molecular orbital localized on the oxygen atom.

In all PCM solvents studied, TD-DFT predicts S_1 as (π, π^*) ($\Gamma = B_2$). The energy of the

S_1 state decreases in the following order: 2.38 eV (λ 521 nm, n-hexane), 2.34 eV (λ 530 nm,

toluene), 2.32 eV (λ 535 nm, carbon disulfide), 2.28 eV (λ 544 nm, dichloromethane), and

2.27 eV (λ 545 nm, methanol). The $^1(n, \pi^*)$ state ($\Gamma = A_2$) is predicted to be S_2 in the gas phase

and S_3 in all solvent environments. The inversion of $^1(n, \pi^*)$ from S_2 to S_3 is attributed to the red

shift of the (π, π^*) state and the blue shift of (n, π^*). The energy of the $^1(n, \pi^*)$ state increases in

the following order: 2.88 eV (λ 430 nm, n-hexane), 2.91 eV (λ 426 nm, toluene), 2.92 eV

(λ 425 nm, carbon disulfide), 2.93 eV (λ 423 nm, methanol), and 2.94 eV (λ 422 nm,

dichloromethane). Further, TD-DFT predicts the following orbital configurations for the triplet

excited states: $T_1(\pi, \pi^*)$ ($\Gamma = B_2$), $T_2(\pi, \pi^*)$ ($\Gamma = A_1$), and $T_3(n, \pi^*)$ ($\Gamma = A_2$).

For bis-juldmac, in the gas phase, TD-DFT predicts S_1 as a strong symmetry allowed $B_2 \leftarrow A_1$ transition of (π, π^*) orbital nature localized at 2.45 eV (λ 505 nm, f = 2.03), arising from the orbital excitation $a_2(\pi) \rightarrow b_1(\pi^*)$, where $a_2(\pi)$ is the HOMO and $b_1(\pi^*)$ is the LUMO. The S_3 state is computed to be the forbidden $A_2 \leftarrow A_1$ transition of the (n, π^*) type localized at 2.81 eV (λ 441 nm, f = 0.011), arising from the orbital excitation $b_2(n) \rightarrow b_1(\pi^*)$, where $b_2(n)$ is the HOMO-2 nonbonding molecular orbital localized on the oxygen atom. In solvents, TD-DFT predicts S_1 as (π, π^*) and S_3 as (n, π^*). In the triplet state manifold, T_3 is predicted to be (n, π^*) in the gas phase, n-hexane, and toluene, switching to T_4 in dichloromethane and methanol. The inversion is attributed to hypsochromic shifting of (n, π^*) with respect to increased solvent polarity. It can be concluded that S_1 and T_1 of bis-dmac and bis-juldmac are nearly identical in their electronic structure.

(A$_1$) S$_3$ (π, π*) $\underline{\quad 2.89 \quad}$

(A$_2$) S$_2$ (n, π*) $\underline{\quad 2.80 \quad}$

(B$_2$) S$_1$ (π, π*) $\underline{\quad 2.54 \quad}$ $\underline{\quad 2.47 \quad}$ T$_3$ (n, π*) (A$_2$)

$\underline{\quad 1.73 \quad}$ T$_2$ (π, π*) (A$_1$)

$\underline{\quad 1.59 \quad}$ T$_1$ (π, π*) (B$_2$)

S$_0$ $\quad$ ——

bis-dmac

(A$_2$) S$_3$ (n, π*) $\underline{\quad 2.81 \quad}$

(A$_1$) S$_2$ (π, π*) $\underline{\quad 2.78 \quad}$

(B$_2$) S$_1$ (π, π*) $\underline{\quad 2.45 \quad}$ $\underline{\quad 2.47 \quad}$ T$_3$ (n, π*) (A$_2$)

$\underline{\quad 1.70 \quad}$ T$_2$ (π, π*) (A$_1$)

$\underline{\quad 1.55 \quad}$ T$_1$ (π, π*) (B$_2$)
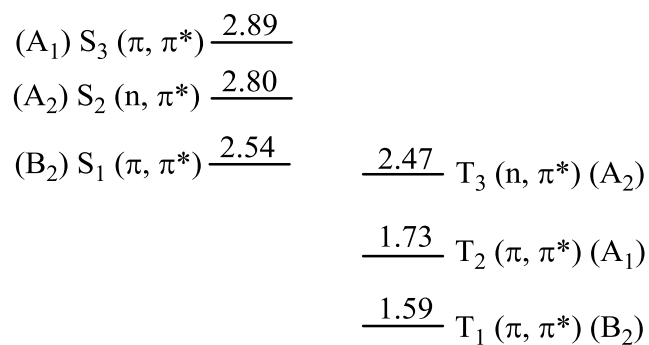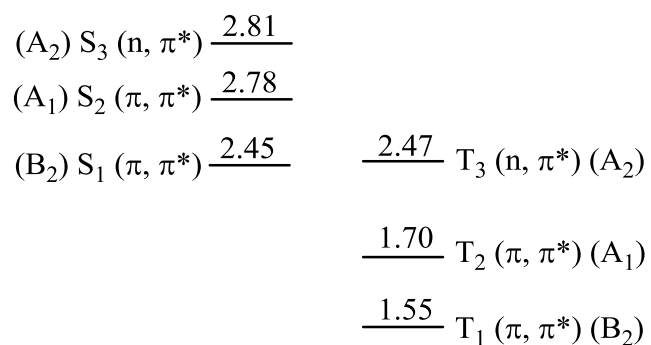
S$_0$ $\quad$ ——

bis-juldmac

Figure 65. Gas phase electronic energies of bis-dmac and bis-juldmac (in eV) at the TD-DFT

B3LYP/6-31G(d) level of theory.

Table 25. TD-DFT spectral calculations of bis-dmac both in the gas phase and in solvent environments at the B3LYP/6-31G(d) level of theory.[†]

Solvent	State	Transition Energy			f	MO	CI Coef.
		eV	cm^{-1}	nm			
Gas (μ = 5.84 D)	T_1 (π, π*) (B$_2$)	1.59	12788	782	0.00	104→108	-0.17988
						106→109	0.22564
						107→108	0.63926
	T_2 (π, π*) (A$_1$)	1.73	13986	715	0.00	103→108	-0.23667
						106→108	0.57600
						107→109	0.31931
	T_3 (n, π*) (A$_2$)	2.47	19920	502	0.00	105→108	0.68431
						105→112	0.13230
	S_1 (π, π*) (B$_2$)	2.54	20492	488	2.02	107→108	0.70744
	S_2 (n, π*) (A$_2$)	2.80	22523	444	0.0009	105→108	0.67820
						105→112	0.10066
						106→108	0.14535
	S_3 (π, π*) (A$_1$)	2.89	23310	429	0.028	105→108	-0.15053
						106→108	0.65616
						107→109	-0.20778
n-Hexane (μ = 6.58 D)	T_1 (π, π*) (B$_2$)	1.56	12594	794	0.00	104→108	-0.18543
						106→109	0.21226
						107→108	0.64230
	T_2 (π, π*) (A$_1$)	1.74	14065	711	0.00	103→108	-0.23711
						106→108	0.57763
						107→109	0.31415
	S_1 (π, π*) (B$_2$)	2.38	19194	521	2.22	107→108	0.70641
	T_3 (n, π*) (A$_2$)	2.56	20661	484	0.00	105→108	0.68275
						105→112	0.12638
	S_2 (π, π*) (A$_1$)	2.77	22371	447	0.042	106→108	0.68420
						107→109	-0.14120
	S_3 (n, π*) (A$_2$)	2.88	23256	430	0.0013	105→108	0.68587

						104→108	-0.18703
	$T_1(\pi, \pi^*)$	1.55	12500	800	0.00	106→109	0.20673
	(B_2)					107→108	0.64373
						103→108	-0.23464
	$T_2(\pi, \pi^*)$	1.75	14085	710	0.00	106→108	0.57939
Carbon	(A_1)					107→109	0.31126
Disulfide	$S_1(\pi, \pi^*)$						
(μ = 6.91 D)	(B_2)	2.32	18692	535	2.29	107→108	0.70579
	$T_3(n, \pi^*)$					105→108	0.68014
	(A_2)	2.60	20964	477	0.00	105→112	0.12324
	$S_2(\pi, \pi^*)$					106→108	0.69460
	(A_1)	2.72	21978	455	0.050	107→109	-0.11361
	$S_3(n, \pi^*)$					103→108	0.10800
	(A_2)	2.92	23529	425	0.0006	105→108	0.68674
						104→108	-0.18664
	$T_1(\pi, \pi^*)$	1.55	12531	798	0.00	106→109	0.20823
	(B_2)					107→108	0.64333
						103→108	-0.23555
	$T_2(\pi, \pi^*)$	1.74	14065	711	0.00	106→108	0.57885
Toluene	(A_1)					107→109	0.31209
(μ = 6.82 D)	$S_1(\pi, \pi^*)$						
	(B_2)	2.34	18868	530	2.26	107→108	0.70610
	$T_3(n, \pi^*)$					105→108	0.68109
	(A_2)	2.59	20877	479	0.00	105→112	0.12416
	$S_2(\pi, \pi^*)$					106→108	0.69139
	(A_1)	2.74	22124	452	0.047	107→109	-0.12682
	$S_3(n, \pi^*)$						
	(A_2)	2.91	23474	426	0.0007	105→108	0.68735
						105→108	-0.18894
	$T_1(\pi, \pi^*)$	1.52	12285	814	0.00	106→109	0.19421
	(B_2)					107→108	0.64743
						103→108	-0.20642
	$T_2(\pi, \pi^*)$	1.74	14065	711	0.00	104→108	0.11710
	(A_1)					106→108	0.58607
Dichloro-						107→109	0.30266
methane	$S_1(\pi, \pi^*)$						
(μ = 7.72 D)	(B_2)	2.28	18382	544	2.26	107→108	0.70646
	$S_2(\pi, \pi^*)$					106→108	0.69336
	(A_1)	2.68	21645	462	0.048	107→109	-0.12946
						103→108	0.25841
	$T_3(n, \pi^*)$	2.68	21645	462	0.00	104→108	0.63659
	(A_2)					104→112	-0.10735
	$S_3(n, \pi^*)$					103→108	0.29374
	(A_2)	2.94	23697	422	0.0002	104→108	0.63207

						105→108	-0.18898
Methanol (μ = 8.04 D)	T_1 (π, π*) (B₂)	1.51	12180	821	0.00	106→109	0.18965
						107→108	0.64896
	T_2 (π, π*) (A₁)	1.74	14045	712	0.00	103→108	-0.16474
						104→108	0.16698
						106→108	0.58948
						107→109	0.29872
	S_1 (π, π*) (B₂)	2.27	18349	545	2.23	107→108	0.70685
	S_2 (π, π*) (A₁)	2.67	21505	465	0.046	106→108	0.69171
						107→109	-0.13902
	T_3 (n, π*) (A₂)	2.71	21882	457	0.00	103→108	0.39911
						104→108	0.55890
	S_3 (n, π*) (A₂)	2.93	23641	423	0.0001	103→108	0.45522
						104→108	0.52836

[†]In the gas phase, n-hexane, carbon disulfide, and toluene, HOMO-2 (#105) is the nonbonding orbital. In dichloromethane, HOMO-3 (#104) is the nonbonding orbital. In methanol, both HOMO-3 (#104) and HOMO-4 (#103) are mixes of both π-bonding and nonbonding characters (primarily nonbonding).

Table 26. TD-DFT spectral calculations of bis-juldmac both in the gas phase and in solvent environments at the B3LYP/6-31G(d) level of theory. [†]

Solvent	State	Transition Energy			f	MO	CI Coef.
		eV	cm^{-1}	nm			
Gas (μ = 5.76 D)	T_1 (π, π^*) (B$_2$)	1.55	12484	801	0.00	132$\rightarrow$136	0.18887
						134$\rightarrow$137	0.22327
						135$\rightarrow$136	0.63673
	T_2 (π, π^*) (A$_1$)	1.70	13717	729	0.00	131$\rightarrow$136	-0.24262
						134$\rightarrow$136	0.57294
						135$\rightarrow$137	0.31844
	S_1 (π, π^*) (B$_2$)	2.45	19802	505	2.03	135$\rightarrow$136	0.70744
	T_3 (n, π^*) (A$_2$)	2.47	19960	501	0.00	133$\rightarrow$136	0.68370
						133$\rightarrow$140	0.13181
	S_2 (π, π^*) (A$_1$)	2.78	22422	446	0.019	133$\rightarrow$136	0.40141
						134$\rightarrow$136	0.55053
						135$\rightarrow$137	-0.15598
	S_3 (n, π^*) (A$_2$)	2.81	22676	441	0.011	133$\rightarrow$136	0.56552
						134$\rightarrow$136	-0.39302
						135$\rightarrow$137	0.11924
n-Hexane (μ = 6.54 D)	T_1 (π, π^*) (B$_2$)	1.52	12255	816	0.00	132$\rightarrow$136	-0.17398
						134$\rightarrow$137	0.20999
						135$\rightarrow$136	0.64081
	T_2 (π, π^*) (A$_1$)	1.70	13736	728	0.00	131$\rightarrow$136	-0.23540
						134$\rightarrow$136	0.57814
						135$\rightarrow$137	0.31206
	S_1 (π, π^*) (B$_2$)	2.30	18519	540	2.22	135$\rightarrow$136	0.70631
	T_3 (n, π^*) (A$_2$)	2.57	20704	483	0.00	132$\rightarrow$136	0.28131
						133$\rightarrow$136	0.61886
						133$\rightarrow$140	0.11394
	S_2 (π, π^*) (A$_1$)	2.68	21598	463	0.045	134$\rightarrow$136	0.69182
						135$\rightarrow$137	-0.13248
	S_3 (n, π^*) (A$_2$)	2.86	23041	434	0.0003	131$\rightarrow$136	0.11665
						132$\rightarrow$136	0.28501
						133$\rightarrow$136	0.62394

	T$_1$ (π, π*) (B$_2$)	1.51	12180	821	0.00	133→136	-0.19164
						134→137	0.20602
						135→136	0.64220
	T$_2$ (π, π*) (A$_1$)	1.70	13736	728	0.00	131→136	-0.22997
						134→136	0.58056
Toluene (μ = 6.80 D)						135→137	0.30953
	S$_1$ (π, π*) (B$_2$)	2.26	18215	549	2.26	135→136	0.70600
	T$_3$ (n, π*) (A$_2$)	2.59	20921	478	0.00	131→136	0.12364
						132→136	0.67408
						132→140	0.12224
	S$_2$ (π, π*) (A$_1$)	2.64	21322	469	0.049	134→136	0.69510
						135→137	-0.11833
	S$_3$ (n, π*) (A$_2$)	2.85	23041	434	0.0002	131→136	0.15345
						132→136	0.67830
	T$_1$ (π, π*) (B$_2$)	1.47	11891	841	0.00	133→136	-0.19032
						134→137	0.19232
						135→136	0.64770
	T$_2$ (π, π*) (A$_1$)	1.69	13643	733	0.00	131→136	-0.13878
						132→136	0.18235
						134→136	0.59217
Dichloro-methane (μ = 7.79 D)						135→137	0.29808
	S$_1$ (π, π*) (B$_2$)	2.19	17668	566	2.25	135→136	0.70641
	S$_2$ (π, π*) (A$_1$)	2.57	20747	482	0.049	134→136	0.69526
						135→137	-0.12194
	T$_3$ (π, π*) (A$_1$)	2.66	21459	466	0.00	132→136	0.26898
						133→137	-0.20245
						134→136	-0.37936
						135→137	0.46064
	S$_3$ (n, π*) (A$_2$)	2.84	22936	436	0.0001	131→136	0.52204
						132→136	0.46288

	T_1 (π, π^*) (B$_2$)	1.46	11765	850	0.00	133→136	-0.18896
						134→137	0.18791
						135→136	0.64972
	T_2 (π, π^*) (A$_1$)	1.69	13605	735	0.00	132→136	-0.20659
						134→136	0.59697
						135→137	0.29337
Methanol (μ = 8.15 D)	S_1 (π, π^*) (B$_2$)	2.18	17606	568	2.23	135→136	0.70683
	S_2 (π, π^*) (A$_1$)	2.56	20661	484	0.047	134→136	0.69362
						135→137	-0.13152
	T_3 (π, π^*) (A$_1$)	2.64	21277	470	0.00	132→136	-0.27016
						133→137	-0.20718
						134→136	-0.37459
						135→137	0.46498
	S_3 (n, π^*) (A$_2$)	2.84	22883	437	0.0001	131→136	0.62180
						132→136	-0.31729

[†]In both the gas phase and n-hexane, HOMO-2 (#133) is the nonbonding orbital. In toluene, HOMO-3 (#132) is the nonbonding orbital. In both dichloromethane and methanol, HOMO-4 (#131) is the nonbonding orbital.

Table 27. Gas phase electronic energies (Hartree) and irreducible representations of the MOs important in configuration interaction (CI) for bis-dmac.

113	0.04936	a_2
112	0.01626	b_1
111	0.00462	a_2
110	0.00348	b_1
109	-0.03159	a_2
108	-0.06901	b_1 LUMO
107	-0.17088	a_2 HOMO
106	-0.17999	b_1
105	-0.21195	b_2
104	-0.22120	a_2
103	-0.22465	b_1
102	-0.24804	b_1
101	-0.24804	b_1
100	-0.27841	b_1

Table 28. Gas phase electronic energies (Hartree) and irreducible representations of the MOs important in configuration interaction (CI) for bis-juldmac.

141	0.04575	a_2
140	0.01632	b_1
139	0.00412	a_2
138	0.00321	b_1
137	-0.02981	a_2
136	-0.06709	b_1 LUMO
135	-0.16596	a_2 HOMO
134	-0.17449	b_1
133	-0.20991	b_2
132	-0.21551	a_2
131	-0.21977	b_1
130	-0.23251	b_1
129	-0.23254	b_1
128	-0.27593	b_1

4.2.3.1.4 Fluorescence Quantum Yields, Lifetimes, and Decay Constants

Experimental data demonstrate that both Φ_f and τ_f values show solvent dependence with quantum yields ranging between 0.007 (in trifluoroethanol) to 0.48 (in dichloromethane) for bis-dmac and between 0.008 (in trifluoroethanol) and 0.30 (in benzene and toluene) for bis-juldmac. Lifetimes of bis-dmac range between 0.14 ns (in trifluoroethanol) and 1.17 ns (in pyridine) and those of bis-juldmac between 0.28 ns (in trifluoroethanol) and 1.17 ns (in diethyl ether).

Table 29. Photophysical properties of bis-dmac in various solvents.

	Solvent	Φ_f	τ_f (ns)	k_f (s^{-1})	k_{nr} (s^{-1})
1	Trifluoroethanol	0.007	0.14	5.00×10^7	7.09×10^9
2	Methanol	0.022	0.21	1.05×10^8	4.66×10^9
3	Ethanol	0.076	0.24	3.17×10^8	3.85×10^9
4	1-Propanol	0.12	0.19	6.32×10^8	4.63×10^9
5	1-Butanol	0.17	0.37	4.59×10^8	2.24×10^9
6	2-Propanol	0.15	0.56	2.68×10^8	1.52×10^9
7	Dimethyl sulfoxide	0.14	0.58	2.41×10^8	1.48×10^9
8	Acetonitrile	0.075	0.49	1.53×10^8	1.89×10^9
9	Dimethylformamide	0.18	0.67	2.69×10^8	1.22×10^9
10	Acetone	0.24	0.80	3.00×10^8	9.50×10^8
11	Pyridine	0.40	1.17	3.42×10^8	5.13×10^8
12	Dichloromethane	0.48	1.08	4.44×10^8	4.81×10^8
13	Ethyl acetate	0.35	0.69	5.07×10^8	9.42×10^8
14	Carbon disulfide	0.43	0.83	5.18×10^8	6.87×10^8
15	Diethyl ether	0.26	0.76	3.42×10^8	9.74×10^8
16	Benzene	0.42	0.81	5.19×10^8	7.16×10^8
17	Toluene	0.40	0.86	4.65×10^8	6.98×10^8
18	Carbon tetrachloride	0.25	0.76	3.29×10^8	9.87×10^8
19	n-Hexane	0.041	0.86	4.77×10^7	1.12×10^9
20	Cyclohexane	0.069	0.48	1.44×10^8	1.94×10^9

Table 30. Photophysical properties of bis-juldmac in various solvents.

	Solvent	Φ_f	τ_f (ns)	k_f (s^{-1})	k_{nr} (s^{-1})
1	Trifluoroethanol	0.008	0.28	2.86×10^7	3.54×10^9
2	Methanol	0.025	0.35	7.14×10^7	2.78×10^9
3	Ethanol	0.026	0.39	6.67×10^7	2.50×10^9
4	1-Propanol	0.042	0.37	1.14×10^8	2.59×10^9
5	1-Butanol	0.061	0.47	1.30×10^8	2.00×10^9
6	2-Propanol	0.070	0.57	1.23×10^8	1.63×10^9
7	Dimethyl sulfoxide	0.062	0.67	9.25×10^7	1.40×10^9
8	Acetonitrile	0.037	0.45	8.22×10^7	2.14×10^9
9	Dimethylformamide	0.053	0.75	7.07×10^7	1.26×10^9
10	Acetone	0.092	0.96	9.58×10^7	9.46×10^8
11	Pyridine	0.17	0.93	1.83×10^8	8.92×10^8
12	Dichloromethane	0.15	1.15	1.30×10^8	7.39×10^8
13	Ethyl acetate	0.10	0.91	1.10×10^8	9.89×10^8
14	Carbon disulfide	0.078	0.91	8.57×10^7	1.01×10^9
15	Diethyl ether	0.26	1.17	2.22×10^8	6.32×10^8
16	Benzene	0.30	0.87	3.45×10^8	8.05×10^8
17	Toluene	0.30	0.93	3.23×10^8	7.53×10^8
18	n-Hexane	0.13	0.87	1.49×10^8	1.00×10^9

The Φ_f values for bis-dmac and bis-juldmac have been plotted against ν_f (Figures 66 and 67). For both molecules, behavior similar to Asdimcy1 is observed in the quantum yield plots in that Φ_f is low at higher energy gaps, rises in the intermediate region, then drops back down at smaller energy gaps. For bis-dmac, a parabolic trend is seen, where in n-hexane ($\nu_f = 20{,}161$ cm^{-1}), Φ_f is low (0.041). As solvent polarity gradually increases, Φ_f increases, reaching a maximum in dichloromethane at $\nu_f = 14{,}880$ cm^{-1} ($\Phi_f = 0.48$). A further increase in polarity results in lower Φ_f's. A similar parabolic trend, although not as obvious, is seen for bis-juldmac.

Both k_f and k_{nr} values of bis-dmac and bis-juldmac were calculated using equations 4-1 and 4-2, respectively. Both k_f and k_{nr} values show solvent dependence. The k_f values range between 4.77×10^7 s^{-1} (n-hexane) to 6.32×10^8 s^{-1} (1-propanol) (for bis-dmac) and between 2.86×10^7 s^{-1} (TFE) to 3.45×10^8 s^{-1} (benzene) (for bis-juldmac). The k_{nr} values range between 4.81×10^8 s^{-1} (dichloromethane) to 7.09×10^9 s^{-1} (TFE) (for bis-dmac) and between 6.32×10^8 s^{-1} (diethyl ether) to 3.54×10^9 s^{-1} (TFE) (for bis-juldmac). The k_{nr} values have been plotted against the corrected maximum energies of fluorescence in various solvents for both compounds (see Figures 68 and 69). Similar trends are observed in both k_{nr} plots, which can be partitioned into two distinct regions: the region from the minimum to the low frequency side (region 1) and the region from the minimum to the high frequency side (region 2).

For the case of bis-dmac (Figure 68), in region 1, k_{nr} increases from 1.22×10^9 s^{-1} (dimethylformamide, $\nu_f = 13{,}980$ cm^{-1}) to 7.09×10^9 s^{-1} (TFE, $\nu_f = 13{,}089$ cm^{-1}). In region 2, k_{nr} decreases from 1.94×10^9 s^{-1} (cyclohexane, $\nu_f = 20{,}000$ cm^{-1}) to 9.50×10^8 s^{-1} (acetone, $\nu_f = 14{,}400$ cm^{-1}). Recalling that $k_{nr} = k_{ic} + k_{isc}$, where k_{ic} is the rate of internal conversion and

k_{isc} is the rate of intersystem crossing from the singlet to the triplet manifold of states, it is believed that the variation in k_{nr} shown in Figure 68 can be attributed to opposing behavior for these two rates with respect to solvent polarity. In shifting from nonpolar (high ν_f) to polar solvents (low ν_f), k_{ic} increases while k_{isc} decreases. In region 1, where k_{nr} increases with a decrease in ν_f, the increase in k_{ic} dominates the decrease in k_{isc}; whereas in region 2, where k_{nr} decreases with a decrease in ν_f, the decrease in k_{isc} dominates the increase in k_{ic}. The increase in k_{nr} found in region 1 is attributed to the energy gap law for internal conversion. In region 2, where intersystem crossing is the major nonradiative decay channel, it is believed that the solvent modulated location of (n, π^*) states relative to the $S_1(\pi, \pi^*)$ and $T_1(\pi, \pi^*)$ states governs the rate of S → T intersystem crossing.

As with the discussion of Asdimcy1, vibronic spin-orbit coupling can be considered as a second order mechanism in explaining the decrease in k_{nr} shown in region 2 of both k_{nr} plots. Theoretical support is provided to explain the k_{nr} decrease, which involved determining the energy differences between the lowest lying (n, π^*) and (π, π^*) states in both the singlet and triplet manifolds (see Table 31). From the TD-DFT calculations of bis-dmac and bis-juldmac, the decrease in k_{nr} is consistent with a gradual solvent induced increase in the spacing between S_1/T_1 (π, π^*) and the higher energy (n, π^*) states, resulting in an attenuation in the degree of mixing between (n, π^*) and (π, π^*) states in either the singlet and triplet manifolds.
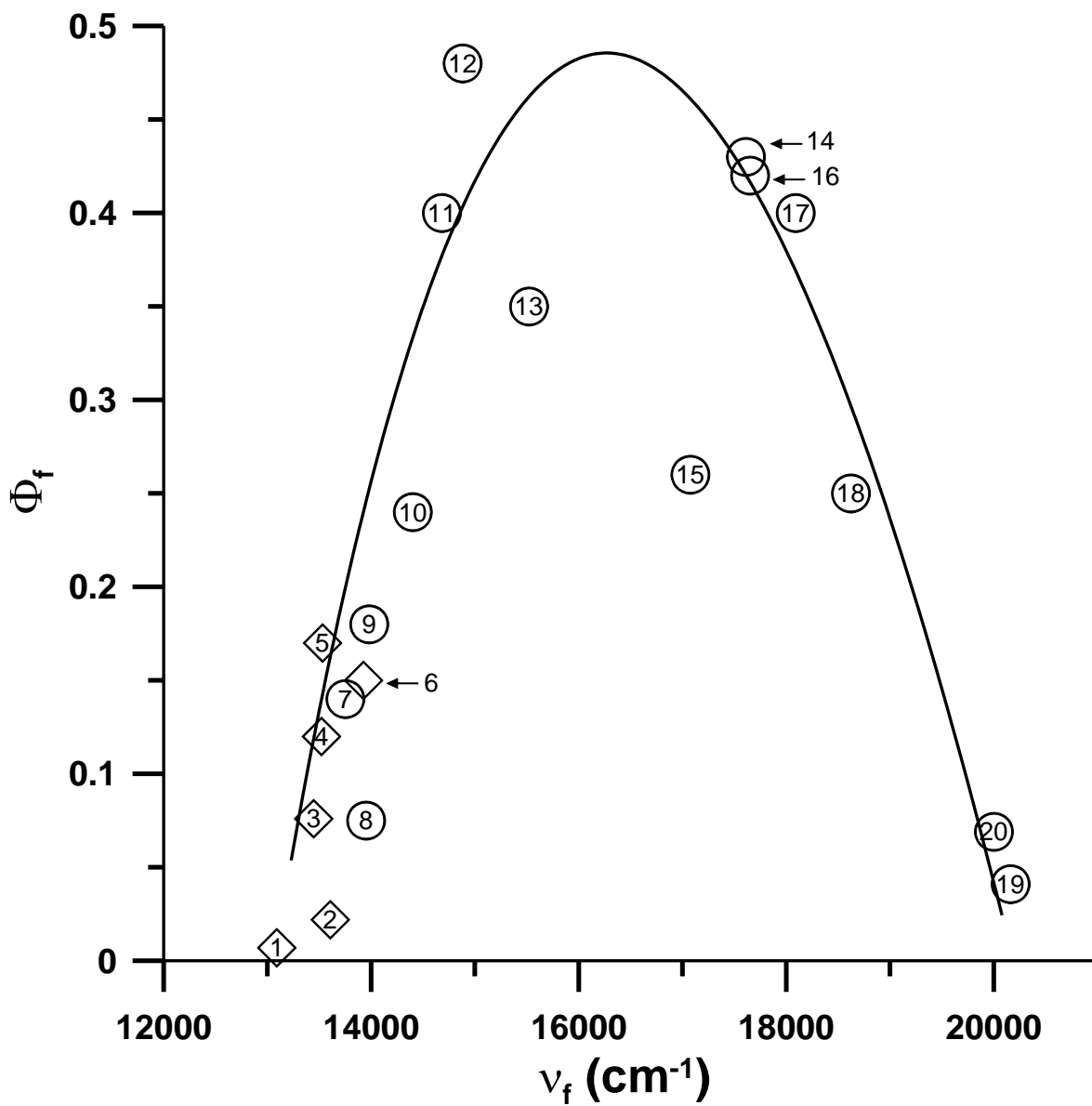
Figure 66. Fluorescence quantum yields (Φ_f) plotted against the fluorescence spectral maxima of bis-dmac in various solvents. Circles represent aprotic solvents; diamonds represent protic solvents.
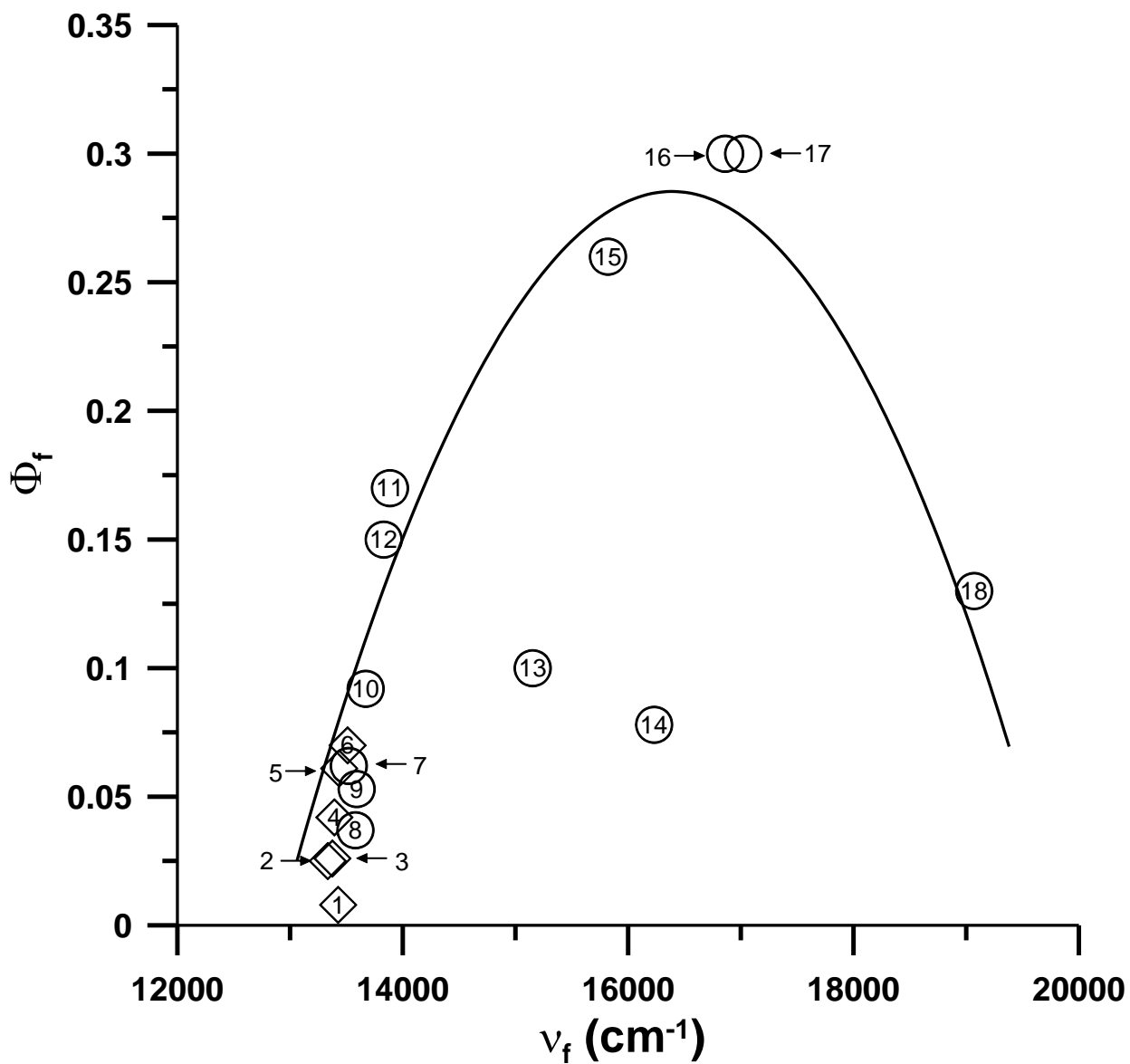
Figure 67. Fluorescence quantum yields (Φ_f) plotted against the fluorescence spectral maxima of bis-juldmac in various solvents. Circles represent aprotic solvents; diamonds represent protic solvents.
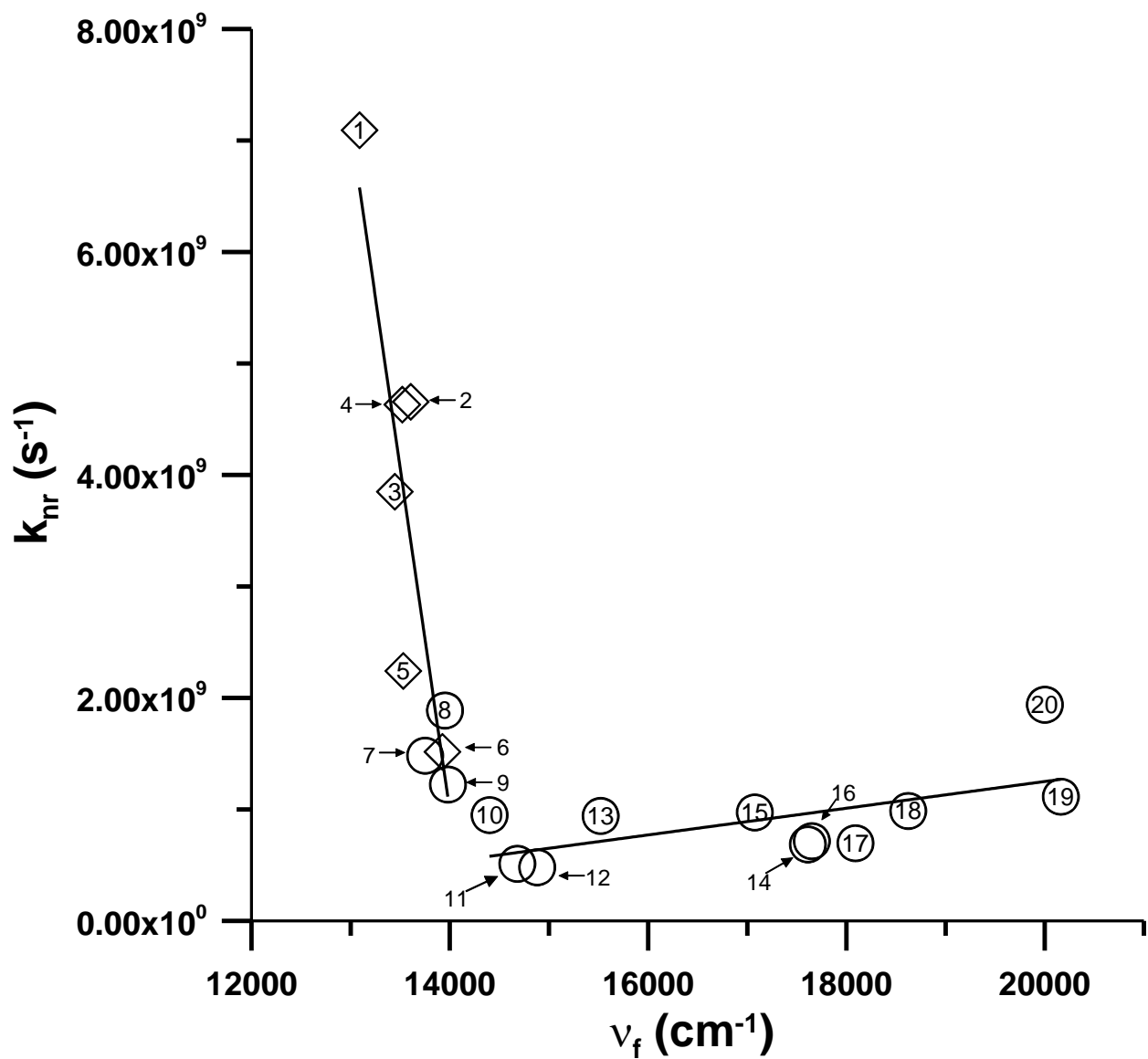
Figure 68. Nonradiative decay constants (k_{nr}) plotted against the fluorescence spectral maxima of bis-dmac in various solvents. Circles represent aprotic solvents; diamonds represent protic solvents.
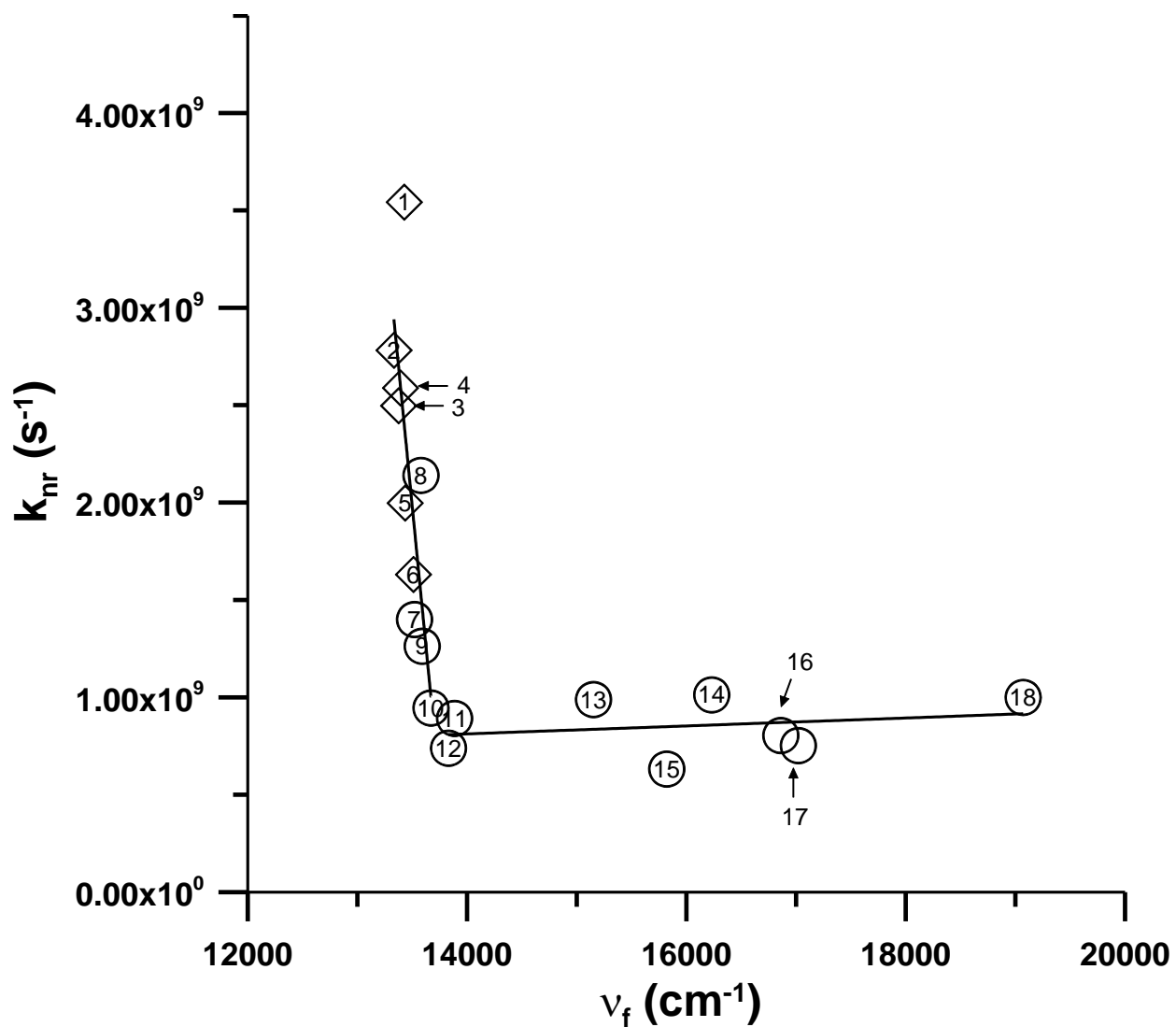
Figure 69. Nonradiative decay constants (k_{nr}) plotted against the fluorescence spectral maxima of bis-juldmac in various solvents. Circles represent aprotic solvents; diamonds represent protic solvents.

Table 31. TD-DFT computed energy gaps between the lowest lying (n, π*) and (π, π*) states and experimental k_{nr} values for bis-dmac and bis-juldmac.

bis-dmac			
	Toluene	Carbon Disulfide	Dichloromethane
$T_3(n, \pi^*)$-$T_1(\pi, \pi^*)$	8346 cm^{-1}	8464 cm^{-1}	9360 cm^{-1}
$S_3(n, \pi^*)$-$S_1(\pi, \pi^*)$	4606 cm^{-1}	4837 cm^{-1}	5315 cm^{-1}
$k_{nr} \times 10^{-8}$ (s^{-1})	6.98	6.87	4.81
bis-juldmac			
	n-Hexane	Toluene	Dichloromethane
$T_m(n, \pi^*)$-$T_1(\pi, \pi^*)^{\dagger}$	8449 cm^{-1}	8741 cm^{-1}	9801 cm^{-1}
$S_3(n, \pi^*)$-$S_1(\pi, \pi^*)$	4522 cm^{-1}	4826 cm^{-1}	5268 cm^{-1}
$k_{nr} \times 10^{-8}$ (s^{-1})	10.0	7.53	7.39

†In n-hexane and toluene, m = 3; in dichloromethane, m = 4.

A linear relationship is observed when plotting the natural logarithm of k_{nr} against the S_0-S_1 energy gap (ν_f) for both bis-dmac and bis-juldmac in alcohols and several polar aprotic solvents that follow the energy gap law of internal conversion (Figure 70). Taking the natural logarithm of both sides of equation 4-3 (energy gap law), algebraic simplification leads to the following:

$$\ln k_{ic} = -\beta \Delta E + \ln \alpha \qquad (4\text{-}4)$$

Hence, both constants α and β can be determined from the linear regression equations. Constant β is expressed in cm and α is referred to as the pre-exponential factor, expressed in s^{-1}. Calculations show that for bis-dmac, $\beta = 0.0019$ cm and $\alpha = 4.21 \times 10^{20}\ s^{-1}$; for bis-juldmac, $\beta = 0.0029$ cm and $\alpha = 1.13 \times 10^{26}\ s^{-1}$. Similar values in β for both compounds suggest similar mechanistic details for deactivation via internal conversion from S_1.

To conclude, from the spectroscopic and photophysical data, the tendency for bis-dmac to undergo fluorescence quenching in polar solvents cannot be attributed to twisting of the $-N(CH_3)_2$ group to form a polar TICT state since its spatially restricted julolidine analogue, bis-juldmac, which cannot form a TICT state, behaves in a similar manner.
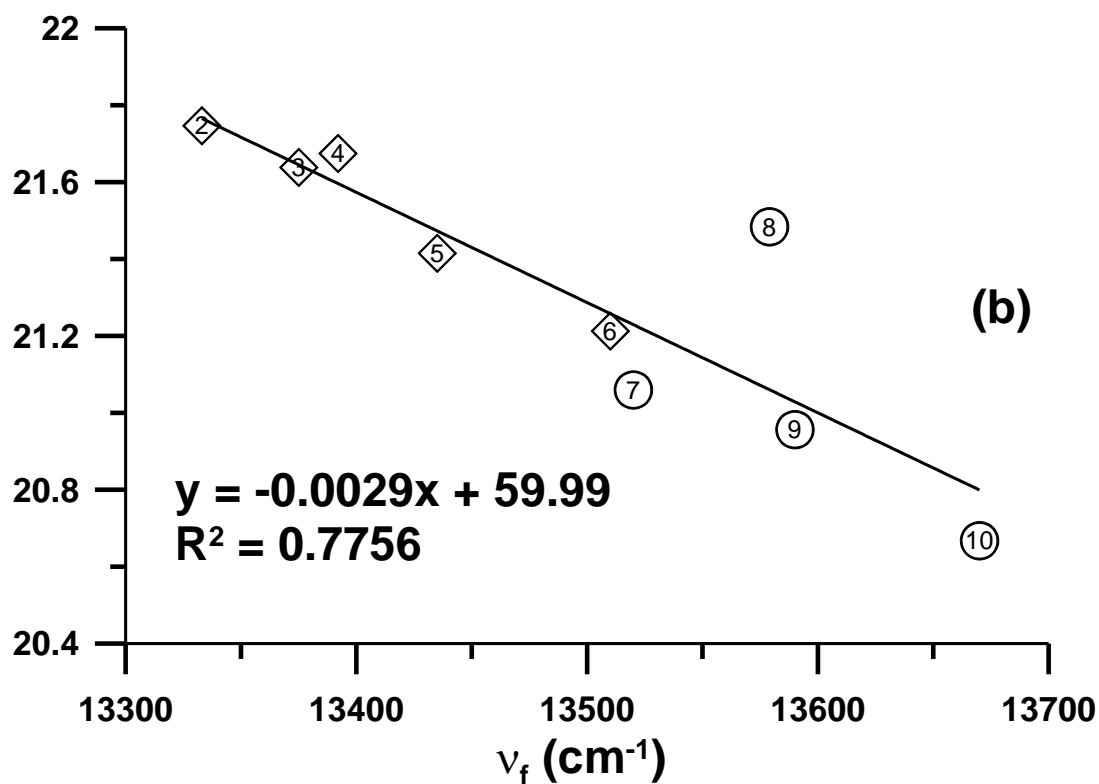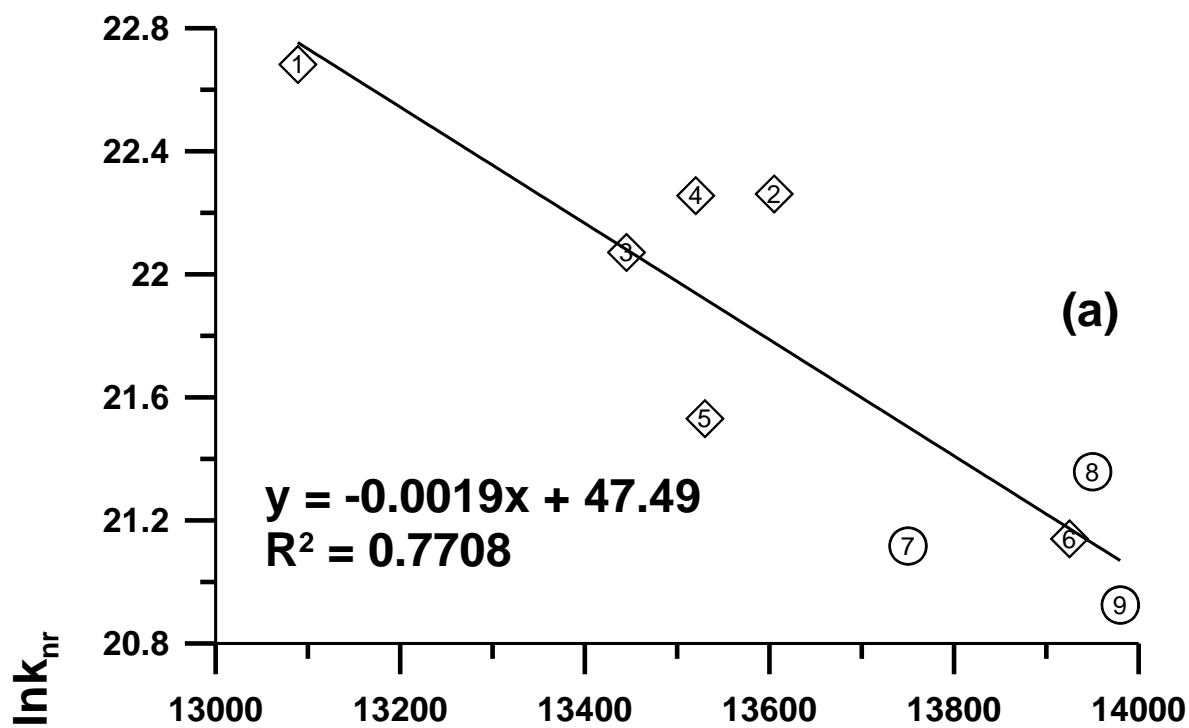
Figure 70. Plot of $\ln k_{nr}$ against the fluorescence spectral maxima of (a) bis-dmac and (b) bis-juldmac.

169

The C_{2V} symmetries of bis-dmac and bis-juldmac can be used to make the discussion of vibronic spin-orbit coupling more specific. Group theory can be used to demonstrate whether or not two excited states mix through first-order spin-orbit coupling. For two singlet and triplet state wavefunctions $^1\Psi_n$ and $^3\Psi_m$ to mix through SOC:

$$\left\langle {}^1\Psi_n \left| \hat{H}_{so} \right| {}^3\Psi_m \right\rangle \neq 0$$

The direct product of the irreducible representations of $^1\Psi_n$, $^3\Psi_m$, and $\hat{H}_{so}$ must equate to the totally symmetric irreducible representation (A_1 in the C_{2v} point group) in order for the wavefunctions to mix through SOC:

$$\Gamma({}^1\Psi_n) \times \Gamma(\hat{H}_{so}) \times \Gamma({}^3\Psi_m) = \Gamma_{totsym} = A_1$$

The spin-orbit coupling Hamiltonian operator involves the orbital angular momentum operators, $\hat{l}_x, \hat{l}_y, \hat{l}_z$, for which the appropriate irreducible representations are the rotations R_x, R_y, and R_z, where $\Gamma(R_x) = B_2$; $\Gamma(R_y) = B_1$; $\Gamma(R_z) = A_2$.

To exemplify, for the case of bis-dmab, group theory is used to demonstrate whether or not the following excited states mix though first-order spin-orbit coupling:

1. $\left\langle {}^1B_2(\pi,\pi^*) \left| \hat{H}_{so} \right| {}^3A_2(n,\pi^*) \right\rangle$

$$\Gamma({}^1B_2) \times \Gamma(R_x) \times \Gamma({}^3A_2) = B_2 \times B_2 \times A_2 = A_1 \times A_2 = A_2 \neq \Gamma_{totsym}$$

$$\Gamma({}^1B_2) \times \Gamma(R_z) \times \Gamma({}^3A_2) = B_2 \times A_2 \times A_2 = B_1 \times A_2 = B_2 \neq \Gamma_{totsym}$$

$$\Gamma({}^1B_2) \times \Gamma(R_y) \times \Gamma({}^3A_2) = B_2 \times B_1 \times A_2 = A_2 \times A_2 = A_1 = \Gamma_{totsym}$$

Hence, since the direct product involving $\Gamma(R_y)$ is equal to A_1, then ${}^1B_2(\pi, \pi^*)$ and ${}^3A_2(n, \pi^*)$ mix through first-order SOC.

2. $\left\langle {}^1B_2(\pi,\pi^*) \left| \hat{H}_{so} \right| {}^3B_2(\pi,\pi^*) \right\rangle$

$$\Gamma({}^1B_2) \times \Gamma(R_x) \times \Gamma({}^3B_2) = B_2 \times B_2 \times B_2 = A_1 \times B_2 = B_2 \neq \Gamma_{totsym}$$

$$\Gamma({}^1B_2) \times \Gamma(R_y) \times \Gamma({}^3B_2) = B_2 \times B_1 \times B_2 = A_2 \times B_2 = B_1 \neq \Gamma_{totsym}$$

$$\Gamma({}^1B_2) \times \Gamma(R_z) \times \Gamma({}^3B_2) = B_2 \times A_2 \times B_2 = B_1 \times B_2 = A_2 \neq \Gamma_{totsym}$$

Since none of the three direct products equate to A_1, then ${}^1B_2(\pi, \pi^*)$ and ${}^3B_2(\pi, \pi^*)$ don't mix through first-order SOC.

3. $\left\langle {}^{1}A_{2}(n,\pi^*)\middle|\hat{H}_{so}\middle|{}^{3}A_{2}(n,\pi^*)\right\rangle$

$$\Gamma({}^{1}A_{2}) \times \Gamma(R_{x}) \times \Gamma({}^{3}A_{2}) = A_{2} \times B_{2} \times A_{2} = B_{1} \times A_{2} = B_{2} \neq \Gamma_{totsym}$$

$$\Gamma({}^{1}A_{2}) \times \Gamma(R_{y}) \times \Gamma({}^{3}A_{2}) = A_{2} \times B_{1} \times A_{2} = B_{2} \times A_{2} = B_{1} \neq \Gamma_{totsym}$$

$$\Gamma({}^{1}A_{2}) \times \Gamma(R_{z}) \times \Gamma({}^{3}A_{2}) = A_{2} \times A_{2} \times A_{2} = A_{1} \times A_{2} = A_{2} \neq \Gamma_{totsym}$$

Since none of the three direct products equate to A_{1}, then ${}^{1}A_{2}(n, \pi^*)$ and ${}^{3}A_{2}(n, \pi^*)$ don't

mix through first-order SOC.

Group theory can also be applied to vibronic coupling (VC). According to the Herzberg-Teller treatment of vibronic coupling, nuclear displacements (or vibrations) have an effect on the mixing between two states of the same spin multiplicity. For two states Φ_k and Φ_m to be vibronically coupled, the following must hold:

$$\left\langle \Phi_k \left| \frac{\delta \hat{H}}{\delta Q_i} Q_i \right| \Phi_m \right\rangle \neq 0$$

where Q is a vibrational normal coordinate.

The direct product of the irreducible representations of Φ_k, Φ_m, and the vibration must equate to the totally symmetric irreducible representation (A_1 in C_{2v}) in order for the electronic states to mix through VC:

$$\Gamma(\Phi_k) \times \Gamma(vib) \times \Gamma(\Phi_m) = \Gamma_{totsym} = A_1$$

This implies that

$$\Gamma(\Phi_k) \times \Gamma(\Phi_m) = \Gamma(vib)$$

Therefore, the irreducible representation of the vibration can be found.

In applying group theory to the vibronic coupling for excited states of bis-dmac and bis-juldmac:

Between $S_1(B_2)$ and $S_m(A_2)$ (m = 2 for bis-dmac; m = 3 for bis-juldmac):

$$\Gamma(S_1) \times \Gamma(vib) \times \Gamma(S_m) = \Gamma_{totsym} = A_1$$
$$\therefore \ \Gamma(vib) = \Gamma(S_1) \times \Gamma(S_m) = B_2 \times A_2 = b_1$$

Likewise, between $T_1(B_2)$ and $T_3(A_2)$:

$$\Gamma(T_1) \times \Gamma(vib) \times \Gamma(T_3) = \Gamma_{totsym} = A_1$$
$$\therefore \; \Gamma(vib) = \Gamma(T_1) \times \Gamma(T_3) = B_2 \times A_2 = b_1$$

Hence, b_1 corresponds to the irreducible representation of the vibration that induces the vibronic coupling between $S_1(\pi, \pi^*)$ and $S_m(n, \pi^*)$ and $T_1(\pi, \pi^*)$ and $T_m(n, \pi^*)$ states for bis-dmac and bis-juldmac.

As shown in Table 31, as solvent polarity increases, the (n, π^*)-(π, π^*) energy spacing also increases, which in turn reduces the vibronic coupling between two states of the same spin multiplicity in reference to equation 2-13. Therefore, the reduction of vibronic coupling attenuates the degree of state mixing between two states of the same spin manifold, which in turn reduces the rate of S → T intersystem crossing. The scheme below shows the vibronic spin-orbit coupling mechanism applied to bis-dmac and bis-juldmac (under C_{2v} symmetry)

$(S_1) \, ^1B_2(\pi, \pi^*) \leftarrow VC(b_1) \rightarrow \, ^1A_2(n, \pi^*) \leftarrow SOC \rightarrow (T_1) \, ^3B_2(\pi, \pi^*)$

$(S_1) \, ^1B_2(\pi, \pi^*) \leftarrow SOC \rightarrow \, ^3A_2(n, \pi^*) \leftarrow VC(b_1) \rightarrow (T_1) \, ^3B_2(\pi, \pi^*)$
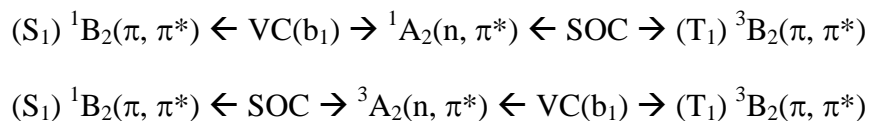
4.2.3.2 bis-dmab

4.2.3.2.1 Molecular Structure of bis-dmab

Compound bis-dmab crystallizes in an orthorhombic system, belonging to the $P2_12_12_1$ space group. Crystallographic data and refinement parameters are listed in Table 32 and the X-ray geometry of bis-dmab, in two views, is shown in Figure 71. As seen, the single crystal structure of bis-dmab is essentially planar, with approximately $3° – 7°$ rotations of the phenyl rings on each end relative to the cyclopentanone ring. Direct comparison between the X-ray geometry and its predicted gas phase geometry at the B3LYP/6-31G(d) level of theory shows excellent agreement in both bond lengths and bond angles (see Table 33). Absolute differences between experimental and calculated bond lengths varies between 0.001 Å $– 0.025$ Å and bond angles between $0.01° – 4.4°$. The predicted DFT geometry of bis-dmab is planar, with a ~$1°$ rotation of the phenyl rings relative to the inner cyclopentanone ring system.

Table 32. Crystallographic data and refinement parameters of bis-dmab.

Crystal Form	
Formula	$C_{23}H_{26}N_2O$
Formula weight (g mol^{-1})	346.46
Crystal system	orthorhombic
Space group	$P2_12_12_1$
Color and habit	Orange, rectangular plates
Crystal size	0.03 mm × 0.20 mm × 0.35 mm
a (Å)	5.8855(2)
b (Å)	7.9754(2)
c (Å)	39.9677(12)
α (deg)	90.00
β (deg)	90.00
γ (deg)	90.00
Volume (Å^3)	1876.05(10)
Z	4
λ (Å)	0.71073
ρ_{calc} (g cm^{-3})	1.227
Temperature (K)	299(2)
F(000)	744
θ range for data collection (deg)	1.02 – 26.41
Ranges of miller indices	$-7 \leq h \leq 7$ $-9 \leq k \leq 9$ $-45 \leq l \leq 49$
Absorption coefficient (mm^{-1})	0.075
Reflections collected	17565
Independent reflections	3700 [R_{int} = 0.0357]
Reflections [I > 2σ(I)]	2313
Data/restraints/parameters	3700/0/239
Goodness of fit on F^2	1.020
R (all data)	R_1 = 0.0480 wR_2 = 0.1093
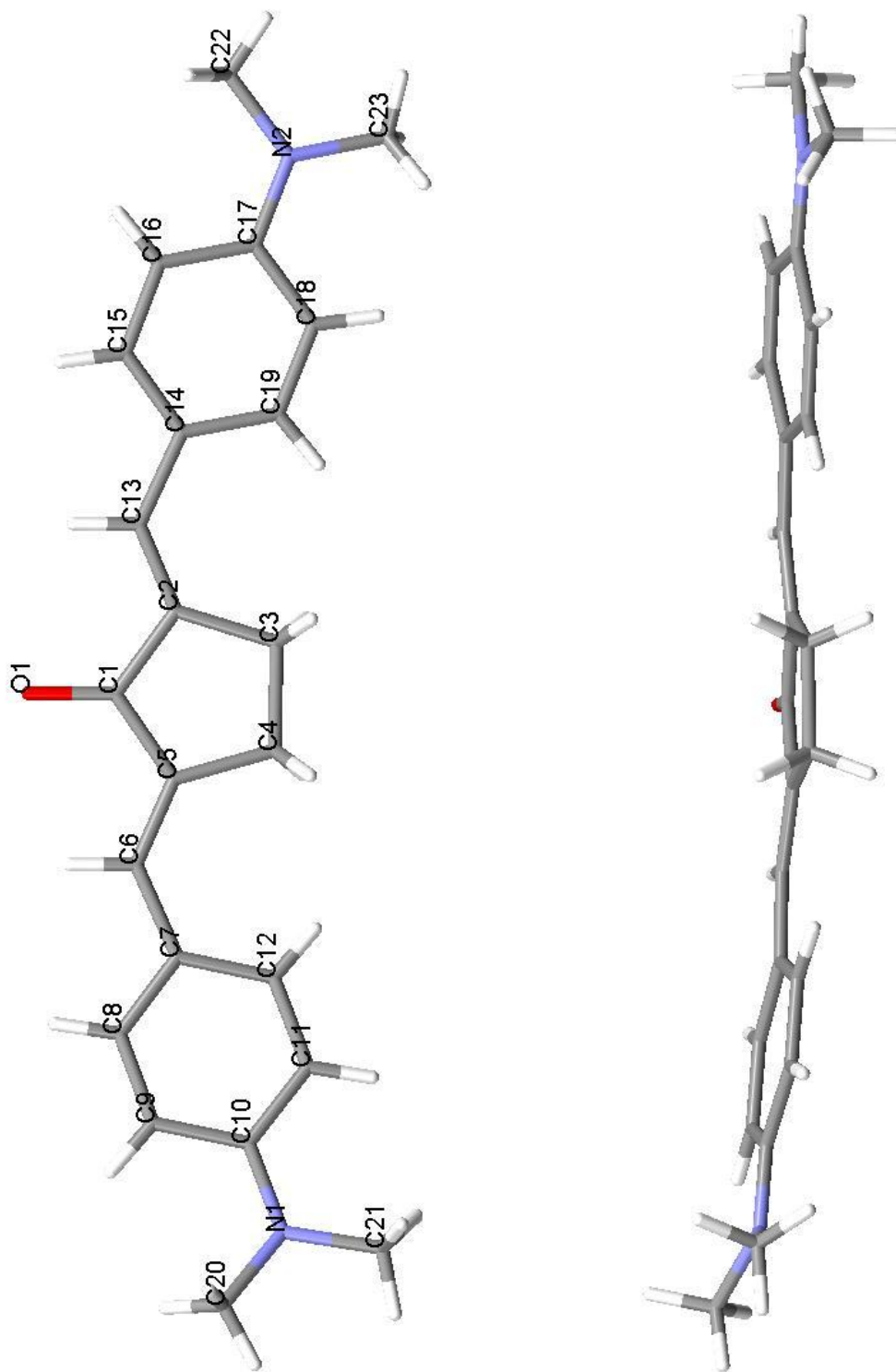
Figure 71. Single crystal X-ray structure of bis-dmab.

Table 33. Single crystal geometry of bis-dmab by X-ray diffractometry and its predicted gas phase geometry at the DFT B3LYP/6-31G(d) level of theory. Δ = X-ray-DFT

Bond Lengths (Å)			
	X-ray	DFT	Δ
C_1-C_2	1.462(3)	1.487	-0.025
C_1-C_5	1.473(3)	1.487	-0.014
C_1-O_1	1.238(3)	1.230	0.008
C_2-C_3	1.503(3)	1.510	-0.007
C_2-C_{13}	1.339(3)	1.354	-0.015
C_3-C_4	1.545(3)	1.561	-0.016
C_4-C_5	1.495(3)	1.510	-0.015
C_5-C_6	1.338(3)	1.354	-0.016
C_6-C_7	1.447(3)	1.452	-0.005
C_7-C_8	1.387(3)	1.411	-0.024
C_7-C_{12}	1.404(3)	1.411	-0.007
C_8-C_9	1.368(3)	1.385	-0.017
C_9-C_{10}	1.395(3)	1.416	-0.021
C_{10}-C_{11}	1.402(3)	1.416	-0.014
C_{10}-N_1	1.367(3)	1.383	-0.016
C_{11}-C_{12}	1.374(3)	1.387	-0.013
C_{13}-C_{14}	1.450(3)	1.452	-0.002
C_{14}-C_{15}	1.395(3)	1.411	-0.016
C_{14}-C_{19}	1.400(3)	1.411	-0.011
C_{15}-C_{16}	1.375(3)	1.385	-0.010
C_{16}-C_{17}	1.395(3)	1.416	-0.021
C_{17}-C_{18}	1.415(3)	1.416	-0.001
C_{17}-N_2	1.361(3)	1.383	-0.022
C_{18}-C_{19}	1.370(3)	1.387	-0.017
C_{20}-N_1	1.449(3)	1.453	-0.004
C_{21}-N_1	1.447(3)	1.453	-0.006
C_{22}-N_2	1.458(3)	1.453	0.005
C_{23}-N_2	1.428(3)	1.453	-0.025

Dihedral Angles (°)		
	X-ray	DFT
C_3-C_{13}-C_{14}-C_{19}	5.6	-0.7
C_3-C_{13}-C_{16}-C_{17}	7.0	-0.3
C_4-C_6-C_7-C_{12}	-3.8	-0.7
C_4-C_6-C_9-C_{10}	-4.2	-0.3

Bond Angles (°)			
	X-ray	DFT	Δ
C_1-C_2-C_3	109.0(2)	109.7	-0.7
C_1-C_2-C_{13}	120.9(2)	119.3	1.6
C_1-C_5-C_4	108.7(2)	109.7	-1.0
C_1-C_5-C_6	121.5(2)	119.3	2.2
C_2-C_1-C_5	109.3(2)	108.1	1.2
C_2-C_1-O_1	125.8(2)	125.9	-0.1
C_2-C_3-C_4	106.2(2)	106.3	-0.1
C_2-C_{13}-C_{14}	132.2(2)	131.6	0.6
C_3-C_2-C_{13}	130.2(2)	131.0	-0.8
C_3-C_4-C_5	106.6(2)	106.3	0.3
C_4-C_5-C_6	129.8(2)	131.0	-1.2
C_5-C_1-O_1	124.9(2)	125.9	-1.0
C_5-C_6-C_7	132.2(2)	131.6	0.6
C_6-C_7-C_8	119.0(2)	118.4	0.6
C_6-C_7-C_{12}	125.4(2)	125.4	0.01
C_7-C_8-C_9	123.1(3)	122.6	0.5
C_7-C_{12}-C_{11}	122.0(2)	122.0	-0.06
C_8-C_7-C_{12}	115.5(2)	116.2	-0.7
C_8-C_9-C_{10}	121.4(2)	120.8	0.6
C_9-C_{10}-C_{11}	116.3(2)	117.0	-0.7
C_9-C_{10}-N_1	121.9(2)	121.5	0.4
C_{10}-C_{11}-C_{12}	121.6(2)	121.4	0.2
C_{10}-N_1-C_{20}	120.1(2)	119.8	0.3
C_{10}-N_1-C_{21}	120.4(2)	119.9	0.5
C_{11}-C_{10}-N_1	121.8(2)	121.5	0.3
C_{13}-C_{14}-C_{15}	119.4(2)	118.4	1.0
C_{13}-C_{14}-C_{19}	125.1(2)	125.4	-0.3
C_{14}-C_{15}-C_{16}	123.1(2)	122.6	0.5
C_{14}-C_{19}-C_{18}	122.4(2)	122.0	0.4
C_{15}-C_{14}-C_{19}	115.5(2)	116.2	-0.7
C_{15}-C_{16}-C_{17}	121.1(2)	120.8	0.3
C_{16}-C_{17}-C_{18}	116.4(2)	117.0	-0.6
C_{16}-C_{17}-N_2	121.9(2)	121.5	0.4
C_{17}-C_{18}-C_{19}	121.5(2)	121.4	0.1
C_{17}-N_2-C_{22}	121.9(2)	119.8	2.1
C_{17}-N_2-C_{23}	122.6(2)	119.9	2.7
C_{18}-C_{17}-N_2	121.7(2)	121.5	0.2
C_{20}-N_1-C_{21}	114.7(2)	119.1	-4.4
C_{22}-N_2-C_{23}	115.1(2)	119.1	-4.0

4.2.3.2.2 Spectroscopic Properties of bis-dmab

Both the absorption and fluorescence spectral properties of bis-dmab were examined in fifteen solvents of differing polarities (Table 34). Experimental absorption and fluorescence spectra in six of the solvents studied are shown in Figure 72. The spectral characteristics of bis-dmab have been compared to its one-sided analogue, dmab, by plotting the absorption spectral maxima of both molecules (Figure 73) and fluorescence spectral maxima of both molecules (Figure 74) on the same plot. Similar to dmab, it is observed that with increasing solvent polarity, there is a small bathochromic shift in the absorption spectral maxima for bis-dmab and the alcohols appear to fall on the same line together with the aprotic solvents. Even though the data points appear to be scattered in the absorption plot (based on their R^2 values), their solvatochromic properties are similar. In taking the difference in wavenumbers for the absorption spectral maxima in carbon tetrachloride and in methanol, bathochromic shifts of 1449 cm^{-1} (dmab) and 1494 cm^{-1} (bis-dmab) are observed.

In the fluorescence plots shown in Figure 74, both dmab and bis-dmab fall on separate lines for aprotic and protic solvents and there are linear correlations when plotting the fluorescence spectral maxima against the $E_T(30)$ scale. In aprotic solvent environments, bathochromic shifts of 2706 cm^{-1} (dmab) and 3857 cm^{-1} (bis-dmab) are observed by subtracting the emission wavenumber data for carbon tetrachloride and acetonitrile. The larger shift in fluorescence to the red for bis-dmab is attributed to the higher degree of internal charge transfer due to the presence of the second electron donating dimethylaminophenyl moiety in the molecule.

Additionally, comparison of the solvatochromic properties of bis-dmab with its more conjugated symmetric analogue, bis-dmac, involved looking at differences in the trendline slopes in fluorescence for aprotic solvents against $E_T(30)$ for both compounds. The slope of bis-dmac (see Figure 59) is found to be approximately 1.4-fold larger in magnitude than that for bis-dmab. In fluorescence, from CCl4 to acetonitrile, bis-dmab undergoes a spectral shift of 4,672 cm^{-1}, larger than that observed for bis-dmab ($\Delta v_f = 3,857$ cm^{-1}). Both the steeper slope and larger spectral maxima shift in fluorescence support the greater solvatofluorochromic behavior of bis-dmac compared to bis-dmab.

Table 34. Spectroscopic properties of bis-dmab in various solvents.

Solvent	λ_{abs} (nm)	λ_f (nm)	ν_{abs} (cm^{-1})	ν_f (cm^{-1})	$E_T(30)$* (kcal mol^{-1})	Δf*	$\Delta\nu$ (cm^{-1})
Methanol	479	635	20,877	15,758	55.4	0.3093	5119
Ethanol	478	613	20,921	16,307	51.9	0.2887	4614
2-Propanol	473	590	21,142	16,955	48.4	0.2769	4187
Acetonitrile	460	587	21,739	17,050	45.6	0.3054	4689
Dimethyl sulfoxide	474	588	21,097	17,018	45.1	0.2637	4079
Dimethylformamide	466	575	21,459	17,378	43.2	0.2752	4081
Acetone	456	565	21,930	17,715	42.2	0.2843	4215
Dichloromethane	464	547	21,552	18,278	40.7	0.2171	3274
Chloroform	468	543	21,368	18,413	39.1	0.1491	2955
Ethyl acetate	450	528	22,222	18,950	38.1	0.1996	3272
Tetrahydrofuran	453	529	22,075	18,893	37.4	0.2104	3182
1,4-Dioxane	452	493	22,124	20,284	36.0	0.0204	1840
Toluene	452	482	22,124	20,727	33.9	0.0131	1397
Carbon disulfide	463	497	21,598	20,132	32.8	-0.0007	1466
Carbon tetrachloride	447	478	22,371	20,907	32.4	0.0119	1464

*Both Δf and $E_T(30)$ values are taken from Suppan, P. and Ghonheim, N., in *Solvatochromism*, The Royal Society of Chemistry, Cambridge, 1997; and Lide, D. R., *CRC Handbook of Chemistry and Physics*, 89th ed., 2008.
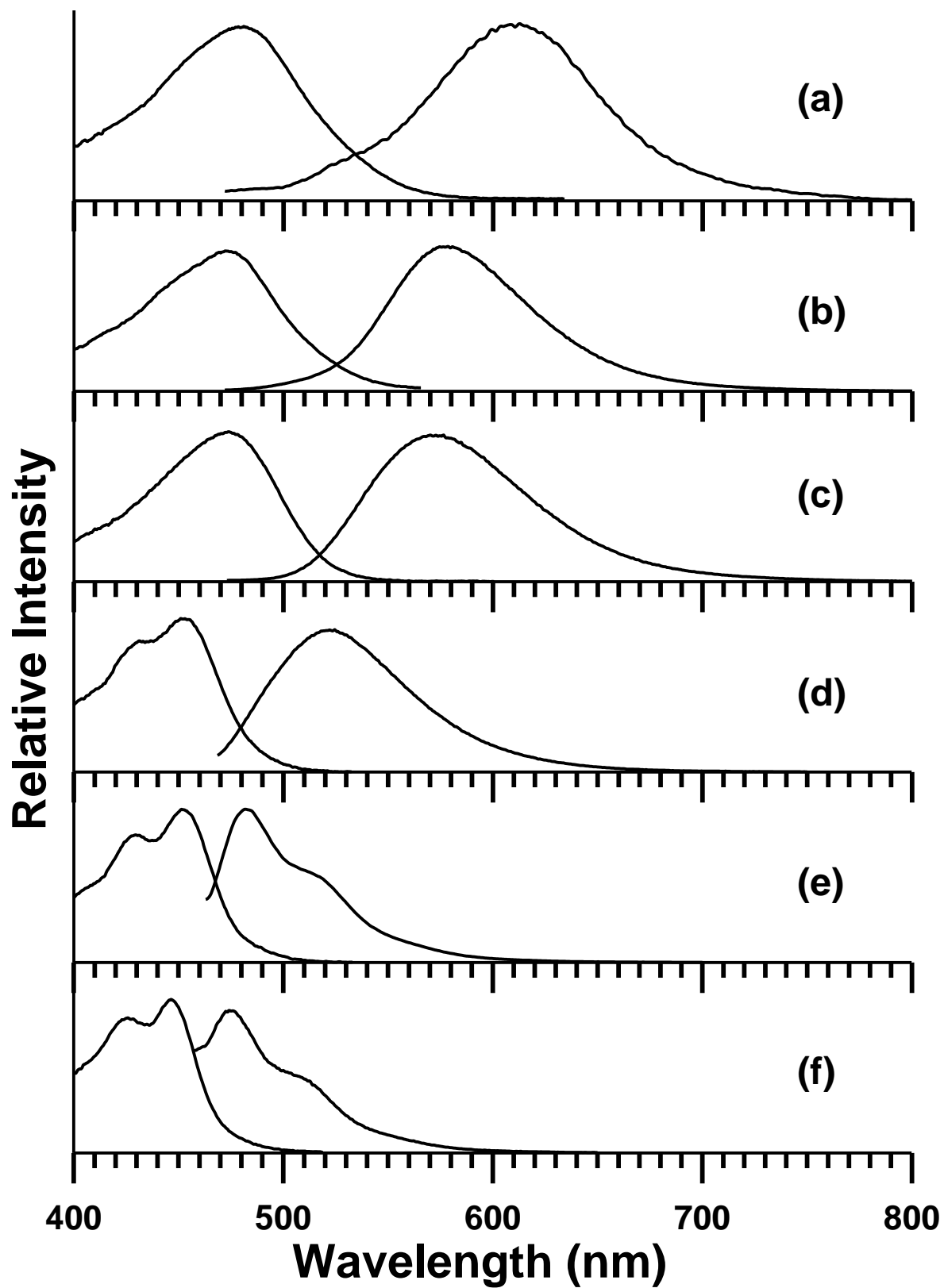
Figure 72. Absorption and fluorescence emission spectra of bis-dmab in (a) methanol, (b) 2-propanol, (c) dimethyl sulfoxide, (d) tetrahydrofuran, (e) toluene, and (f) carbon tetrachloride.

182
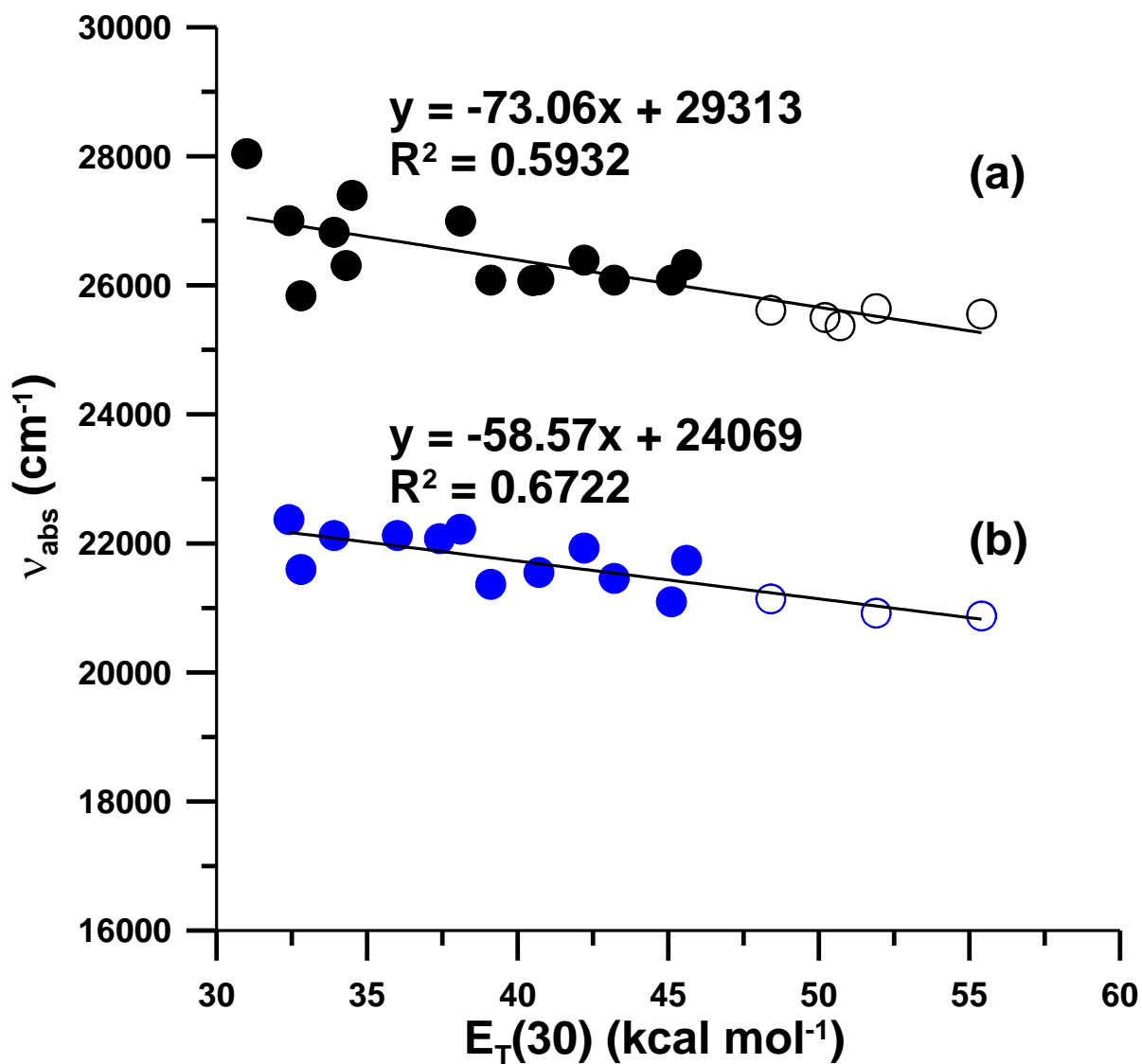
Figure 73. Plot of absorption spectral maxima of (a) dmab and (b) bis-dmab in various solvents against the $E_T(30)$ scale. Solid symbols represent aprotic solvents; open symbols represent protic solvents.
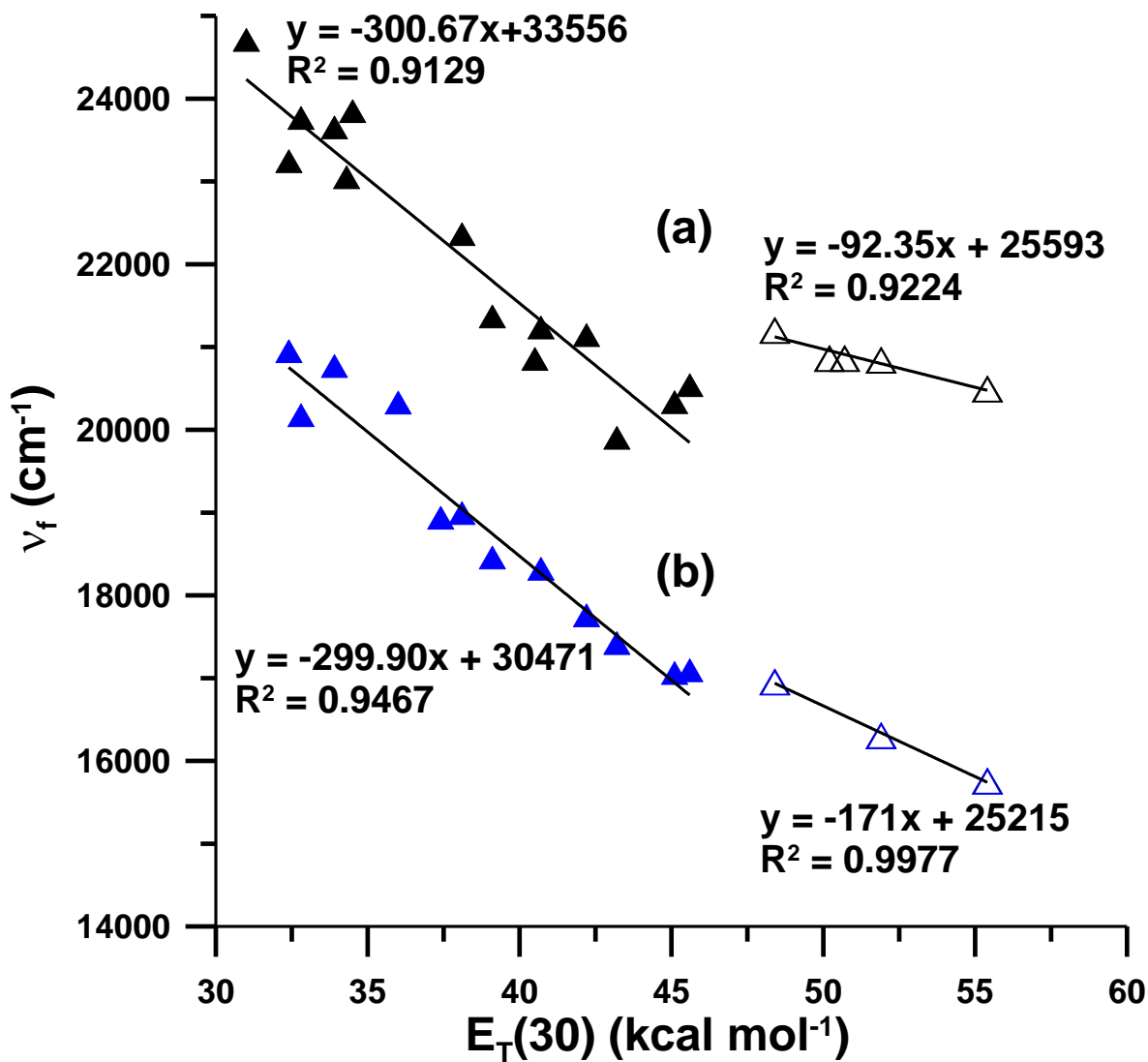
Figure 74. Plot of fluorescence spectral maxima of (a) dmab and (b) bis-dmab in various solvents against the $E_T(30)$ scale. Solid symbols represent aprotic solvents; open symbols represent protic solvents.

The Lippert-Mataga plot of bis-dmab is shown in Figure 75. Using the ground state dipole moment (5.22 D) and the Onsager cavity radius (5.77 Å) that were computed at the B3LYP/6-31G(d) level of theory, the excited state dipole moment is calculated to be 18.9 D ($\Delta\mu$ = 13.7 D) in aprotic solvents, which is 1 D unit larger than for dmac and 2.3 D units larger than for dmab. The larger electronic dipole moment in the excited state is attributed to the higher degree of internal charge transfer exhibited by bis-dmab, which, as previously mentioned, is due to the addition of the second dimethylaminophenyl moiety.
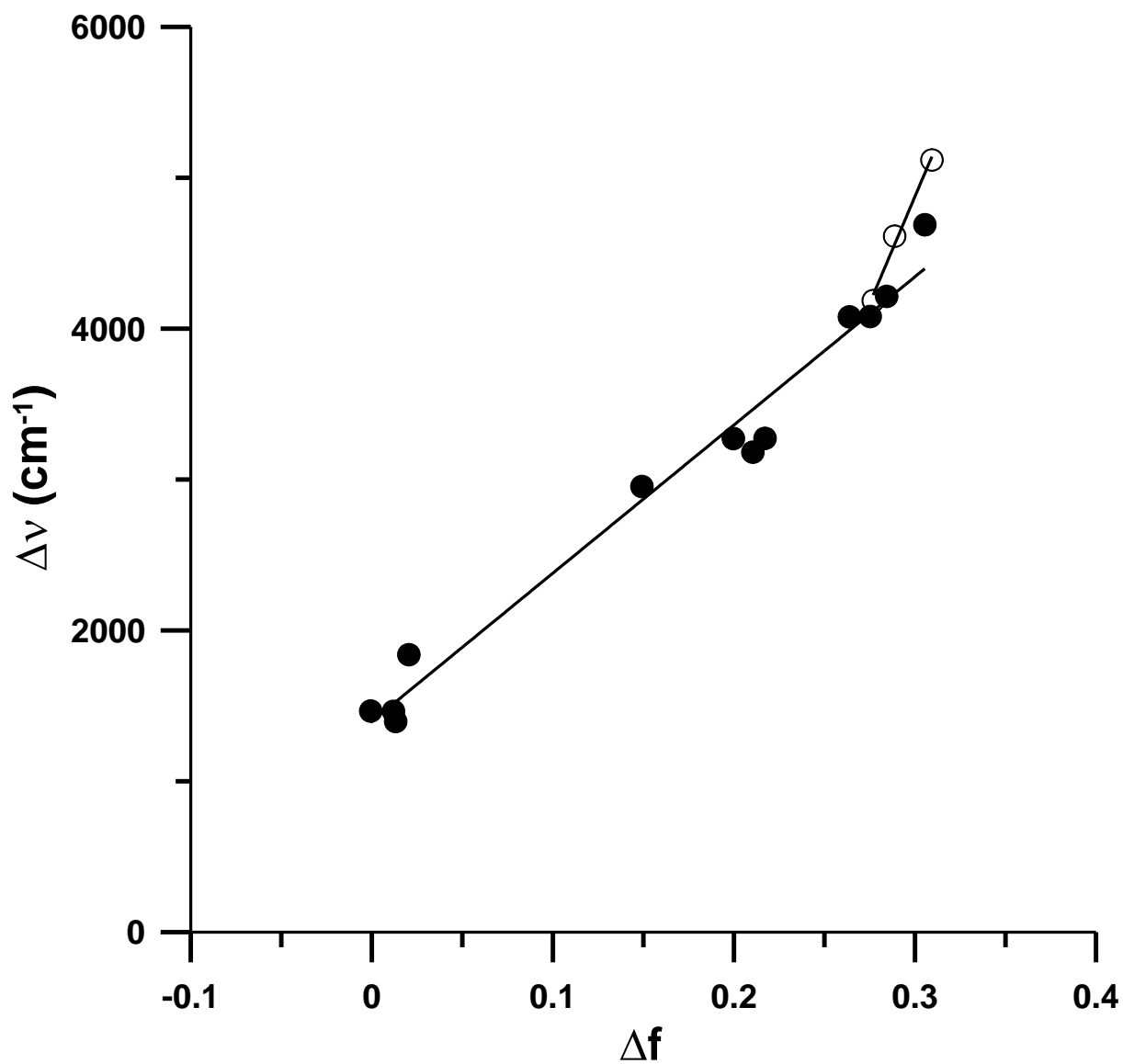
Figure 75. Lippert-Mataga plot of bis-dmab in various solvents. Solid symbols represent aprotic

solvents; open symbols represent protic solvents.

Figure 76 and Table 35 present the computed molecular orbitals of bis-dmab and the TD-DFT spectral calculations both in the gas phase and in solvent environments. Also shown are the irreducible representations of the molecular orbitals and the excited states for bis-dmab. Table 36 presents the molecular orbitals that are important in configuration interaction for bis-dmab. The irreducible representations (under C_{2v} symmetry) of the computed molecular orbitals and the excited states for bis-dmab are the same as for bis-dmac and bis-juldmac.

In the gas phase, TD-DFT computes S_1 as a strong symmetry allowed $B_2 \leftarrow A_1$ transition of the (π, π^*) type localized at 2.93 eV (λ 423 nm, f = 1.45), arising from the orbital excitation $a_2(\pi) \rightarrow b_1(\pi^*)$, where $a_2(\pi)$ is the HOMO and $b_1(\pi^*)$ is the LUMO. The S_2 state is computed to be a symmetry forbidden $A_2 \leftarrow A_1$ transition of the (n, π^*) type localized at 3.04 eV (λ 408 nm, f = 0.00), arising from the orbital excitation $b_2(n) \rightarrow b_1(\pi^*)$, where $b_2(n)$ is the HOMO-2 nonbonding molecular orbital localized on the oxygen atom.

In all PCM solvents studied, TD-DFT also predicts S_1 as (π, π^*) ($\Gamma = B_2$). The energy of the S_1 state decreases in the following order: 2.74 eV (λ 452 nm, carbon tetrachloride), 2.73 eV (λ 454 nm, toluene), 2.71 eV (λ 458 nm, carbon disulfide), 2.68 eV (λ 463 nm, tetrahydrofuran), 2.66 eV (λ 467 nm, methanol), and 2.64 eV (λ 470 nm, dimethylformamide). The $^1(n, \pi^*)$ state ($\Gamma = A_2$) is predicted to be S_2 in the gas phase, carbon tetrachloride, toluene, and carbon disulfide, switching to S_3 in tetrahydrofuran, dichloromethane, dimethylformamide, and methanol. The inversion of $^1(n, \pi^*)$ from S_2 to S_3 is attributed to the red shift of the (π, π^*) state and the blue shift of (n, π^*) in solvents of increasing polarity. The energy of the $^1(n, \pi^*)$ state increases in the following order: 3.13 eV (λ 396 nm, carbon tetrachloride), 3.14 eV (λ 395 nm, toluene), 3.15 eV (λ 394 nm, carbon disulfide), 3.21 eV (λ 386 nm, tetrahydrofuran), 3.22 eV

(λ 386 nm, dichloromethane), and 3.24 eV (λ 382 nm, dimethylformamide and methanol). Furthermore, TD-DFT predicts the following orbital configurations for the triplet excited states: $T_1(\pi, \pi^*)$ ($\Gamma = B_2$), $T_2(\pi, \pi^*)$ ($\Gamma = A_1$), and $T_3(n, \pi^*)$ ($\Gamma = A_2$).

It is also evident that the computed molecular orbitals of bis-dmab provide an illustrative description of the photoinduced internal charge transfer nature of this compound. Similar to bis-dmac and bis-juldmac, in the π-bonding HOMO the electron density is distributed along the cross-conjugated framework, with significant density centered on the tertiary nitrogen atom of the alkylamino group. In the π^*-antibonding LUMO electron density is transferred from the nitrogen atoms to the carbonyl center, signifying a charge transfer process.

LUMO (π^*, b_1)
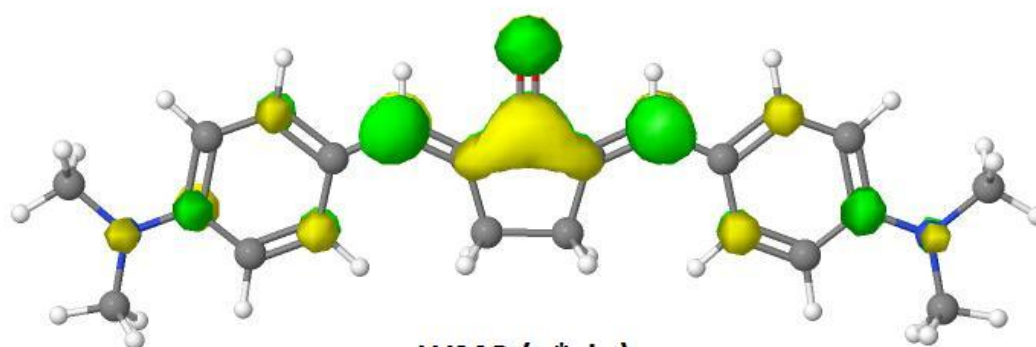
MO 94
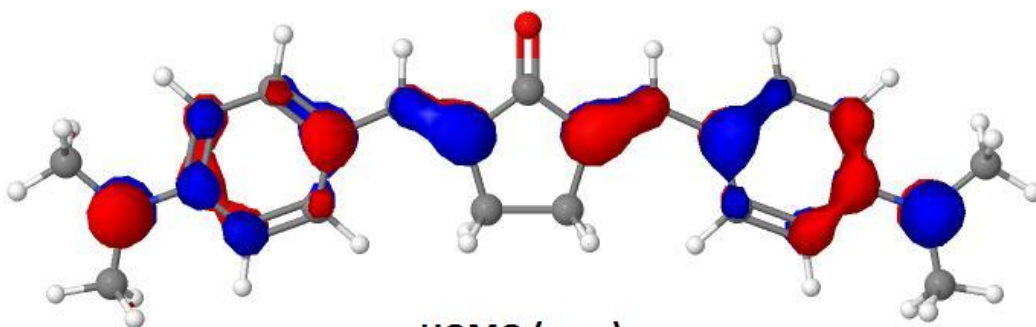
HOMO (π, a_2)

MO 93
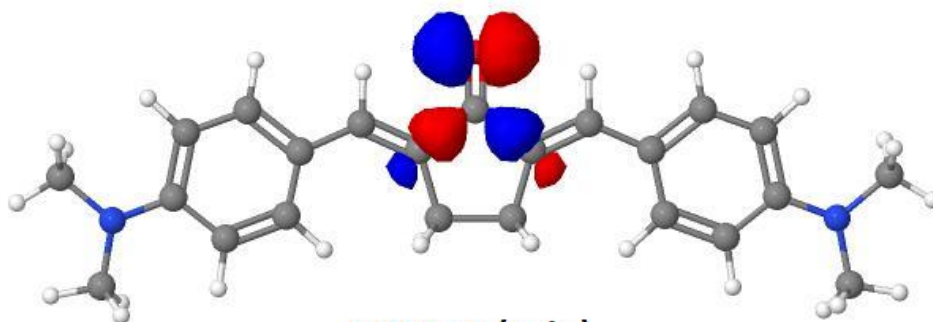
HOMO-2 (n, b_2)

MO 91

Figure 76. Computed molecular orbitals of bis-dmab in the gas phase.

189

Table 35. TD-DFT spectral calculations of bis-dmab both in the gas phase and in solvent environments at the B3LYP/6-31G(d) level of theory.

Solvent	State	Transition Energy			f	MO	CI Coef.
		eV	cm^{-1}	nm			
Gas (μ = 5.22 D)	T_1 (π, π*) (B$_2$)	2.05	16529	605	0.00	90→94	0.15492
						92→95	-0.18274
						93→94	0.65808
	T_2 (π, π*) (A$_1$)	2.19	17699	565	0.00	89→94	0.22087
						92→94	0.61905
						93→95	-0.24156
	T_3 (n, π*) (A$_2$)	2.70	21739	460	0.00	91→94	0.69299
						91→98	-0.11224
	S_1 (π, π*) (B$_2$)	2.93	23641	423	1.45	93→94	0.70717
	S_2 (n, π*) (A$_2$)	3.04	24510	408	0.00	91→94	0.69980
	S_3 (π, π*) (A$_1$)	3.32	26810	373	0.034	92→94	0.68878
						93→95	0.15064
Carbon Tetrachloride (μ = 6.08 D)	T_1 (π, π*) (B$_2$)	2.00	16103	621	0.00	90→94	0.15277
						92→95	-0.17051
						93→94	0.66293
	T_2 (π, π*) (A$_1$)	2.19	17637	567	0.00	89→94	0.21137
						92→94	0.62577
						93→95	-0.23550
	S_1 (π, π*) (B$_2$)	2.74	22124	452	1.66	93→94	0.70649
	T_3 (n, π*) (A$_2$)	2.80	22573	443	0.00	91→94	0.69369
						91→98	-0.10921
	S_2 (n, π*) (A$_2$)	3.13	25253	396	0.0001	91→94	0.69945
	S_3 (π, π*) (A$_1$)	3.18	25707	389	0.049	92→94	0.69748
						93→95	0.10411

						90→94	0.15221
	$T_1(\pi, \pi^*)$	1.99	16051	623	0.00	92→95	-0.16863
	(B_2)					93→94	0.66372
						89→94	0.20933
	$T_2(\pi, \pi^*)$	2.18	17606	568	0.00	92→94	0.62711
Carbon	(A_1)					93→95	-0.23427
Disulfide	$S_1(\pi, \pi^*)$						
($\mu = 6.23$ D)	(B_2)	2.71	21834	458	1.70	93→94	0.70625
	$T_3(n, \pi^*)$					91→94	0.69380
	(A_2)	2.82	22727	440	0.00	91→98	-0.10874
	$S_2(n, \pi^*)$					91→94	0.68561
	(A_2)	3.15	25381	394	0.021	92→94	0.14188
	$S_3(\pi, \pi^*)$					91→94	-0.14206
	(A_1)	3.16	25445	393	0.051	92→94	0.68524
						90→94	0.15255
	$T_1(\pi, \pi^*)$	1.99	16077	622	0.00	92→95	-0.16973
	(B_2)					93→94	0.66326
						89→94	0.21055
	$T_2(\pi, \pi^*)$	2.19	17637	567	0.00	92→94	0.62631
Toluene	(A_1)					93→95	-0.23500
($\mu = 6.14$ D)	$S_1(\pi, \pi^*)$						
	(B_2)	2.73	22026	454	1.67	93→94	0.70644
	$T_3(n, \pi^*)$					91→94	0.69374
	(A_2)	2.81	22624	442	0.00	91→98	-0.10901
	$S_2(n, \pi^*)$						
	(A_2)	3.14	25316	395	0.0002	91→94	0.69890
	$S_3(\pi, \pi^*)$					92→94	0.69732
	(A_1)	3.18	25641	390	0.050	93→95	0.10157
						90→94	0.14889
	$T_1 (\pi, \pi^*)$	1.95	15699	637	0.00	92→95	-0.16035
	(B_2)					93→94	0.66736
						89→94	0.19822
	$T_2 (\pi, \pi^*)$	2.17	17483	572	0.00	92→94	0.63398
Tetrahydro-	(A_1)					93→95	-0.22770
furan	$S_1 (\pi, \pi^*)$						
($\mu = 6.93$ D)	(B_2)	2.68	21598	463	1.66	93→94	0.70676
	$T_3 (n, \pi^*)$					91→94	0.69428
	(A_2)	2.89	23256	430	0.00	91→98	-0.10664
	$S_2 (\pi, \pi^*)$					92→94	0.69780
	(A_1)	3.12	25189	397	0.049	93→95	0.10702
	$S_3 (n, \pi^*)$						
	(A_2)	3.21	25907	386	0.00	91→94	0.70025

Dichloro-methane ($\mu = 7.01$ D)	$T_1(\pi, \pi^*)$ (B$_2$)	1.94	15649	639	0.00	90→94	0.14845
						92→95	-0.15948
						93→94	0.66776
	$T_2(\pi, \pi^*)$ (A$_1$)	2.17	17452	573	0.00	89→94	0.19686
						92→94	0.63479
						93→95	-0.22689
	$S_1(\pi, \pi^*)$ (B$_2$)	2.66	21505	465	1.67	93→94	0.70674
	$T_3(n, \pi^*)$ (A$_2$)	2.89	23365	428	0.00	91→94	0.69433
						91→98	-0.10642
	$S_2(\pi, \pi^*)$ (A$_1$)	3.11	25126	398	0.050	92→94	0.69809
						93→95	0.10562
	$S_3(n, \pi^*)$ (A$_2$)	3.22	25906	386	0.00	91→94	0.70031
Dimethyl-formamide ($\mu = 7.34$ D)	$T_1 (\pi, \pi^*)$ (B$_2$)	1.92	15504	645	0.00	90→94	0.14653
						92→95	-0.15601
						93→94	0.66939
	$T_2 (\pi, \pi^*)$ (A$_1$)	2.16	17391	575	0.00	89→94	0.19091
						92→94	0.63817
						93→95	-0.22346
	$S_1(\pi, \pi^*)$ (B$_2$)	2.64	21277	470	1.67	93→94	0.70679
	$T_3 (n, \pi^*)$ (A$_2$)	2.92	23585	424	0.00	91→94	0.69453
						91→98	-0.10551
	$S_2 (\pi, \pi^*)$ (A$_1$)	3.09	24876	402	0.050	92→94	0.69835
						93→95	0.10505
	$S_3 (n, \pi^*)$ (A$_2$)	3.24	26178	382	0.00	91→94	0.70047
Methanol ($\mu = 7.33$ D)	$T_1 (\pi, \pi^*)$ (B$_2$)	1.92	15504	645	0.00	90→94	0.14663
						92→95	-0.15618
						93→94	0.66931
	$T_2 (\pi, \pi^*)$ (A$_1$)	2.16	17391	575	0.00	89→94	0.19120
						92→94	0.63801
						93→95	-0.22363
	$S_1 (\pi, \pi^*)$ (B$_2$)	2.66	21413	467	1.64	93→94	0.70701
	$T_3 (n, \pi^*)$ (A$_2$)	2.92	23585	424	0.00	91→94	0.69452
						91→98	-0.10556
	$S_2 (\pi, \pi^*)$ (A$_1$)	3.10	25000	400	0.047	92→94	0.69711
						93→95	0.11256
	$S_3 (n, \pi^*)$ (A$_2$)	3.24	26178	382	0.00	91→94	0.70046

Table 36. Gas phase electronic energies (Hartree) and irreducible representations of the MOs important in configuration interaction (CI) for bis-dmab.

98	0.04545	b_1
97	0.00729	a_2
96	0.00659	b_1
95	-0.00680	a_2
94	-0.05770	b_1 LUMO
93	-0.17572	a_2 HOMO
92	-0.18550	b_1
91	-0.21355	b_2
90	-0.23842	a_2
89	-0.23951	b_1
88	-0.24539	b_1
87	-0.24544	a_2
86	-0.29982	b_1

4.2.3.2.3 Fluorescence Quantum Yields, Lifetimes, and Decay Constants

The photophysical properties of bis-dmab are listed in Table 37. Fluorescence quantum yields range from 0.025 (in methanol) to 0.20 (in dimethyl sulfoxide) and lifetimes range from 0.29 ns (in methanol) to 0.92 ns (in dimethylformamide). The fluorescence quantum yields of bis-dmab have been plotted against the maximum frequencies of fluorescence, as shown in Figure 77. It is seen that in carbon tetrachloride, the quantum yield is low ($\Phi_f = 0.043$, $\nu_f = 20,907$ cm^{-1}), rises to 0.20 in dimethyl sulfoxide ($\nu_f = 17,018$ cm^{-1}), then drops to 0.025 in methanol ($\nu_f = 15,758$ cm^{-1}).

In order to test whether hydrogen bonding between the hydroxyl hydrogen atom of methanol and the carbonyl oxygen atom of the excited state molecule is a factor in the low Φ_f value in methanol, a quantum yield study was carried out for bis-dmab in methan(ol-d) (CH$_3$OD). The Franck-Condon factors are generally greatest for high frequency vibrations because the higher the energy of vibration, the fewer the number of quanta required to match an electronic gap with vibrational energy [31]. The replacement of a hydrogen atom with a deuterium atom lowers the vibrational frequency of the O-H stretch, resulting in a smaller vibrational overlap between the lowest vibrational energy level of S_1 and an isoenergetic vibrational energy level of S_0, as predicted by the Franck-Condon overlap factor. If the O-H vibration is an important energy accepting mode in internal conversion, the value of Φ_f for bis-dmab is expected to be higher in methan(ol-d) than in undeuterated methanol. The Φ_f of bis-dmab in methan(ol-d) was measured as 0.025, which is the same as measured in methanol. Therefore, it is concluded from this study that hydrogen bonding is not a factor in explaining the low quantum yield of fluorescence in methanol.

Table 37. Photophysical properties of bis-dmab in various solvents.

	Solvent	Φ_f	τ_f (ns)	k_f (s^{-1})	k_{nr} (s^{-1})
1	Methanol	0.025	0.29	8.62×10^7	3.36×10^9
2	Ethanol	0.11	0.34	3.24×10^8	2.62×10^9
3	2-Propanol	0.18	0.68	2.65×10^8	1.21×10^9
4	Acetonitrile	0.11	0.54	2.04×10^8	1.65×10^9
5	Dimethyl sulfoxide	0.20	0.85	2.35×10^8	9.41×10^8
6	Dimethylformamide	0.19	0.92	2.07×10^8	8.80×10^8
7	Acetone	0.15	0.74	2.03×10^8	1.15×10^9
8	Dichloromethane	0.16	0.77	2.08×10^8	1.09×10^9
9	Chloroform	0.13	0.57	2.28×10^8	1.53×10^9
10	Ethyl acetate	0.090	0.59	1.53×10^8	1.54×10^9
11	Tetrahydrofuran	0.089	0.60	1.48×10^8	1.52×10^9
12	1,4-Dioxane	0.080	0.50	1.60×10^8	1.84×10^9
13	Toluene	0.080	0.48	1.67×10^8	1.92×10^9
14	Carbon disulfide	0.10	0.51	1.96×10^8	1.76×10^9
15	Carbon tetrachloride	0.043	0.37	1.16×10^8	2.59×10^9
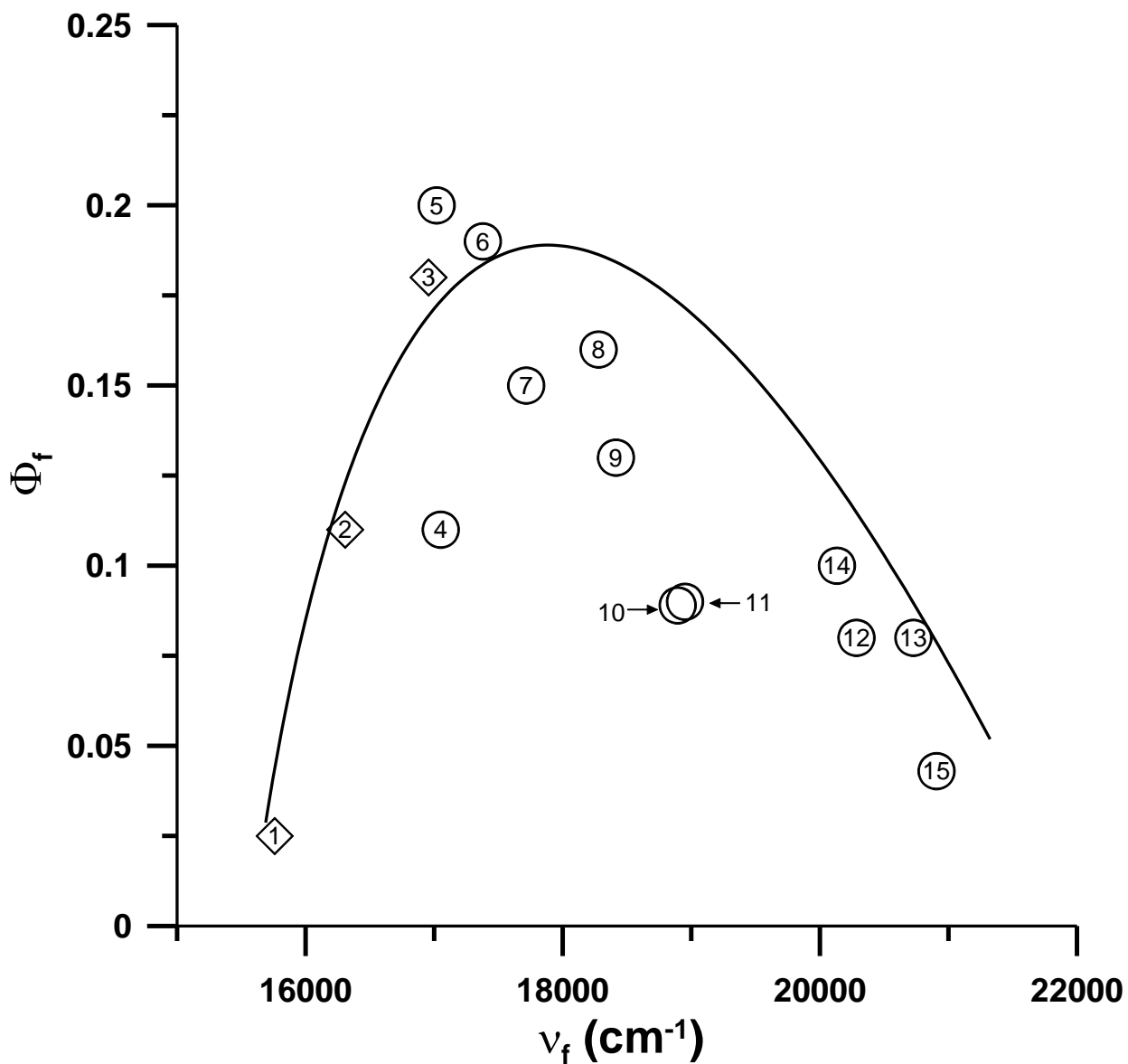
Figure 77. Fluorescence quantum yields (Φ_f) plotted against the fluorescence spectral maxima of bis-dmab in various solvents. Circles represent aprotic solvents; diamonds represent protic solvents.

The calculated k_{nr} values of bis-dmab have been plotted against the corrected S_0-S_1 energy gaps in all solvents studied (Figure 78). As shown, in carbon tetrachloride, k_{nr} is high (2.59×10^9 s^{-1}), reaches a minimum at 17,378 cm^{-1} in dimethylformamide (8.80×10^8 s^{-1}), then rises to 3.36×10^9 s^{-1} in methanol ($\nu_f = 15{,}758$ cm^{-1}). Although the trend in k_{nr} for bis-dmab appears to be more linear rather than parabolic (like that observed for Asdimcy1, see Figure 39), the plot can be subdivided into two regions: region 1: from dimethyl sulfoxide to methanol; and region 2: from carbon tetrachloride to dimethylformamide. In region 1, internal conversion is the major nonradiative route of decay, where the k_{nr} increases by an order of magnitude, consistent with the energy gap law for internal conversion, as discussed in section 4.1.4.

In region 2, intersystem crossing from singlet to triplet state manifolds is believed to be the major nonradiative decay channel from S_1 to S_0. As discussed in section 4.1 for the case of Asdimcy1 and also with bis-dmac and bis-juldmac in the previous section, vibronic spin-orbit coupling can be used to explain the decrease in k_{nr} depicted in region 2 of Figure 78. Theoretical support is provided to explain the k_{nr} decrease. In accordance with Table 38, the decrease in k_{nr} is consistent with a gradual solvent induced increase in the spacing between S_1/T_1 (π, π*) and the appropriate intermediate (n, π*) states, which results in an attenuation in the degree of state mixing between (n, π*) and (π, π*) in either the singlet or triplet manifolds.

In reference to Table 38, direct comparison of the TD-DFT computed energy gaps and experimental k_{nr} values of bis-dmab with those of bis-dmac in toluene, carbon disulfide, and dichloromethane led to another interesting observation. A larger change in the k_{nr} value of bis-dmab than bis-dmac was observed between toluene and dichloromethane, which correlates with the magnitudes of the changes in the energy spacings between S_1/T_1(π, π*) and the

appropriate (n, π*) states. Specifically, for bis-dmab, the k_{nr} value is reduced from 19.2×10^8 s^{-1} to 10.9×10^8 s^{-1} ($\Delta = 8.3 \times 10^8$ s^{-1}). The differences in the lowest lying (π, π*)-(n, π*) energy gaps are calculated to be 1168 cm^{-1} (triplet) and 1112 cm^{-1} (singlet). Similarly, for bis-dmac, the k_{nr} value is reduced from 6.98×10^8 s^{-1} to 4.81×10^8 s^{-1} ($\Delta = 2.17 \times 10^8$ s^{-1}) and the corresponding changes in the lowest lying (π, π*)-(n, π*) energy gaps are calculated to be 1014 cm^{-1} (triplet) and 709 cm^{-1} (singlet).

From a conceptual perspective, the larger change in k_{nr} observed for bis-dmab compared to bis-dmac in changing solvent from toluene to dichloromethane is attributed to larger (π, π*)-(n, π*) energy spacings for bis-dmab. For bis-dmac, the larger energy gaps imply a smaller degree of vibronic coupling between (n, π*) and (π, π*) states of the same spin manifold, which in turn results in a smaller reduction of k_{nr} in going from toluene to dichloromethane. The smaller change in k_{nr} seen for bis-dmac with solvent is attributed to a smaller difference in the (n, π*)-(π, π*) energy spacings.

Since the irreducible representations of the molecular orbitals and excited states of bis-dmab are in parallel with bis-dmac and bis-juldmac, the same arguments hold in the group theory applications for spin-orbit coupling and vibronic coupling of bis-dmac and bis-juldmac (refer back to section 4.2.3.1). Hence, as with bis-dmac and bis-juldmac, b_1 corresponds to the irreducible representation of the vibration that induces the vibronic coupling between S_1(π, π*) and S_n(n, π*) (n = 2 for bis-dmac and n = 3 for bis-juldmac) and T_1(π, π*) and T_3(n, π*) states.

Similar to the argument for bis-dmac and bis-juldmac, as solvent polarity increases, the lowest lying (n, π*)-(π, π*) energy spacing also increases, which in turn reduces the vibronic coupling between two states of the same spin multiplicity. Therefore, the reduction of vibronic

198

coupling attenuates the degree of state mixing between two states of the same spin manifold, which in turn reduces the rate of S → T intersystem crossing. The scheme below for the vibronic spin-orbit coupling mechanism still holds for bis-dmab (under C_{2v} symmetry)

$$(S_1)\ ^1B_2(\pi, \pi^*) \leftarrow VC(b_1) \rightarrow\ ^1A_2(n, \pi^*) \leftarrow SOC \rightarrow (T_1)\ ^3B_2(\pi, \pi^*)$$

$$(S_1)\ ^1B_2(\pi, \pi^*) \leftarrow SOC \rightarrow\ ^3A_2(n, \pi^*) \leftarrow VC(b_1) \rightarrow (T_1)\ ^3B_2(\pi, \pi^*)$$
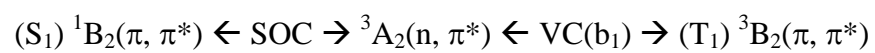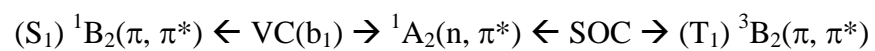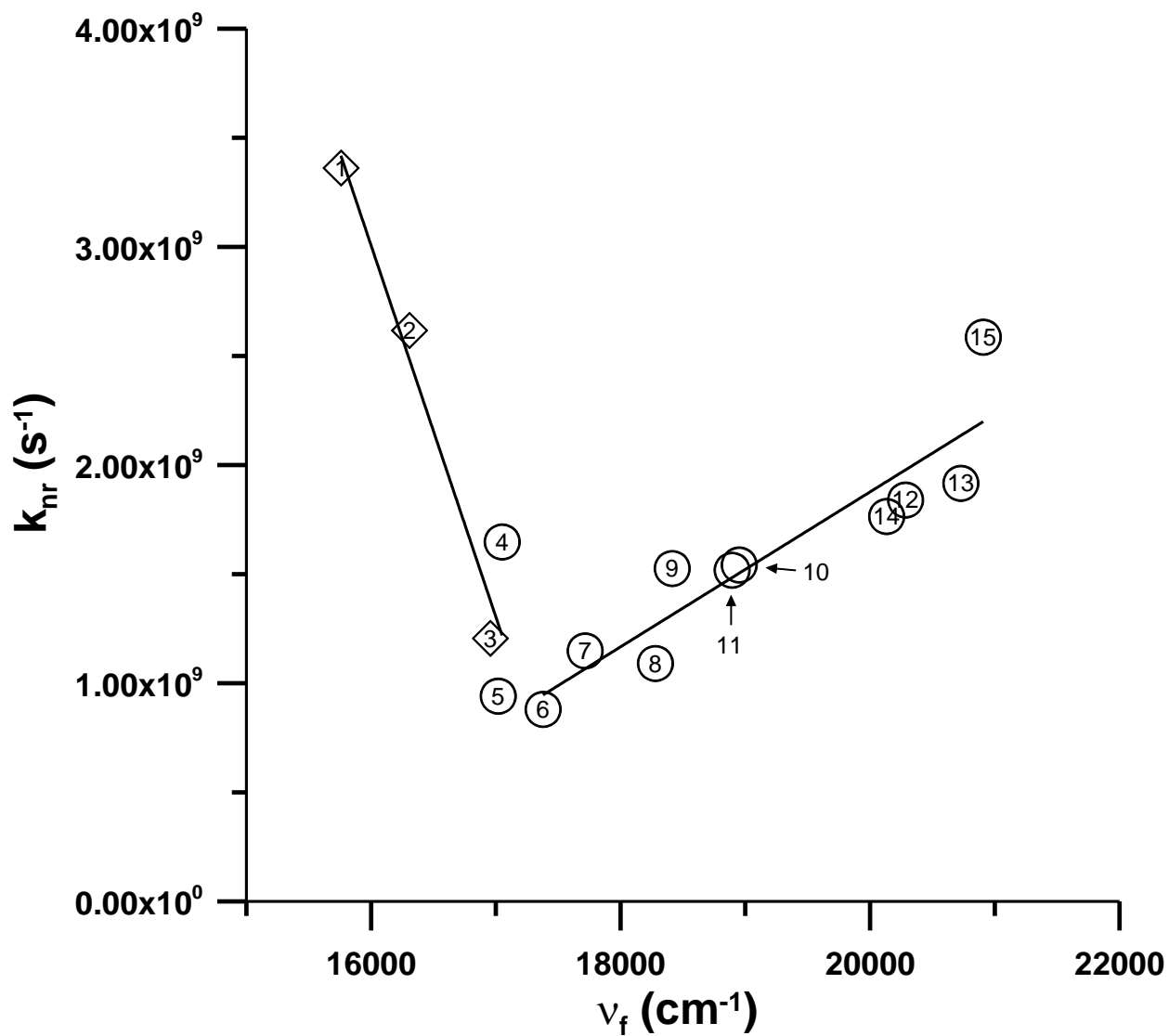
Figure 78. Nonradiative decay constants (k_{nr}) plotted against the fluorescence spectral maxima of bis-dmab in various solvents. Circles represent aprotic solvents; diamonds represent protic solvents.

Table 38. TD-DFT computed energy gaps between the lowest lying (n, π*) and (π, π*) states and experimental k_{nr} values for bis-dmab in comparison to bis-dmac in the same solvents.

	Toluene	Carbon Disulfide	Dichloromethane	Δ(DCM/Toluene)
bis-dmab				
T_3(n, π*)-T_1(π, π*)	6547 cm^{-1}	6676 cm^{-1}	7715 cm^{-1}	1168 cm^{-1}
S_n(n, π*)-S_1(π,π*)†	3290 cm^{-1}	3547 cm^{-1}	4402 cm^{-1}	1112 cm^{-1}
$k_{nr} \times 10^{-8}$ (s^{-1})	19.2	17.6	10.9	8.3
bis-dmac				
T_3(n, π*)-T_1(π, π*)	8346 cm^{-1}	8464 cm^{-1}	9360 cm^{-1}	1014 cm^{-1}
S_3(n, π*)-S_1(π,π*)†	4606 cm^{-1}	4837 cm^{-1}	5315 cm^{-1}	709 cm^{-1}
$k_{nr} \times 10^{-8}$ (s^{-1})	6.98	6.87	4.81	2.17

†In toluene and carbon disulfide, n = 2; in dichloromethane, n = 3.

4.2.3.3 Ashrbor

4.2.3.3.1 Computed Structure of Ashrbor

The last portion of this section is a presentation and discussion of the spectroscopic and photophysical data of Ashrbor, an asymmetric alkylamino substituted 2,5-diarylidene cyclopentanone compound, considered to be a combination of both bis-dmab and bis-dmac, falling intermediate in terms of polyene chain length. Similar to bis-dmab, the ground state optimized geometry of Ashrbor shown in Figure 79 and tabulated parameters presented in Table 39 is essentially planar, with ~1° rotation of the phenyl ring groups.
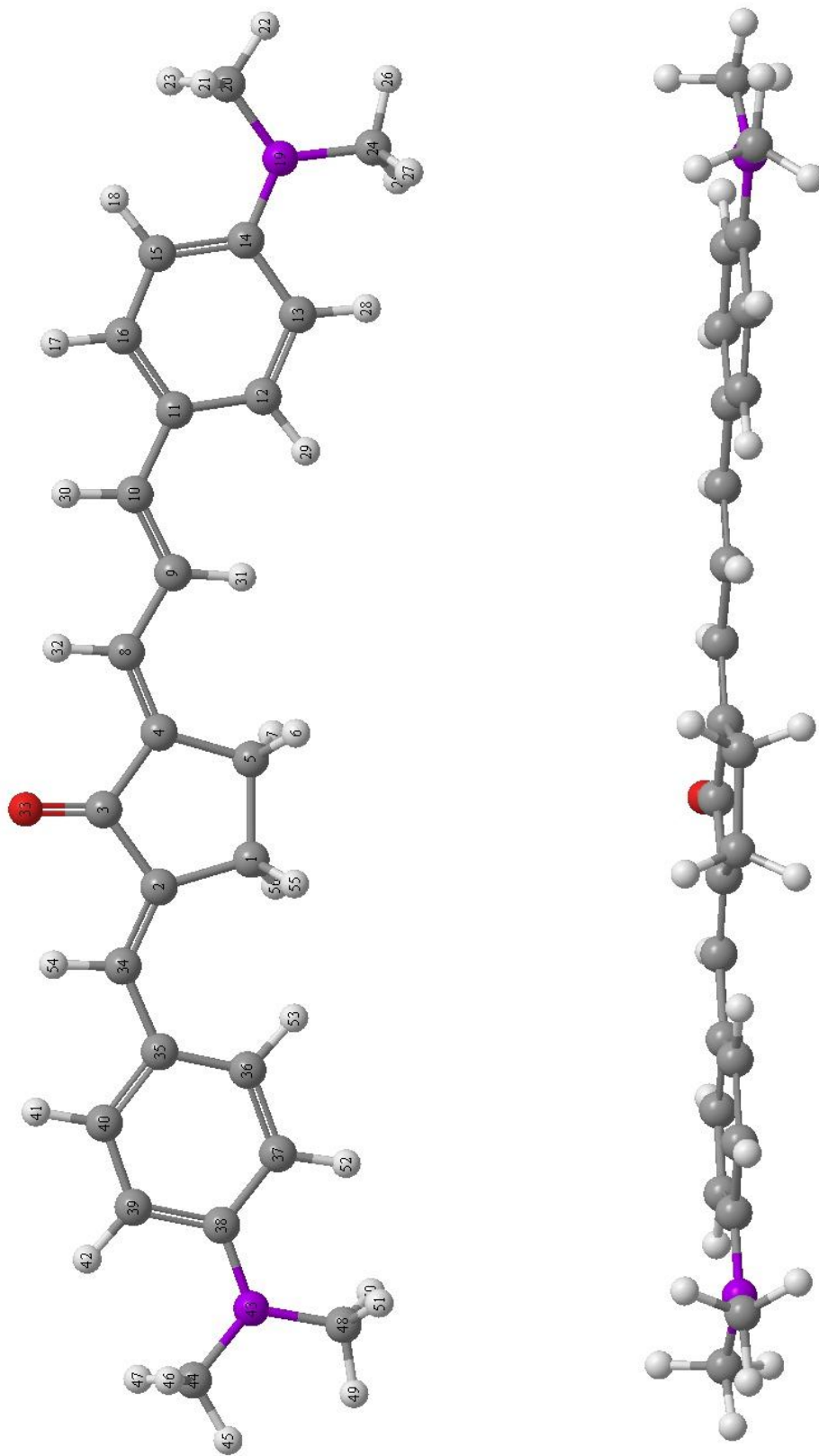
Figure 79. Optimized geometry of Ashrbor at the B3LYP/6-31G(d) level of theory. Gas phase

dipole moment = 5.60 D.

Table 39. B3LYP/6-31G(d) calculated ground state optimized geometry of Ashrbor.

Bond Lengths (Å)	
C_1-C_2	1.51
C_1-C_5	1.56
C_2-C_3	1.49
C_2-C_{34}	1.35
C_3-C_4	1.48
C_3-O_{33}	1.23
C_4-C_5	1.51
C_4-C_8	1.36
C_8-C_9	1.44
C_9-C_{10}	1.36
C_{10}-C_{11}	1.45
C_{11}-C_{12}	1.41
C_{11}-C_{16}	1.41
C_{12}-C_{13}	1.38
C_{13}-C_{14}	1.42
C_{14}-C_{15}	1.41
C_{14}-N_{19}	1.38
C_{15}-C_{16}	1.39
N_{19}-C_{20}	1.45
N_{19}-C_{24}	1.45
C_{34}-C_{35}	1.45
C_{35}-C_{36}	1.41
C_{35}-C_{40}	1.41
C_{36}-C_{37}	1.39
C_{37}-C_{38}	1.42
C_{38}-C_{39}	1.42
C_{38}-N_{43}	1.38
C_{39}-C_{40}	1.39
N_{43}-C_{44}	1.45
N_{43}-C_{48}	1.45

Bond Angles (°)	
C_1-C_2-C_3	109.71
C_1-C_2-C_{34}	131.01
C_1-C_5-C_4	105.95
C_2-C_1-C_5	106.28
C_2-C_3-C_4	107.89
C_2-C_3-O_{33}	126.14
C_2-C_{34}-C_{35}	131.63
C_3-C_2-C_{34}	119.29
C_3-C_4-C_5	110.14
C_3-C_4-C_8	121.24
C_4-C_3-O_{33}	125.97
C_4-C_8-C_9	126.42
C_5-C_4-C_8	128.62
C_8-C_9-C_{10}	122.75
C_9-C_{10}-C_{11}	128.21
C_{10}-C_{11}-C_{12}	124.05
C_{10}-C_{11}-C_{16}	119.57
C_{11}-C_{12}-C_{13}	122.03
C_{11}-C_{16}-C_{15}	122.44
C_{12}-C_{11}-C_{16}	116.38
C_{12}-C_{13}-C_{14}	121.24
C_{13}-C_{14}-C_{15}	117.04
C_{13}-C_{14}-N_{19}	121.38
C_{14}-C_{15}-C_{16}	120.86
C_{14}-N_{19}-C_{20}	119.72
C_{14}-N_{19}-C_{24}	119.87
C_{15}-C_{14}-N_{19}	121.58
C_{20}-N_{19}-C_{24}	119.02
C_{34}-C_{35}-C_{36}	125.40
C_{34}-C_{35}-C_{40}	118.45
C_{35}-C_{36}-C_{37}	122.01
C_{35}-C_{40}-C_{39}	122.63
C_{36}-C_{35}-C_{40}	116.15
C_{36}-C_{37}-C_{38}	121.36
C_{37}-C_{38}-C_{39}	117.02
C_{37}-C_{38}-N_{43}	121.46
C_{38}-C_{39}-C_{40}	120.82
C_{38}-N_{43}-C_{44}	119.77
C_{38}-N_{43}-C_{48}	119.85
C_{39}-C_{38}-N_{43}	121.52
C_{44}-N_{43}-C_{48}	119.04

Atomic Charges	
C_1	-0.371
C_2	0.0995
C_3	0.350
C_4	0.0780
C_5	-0.364
C_8	-0.169
C_9	-0.120
C_{10}	-0.189
C_{11}	0.177
C_{12}	-0.190
C_{13}	-0.193
C_{14}	0.372
C_{15}	-0.195
C_{16}	-0.204
N_{19}	-0.472
C_{20}	-0.313
C_{24}	-0.312
O_{33}	-0.524
C_{34}	-0.264
C_{35}	0.188
C_{36}	-0.193
C_{37}	-0.197
C_{38}	0.374
C_{39}	-0.198
C_{40}	-0.198
N_{43}	-0.472
C_{44}	-0.312
C_{48}	-0.312

Dihedral Angles (°)	
C_1-C_2-C_{35}-C_{36}	1.13
C_5-C_4-C_{11}-C_{12}	-0.63

4.2.3.3.2 Spectroscopic Properties of Ashrbor

The spectroscopic properties of Ashrbor have been measured in a total of twenty three solvents, seven of which are displayed in Figure 80. Absorption maxima ranged from 435 nm (22,989 cm^{-1}) in n-hexane to 500 nm (20,000 cm^{-1}) in methanol. Fluorescence ranged from 504 nm (19,844 cm^{-1}) in n-hexane to 737 nm (13,570 cm^{-1}) in methanol. Noteworthy to consider is that the spectral maxima of Ashrbor fall intermediate to bis-dmab and bis-dmac. This is attributed to the polyene chain length of Ashrbor being in between those of bis-dmab and bis-dmac. To demonstrate the effect of π conjugated chain length on spectroscopic properties, the absorption and fluorescence maxima of bis-dmab, Ashrbor, and bis-dmac in four solvents of differing polarities, have been compared (see Table 40). As shown in Table 40, in all four solvents presented, the absorption and fluorescence spectral maxima shift to smaller energies in the order bis-dmab to Ashrbor to bis-dmac.

Table 40. Absorption and fluorescence spectral maxima of bis-dmab, Ashrbor, and bis-dmac in carbon tetrachloride, ethyl acetate, dichloromethane, and ethanol.

Compound	Carbon Tetrachloride	Ethyl Acetate	Dichloromethane	Ethanol
bis-dmab	$\nu_a = 22371$ cm^{-1} (447 nm)	$\nu_a = 22222$ cm^{-1} (450 nm)	$\nu_a = 21552$ cm^{-1} (464 nm)	$\nu_a = 20921$ cm^{-1} (478 nm)
	$\nu_f = 20907$ cm^{-1} (478 nm)	$\nu_f = 18950$ cm^{-1} (528 nm)	$\nu_f = 18278$ cm^{-1} (547 nm)	$\nu_f = 16307$ cm^{-1} (613 nm)
Ashrbor	$\nu_a = 22272$ cm^{-1} (449 nm)	$\nu_a = 21552$ cm^{-1} (464 nm)	$\nu_a = 20661$ cm^{-1} (484 nm)	$\nu_a = 20080$ cm^{-1} (498 nm)
	$\nu_f = 19402$ cm^{-1} (515 nm)	$\nu_f = 16920$ cm^{-1} (591 nm)	$\nu_f = 15747$ cm^{-1} (635 nm)	$\nu_f = 13790$ cm^{-1} (725 nm)
bis-dmac	$\nu_a = 21505$ cm^{-1} (465 nm)	$\nu_a = 20833$ cm^{-1} (480 nm)	$\nu_a = 19901$ cm^{-1} (503 nm)	$\nu_a = 19608$ cm^{-1} (510 nm)
	$\nu_f = 18622$ cm^{-1} (537 nm)	$\nu_f = 15520$ cm^{-1} (644 nm)	$\nu_f = 14880$ cm^{-1} (672 nm)	$\nu_f = 13445$ cm^{-1} (744 nm)
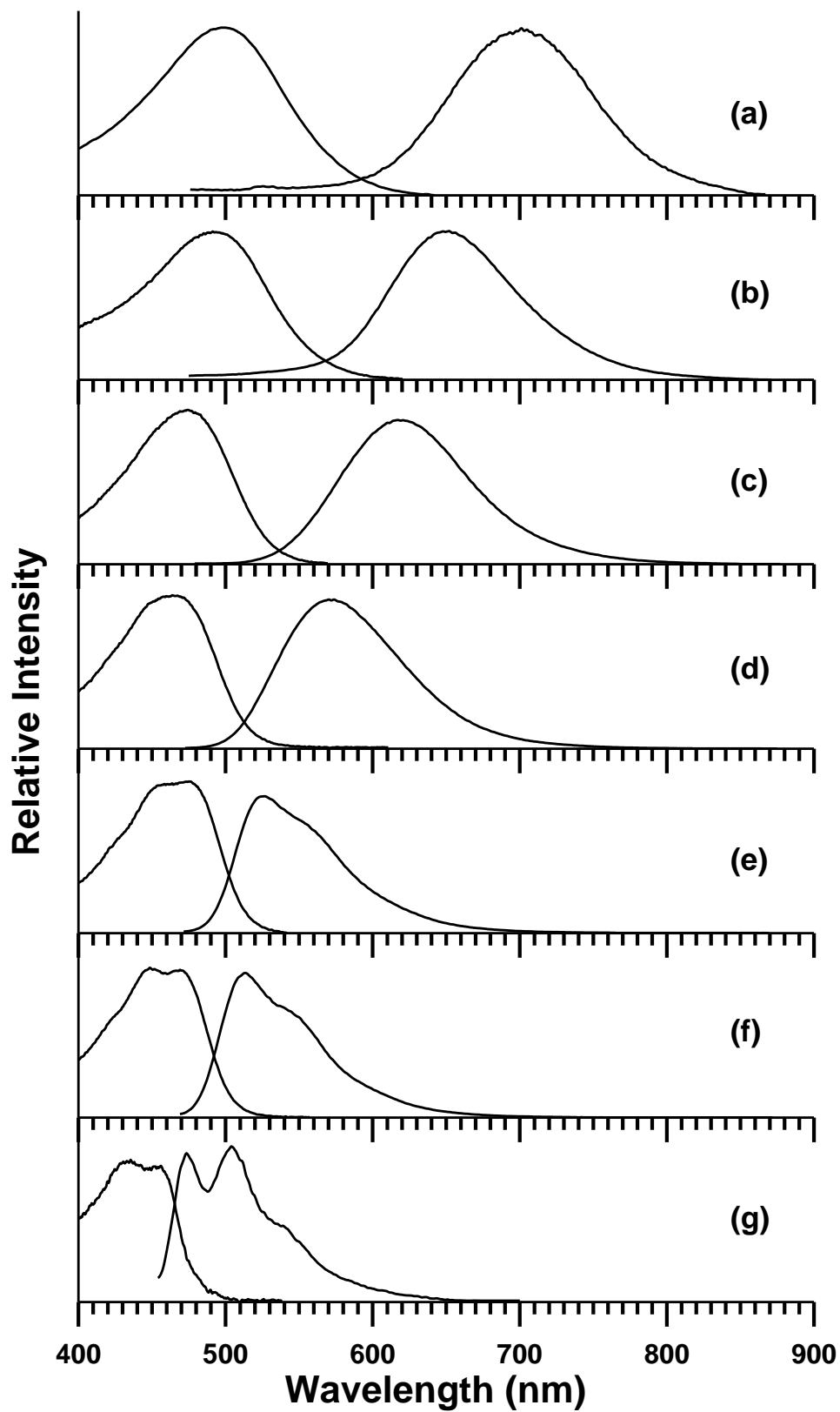
Figure 80. Absorption and fluorescence emission spectra of Ashrbor in (a) methanol, (b) 2-propanol, (c) acetone, (d) ethyl acetate, (e) toluene, (f) carbon tetrachloride, and (g) n-hexane.

Table 41. Spectroscopic properties of Ashrbor in various solvents.

Solvent	λ_{abs} (nm)	λ_f (nm)	ν_{abs} (cm^{-1})	ν_f (cm^{-1})	$E_T(30)$* (kcal mol^{-1})	Δf*	$\Delta\nu$ (cm^{-1})
Methanol	500	737	20,000	13,570	55.4	0.3093	6430
Ethanol	498	725	20,080	13,790	51.9	0.2887	6290
1-Propanol	499	717	20,040	13,953	50.7	0.2746	6087
1-Butanol	499	712	20,040	14,038	50.2	0.2642	6002
2-Propanol	493	687	20,284	14,557	48.4	0.2769	5727
Acetonitrile	478	666	20,921	15,016	45.6	0.3054	5905
Dimethyl sulfoxide	496	676	20,161	14,786	45.1	0.2637	5375
Dimethylformamide	486	656	20,576	15,237	43.2	0.2752	5339
Acetone	474	650	21,097	15,390	42.2	0.2843	5707
Dichloromethane	484	635	20,661	15,747	40.7	0.2171	4914
Pyridine	488	643	20,492	15,560	40.5	0.2124	4932
Chloroform	486	623	20,576	16,040	39.1	0.1491	4536
n-Butyl acetate	468	581	21,368	17,209	38.5	0.1709	4159
Ethyl acetate	464	591	21,552	16,920	38.1	0.1996	4632
Ethyl benzoate	481	604	20,790	16,554	38.1	0.1581	4236
o-Dichlorobenzene	488	608	20,492	16,445	38.0	0.1867	4047
Tetrahydrofuran	479	649	20,877	15,398	37.4	0.2104	5479
Diethyl ether	448	546	22,321	18,331	34.5	0.1669	3990
Benzene	475	532	21,053	18,807	34.3	0.0031	2246
Toluene	475	530	21,053	18,858	33.9	0.0131	2195
Carbon disulfide	489	540	20,450	18,518	32.8	-0.0007	1932
Carbon tetrachloride	449	515	22,272	19,402	32.4	0.0119	2870
n-Hexane	435	504	22,989	19,844	31.0	-0.0004	3145

*Both Δf and $E_T(30)$ values are taken from Suppan, P. and Ghonheim, N., in *Solvatochromism*, The Royal Society of Chemistry, Cambridge, 1997; and Lide, D. R., *CRC Handbook of Chemistry and Physics*, 89th ed., 2008.
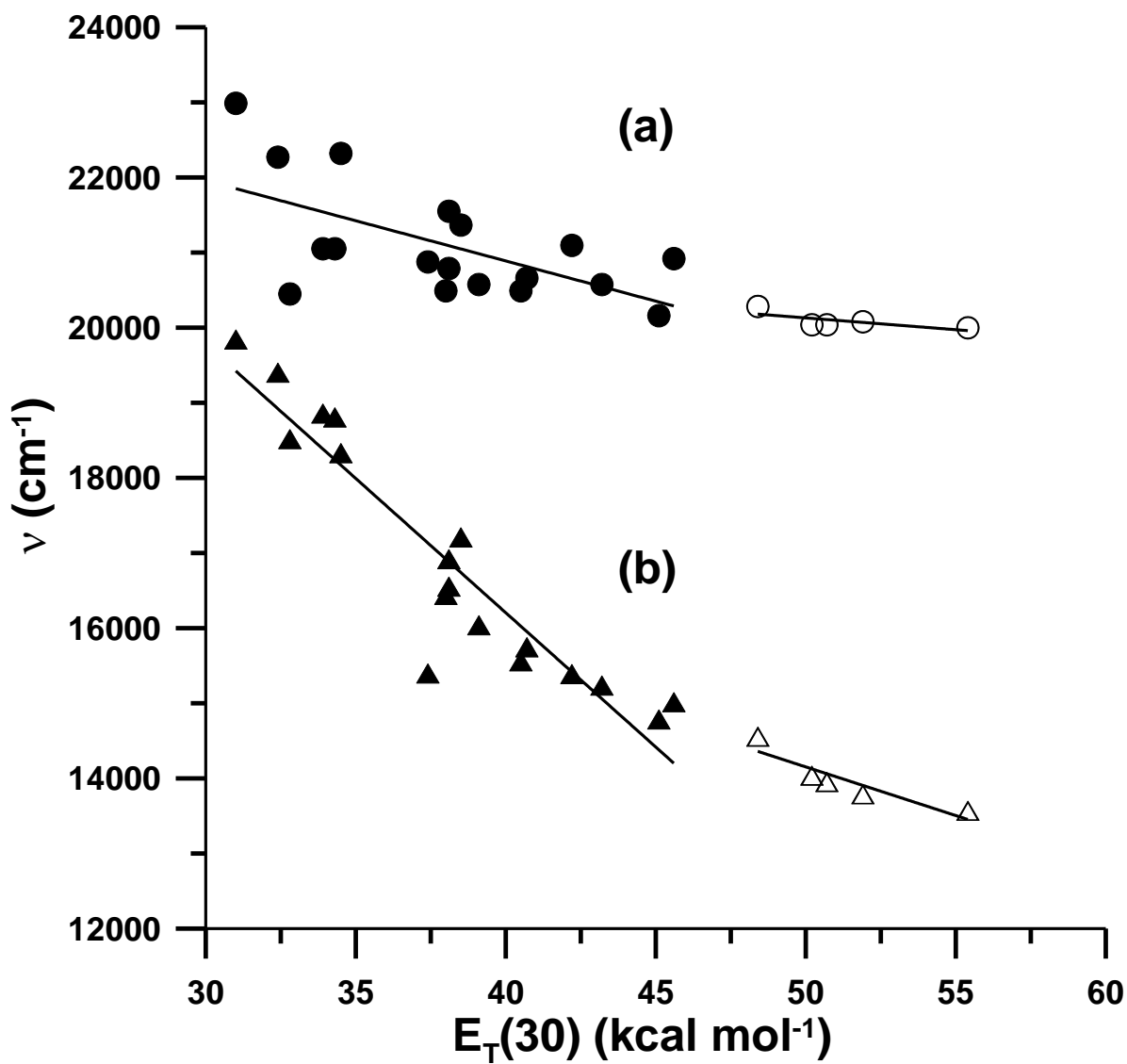
Figure 81. Plot of (a) absorption and (b) fluorescence spectral maxima of Ashrbor in various solvents against the $E_T(30)$ scale. Solid symbols represent aprotic solvents; open symbols represent protic solvents.

The room temperature absorption spectrum of Ashrbor in chloroform along with the results of the TD-DFT (PCM = chloroform) calculations are shown in Figure 82. Results for the first five computed singlet excitations both in the gas phase and in solvent along with experimental data are summarized in Table 42. The $S_0 \rightarrow S_1$ excitation is observed at 486 nm in chloroform and is predicted by TD-DFT to be a strong electronic transition appearing at 458 nm in the gas phase and 502 nm in chloroform, arising from the HOMO $\rightarrow$ LUMO orbital configuration. Examination of the HOMO and LUMO of Ashrbor in Figure 83 reveals the internal charge transfer nature of this excitation. Due to the asymmetric structure of Ashrbor, electron density is not equally proportional on either end of the molecule, unlike symmetric bis-dmab. Qualitatively, it is observed that in the HOMO, electron density is mainly centered on the longer polyene chain end of the molecule, with significant density centered on the nitrogen atom of the dimethylamino group. In the LUMO, electron density becomes larger at the carbonyl center with donor-acceptor charge transfer mainly seen on the longer polyene chain end. Excitation to the predicted S_2 state was not observed experimentally. TD-DFT predicts S_2 to be a forbidden (n, π^*) state in the gas phase occurring at 427 nm, and a weakly allowed (π, π^*) state in chloroform at 428 nm.

The $S_0 \rightarrow S_3$ transition is computed to be a forbidden (n, π^*) excitation in chloroform arising from HOMO-3 $\rightarrow$LUMO, where HOMO-3 is a nonbonding orbital localized on the oxygen atom. The $S_0 \rightarrow S_3$ transition state energy is calculated to occur at 405 nm in chloroform. Excitation to S_4 is predicted to be a weak transition occurring at 366 nm in chloroform with HOMO (π) $\rightarrow$ LUMO + 1 (π^*) as the major CI configuration. Lastly, excitation to S_5 is predicted to be a weak transition of (π, π^*) orbital nature, calculated to occur at 354 nm in chloroform. Absorption bands observed at 318 nm and 301 nm are assigned to the computed S_4 and S_5

excitations due to good agreement with (i) TD-DFT predictions and (ii) spacing of these two excitations.
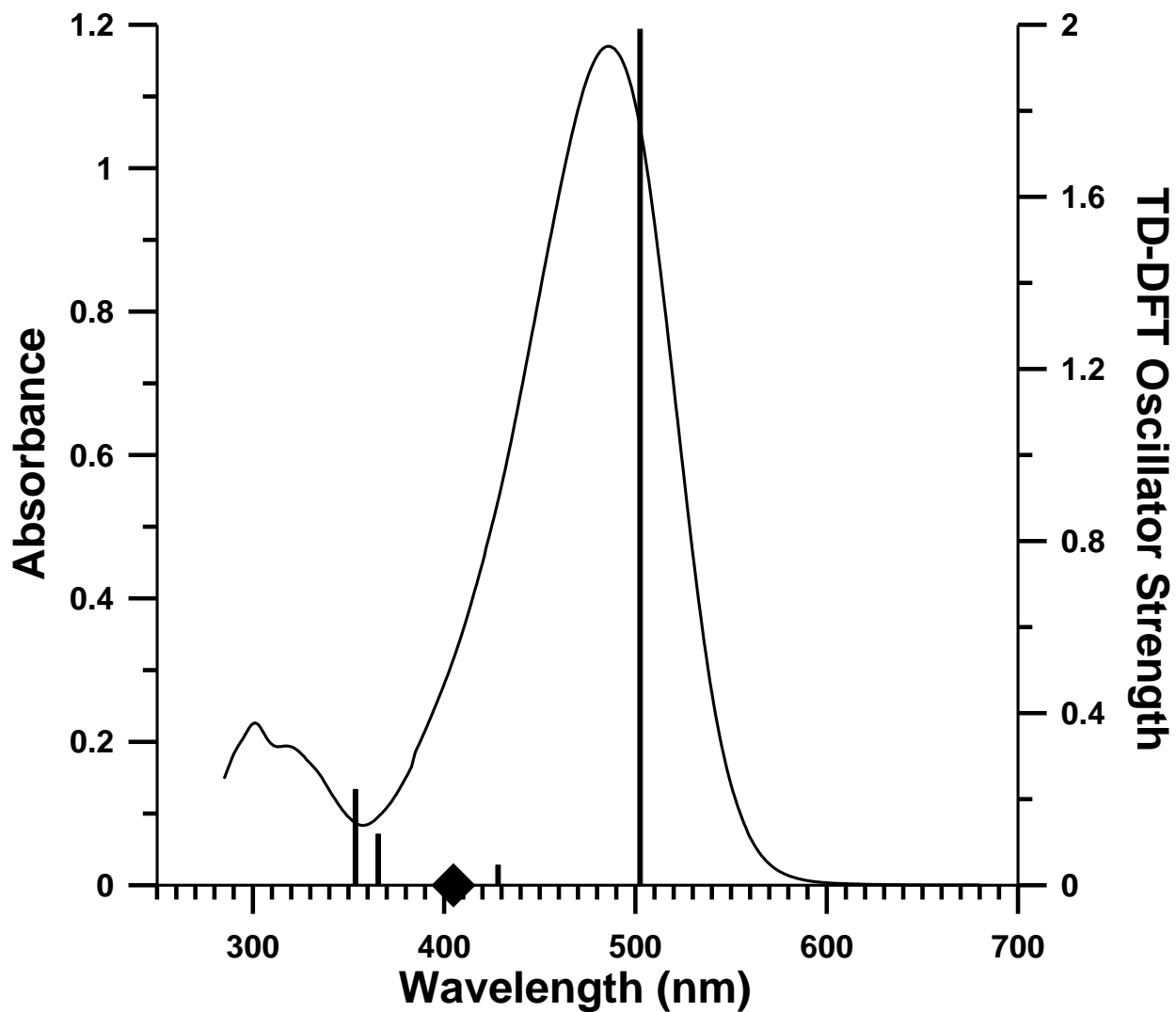
Figure 82. Experimental absorption spectrum of Ashrbor in chloroform and TD-DFT oscillator strengths at the B3LYP/6-31G(d) level of theory. The forbidden $S_3(n, \pi^*)$ excited state is represented by the filled diamond.

Table 42. Experimental spectral data and TD-DFT calculated results for Ashrbor.

Gas phase (calc.)			CHCl₃		CHCl₃ (calc.)	CHCl₃ (expt.)
S_1 (ICT, π, π*)	λ_{max}	458 nm	S_1 (ICT, π, π*)	λ_{max}	502 nm	486 nm
	f	1.76		f	1.99	-
S_2 (n, π*)	λ_{max}	427 nm	S_2 (π, π*)	λ_{max}	428 nm	Not observed
	f	0.0002		f	0.047	
S_3 (π, π*)	λ_{max}	404 nm	S_3 (n, π*)	λ_{max}	405 nm	Not observed
	f	0.054		f	0.00	
S_4 (π, π*)	λ_{max}	359 nm	S_4 (π, π*)	λ_{max}	366 nm	318 nm
	f	0.24		f	0.12	-
S_5 (π, π*)	λ_{max}	347 nm	S_5 (π, π*)	λ_{max}	354 nm	301 nm
	f	0.15		f	0.22	-

LUMO (π*)

HOMO (π)

HOMO-2 (n)
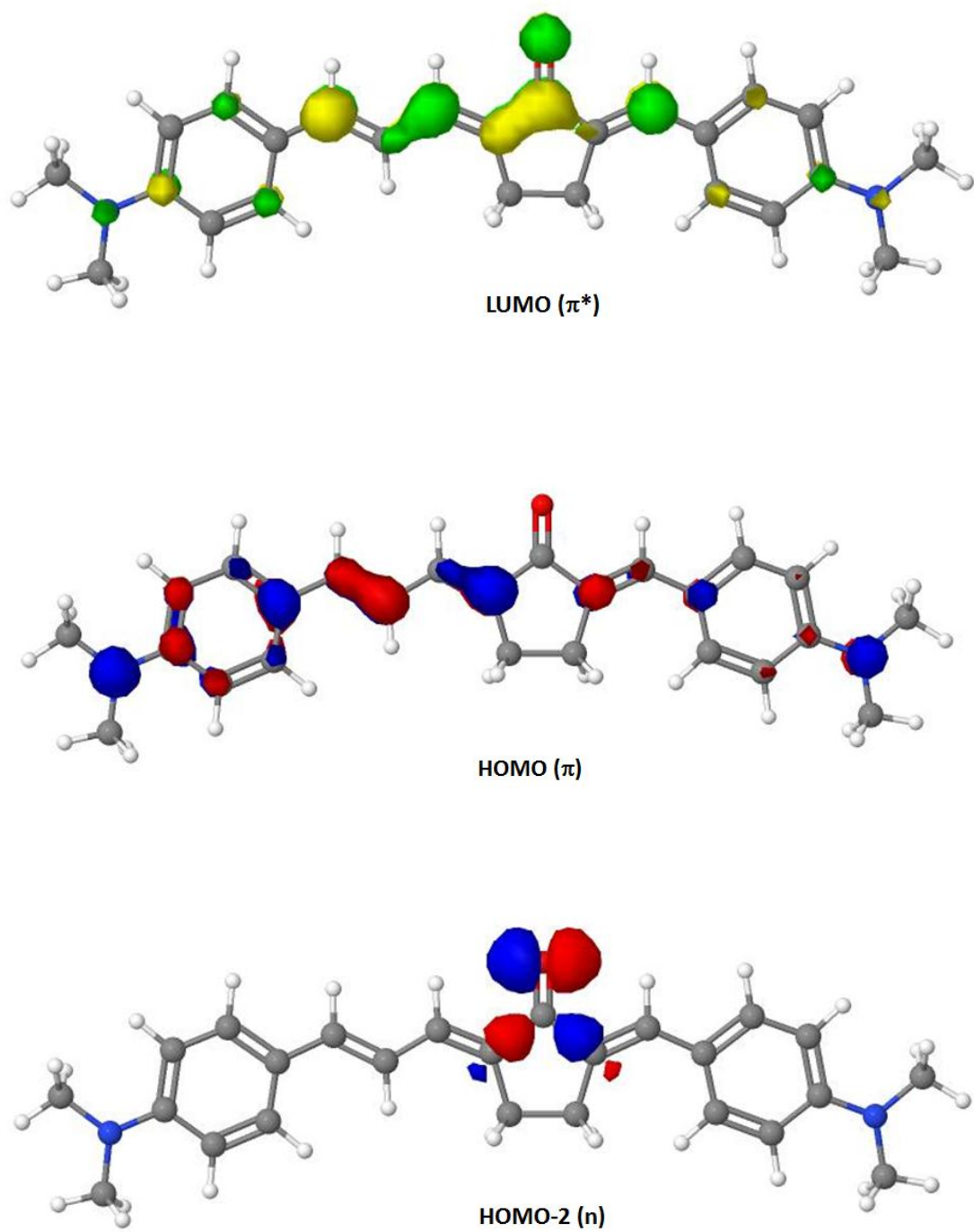
Figure 83. Computed molecular orbitals of Ashrbor in the gas phase.

Treatment of the Lippert-Mataga method for Ashrbor in aprotic solvents (plot shown in Figure 84) and knowledge that the ground state dipole moment and Onsager cavity radius are 5.60 D and 5.97 Å, computed at the B3LYP/6-31G(d) level of theory, the excited state dipole moment is calculated to be 21.1 D ($\Delta\mu$ = 15.5 D), which is 2.2 D larger in magnitude than that of bis-dmab. The ~4-fold enhancement in the electronic dipole moment between S_0 and S_1 is consistent with $S_0 \rightarrow S_1$ being charge transfer in nature.
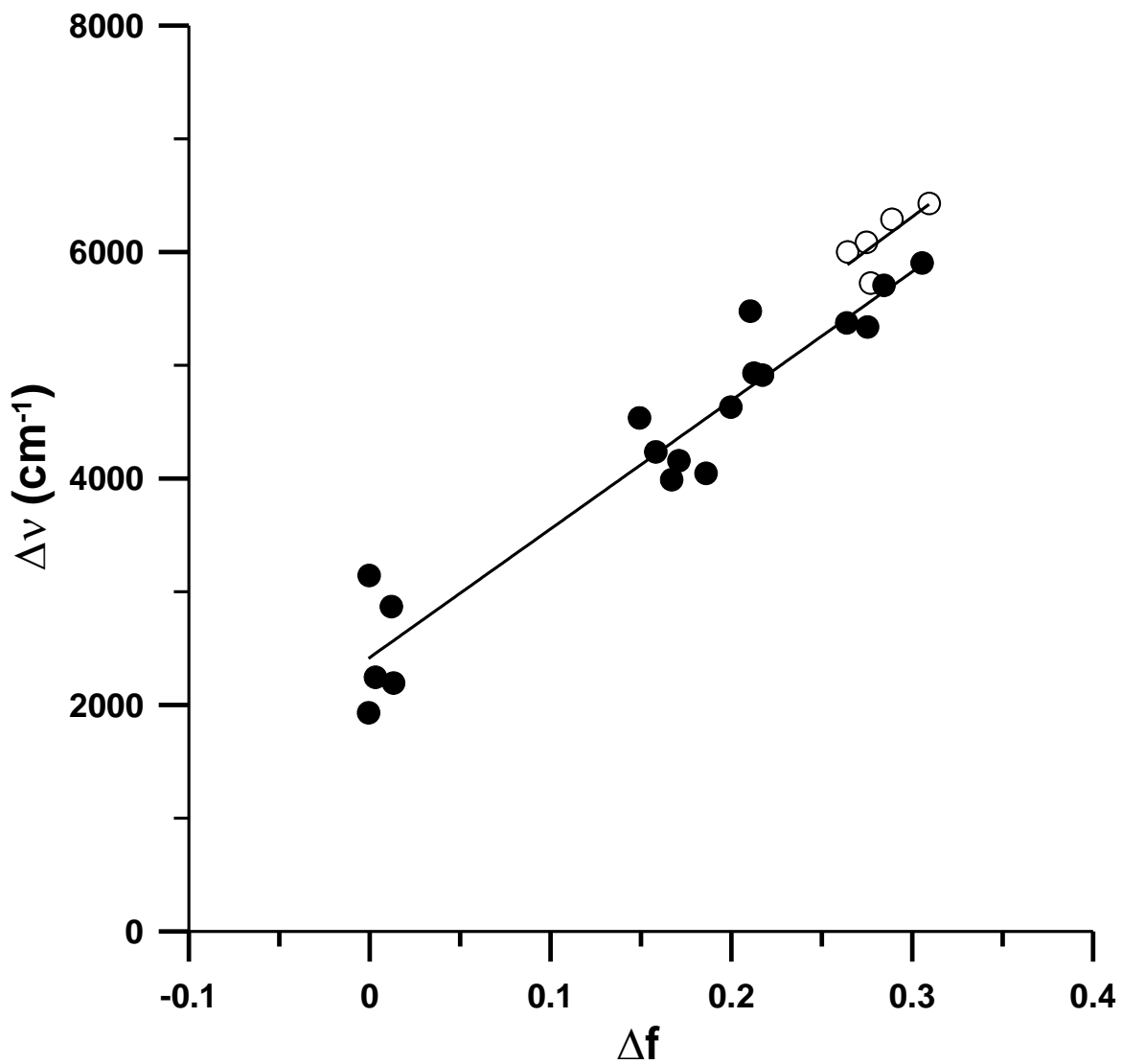
Figure 84. Lippert-Mataga plot of Ashrbor in various solvents. Solid symbols represent aprotic solvents; open symbols represent protic solvents.

4.2.3.3.3 Fluorescence Quantum Yields, Lifetimes, and Decay Constants

       As listed in Table 43, the photophysical properties of Ashrbor showed solvent dependence, with quantum yields varying from 0.007 (in n-hexane) to 0.40 (in dimethyl sulfoxide) and lifetimes between 0.29 ns (carbon tetrachloride) to 1.40 ns (in dimethyl sulfoxide).

Table 43. Photophysical properties of Ashrbor in various solvents.

	Solvent	Φ_f	τ_f (ns)	k_f (s^{-1})	k_{nr} (s^{-1})
1	Methanol	0.11	0.30	3.67×10^8	2.97×10^9
2	Ethanol	0.23	0.82	2.80×10^8	9.39×10^8
3	1-Propanol	0.34	1.13	3.01×10^8	5.84×10^8
4	1-Butanol	0.36	1.25	2.88×10^8	5.12×10^8
5	2-Propanol	0.33	1.24	2.66×10^8	5.40×10^8
6	Acetonitrile	0.29	0.91	3.19×10^8	7.80×10^8
7	Dimethyl sulfoxide	0.40	1.40	2.86×10^8	4.29×10^8
8	Dimethylformamide	0.36	1.32	2.73×10^8	4.85×10^8
9	Acetone	0.31	1.15	2.70×10^8	6.00×10^8
10	Dichloromethane	0.36	1.13	3.19×10^8	5.66×10^8
11	Pyridine	0.38	1.26	3.02×10^8	4.92×10^8
12	Chloroform	0.27	0.98	2.76×10^8	7.45×10^8
13	n-Butyl acetate	0.16	0.63	2.54×10^8	1.33×10^9
14	Ethyl acetate	0.20	0.71	2.82×10^8	1.13×10^9
15	Ethyl benzoate	0.24	0.83	2.89×10^8	9.16×10^8
16	o-Dichlorobenzene	0.24	0.83	2.89×10^8	9.16×10^8
17	Tetrahydrofuran	0.16	0.42	3.81×10^8	2.00×10^9
18	Diethyl ether	0.073	0.31	2.35×10^8	2.99×10^9
19	Benzene	0.13	0.38	3.42×10^8	2.29×10^9
20	Toluene	0.11	0.36	3.06×10^8	2.47×10^9
21	Carbon disulfide	0.13	0.43	3.02×10^8	2.02×10^9
22	Carbon tetrachloride	0.068	0.29	2.34×10^8	3.21×10^9
23	n-Hexane	0.007	-	-	-

From the plot of Φ_f against ν_f of Ashrbor shown in Figure 85, the quantum yield is initially low in n-hexane ($\Phi_f = 0.007$), then increases with respect to a decrease in ν_f, reaching a maximum value of 0.40 in DMSO at 14,786 cm^{-1}, then eventually drops off, but rather still large, in ethanol ($\Phi_f = 0.23$) and methanol ($\Phi_f = 0.11$).
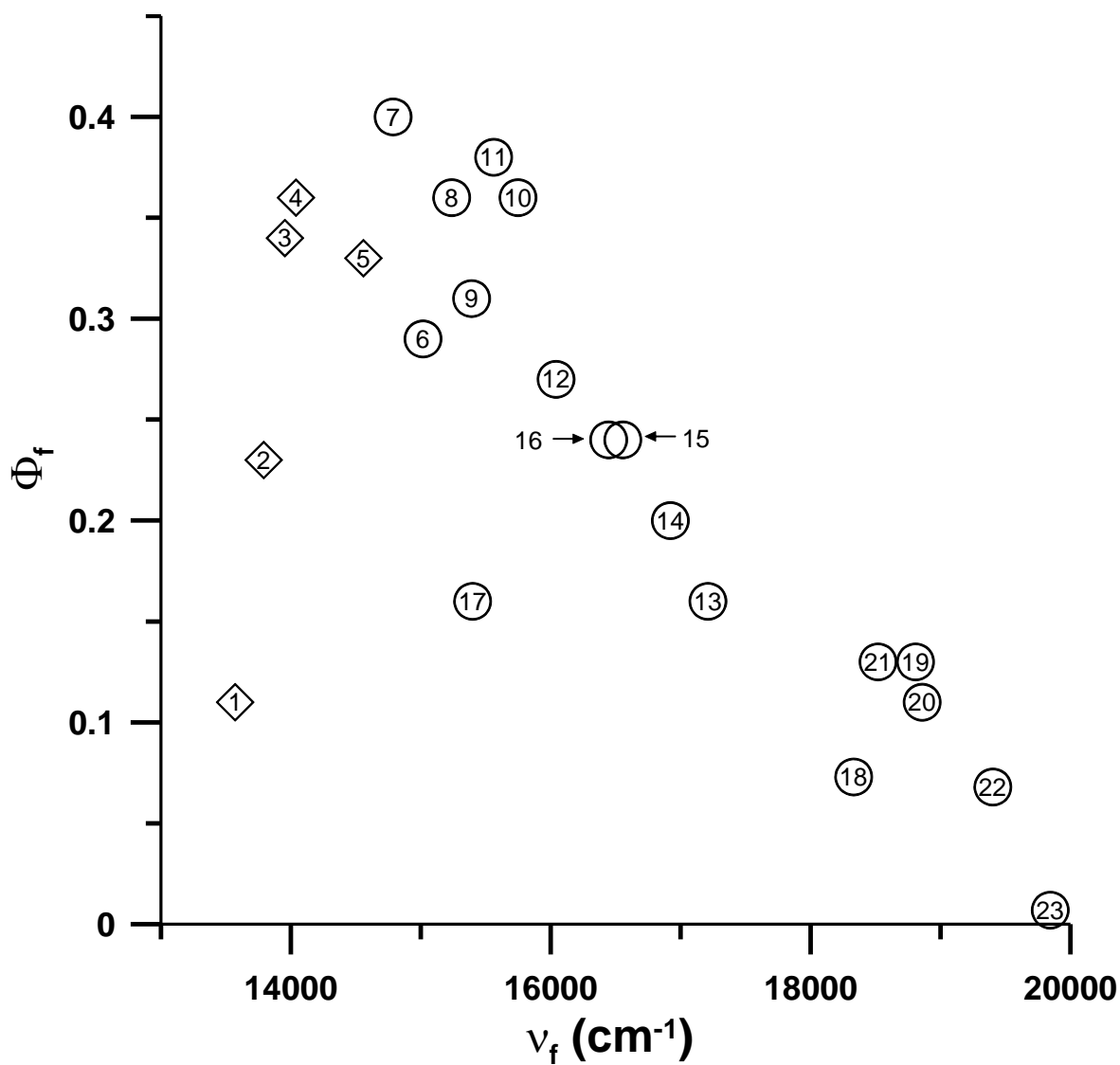
Figure 85. Fluorescence quantum yields (Φ_f) plotted against the fluorescence spectral maxima of Ashrbor in various solvents. Circles represent aprotic solvents; diamonds represent protic solvents.

To explain the relatively high quantum yields observed in highly polar solvent environments, particularly protic solvents, TD-DFT calculations in several alcohols were investigated and compared to bis-dmab and bis-dmac, in which fluorescence quenching was noticeable (see Table 44). In the PCM studied alcohols for Ashrbor, bis-dmab, and bis-dmac, the predicted $^3(n, \pi^*)$ state is localized above the $S_1(\pi, \pi^*)$ state, suggesting that direct spin-orbit coupling between $S_1(\pi, \pi^*)$ and $T_1(\pi, \pi^*)$ is weak (low k_{isc}). Vibronic spin-orbit coupling can be offered as a mechanism in explaining the higher quantum yields observed for Ashrbor in alcohols. As presented in Table 44, even though the lowest lying triplet (n, π^*)-(π, π^*) energy gaps of Ashrbor in alcohols fall in between bis-dmab and bis-dmac, the corresponding singlet (n, π^*)-(π, π^*) energy spacings of Ashrbor are larger than for both bis-dmab and bis-dmac. The larger energy gap between $^1(\pi, \pi^*)$ and $^1(n, \pi^*)$ suggests an attenuation in the degree of vibronic coupling between these two states, resulting in a slower rate of singlet → triplet intersystem crossing. Therefore, these data provide theoretical support for the higher Φ_f values observed for Ashrbor in alcohols.

In order to test whether the low fluorescence quantum yield of Ashrbor in methanol is due to hydrogen bonding between the hydroxyl hydrogen atom of methanol and the carbonyl oxygen atom of the excited state molecule, a quantum yield study was carried out in methan(ol-d). It was found that $\Phi_f = 0.12$ in CH_3OD, compared to $\Phi_f = 0.11$. Therefore, the insignificant change in Φ_f between undeuterated methanol and methan(ol-d) suggests that hydrogen bonding is not a factor in the low quantum yield of fluorescence in methanol.

Table 44. TD-DFT computed energy gaps of bis-dmab, Ashrbor, and bis-dmac in methanol, ethanol, 2-propanol, and 1-butanol (with observed Φ_f values).[†]

Compound	Methanol	Ethanol	2-Propanol	1-Butanol
bis-dmab	$\Delta E_S = 4765$ cm^{-1} $\Delta E_T = 8081$ cm^{-1} ($\Phi_f = 0.025$)	$\Delta E_S = 4697$ cm^{-1} $\Delta E_T = 8001$ cm^{-1} ($\Phi_f = 0.11$)	$\Delta E_S = 4697$ cm^{-1} $\Delta E_T = 7977$ cm^{-1} ($\Phi_f = 0.18$)	-
Ashrbor	$\Delta E_S = 5543$ cm^{-1} $\Delta E_T = 9672$ cm^{-1} ($\Phi_f = 0.11$)	$\Delta E_S = 5480$ cm^{-1} $\Delta E_T = 9622$ cm^{-1} ($\Phi_f = 0.23$)	$\Delta E_S = 5480$ cm^{-1} $\Delta E_T = 9603$ cm^{-1} ($\Phi_f = 0.33$)	$\Delta E_S = 5518$ cm^{-1} $\Delta E_T = 9552$ cm^{-1} ($\Phi_f = 0.36$)
bis-dmac	$\Delta E_S = 5292$ cm^{-1} $\Delta E_T = 9702$ cm^{-1} ($\Phi_f = 0.022$)	$\Delta E_S = 5326$ cm^{-1} $\Delta E_T = 9624$ cm^{-1} ($\Phi_f = 0.076$)	$\Delta E_S = 5326$ cm^{-1} $\Delta E_T = 9639$ cm^{-1} ($\Phi_f = 0.15$)	$\Delta E_S = 5326$ cm^{-1} $\Delta E_T = 9576$ cm^{-1} ($\Phi_f = 0.17$)

[†]ΔE values are between $S_1/T_1(\pi, \pi^*)$ and the appropriate intermediate (n, π^*) states for singlet (S) and triplet (T) manifolds.

From the k_{nr} plot of Ashrbor shown in Figure 86, the k_{nr} value is initially large at higher S_0-S_1 energy gaps ($k_{nr} = 3.21 \times 10^9$ s^{-1} in CCl$_4$), then continuously decreases with respect to a decrease in energy gap, reaching a minimum at 14,786 cm^{-1} in DMSO ($k_{nr} = 4.29 \times 10^8$ s^{-1}). The decrease in k_{nr} from CCl$_4$ to DMSO is related to the interpretation in the trend in the quantum yield plot. As was seen with all three symmetric alkylamino substituted 2,5-diarylidene cyclopentanones, it is also seen in Table 45 for the case of Ashrbor that the energy spacing between the lowest lying singlet and triplet $(\pi, \pi^*)/(n, \pi^*)$ states becomes continuously larger with respect to an increase in solvent polarity. As stated before, the solvent induced increase in the (n, π^*)-(π, π^*) energy gaps attenuates the degree of vibronic coupling among energy states of same spin multiplicities, thereby reducing the overall rate of intersystem crossing between singlet and triplet state manifolds.

Table 45. TD-DFT computed energy gaps between the lowest lying (n, π*) and (π, π*) states and experimental k_{nr} values for Ashrbor.

	Toluene	Carbon Disulfide	Dichloromethane
$T_3(n, \pi^*)$-$T_1(\pi, \pi^*)$	8429 cm^{-1}	8494 cm^{-1}	9350 cm^{-1}
$S_3(n, \pi^*)$-$S_1(\pi, \pi^*)$	4070 cm^{-1}	4331 cm^{-1}	5214 cm^{-1}
$k_{nr} \times 10^{-8}$ (s^{-1})	24.7	20.2	5.66
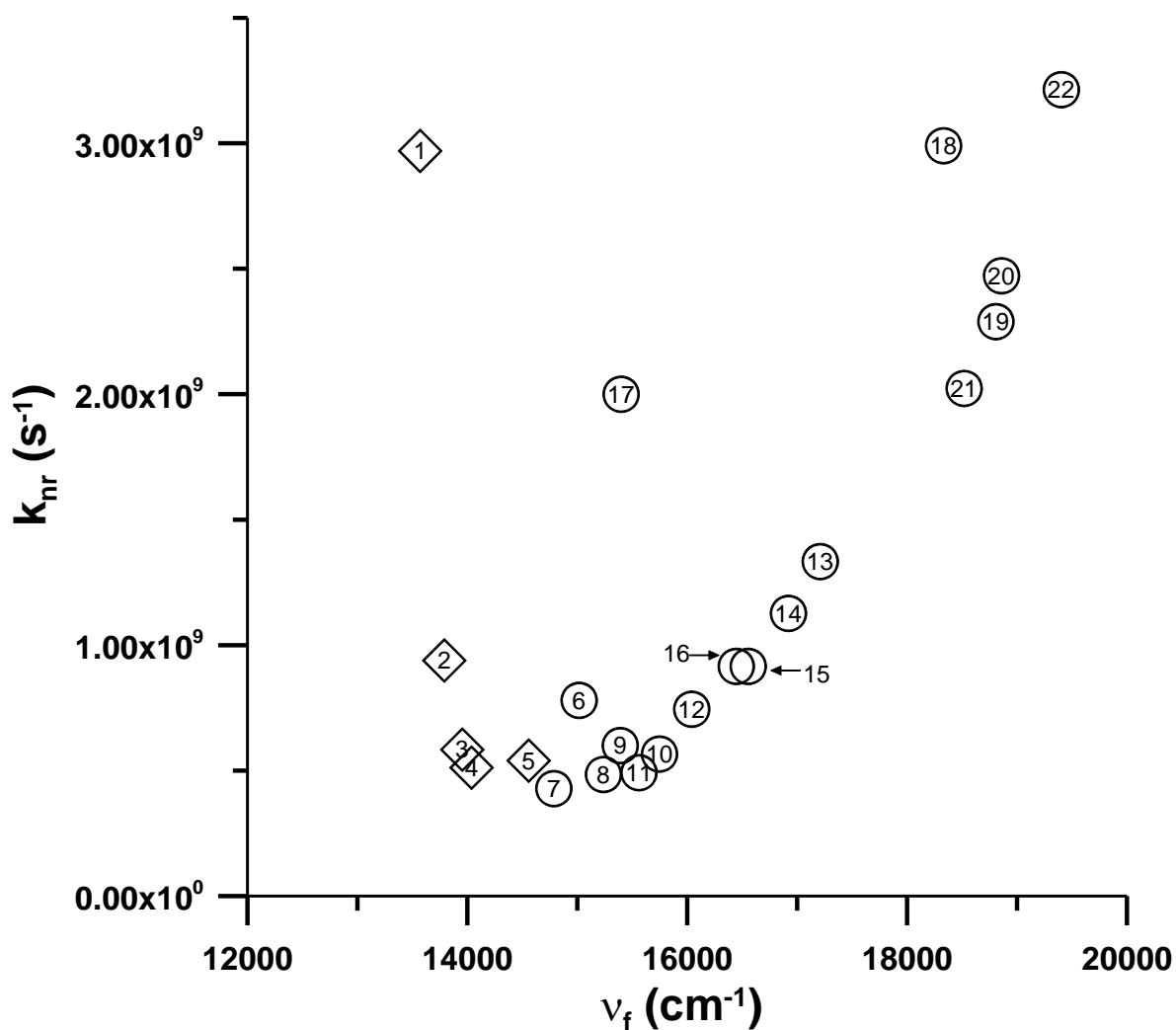
Figure 86. Nonradiative decay constants (k_{nr}) plotted against the fluorescence spectral maxima of Ashrbor in various solvents. Circles represent aprotic solvents; diamonds represent protic solvents.
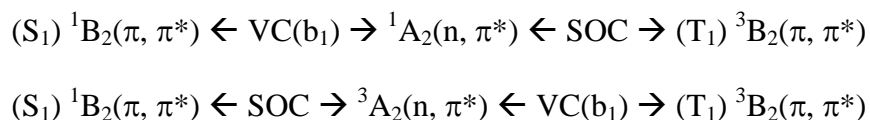
4.2.4   Conclusions

The alkylamino substituted 2-arylidene cyclopentanones, dmab and dmac, exhibit similar solvatochromic properties in their absorption and fluorescence spectra, with smaller red shifts in absorption and fluorescence energies for dmac, consistent with the longer polyene chain length. In addition, the larger $\Delta\mu$ and μ_e values of dmac support its higher degree of internal charge transfer. Fluorescence was observed to be very weak for both compounds in all solvents. The weak fluorescence is attributed to highly efficient singlet $\rightarrow$ triplet intersystem crossing between excited states of different orbital configurations in accordance with El-Sayed's rules. TD-DFT spectral calculations support this argument.

Comparative studies for absorption and fluorescence of dmab and dmac with their symmetric two-sided analogues, bis-dmab and bis-dmac, showed more pronounced solvatochromism in spectral maxima and larger dipole moments in the excited states for both bis-dmab and bis-dmac. The higher degree of bathochromic shifting and higher excited state dipole moments exhibited by bis-dmab and bis-dmac are attributed to longer π-conjugated chain lengths and the presence of a second electron donating group.

From their DFT optimized geometries, all four alkylamino substituted 2,5-diarylidene cyclopentanone dyes exhibit similar planar structures. There was excellent agreement between the X-ray crystal structure of bis-dmab and its predicted DFT geometry. Spectroscopic properties of all four compounds showed strong solvent dependence with absorption and fluorescence spectra shifted bathochromically with respect to an increase in solvent polarity. Energy maxima shifted further to the red with respect to increased polyene chain length. For bis-dmab, bis-dmac, and bis-juldmac (under assumed C_{2v} symmetry), S_1 is computed to be strong symmetry allowed

$B_2 \leftarrow A_1$ transition of the (π, π^*) type, arising from the orbital excitation $a_2(\pi) \rightarrow b_1(\pi^*)$, where $a_2(\pi)$ is the HOMO and $b_1(\pi^*)$ is the LUMO. The S_2 state is computed to be a symmetry forbidden $A_2 \leftarrow A_1$ transition of the (n, π^*) type, arising from the orbital excitation $b_2(n) \rightarrow b_1(\pi^*)$, where $b_2(n)$ is the nonbonding molecular orbital localized on the oxygen atom.

Application of group theory to spin-orbit coupling of these three compounds demonstrates that the excited states $^1B_2(\pi, \pi^*)$ and $^3A_2(n, \pi^*)$ mix through first-order spin-orbit coupling, but $^1B_2(\pi, \pi^*)/^3B_2(\pi, \pi^*)$ and $^1A_2(n, \pi^*)/^3A_2(n, \pi^*)$ don't mix through first-order spin-orbit coupling. Application of group theory to vibronic coupling shows that b_1 corresponds to the irreducible representation of the vibration that promotes the vibronic coupling between $S_1(\pi, \pi^*)$ and $S_m(n, \pi^*)$ as well as between $T_1(\pi, \pi^*)$ and $T_m(n, \pi^*)$ states for these compounds. Therefore, under C_{2v}, the following scheme below shows the vibronic spin-orbit coupling mechanism applied to bis-dmab, bis-dmac, and bis-juldmac.

$$(S_1)\ ^1B_2(\pi, \pi^*) \leftarrow VC(b_1) \rightarrow\ ^1A_2(n, \pi^*) \leftarrow SOC \rightarrow (T_1)\ ^3B_2(\pi, \pi^*)$$

$$(S_1)\ ^1B_2(\pi, \pi^*) \leftarrow SOC \rightarrow\ ^3A_2(n, \pi^*) \leftarrow VC(b_1) \rightarrow (T_1)\ ^3B_2(\pi, \pi^*)$$

Both the fluorescence quantum yields (Φ_f) and lifetimes (τ_f) varied depending on solvent polarity. Similar parabolic trends were observed in the Φ_f against ν_f plots for bis-dmab, bis-dmac, and bis-juldmac. At higher energy gaps, Φ_f is low, rises in the intermediate region, then drops back down at smaller energy gaps. The rise in Φ_f from the high energy end to the middle (nonpolar to several polar aprotic solvents) is due to the decreasing rate of intersystem crossing. The drop in Φ_f at smaller energies (in several aprotic and protic solvents) is attributed to the increase in the rate of internal conversion, as predicted by the energy gap law.

Related to the Φ_f plots are the plots of k_{nr} against ν_f, which are separated into two distinct regions: region 1 (polar protic and several polar aprotic), where internal conversion is the major nonradiative decay channel from S_1 (energy gap law); and region 2 (polar aprotic and nonpolar), where intersystem crossing is the major nonradiative decay channel from S_1. Vibronic spin-orbit coupling is considered to be a second-order mechanism for explaining the change in k_{nr} seen in region 2. TD-DFT calculations show computed energy gaps between $S_1/T_1(\pi, \pi^*)$ and the appropriate intermediate (n, π^*) states in several 'region 2' solvents that are supportive of the vibronic spin-orbit coupling mechanism. It was proposed that the solvent induced increase in the spacing between $S_1/T_1(\pi, \pi^*)$ and (n, π^*) states attenuates the degree of state mixing (of the same spin manifold), which in turn reduces the rate of S → T intersystem crossing, as was experimentally shown from the k_{nr} decrease in this region. Additionally, direct comparison of the TD-DFT computed energy gaps of bis-dmab and bis-dmac in the same 'region 2' solvents showed larger differences in the $S_1/T_1(\pi, \pi^*)$-(n, π^*) energy spacings between toluene and dichloromethane for bis-dmab, which thereby provides theoretical support in explaining the large change in k_{nr} from the high frequency end to the mid frequency end of this region for bis-dmab.

The tendency for bis-dmac to undergo fluorescence quenching in polar aprotic and protic solvents cannot be attributed to twisting of the dimethylamino group to form a polar TICT state since its spatially-restricted julolidinic analogue, bis-juldmac, behaves in a similar manner and is incapable of twisting to form a TICT compound.

Furthermore, the asymmetric alkylamino substituted 2,5-diarylidene cyclopentanone compound, Ashrbor, falling intermediate in polyene chain length between bis-dmab and bis-dmac, exhibits similar solvatochromic trends in both absorption and fluorescence. Therefore,

due to its unsaturated chain length, the absorption and fluorescence spectral maxima of Ashrbor fall between those of bis-dmab and bis-dmac. The higher Φ_f values of Ashrbor in alcohols are indicative of less fluorescence quenching than observed for bis-dmab and bis-dmac in alcohols. The larger ^{1}(n, π*)-^{1}(π, π*) energy gaps of Ashrbor, predicted by TD-DFT, are consistent with the higher quantum yield values in alcohols.

### 4.3 Spectroscopic and Photophysical Properties of Additional 2,5-Diarylidene Cyclopentanone Dyes

4.3.1 Introduction

This section is subdivided into two parts. Section 4.3.2 deals with the spectroscopic and photophysical properties of (2E,5E)-2,5-bis(p-methoxycinnamylidene)-cyclopentanone (2dbmxcp), relating them to the dimethylamino derivative, bis-dmac. Particular attention in this section will be devoted to looking at the internal charge transfer nature of 2dbmxcp and how it compares to the charge transfer nature of bis-dmac, through examination of absorption and fluorescence spectra, Lippert-Mataga analyses for electronic state dipole moments and semi-empirical partial charge calculations for atoms of both molecules in the ground and excited states.

Section 4.3.3 will present and discuss the structural and spectroscopic properties of an asymmetrically unsubstituted 2,5-diarylidene-cyclopentanone dye, namely (2E,5E)-2-benzylidene-5-cinnamylidene-cyclopentanone (Asunsub), briefly comparing its properties to previously published work for symmetrically unsubstituted 2,5-diarylidene-cyclopentanone dyes.

4.3.2 Spectroscopic and Photophysical Properties of 2dbmxcp

The objective of this section is to not only present experimental and theoretical work for 2dbmxcp, but also to compare and contrast the spectral and photophysical properties with the dimethylamino derivative, bis-dmac. As illustrated in Figure 87, bis-dmac has a higher degree of solvatochromism than 2dbmxcp, in that its color changes from yellow → orange → red → purple in going from nonpolar to polar, aprotic and protic solvents; whereas 2dbmxcp remains yellow and changes to orange in 2,2,2-trifluoroethanol.
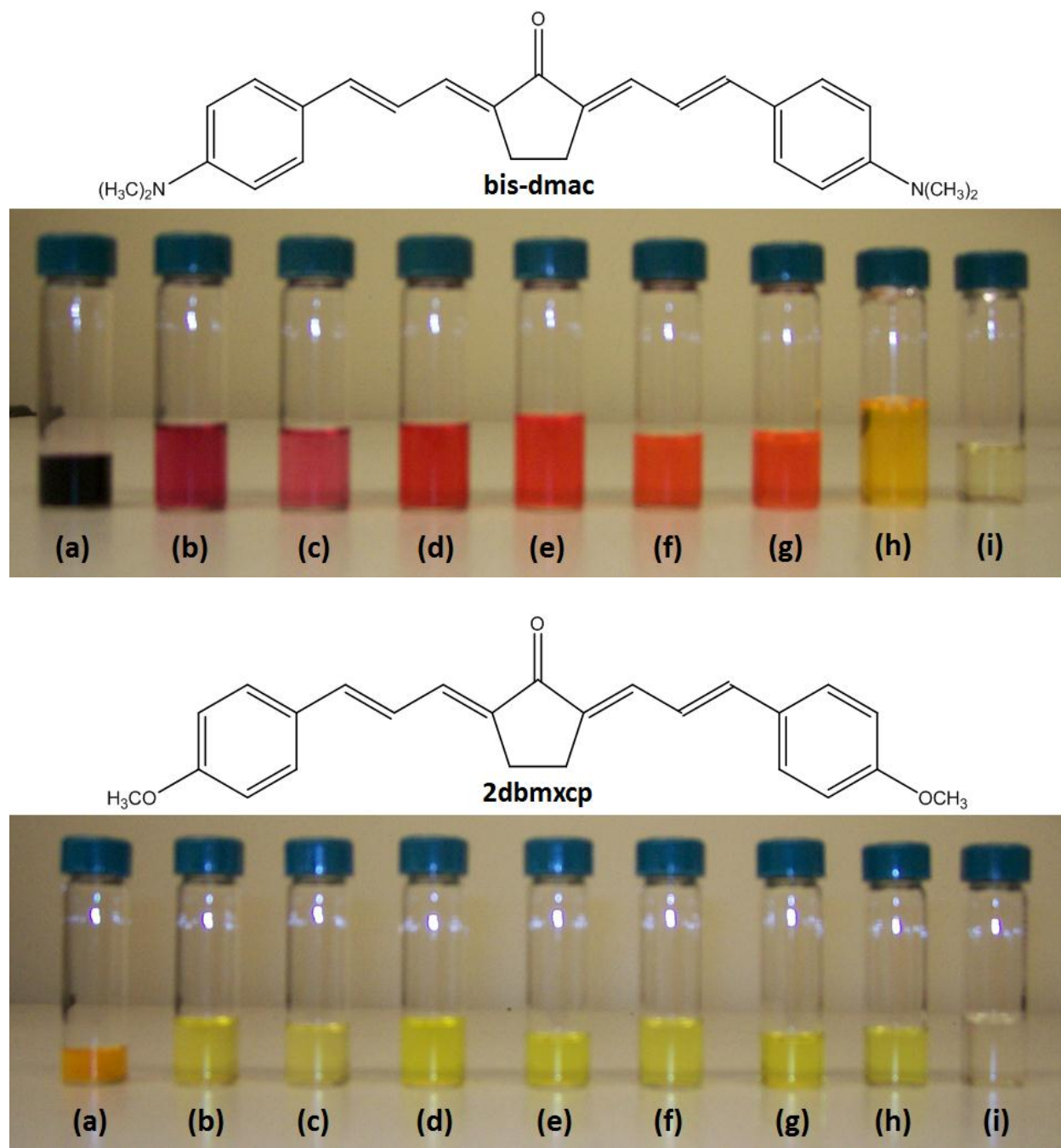
Figure 87. Solutions of bis-dmac and 2dbmxcp in (a) 2,2,2-trifluoroethanol, (b) ethanol, (c) 2-propanol, (d) acetonitrile, (e) acetone, (f) ethyl acetate, (g) benzene, (h) toluene, and (i) cyclohexane.

Figure 88 shows the gas phase optimized geometry of 2dbmxcp at the DFT

B3LYP/6-31G(d) level of theory. Similar to the alkylamino substituted 2,5-diarylidene

cyclopentanone dyes, the predicted geometry of the molecule is essentially planar, with the

exception of ~10° nonplanarity within the cyclopentanone ring.
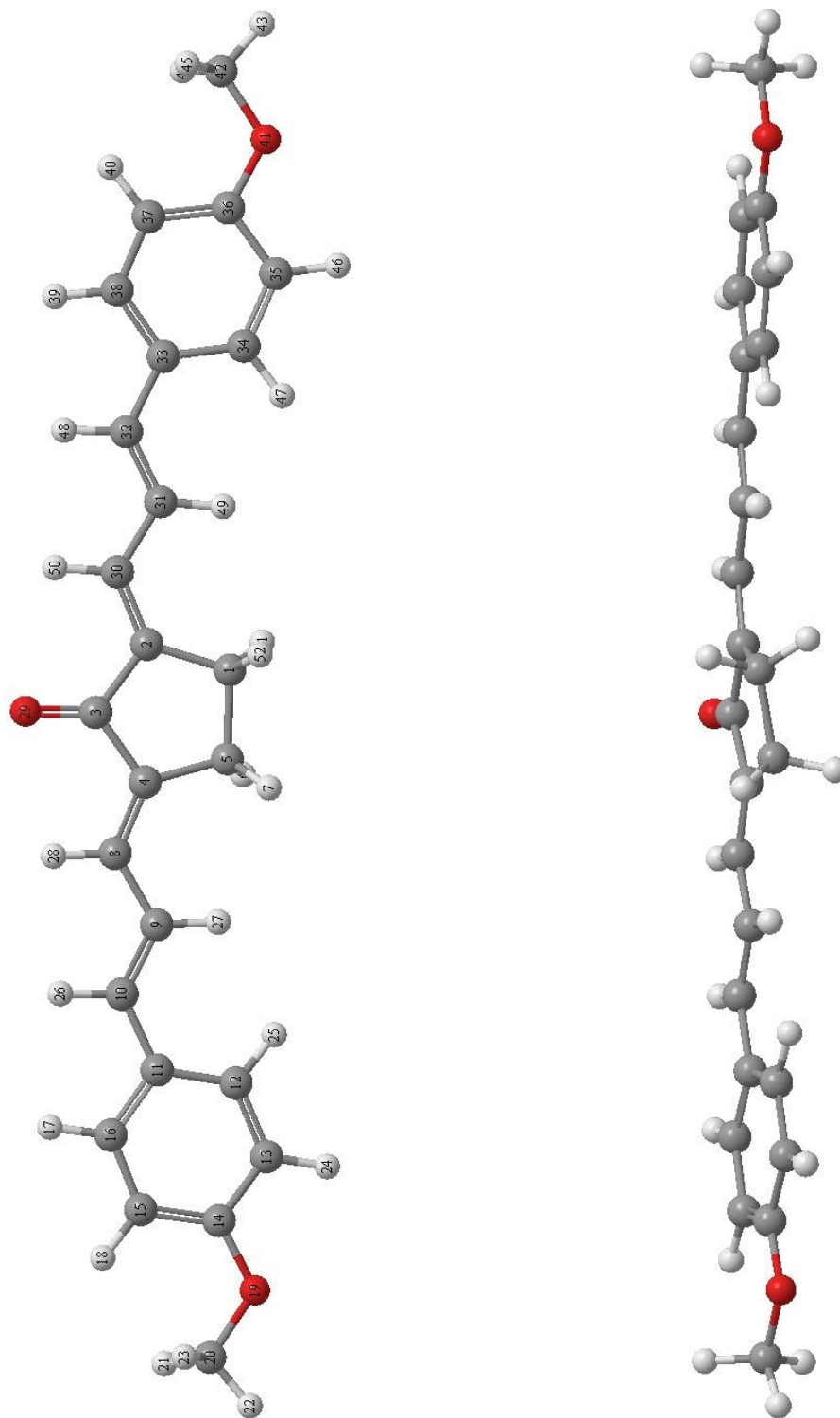
Figure 88. Optimized geometry of 2dbmxcp at the B3LYP/6-31G(d) level of theory. Gas phase

dipole moment = 2.04 D.

Table 46. B3LYP/6-31G(d) calculated ground state optimized geometry of 2dbmxcp.

Bond Lengths (Å)	
C_1-C_2	1.51
C_1-C_5	1.56
C_2-C_3	1.48
C_3-O_{29}	1.23
C_4-C_8	1.35
C_8-C_9	1.44
C_9-C_{10}	1.36
C_{10}-C_{11}	1.46
C_{11}-C_{12}	1.41
C_{11}-C_{16}	1.41
C_{12}-C_{13}	1.38
C_{13}-C_{14}	1.41
C_{14}-C_{15}	1.40
C_{14}-O_{19}	1.36
C_{15}-C_{16}	1.39
O_{19}-C_{20}	1.42

Bond Angles (°)	
C_1-C_2-C_3	109.75
C_1-C_5-C_4	105.61
C_2-C_3-C_4	107.58
C_2-C_3-O_{29}	126.21
C_3-C_4-C_8	121.20
C_4-C_8-C_9	126.45
C_5-C_4-C_8	129.04
C_8-C_9-C_{10}	122.67
C_9-C_{10}-C_{11}	128.05
C_{10}-C_{11}-C_{12}	123.70
C_{10}-C_{11}-C_{16}	119.18
C_{11}-C_{12}-C_{13}	121.39
C_{11}-C_{16}-C_{15}	122.21
C_{12}-C_{11}-C_{16}	117.12
C_{12}-C_{13}-C_{14}	120.41
C_{13}-C_{14}-C_{15}	119.41
C_{13}-C_{14}-O_{19}	115.68
C_{14}-C_{15}-C_{16}	119.45
C_{14}-O_{19}-C_{20}	118.33
C_{14}-N_{19}-C_{24}	119.84
C_{15}-C_{14}-O_{19}	124.91

Atomic Charges	
C_1	-0.360
C_2	0.0777
C_3	0.352
C_8	-0.170
C_9	-0.117
C_{10}	-0.187
C_{11}	0.174
C_{12}	-0.180
C_{13}	-0.173
C_{14}	0.379
C_{15}	-0.196
C_{16}	-0.203
O_{19}	-0.503
C_{20}	-0.218
O_{29}	-0.514

| Dihedral Angles (°)	
C_1-C_2-C_{33}-C_{34}	-0.47
C_3-C_2-C_1-C_5	10.95

Absorption and fluorescence properties of 2dbmxcp were examined in a total of seventeen solvents, six of which whose spectra are displayed in Figure 89. As shown, 2dbmxcp undergoes a red shift with respect to an increase in solvent polarity. To further discuss the solvatochromic properties, both absorption and fluorescence spectral maxima of 2dbmxcp have been plotted against the $E_T(30)$ scale and are compared to the spectral data of bis-dmac. It is clearly seen in both the absorption and fluorescence plots (see Figures 90 and 91) that bis-dmac exhibits greater red shifted spectral characteristics. In the absorption plot, 2dbmxcp ranges between 23,923 cm^{-1} (λ 418 nm) in ethyl acetate and 22,124 cm^{-1} (λ 452 nm) in trifluoroethanol (Δv_{abs} = 1799 cm^{-1}). This is compared to the absorption shift of bis-dmac: 21,505 cm^{-1} (λ 465 nm) in carbon tetrachloride to 18,727 cm^{-1} (λ 534 nm) in trifluoroethanol (Δv_{abs} = 2778 cm^{-1}). In the fluorescence plot of 2dbmxcp, the spectral maxima range between 19,087 cm^{-1} (λ 524 nm) in carbon disulfide and 15,407 cm^{-1} (λ 649 nm) in trifluoroethanol (Δv_f = 3680 cm^{-1}). This is compared to the fluorescence shift observed for bis-dmac: 20,161 cm^{-1} (λ 496 nm) in n-hexane to 13,089 cm^{-1} (λ 764 nm) in trifluoroethanol (Δv_f = 7072 cm^{-1}). Also, it is clearly seen in Figure 91 that the slope of the linear regression fit for bis-dmac in aprotic solvents is ~3-fold greater in magnitude than that for 2dbmxcp. The observed solvatochromic properties of these two compounds are consistent with a charge transfer electronic transition. However, it is also asserted that since the spectral energy shifts of bis-dmac are larger than those for 2dbmxcp, bis-dmac exhibits a higher degree of internal charge transfer.

Table 47. Spectroscopic properties of 2dbmxcp in various solvents.

| Solvent	λ_{abs} (nm)	λ_f (nm)	ν_{abs} (cm^{-1})	ν_f (cm^{-1})	$E_T(30)^*$ (kcal mol^{-1})	Δf^*	$\Delta\nu$ (cm^{-1})
Trifluoroethanol	452	649	22,124	15,407	59.4	0.3159	6717
Methanol	438	620	22,831	16,119	55.4	0.3093	6712
Ethanol	438	599	22,831	16,689	51.9	0.2887	6142
1-Propanol	439	595	22,779	16,813	50.7	0.2746	5966
1-Butanol	440	593	22,727	16,860	50.2	0.2642	5867
2-Propanol	435	583	22,989	17,166	48.4	0.2769	5823
Acetonitrile	427	570	23,419	17,558	45.6	0.3054	5861
Dimethyl sulfoxide	439	575	22,779	17,392	45.1	0.2637	5387
Dimethylformamide	434	564	23,041	17,730	43.2	0.2752	5311
Acetone	425	565	23,529	17,696	42.2	0.2843	5833
Dichloromethane	433	538	23,095	18,580	40.7	0.2171	4515
Pyridine	437	540	22,883	18,520	40.5	0.2124	4363
Chloroform	435	539	22,989	18,561	39.1	0.1491	4428
Ethyl acetate	418	529	23,923	18,903	38.1	0.1996	5020
Benzene	424	527	23,585	18,979	34.3	0.0031	4606
Toluene	421	527	23,753	18,979	33.9	0.0131	4774
Carbon disulfide	432	524	23,148	19,087	32.8	-0.0007	4061

*Both Δf and $E_T(30)$ values are taken from Suppan, P. and Ghonheim, N., in *Solvatochromism*, The Royal Society of Chemistry, Cambridge, 1997; and Lide, D. R., *CRC Handbook of Chemistry and Physics*, 89th ed., 2008.
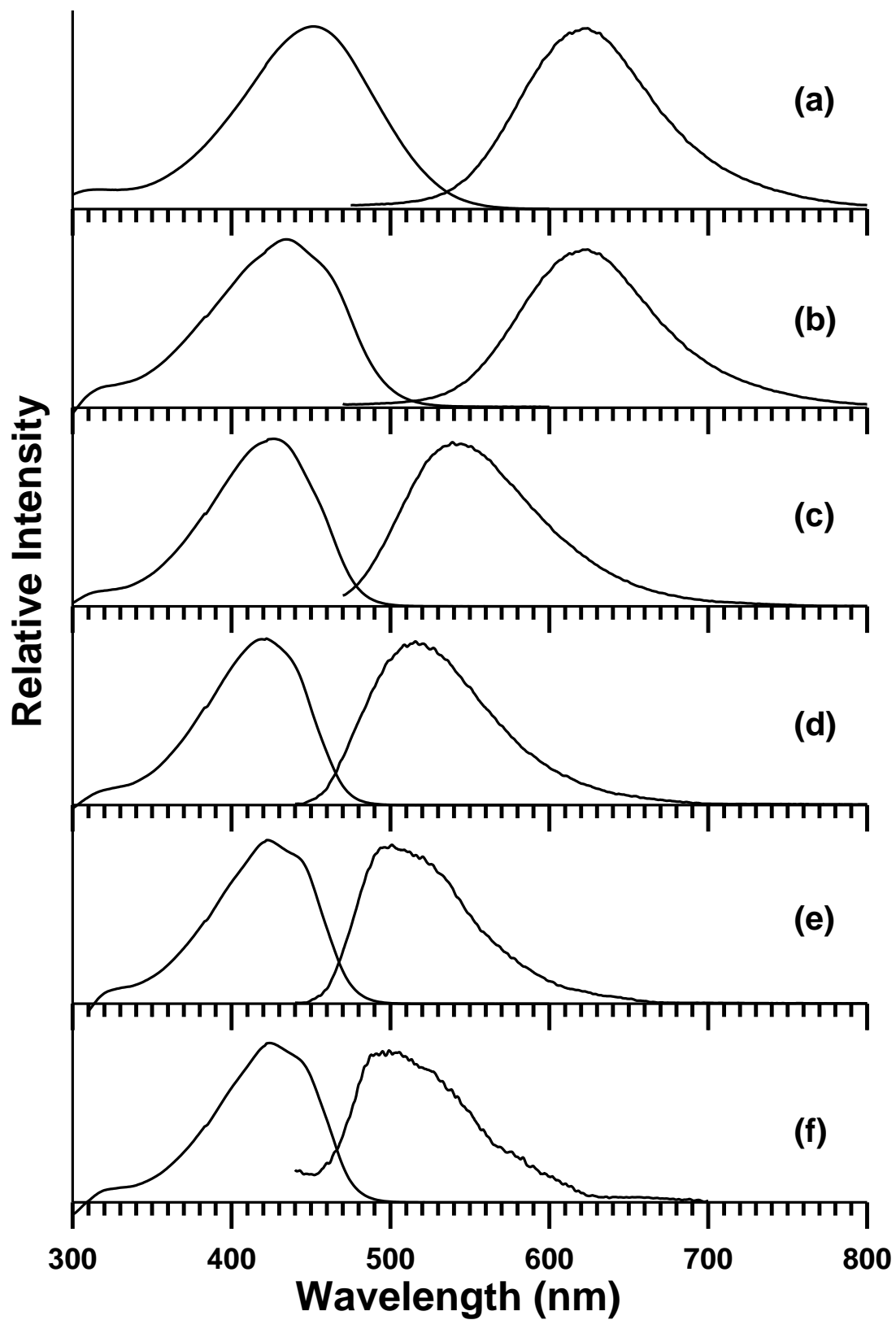
Figure 89. Absorption and fluorescence emission spectra of 2dbmxcp in (a) 2,2,2-trifluoroethanol, (b) 2-propanol, (c) acetonitrile, (d) ethyl acetate, (e) benzene, and (f) toluene.
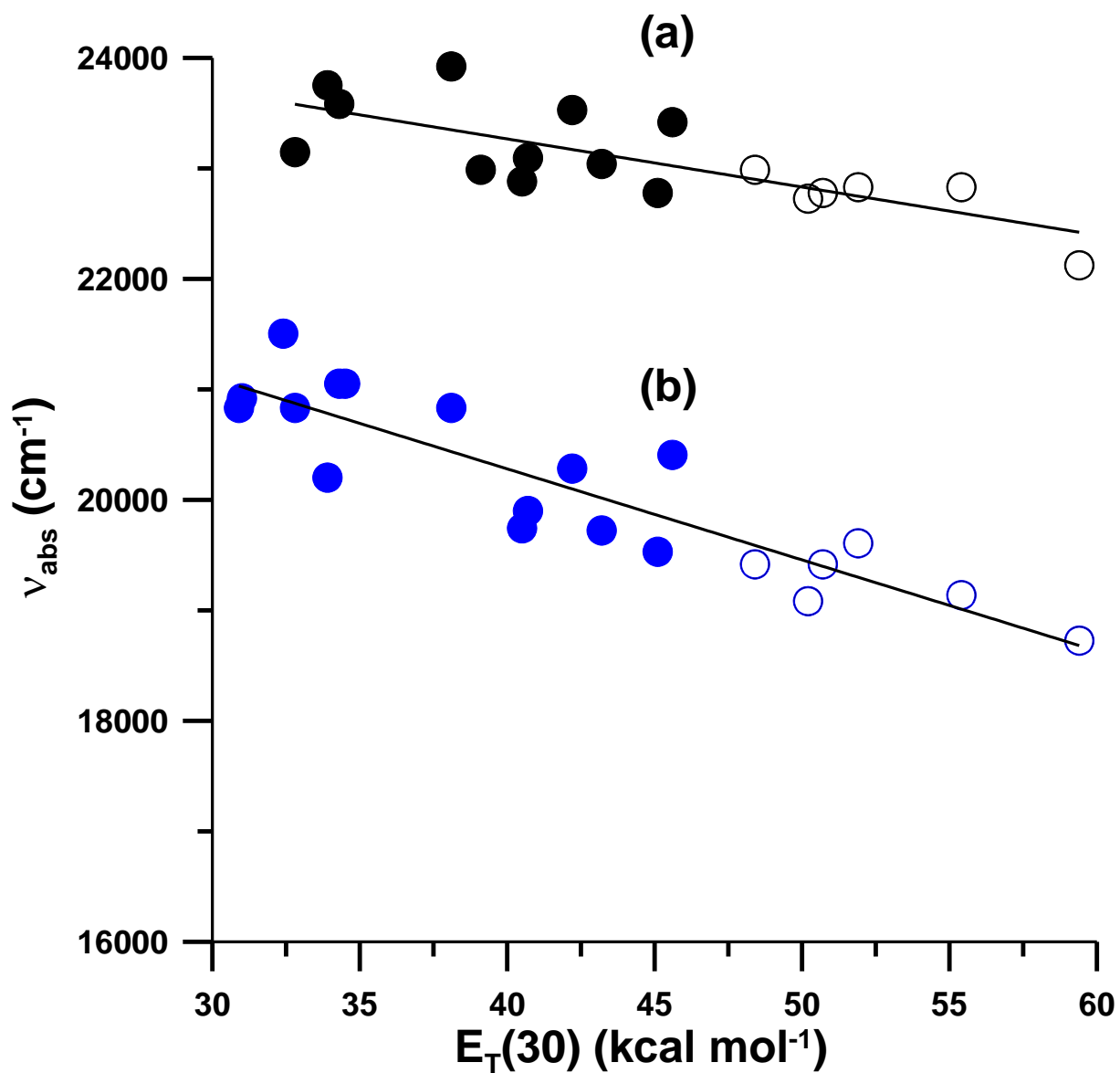
Figure 90. Plot of absorption spectral maxima of (a) 2dbmxcp and (b) bis-dmac in various solvents against the $E_T(30)$ scale. Solid symbols represent aprotic solvents; open symbols represent protic solvents.
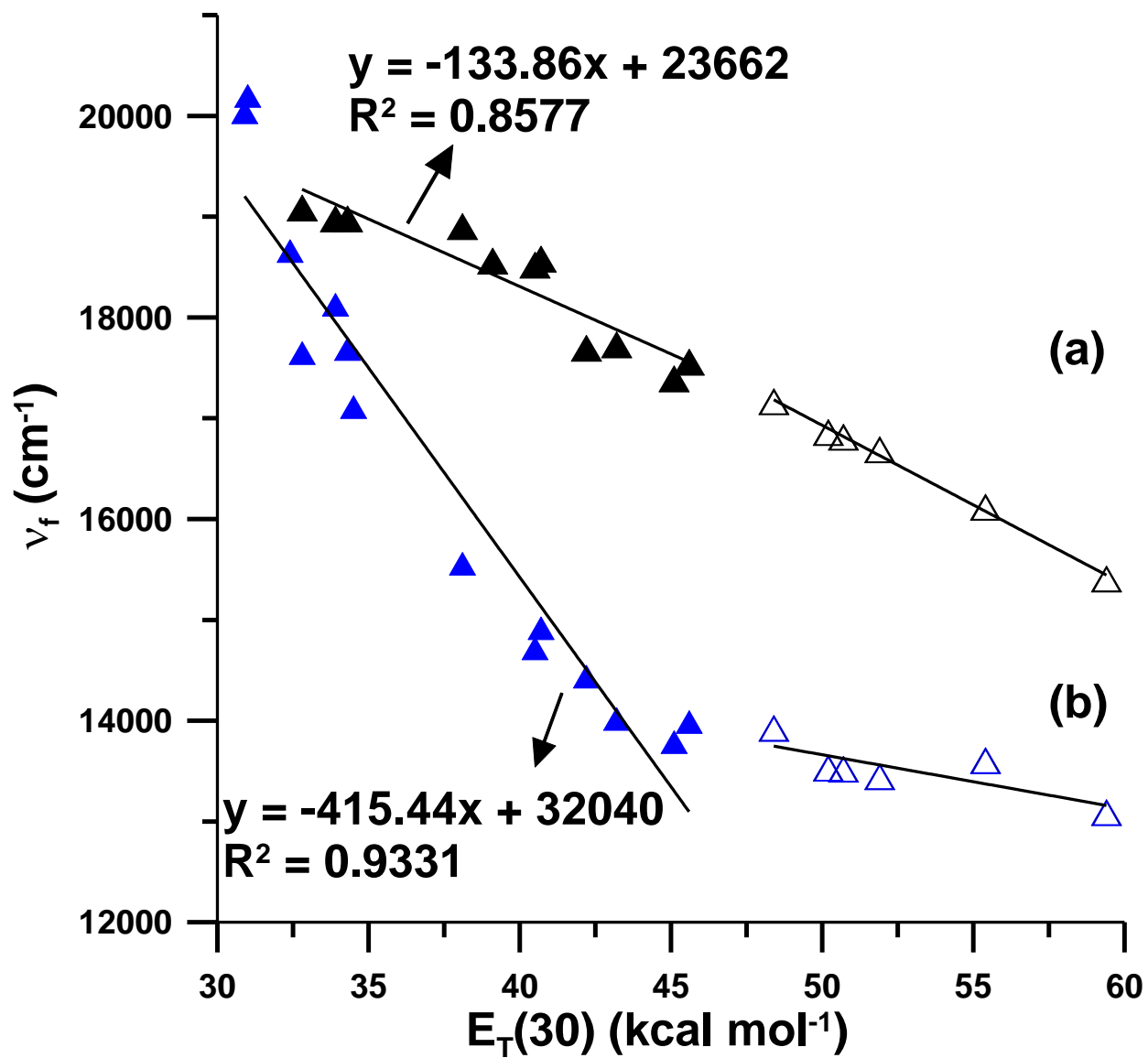
Figure 91. Plot of fluorescence spectral maxima of (a) 2dbmxcp and (b) bis-dmac in various

solvents against the $E_T(30)$ scale. Solid symbols represent aprotic solvents; open symbols

represent protic solvents.

Further studies of the charge transfer behavior of 2dbmxcp involved calculating the electronic dipole moment in the excited state via the Lippert-Mataga method and comparing it to that of its dimethylamino analogue. Figure 92 shows the Lippert-Mataga plot for 2dbmxcp. By DFT B3LYP/6-31G(d), the ground state dipole moment and the Onsager cavity radius of 2dbmxcp are calculated as 2.04 D and 5.86 Å, respectively. The excited state dipole moment is found to be 10.6 D ($\Delta\mu$ = 8.6 D), excluding data for protic solvents. As mentioned earlier, the excited state dipole moment of bis-dmac is calculated to be 21.0 D ($\Delta\mu$ = 15.2 D). The ~2-fold enhancement in both μ_{exc} and $\Delta\mu$ for bis-dmac implies that the electron distribution is internally transferred to a larger degree for bis-dmac than 2dbmxcp in going from the ground state to the excited singlet state, thereby supporting its higher internal charge transfer nature compared to that for 2dbmxcp.
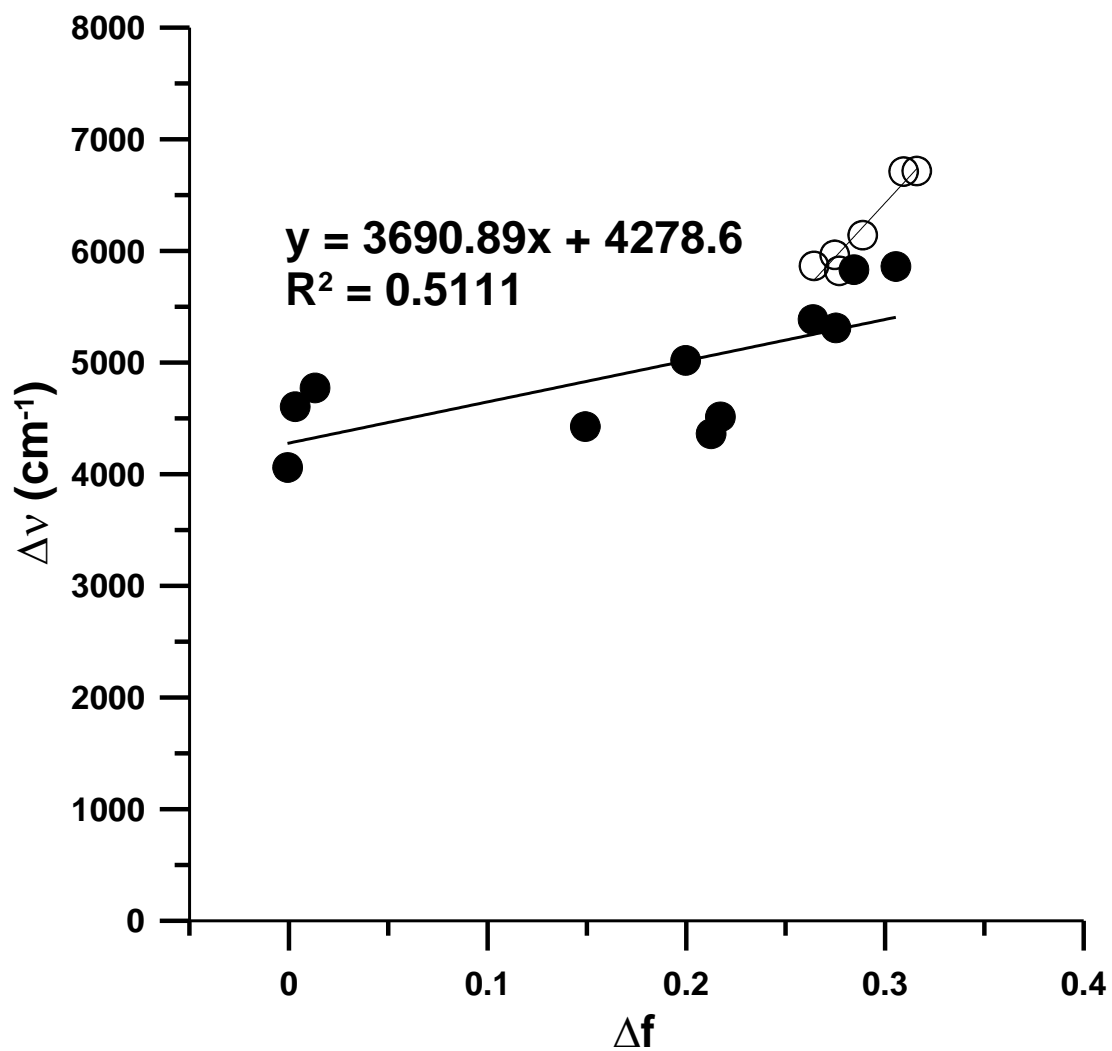
Figure 92. Lippert-Mataga plot of 2dbmxcp in various solvents. Solid symbols represent aprotic

solvents; open symbols represent protic solvents.

Further quantitative support for the higher degree of internal charge transfer for bis-dmac compared to 2dbmxcp involved calculating partial charges of atoms both in the ground state and in the singly excited (π, π^*) state for both molecules at the MOSF semi-empirical level of theory [62]. MOSF calculated values are presented in Tables 48 (2dbmxcp) and 49 (bis-dmac). Under assumed C_{2v} symmetry, the atomic charges for one half of each molecule are presented and included beneath each table are the optimized DFT geometries, with the appropriate atom labels, for direct comparison. Atoms are arranged from electron donating (outer) end to electron withdrawing (central) end.

A positive change in atomic charge implies that an atom loses electronic charge in going from S_0 to the $^1(\pi, \pi^*)$ state, whereas for a negative change, a gain of electronic charge is found on the atom of interest. The general trend seen for both compounds is that atoms on the electron donor end of the molecules become more positive in charge, whereas atoms closer to the carbonyl group become more negative in charge (in going from S_0 to $^1(\pi, \pi^*)$). This means that electron density along the π-conjugated framework becomes greater closer to the carbonyl center, demonstrating the occurrence of electronic charge transfer in both compounds. In comparing the partial charge differences between the tertiary nitrogen atom (N_{19}) of bis-dmac and the methoxy oxygen atom (O_{19}) of 2dbmxcp, the magnitude of N_{19} is ~4.2 times larger than that of O_{19}, implying a larger loss of electron density on the nitrogen atom. In addition, the ΔQ values of the C_{14}, C_{12}, C_{16}, C_{10}, C_9, C_8, and C_4 atoms are more negative in bis-dmac than the corresponding carbon atoms in 2dbmxcp. Both the larger ΔQ value of N and smaller ΔQ values of the specified conjugated carbon atoms of bis-dmac imply a higher degree of internal charge transfer character.

239

Furthermore, calculation of the sums of (i) atomic charge differences and (ii) atomic charges in the $^1(\pi, \pi^*)$ state for atoms belonging to the electron donating phenyl moieties provides further insight into the internal charge transfer natures of these two compounds. For 2dbmxcp, the sums were calculated to be 0.0964 ($\Sigma\Delta Q$) and 0.127 ($\Sigma Q^1(\pi, \pi^*)$). For bis-dmac, the sums were found to be 0.166 ($\Sigma\Delta Q$) and 0.211 ($\Sigma Q^1(\pi, \pi^*)$). The larger sums calculated for bis-dmac suggest a larger loss of electron charge in the dimethylamino phenyl moiety from S_0 to $^1(\pi, \pi^*)$, which provides additional support on the higher degree of ICT character seen for bis-dmac.

Table 48. MOSF calculated atomic charges of 2dbmxcp both in S_0 and $^1(\pi, \pi^*)$ states along with their differences.

Atom	$Q(S_0)$	$Q(^1(\pi, \pi^*))$	ΔQ
C_{20}	0.112	0.112	0.00011
H_{21}	0.0246	0.0248	0.00023
H_{22}	0.0197	0.0198	0.00007
H_{23}	0.0246	0.0248	0.00023
O_{19}	-0.307	-0.292	0.0154
C_{12}	-0.0145	-0.0139	0.0006
C_{13}	-0.0316	-0.0181	0.0135
C_{14}	0.162	0.179	0.0175
C_{15}	-0.0409	-0.0312	0.0097
C_{16}	-0.0169	-0.0098	0.0071
C_{11}	-0.0010	0.0310	0.0319
H_{17}	0.0225	0.0225	0.00000
H_{18}	0.0264	0.0264	0.00001
H_{24}	0.0285	0.0285	0.00001
H_{25}	0.0230	0.0230	0.00000
C_{10}	-0.0045	-0.0302	-0.0257
H_{26}	0.0256	0.0256	0.00000
C_9	-0.0380	-0.0020	0.0360
H_{27}	0.0268	0.0268	-0.00001
C_8	0.0168	-0.0408	-0.0576
H_{28}	0.0421	0.0421	-0.00001
C_4	-0.0172	0.0168	0.0340
C_3	0.320	0.213	-0.107
O_{29}	-0.547	-0.621	-0.0740
C_5	-0.0028	0.00019	0.0030
H_6	0.019	0.0223	0.0033
H_7	0.0148	0.0158	0.0010
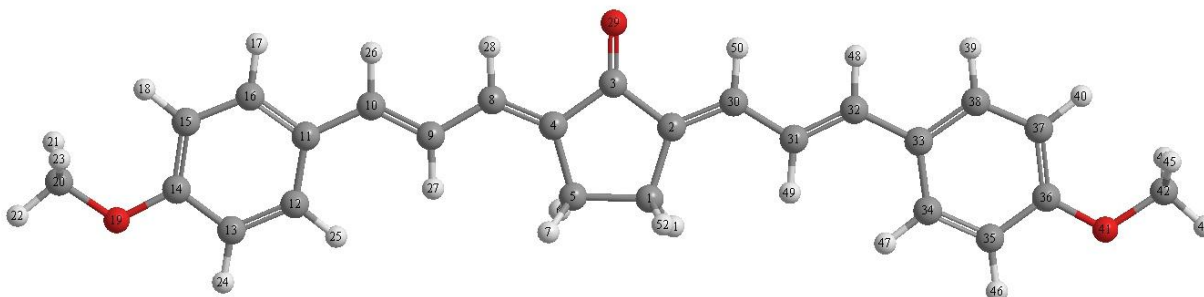
Table 49. MOSF calculated atomic charges of bis-dmac both in S_0 and $^1(\pi, \pi^*)$ states along with their differences.

Atom	$Q(S_0)$	$Q(^1(\pi, \pi^*))$	ΔQ
N_{19}	-0.203	-0.138	0.0653
C_{20}	0.0621	0.0628	0.00068
C_{24}	0.0622	0.0629	0.00067
H_{21}	0.0179	0.0191	0.0012
H_{22}	0.0176	0.0192	0.0016
H_{23}	0.0114	0.0114	0.00005
H_{25}	0.0176	0.0188	0.0012
H_{26}	0.0115	0.0115	0.00004
H_{27}	0.0173	0.0189	0.0016
C_{12}	-0.0125	-0.0175	-0.0050
C_{13}	-0.0635	-0.0384	0.0251
C_{14}	0.117	0.125	0.0076
C_{15}	-0.0634	-0.0394	0.0240
C_{16}	-0.0124	-0.0156	-0.0032
C_{11}	-0.0146	0.0300	0.0446
H_{17}	0.0201	0.0201	0.00001
H_{18}	0.0209	0.0209	0.00003
H_{28}	0.0198	0.0198	0.00001
H_{29}	0.0198	0.0198	0.00001
C_{10}	-0.0012	-0.0507	-0.0496
H_{30}	0.0248	0.0248	0.00000
C_9	-0.0454	-0.0181	0.0273
H_{31}	0.0250	0.0250	0.00000
C_8	0.0178	-0.0522	-0.0700
H_{32}	0.0416	0.0416	-0.00001
C_4	-0.0212	-0.0084	0.0128
C_3	0.319	0.215	-0.105
O_{33}	-0.551	-0.625	-0.0737
C_5	-0.0034	-0.0014	0.0020
H_6	0.0178	0.0198	0.0020
H_7	0.0141	0.0146	0.00053

242
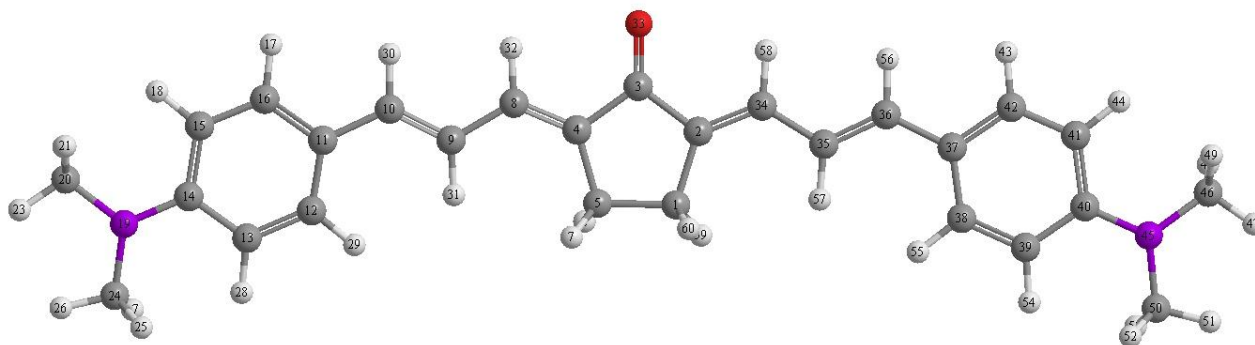
Experimental findings for both the fluorescence quantum yields and fluorescence lifetimes show a solvent dependence for 2dbmxcp (Table 50). Fluorescence quantum yields of 2dbmxcp range from 0.003 (in carbon disulfide) to 0.16 (in n-butanol) and lifetimes vary from 0.2 ns (in ethyl acetate and carbon disulfide) to 0.72 ns (in 1-propanol). Interestingly, 2dbmxcp, unlike bis-dmac, had the largest quantum yields and lifetime values in the alcohols out of the entire set of solvents.

Fluorescence quantum yields have been plotted against the maximum fluorescence energies in all solvents studied, as shown in Figure 93. This plot can be partitioned into two regions: region 1 (protic solvents): from $v_f = 17,166$ cm^{-1} (2-PrOH, $\Phi_f = 0.14$) to $v_f = 15,407$ cm^{-1} (TFE, $\Phi_f = 0.11$); region 2 (aprotic solvents): from $v_f = 19,087$ cm^{-1} (CS$_2$, $\Phi_f = 0.003$) to $v_f = 17,392$ cm^{-1} (DMSO, $\Phi_f = 0.13$). In region 2, Φ_f is found to increase as the S_0-S_1 energy gap decreases, attributing this to the decreasing rate of intersystem crossing, as was previously seen with Asdimcy1, bis-dmab, bis-dmac, and bis-juldmac. In region 1, Φ_f essentially remains level at high values. In region 1 for bis-dmac (Figure 66), Φ_f dropped in more polar solvents, particularly in alcohols, but this trend does not hold for 2dbmxcp.

The k_{nr} values of 2dbmxcp have been plotted against v_f in various solvents, shown in Figure 94. This plot is also separated into two regions: region 1 (protic solvents): $v_f = 17,166$ cm^{-1} (2-PrOH, $k_{nr} = 1.28 \times 10^9$ s^{-1}) to $v_f = 15,407$ cm^{-1} (TFE, $k_{nr} = 1.71 \times 10^9$ s^{-1}); region 2 (aprotic solvents): $v_f = 19,087$ cm^{-1} (CS$_2$, $k_{nr} = 4.99 \times 10^9$ s^{-1}) to $v_f = 17,392$ cm^{-1} (DMSO, $k_{nr} = 1.78 \times 10^9$ s^{-1}). In region 2, the k_{nr} value decreases with respect to a decrease in v_f, consistent with less efficient intersystem crossing, as discussed for Asdimcy1 (section 4.1.4) and

the alkylamino substituted 2,5-diarylidene cyclopentanones (section 4.2.3). A smaller change in k_{nr} is observed in region 1.

The higher Φ_f and smaller k_{nr} values observed for 2dbmxcp in region 1 are attributed to the larger S_0-S_1 energy gaps in protic solvents, contrary to the observations for bis-dmab and bis-dmac in the same region. As seen in Figures 95 and 96, direct comparison of the Φ_f and k_{nr} values for 2dbmxcp to those of bis-dmab and bis-dmac in region 1 clearly shows that 2dbmxcp is higher in Φ_f and lower in k_{nr} and have higher energy gaps than in corresponding solvents for bis-dmab and bis-dmac. For instance, the experimental ν_f (along with Φ_f and k_{nr}) values for 2dbmxcp in methanol and ethanol are 16,119 cm^{-1} ($\Phi_f = 0.15$; $k_{nr} = 1.60 \times 10^9$ s^{-1}) and 16,689 cm^{-1} ($\Phi_f = 0.15$; $k_{nr} = 1.20 \times 10^9$ s^{-1}). In the same order, the corresponding values for bis-dmab are 15,758 cm^{-1} ($\Phi_f = 0.025$; $k_{nr} = 3.36 \times 10^9$ s^{-1}) and 16,307 cm^{-1} ($\Phi_f = 0.11$; $k_{nr} = 2.62 \times 10^9$ s^{-1}) and those for bis-dmac are 13,605 cm^{-1} ($\Phi_f = 0.022$; $k_{nr} = 4.66 \times 10^9$ s^{-1}) and 13,445 cm^{-1} ($\Phi_f = 0.076$; $k_{nr} = 3.85 \times 10^9$ s^{-1}). Furthermore, the $\ln k_{nr}$ values for these three compounds have been plotted against ν_f (see Figure 96(b)). Steeper slopes are seen for both bis-dmac and bis-dmab than for 2dbmxcp, suggesting that the energy gap law for internal conversion is greater for both alkylamino compounds than for 2dbmxcp.

In addition to the energy gap law argument, according to research conducted by Morimoito, *et al.* [68], fluorescence of an excited state molecule with a smaller degree of internal charge transfer cannot be quenched efficiently by an alcohol because of weak hydrogen bonding interaction on the carbonyl oxygen atom, which is also consistent with the results reported here for 2dbmxcp. In their studies, the photophysical properties for three classes of electron donor-acceptor polyenes and fluorescence quenching of these molecules by ethanol were investigated.

The three classes of compounds were (i) 9,10-aminoanthraquinones and 9-fluorenones,

(ii) aminophthalimides, and (iii) aminocoumarins. Greater fluorescence quenching was found for

the class (i) and (ii) compounds, but hardly any quenching for the class (iii) compounds, in the

presence of ethanol as the quencher. It was argued in their studies that a probable answer as to

why the excited states of the class (i) and (ii) compounds behaved differently than class (iii) is

the local charge density on the carbonyl oxygen atom within the molecule. It was found that the

transferred negative charge was specifically localized on the carbonyl oxygen atoms for both

class (i) and (ii) compounds, whereas substantial delocalization of electronic charge over the

entire molecule was observed for the class (iii) compounds.

These differences in the localization and delocalization of charge can be discussed within

the hard-soft acid-base (HSAB) theory [69]. According to the HSAB theory, a hard base such as

an alkylamine or hydroxide ion has its negative charge localized on a specific atom of high

electronegativity, whereas benzene is a common soft base, in which electrons are delocalized

over the entire conjugated system. The hydroxyl hydrogen atom of the quencher alcohol is protic

and is hence classified as a "hard cation".

From their studies, Morimoito, *et al.* were able to conclude that because electron charge

is localized specifically on the carbonyl oxygen atoms in the excited states of both class (i) and

class (ii) molecules, these two classes of molecules are classified as hard anions. The larger

electron charge on the carbonyl oxygen atoms implies stronger hydrogen bonding interaction

with the hydroxyl hydrogen atom ("hard cation") of ethanol, explaining the observed

fluorescence quenching of these compounds. The absence of fluorescence quenching for the

excited state molecules of class (iii) compounds by ethanol is attributed to the soft anion

properties of this class, in that electron charge is not explicitly localized on the carbonyl oxygen

atom, but rather delocalized over the entire molecule. The excited state molecule of bis-dmac can be classified as a 'harder anion' than that for 2dbmxcp due to its higher degree of internal charge transfer upon photon absorption, which can thereby strengthen hydrogen bonding interaction between the carbonyl oxygen atom and the alcohol, giving rise to efficient fluorescence quenching.

Table 50. Photophysical properties of 2dbmxcp in various solvents.

	Solvent	Φ_f	τ_f (ns)	k_f (s^{-1})	k_{nr} (s^{-1})
1	Trifluoroethanol	0.11	0.52	2.12×10^8	1.71×10^9
2	Methanol	0.15	0.53	2.83×10^8	1.60×10^9
3	Ethanol	0.15	0.71	2.11×10^8	1.20×10^9
4	1-Propanol	0.15	0.72	2.08×10^8	1.18×10^9
5	1-Butanol	0.16	0.62	2.58×10^8	1.35×10^9
6	2-Propanol	0.14	0.67	2.09×10^8	1.28×10^9
7	Acetonitrile	0.07	0.49	1.43×10^8	1.90×10^9
8	Dimethyl sulfoxide	0.13	0.49	2.65×10^8	1.78×10^9
9	Dimethylformamide	0.07	0.57	1.23×10^8	1.63×10^9
10	Acetone	0.04	0.46	8.70×10^7	2.09×10^9
11	Dichloromethane	0.10	0.49	2.04×10^8	1.84×10^9
12	Pyridine	0.07	0.42	1.67×10^8	2.21×10^9
13	Chloroform	0.15	0.53	2.83×10^8	1.60×10^9
14	Ethyl acetate	0.004	0.2	2.00×10^7	4.98×10^9
15	Benzene	0.005	0.39	1.28×10^7	2.55×10^9
16	Toluene	0.004	0.27	1.48×10^7	3.69×10^9
17	Carbon disulfide	0.003	0.2	1.50×10^7	4.99×10^9
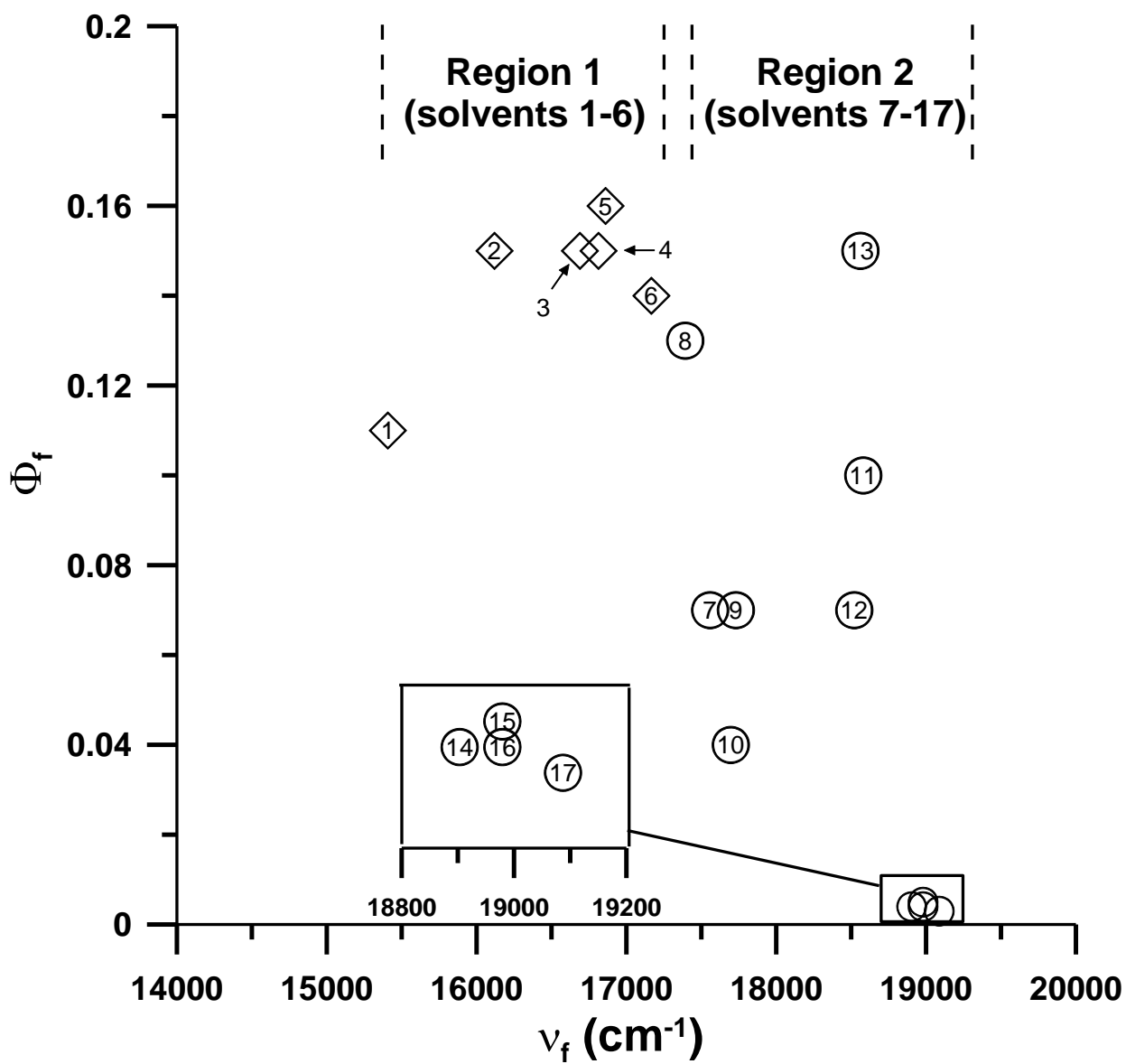
Figure 93. Fluorescence quantum yields (Φ_f) plotted against the fluorescence spectral maxima of 2dbmxcp in various solvents. Circles represent aprotic solvents; diamonds represent protic solvents.
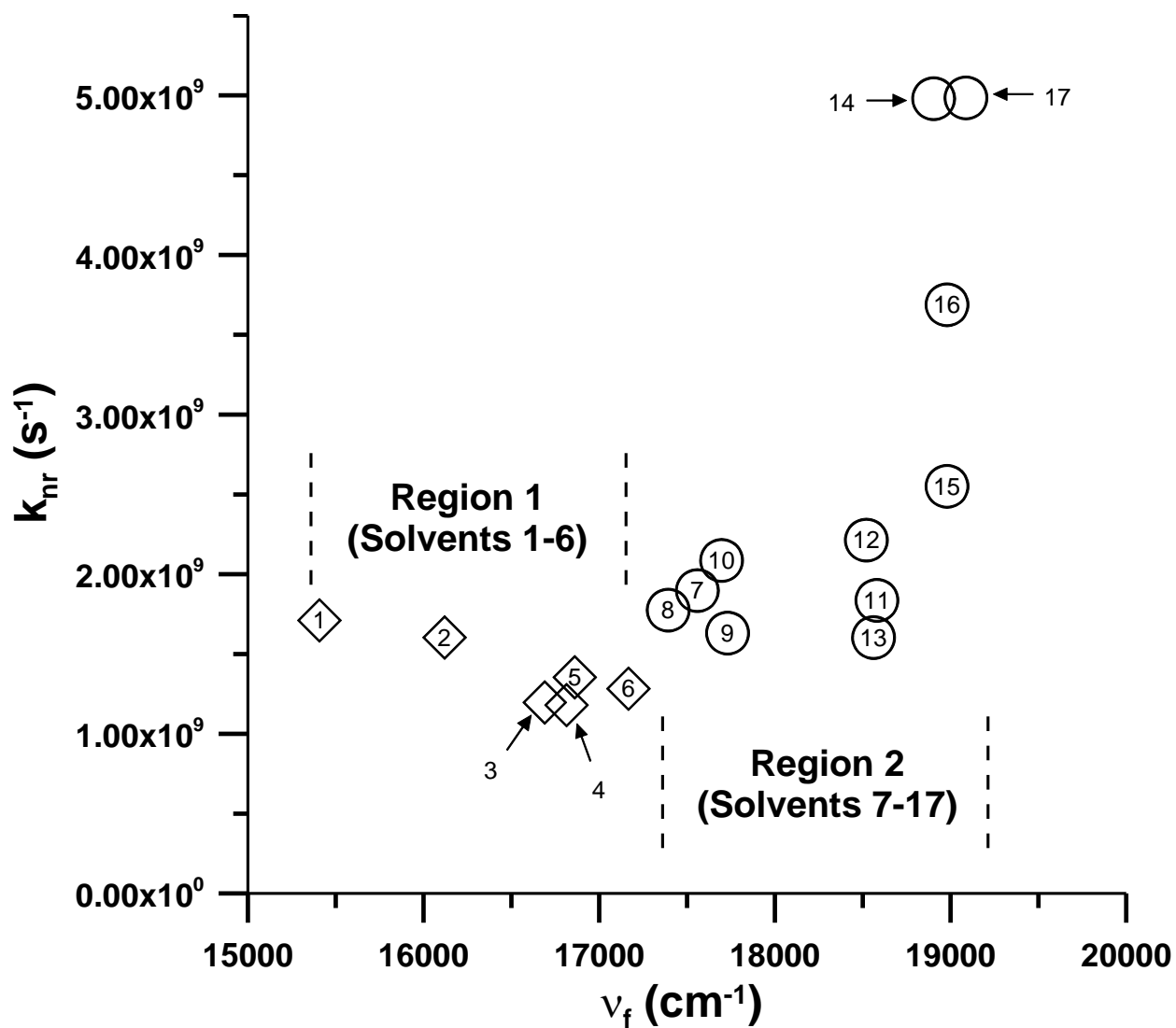
Figure 94. Nonradiative decay constants (k_{nr}) plotted against the fluorescence spectral maxima of 2dbmxcp in various solvents. Circles represent aprotic solvents; diamonds represent protic solvents.
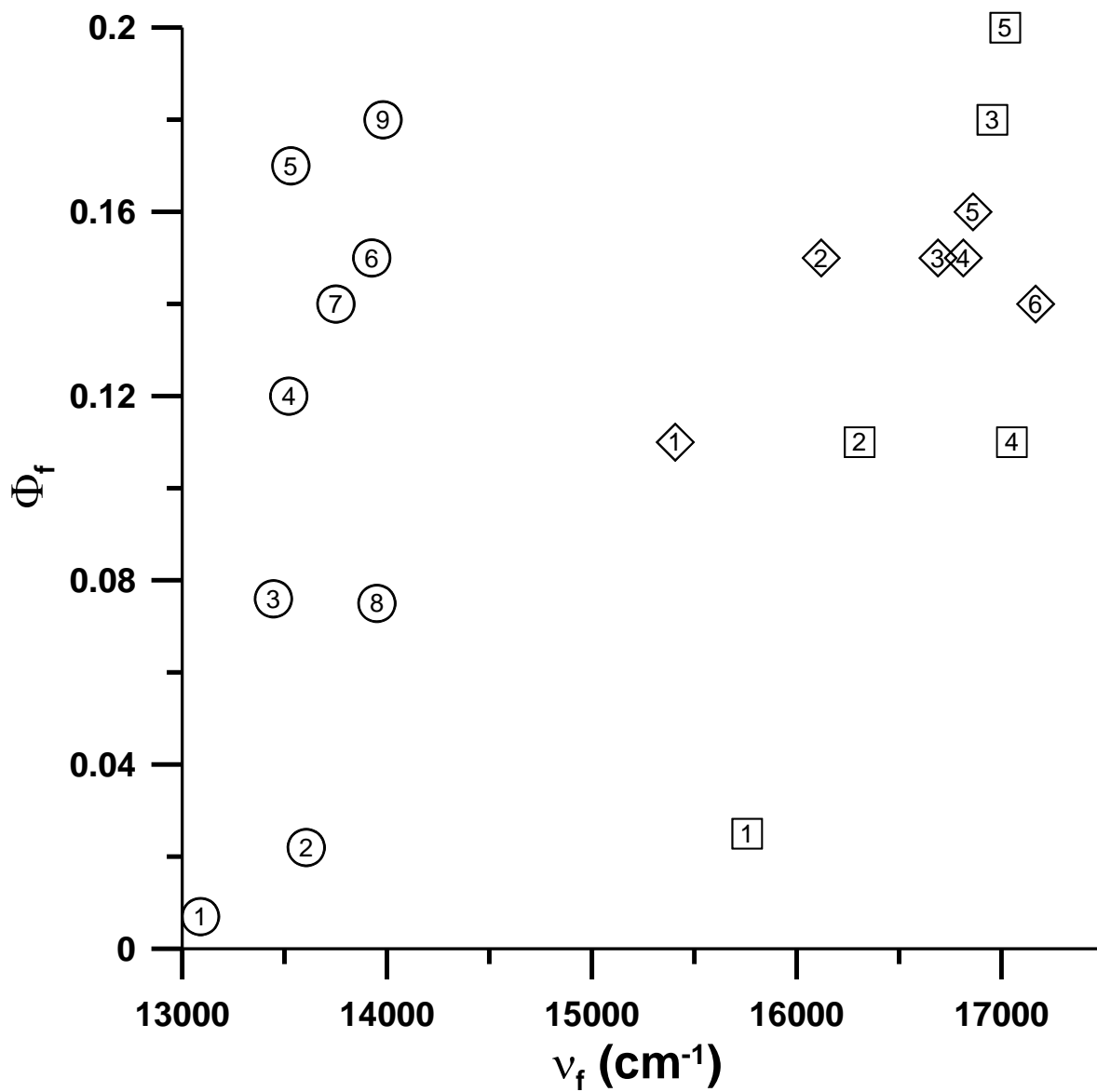
Figure 95. Plot of Φ_f of 2dbmxcp (unfilled diamonds), bis-dmac (unfilled circles), and bis-dmab (unfilled squares) against ν_f for region 1 solvents. Solvents are numbered accordingly as presented in Tables 50 (2dbmxcp), 29 (bis-dmac), and 37 (bis-dmab).
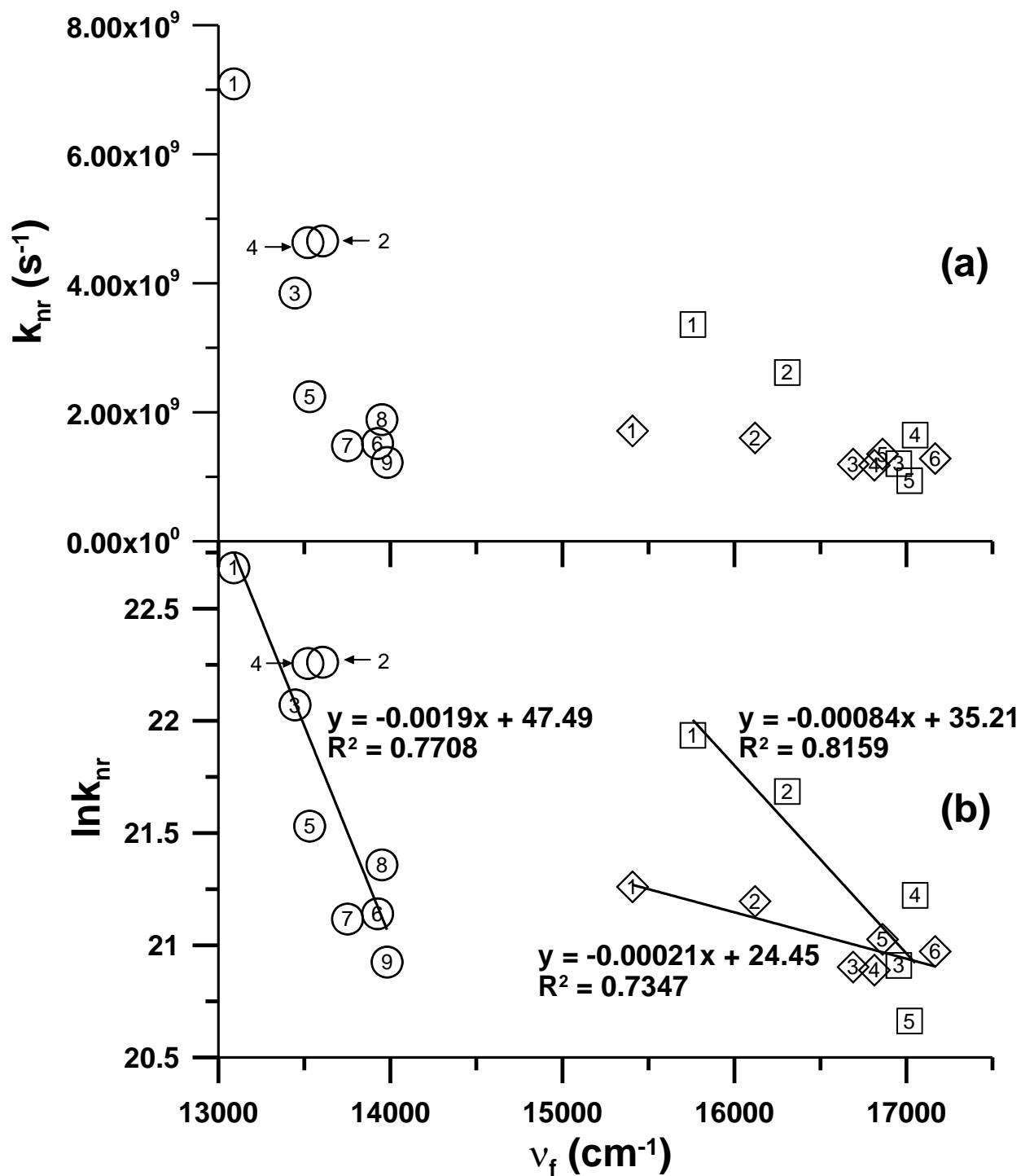
Figure 96. Plots of (a) k_{nr} and (b) $\ln k_{nr}$ of 2dbmxcp (unfilled diamonds), bis-dmac (unfilled circles), and bis-dmab (unfilled squares) against ν_f for region 1 solvents. Solvents are numbered accordingly as presented in Tables 50 (2dbmxcp), 29 (bis-dmac), and 37 (bis-dmab).

4.3.3   Structural and Spectroscopic Properties of Asunsub

Asunsub crystallizes in a monoclinic system, belonging to the C2/c space group. The crystallographic data and refinement parameters of Asunsub are presented in Table 51. The X-ray crystal structure of Asunsub, from two views, is shown in Figure 97 and tabulated data, directly compared to its predicted DFT gas phase geometry, is presented in Table 52. As shown from the X-ray crystal structure, a higher degree of phenyl ring torsion is seen on the benzylidene end ($35.0°$) than on the more conjugated cinnamylidene end of the molecule ($\sim13°$). An overall dihedral angle of $\sim53°$ from the phenyl ring on one end of the molecule to the phenyl ring of the other end is seen.

Direct comparison between the geometry of Asunsub in the crystalline state and its predicted gas phase geometry at the DFT B3LYP/6-31G(d) level of theory shows nearly no differences in the bond lengths and bond angles. The absolute differences between experimental and calculated bond lengths varied 0.001 Å $– 0.023$ Å and bond angles varying between $0.01° – 3.5°$. The much higher twisting conformation of the phenyl rings seen in the experimental X-ray structure differs from the predicted DFT geometry. A nearly planar geometry is seen in the DFT structure ($\sim10°$ rotation of the phenyl rings on each end relative to the cyclopentanone ring).

The larger twisting conformation of the phenyl ring on the less conjugated benzylidene end of the molecule is likely influenced not only by the molecular structure and energy, but also by the molecular packing arrangement in the single crystal. Figure 98 shows the unit cell packing arrangement of Asunsub in wireframe style and as seen, the total occupancy number of molecules per unit cell was calculated to be eight. Noteworthy to consider is that in the electron cloud arrangement of the unit cell (see Figure 99), the phenyl group on the lesser conjugated end

of the molecule may twist to allow C-H…π interactions to occur between the C-H protons and the π electron cloud of neighboring aromatic rings. This type of intermolecular interaction is energetically favorable and is commonly observed when aromatic ring systems pack in the solid crystalline state. For instance, Marjani, *et al.* [70] have solved the crystal structure of N-(2-pyridylmethylene)benzene-1,4-diamine, an aza-conjugated compound, and have measured, from their studies, a ~25° out-of-plane rotation of the p-aminophenyl moiety and observed a C-H…π stacking interaction among adjacent molecules. Another observation to consider when comparing the experimental structure to its predicted DFT structure is that the aromatic ring may twist out of the plane to a higher degree more in the crystalline state than in the gas phase to better allow more efficient packing of the molecules.

Table 51. Crystallographic data and refinement parameters of Asunsub.

Crystal Form	
Formula	$C_{21}H_{18}O$
Formula weight (g mol^{-1})	286.35
Crystal system	monoclinic
Space group	C2/c
Color and habit	Yellow, needles
Crystal size	0.15 mm × 0.20 mm × 1.00 mm
a (Å)	33.4281(10)
b (Å)	11.9668(4)
c (Å)	7.8031(2)
α (deg)	90.00
β (deg)	92.785(2)
γ (deg)	90.00
Volume (Å^3)	3117.77(16)
Z	8
λ (Å)	0.71073
ρ_{calc} (g cm^{-3})	1.220
Temperature (K)	296(2)
F(000)	1216
θ range for data collection (deg)	1.22 − 28.30
Ranges of Miller Indices	$-44 \leq h \leq 44$ $-15 \leq k \leq 15$ $-10 \leq l \leq 9$
Absorption coefficient (mm^{-1})	0.073
Reflections collected	23582
Independent reflections	3876 [R_{int} = 0.0275]
Reflections [I > 2σ(I)]	2519
Data/restraints/parameters	3876/0/200
Goodness of fit on F^2	1.023
R (all data)	R_1 = 0.0414 wR_2 = 0.1112
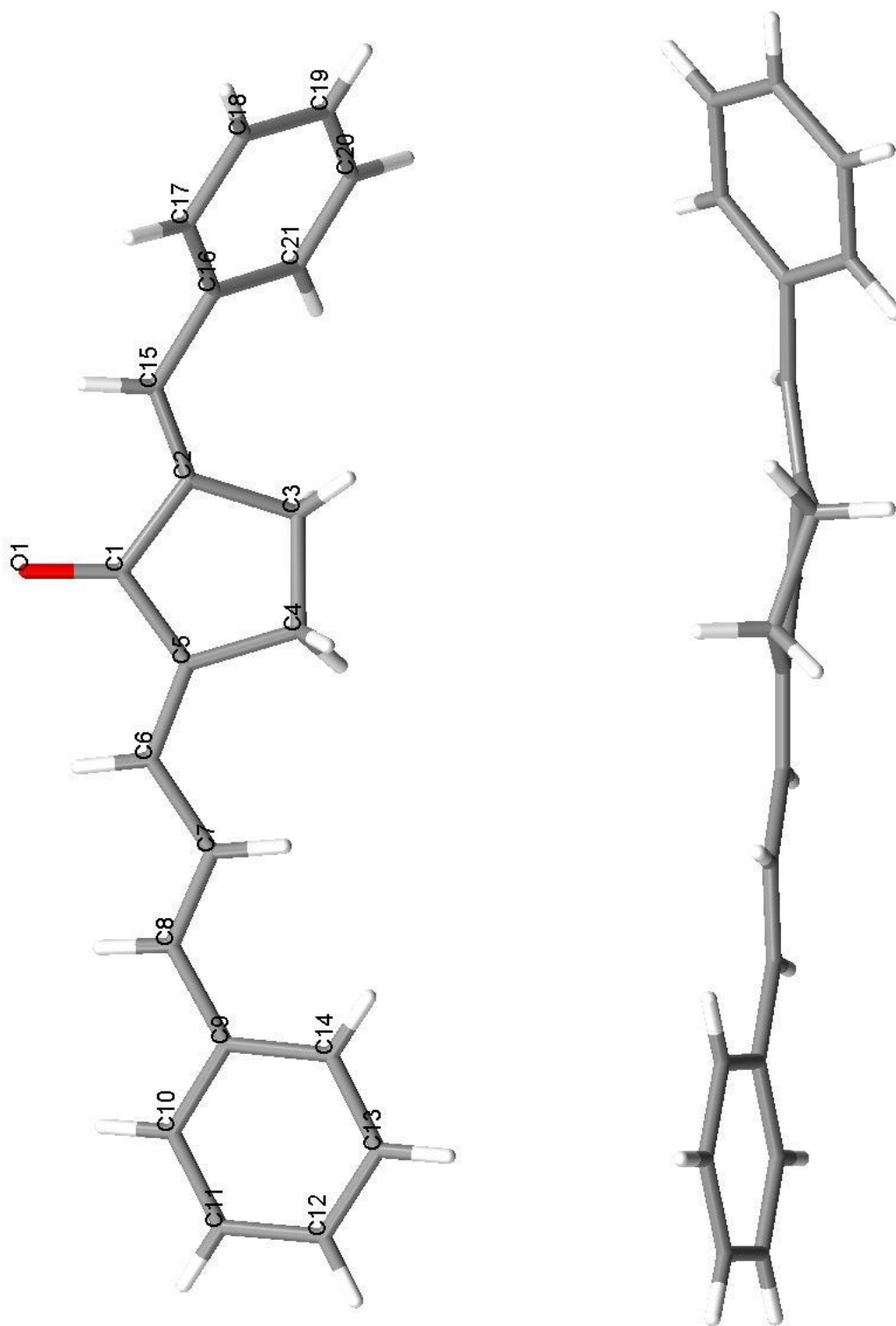
Figure 97. Single crystal X-ray structure of Asunsub.

Table 52. Single crystal geometry of Asunsub by X-ray diffractometry and its predicted gas phase geometry at the DFT B3LYP/6-31G(d) level of theory. Δ = X-ray-DFT

Bond Lengths (Å)			
	X-ray	DFT	Δ
C_1-C_2	1.490(2)	1.493	-0.003
C_1-C_5	1.478(2)	1.484	-0.006
C_1-O_1	1.225(2)	1.227	-0.002
C_2-C_3	1.504(2)	1.512	-0.008
C_2-C_{15}	1.336(2)	1.351	-0.015
C_3-C_4	1.541(2)	1.560	-0.019
C_4-C_5	1.503(2)	1.510	-0.007
C_5-C_6	1.336(2)	1.354	-0.018
C_6-C_7	1.440(2)	1.439	0.001
C_7-C_8	1.333(2)	1.356	-0.023
C_8-C_9	1.463(2)	1.460	0.003
C_9-C_{10}	1.388(2)	1.409	-0.021
C_9-C_{14}	1.395(2)	1.410	-0.015
C_{10}-C_{11}	1.383(2)	1.393	-0.010
C_{11}-C_{12}	1.374(3)	1.396	-0.022
C_{12}-C_{13}	1.376(2)	1.399	-0.023
C_{13}-C_{14}	1.378(2)	1.390	-0.012
C_{15}-C_{16}	1.464(2)	1.460	0.004
C_{16}-C_{17}	1.397(2)	1.411	-0.014
C_{16}-C_{21}	1.395(2)	1.411	-0.016
C_{17}-C_{18}	1.382(2)	1.391	-0.009
C_{18}-C_{19}	1.379(2)	1.397	-0.018
C_{19}-C_{20}	1.377(2)	1.397	-0.020
C_{20}-C_{21}	1.381(2)	1.393	-0.012

Bond Angles (°)			
	X-ray	DFT	Δ
C_1-C_2-C_3	108.3(1)	109.3	-1.0
C_1-C_2-C_{15}	121.5(1)	119.2	2.3
C_1-C_5-C_4	108.7(1)	109.8	-1.1
C_1-C_5-C_6	123.5(1)	121.1	2.4
C_2-C_1-C_5	107.6(1)	108.8	-1.2
C_2-C_1-O_1	125.8(1)	126.1	-0.3
C_2-C_3-C_4	104.9(1)	106.0	-1.1
C_2-C_{15}-C_{16}	127.7(1)	131.2	-3.5
C_3-C_2-C_{15}	130.0(1)	131.5	-1.5
C_3-C_4-C_5	105.3(1)	105.7	-0.4
C_4-C_5-C_6	127.8(1)	129.1	-1.3
C_5-C_1-O_1	126.6(1)	126.1	0.5
C_5-C_6-C_7	125.6(1)	126.3	-0.7
C_6-C_7-C_8	123.2(1)	122.6	0.6
C_7-C_8-C_9	127.8(1)	127.9	-0.1
C_8-C_9-C_{10}	119.3(1)	118.7	0.6
C_8-C_9-C_{14}	122.8(1)	123.4	-0.6
C_9-C_{10}-C_{11}	121.0(1)	121.3	-0.3
C_9-C_{14}-C_{13}	120.9(1)	120.9	0.05
C_{10}-C_9-C_{14}	117.9(1)	117.9	-0.02
C_{10}-C_{11}-C_{12}	120.2(2)	120.0	0.2
C_{11}-C_{12}-C_{13}	119.8(2)	119.5	0.3
C_{12}-C_{13}-C_{14}	120.3(2)	120.4	-0.1
C_{15}-C_{16}-C_{17}	119.3(1)	117.8	1.5
C_{15}-C_{16}-C_{21}	122.8(1)	124.5	-1.7
C_{16}-C_{17}-C_{18}	120.7(1)	121.4	-0.7
C_{16}-C_{21}-C_{20}	120.9(1)	120.8	0.1
C_{17}-C_{16}-C_{21}	118.0(1)	117.7	0.3
C_{17}-C_{18}-C_{19}	120.3(2)	120.0	0.3
C_{18}-C_{19}-C_{20}	119.7(2)	119.5	0.2
C_{19}-C_{20}-C_{21}	120.3(1)	120.5	-0.2

Dihedral Angles (°)		
	X-ray	DFT
C_1-C_2-C_3-C_4	-20.1	9.9
C_1-C_5-C_4-C_3	-17.5	10.3
C_{21}-C_{16}-C_9-C_{14}	52.8	-15.4
C_4-C_6-C_9-C_{14}	12.9	-1.1
C_3-C_{15}-C_{16}-C_{21}	35.0	-9.7
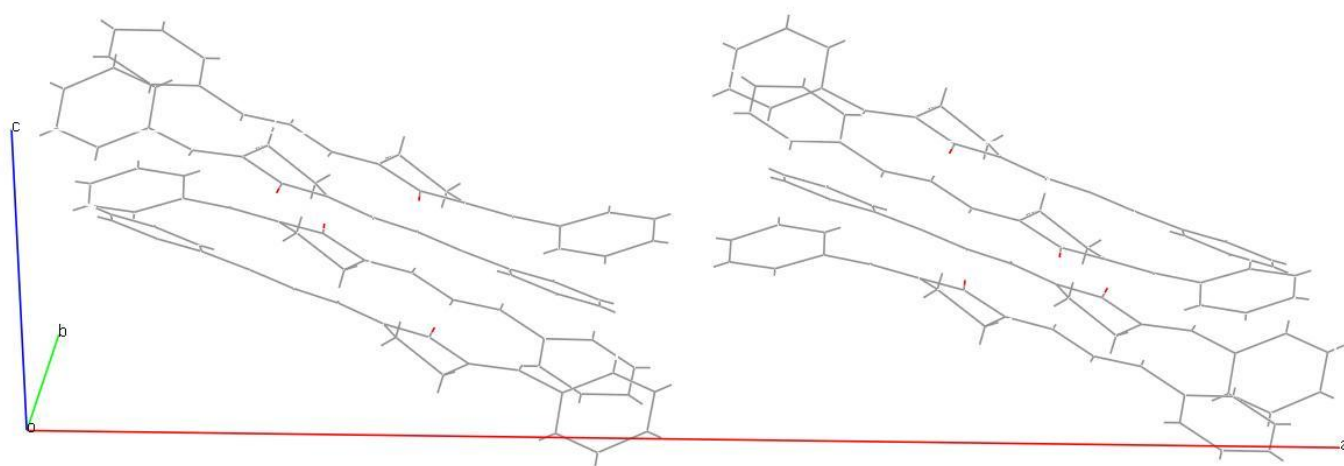
**Figure 98**. Unit cell packing arrangement of Asunsub with wireframe style.
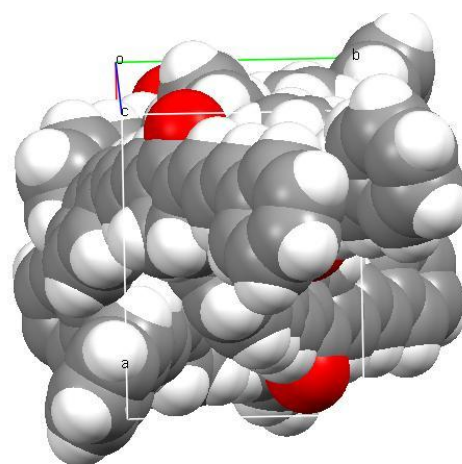
Figure 99. Unit cell packing arrangement of Asunsub with electron cloud spacefill style. Color designations: Gray: carbon; White: hydrogen; Red: oxygen.

Spectroscopic measurements were carried out on Asunsub and it was found that this compound fluoresces only in polar protic solvents (Figure 100). This is attributed to S_1 being (π, π^*) in the protic solvents and (n, π^*) in the aprotic solvents. As previously noted, as solvent polarity increases, (n, π^*) excited states undergo hypsochromic (blue) shifts and (π, π^*) excited states undergo bathochromic (red) shifts. In order to support the argument that S_1 is (n, π^*) in aprotic solvents but (π, π^*) in protic solvents, a series of TD-DFT spectral calculations were carried out both in the gas phase and in solvent (PCM = cyclohexane and ethanol) (Table 53).

The $S_0 \rightarrow S_1$ excitation was predicted by TD-DFT to be a forbidden (n, π^*) state in the gas phase with a calculated transition energy of 23,041 cm^{-1} (λ 434 nm) and an essentially forbidden (n, π^*) state in cyclohexane, with a calculated transition wavelength of 23,585 cm^{-1} (λ 424 nm). Excitation to S_2 is predicted to be a strongly absorbing (π, π^*) state localized at 25,316 cm^{-1} (λ 395 nm) in the gas phase and 24,096 cm^{-1} (λ 415 nm) in cyclohexane, with HOMO $\rightarrow$ LUMO being the major CI configuration.

In ethanol, the $^1(\pi, \pi^*)$ state shifts below that of $^1(n, \pi^*)$, making it the S_1 state, thereby inducing fluorescence, as was experimentally observed. From TD-DFT, calculated transition energies for S_1 and S_2 were 23,810 cm^{-1} (λ 420 nm) and 24,390 cm^{-1} (λ 410 nm) in ethanol.
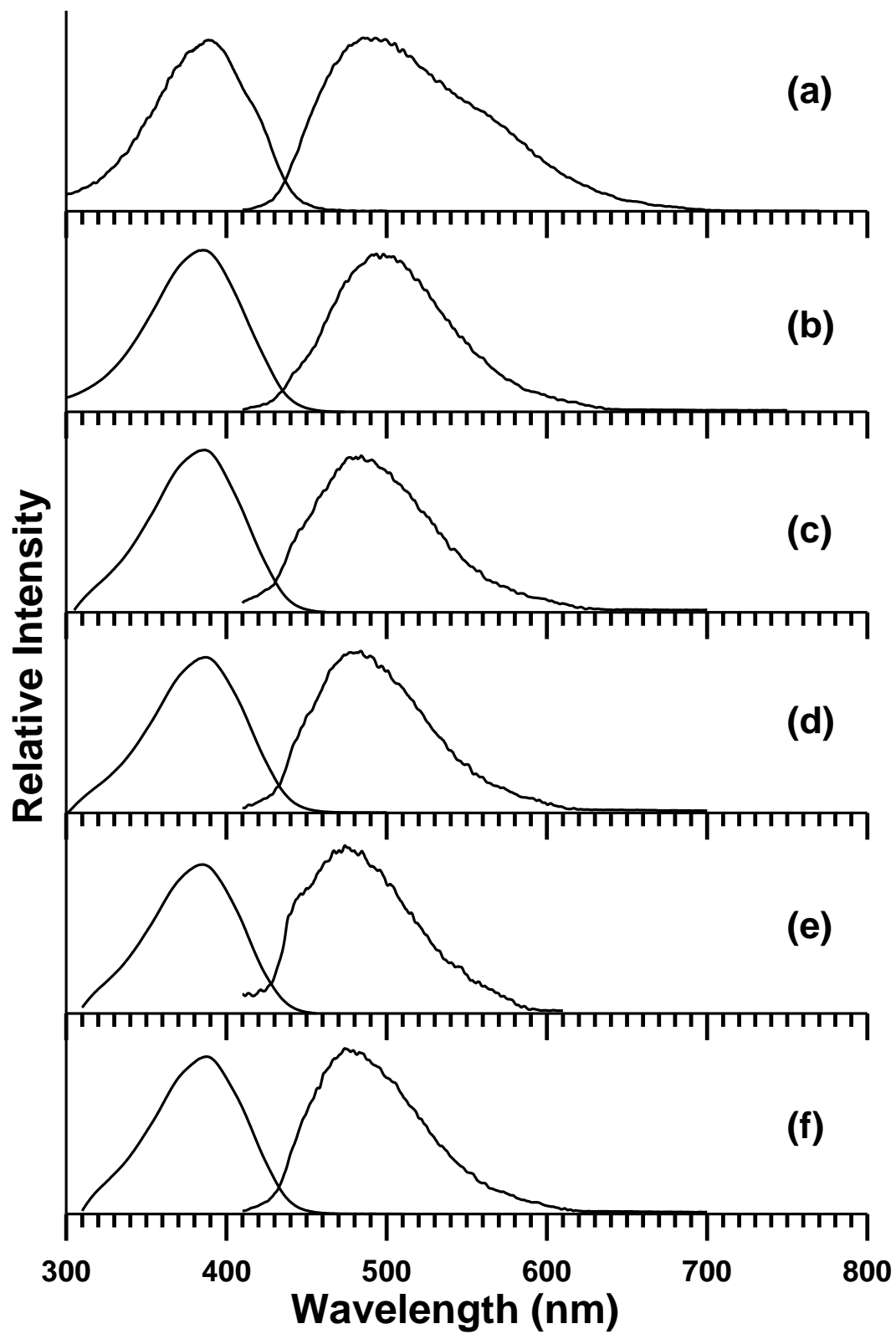
Figure 100. Absorption and fluorescence emission spectra of Asunsub in (a) concentrated acetic acid, (b) methanol, (c) ethanol, (d) 1-propanol, (e) 2-propanol, and (f) 1-butanol.

259

Table 53. TD-DFT spectral calculations of Asunsub in the gas phase, cyclohexane, and ethanol at the B3LYP/6-31G(d) level of theory.

Solvent	State	Transition Energy			f	MO	CI Coef.
		eV	cm^{-1}	nm			
Gas (μ = 3.55 D)	S$_1$ (n, π*)	2.86	23041	434	0.00	74→77	0.67366
						75→77	-0.16783
	S$_2$ (π, π*)	3.14	25316	395	1.41	75→77	-0.15681
						76→77	0.68673
	S$_3$ (π, π*)	3.57	28736	348	0.018	74→77	0.16410
						75→77	0.63951
						76→77	0.13083
						76→78	-0.19737
Cyclohexane (μ = 4.03 D)	S$_1$ (n, π*)	2.93	23585	424	0.001	74→77	0.68000
						75→77	-0.13898
	S$_2$ (π, π*)	2.99	24096	415	1.60	75→77	-0.12970
						76→77	0.69358
	S$_3$ (π, π*)	3.52	28409	352	0.034	74→77	0.14249
						75→77	0.66292
						76→77	0.11052
						76→78	-0.15223
Ethanol (μ = 4.86 D)	S$_1$ (π, π*)	2.95	23810	420	1.58	75→77	-0.10736
						76→77	0.69715
	S$_2$ (n, π*)	3.03	24390	410	0.0035	74→77	0.68434
						75→77	-0.12703
	S$_3$ (π, π*)	3.52	28329	353	0.044	74→77	0.12321
						75→77	0.66710
						76→78	-0.16118

This compound is reminiscent to previous work done on a series of three symmetrically unsubstituted 2,5-diarylidene cyclopentanones, compounds 1dbcp, 2dbcp, and 3dbcp discussed in chapter 2 [11]. It was found in their studies that 1dbcp doesn't fluoresce in any solvents, 2dbcp fluoresces only in polar protic solvents, and 3dbcp fluoresces in a number of protic and aprotic solvents. Solvents which are able to induce fluorescence are believed to do so by inverting the order of the ^{1}(n, π^*) and ^{1}(π, π^*) states. The absence of measurable fluorescence when S_1 is (n, π^*) is attributed to efficient ^{1}(n, π^*) $\rightarrow$ ^{3}(π, π^*) intersystem crossing, in accordance to El-Sayed's rule. A solvent-induced inversion of state order such that S_1 becomes (π, π^*) is believed to occur in those situations where fluorescence was observed.

The room temperature absorption spectrum of Asunsub was measured in cyclohexane, shown in Figure 101. Excitation to S_2 was experimentally observed as the major absorption band with vibronic structure between 290 nm to 410 nm. Two weakly intense absorption bands between 420 nm to 470 nm were also observed, which are assigned to excitation to the S_1 (n, π^*) excited state. The approximate spacing of these two weak bands was found to be 1250 cm^{-1}. The absorption characteristics of 1dbcp, 2dbcp, and 3dbcp in cyclohexane have previously been studied [11]. Similar features were observed as with Asunsub. A dominant spectral band for 1dbcp was observed between 270 nm to 370 nm, representing the ^{1}(π, π^*) state, and was found to shift bathochromically with respect to increased polyene chain length (as seen for 2dbcp and 3dbcp). A set of three weak bands localized at longer wavelengths between 370 nm to 460 nm was also observed for 1dbcp, which was assigned to the ^{1}(n, π^*) state. The (n, π^*) bands shift hypsochromically and overlap with the red shifted (π, π^*) band in going from 1dbcp to 2dbcp to 3dbcp. This explains why there are three well resolved (n, π^*) absorption bands for 1dbcp, and only one less resolved absorption band for 2dbcp.
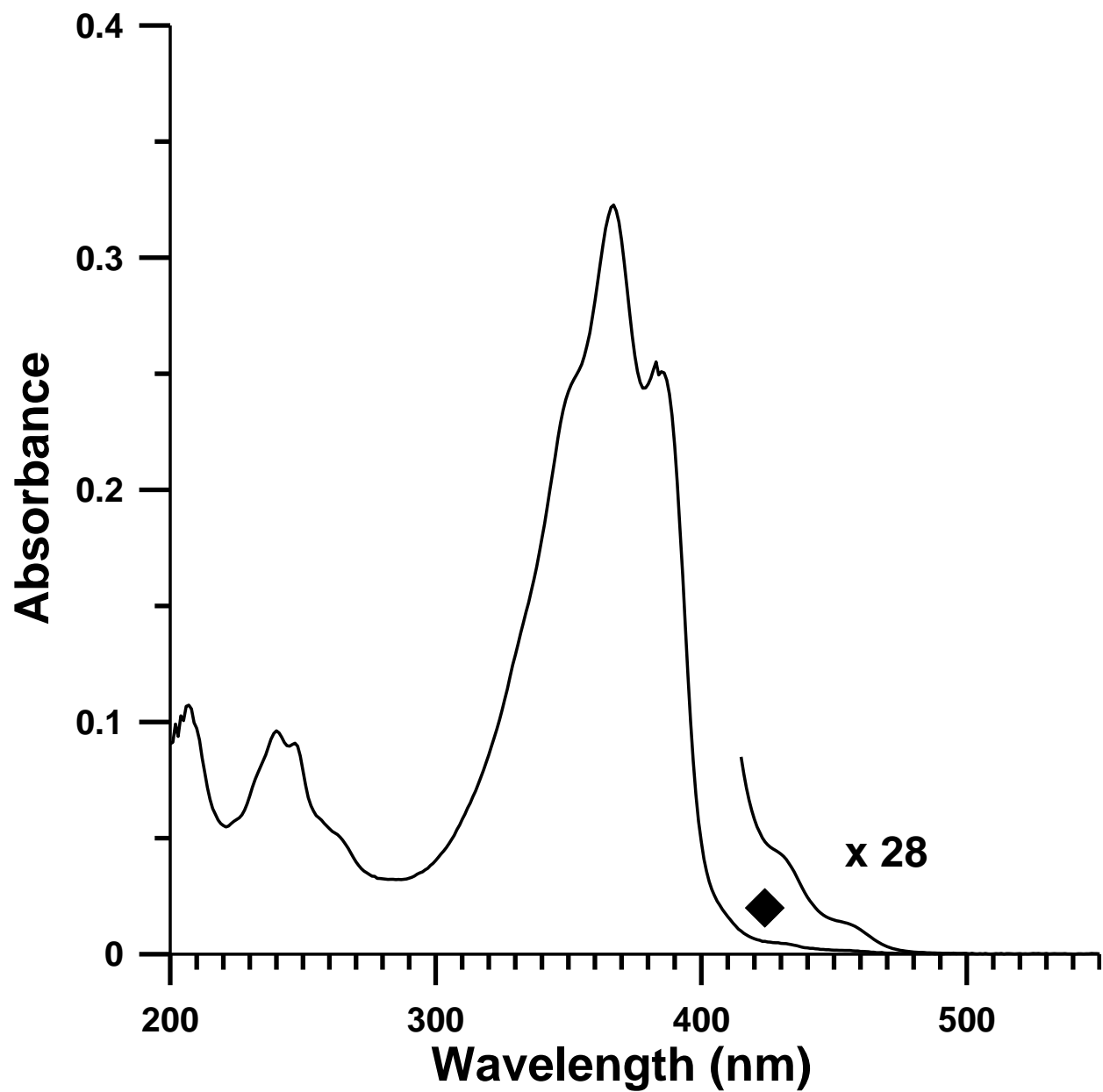
Figure 101. Experimental absorption spectrum of Asunsub in cyclohexane. The filled diamond

is the location of the weakly observed $S_1(n, \pi^*)$ state (TD-DFT: $\lambda = 424$ nm, $f = 0.001$).

4.3.4   Conclusions

Comparative studies of the electronic absorption and fluorescence properties of 2dbmxcp and its dimethylamino analogue, bis-dmac, provide experimental and theoretical support of the internal charge transfer properties of these two compounds. The larger bathochromic shifts in absorption and fluorescence energies (~2-fold greater red shift in fluorescence), the ~2-fold increase on the magnitudes of μ_{exc} and $\Delta\mu$, and MOSF calculated data on ground state and excited state atomic charges demonstrate a higher degree of internal charge transfer behavior exhibited by bis-dmac. The larger Φ_f and smaller k_{nr} values observed for 2dbmxcp in region 1 are attributed to the larger S_0-S_1 energy gaps (energy gap law), compared to the S_0-S_1 energy gaps of bis-dmac and bis-dmab.

The single crystal X-ray structure of Asunsub has a higher degree of phenyl ring torsion on the benzylidene end than on the more conjugated cinnamylidene end of the molecule. The larger twisting conformation of the phenyl ring on the less conjugated end of the molecule is likely influenced not only by the molecular structure and energy of the isolated molecule, but also by the packing arrangement in the crystal. Twisting of phenyl groups can be due to intermolecular C-H…π interactions between the C-H protons and π electron clouds of neighboring aromatic rings. Direct comparison between the X-ray crystal structure of Asunsub and its predicted DFT geometry in the gas phase showed excellent agreement in bond lengths and bond angles. However, a nearly planar geometry was seen in the predicted DFT structure.

Fluorescence of Asunsub was observed only in protic solvents which is attributed to S_1 being (π, π^*). The absence of measurable fluorescence in aprotic solvents, where S_1 is (n, π^*) is due to efficient intersystem crossing from the singlet state to triplet state manifold. The room

temperature absorption spectrum of Asunsub in cyclohexane consisted of a major absorption

band between 290 nm and 410 nm. Two weak absorption bands between 420 nm and 470 nm

were also observed and assigned as excitation to the $S_1(n, \pi^*)$ state. Furthermore, the

spectroscopic work carried out for Asunsub is consistent with previous work done on

symmetrically unsubstituted 2,5-diarylidene cyclopentanone dyes [11].

4.4   Excited State Protonation Studies in Acetic Acid

4.4.1   Introduction

This portion of the results presents the spectroscopic findings of 2,5-diarylidene cyclopentanone dyes that exhibited dual emission in their fluorescence emission spectra. The longer wavelength fluorescence band is due to emission from the protonated species. The following compounds were experimentally observed to undergo excited state protonation at room temperature: bis-dmab, Ashrbor, 2dbmxcp, and two additional compounds that have not been discussed up to now, (2E,5E)-2,5-bis(p-methoxybenzylidene)-cyclopentanone (1dbmxcp), and (2E,5E)-2,5-bis(benzofuran-2-ylmethylene)-cyclopentanone (1dbzfcp). The Forster cycle is used in calculating the ΔpKa for each compound from the fluorescence spectral data. Furthermore, correlations are made among the experimentally determined ΔpKa values and calculated formal charges of the carbonyl oxygen atom in both the ground singlet and singly excited (π, π^*) states.

4.4.2   Spectroscopic Analyses of Dyes in Acetic Acid

Acetic acid, being a weak monocarboxylic acid, is a suitable solvent for excited state protonation studies, contrary to stronger acids such as sulfuric acid and phosphoric acid, which protonate the ground state as well [15]. Evidence for the lack of ground state protonation and the presence of excited state protonation is seen by the presence of a single band in the absorption spectrum and the observation of dual emission in the fluorescence spectrum. The fluorescence excitation spectra for the emission of unprotonated and protonated forms are identical with eachother and in agreement with the absorption spectra, indicating that the protonated and unprotonated states arise from the same chromophore [15]. The absorption and fluorescence

265

emission spectra of bis-dmab, Ashrbor, 1dbmxcp, 2dbmxcp, and 1dbzfcp in glacial acetic acid

are shown in Figures 102 – 104. The ΔpKa values for various 2,5-diarylidene cyclopentanone

dyes were calculated knowing the fluorescence energies for both unprotonated and protonated

forms, represented by the two local maxima in the fluorescence emission spectra (equation 2-4).

Table 54 lists the experimentally observed absorption and fluorescence energies (both protonated

and unprotonated forms) for each compound, along with their calculated ΔpKa values. The

experimentally observed ΔpKa values are positive for all compounds, indicating that the

compound is more basic in the S_1 state than in the ground singlet state (pKa* > pKa).

Table 54. Experimental absorption and fluorescence energies of 2,5-diarylidene cyclopentanone
dyes in acetic acid with their corresponding ΔpKa values.

Compound	ν_{abs} (cm^{-1})	$\nu_{f,A}$ (cm^{-1})	$\nu_{f,HA+}$ (cm^{-1})	ΔpKa
bis-dmab	20,619 (λ = 485 nm)	16,750 (λ = 597 nm)	13,569 (λ = 737 nm)	6.7
Ashrbor	20,040 (λ = 499 nm)	15,576 (λ = 642 nm)	12,225 (λ = 818 nm)	7.1
1dbmxcp	25,381 (λ = 394 nm)	20,161 (λ = 496 nm)	17,153 (λ = 583 nm)	6.4
2dbmxcp	22,371 (λ = 447 nm)	17,153 (λ = 583 nm)	13,889 (λ = 720 nm)	6.9
1dbzfcp	23,474 (λ = 426 nm)	18,519 (λ = 540 nm)	15,823 (λ = 632 nm)	5.7
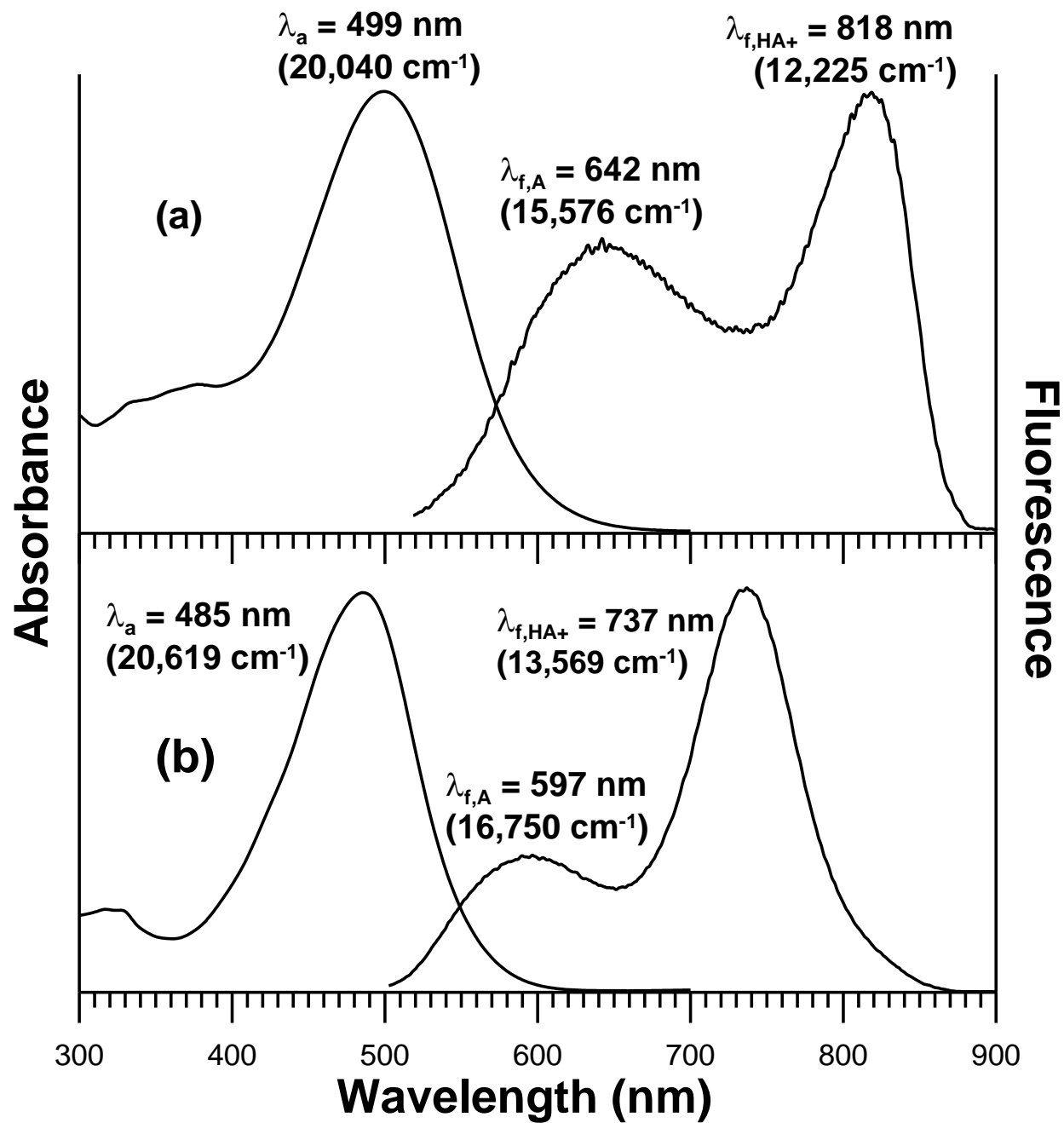
Figure 102. Absorption and fluorescence emission spectra of (a) Ashrbor and (b) bis-dmab in glacial acetic acid.
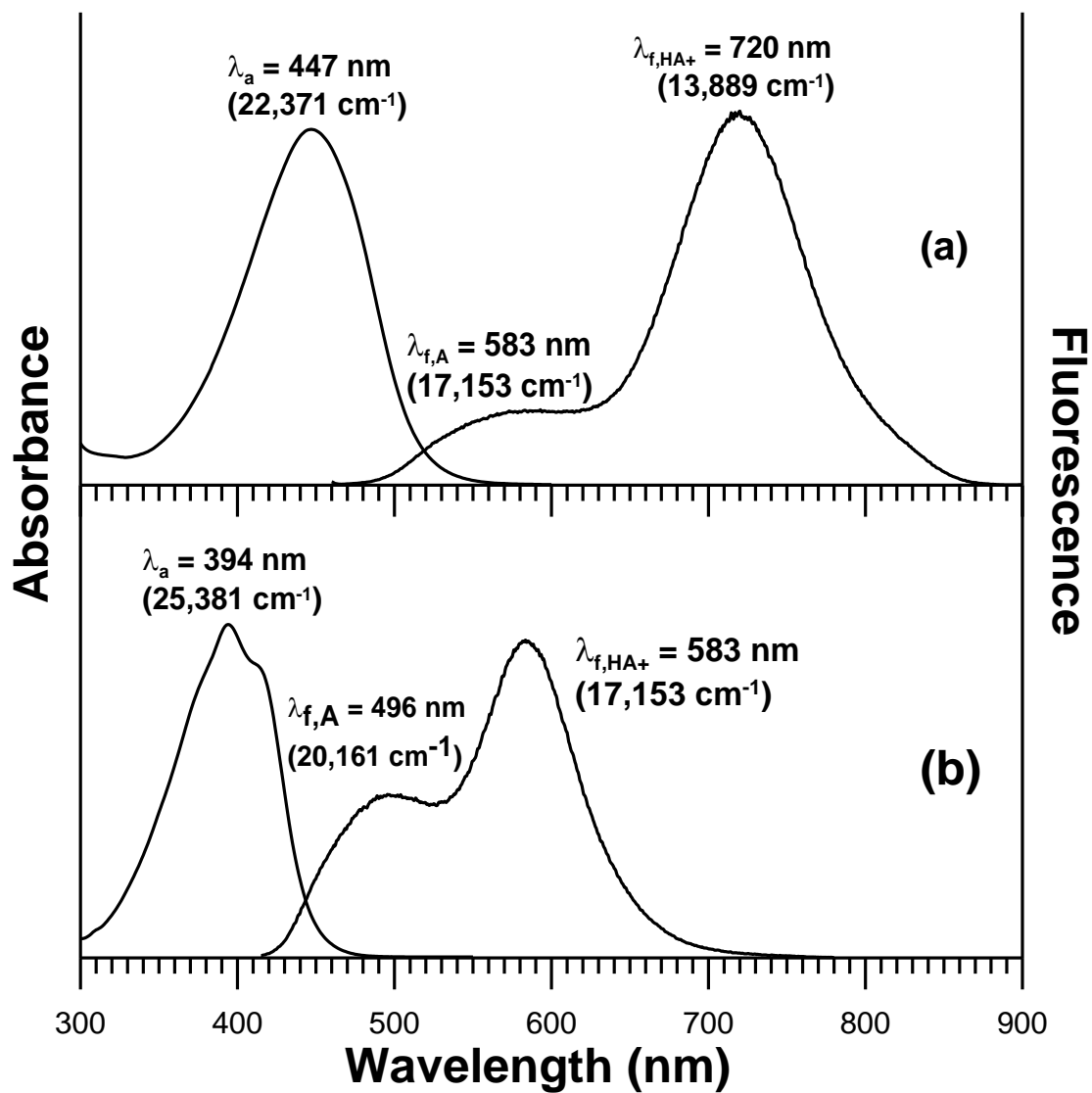
Figure 103. Absorption and fluorescence emission spectra of (a) 1dbmxcp and (b) 2dbmxcp in glacial acetic acid.
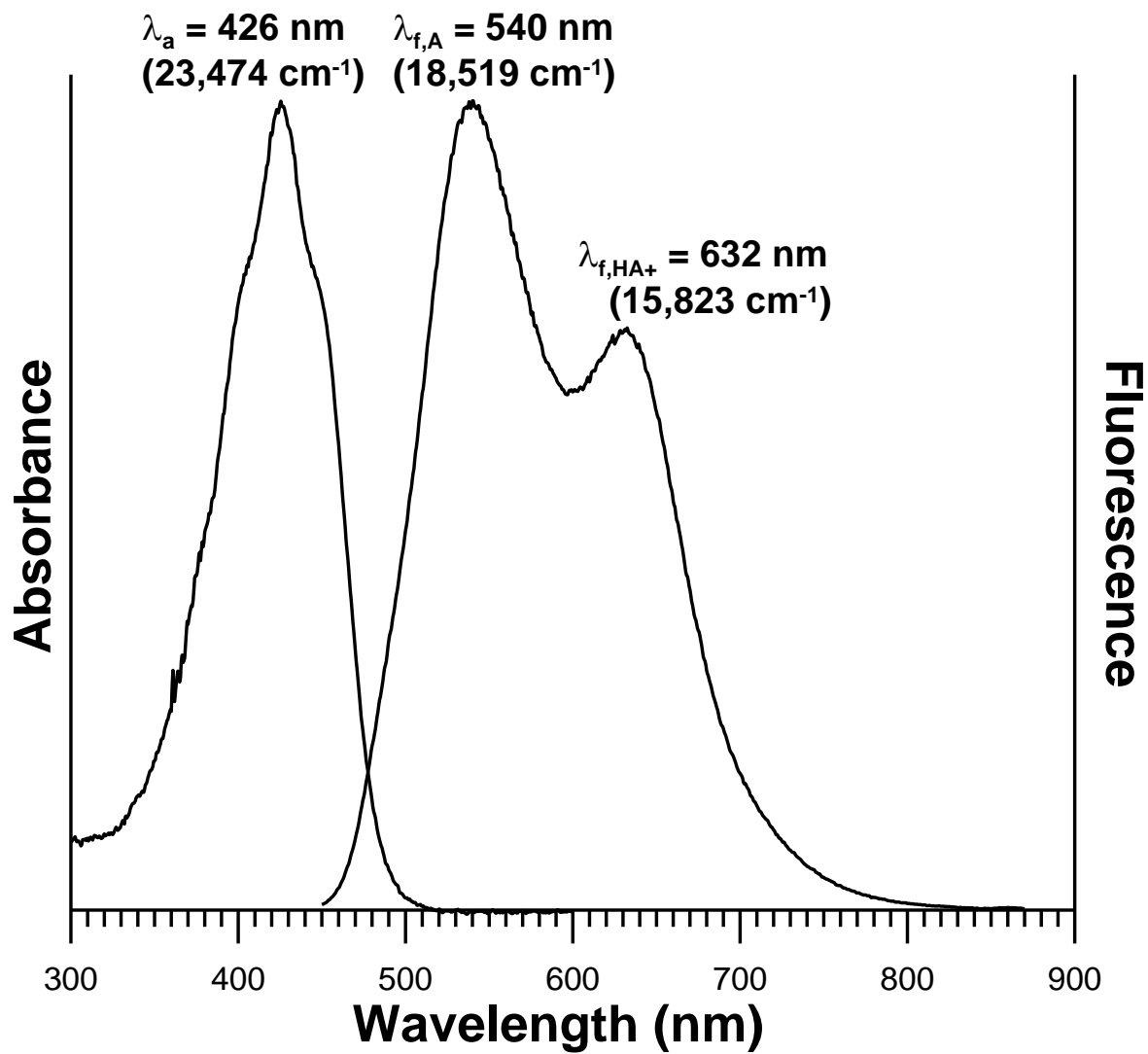
Figure 104. Absorption and fluorescence emission spectra of 1dbzfcp in glacial acetic acid.

4.4.3 Comparisons of Atomic Charges with Experimental ΔpKa's

Further quantitative support on the excited state protonation studies of these compounds in glacial acetic acid involved calculating atomic charges in both the ground singlet and singly excited (π, π^*) states and correlating them to experimentally determined ΔpKa values. Specifically, the atomic charge of the carbonyl oxygen atom both in the S_0 and $^1(\pi, \pi^*)$ states and its difference (ΔQ) were computationally determined for each compound and are presented in Table 55. The observation of excited state proton transfer from $S_1(\pi, \pi^*)$ can be understood by considering that there is an internal transfer of electron charge density from the electron donating ends of the molecule to the carbonyl oxygen atom, thereby causing the molecule to become a stronger base in the excited state. This is supported by the fact that the charge of O becomes more negative from S_0 to $^1(\pi, \pi^*)$, hence the negative values in ΔQ_O. Although a direct quantitative correlation cannot be made on the relationship of ΔpKa with either $Q_O(S_0)$ or ΔQ_O, it is clear that the positive values in ΔpKa are attributed to the more negative charge of the carbonyl oxygen atom in the singly excited state than in the ground state. Also included are the experimentally observed ΔpKa values for two symmetrically unsubstituted analogues, compounds 2dbcp and 3dbcp, previously studied [15].

Table 55. Experimental ΔpKa values and computed formal charges of the carbonyl oxygen atoms at both the S_0 and $^1(\pi, \pi^*)$ states.

Compound	ΔpKa	Q_O (S_0)	Q_O ($^1(\pi, \pi^*)$)	ΔQ_O
bis-dmab	6.7	-0.553	-0.664	-0.111
Ashrbor	7.1	-0.553	-0.630	-0.077
1dbmxcp	6.4	-0.547	-0.641	-0.094
2dbmxcp	6.9	-0.548	-0.622	-0.074
1dbzfcp	5.7	-0.542	-0.625	-0.083
2dbcp	5.2*	-0.543	-0.618	-0.075
3dbcp	4.1*	-0.547	-0.606	-0.059

*ΔpKa values for 2dbcp and 3dbcp were taken from [15]

4.4.4 Conclusions

Dual fluorescence emission from the S_1 excited states of the studied 2,5-diarylidene cyclopentanones in glacial acetic acid is attributed to the increase in basicity in the excited state. Examination of the computed charges of the carbonyl oxygen atoms demonstrates that the compounds are stronger bases in the $^1(\pi, \pi^*)$ state than in the ground state. Both the positive values in ΔpKa (pKa* > pKa) and the decrease in formal charge of the carbonyl oxygen atom in the $^1(\pi, \pi^*)$ state explains the observable excited state protonation of these compounds.

4.5 Photochemistry of bis-dmab

4.5.1 Introduction

This portion of the results and discussion is divided into four sections:

1. The screening of bis-dmab as a photosensitizer for singlet oxygen in the presence of tetramethylethylene (TME) in chloroform-d, toluene-d_8, and methanol-d_4.

2. ^{1}H NMR studies carried out on the self-sensitized photooxidation of bis-dmab in CDCl$_3$.

3. UV-Vis absorption studies of the photochemistry of bis-dmab in the presence and absence of oxygen in various solvents.

4. LC/MS results carried out for further identification of photooxidized products of bis-dmab.

4.5.2 Testing of bis-dmab as a Singlet Oxygen Photosensitizer

The singlet oxygen (Schenck) ene reaction has been known since the 1940's [46, 47]. In the Schenck reaction, the combination between an alkene with an allylic hydrogen atom and ^{1}O$_2$ (acting as the enophile) results in the production of an allylic hydroperoxide. For example, from Figure 15(a), the reaction between 2,3-dimethyl-2-butene (tetramethylethylene, TME) and ^{1}O$_2$ results in the formation of 3-hydroperoxy-2,3-dimethyl-1-butene. Previous work done by Matsumoto, *et al.* [48a] has shown that the sensitized photooxygenation of a catalytic amount of N-substituted 2-pyridones in the presence of TME yields 3-hydroperoxy-2,3-dimethyl-1-butene as the resulting product.

Compound bis-dmab was tested as a photosensitizer for singlet oxygen in the presence of TME as the indicator for ^{1}O$_2$ production. In this section, ^{1}H NMR will show that a catalytic amount of bis-dmab in the presence of TME (acting as an indicator for ^{1}O$_2$ production) and deuterated solvent results in the conversion from TME to the allylic hydroperoxide. TME has

one singlet at δ *ca* 1.6 ppm (12H). Figure 105 provides the following ^{1}H NMR assignments of 3-hydroperoxy-2,3-dimethyl-1-butene. The ^{1}H NMR data of the allylic hydroperoxide is in agreement to values reported in the literature [71]. The 'a', 'b', 'c', and 'd' labeled H's are experimentally observed, and the 'e' labeled hydroperoxy H atom is observed only in chloroform-d. The ^{1}H NMR spectrum of a final irradiation/oxygen bubbling interval of catalytic bis-dmab in CDCl$_3$, provided in Figures 106 – 109, confirms the chemical identity of 3-hydroperoxy-2,3-dimethyl-1-butene.

H	δ (ppm)	Multiplicity
a, b	4.9-5.1	2 x m (2H)
c	1.7-1.8	m (3H)
d	1.3-1.4	s (6H)
e	7.3-7.35	s (1H)
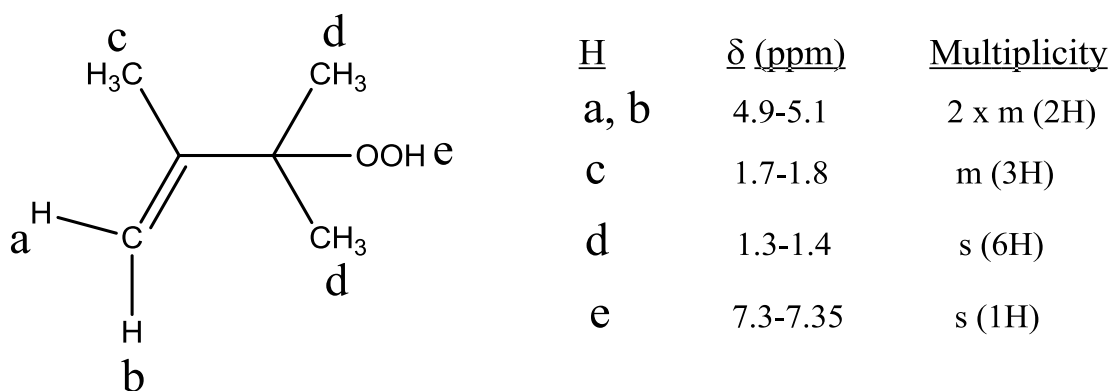
Figure 105. Structure and ^{1}H NMR assignments of 3-hydroperoxy-2,3-dimethyl-1-butene.

273
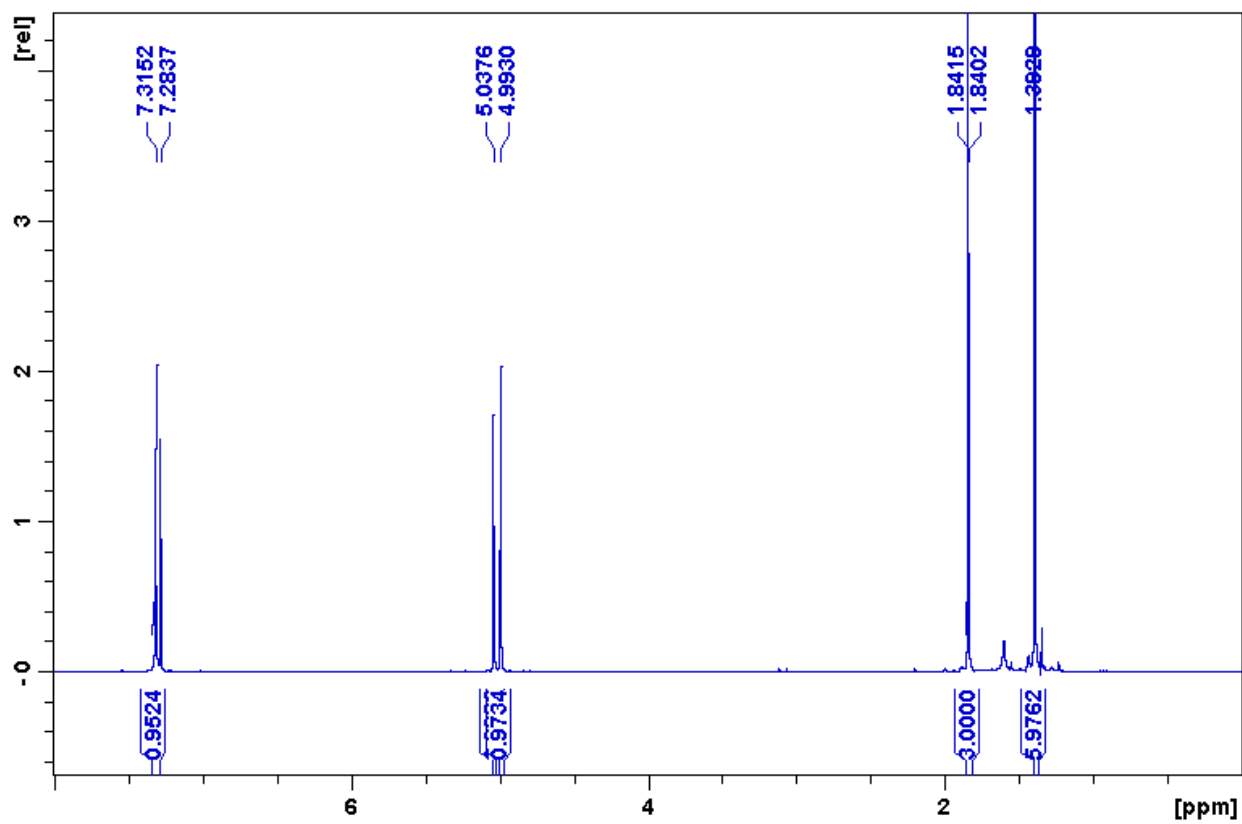
Figure 106. ^{1}H NMR spectrum of bis-dmab/TME/CDCl$_3$ solution at a final irradiation/bubbling

interval δ 0 – 8.0 ppm.
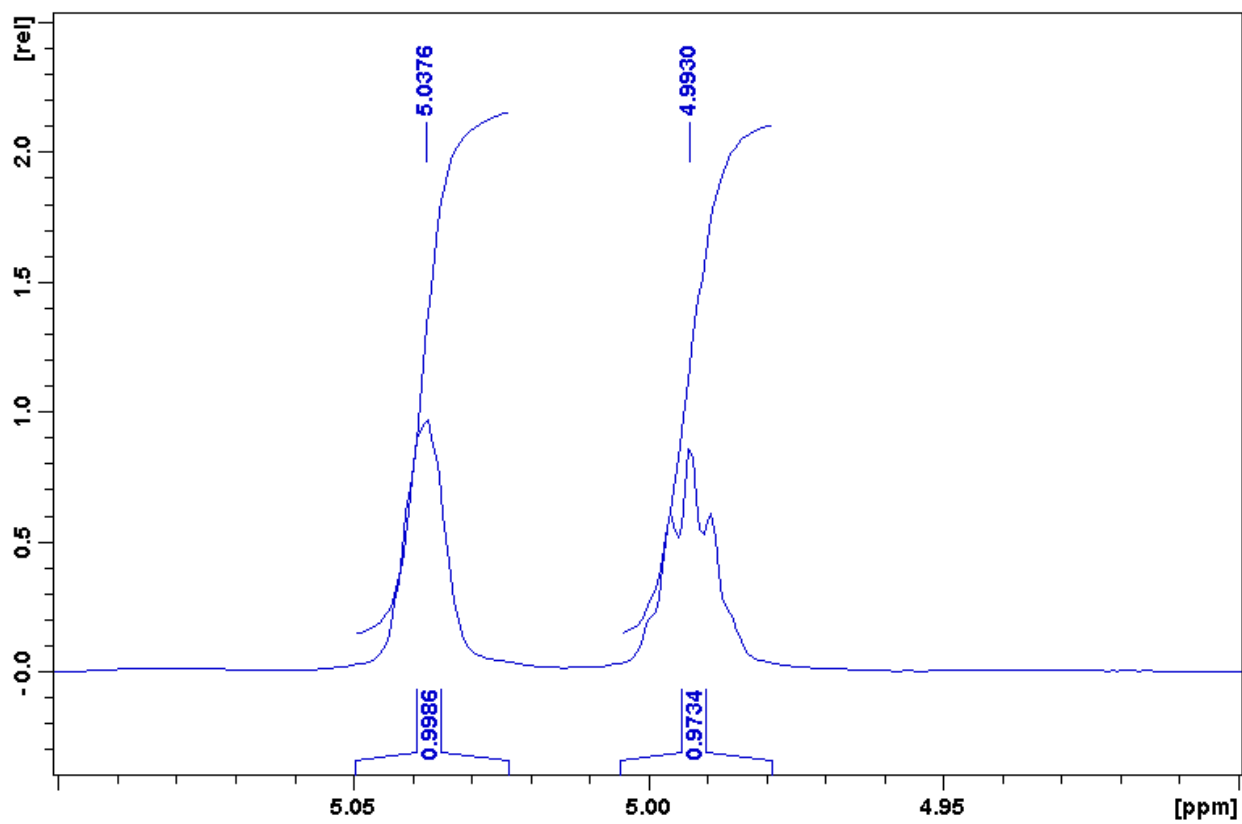
Figure 107. ^{1}H NMR spectrum of bis-dmab/TME/CDCl$_3$ solution at a final irradiation/bubbling interval δ 4.9 – 5.1 ppm.
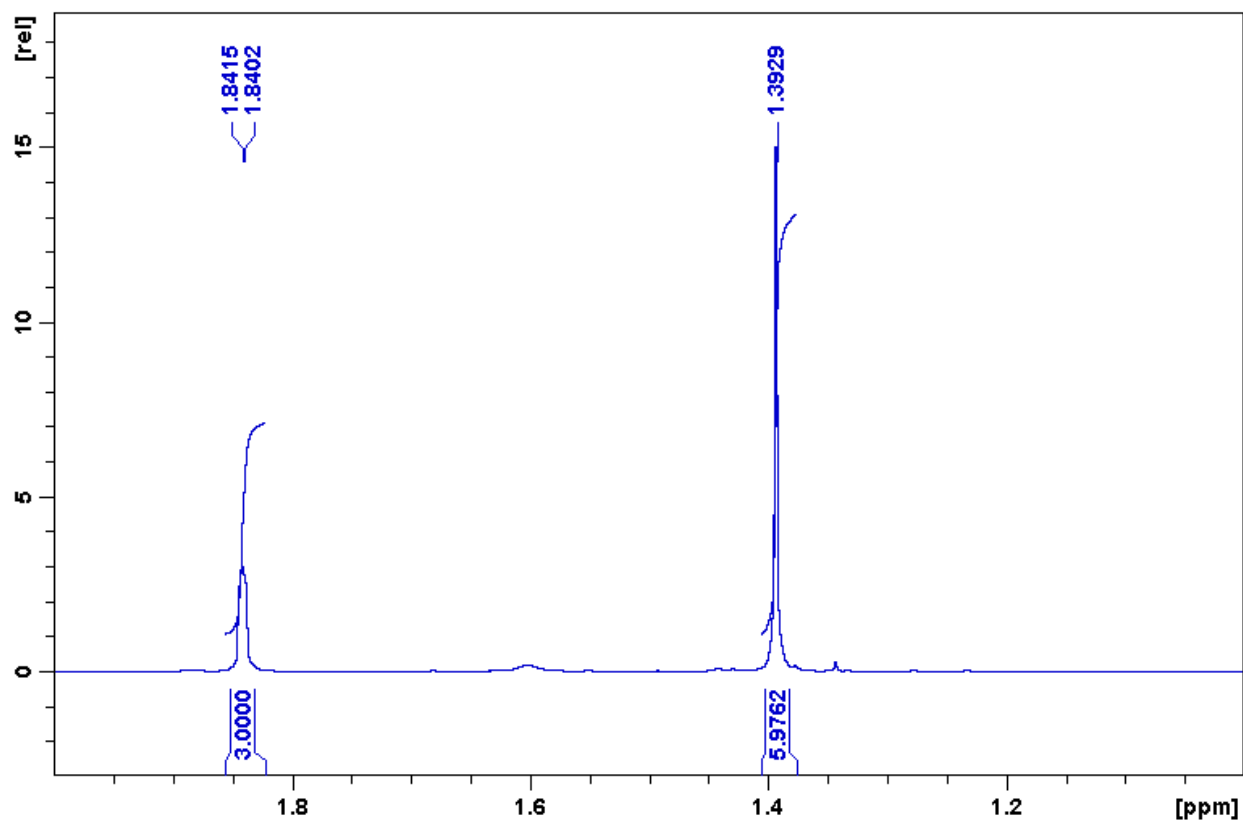
Figure 108. ^{1}H NMR spectrum of bis-dmab/TME/CDCl$_3$ solution at a final irradiation/bubbling interval δ 1.0 – 2.0 ppm.
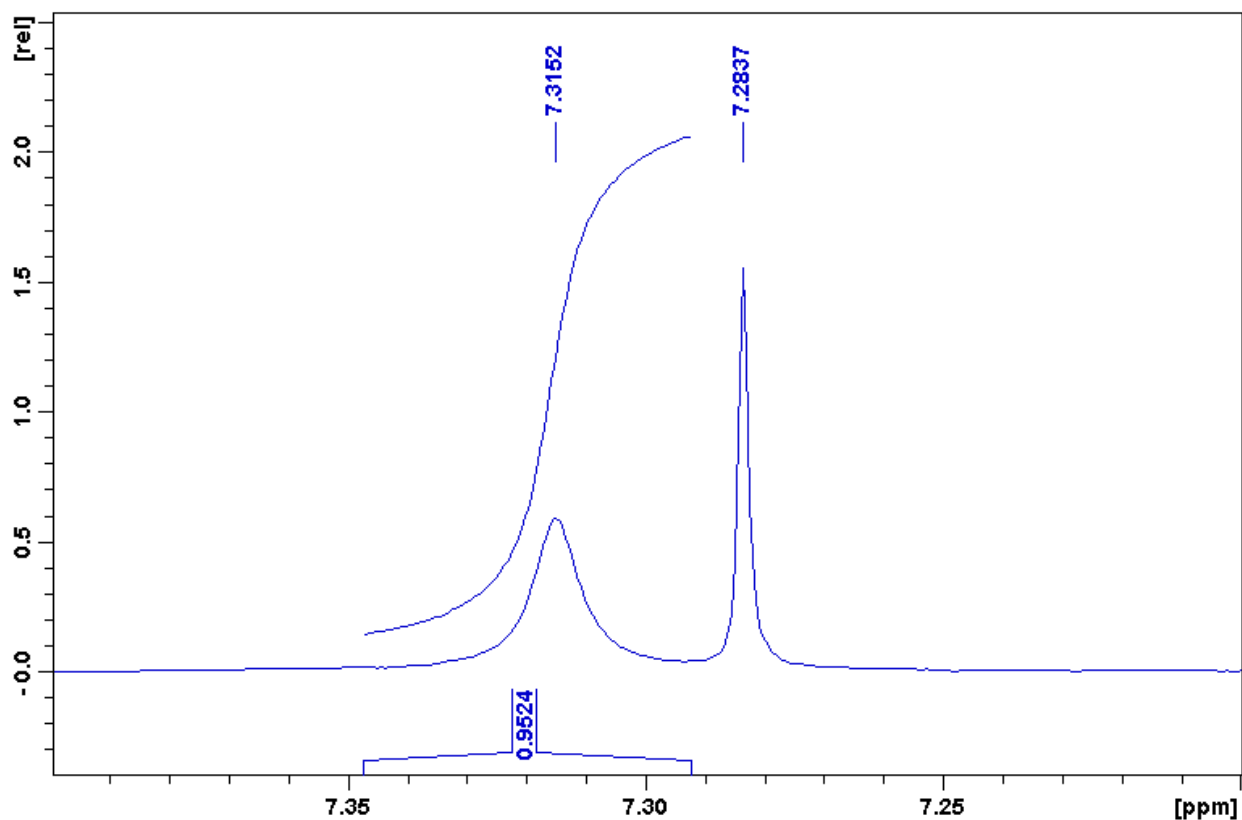
Figure 109. ^{1}H NMR spectrum of bis-dmab/TME/CDCl$_3$ solution at a final irradiation/bubbling interval δ 7.2 – 7.4 ppm.

A control experiment was carried out, which involved irradiating while bubbling O$_2$ through a solution of TME (10 µL) in CDCl$_3$ (1.80 mL) in the absence of sensitizer for a period of 30 minutes ([TME] = 46.5 mM). Figures 110 - 112 show the ^{1}H NMR spectra for the control experiment at various chemical shifts both before and after irradiation. Hardly any change in both the reactant and product signals was observed in the 30 minute irradiation interval, with only 0.15 % increase in the growth of the allylic hydroperoxide, concluding that TME does not react in the absence of bis-dmab.
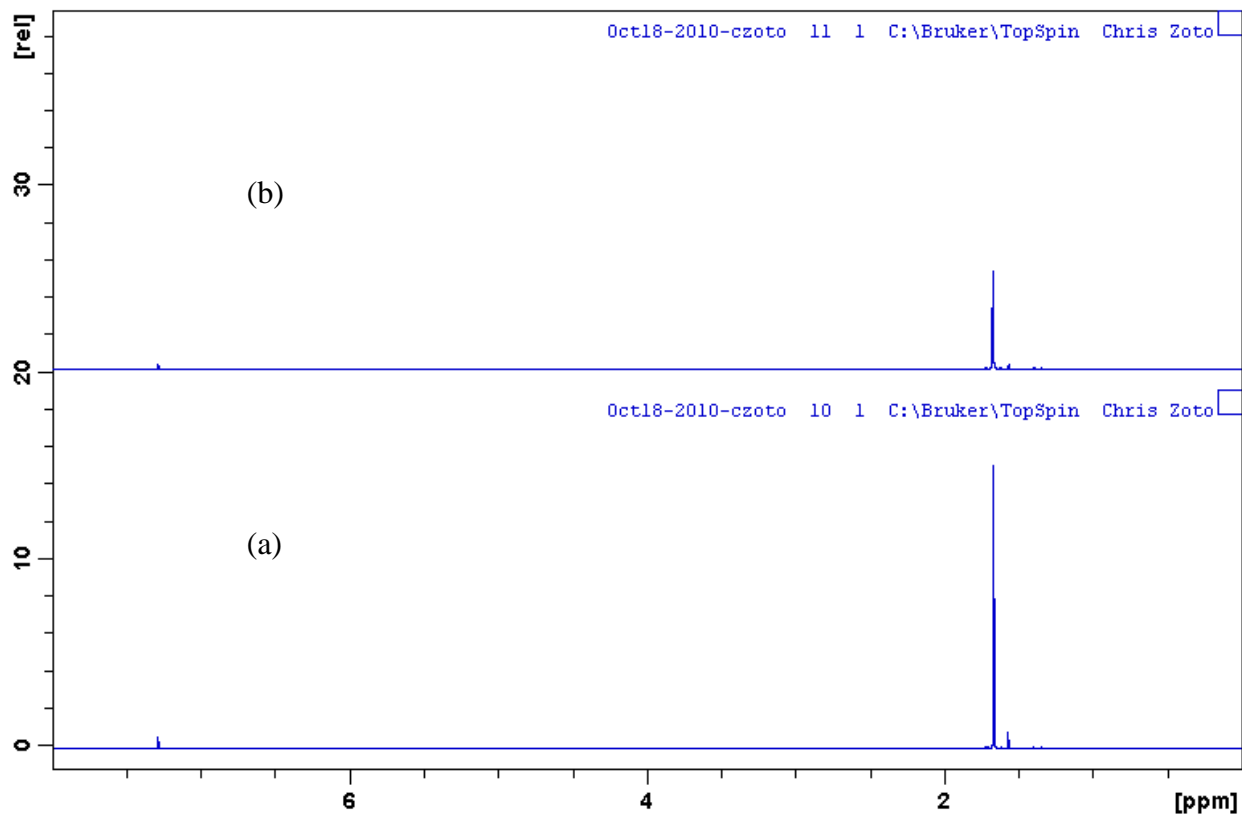
Figure 110. ^{1}H NMR spectra of TME in CDCl$_3$ δ 0 – 8.0 ppm at (a) 0 min and (b) 30 min

irradiation and bubbling.
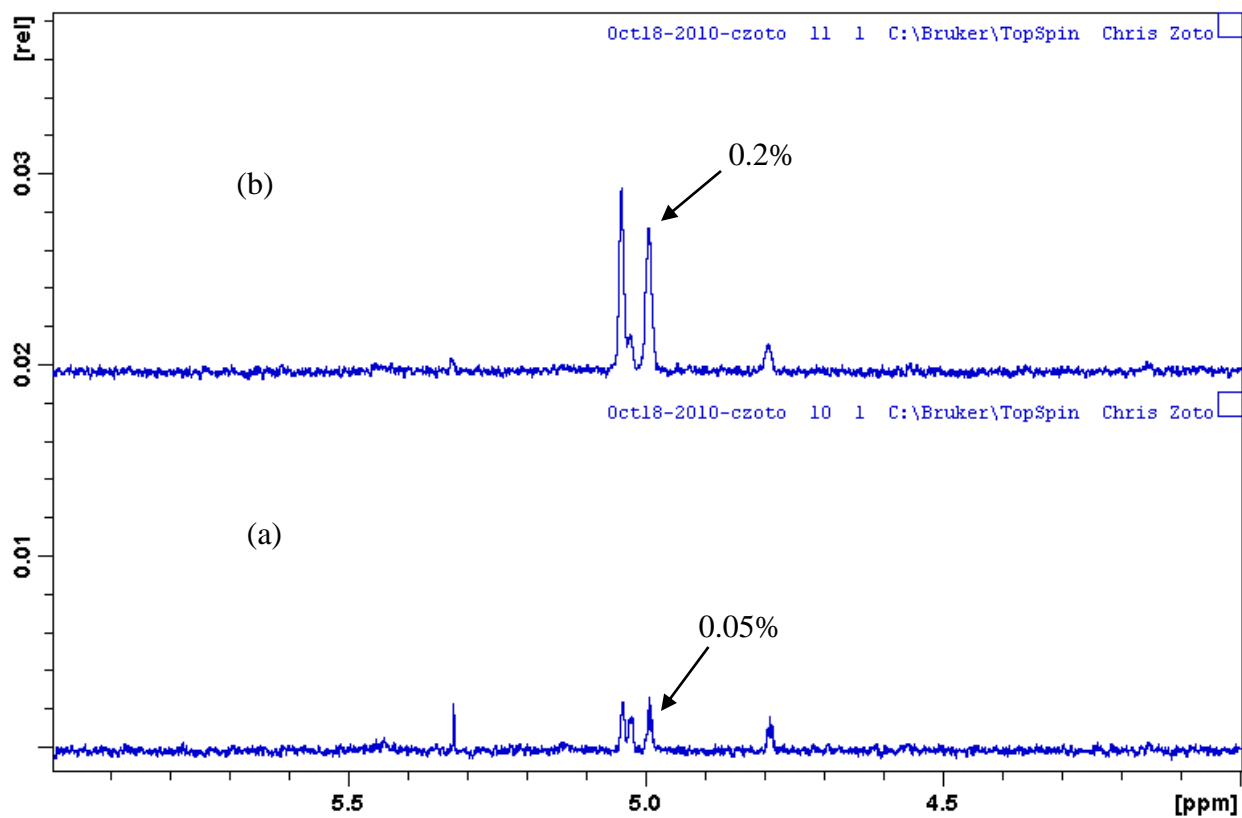
Figure 111. ^{1}H NMR spectra of TME in $CDCl_3$ δ 4.0 – 6.0 ppm at (a) 0 min and (b) 30 min irradiation and bubbling.
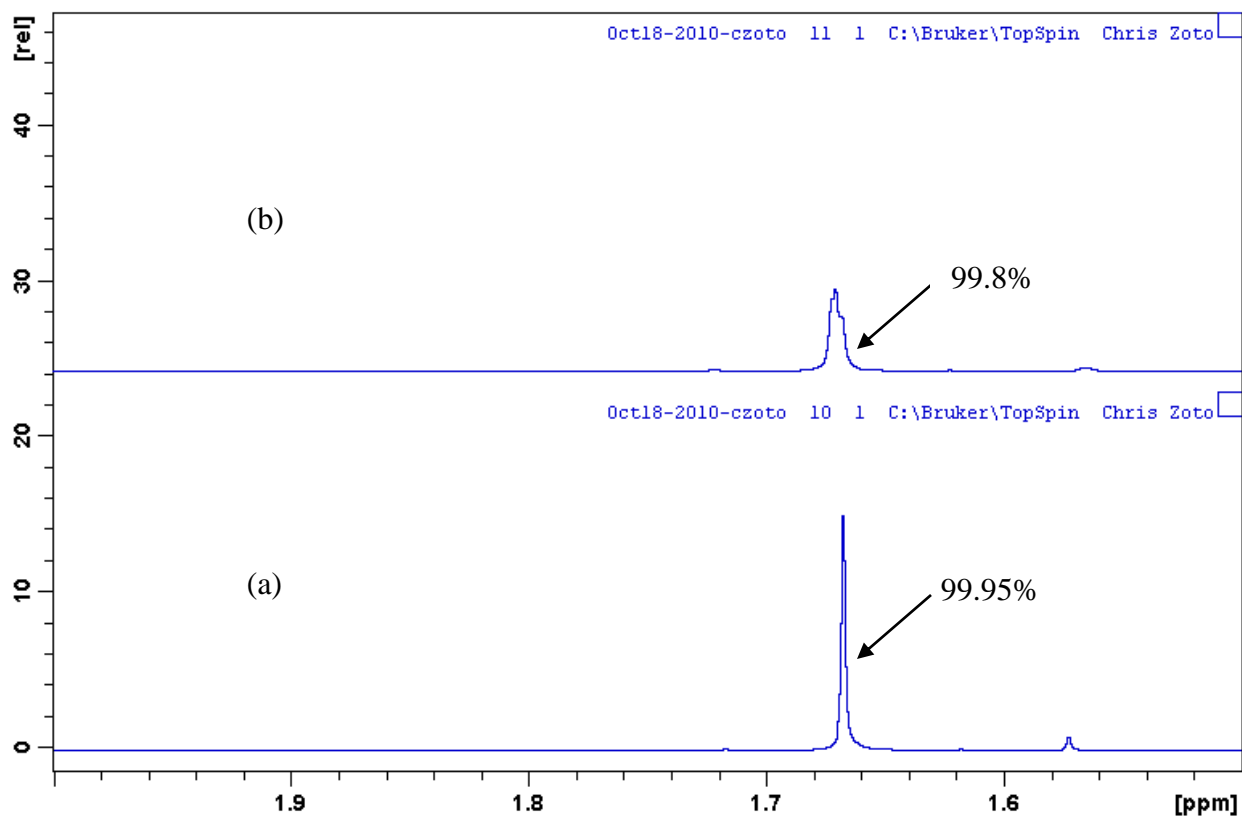
Figure 112. ^{1}H NMR spectra of TME in CDCl$_3$ δ 1.5 – 2.0 ppm at (a) 0 min and (b) 30 min

irradiation and bubbling.

The testing of bis-dmab as a singlet oxygen sensitizer has been carried out in chloroform-d, toluene-d_8, and methanol-d_4, monitoring the ^{1}H NMR spectra at various irradiation/bubbling intervals, as shown in Figures 113 – 116 (in chloroform-d), Figures 117 – 119 (toluene-d_8), and Figures 120 – 121 (in methanol-d_4). It has been shown that bis-dmab sensitizes singlet oxygen in all three solvents, as confirmed from the production of 3-hydroperoxy-2,3-dimethyl-1-butene (Schenck reaction).

In chloroform-d, the molar concentrations of bis-dmab and TME were 0.14 mM (approximate) and 46.6 mM, respectively. The molar concentration of bis-dmab was measured assuming the molar extinction coefficient to be 65,000 $M^{-1}cm^{-1}$ [72]. As observed in deuterated chloroform, 100% conversion from TME to hydroperoxide occurred after approximately 24 minutes. In toluene-d_8, the molar concentrations of bis-dmab and TME were 0.15 mM (approximate) and 46.5 mM. The concentration of bis-dmab was measured assuming the molar extinction coefficient to be the same as in chloroform. Partial conversion from TME to hydroperoxide was observed in toluene-d_8. From ^{1}H NMR spectral data, normalized percent conversion was 16.5% after 60 minutes of irradiation and O_2 bubbling. In methanol-d_4, the molar concentrations of bis-dmab and TME were 0.03 mM (approximate; poor solubility) and 46.4 mM. The concentration of bis-dmab was measured assuming the molar extinction coefficient to be the same as in chloroform. Integration of emerged ^{1}H NMR signals at δ 1.3 and 1.7 ppm verified the chemical identity of the hydroperoxide. As observed in methanol-d_4, ~100% conversion from TME to hydroperoxide occurred after approximately 80 minutes.

To conclude from these studies, bis-dmab sensitizes singlet oxygen in all three solvents. However, it is not possible from these data to report quantitative rates of TME consumption and hydroperoxide production in these three solvents.

281
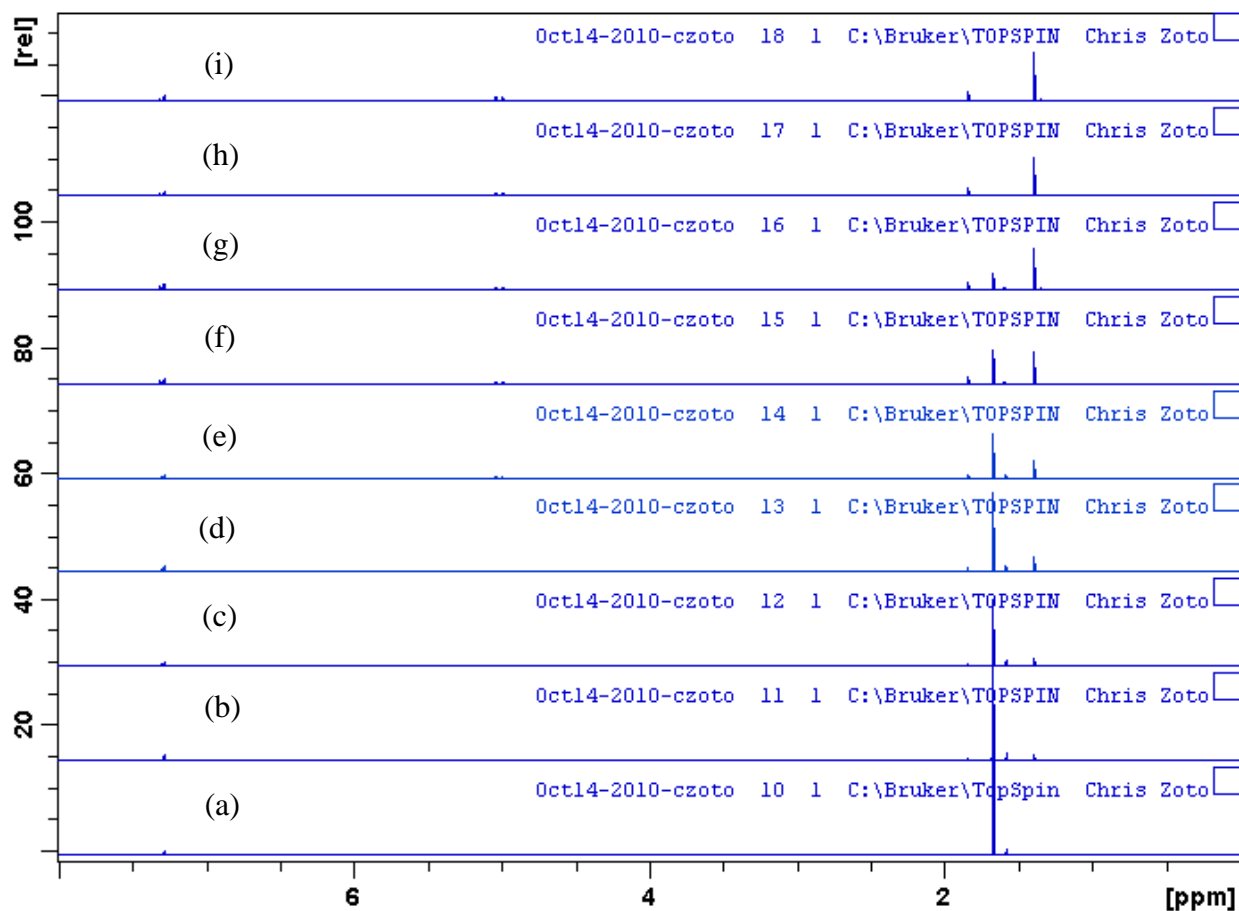
Figure 113. ^{1}H NMR spectra of bis-dmab/TME in CDCl$_3$ δ 0 – 8 ppm at (a) 0 min, (b) 2 min, (c) 4 min, (d) 6 min, (e) 10 min, (f) 14 min, (g) 18 min, (h) 22 min, and (i) 24 min of irradiation and O$_2$ bubbling.
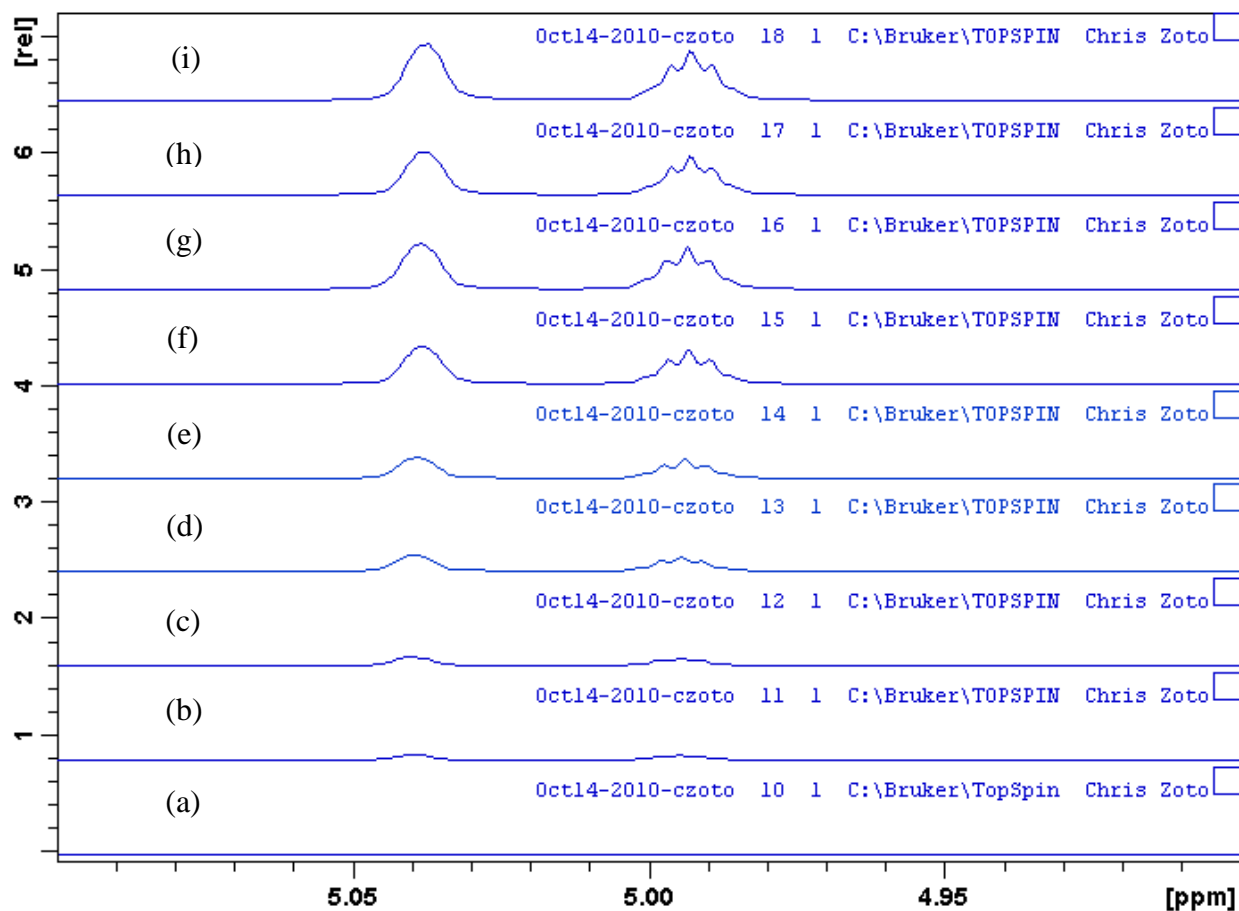
Figure 114. ^{1}H NMR spectra of bis-dmab/TME in $CDCl_3$ δ 4.90 – 5.10 ppm at (a) 0 min, (b) 2 min, (c) 4 min, (d) 6 min, (e) 10 min, (f) 14 min, (g) 18 min, (h) 22 min, and (i) 24 min of irradiation and O_2 bubbling.
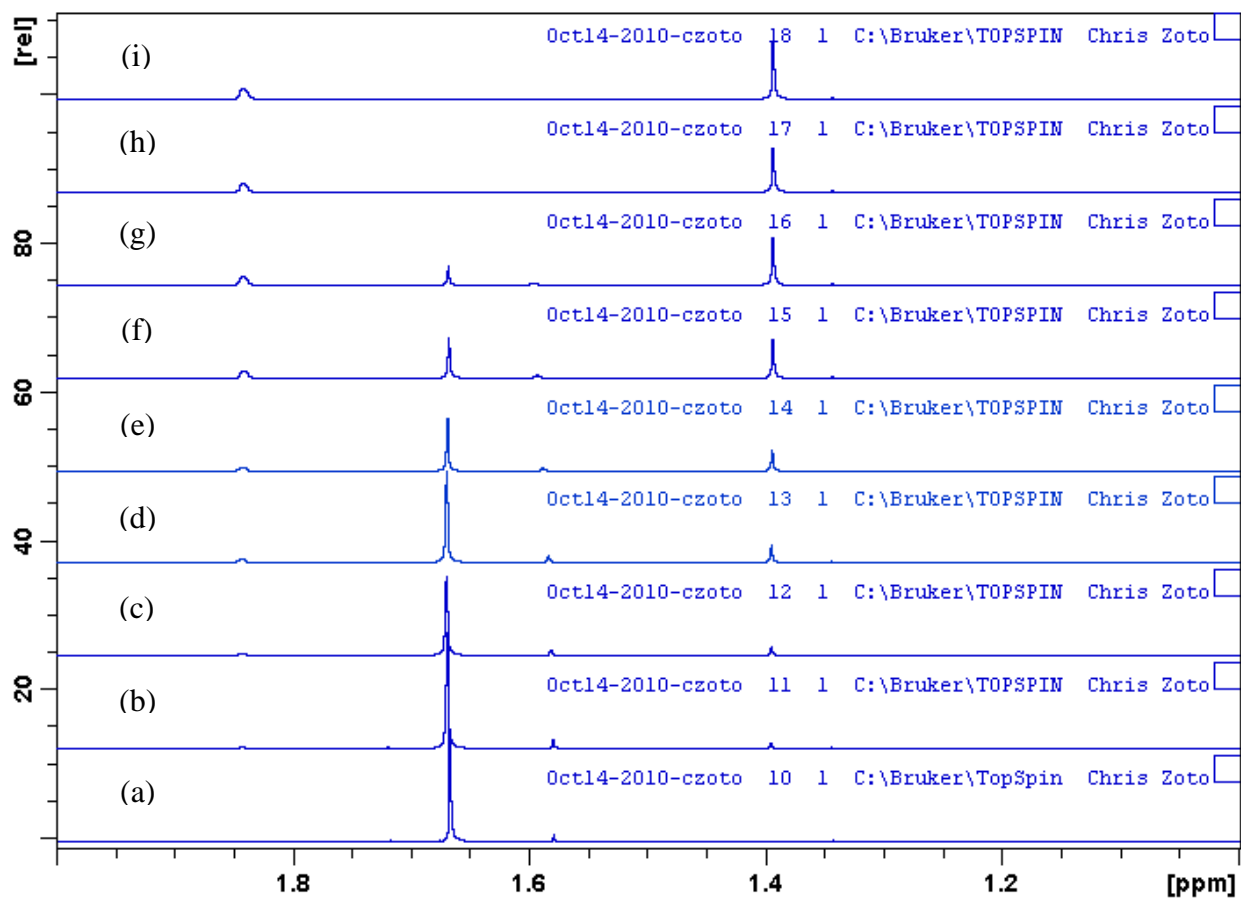
Figure 115. ^{1}H NMR spectra of bis-dmab/TME in CDCl$_3$ δ 1.0 − 2.0 ppm at (a) 0 min,

(b) 2 min, (c) 4 min, (d) 6 min, (e) 10 min, (f) 14 min, (g) 18 min, (h) 22 min, and (i) 24 min of

irradiation and O$_2$ bubbling.
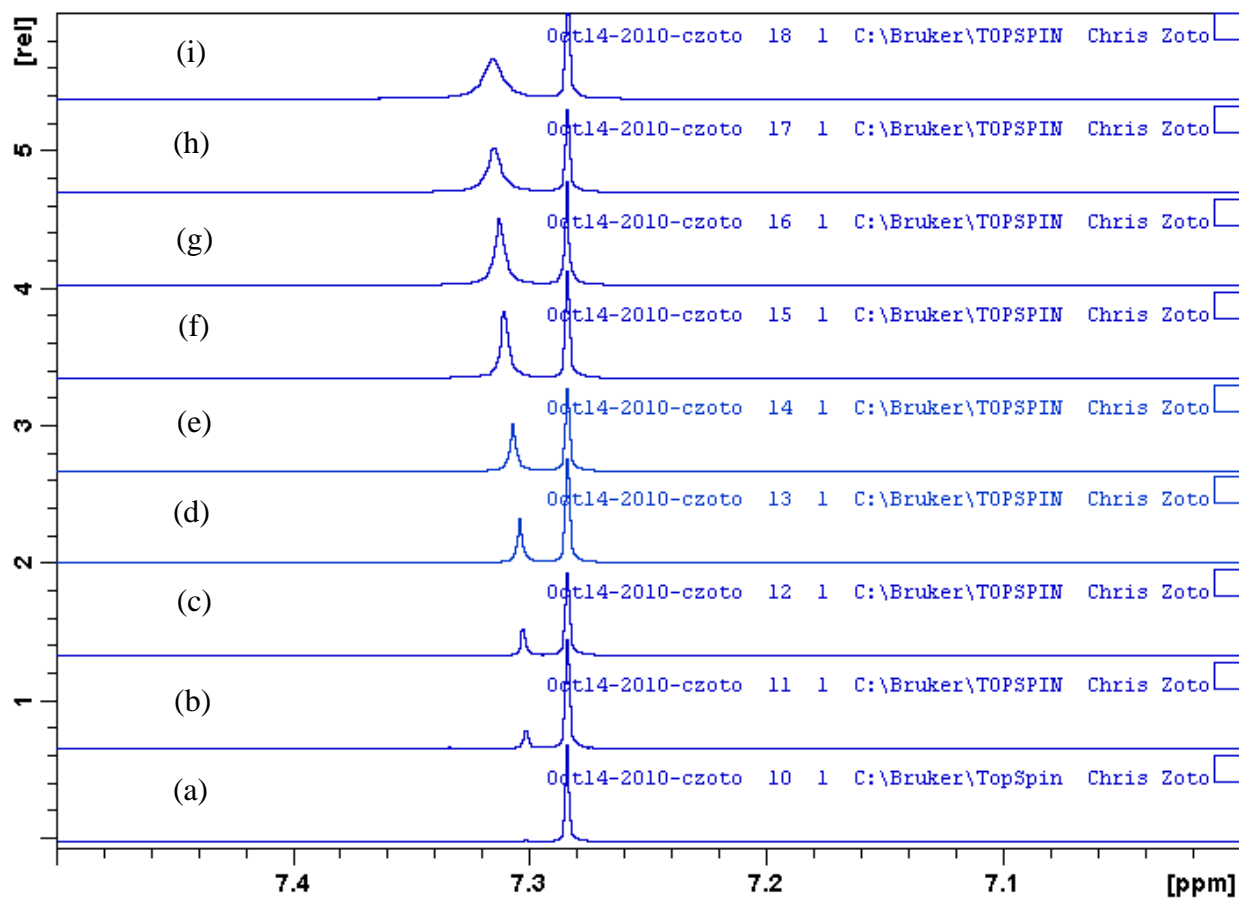
Figure 116. ^{1}H NMR spectra of bis-dmab/TME in CDCl$_3$ δ 7.0 – 7.5 ppm at (a) 0 min,

(b) 2 min, (c) 4 min, (d) 6 min, (e) 10 min, (f) 14 min, (g) 18 min, (h) 22 min, and (i) 24 min

irradiation and O$_2$ bubbling.
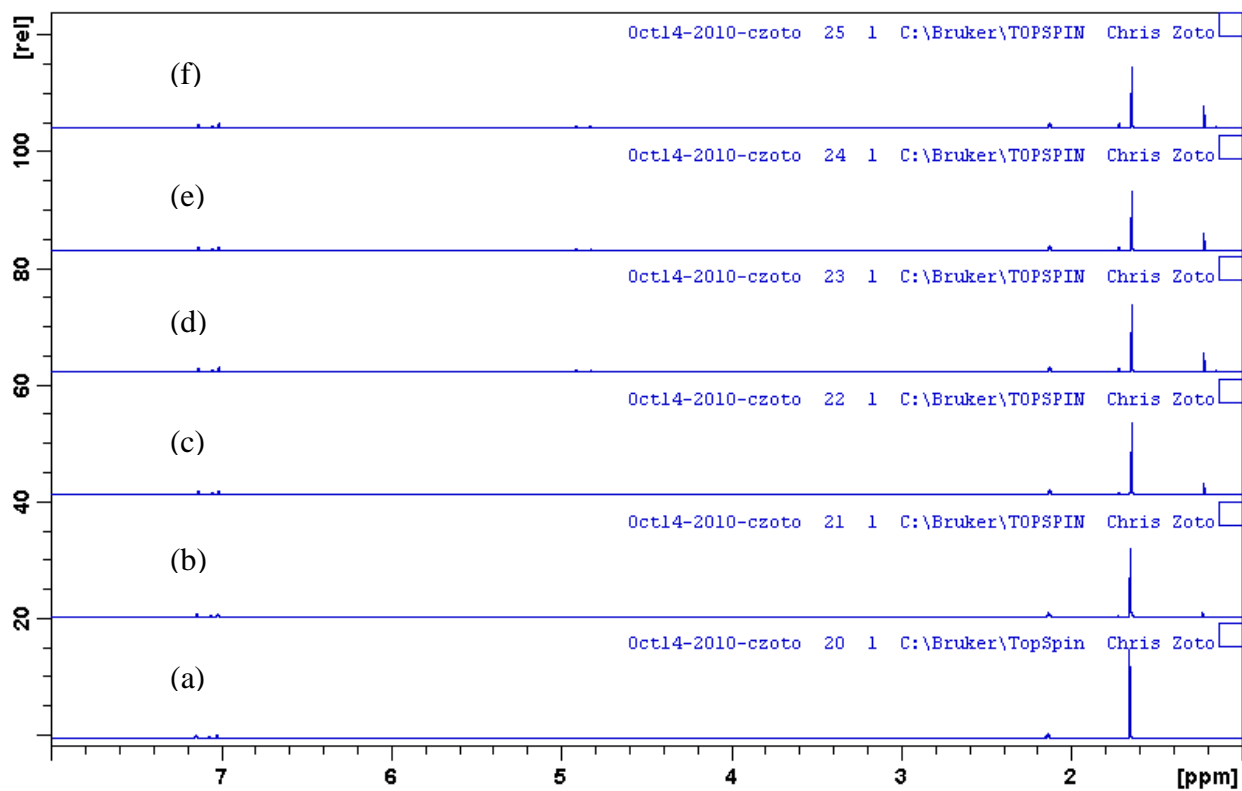
Figure 117. ^{1}H NMR spectra of bis-dmab/TME in toluene-d$_8$ δ 1.0 – 8.0 ppm at (a) 0 min, (b) 5 min, (c) 10 min, (d) 20 min, (e) 30 min, and (f) 60 min of irradiation and O$_2$ bubbling.
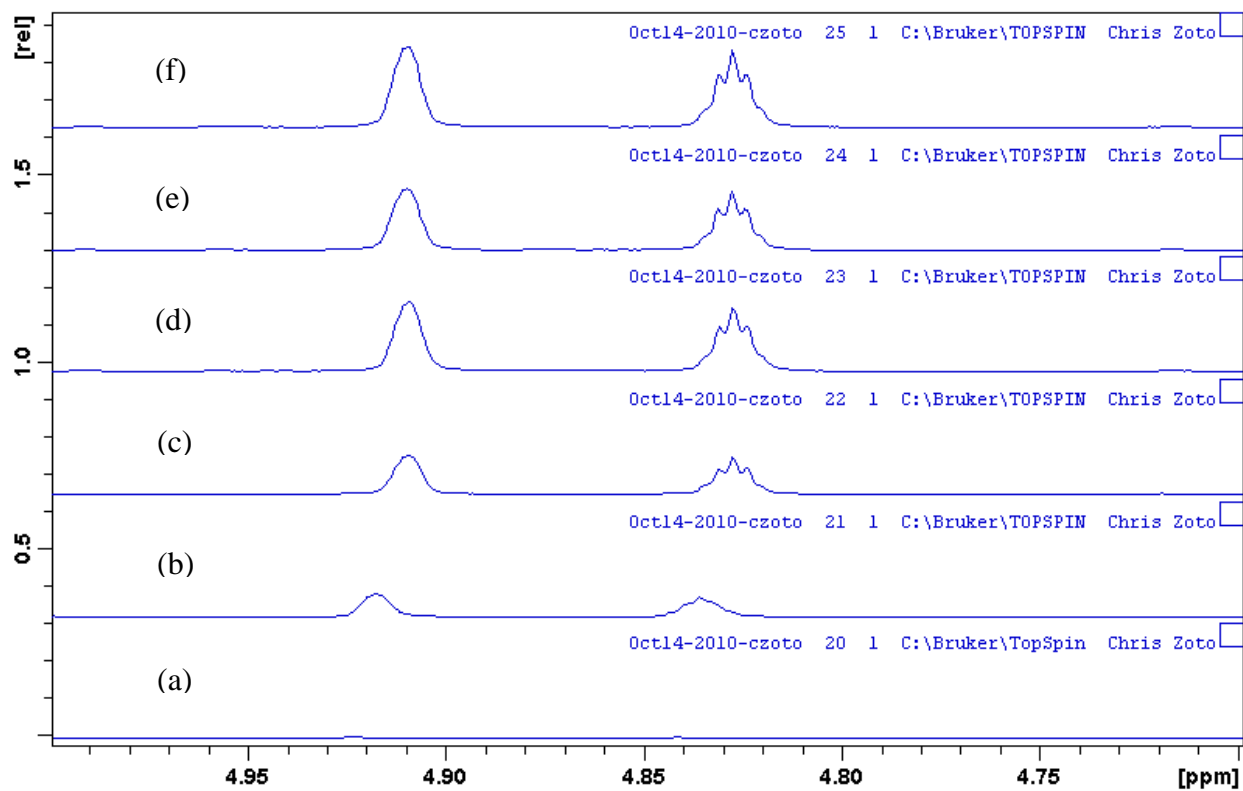
Figure 118. ^{1}H NMR spectra of bis-dmab/TME in toluene-d$_8$ δ 4.7 – 5.0 ppm at (a) 0 min,

(b) 5 min, (c) 10 min, (d) 20 min, (e) 30 min, and (f) 60 min of irradiation and O$_2$ bubbling.
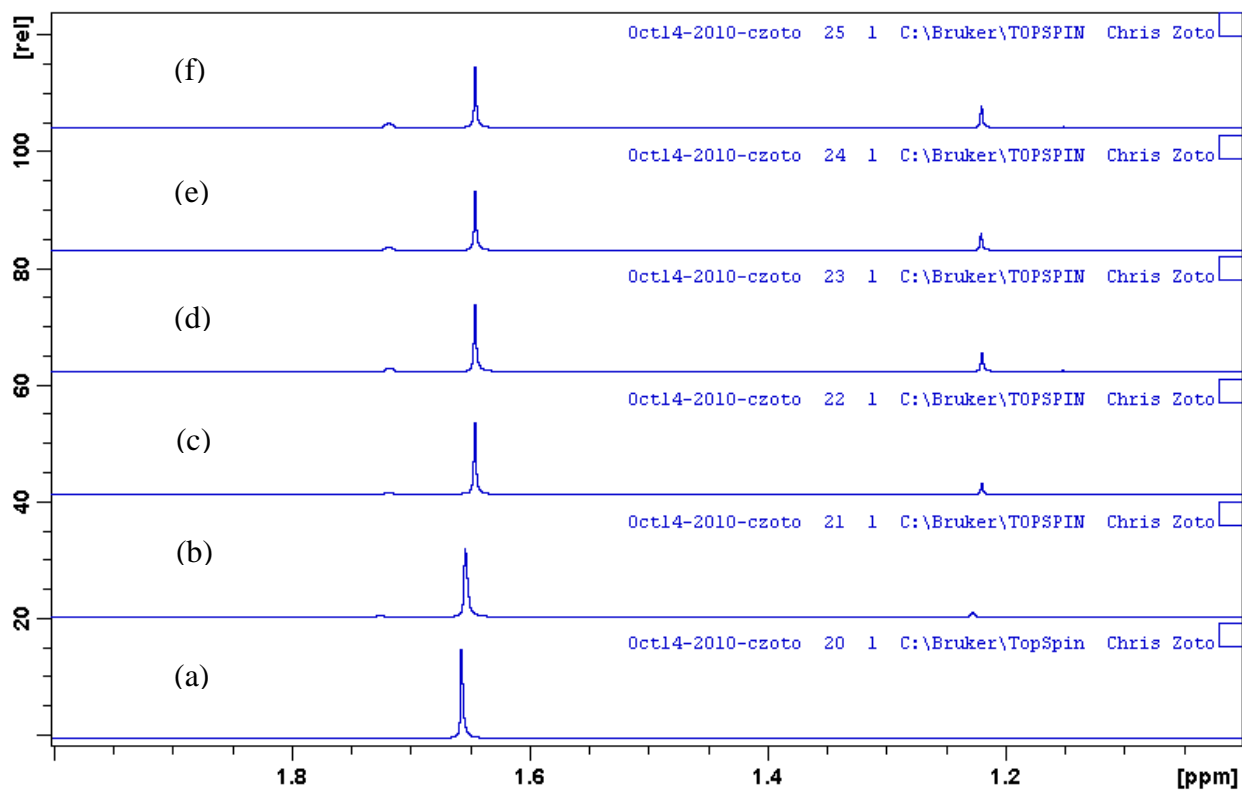
Figure 119. ^{1}H NMR spectra of bis-dmab/TME in toluene-d_8 δ 1.0 – 2.0 ppm at (a) 0 min, (b) 5 min, (c) 10 min, (d) 20 min, (e) 30 min, and (f) 60 min of irradiation and O_2 bubbling.
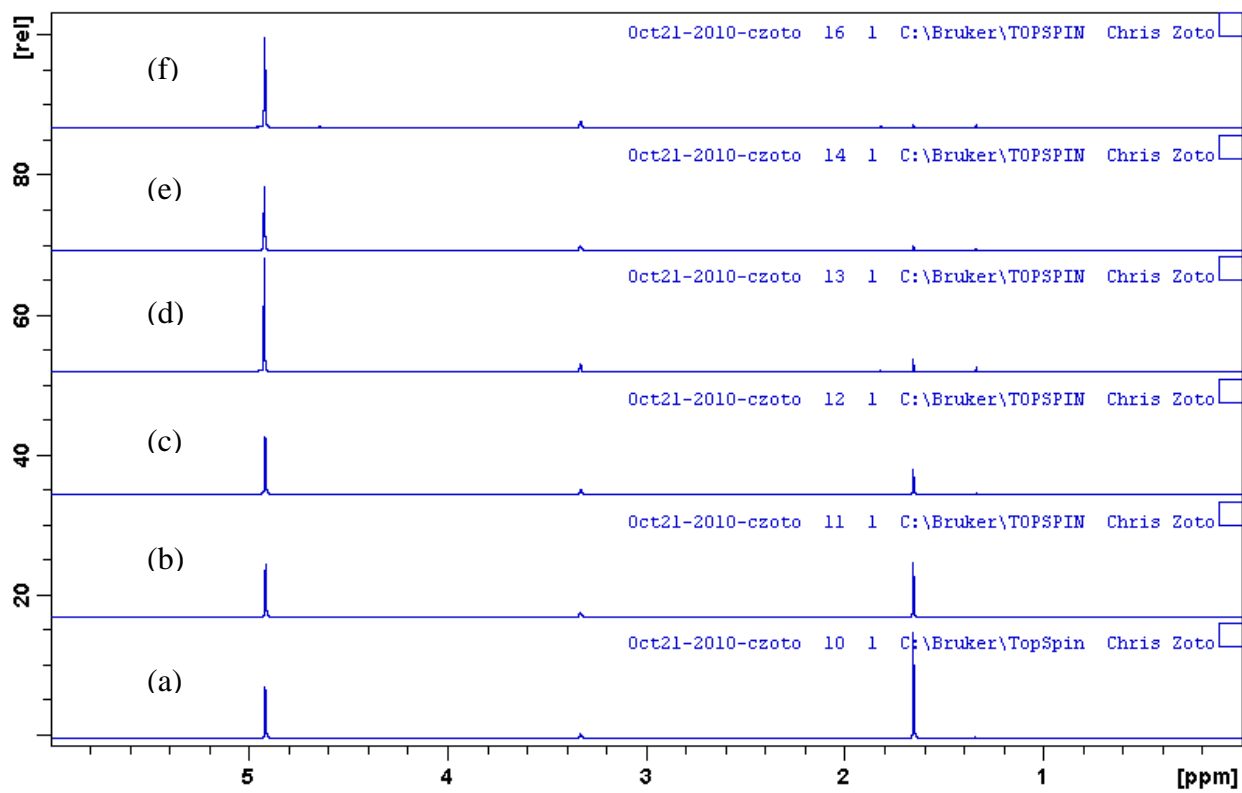
Figure 120. ^{1}H NMR spectra of bis-dmab/TME in methanol-d$_4$ δ 0 – 6.0 ppm at (a) 0 min,

(b) 10 min, (c) 30 min, (d) 60 min, (e) 70 min, and (f) 80 min of irradiation and O$_2$ bubbling.
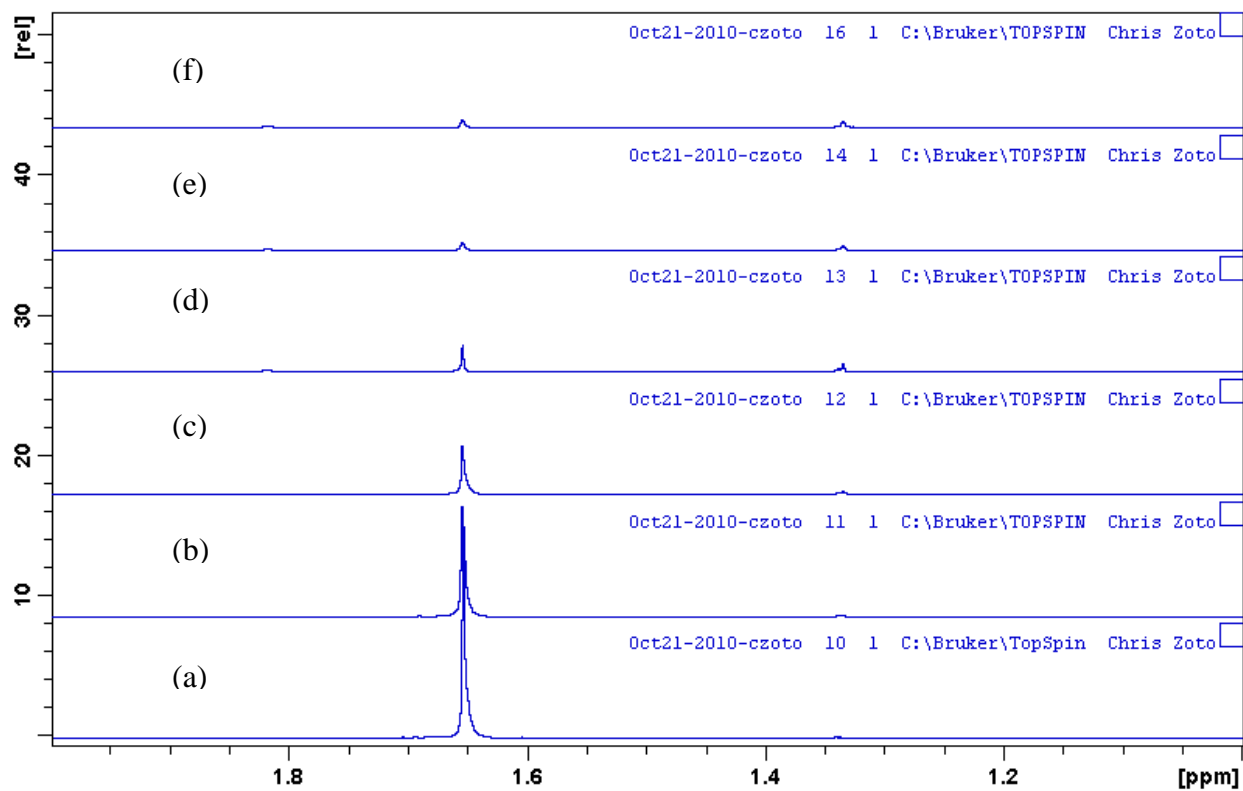
Figure 121. ^{1}H NMR spectra of bis-dmab/TME in methanol-d_4 δ 1.0 – 2.0 ppm at (a) 0 min, (b) 10 min, (c) 30 min, (d) 60 min, (e) 70 min, and (f) 80 min of irradiation and O_2 bubbling.

4.5.3 Self-Sensitized Photooxidation of bis-dmab: ^{1}H NMR Study

The self-sensitized photooxidation of bis-dmab was carried out in chloroform-d with a 400 nm cut-on filter. A concentrated solution of bis-dmab in chloroform-d was prepared, simultaneously irradiated and bubbled with O_2, monitoring the course of the photooxidation reaction by ^{1}H NMR spectroscopy at various irradiation/oxygen bubbling intervals. Figures 122 - 127 show both zoomed in and zoomed out ^{1}H NMR spectral data for the photooxidation study of bis-dmab in chloroform-d at 0, 75, 150, 175, and 225 minutes of irradiation and bubbling. As shown in the ^{1}H NMR spectra, starting bis-dmab peaks at t = 0 mins decrease with respect to increased irradiation and bubbling. The emergence of signal peaks at δ 9.68 (s), 8.52 (s), 7.68 (d), 7.58 (d), 6.65 (d), 3.02 (s), 2.993 (s), and 2.990 (s) ppm were observed. Specifically, accurate integration of emerged ^{1}H NMR signals at δ 9.68 (s, 1H), 7.68 (d, 2H), and 3.02 ppm (s, 6H) confirmed the structural identity of 4-dimethylaminobenzaldehyde as one of the observed photooxidized products of bis-dmab. However, accurate integration of the emerged doublet at δ 6.65 ppm could not be obtained due to off-baselining. Emerged peaks of 4-dimethylaminobenzaldehyde are identified by the asterisks.

In addition, the ^{1}H NMR spectrum of the bis-dmab/CDCl$_3$ solution at t = 225 minutes of irradiation/bubbling was compared to the ^{1}H NMR spectrum of commercially available 4-dimethylaminobenzaldehyde (99%, Sigma-Aldrich) in CDCl$_3$ and the peaks consistently lined up (as shown in Figures 128 - 131). The ^{1}H NMR spectrum of 4-dimethylaminobenzaldehyde consists of a singlet at δ 9.77 ppm (1H, aldehyde proton), two doublets at δ 7.68 (2H) and 6.64 ppm (2H), which are aromatic protons and a singlet at δ 3.01 ppm (6H, -N(CH$_3$)$_2$ protons).
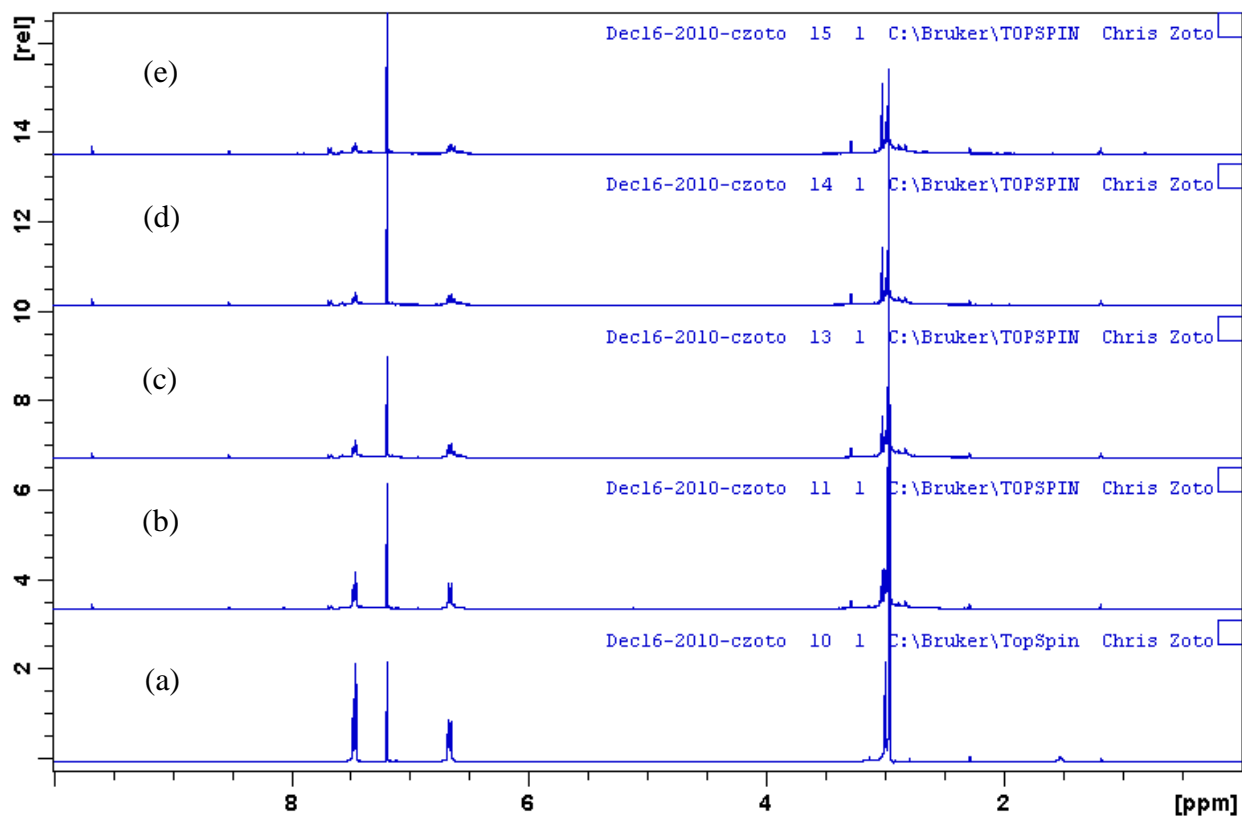
Figure 122. ^{1}H NMR spectra of bis-dmab in CDCl$_3$ δ 0 – 10.0 ppm at (a) 0 min, (b) 75 min, (c) 150 min, (d) 175 min, and (e) 225 min of irradiation and O$_2$ bubbling.
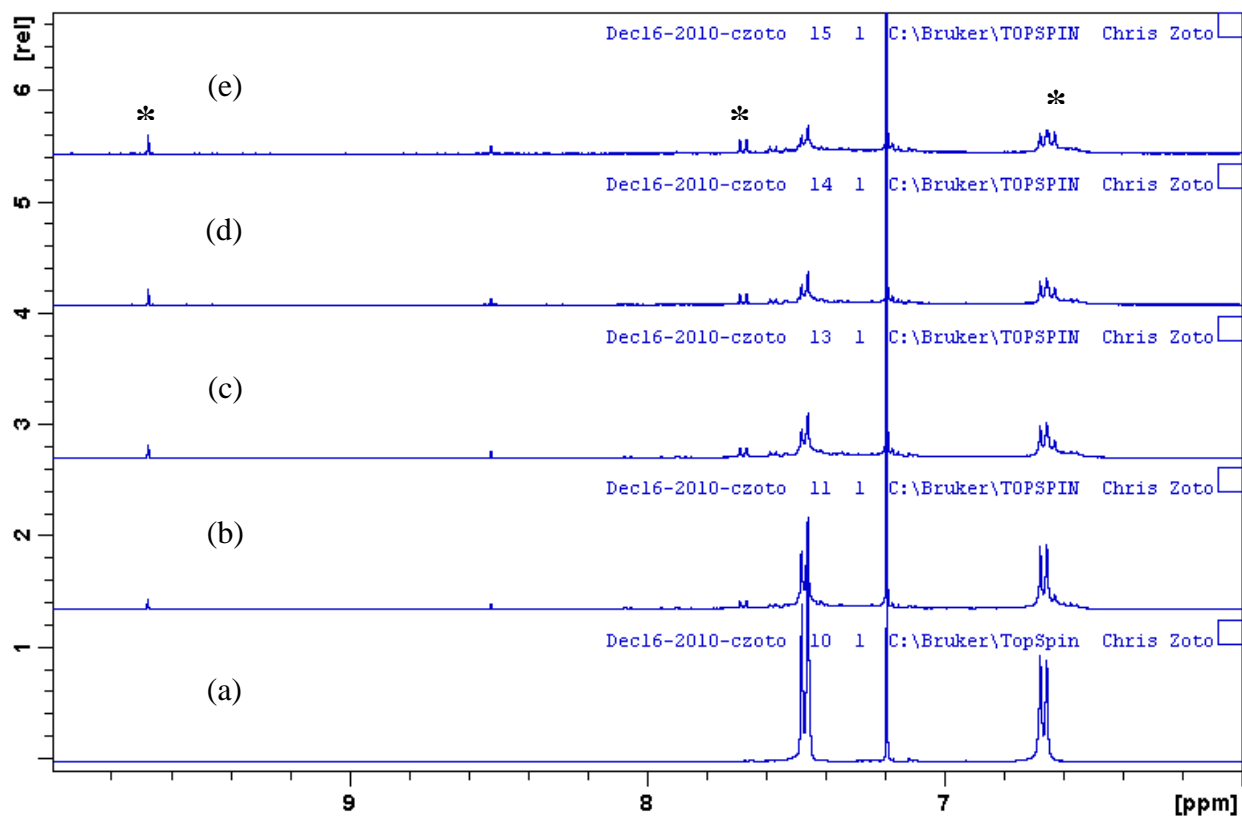
Figure 123. ^{1}H NMR spectra of bis-dmab in $CDCl_3$ δ 6.0 − 10.0 ppm at (a) 0 min, (b) 75 min, (c) 150 min, (d) 175 min, and (e) 225 min of irradiation and O_2 bubbling.
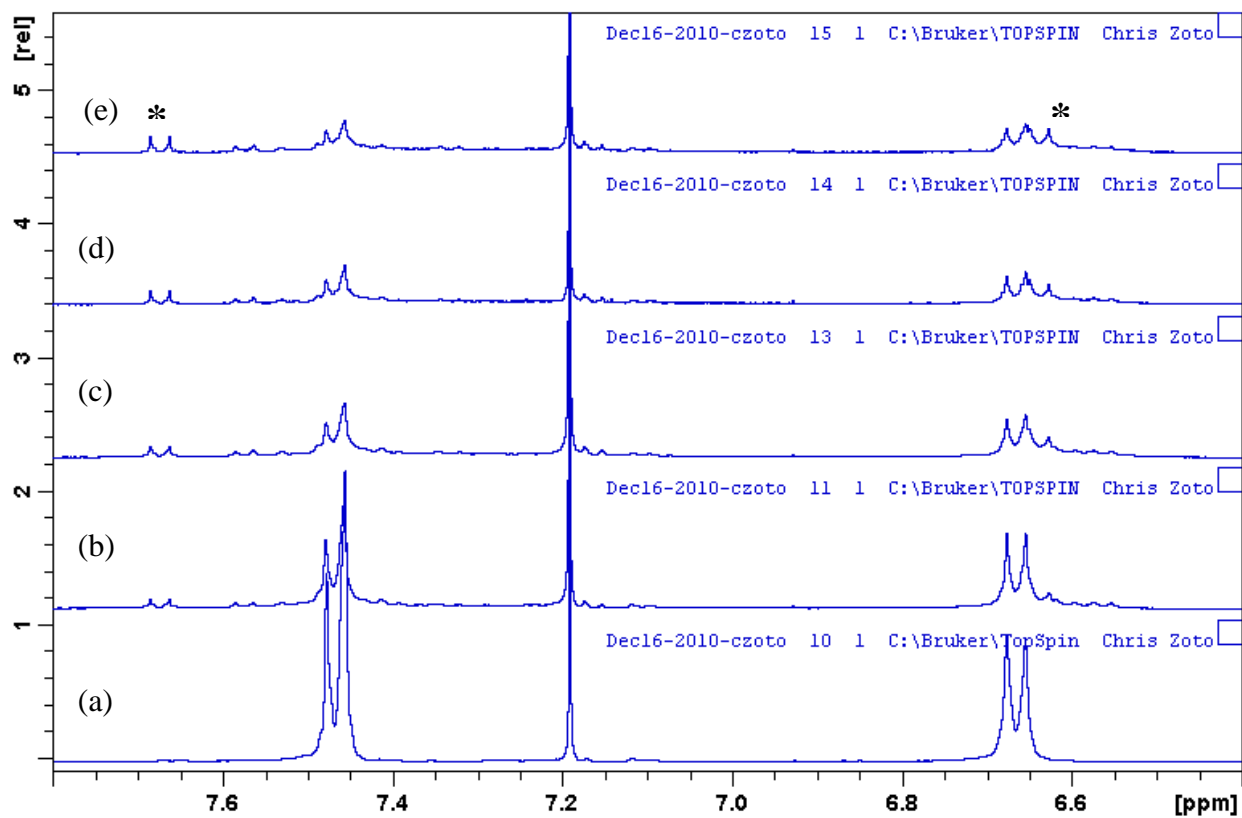
Figure 124. ^{1}H NMR spectra of bis-dmab in $CDCl_3$ δ 6.4 – 7.8 ppm at (a) 0 min, (b) 75 min, (c) 150 min, (d) 175 min, and (e) 225 min of irradiation and O_2 bubbling.
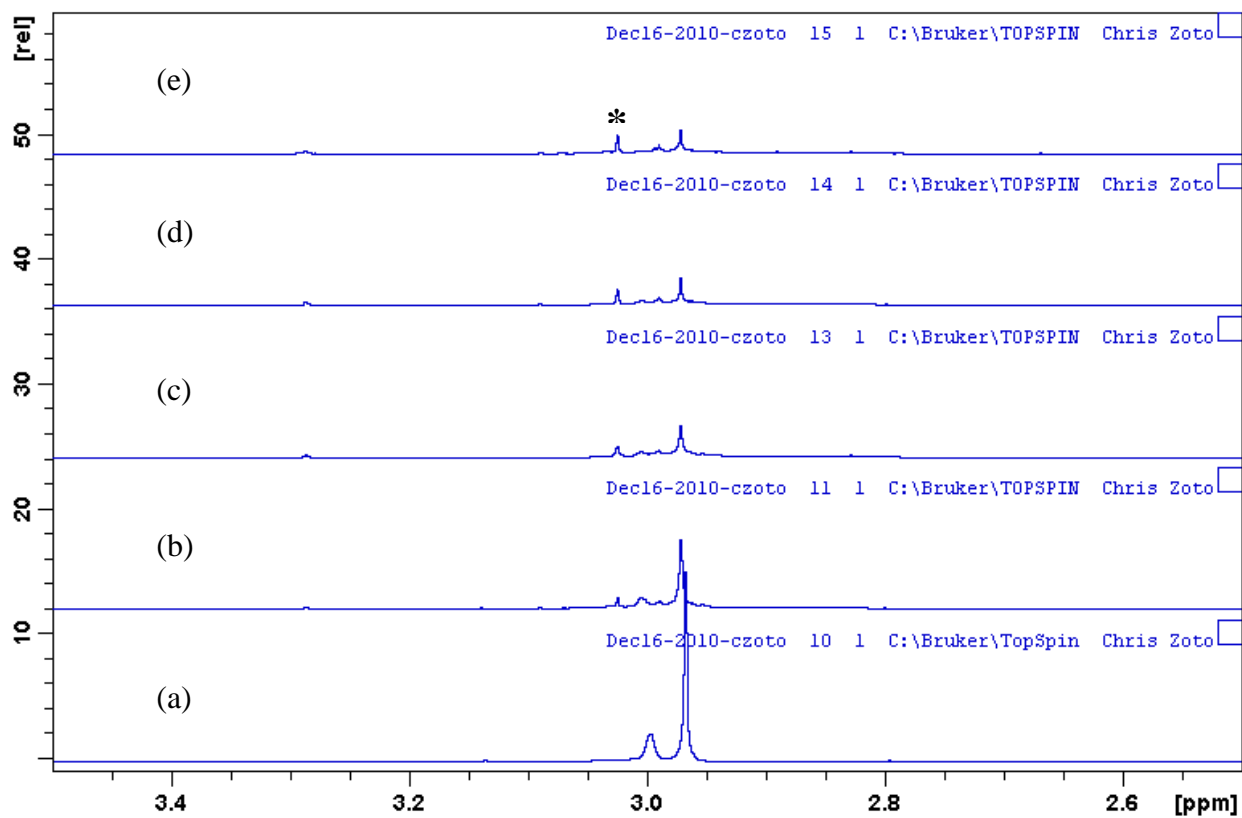
Figure 125. ^{1}H NMR spectra of bis-dmab in CDCl$_3$ δ 2.5 – 3.5 ppm at (a) 0 min, (b) 75 min, (c) 150 min, (d) 175 min, and (e) 225 min of irradiation and O$_2$ bubbling.
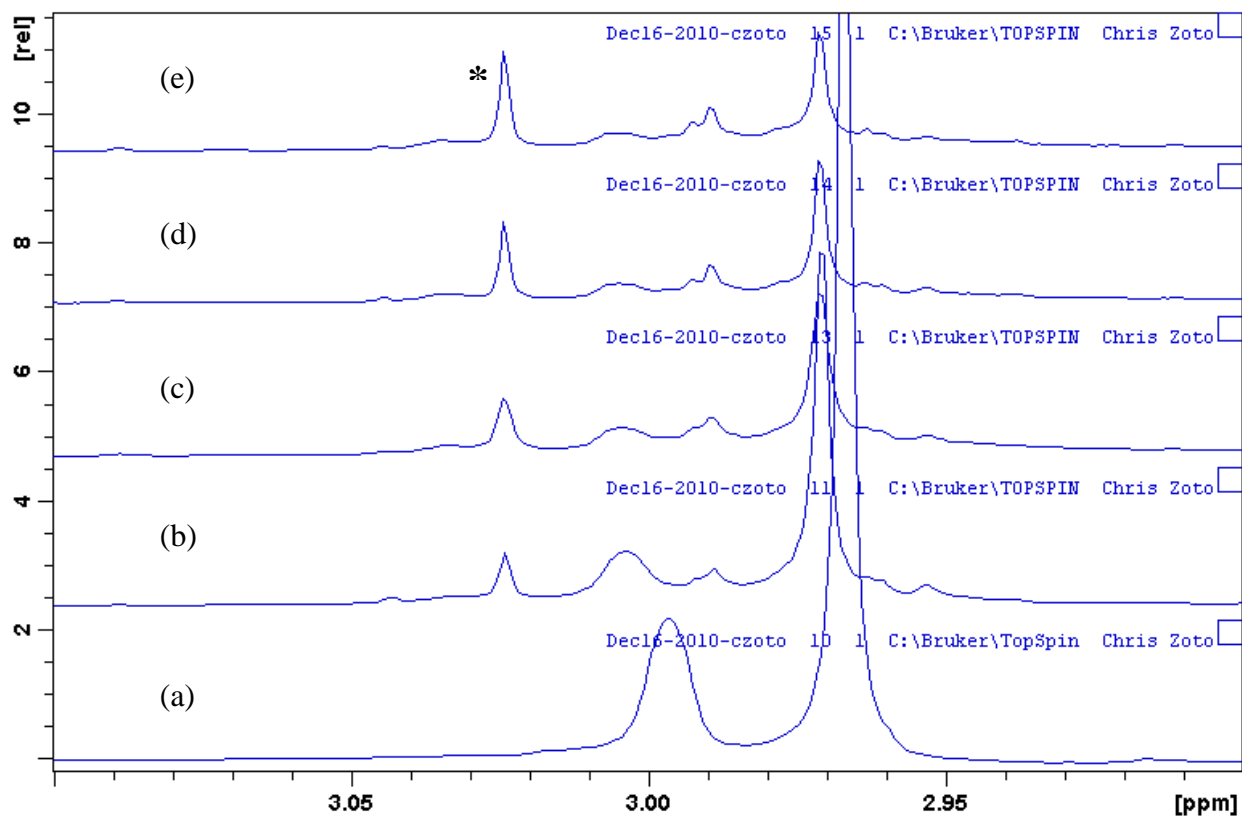
Figure 126. ^{1}H NMR spectra of bis-dmab in CDCl$_3$ δ 2.9 – 3.1 ppm at (a) 0 min, (b) 75 min, (c) 150 min, (d) 175 min, and (e) 225 min of irradiation and O$_2$ bubbling.
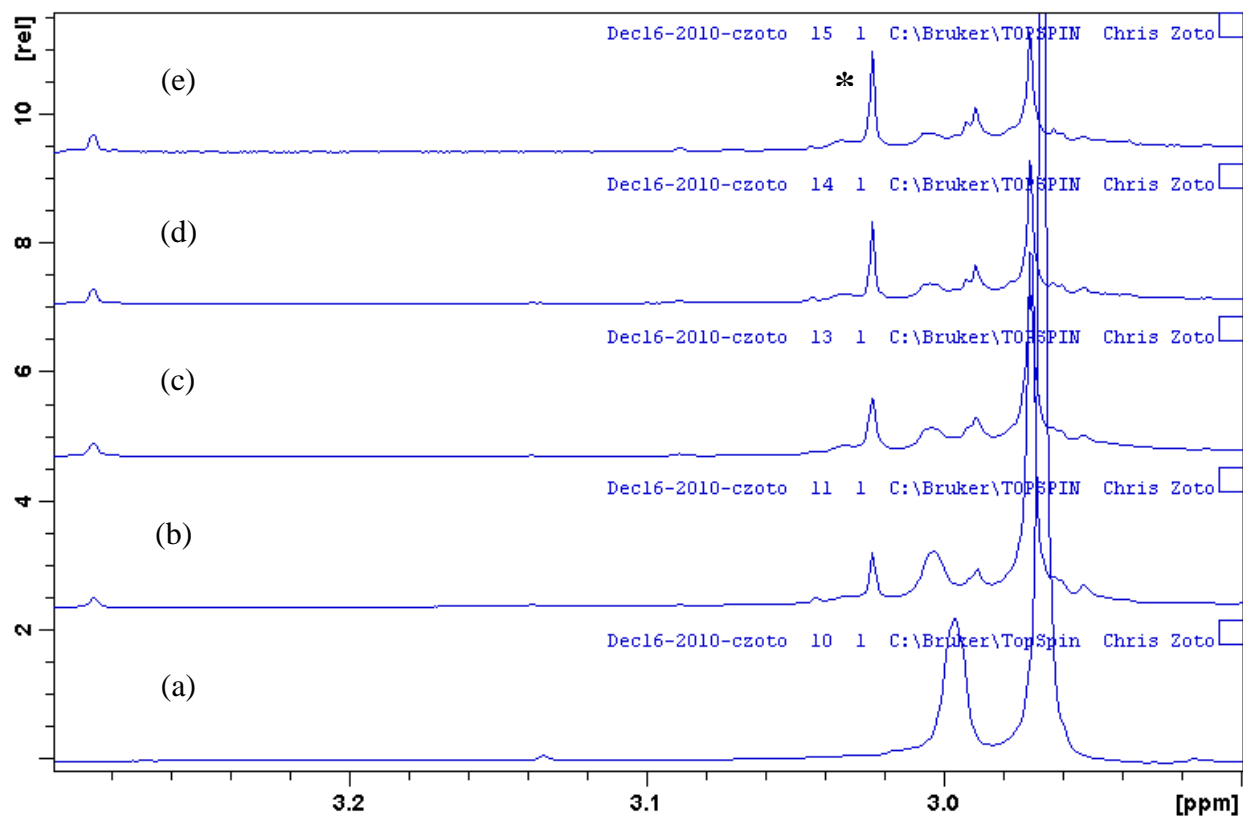
Figure 127. ^{1}H NMR spectra of bis-dmab in $CDCl_3$ δ 2.9 – 3.3 ppm at (a) 0 min, (b) 75 min, (c) 150 min, (d) 175 min, and (e) 225 min of irradiation and O_2 bubbling.
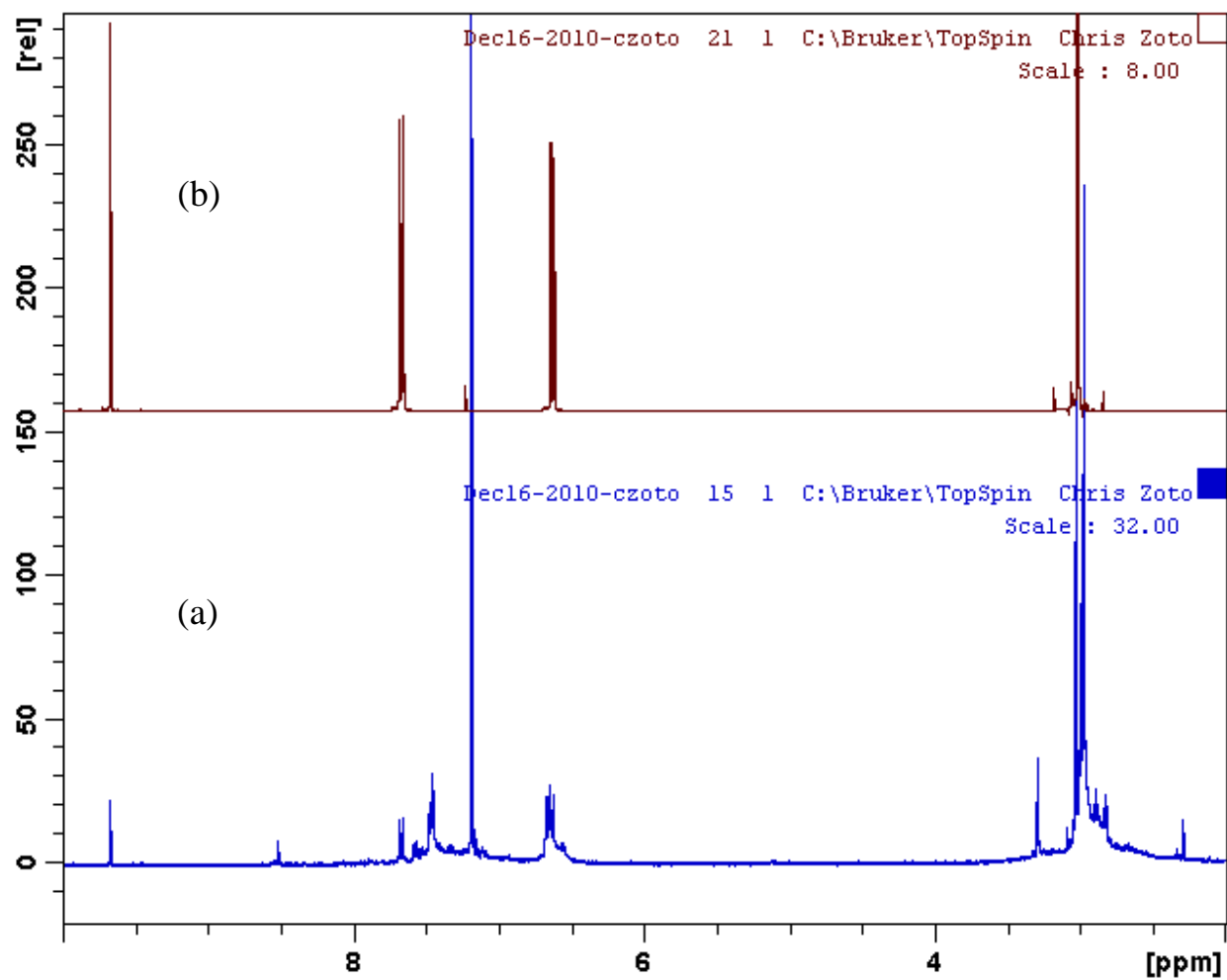
Figure 128. ^{1}H NMR spectra of (a) bis-dmab in CDCl$_3$ at t = 225 min irradiation/bubbling, and

(b) 4-dimethylaminobenzaldehyde in CDCl$_3$ δ 2.0 – 10.0 ppm.
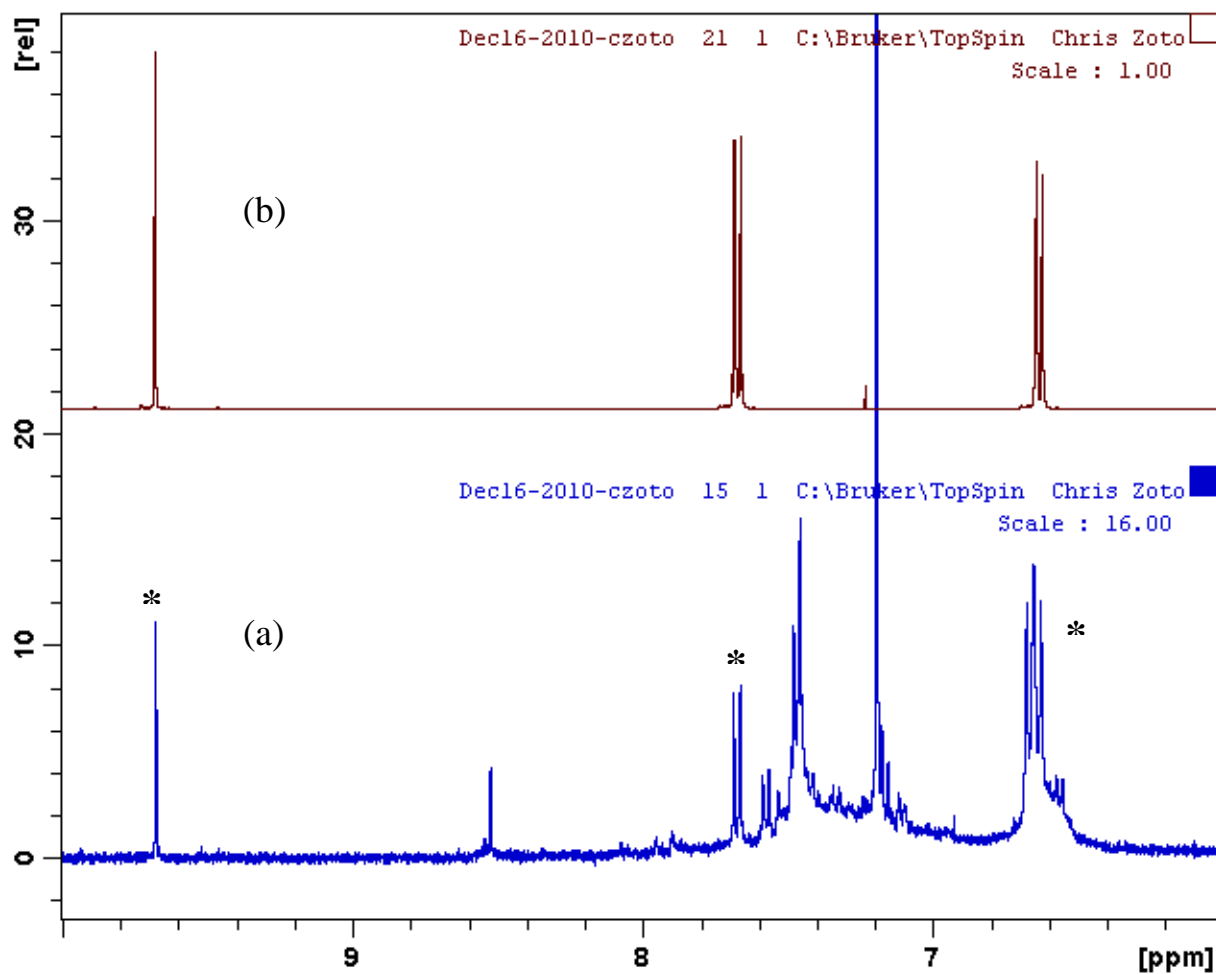
Figure 129. ^{1}H NMR spectra of (a) bis-dmab in CDCl$_3$ at t = 225 min irradiation/bubbling, and (b) 4-dimethylaminobenzaldehyde in CDCl$_3$ δ 6.0 − 10.0 ppm.
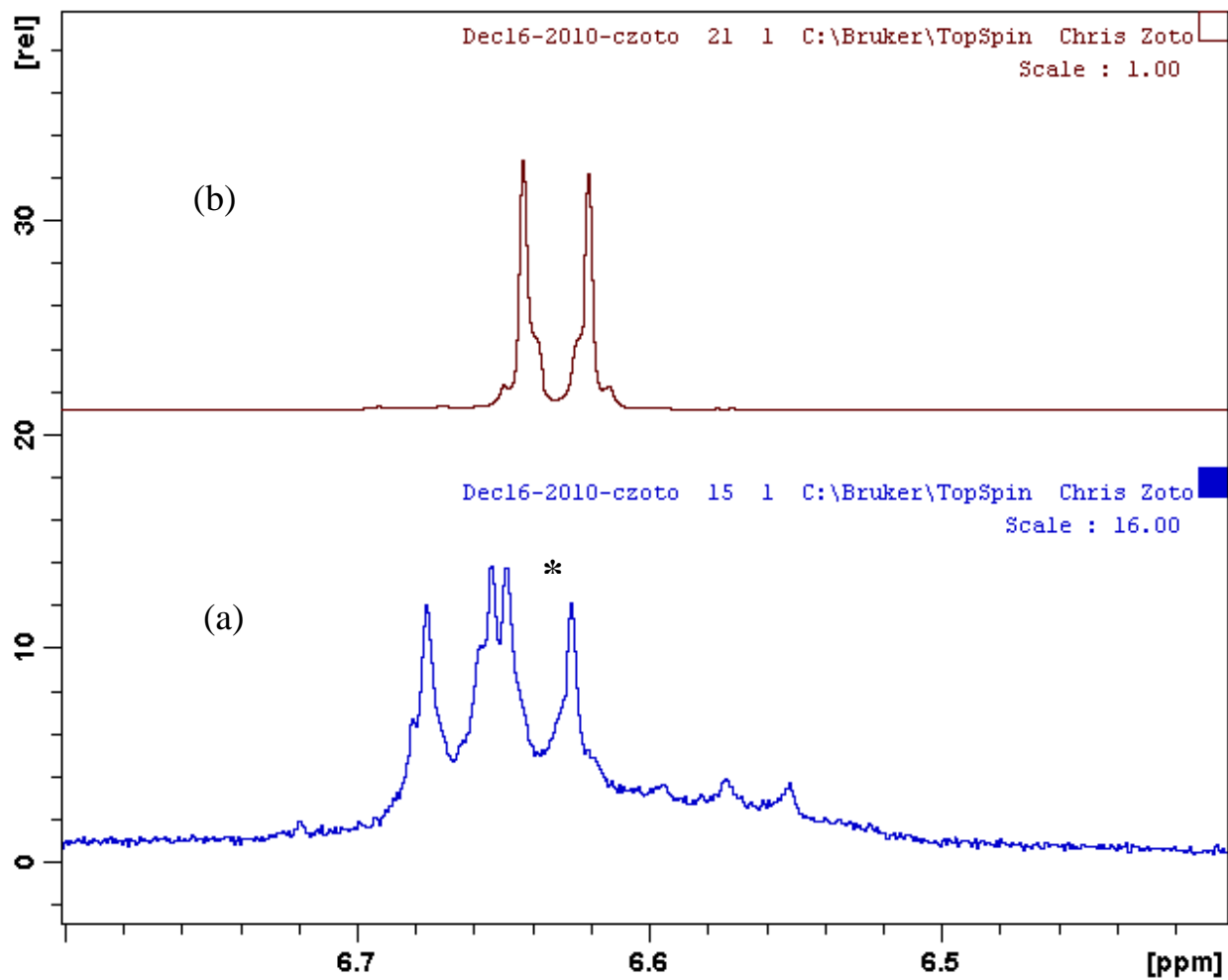
Figure 130. ^{1}H NMR spectra of (a) bis-dmab in CDCl$_3$ at t = 225 min irradiation/bubbling, and

(b) 4-dimethylaminobenzaldehyde in CDCl$_3$ δ 6.4 – 6.8 ppm.
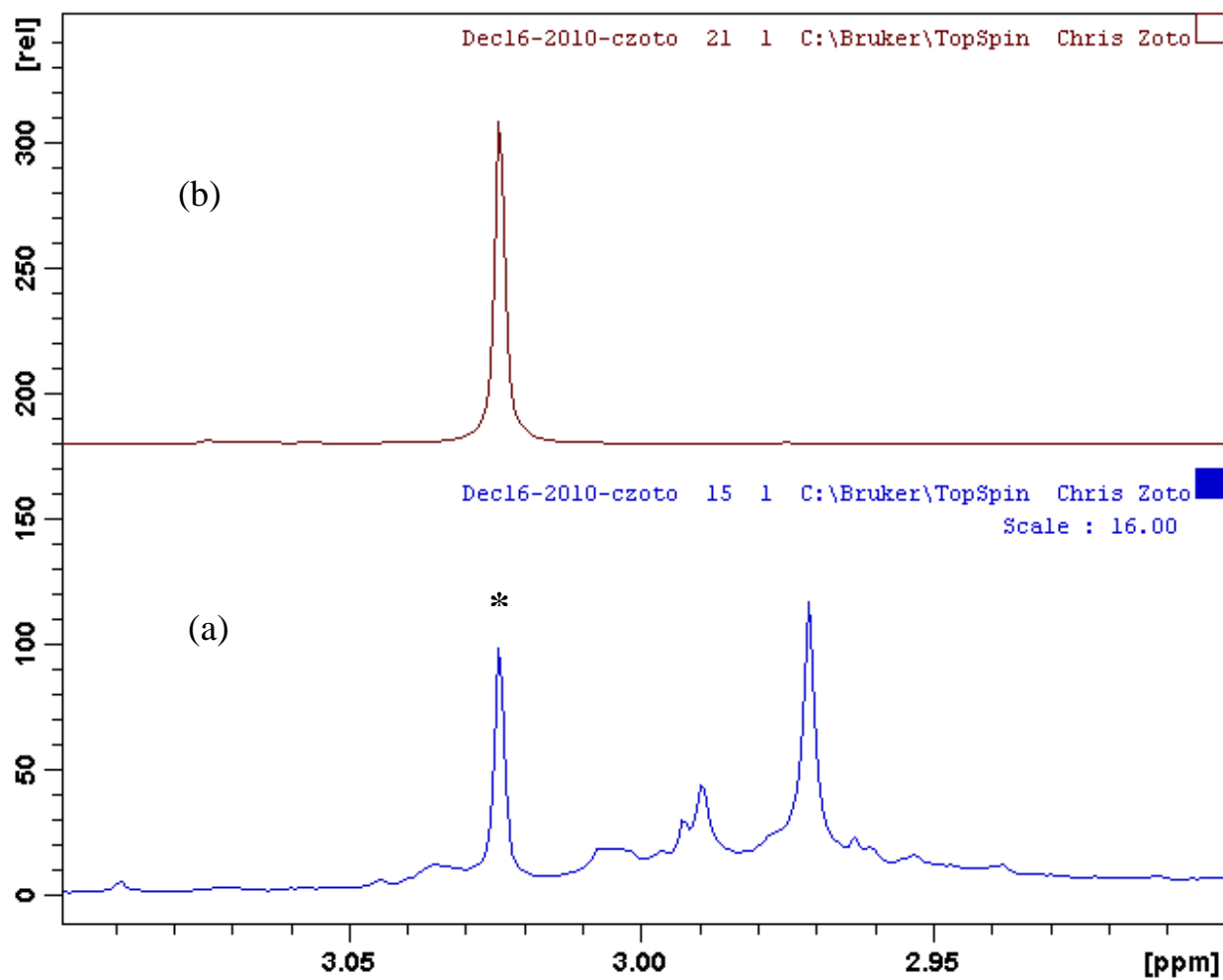
Figure 131. ^{1}H NMR spectra of (a) bis-dmab in CDCl$_3$ at t = 225 min irradiation/bubbling, and

(b) 4-dimethylaminobenzaldehyde in CDCl$_3$ δ 2.9 − 3.1 ppm.

A proposed two step mechanism for the photooxidation reaction (Figure 132) involves the $[2\pi + 2\pi]$ cycloaddition of bis-dmab with $^1O_2$, producing the corresponding endoperoxide as an intermediate, which due to its thermal instability, breaks down into 4-dimethylaminobenzaldehyde and (E)-3-(4-dimethylaminobenzylidene)-1,2-cyclopentadione. Hypothetically, the emerged ^1H NMR signals at δ 8.52 (s), 7.58 (d), 2.993 (s), and 2.990 (s) ppm represent the dione. Integrations were carried out on the other emerged ^1H NMR signals and it is shown that when calibrating the singlet at δ 8.52 ppm to 1, believed to be the vinyl H, the doublet at δ 7.58 ppm integrates to approximately 4 (aromatic doublets), and the closely spaced peaks at δ 2.993 and 2.990 ppm approximately integrate to 4 and 6 (2 x CH_2 and $-N(CH_3)_2$ protons), which are consistent with the chemical structure of the dione.

The proposed mechanism for the photooxidation of bis-dmab shown in Figure 132 is supported by previously published work on 1,2-cycloaddition reactions of olefinic (ene) systems with $^1O_2$, followed by cleavage of endoperoxide intermediates [73, 74]. Murthy, *et al.* [73] tested the singlet oxygen photosensitization of a series of olefinic systems and have demonstrated in their studies that $^1O_2$ reacts with the 'ene' photosensitizer in a 1,2-cycloaddition reaction, generating an endoperoxide intermediate, which breaks down into two carbonyl compounds. In addition, Cabrerizo, *et al.* [74] have studied the reactions of $^1O_2$ with heteroaromatic compounds, specifically multisubstituted pyrazines, that react with $^1O_2$, yielding an endoperoxide, which breaks down into a unimolecular dicarbonyl compound.
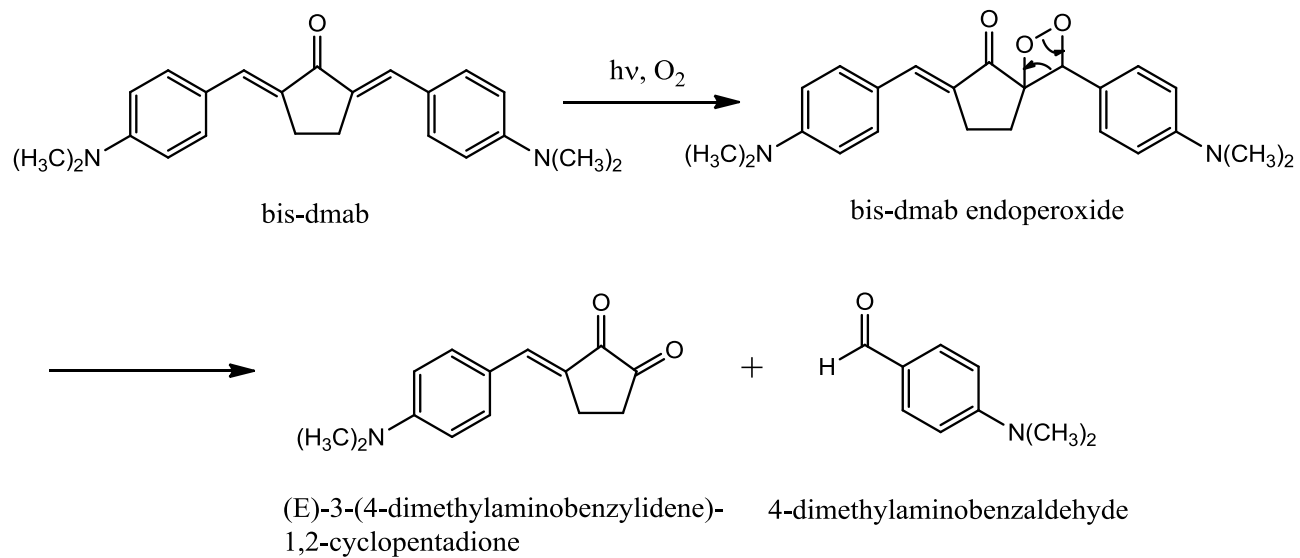
Figure 132. Proposed two step reaction scheme for the photooxidation of bis-dmab.

4.5.4 Photochemistry of bis-dmab: UV-Vis Absorption Study

Photochemistry experiments presented in this section were monitored by UV-Vis absorption spectroscopy, scanning the absorption spectrum at various irradiation/bubbling intervals. Two sets of photochemistry experiments were carried out for each bis-dmab/solvent system. The first set consisted of examining the photochemistry of bis-dmab in the presence of oxygen as a means of studying the photooxidized products. The second set consisted of studying the photochemistry of bis-dmab in a deoxygenated solvent; that is, with continuous degassing by N_2 as a means of studying the resulting photoproduct.

As mentioned in Chapter 2, Doroshenko and Pivovarenko have studied the photochemistry of the julolidine analogue of bis-dmab in toluene and methanol, their compound V [22]. In their irradiation experiments, they found phototransformation of V in toluene, which they attributed the spectral changes to (E,E) → (E,Z) photoisomerization. They asserted that photoisomerization is dependent upon the population of the excited triplet state. However, it was found that no photochemistry of V was observed in methanol.

Figure 133 shows the absorption spectra of bis-dmab in toluene under N_2 at various irradiation times. As shown in Figure 133, the absorption band with $\lambda_{max} = 453$ nm is reduced and the band at $\lambda = 330$ nm increases with an isosbestic point at $\lambda = 367$ nm. The spectral changes and isosbestic point are typical of *trans-cis* photoisomerization of α,β-unsaturated ketones, as observed with the photochemistry of V reported by Doroshenko and Pivovarenko [22].

Figure 134 shows the series of UV-Vis absorption spectra of bis-dmab in toluene with a stream of O_2 bubbling at various irradiation times. As observed, the first absorption band at

453 nm decreases and the band at 330 nm increases with respect to irradiation time. However, the emergence of a spectral band centered at λ 370 nm is observed, which was not seen in the absorption spectral data for the deoxygenated sample. From ^{1}H NMR studies, the photooxidized product at 330 nm was confirmed to be 4-dimethylaminobenzaldehyde, and as depicted in Figure 134, the emerged spectral band centered at λ 330 nm conforms well with the absorption spectrum of commercially available 4-dimethylaminobenzaldehyde in toluene (represented by the dashed line). It is proposed that the emerged spectral band centered at λ 390 nm represents absorption of the alkylaminosubstituted 1,2-cyclopentadione.
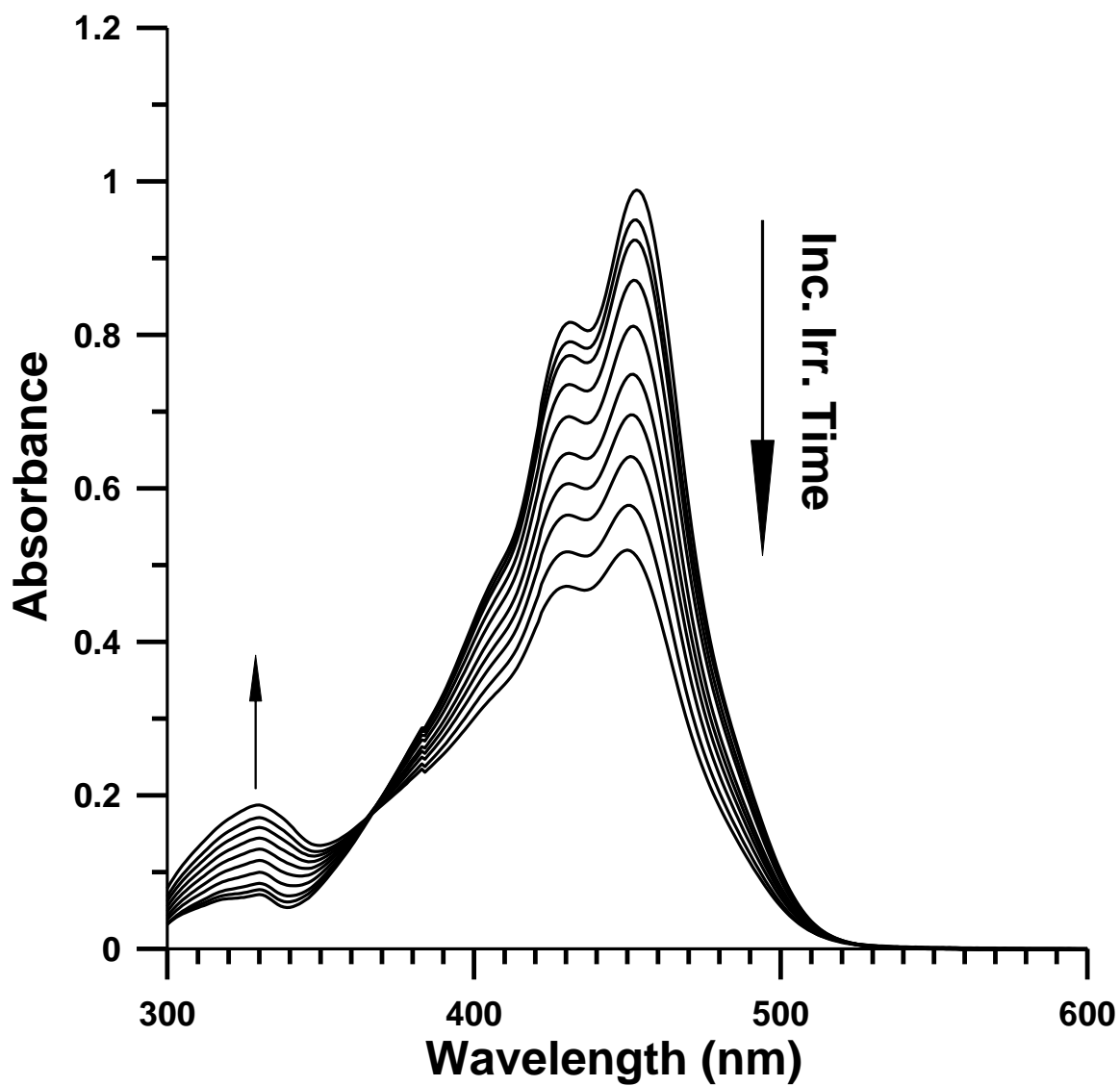
Figure 133. Absorption spectra of bis-dmab in toluene under bubbling of N_2 at t = 0, 10, 30, 60, 90, 120, 150, 180, 210 and 240 minutes of irradiation.
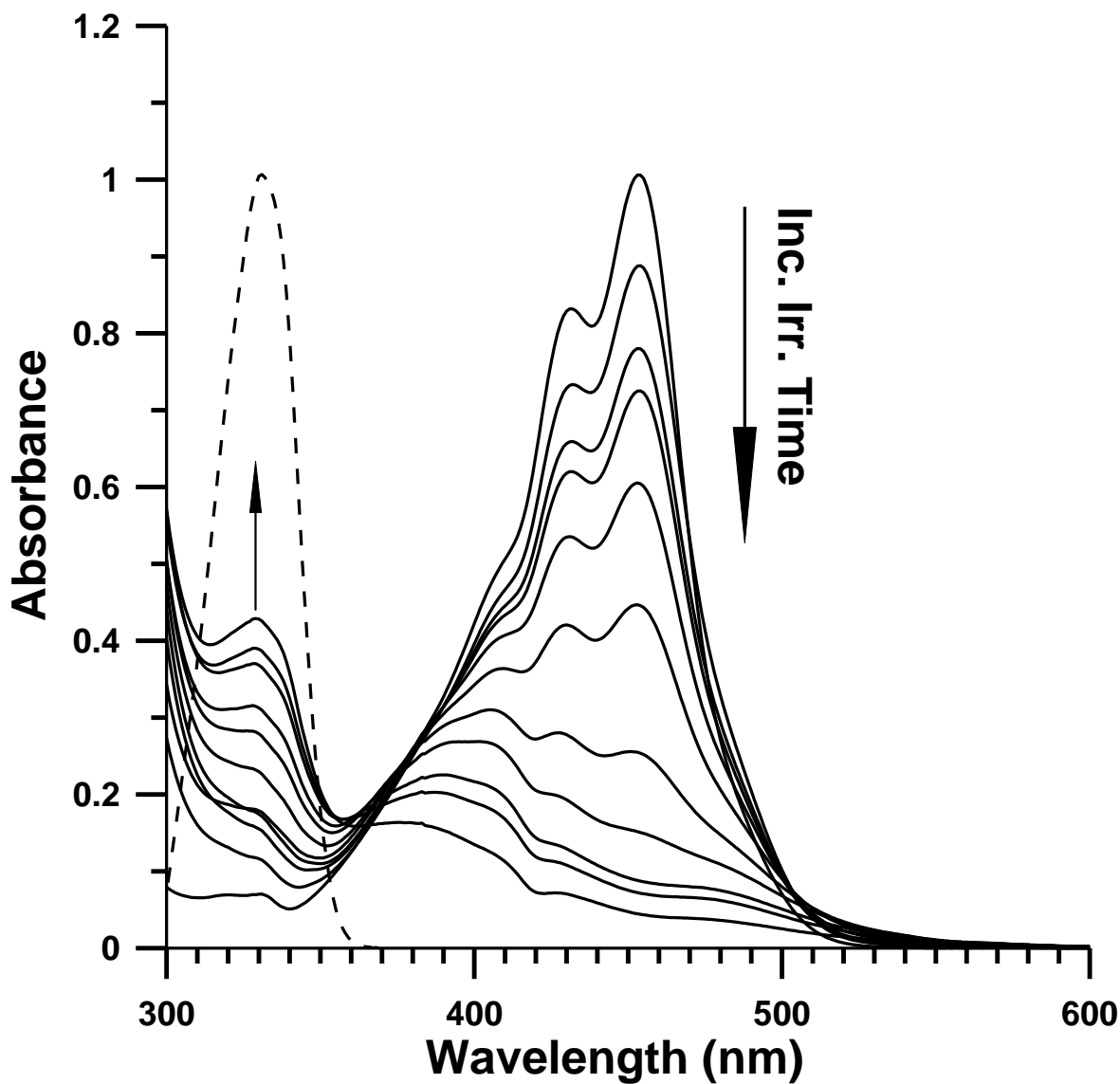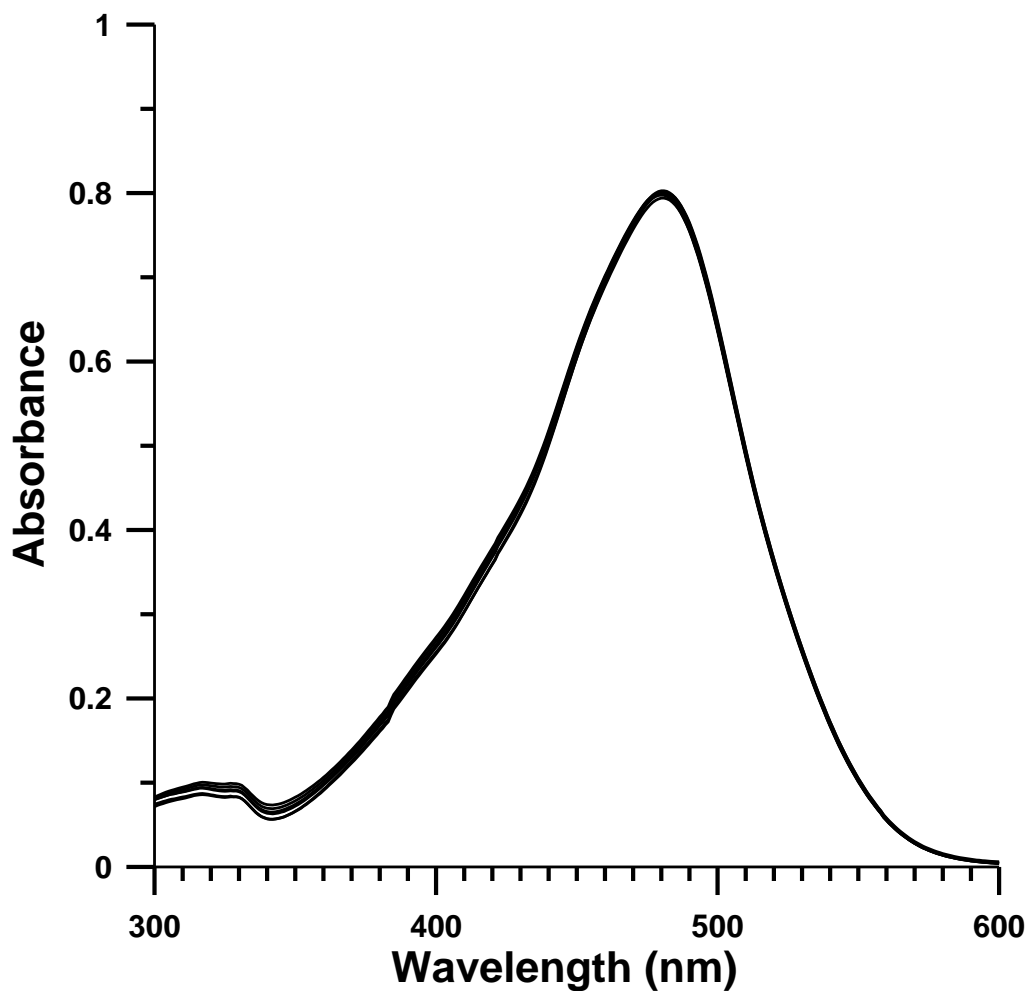
Figure 134. Absorption spectra of bis-dmab in toluene under bubbling of O_2 at t = 0, 1, 2, 3, 5, 7, 10, 16, 20, 25, and 40 minutes of irradiation. Absorption spectrum of 4-dimethylaminobenzaldehyde in toluene is represented by the dashed line (λ_{max} = 331 nm).

A dark experiment was carried out for a solution of bis-dmab in toluene, which involved wrapping the solution with Al foil and bubbling the sample with O_2. The purpose of this experiment was to confirm that bis-dmab is reacting with singlet oxygen and not ground state triplet oxygen. Figure 135 shows the absorption spectra of bis-dmab in toluene for the dark experiment at t = 0 mins and t = 40 mins with no spectral changes observed. From this experiment, it was confirmed that bis-dmab reacts with $^1O_2$ and not $^3O_2$.
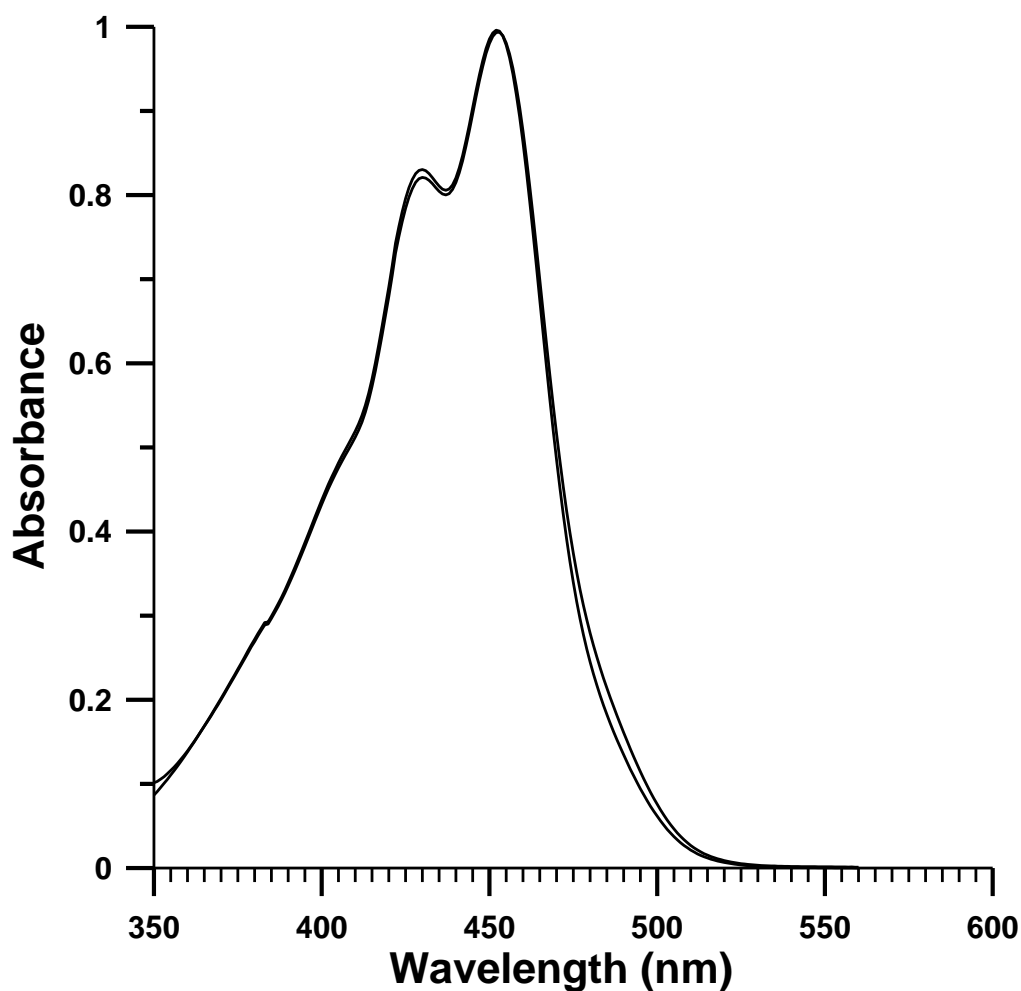
Figure 135. Absorption spectra of bis-dmab in toluene under bubbling of $^3O_2$ at t = 0 and 40 minutes (dark experiment).

Figure 136 shows the set of UV-Vis absorption spectra of bis-dmab in chloroform under a deoxygenated environment. The same trend was observed in chloroform as with in toluene. In Figure 136, the absorption band at $\lambda_{max} = 467$ nm decreases and the minor band centered at $\lambda = 330$ nm increases with an isosbestic point at $\lambda = 407$ nm.
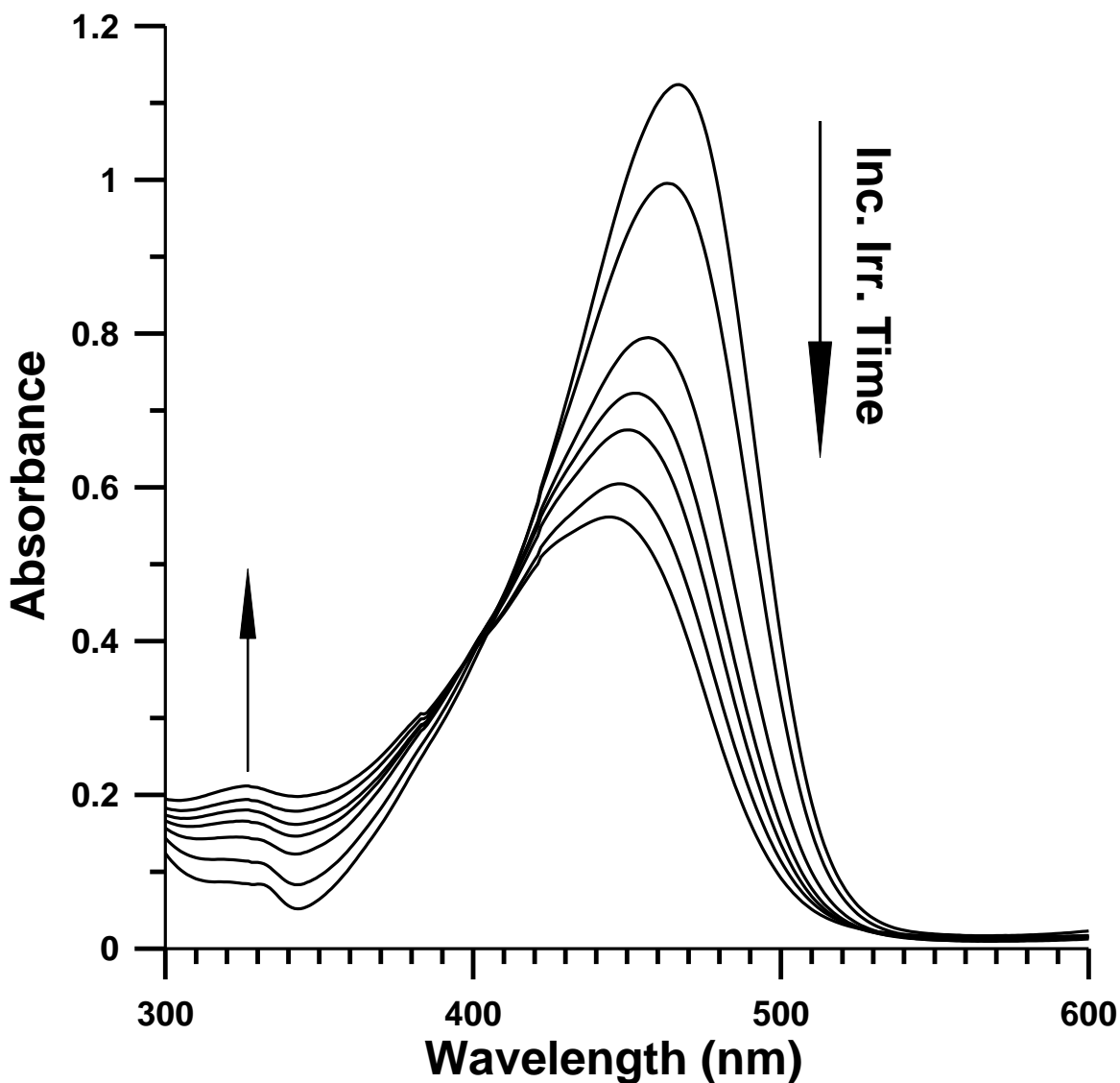
Figure 136. Absorption spectra of bis-dmab in chloroform under bubbling of N_2 at t = 0, 25, 45, 65, 85, 105, and 135 minutes of irradiation.

Figure 137 shows the set of absorption spectra of bis-dmab in chloroform under bubbling of O_2 at various irradiation times. The same trend was observed in chloroform as with in toluene under O_2. The emergence of two absorption bands centered at $\lambda \sim 330$ nm (confirmed to be absorption of 4-dimethylaminobenzaldehyde) and $\lambda \sim 400$ nm (proposed secondary photooxidized product) were observed.
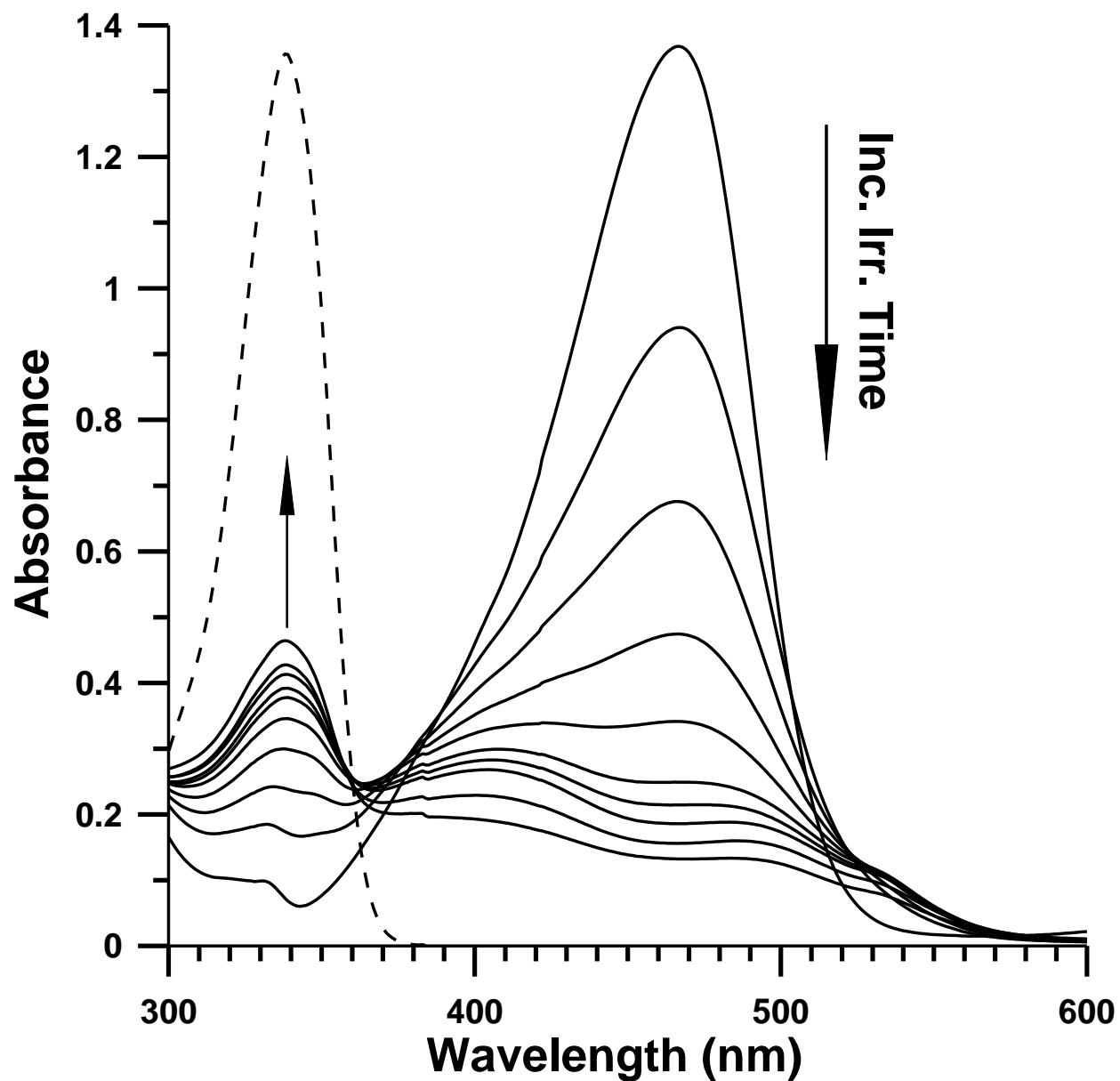
Figure 137. Absorption spectra of bis-dmab in chloroform under bubbling of O_2 at t = 0, 2, 4, 6, 8, 11, 14, 20, 30, and 60 minutes of irradiation. Absorption spectrum of 4-dimethylaminobenzaldehyde in chloroform is represented by the dashed line (λ_{max} = 338 nm).

Photolysis studies of bis-dmab under O_2 and N_2 were also carried out in acetonitrile, as shown in Figures 138 and 139, respectively. Figure 138 shows an analogous trend for the photochemistry of bis-dmab under N_2, with a decrease in the absorption band at $\lambda_{max} = 455$ nm and an increase in the spectral band centered at $\lambda = 323$ nm with an isosbestic point centered at approximately λ 370 nm in between both absorption bands. Figure 139 shows that irradiation and O_2 bubbling of a solution of bis-dmab in acetonitrile results in reduction of the S_1 absorption band of the starting material at $\lambda_{max} = 460$ nm and the emergence of two spectral bands centered at $\lambda = 334$ nm (representing 4-dimethylaminobenzaldehyde) and proposed secondary photooxidized material (centered at $\lambda = 410$ nm).
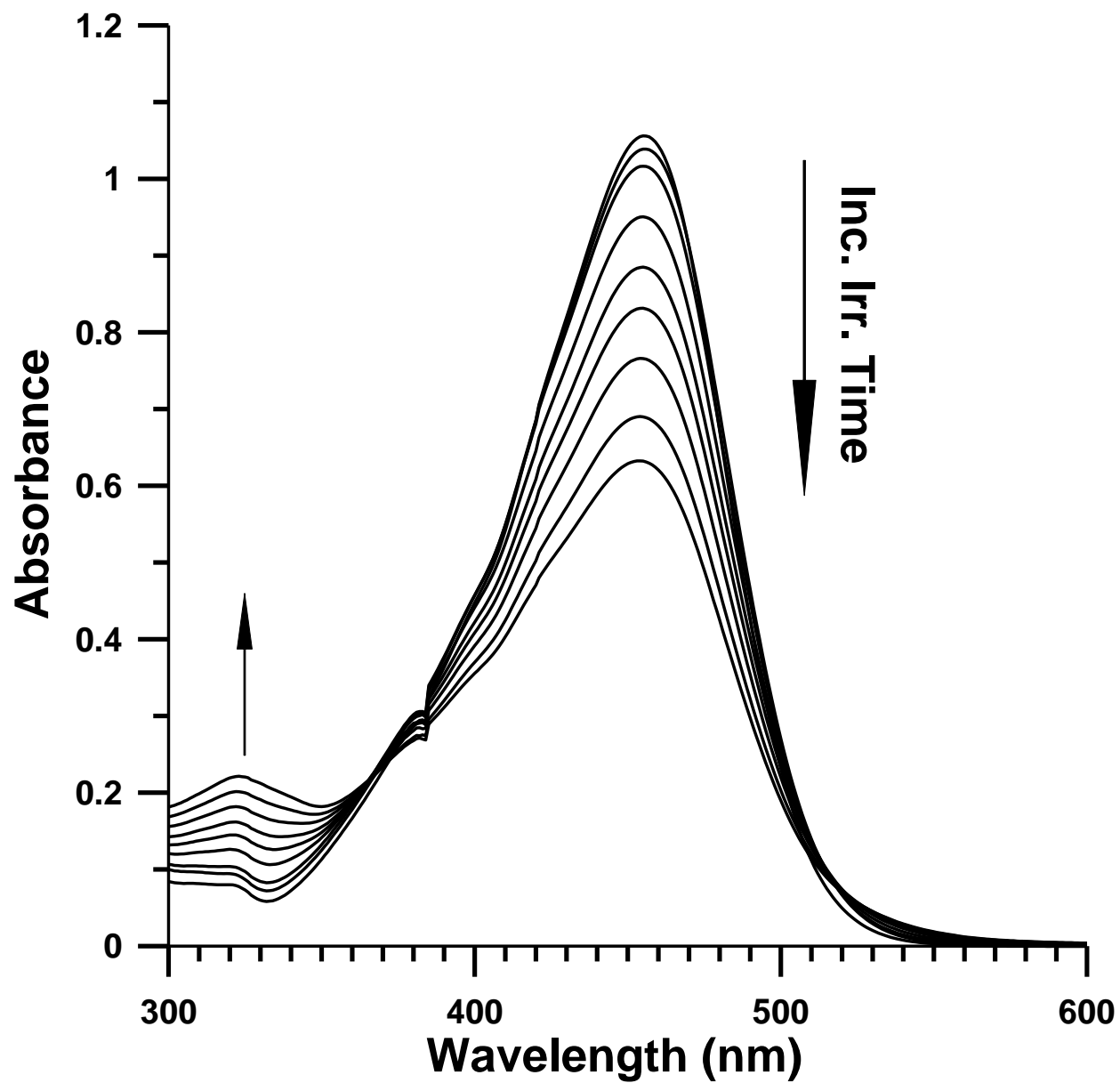
Figure 138. Absorption spectra of bis-dmab in acetonitrile under bubbling of N_2 at t = 0, 1, 8, 28, 48, 68, 88, 108, and 128 minutes of irradiation.
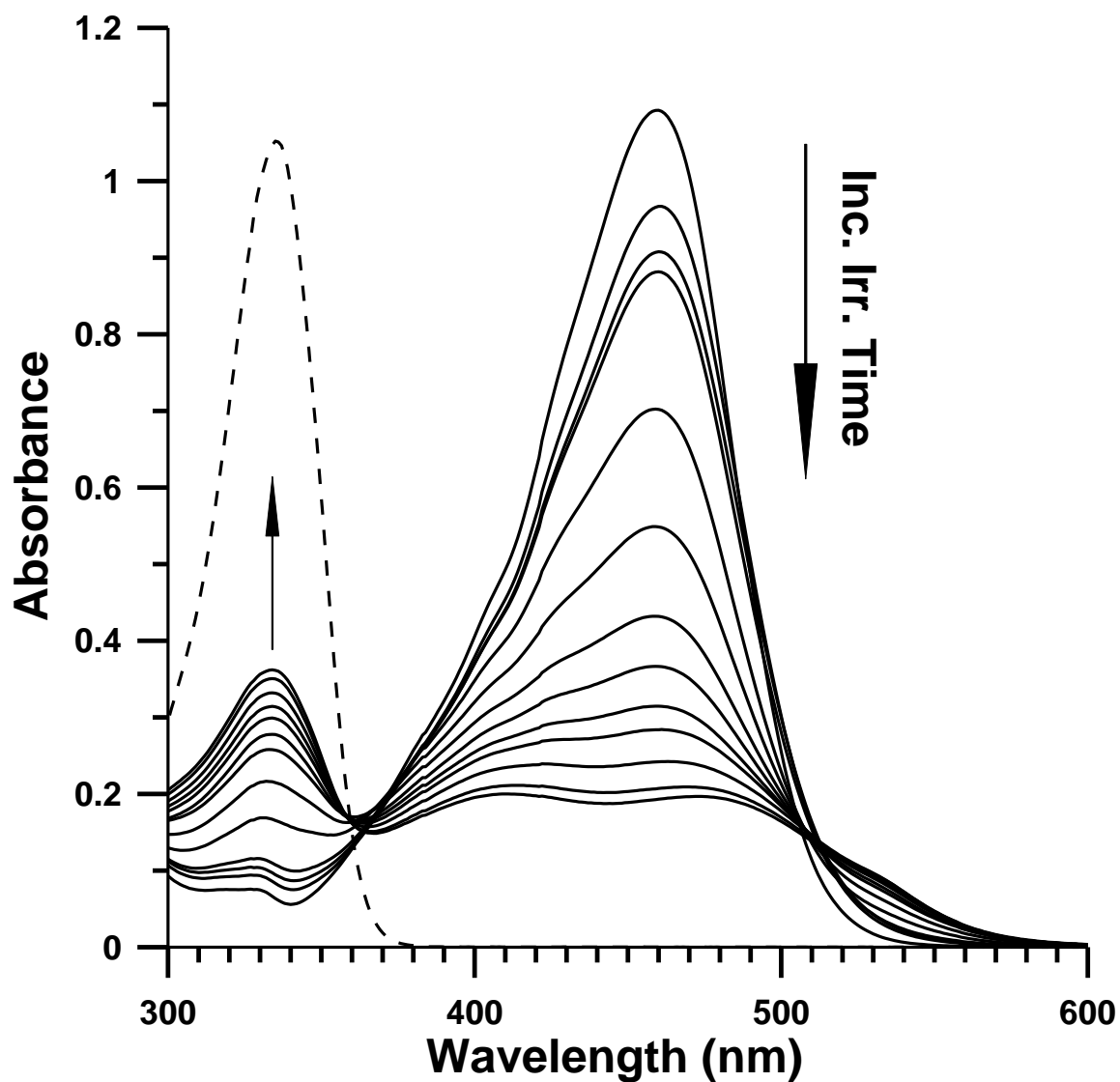
Figure 139. Absorption spectra of bis-dmab in acetonitrile under bubbling of O_2 at t = 0, 1, 2, 3, 6, 9, 12, 15, 18, 21, 26, 36, and 46 minutes of irradiation. Absorption spectrum of 4-dimethylaminobenzaldehyde in acetonitrile is represented by the dashed line (λ_{max} = 335 nm).

The same spectral behavior is observed in the irradiation experiment of bis-dmab in methanol under nitrogen. As shown in Figure 140, the absorption band at λ_{max} = 481 nm is decreased and the band centered at λ = 330 nm is increased with an isosbestic point at 380 nm.
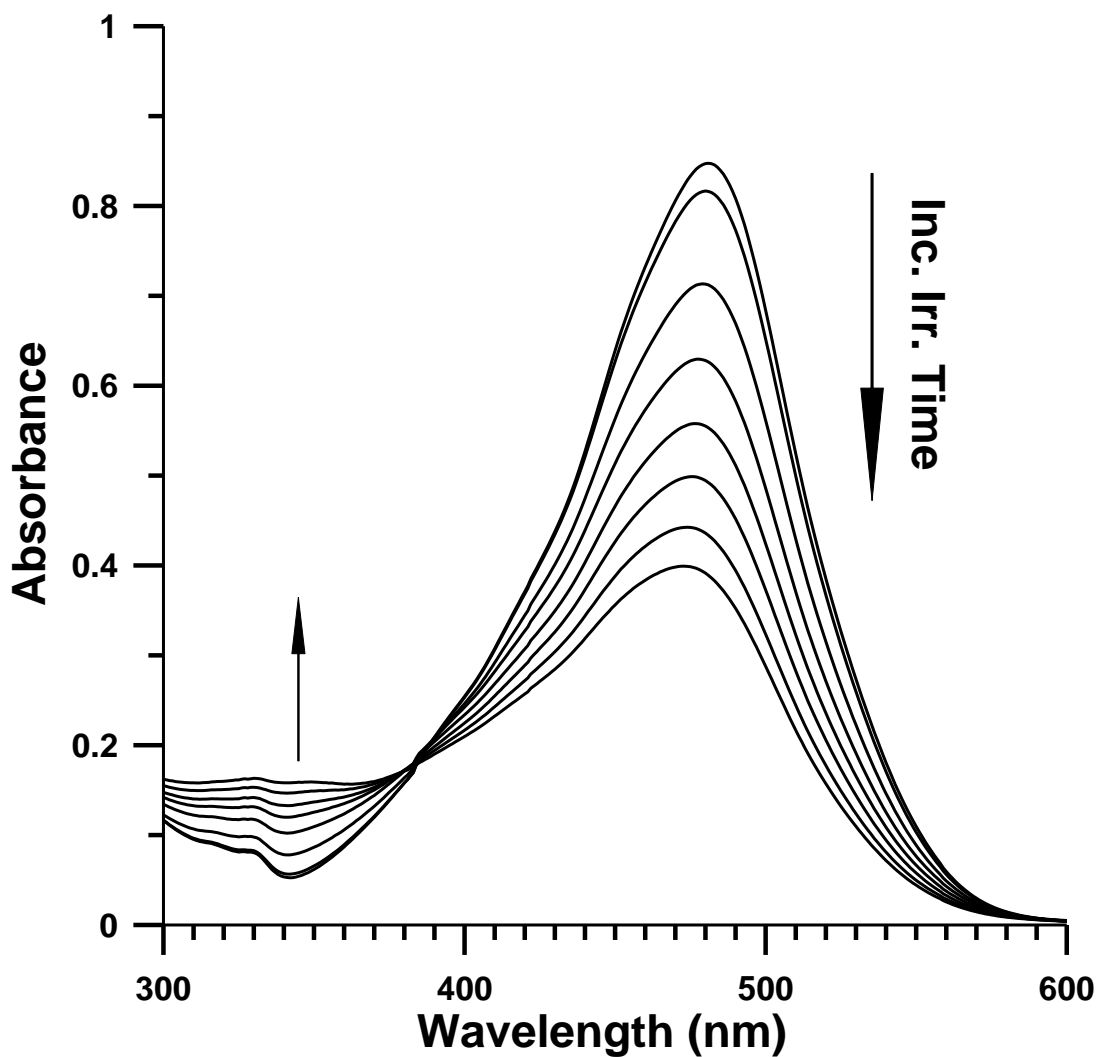
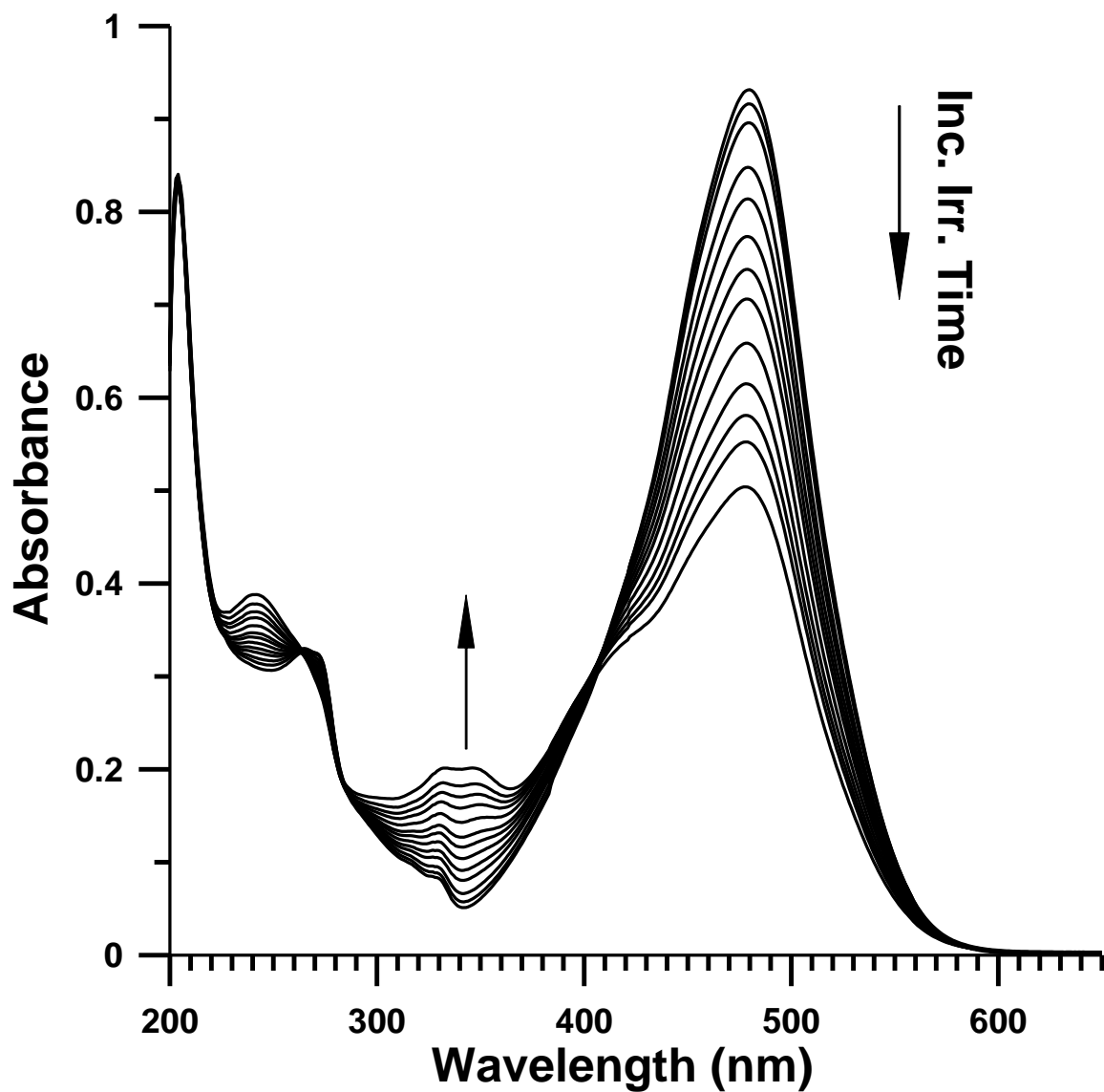**Figure 140.** Absorption spectra of bis-dmab in methanol under bubbling of N_2 at t = 0, 10, 40, 70, 100, 130, 160, and 190 minutes of irradiation.

Interestingly, unlike with the other solvents studied, irradiation and O_2 bubbling studies carried out for bis-dmab in MeOH showed no change in the absorption spectrum over the course of 120 minutes, as depicted in Figure 141. Further experiments consisted of examining the photochemistry of bis-dmab in methanol using a catalytic amount of an aluminum phthalocyanine dye (abbreviated for simplicity as AlPc) as the singlet oxygen photosensitizer and a 515 nm (yellow) cut-on filter. The purpose of conducting this experiment was to determine if $^1O_2$ does react with bis-dmab in methanol and from Figure 142, bis-dmab does react with $^1O_2$, resulting in photooxidized conversion. This demonstrates clearly that $^1O_2$ does react with bis-dmab in methanol.

Figure 141. Absorption spectra of bis-dmab in methanol under bubbling of O_2 at t = 0, 5, 10, 20, 30, 40, 50, 60, 75, 90, 105, and 120 minutes of irradiation.
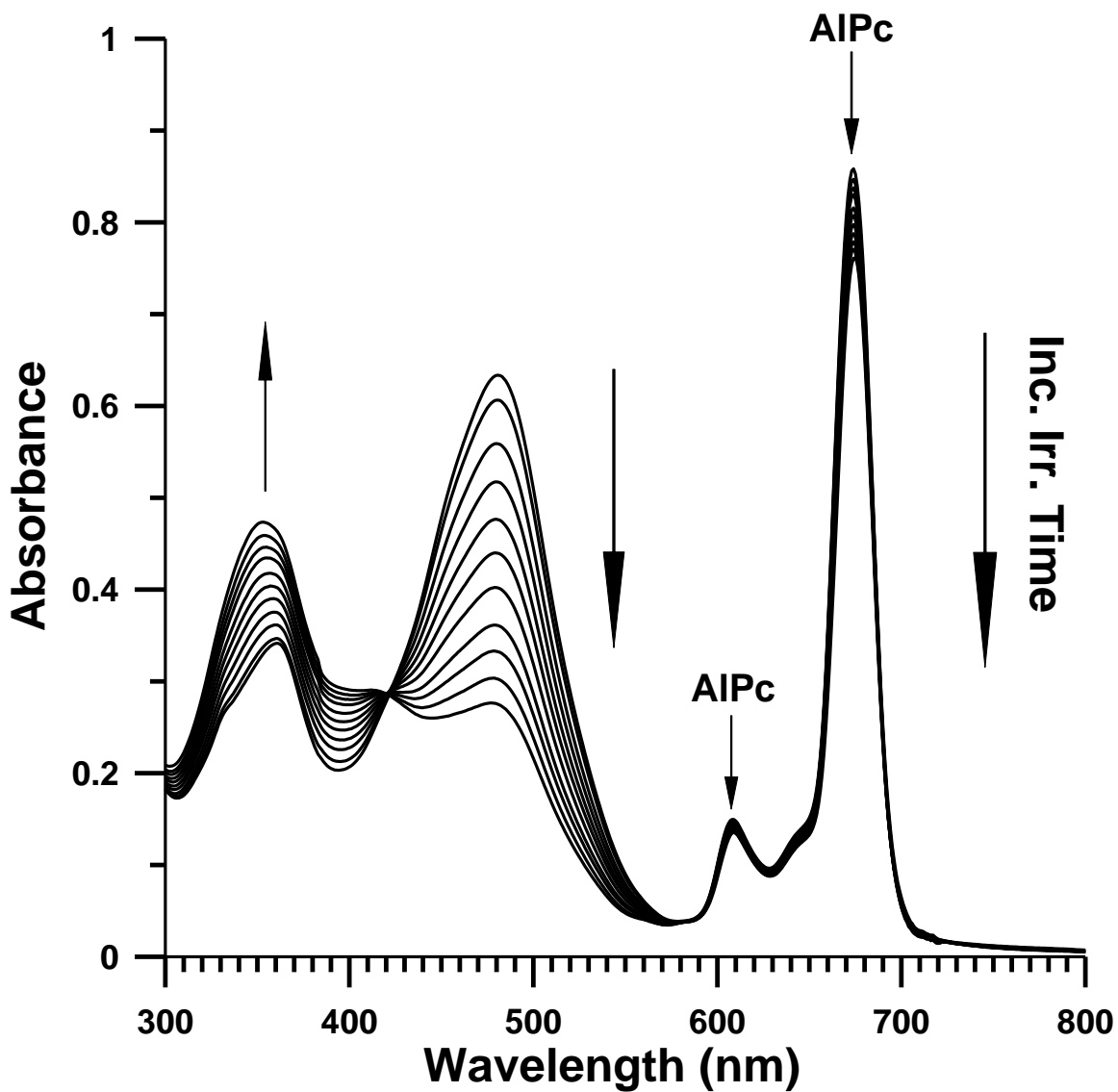
Figure 142. Absorption spectra of bis-dmab/AlPc binary solution under bubbling of O_2 at t = 0, 5, 15, 25, 35, 45, 55, 65, 75, 85, and 95 minutes of irradiation.

Knowledge of the lifetime of singlet oxygen in solution plays an important role in interpreting many of the photooxidation studies being carried out [75]. It is reported that the singlet oxygen lifetime is higher in deuterated solvents than in their undeuterated analogues (see Table 56). Particularly, methanol appears to be a suitable solvent for characterization of singlet oxygen reactions since an order of magnitude increase in the $^1O_2$ lifetime (τ_Δ) upon deuteration has been observed, with a reported value of 270 μs [76]. It is reported that τ_Δ in methanol is 7 μs [75].

Table 56. Reported singlet oxygen lifetimes (τ_Δ) in various solvents [75-80].

Solvent	τ_Δ (μs)
$CHCl_3$	60
$CDCl_3$	300
CH_3OH	7
CD_3OD	270
C_7H_8	29
C_7D_8	320
H_2O	2
D_2O	20
C_6H_6	24
CH_3CN	30

Knowing that the lifetime of singlet oxygen is an order of magnitude larger in methanol-d_4 than in methanol led to examining the photochemistry of bis-dmab in methanol-d_4 under O_2. Both the same concentration of bis-dmab and similar irradiation intervals were taken as with the study conducted in undeuterated methanol. It is shown from Figure 143 that photooxidation of bis-dmab occurs in methanol-d_4. This is attributed to the order of magnitude longer lifetime of $^1O_2$ in methanol-d_4 than in undeuterated methanol.
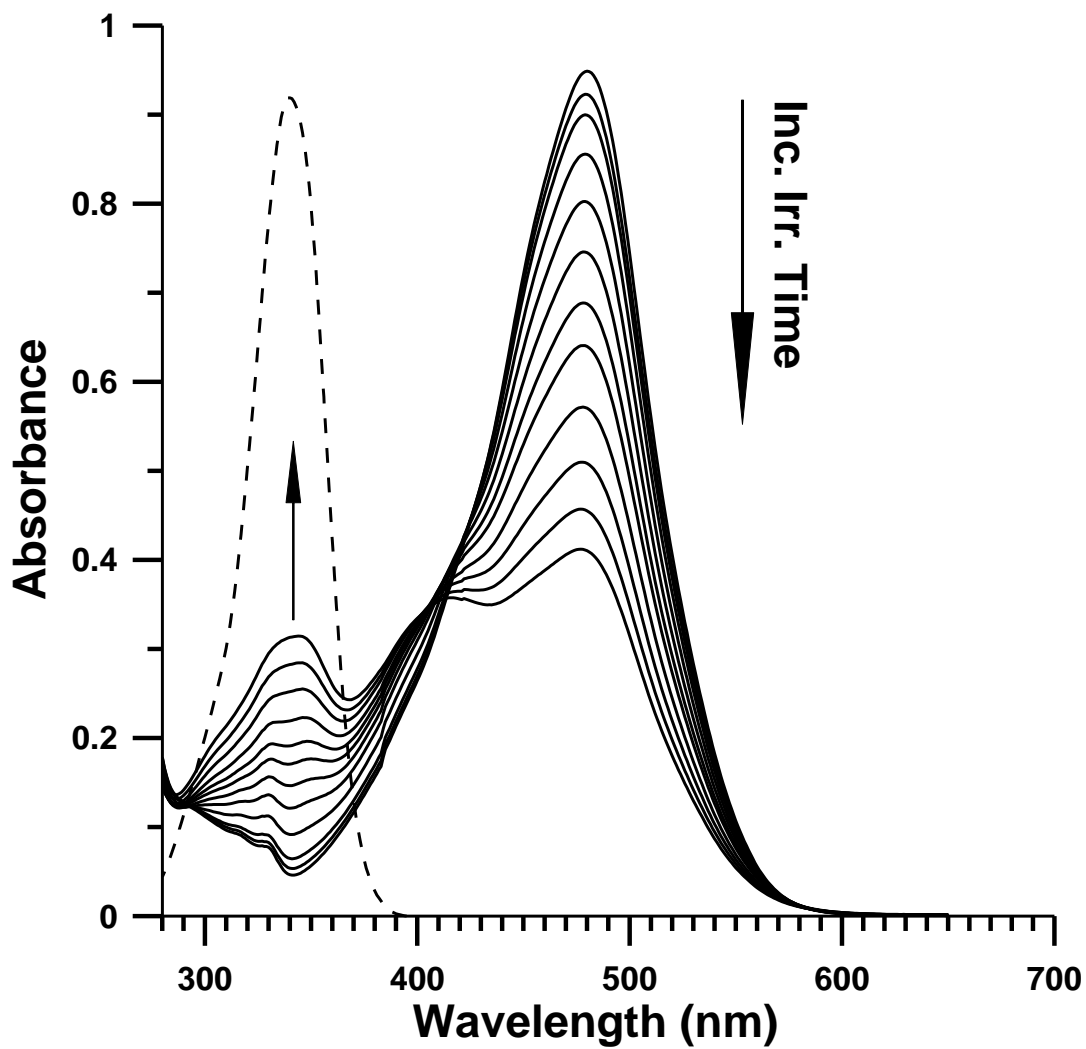
Figure 143. Absorption spectra of bis-dmab in methanol-d_4 under bubbling of O_2 at t = 0, 5, 10, 20, 30, 40, 50, 60, 75, 90, 105, and 120 minutes of irradiation. Absorption spectrum of 4-dimethylaminobenzaldehyde in methanol is represented by the dashed line (λ_{max} = 340 nm).

Further photochemistry experiments involved carrying out individual irradiations of air-saturated solutions of bis-dmab in methanol-d_4 (Figure 144) and methanol (Figure 145). Photooxidation in methanol-d_4 was observed with a continuous decrease in the primary absorption band and emerged bands localized at λ ~340 nm and 410 nm. Minimal change of spectral behavior in methanol was observed over the entire irradiation period of 330 minutes. A gradual decline in absorbance of the major absorption band (λ_{max} = 480 nm) and an increase in absorbance between 240 nm and 350 nm were observed.

The irradiation studies of bis-dmab in undeuterated methanol raise an important question on the photochemistry of this compound and that is "does oxygen completely quench the photoisomerization of bis-dmab?" To assist in answering this question, a reaction scheme on the photochemistry of bis-dmab is shown in Figure 146. Photoexcitation of bis-dmab causes the molecule to be promoted to the first excited singlet state, where it undergoes intersystem crossing to the underlying triplet state manifold (whose rate is dependent upon the solvent environment the molecule is localized in). At the excited triplet state, both photooxidation and (E,E) → (E,Z) photoisomerization are two simultaneous photoprocesses that occur. In the route of photooxidation, ^{3}bis-dmab* reacts with $^3O_2$, affording ground state bis-dmab and $^1O_2$, which react together to produce the photooxidized products, as observed in the solvents other than methanol. The observed photooxidation was attributed to the longer lifetimes of singlet oxygen in those solvents. In the special case with MeOH, the small τ_Δ value implies a high rate of $^1O_2 \to {}^3O_2$ intersystem crossing and as was observed with the dark experiment of bis-dmab in toluene (Figure 135), there was no reaction between bis-dmab and $^3O_2$. In the absence of oxygen, only (E,E) → (E,Z) photoisomerization occurs, recalling that photoisomerization is dependent upon the population of the molecule's triplet state [22].

321

Figure 144. Absorption spectra of an air-saturated solution of bis-dmab in methanol-d$_4$ (no bubbling) at t = 0, 5, 10, 20, 30, 40, 50, 60, 75, 90, 105, 120, and 150 minutes of irradiation.
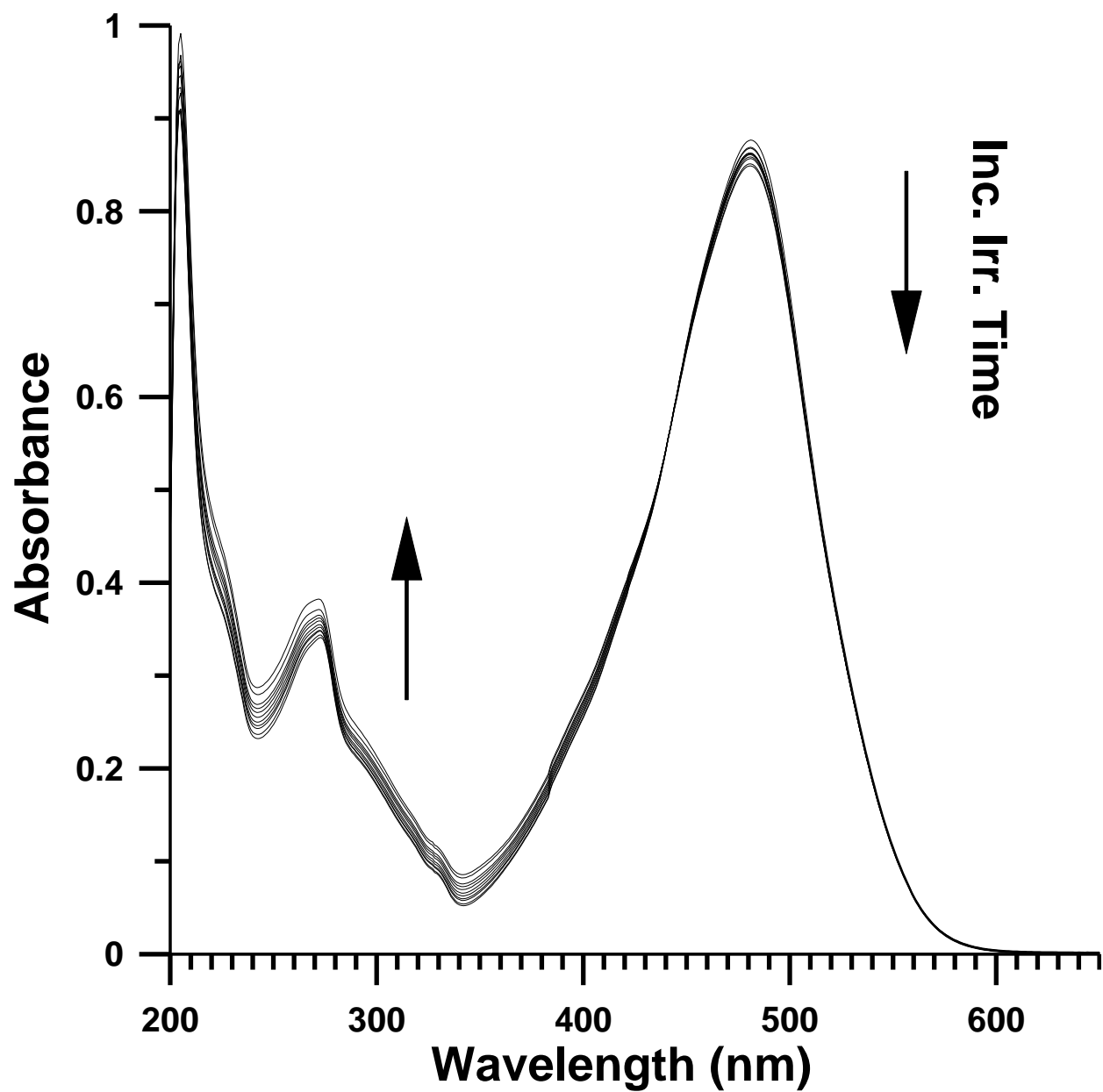
Figure 145. Absorption spectra of an air-saturated solution of bis-dmab in methanol (no

bubbling) at t = 0, 30, 60, 90, 120, 150, 180, 210, 240, 300, and 330 minutes of irradiation.

^{1}bis-dmab $\xrightarrow{h\nu}$ ^{1}bis-dmab* $\xrightarrow{k_{isc}}$ ^{3}bis-dmab*

^{3}bis-dmab* + $^3O_2$ $\longrightarrow$ ^{1}bis-dmab + $^1O_2$ $\longrightarrow$ POX products

$k_{O2} = 1/\tau_\Delta$

no O_2

^{1}bis-dmab + $^3O_2$ $\xrightarrow{\quad\times\quad}$
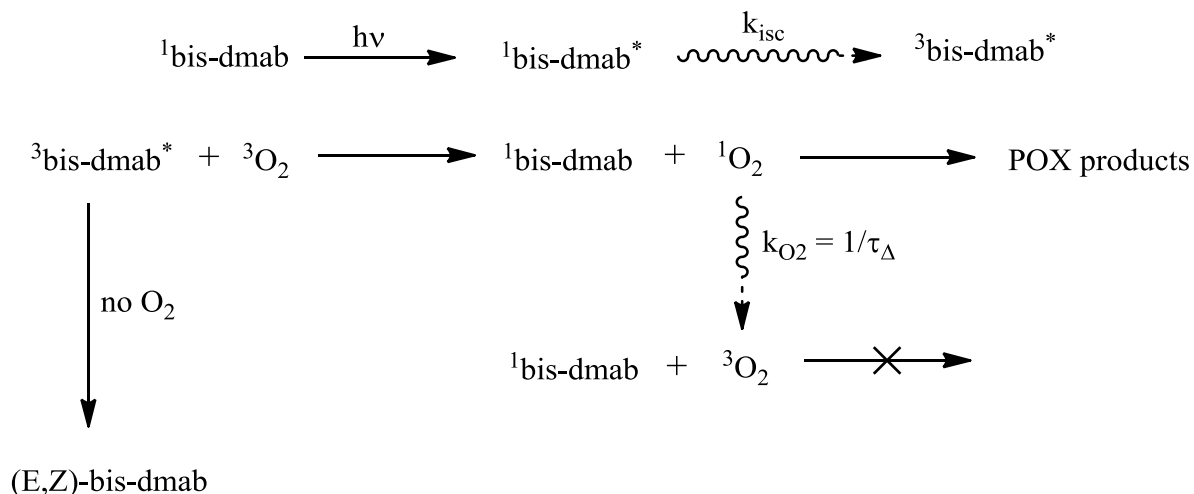
(E,Z)-bis-dmab

Figure 146. Reaction sequences for competition between photooxidation and photoisomerization of bis-dmab.

As a means of better understanding the photoisomerization experiments of bis-dmab, the photoisomerization of (2E,5E)-2,5-dibenzylidene-cyclopentanone (1dbcp) was revisited and studied. Previous experiments have been carried out on the (E,E) → (E,Z) photoisomerization of 1dbcp (reaction shown in Figure 147) with reported λ_{max} absorbance values at 350 nm [12, 23]. A solution of 1dbcp in tetrahydrofuran (THF) was irradiated for various irradiation intervals with a 150 W Xe arc lamp filtered through 12 cm of deionized water. As shown in Figure 148, the absorption band at λ_{max} = 344 nm overall decreases from 0 to 13 minutes of irradiation. In addition, a spectral band centered at λ = 305 nm emerges during the total 13 minute irradiation period. It was found in previous HPLC studies from this laboratory that there was a 34.6 % growth in the (E,Z)-photoisomer of 1dbcp after 5 minutes of irradiation, with established photoequilibrium with the starting (E,E) conformer at 45 minutes (52.0% (E,E) and 48.0% (E,Z))

[12]. In addition, UV-Vis results showed that the maximum absorbance intensity for (E,E)-1dbcp was reduced at λ 350 nm with a slight shoulder appearing at λ ~420 nm [12].
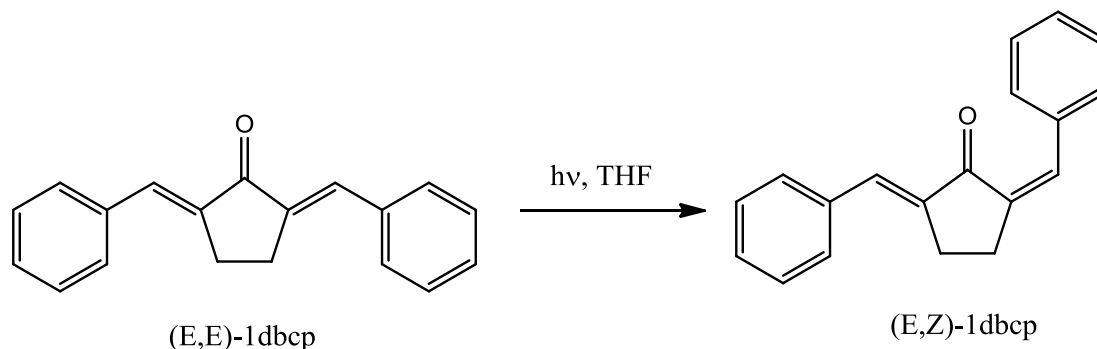
Figure 147. (E,E) → (E,Z) photoisomerization of 1dbcp in THF.

Photochemistry experiments were also performed for 1dbcp in THF, maintaining a continuous flow of N_2 and measuring the absorption spectrum at various irradiation intervals, as depicted in Figures 148 - 150, respectively. Maximum absorbance intensity of the starting (E,E)-1dbcp was reduced approximately 40% from 0 to 5 minutes of irradiation with a spectral band appearing at λ ~440 nm, which is consistent with previously reported results on 1dbcp photoisomerization [12, 23]. Prolonged irradiation resulted in the appearance of a spectral band centered at λ ~ 310 nm, which may represent absorption of the (Z,Z)-photoisomer. Similar trends were observed for the photochemistry experiments of 1dbcp and bis-dmab under N_2. The photochemistry of 1dbcp was found to be faster than that for bis-dmab, attributing this to S_1 being (n, π*); hence, faster S → T intersystem crossing (El-Sayed's Rule).

325
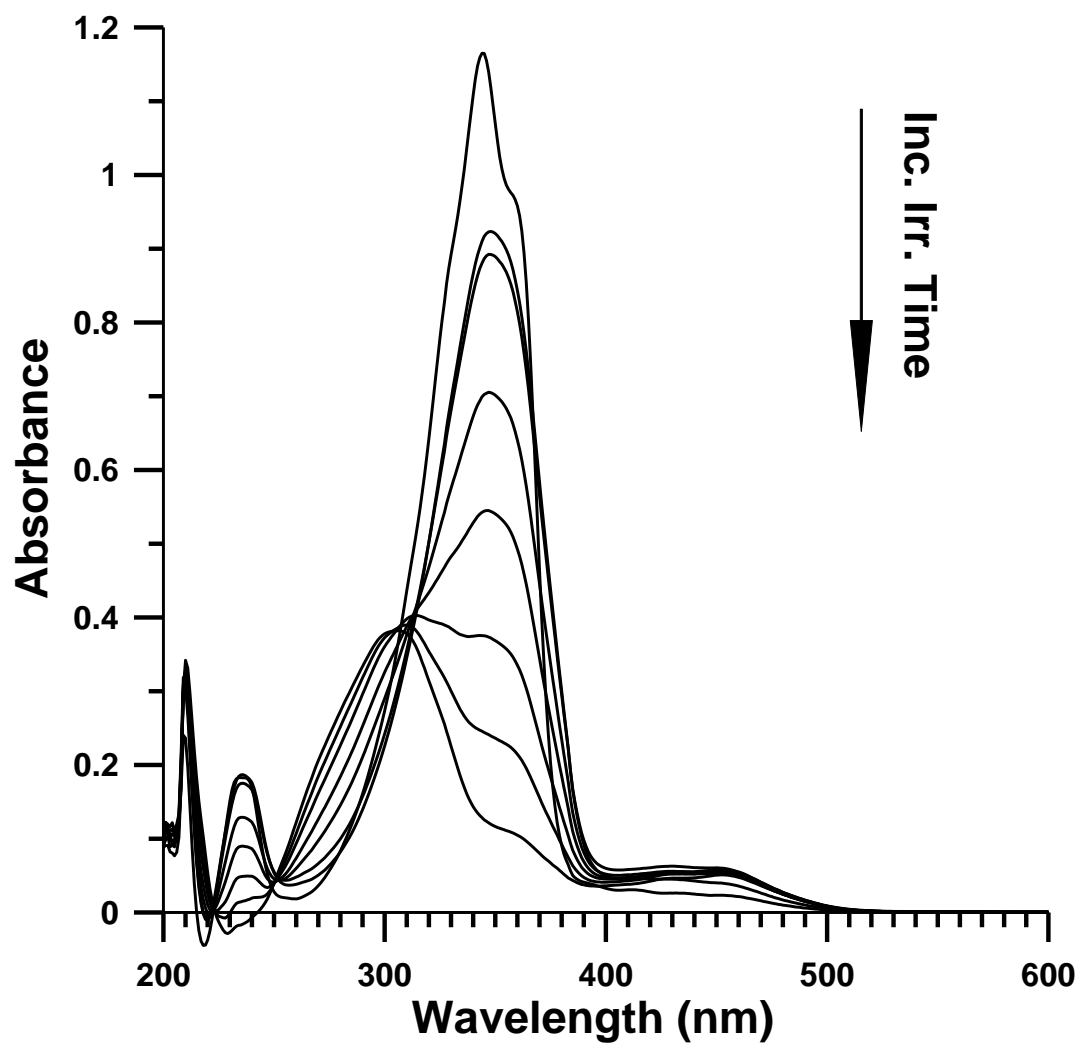
Figure 148. Absorption spectra of 1dbcp in tetrahydrofuran under bubbling of N_2 at t = 0, 2, 3, 5, 7, 9, 11, and 13 minutes of irradiation.
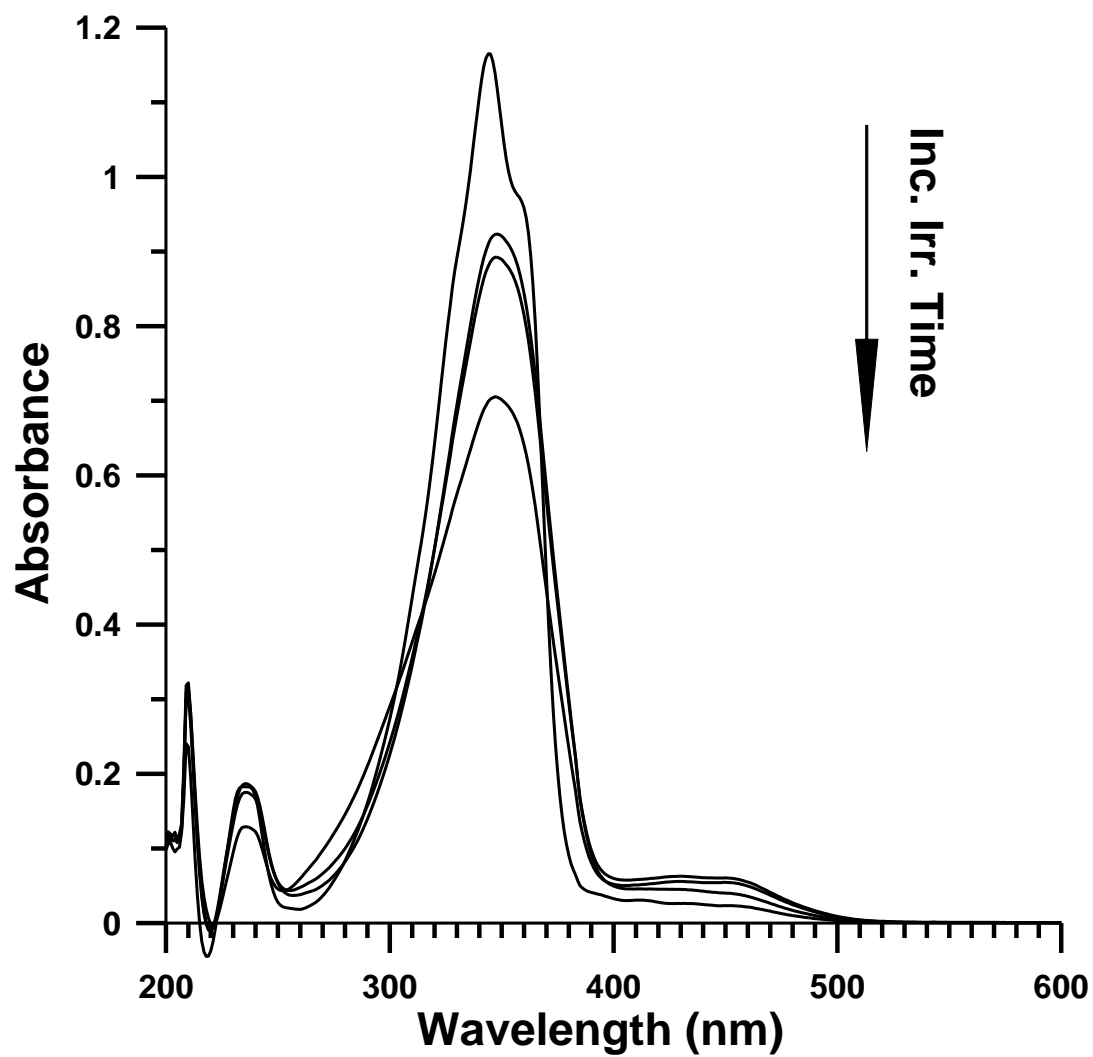
Figure 149. Absorption spectra of 1dbcp in tetrahydrofuran under bubbling of N_2 at t = 0, 2, 3, and 5 minutes of irradiation.
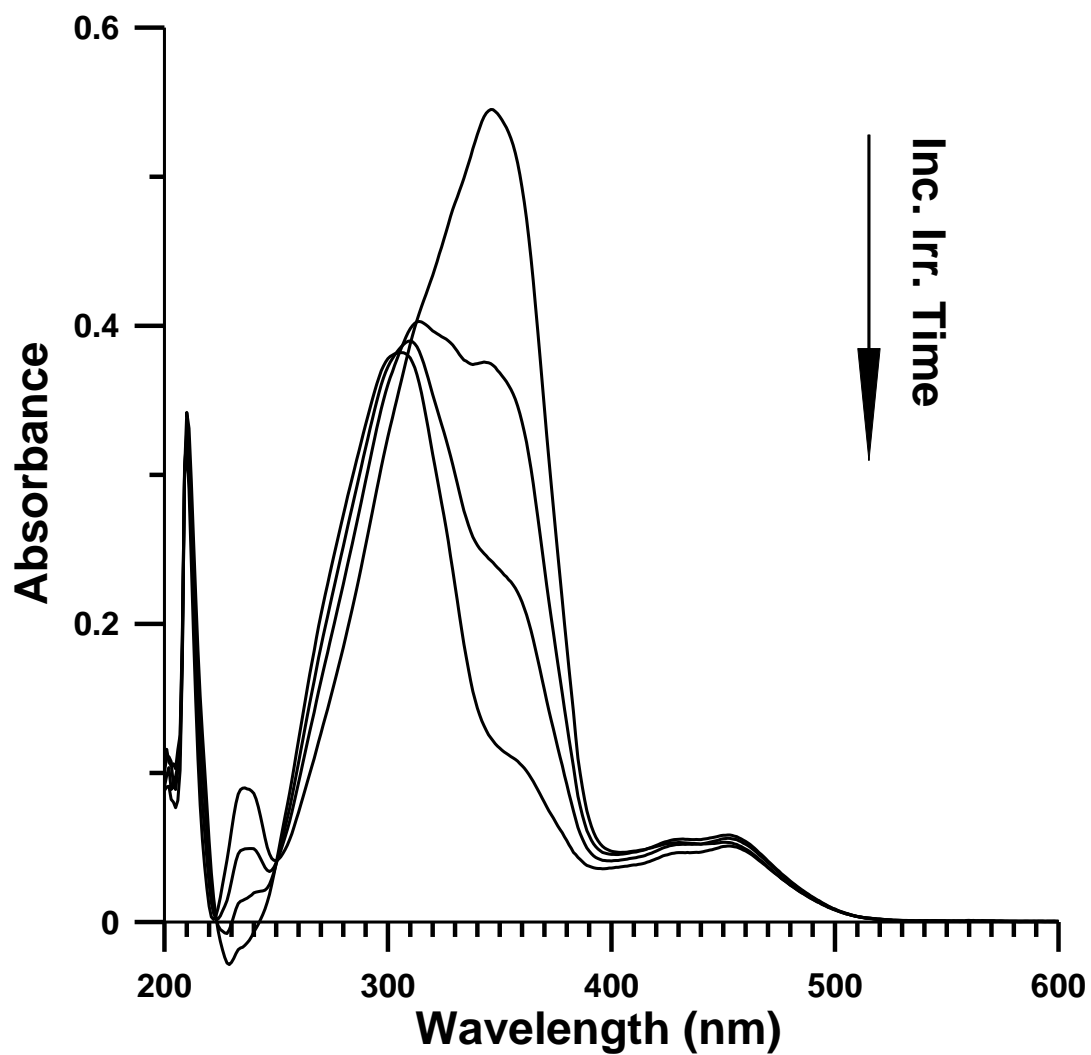
Figure 150. Absorption spectra of 1dbcp in tetrahydrofuran under bubbling of N_2 at t = 7, 9, 11, and 13 minutes of irradiation.

4.5.5   Photooxidation of bis-dmab: LC/MS Study

This section presents the LC/MS results for the photooxidation of bis-dmab. A series of

solutions of bis-dmab in CDCl$_3$ were simultaneously irradiated and bubbled with O$_2$ and

photooxidized conversion was verified by ^{1}H NMR. Irradiated/bubbled solutions were combined,

concentrated *in vacuo*, and components were separated by silica gel column chromatography.

The LC/MS data presented in this section is an analysis of a column fraction that is interpreted to

be composed of a mixture of 4-dimethylaminobenzaldehyde and proposed dione product. The

purpose of conducting LC/MS studies is to (i) further verify the identity of 4-

dimethylaminobenzaldehyde and to (ii) verify identification of the dione.

The chromatogram of a photooxidized solution of bis-dmab in acetonitrile (sample

denoted as 'LONGPOX#5', shown in Figure 151, was obtained. The major component at 6.7

minutes was confirmed to be 4-dimethylaminobenzaldehyde (M = 149 g/mol), and the positive

ion mass spectrum gave a m/z ratio of 150, corresponding to M+1 of the aldehyde (see Figure

152). The absorption spectrum of the major component (Figure 153) gives a λ_{max} centered at

approximately 350 nm, consistent with the UV-Vis experiments discussed in the previous section

on bis-dmab photooxidation. It was found that a mixture containing 4-

dimethylaminobenzaldehyde and what is believed to be (E)-3-(4-dimethylaminobenzylidene)-

1,2-cyclopentadione (M = 229 g/mol) eluted between 5 - 6 minute retention times. As seen in

Figures 154 and 155, the mass spectra for component separation between 5 - 6 minutes contained

m/z values of 150 and 230 and absorption spectra (shown in Figures 156 - 158) showed a major

band centered at λ ~330 nm and a secondary band centered at $\lambda \sim$ 410 nm, consistent with the

UV-Vis experiments presented in section 4.5.4.

Figure 151. Chromatogram of LONGPOX#5 in acetonitrile.
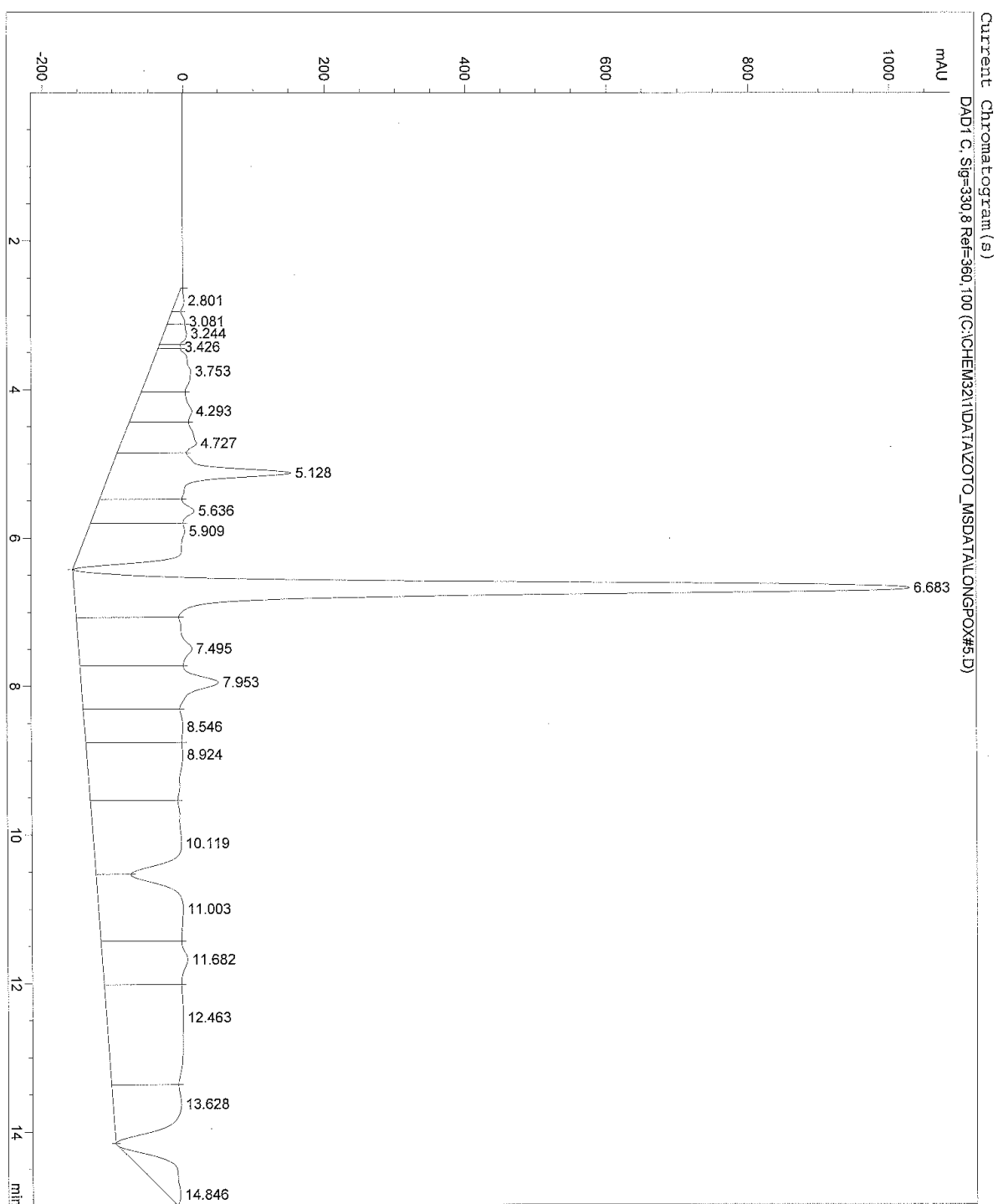
Figure 152. Average mass spectrum of LONGPOX#5 between 6.6 – 7.3 minutes.
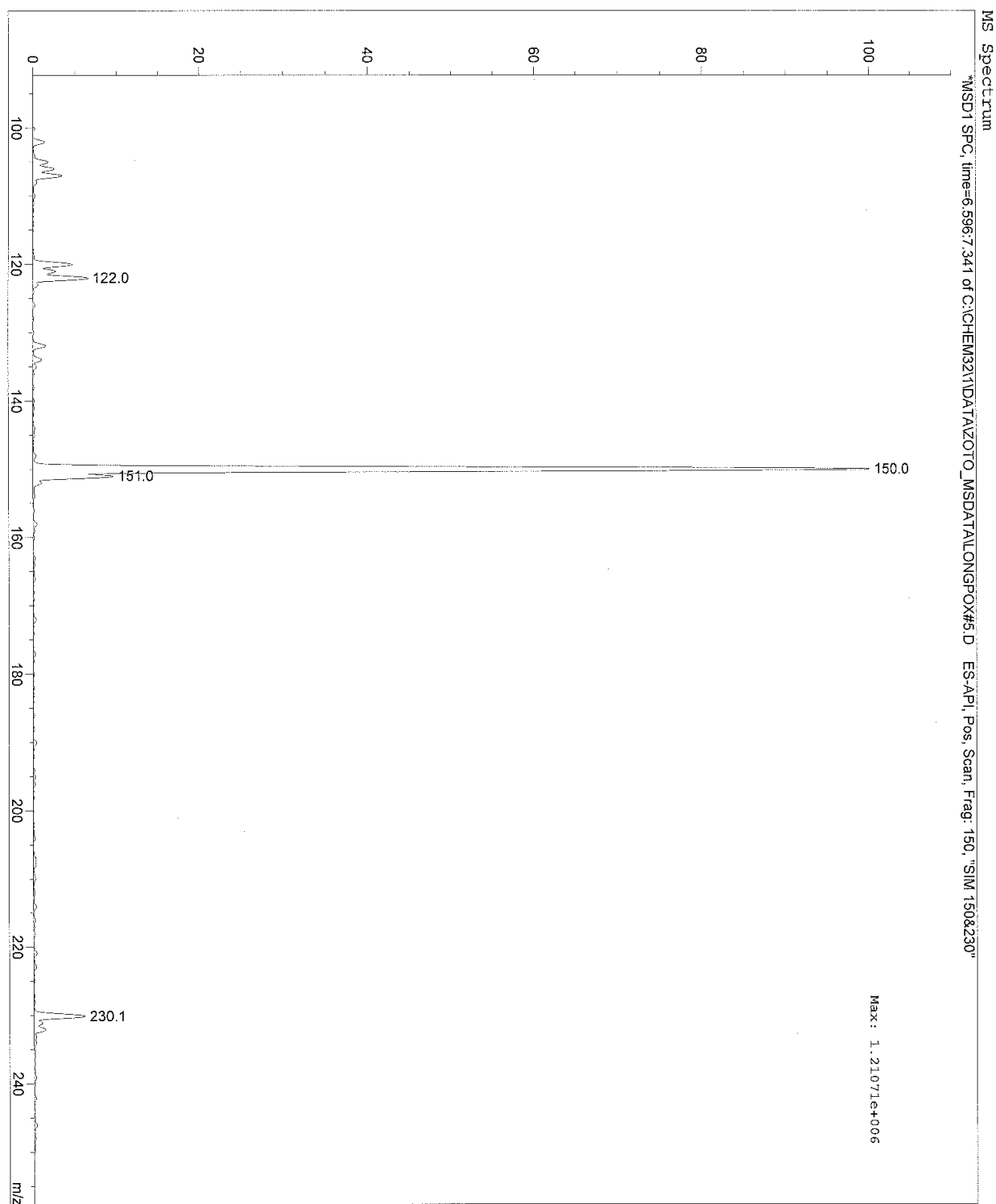
Figure 153. Average absorption spectrum of LONGPOX#5 between 6.6 – 7.1 minutes.
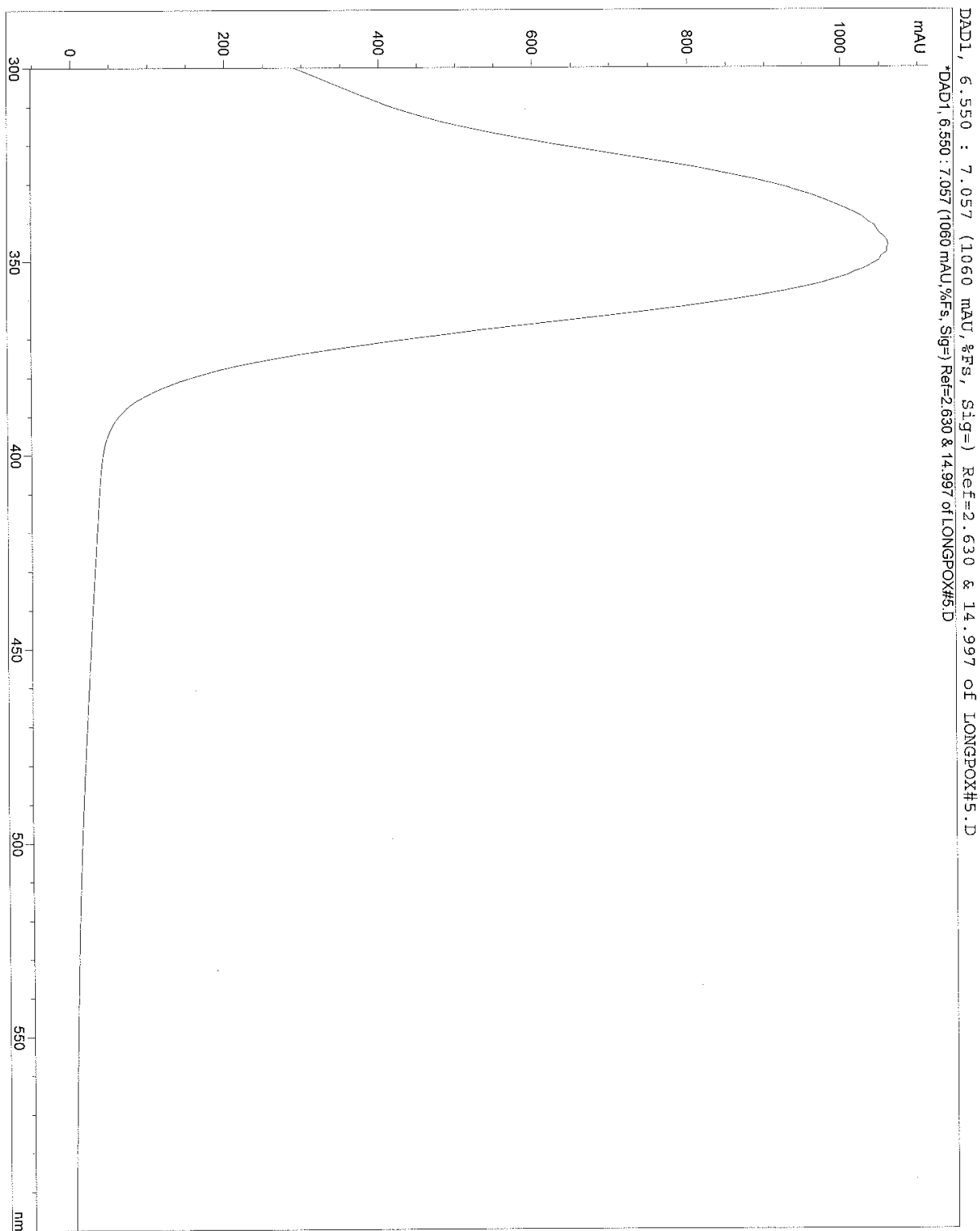
Figure 154. Average mass spectrum of LONGPOX#5 between 4.3 – 6.4 minutes.
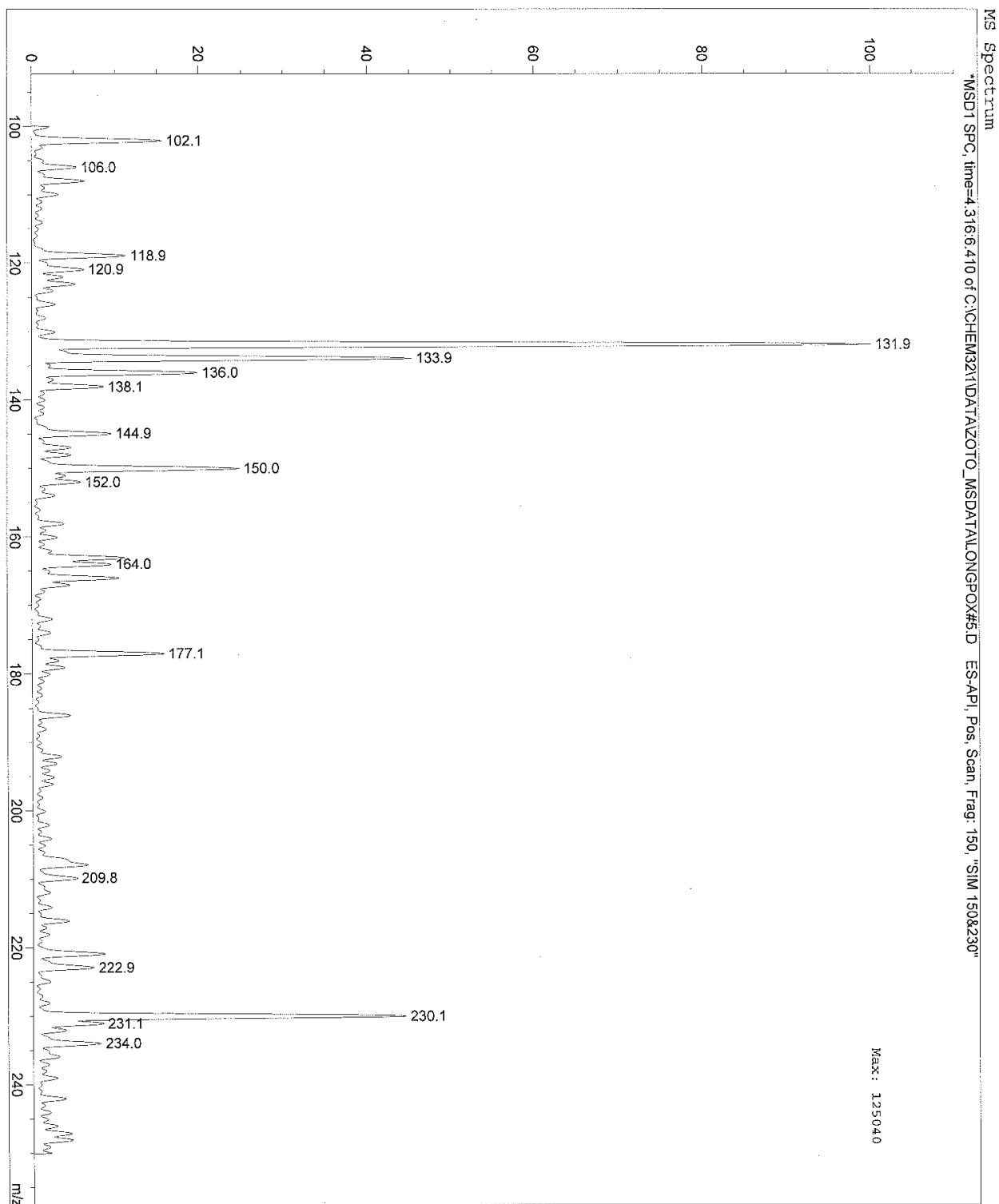
Figure 155. Average mass spectrum of LONGPOX#5 between 5.5 − 5.9 minutes.
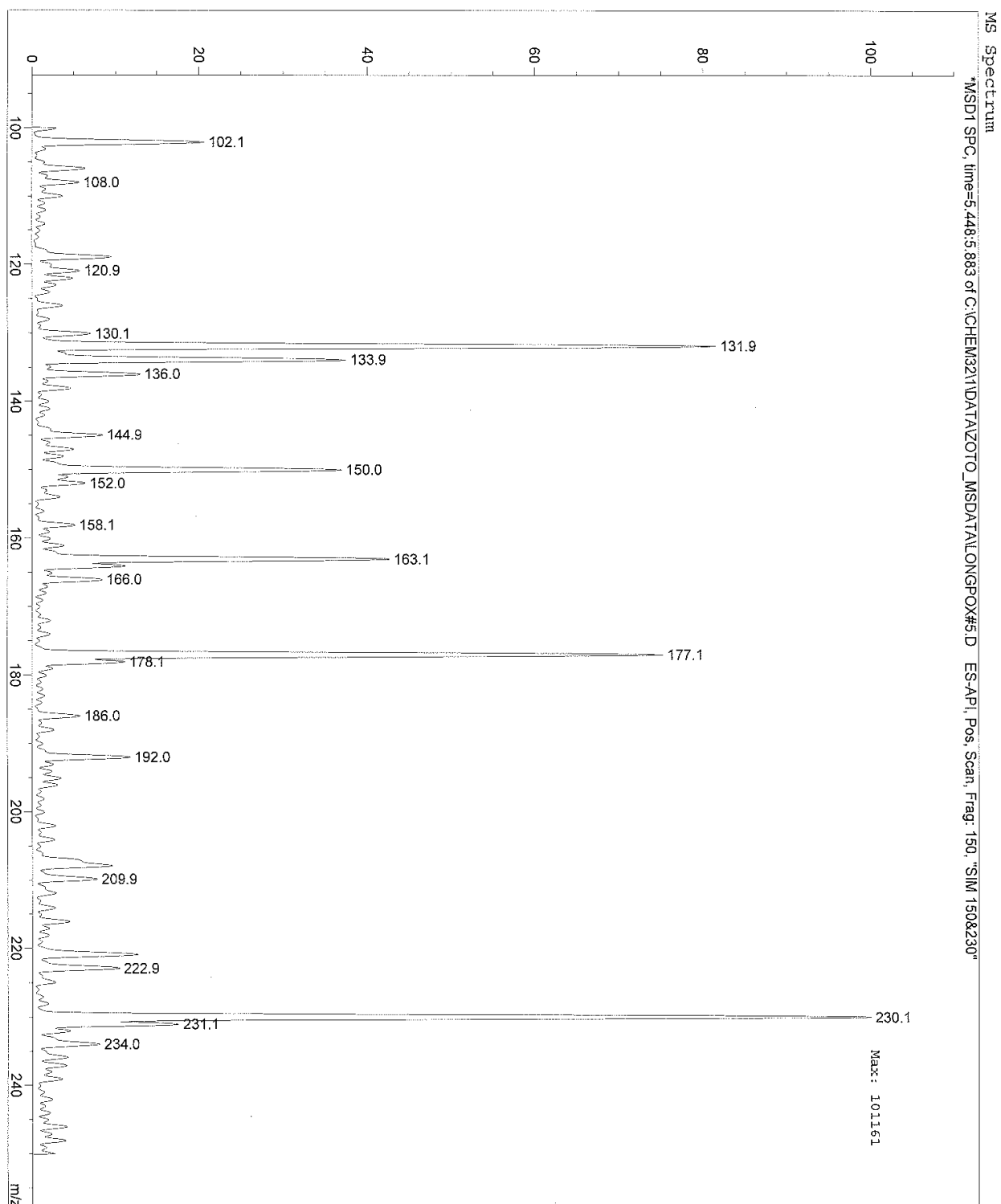
Figure 156. Average absorption spectrum of LONGPOX#5 between 4.9 – 5.5 minutes.
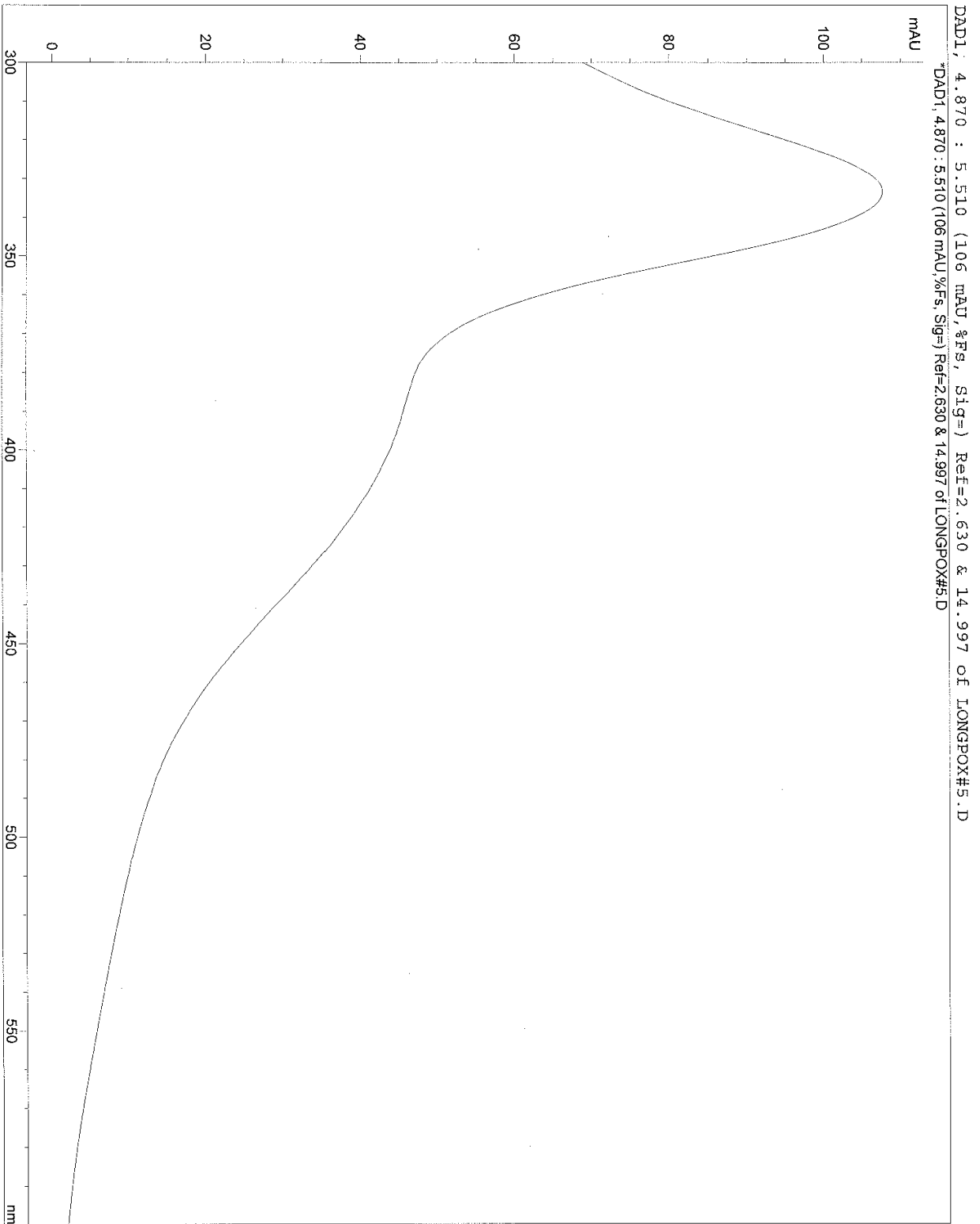
Figure 157. Absorption spectrum of LONGPOX#5 at 5.6 minutes.
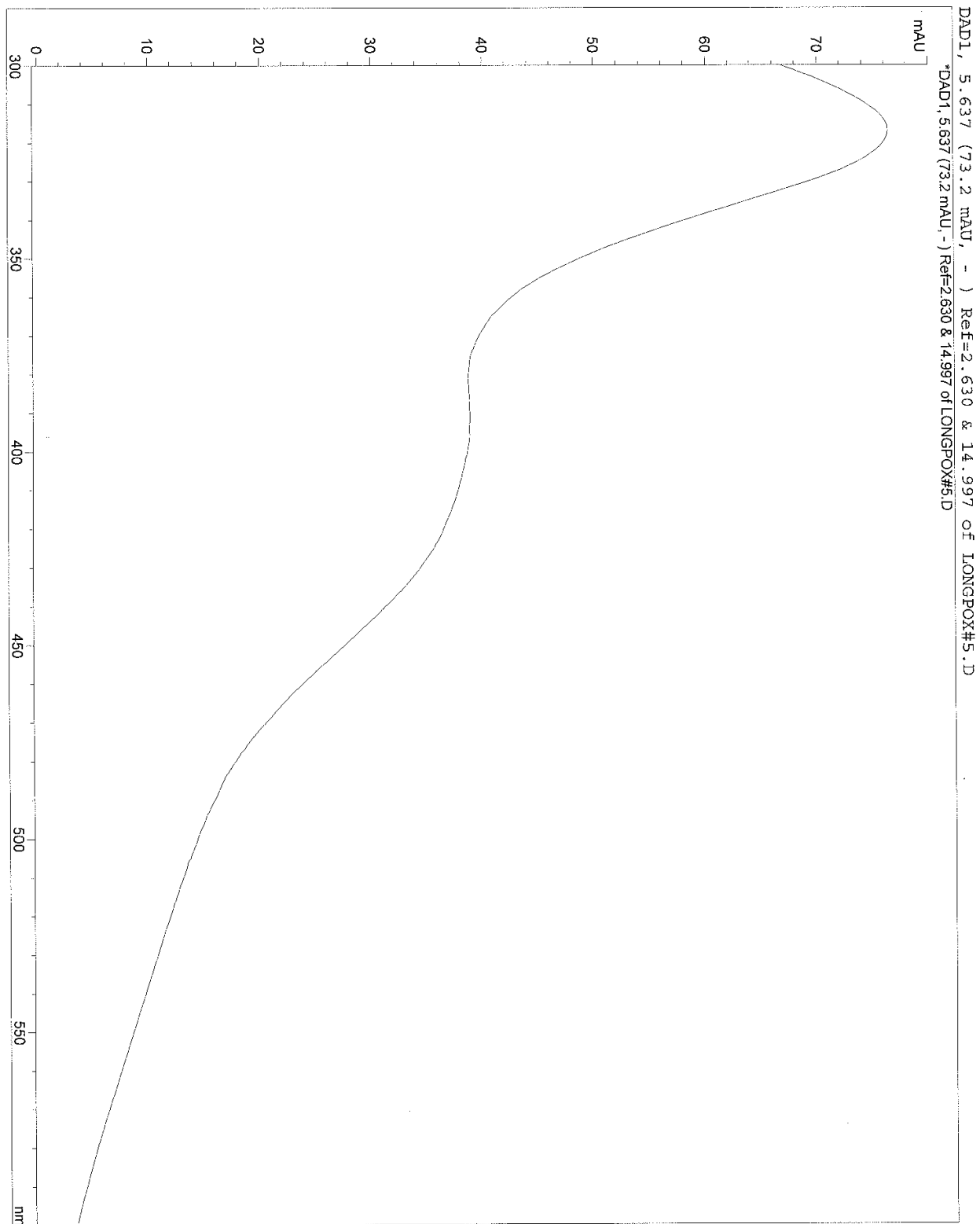
Figure 158. Absorption spectrum of LONGPOX#5 at 5.8 minutes.
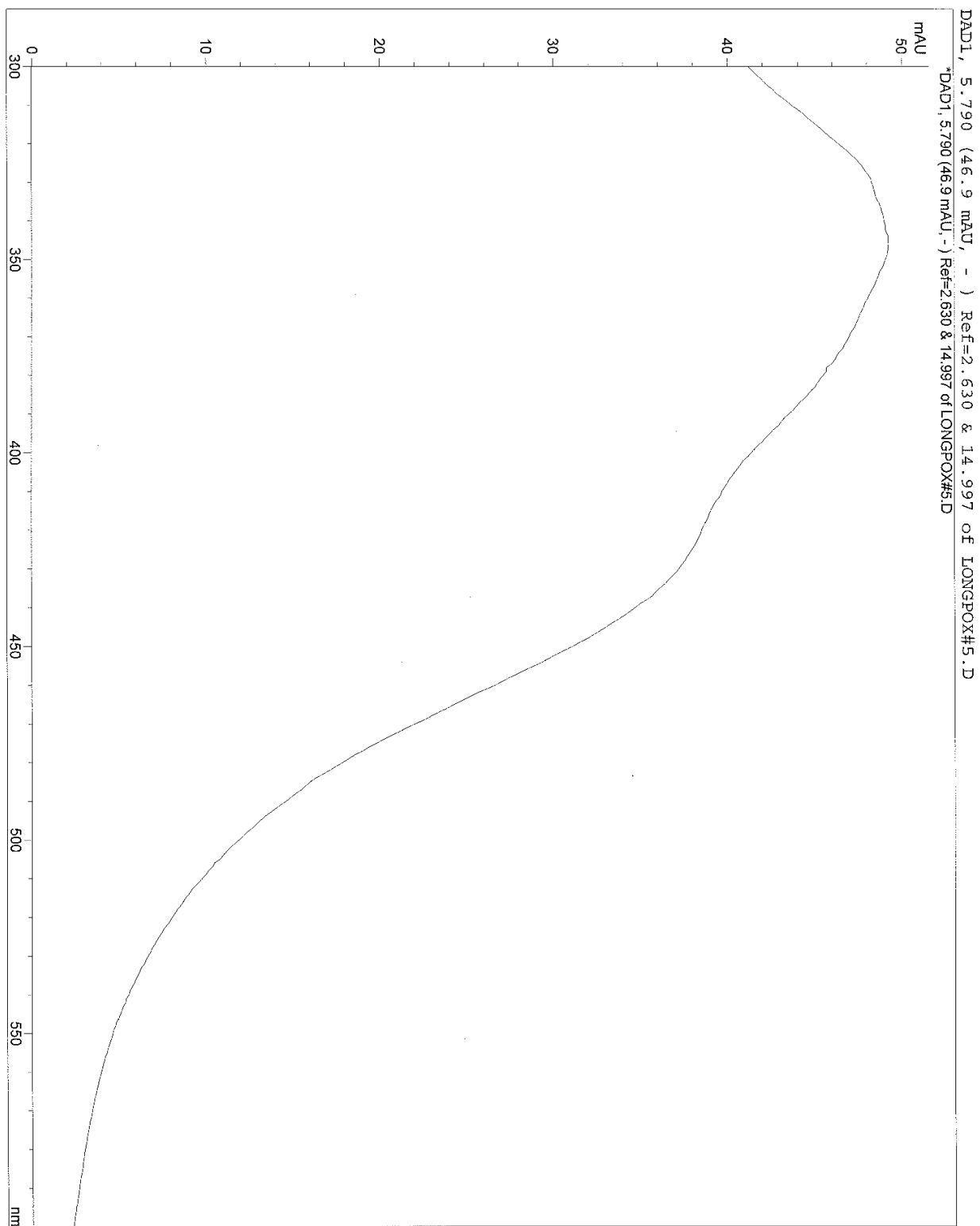
4.5.6 Conclusions

(2E,5E)-2,5-bis(p-dimethylaminobenzylidene)-cyclopentanone (bis-dmab) has been shown to sensitize singlet state oxygen ($^1O_2$) that reacts with tetramethylethylene (TME) in chloroform-d, toluene-d_8, and methanol-d_4. Noticeable photobleaching in toluene-d_8 led to further studying the photochemistry of bis-dmab, specifically self-sensitized photooxidation and *trans-cis* photoisomerization, monitoring the reaction progress by ^1H NMR and UV-Vis absorption spectroscopy. ^1H NMR photooxidation studies led to the conclusion that bis-dmab does react with $^1O_2$ in a $[2\pi + 2\pi]$ cycloaddition reaction, giving an endoperoxide intermediate, which breaks down to 4-dimethylaminobenzaldehyde and a secondary photooxidized product, likely (E)-3-(4-dimethylaminobenzylidene)-1,2-cyclopentadione. ^1H NMR analysis on the structural identification of the dione remained inconclusive.

UV-Vis absorption studies on the photooxidation of bis-dmab in chloroform, toluene, acetonitrile, and methanol-d_4 confirmed conversion of 4-dimethylaminobenzaldehyde localized at λ_{max} ~330 - 340 nm and an emerged spectral band centered at λ ~400 nm, which is proposed to be (E)-3-(4-dimethylaminobenzylidene)-1,2-cyclopentadione. LC/MS analysis on the photooxidized material also confirmed 4-dimethylaminobenzaldehyde (m/z = 150) and a component with m/z = 230, which is M+1 of the proposed dione. Besides ^1H NMR and UV-Vis studies, LC/MS became more convincing on production of the dione.

However, photooxidation of bis-dmab in methanol was not observed. This was attributed to the 7 µs lifetime of singlet oxygen in methanol, contrary to the longer lifetimes in other solvents, particularly the order of magnitude increase in CD_3OD. Further irradiation studies of air saturated solutions of bis-dmab in methanol and methanol-d_4 led to the conclusion that photooxidized conversion, although slower than in the continuous bubbling experiment, was

338

observed in methanol-d$_4$ and that photochemistry in undeuterated methanol is very slow, attributed to the low τ_Δ in methanol and therefore a higher rate of $^1O_2 \rightarrow {}^3O_2$ intersystem crossing.

UV-Vis absorption monitoring of the photochemistry of bis-dmab in degassed environments (that is, under N$_2$) led to the conclusion of (E,E) $\rightarrow$ (E,Z) photoisomerization. With respect to increased irradiation time, decline of the first (lower energy) absorption band, representing absorption of the starting (E,E) conformer, and growth of a higher energy absorption band (ca. λ 330 nm) with an observed isosbestic point in between, provided support of *trans-cis* photoisomerization. In addition, comparative studies with the photoisomerization of its unsubstituted analogue (1dbcp) showed similar spectral behavior, thereby providing additional experimental support.

5   SUMMARY AND RECOMMENDATIONS FOR FUTURE WORK

5.1   Summary

1.   Excellent agreement was observed between the computed molecular structure and the experimental X-ray structural data of Asdimcy1. The spectroscopic and photophysical properties have been found to vary considerably with solvent. The significant internal charge transfer character of Asdimcy1 is clearly supported by solvatochromic plots, computed molecular orbitals, and the large electronic dipole moment in the excited state. Substantial variation with solvent in the nonradiative rate of decay is interpreted in terms of a competition between internal conversion and intersystem crossing.

2.   Both of the alkylamino substituted 2-arylidene cyclopentanones dmab and dmac behave similarly in their spectroscopic and photophysical properties. Compound dmac is slightly more red shifted in its absorption and fluorescence energies than dmab, and it exhibits larger $\Delta\mu$ and μ_e values which are attributed to the extended π conjugation. Fluorescence was observed to be very weak for both compounds in all solvents studied, consistent with highly efficient S $\rightarrow$ T intersystem crossing between excited states of different orbital configurations in accordance with El-Sayed's rule.

3.   According to DFT optimized geometries, all four alkylamino substituted 2,5-diarylidene cyclopentanones, bis-dmab, bis-dmac, bis-juldmac, and Ashrbor, exhibit similar planar structures. Excellent agreement was found between the X-ray crystal structure of bis-dmab and its computed molecular structure. Spectroscopic properties of all four compounds showed strong solvent dependence with absorption and fluorescence spectra shifted bathochromically with respect to an increase in solvent polarity. Energy maxima shifted further to the red with respect to increased chain length.

4.   For bis-dmab, bis-dmac, and bis-juldmac, S_1 is computed to be a strong symmetry allowed $B_2 \leftarrow A_1$ transition of the (π, π^*) type, arising from the orbital excitation $a_2(\pi) \rightarrow b_1(\pi^*)$. The S_2 state is computed to be a symmetry forbidden $A_2 \leftarrow A_1$ transition of the (n, π^*) type, arising from the orbital excitation $b_2(n) \rightarrow b_1(\pi^*)$. Group theory demonstrates that two excited states of different orbital configurations mix through first-order spin-orbit coupling, but excited states of the same orbital configuration do not mix through first-order spin-orbit coupling. In addition, group theory shows that b_1 corresponds to the irreducible representation of the vibration that promotes the vibronic coupling between $S_1(\pi, \pi^*)$ and $S_m(n, \pi^*)$ as well as between $T_1(\pi, \pi^*)$ and $T_m(n, \pi^*)$ states for these compounds.

5.   Both Φ_f and τ_f values vary depending on solvent polarity for all alkylamino substituted 2,5-diarylidene cyclopentanone compounds. The k_{nr} values also show solvent dependence. Variations in k_{nr} are interpreted in terms of a competition between internal conversion and intersystem crossing.

6.   Spectroscopic studies of 2dbmxcp and bis-dmac reveal a higher degree of internal charge transfer character for bis-dmac, with supporting evidence of larger solvatochromic shifts in absorption and fluorescence, larger electronic dipole moment in the excited state, and computed data on the partial charges of atoms both in the ground and excited states. The larger Φ_f and smaller k_{nr} values observed for 2dbmxcp in region 1 solvents are attributed to larger S_0-S_1 energy gaps, contrary to the observations seen for both bis-dmab and bis-dmac.

7.   The single crystal X-ray structure of Asunsub has a higher degree of phenyl ring torsion on the benzylidene end than on the more conjugated cinnamylidene end of the molecule. The larger twisting conformation of the phenyl ring on the less conjugated end of the molecule is

341

likely influenced not only by the molecular structure and energy, but also by the packing

arrangement in the crystal. Fluorescence of Asunsub is observed only in protic solvents,

suggesting the orbital nature of the S_1 state to be (π, π^*). In aprotic solvents, where fluorescence

is not observed, the orbital nature of the S_1 state is (n, π^*).

8.   For dyes that exhibit excited state proton transfer in acetic acid, the dual fluorescence

emission fr om S_1 is attributed to the increase in basicity in the excited state. Examination of the

computed charges of the carbonyl oxygen atoms demonstrates that the compounds are stronger

bases in the $^1(\pi, \pi^*)$ state than in the ground state. The positive values in ΔpKa (pKa* > pKa)

and the decrease in formal charge of the carbonyl oxygen atom in the $^1(\pi, \pi^*)$ state explain the

observable excited state protonation of these compounds.

9.   Compound bis-dmab has been shown to sensitize singlet oxygen ($^1O_2$) in various solvents

in the presence of tetramethylethylene (TME) as the indicator of $^1O_2$ formation. TME reacts with

$^1O_2$ through a concerted Schenck reaction to yield 3-hydroperoxy-2,3-dimethyl-1-butene.

Photooxidation and photoisomerization of bis-dmab were examined in various solvents and

analyzed by ^{1}H NMR, UV-Vis, and LC/MS. The spectral data presented is indicative that

bis-dmab reacts with $^1O_2$ in a $[2\pi + 2\pi]$ cycloaddition reaction, giving an endoperoxide

intermediate, which breaks down to 4-dimethylaminobenzaldehyde and proposed (E)-3-(4-

dimethylaminobenzylidene)-1,2-cyclopentadione. The two step mechanism for the photoxidation

of bis-dmab is further supported by similar work carried out on 1,2-cycloaddition reactions of

olefinic systems with $^1O_2$, followed by the oxidative cleavage of endoperoxides. UV-Vis

absorption monitoring of the photochemistry of bis-dmab in degassed environments (that is,

under N_2) led to the conclusion of (E,E) → (E,Z) photoisomerization. With respect to increased

irradiation time, decline of the first (lower energy) absorption band, representing absorption of the starting (E,E) conformer, and growth of a higher energy absorption band (ca. λ 330 nm) with an observed isosbestic point in between, provides support of *trans-cis* photoisomerization. In addition, comparative studies with the photoisomerization of its unsubstituted symmetric analogue showed similar spectral behavior, thereby providing additional experimental support.

5.2   Recommendations for Future Work

5.2.1   Additional Asymmetrical 2,5-Diarylidene Cyclopentanone Dyes

Further extensive work on the asymmetric charge transfer D-A-A diarylpolyene cyclopentanone series will be to examine the spectroscopic and photophysical properties of (2E,5E)-2-(p-cyanocinnamylidene)-5-(p-dimethylaminobenzylidene)-cyclopentanone (Asdimcy3) and (2E,5E)-2-(p-cyanocinnamylidene)-5-(p-dimethylaminocinnamylidene)-cyclopentanone (Asdimcy4) in a variety of solvents (structures shown in Figure 159). It will be interesting to observe how the solvatochromic and photophysical properties compare and contrast from Asdimcy1 and Chen's compound 1 [81]. Figures 160 and 161 show proposed reaction schemes for the syntheses of Asdimcy3 and Asdimcy4.

As shown in Figure 160, the proposed two step reaction for the synthesis of Asdimcy3 consists of the two carbon homologation of 4-cyanobenzaldehyde via hydrozirconation to produce (E)-4-cyanocinnamaldehyde followed by a crossed aldol condensation with an equimole amount of (E)-2-(p-dimethylaminobenzylidene)-cyclopentanone (dmab) in the presence of NaOH. Shown in Figure 161 is the proposed reaction scheme for the synthesis of Asdimcy4, consisting of three steps. (i) The two carbon homologation of 4-cyanobenzaldehyde to (E)-4-cyanocinnamaldehyde via hydrozirconation. (ii) The synthesis of (E)-2-(p-cyanocinnamylidene)-

cyclopentanone (2pdbcy), which involves combining cyclopentanone and morpholine, giving

in situ N-(1-cyclopenten-1-yl)morpholine (enamine), followed by the addition of (E)-4-

cyanocinnamaldehyde to the enamine, and finally, acid-catalyzed dehydration. (iii) An

intermolecular base-catalyzed crossed aldol condensation between an equimole amount of

2pdbcy with (E)-4-dimethylaminocinnamaldehyde in the presence of NaOH, yielding Asdimcy4.

The proposed reaction scheme for the synthesis of intermediate 2pdbcy is in reference to

previous work carried out for the synthesis of its unsubstituted analogue, namely (E)-2-

cinnamylidene-cyclopentanone in moderate yield (47%) [82].
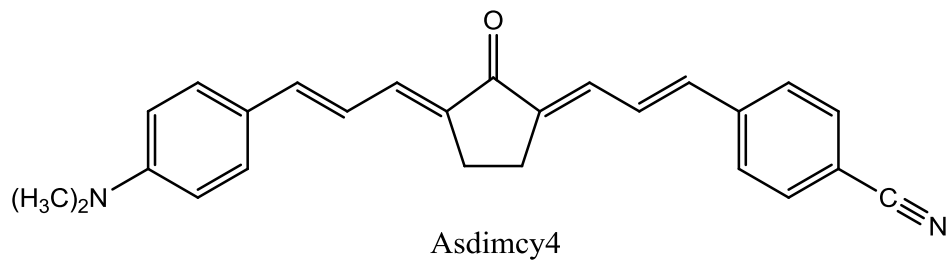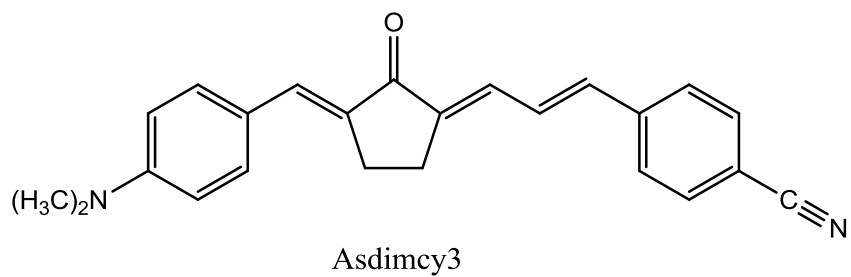
Asdimcy3

Asdimcy4

Figure 159. Structures of Asdimcy3 and Asdimcy4.

1 mol eq

dmab, 1 mol eq
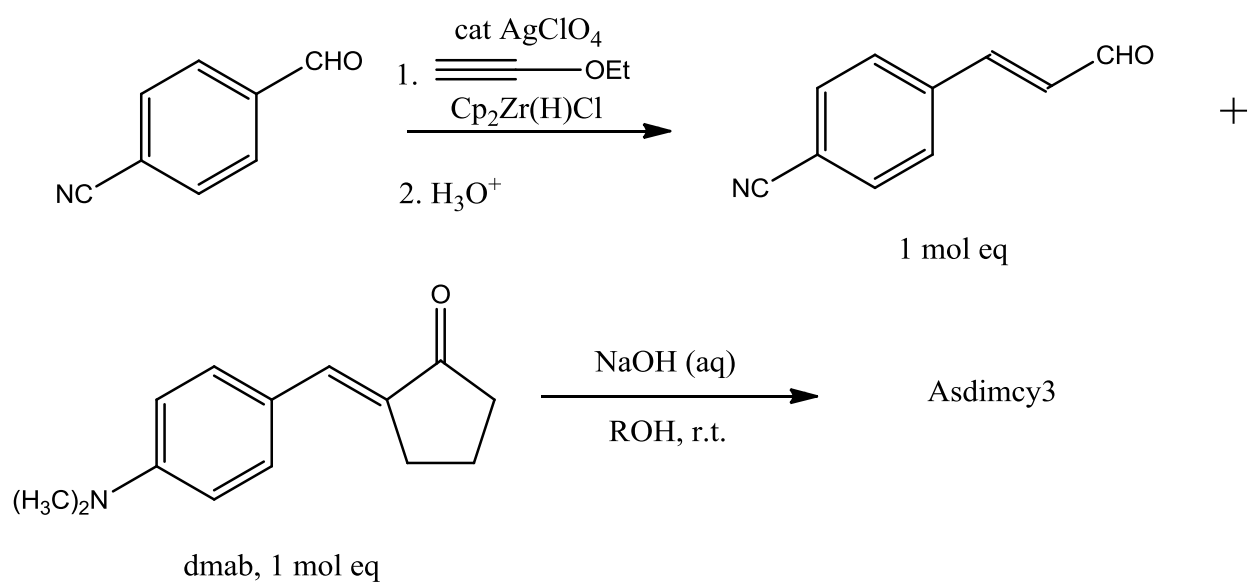
Figure 160. Proposed reaction scheme for the synthesis of Asdimcy3.
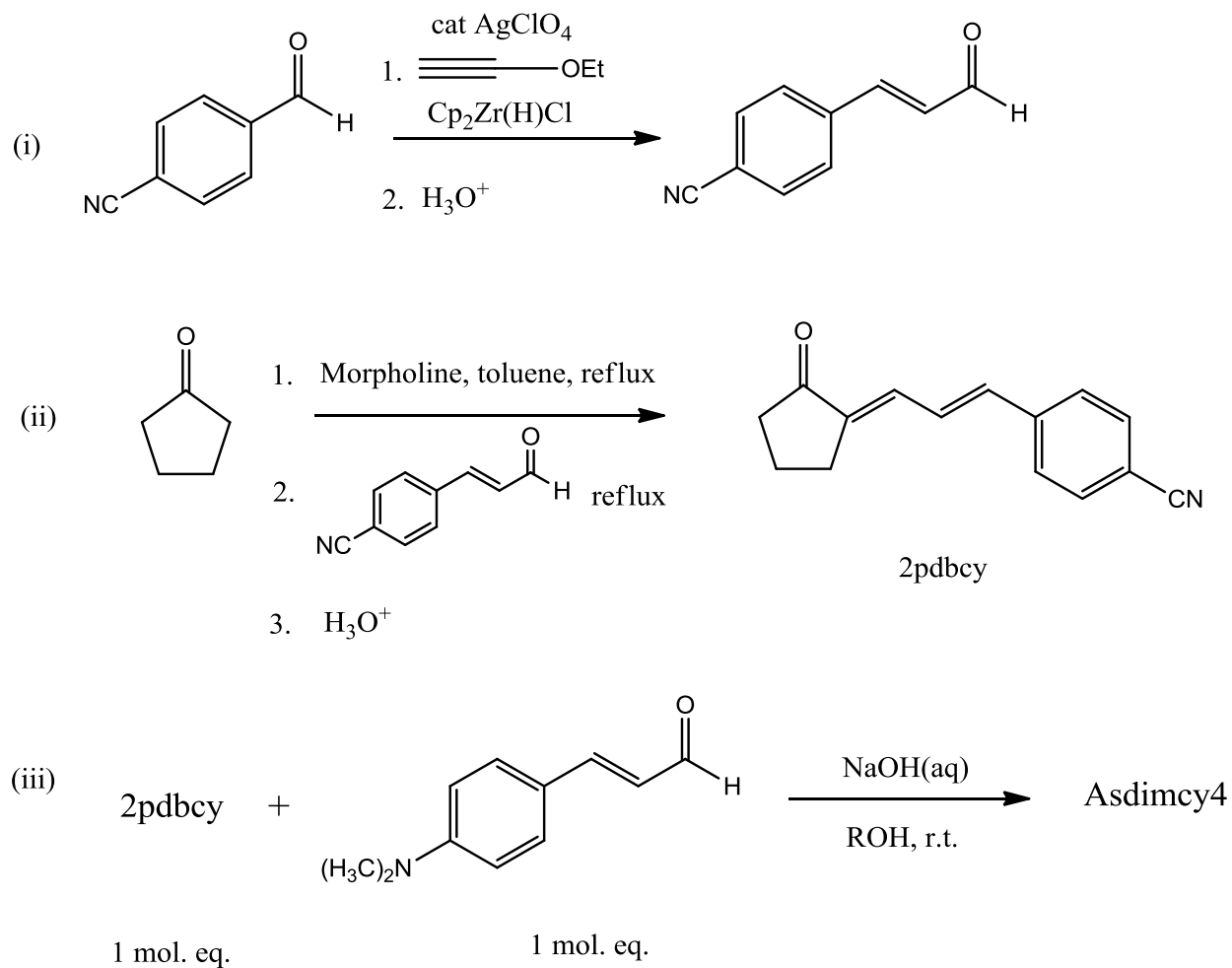
Figure 161. Proposed reaction scheme for the synthesis of Asdimcy4.

5.2.2 (2E,5E)-2,5-bis(5-p-dimethylaminophenyl-penta-2,4-dienylidene)-cyclopentanone (3dbma)

The two carbon homologue of bis-dmac, (2E,5E)-2,5-bis(5-p-dimethylaminophenyl-penta-2,4-dienylidene)-cyclopentanone (3dbma), is of considerable interest (see Figure 162). The extension of polyene chain length will red shift both absorption and fluorescence spectral bands to longer wavelengths, which could push the fluorescence of 3dbma into the near-infrared (NIR) region. There is considerable interest in efficient NIR emitting dyes, ranging from biological to military applications [83, 84]. A proposed synthesis of 3dbma involves first running a two carbon homologation of (E)-4-dimethylaminocinnamaldehyde via $AgClO_4$-catalyzed hydrozirconation, yielding (2E,4E)-5-(4-(dimethylamino)phenyl)-penta-2,4-dienal, followed by an intermolecular base-catalyzed crossed aldol condensation between cyclopentanone (1 mol eq) and the (E)-α,β-unsaturated aldehyde (2 mol eq). A proposed reaction scheme is shown in Figure 163.
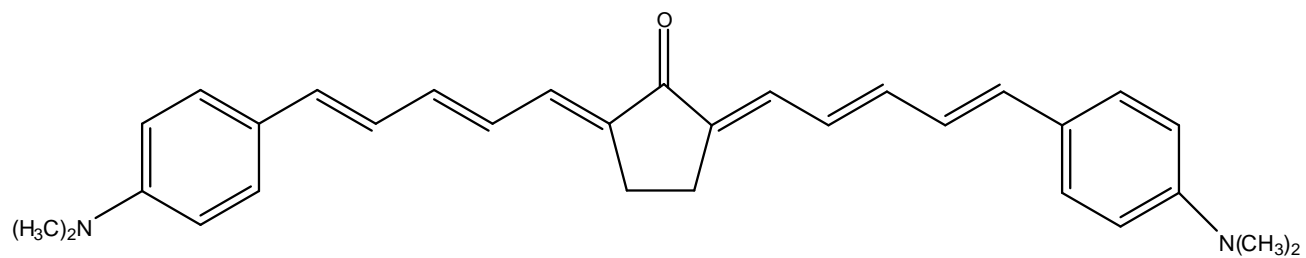
Figure 162. Structure of 3dbma.
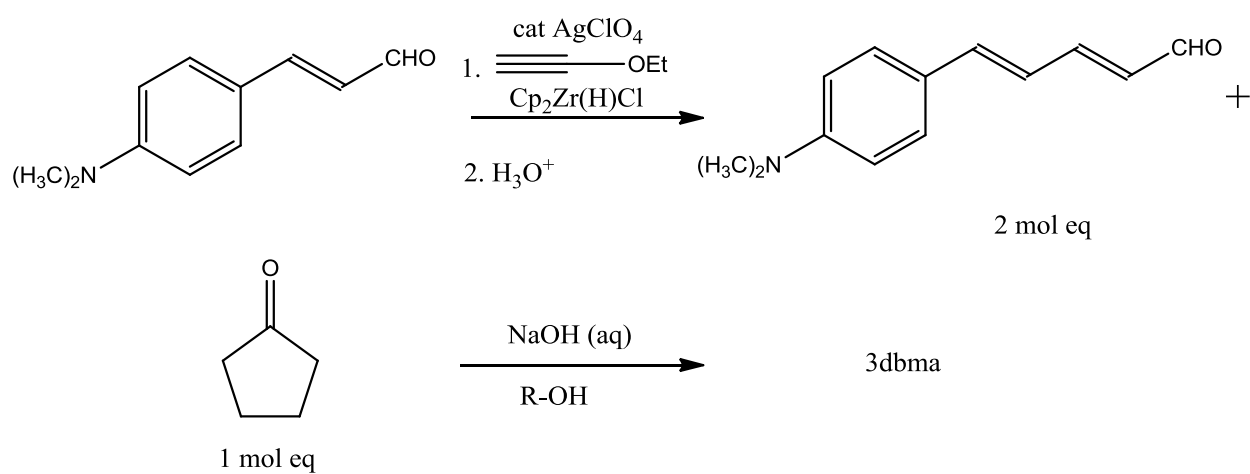
Figure 163. Proposed reaction scheme for the synthesis of 3dbma.

5.2.3 Spectral and Photophysical Properties in Mixed Solvent Systems

This dissertation reports the spectroscopic and photophysical properties of 2-arylidene and 2,5-diarylidene cyclopentanones in single solvent systems. Previous work on the spectral and photophysical properties of electron donor/acceptor charge transfer dyes in binary solvent systems have been carried out [16, 17]. For instance, Pal, *et al.* [17] have investigated the photophysical properties of two aminostyryl dyes, one of which structurally contains a flexible diphenylamino group moiety and the other contains a structurally rigid julolidine moiety, showing the influence of solvent polarity on both the absorption and fluorescence properties. Examination of the 2-arylidene and 2,5-diarylidene cyclopentanone compounds discussed in this dissertation in binary solvent systems should provide further insight into the spectroscopic and photophysical properties of these compounds.

5.2.4 Temperature Dependent Studies

Previous work done by Nad and Pal [16] involved an investigation on the effect of temperature on the photophysical properties of coumarin-151. It was shown that the fluorescence quantum yield of coumarin-151 in hexane decreased relative to an increase in solution temperature, implying an enhancement in the nonradiative deactivation back to the ground state. In other words, an increase in solution temperature resulted in the fluorescence quenching of coumarin-151. Temperature dependent studies of the photophysical properties of the compounds reported here may also provide useful information.

5.2.5   Additional Photochemistry Studies

In addition to the photochemistry of bis-dmab, experiments could be performed to examine the photooxidation and *trans-cis* photoisomerization of additional 2,5-diarylidene cyclopentanone dyes, particularly the asymmetrically substituted 2,5-diarylidene cyclopentanone compound Asdimcy1. Brief studies have been carried out on the singlet oxygen photosensitization of Asdimcy1 in $CDCl_3$ in the presence of 2,2'-thiodiethanol, which reacts with $^1O_2$ to give 2,2'-sulfinylbisethanol. As presented in this dissertation, TME is a good substitute for 2,2'-thiodiethanol for the screening of Asdimcy1 for $^1O_2$. However, studies on both the reactivity of Asdimcy1 with $^1O_2$ and the *trans-cis* photoisomerization have yet to be performed. It would be noteworthy to examine the chemical reactivity of Asdimcy1 with $^1O_2$, especially if the same mechanism holds as that with bis-dmab and whether the $[2\pi + 2\pi]$ cycloaddition reaction occurs on the electron donor end of the molecule or on the electron acceptor end of the molecule.

REFERENCES

[1]   Barnabus, M. V.; Liu, A.; Trifunac, A. D.; Krongauz, V. V.; Chang, C. T. *J. Phys. Chem.* **1992**, *96*, 212.

[2]   Pivovarenko, V. G.; Klueva, A. V.; Doroshenko, A. O.; Demchenko, A. P. *Chem. Phys. Lett.* **2000**, *325*, 389.

[3]   Das, P. K.; Pramanik, R.; Banerjee, D.; Bachi, S. *Spectrochim Acta A* **2000**, *56*, 2763.

[4]   Doroshenko, A. O.; Grigorivich, A. V.; Posokhov, E. A.; Pivovarenko, V. G.; Demchenko, A. P. *Mol. Eng.* **1999**, *8*, 199.

[5]   Kawamata, J.; Inoue, K.; Inabe, T. *Bull. Chem. Soc. Jpn.* **1998**, *71*, 2777.

[6]   Kaatz, P.; Shelton, D. P. *J. Chem. Phys.* **1996**, *105*, 3918.

[7]   Kawamata, J.; Inoue, K.; Inabe, T.; Kiguchi, M.; Kato, M.; Taniguchi, Y. *Chem. Phys. Lett.* **1996**, *249*, 29.

[8]   Kawamata, J.; Akiba, M.; Inagaki, Y. *Jpn. J. Appl. Phys.* **2003**, *42*, L17.

[9]   Wu, J.; Shi, M.; Zhao, Y.; Wu, F. *Dyes Pigm.* **2008**, *76*, 690.

[10]   Tao, W.; Fei-peng, W.; Men-quan, S. *Chem. Res. Chin. Univ.* **2003**, *19*, 470.

[11]   Connors, R. E.; Ucak-Astarlioglu, M. G. *J. Phys. Chem. A* **2003**, *107*, 7684.

[12]   Ucak-Astarlioglu, M. G. *The Electronic Structure and Spectroscopy of Diarylidene-Cycloalkanones and Their Protonated Cations*, Ph. D. Dissertation, Worcester Polytechnic Institute, 2003.

[13]   Zoto, C. A.; Connors, R. E. *J. Mol. Struct.* **2010**, *982*, 121.

[14]   Hutter, W.; Bodenseh, H-K; Koch, A. *J. Mol. Struct.* **1994**, *319*, 73.

[15]   Ucak-Astarlioglu, M. G.; Connors, R. E. *J. Phys. Chem. A* **2005**, *109*, 8275.

[16]   Nad, S.; Pal, H. *J. Phys. Chem. A* **2001**, *105*, 1097.

[17]   Shaikh, M.; Mohanty, J.; Singh, P. K.; Bhasikuttan, A. C.; Rajule, R. N.; Satam, V. S.; Bendre, S. R.; Kanetkar, V. R.; Pal, H. *J. Phys. Chem. A* **2010**, *114*, 4507.

[18]   Chudomel, J. M.; Yang, B.; Barnes, M. D.; Achermann, M.; Mague, J. T.; Lahti, P. M. *J. Phys. Chem. A* **2011**, *115*, 8361.

[19]   Klymchenko, A. S.; Ozturk, T.; Pivovarenko, V. G.; Demchenko, A. P. *Tet. Lett.* **2001**, *42*, 7967.

[20]   Doroshenko, A. O.; Bilokin, M. D.; Pivovarenko, V. G. *J. Photochem. & Photobiol. A: Chemistry* **2004**, *163*, 95.

[21]   Marcotte, N.; Fery-Forgues, S.; Lavabre, D.; Marguet, S.; Pivovarenko, V. G. *J. Phys. Chem. A* **1999**, *103*, 3163.

[22]   Doroshenko, A. O.; Pivovarenko, V. G. *J. Photochem & Photobiol. A: Chemistry* **2003**, *156*, 55.

[23]   George, H.; Roth, R. J. *Tet. Lett.* **1971**, *43*, 4057.

[24]   Zhang, S.; Liu, S.; Zhang, Q.; Deng, Y. *Chem. Commun.* **2011**, *47*, 6641.

[25]   Suppan, P.; Ghonheim, N. *Solvatochromism*; The Royal Society of Chemistry: Cambridge, United Kingdom, 1997.

[26]   (a) Lippert, E. Z. Z. *Naturforschung* **1955**, *10a*, 541. (b) Mataga, N.; Kaifu, Y.; Koizumi, M. *Bull. Chem. Soc. Jpn.* **1956**, *29*, 465.

[27]   Pierola, I. F.; Turro, N. J.; Kuo, P. *Macromolecules* **1985**, *18*, 508.

[28]   Sharma, A. S.; Schulman, S. G. *Introduction to Fluorescence Spectroscopy*; Wiley-Interscience Publication: Canada, 1999.

[29]   Lacowicz, J. R. *Principles of Fluorescence Spectroscopy*; 2nd ed.; Springer: New York, 2004.

[30]   Clarke, R. H.; Frank, H. A. *J. Chem. Phys.* **1976**, *65*, 39.

[31]   Turro, N. J.; Ramamurthy, V.; Scaiano, J. C. *Principles of Molecular Photochemistry An Introduction*; University Science Books: Sausalito, CA, 2009.

[32]   Turro, N. J. *Modern Molecular Photochemistry*; University Science Books: Sausalito, CA, 1991.

[33]   El-Sayed, M. A. *J. Chem. Phys.* **1963**, *38*, 2834.

[34]   Frediani, L.; Rinkevicius, Z.; Ågren, H. *J. Chem. Phys.* **2005**, *122*, 244104.

[35]   Göeppert-Mayer, M. *Ann. Physik.* **1931**, *9*, 273.

[36]   Peticolas, W. L. *Annu. Rev. Phys. Chem.* **1967**, *18*, 233.

[37]   Mukherjee, A. *Appl. Phys. Lett.* **1993**, *62*, 3423.

[38]   He, G. S.; Xu, G. C.; Prasad, P. N., *et. al.*, *Opt. Lett.* **1995**, *20*, 435.

[39]   Strickler, J. H.; Webb, W. W. *Opt. Lett.* **1991**, *16*, 1780.

[40]   Yu, X-Q; Wang, C.; Jiang, M-H *Chem. J. Chin. Univ.* **2000**, *21*, 1953.

[41]   Monnereau, C.; Gallavardin, T.; Armagnat, C.; Lanoé, P-H; Maury, O.; Marcotte, S.; Leverrier, Y.; Baldeck, P. L.; Andraud, C. *Proc. of SPIE*, **8103**, 81030N-2.

[42]   Ahn, H-Y; Fairfull-Smith, K. E.; Morrow, B. J.; Lussini, V.; Kim, B.; Bondar, M. V.; Bottle, S. E.; Belfield, K. D. *J. Am. Chem. Soc.* **2012**, *134*, 4721.

[43]   Lovell, J. F.; Chen, J.; Jarvi, M. T.; Cao, W-G; Allen, A. D.; Liu, Y.; Tidwell, T. T.; Wilson, B. C.; Zheng, G. *J. Phys. Chem. B* **2009**, *113*, 3203.

[44]   (a) Woodburn, K. W.; Engelman, C. J.; Blumenkranz, M. S. *Retina* **2002**, *22*, 391. (b) Brown, S. B.; Brown, E. A.; Walker, I. *Lancet. Oncol.* **2004**, *5*, 497.

[45]   Dougherty, T. J.; Gomer, C. J.; Henderson, B. W.; Jori, G.; Kessel, O.; Korbelik, M.; Moan, J.; Peng, Q. *J. Natl. Cancer. Inst.* **1998**, *90*, 889.

[46]   Wassermann, H. H.; Ives, J. L. *Tetrahedron* **1981**, *37*, 1825.

[47]   (a) Schenck, G. O. *Naturwissenschaften* **1948**, *35*, 28. (b) Wassermann, H. H.; Murray, R. W. *Singlet Oxygen*; Academic Press: New York, 1979.

[48]   (a) Matsumoto, M.; Yamada, M.; Watanabe, N. *Chem. Commun.* **2005**, 483. (b) Kearns, D. R. *Chem. Rev.* **1971**, *71*, 395.

[49]   (a) Turro, N. J.; Chow, M-F; Rigaudy, J. *J. Am. Chem. Soc.* **1979**, *101*, 1300. (b) Turro, N. J.; Chow, M-F; Rigaudy, J. *J. Am. Chem. Soc.* **1981**, *103*, 7218.

[50]   Yuan, Z.; Zheng, S.; Zeng, Y.; Chen, J.; Han, Y.; Li, Y.; Li, Y. *New. J. Chem.* **2010**, *3411*, 718.

[51]   Cai, G.; Bozhkova, N.; Odingo, J.; Berova, N.; Nakanishi, K. *J. Am. Chem. Soc.* **1993**, *115*, 7192.

[52]   Maeta, H.; Suzuki, K. *Tet. Lett.* **1993**, *34*, 341.

[53]   Duff, Jr., M. R. *Charge Transfer Spectra of 2,N-Di-(p-dimethylaminobenzylidene)-cycloalkanones*, MQP Report, Worcester Polytechnic Institute, 2002.

[54]   Kreher, U. P.; Rosamilia, A. E.; Raston, C. L.; Scott, J. L.; Strauss, C. R. *Org. Lett.* **2003**, *5*, 3107.

[55]   Rosamilia, A. E.; Giarrusso, M. A.; Scott, J. L.; Strauss, C. R. *Green. Chem.* **2006**, *8*, 1042.

[56]   Kreher, U. P., *et. al.*, *Acta. Cryst.* **2002**, E**58**, o948.

[57]   Rechthaler, K.; Kohler, G. *Chem. Phys. Lett.* **1994**, *189*, 99.

[58]   Bruker, SAINT (Version 6.14).

[59]   SHELXTL (Version 6.14) for WNT/2003; Bruker AXS Inc.: Madison, WI, 1999.

[60]   CCDC. Mercury 2.4; CCDC: Cambridge, U. K., 2009.

[61]   Gaussian 09, Revision A.02, M. J. Frisch, G. W. Trucks, H. B. Schlegel, G. E. Scuseria, M. A. Robb, J. R. Cheeseman, G. Scalmani, V. Barone, B. Mennucci, G. A. Petersson, H. Nakatsuji, M. Caricato, X. Li, H. P. Hratchian, A. F. Izmaylov, J. Bloino, G. Zheng, J. L. Sonnenberg, M. Hada, M. Ehara, K. Toyota, R. Fukuda, J. Hasegawa, M. Ishida, T. Nakajima, Y. Honda, O. Kitao, H. Nakai, T. Vreven, J. A. Montgomery, Jr., J. E. Peralta, F. Ogliaro, M. Bearpark, J. J. Heyd, E. Brothers, K. N. Kudin, V. N. Staroverov, R. Kobayashi, J. Normand, K. Raghavachari, A. Rendell, J. C. Burant, S. S. Iyengar, J. Tomasi, M. Cossi, N. Rega, J. M. Millam, M. Klene, J. E. Knox, J. B. Cross, V. Bakken, C. Adamo, J. Jaramillo, R. Gomperts, R. E. Stratmann, O. Yazyev, A. J. Austin, R. Cammi, C. Pomelli, J. W. Ochterski, R. L. Martin, K. Morokuma, V. G. Zakrzewski, G. A. Voth, P. Salvador, J. J. Dannenberg, S. Dapprich, A. D. Daniels, O. Farkas, J. B. Foresman, J. V. Ortiz, J. Cioslowski, and D. J. Fox, Gaussian, Inc., Wallingford CT, 2009.

[62]   MOS-F version 4.2B, Microsoft® Windows 95/98/NT, Matsuura, A., Fujitsu Labs Ltd.

[63]   Papanikolas, J.; Walker, G. C.; Shamamian, V. A.; Christensen, R. L.; Baum, J. C. *J. Am. Chem. Soc.* **1990**, *112*, 1912.

[64]   (a) Klessinger, M.; Michl, J. *Excited States and Photochemistry of Organic Molecules*; VCH Publishers: New York, 1995. (b) Englman, R.; Jortner, J. *Mol. Phys.* **1970**, *18*, 145. (c) Barltrop, J.; Coyle, J. D. *Principles of Photochemistry*; Wiley & Sons: New York, 1978.

[65]   Tatchen, J.; Gilka, N.; Marian, C. M. *Phys. Chem. Chem. Phys.* **2007**, *9*, 5209 (and references therein).

[66]   Furche, F.; Rappoport, D. (2005). Density functional methods for excited states: equilibrium structure and electronic spectra. In M. Olivucci (Ed.), *Computational Photochemistry* (pp. 93-128). Amsterdam: Elsevier.

[67]   Kessler, M. A.; Wolfbeis, O. S. *Spectrochimica Acta.* **1991**, *47A*, 187.

[68]   Morimoito, A.; Yatsuhashi, T.; Shimada, T.; Biczók, L.; Tryk, D.; Inoue, H. *J. Phys. Chem. A* **2001**, *105*, 10488.

[69]   (a) Pearson, R. G. Ed. *Hard and Soft Acids and Bases*; Hutchingson and Ross: Stroudsburg, PA, 1973. (b) Ho, T.-I. *The Hard and Soft Acid and Base Principle in Organic Chemistry*; Academic Press: New York, 1977.

[70]   Marjani, K.; Mousavi, M.; Namazian, F. *J. Chem. Crystallogr.* **2011**, 41, 1451.

[71]   Murray, R. W.; Kong, W.; Rajadhyaksha, S. N. *J. Org. Chem.*, **1993**, *58*, 315.

[72]   Xue, J.; Zhao, Y.; Wu, J.; Wu, F. *J. Photochem. & Photobiol. A: Chemistry* **2008**, *195*, 261.

[73]   Murthy, R. S.; Bio, M.; You, Y. *Tet. Lett.* **2009**, *50*, 1041.

[74]   Cabrerizo, F. M.; Dántola, M. L.; Petroselli, G.; Capparelli, A. L. *Photochem. & Photobiol.* **2007**, *83*, 526.

[75]   Merkel, P. B.; Kearns, D. R. *J. Am. Chem. Soc.* **1972**, *94*, 1029.

[76]   Jockusch, S.; Ren, R. X.; Jang, Y. P.; Itagaki, Y.; Vollmer-Snarr, H. R.; Sparrow, J. R.; Nakanishi, K.; Turro, N. J. *J. Am. Chem. Soc.* **2004**, *126*, 4646.

[77]   Merkel, P. B.; Nilsson, R.; Kearns, D. R. *J. Am. Chem. Soc.* **1972**, *94*, 1030.

[78]   Long, C. A.; Kearns, D. R. *J. Am. Chem. Soc.* **1975**, *97*, 2018.

[79]   Merkel, P. B.; Kearns, D. R. *J. Am. Chem. Soc.* **1972**, *94*, 7244.

[80]   Salokhiddinov, K. I.; Byteva, I. M.; Gurinovich, G. P. *J. Applied. Spectroscopy* **1981**, *34*, 561.

[81]   Chen, Z. *Synthesis and Properties of a Visible-to-Near-IR-Fluorescing 2,5-Diarylidene Cyclopentanone Charge-Transfer Dye*, MQP Report, Worcester Polytechnic Institute, 2011.

[82]   Austin, M.; Egan, O. J.; Tully, R.; Pratt, A. C. *Org. Biomol. Chem.* **2007**, *5*, 3778.

[83]   Amiot, C. L.; Xu, S.; Liang, S.; Pan, L.; Zhao, J. X. *Sensors* **2008**, *8*, 3082.

[84]   Vilaseca, M.; Pujol, J.; Arjona, M.; Martínez-Verdú, F. M. *CGIV 2004: The Second European Conference on Colour Graphics, Imaging and Vision*, 431.

APPENDICES

APPENDIX A

QUANTUM MECHANICS BEHIND SPIN-ORBIT COUPLING

To demonstrate the basis of El-Sayed's rule, the mode of action of each orbital angular momentum operator on p-atomic orbitals will be examined. The p-orbital atomic wavefunctions in general form are defined by the following, provided that c is the normalization constant, α is proportional to Z/a_0 (Z = nuclear charge and $a_0 = 0.529$ Å), and the radial and spherical (polar) dimensions are $r > 0$, $0 \le \theta \le \pi$, and $0 \le \phi \le 2\pi$:

$$p_x = c\exp(-\alpha r)\sin\theta\cos\phi \qquad (A\text{-}1)$$

$$p_y = c\exp(-\alpha r)\sin\theta\sin\phi \qquad (A\text{-}2)$$

$$p_z = c\exp(-\alpha r)\cos\theta \qquad (A\text{-}3)$$

The orbital angular momentum operator components are defined by the following:

$$\hat{l}_x = -i\hbar\left(-\sin\phi\frac{\partial}{\partial\theta} - \cot\theta\cos\phi\frac{\partial}{\partial\phi}\right) \qquad (A\text{-}4)$$

$$\hat{l}_y = -i\hbar\left(\cos\phi\frac{\partial}{\partial\theta} - \cot\theta\sin\phi\frac{\partial}{\partial\phi}\right) \qquad (A\text{-}5)$$

$$\hat{l}_z = -i\hbar\frac{\partial}{\partial\phi} \qquad (A\text{-}6)$$

356

Consider two simple organic systems: 1,3-butadiene and a generic carbonyl compound (see Figure A-1).

(a)

(b)
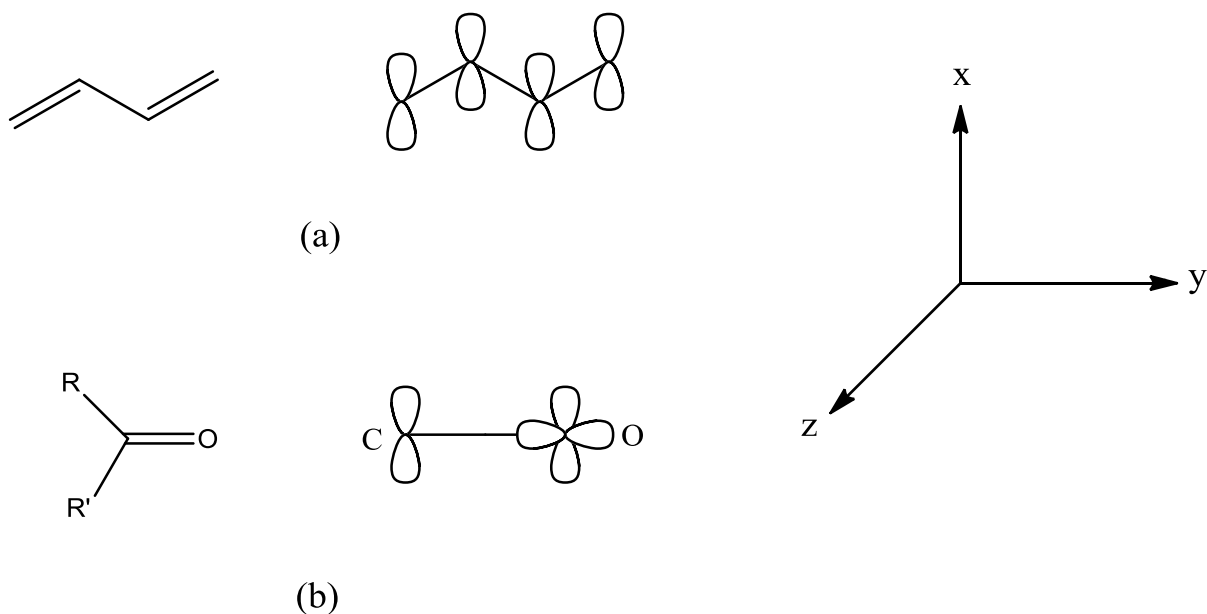
Figure A-1. Structures and orbital depictions of (a) 1,3-butadiene and (b) a generic carbonyl compound, along with assignment of the three-dimensional axis system.

For the case of 1,3-butadiene, which is composed of four π-molecular orbitals, consider the spin-orbit coupling matrix element $< {}^{1}(\pi, \pi *) \left| \hat{H}_{SO} \right| {}^{3}(\pi, \pi *) >$. In knowing that π-molecular orbitals are formed from the linear combination of out of plane p atomic orbitals, solution to the one-center term matrix elements (that is, localization on the same atom i) show that they are equal to zero:

357

(i) $\quad < p_{x,i} \left| \hat{\ell}_{x,i} \right| p_{x,i} >$

$$\hat{\ell}_{x,i} \left| p_{x,i} >= \left[-i\hbar \left(-\sin\phi \frac{\partial}{\partial\theta} - \cot\theta\cos\phi \frac{\partial}{\partial\phi} \right) \right] cre^{-\alpha r}\sin\theta\cos\phi =$$

$$-i\hbar \left(-\sin\phi \frac{\partial}{\partial\theta} \left(cre^{-\alpha r}\sin\theta\cos\phi \right) - \cot\theta\cos\phi \frac{\partial}{\partial\phi} \left(cre^{-\alpha r}\sin\theta\cos\phi \right) \right) =$$

$$-i\hbar \left(-\sin\phi\, cre^{-\alpha r}\cos\phi \frac{\partial}{\partial\theta}(\sin\theta) - \cot\theta\cos\phi\, cre^{-\alpha r}\sin\theta \frac{\partial}{\partial\phi}(\cos\phi) \right) =$$

$$-i\hbar \left(-cre^{-\alpha r}\sin\phi\cos\phi\cos\theta + cre^{-\alpha r}\cot\theta\cos\phi\sin\theta\sin\phi \right) =$$

$$-i\hbar \left(-cre^{-\alpha r}\sin\phi\cos\phi\cos\theta + cre^{-\alpha r}\frac{\cos\theta}{\sin\theta}\cos\phi\sin\theta\sin\phi \right) =$$

$$-i\hbar \left(-cre^{-\alpha r}\sin\phi\cos\phi\cos\theta + cre^{-\alpha r}\cos\theta\cos\phi\sin\phi \right) = -i\hbar(0) = 0$$

$$\therefore < p_{x,i} \left| \hat{l}_{x,i} \right| p_{x,i} >= 0$$

(ii) $\quad < p_{x,i} \left| \hat{\ell}_{y,i} \right| p_{x,i} >$

$$\hat{l}_{y,i} \left| p_{x,i} >= \left[-i\hbar \left(\cos\phi \frac{\partial}{\partial\theta} - \cot\theta\sin\phi \frac{\partial}{\partial\phi} \right) \right] cre^{-\alpha r}\sin\theta\cos\phi =$$

$$-i\hbar \left(\cos\phi \frac{\partial}{\partial\theta} \left(cre^{-\alpha r}\sin\theta\cos\phi \right) - \cot\theta\sin\phi \frac{\partial}{\partial\phi} \left(cre^{-\alpha r}\sin\theta\cos\phi \right) \right) =$$

$$-i\hbar \left(\cos\phi\, cre^{-\alpha r}\cos\phi \frac{\partial}{\partial\theta}(\sin\theta) - \cot\theta\sin\phi\, cre^{-\alpha r}\sin\theta \frac{\partial}{\partial\phi}(\cos\phi) \right) =$$

$$-i\hbar \left(cre^{-\alpha r}\cos^2\phi\cos\theta + cre^{-\alpha r}\cot\theta\sin^2\phi\sin\theta \right) =$$

$$-i\hbar \left(cre^{-\alpha r}\cos^2\phi\cos\theta + cre^{-\alpha r}\frac{\cos\theta}{\sin\theta}\sin^2\phi\sin\theta \right) =$$

$$-i\hbar \left(cre^{-\alpha r}\cos\theta \right)\left(\cos^2\phi + \sin^2\phi \right) = -i\hbar(p_{z,i})(1) = -i\hbar(p_{z,i})$$

$$\therefore < p_{x,i} \left| \hat{l}_{y,i} \right| p_{x,i} >= -i\hbar < p_{x,i} \left| p_{z,i} >= -i\hbar(0) = 0$$

(iii) $< p_{x,i} | \hat{l}_{z,i} | p_{x,i} >$

$$\hat{l}_{z,i} | p_{x,i} > = \left[-i\hbar \frac{\partial}{\partial \phi} \right] cre^{-\alpha r} \sin \theta \cos \phi = -i\hbar cre^{-\alpha r} \sin \theta \frac{\partial}{\partial \phi} (\cos \phi) =$$

$$- i\hbar cre^{-\alpha r} \sin \theta (-\sin \phi) = i\hbar cre^{-\alpha r} \sin \theta \sin \phi = i\hbar p_{y,i}$$

$$\therefore < p_{x,i} | \hat{l}_{z,i} | p_{x,i} > = i\hbar < p_{x,i} | p_{y,i} > = i\hbar(0) = 0$$

Therefore, no one-center terms survive.

For two-center terms (that is, localization on adjacent atoms i and j), the matrix elements for spin-orbit coupling also come out to equal zero because of the Hermitian nature of the $\hat{l}$ operator:

$$< p_{x,i} \left| \hat{\ell}_{x,i} \right| p_{x,j} > = < p_{x,j} \left| \hat{\ell}_{x,i} \right| p_{x,i} >* = i\hbar(0) = 0$$

$$< p_{x,i} \left| \hat{\ell}_{y,i} \right| p_{x,j} > = < p_{x,j} \left| \hat{\ell}_{y,i} \right| p_{x,i} >* = -i\hbar(0) = 0$$

$$< p_{x,i} \left| \hat{\ell}_{z,i} \right| p_{x,j} > = < p_{x,j} \left| \hat{\ell}_{z,i} \right| p_{x,i} >* = i\hbar(0) = 0$$

Therefore, no two-center terms survive.

It is only the three-center terms that survive, giving a very small value for

$< {}^1(\pi, \pi *) \left| \hat{H}_{SO} \right| {}^3(\pi, \pi *) >$, which explains why the rate of $S(\pi, \pi^*) \rightarrow T(\pi, \pi^*)$ intersystem crossing is slow.

For the case of a carbonyl compound, which is composed of a nonbonding orbital localized on the carbonyl oxygen atom, the spin-orbit coupling matrix element

$< {}^1(\pi, \pi *) \left| \hat{H}_{SO} \right| {}^3(n, \pi *) >$ is considered. The nonbonding orbital on oxygen is treated to be approximately equivalent to a p_y orbital and evaluation of the following one-center matrix element does not equal zero:

$$< p_{x,O} \left| \hat{l}_{z,i} \right| p_{y,O} >$$

$$\hat{l}_{z,i} | p_{y,O} > = \left[-i\hbar \frac{\partial}{\partial \phi} \right] cre^{-\alpha r} \sin\theta \sin\phi = -i\hbar cre^{-\alpha r} \sin\theta \frac{\partial}{\partial \phi} \sin\phi = -i\hbar cre^{-\alpha r} \sin\theta \cos\phi = -i\hbar p_{x,O}$$

$$\therefore < p_{x,O} \left| \hat{l}_{z,i} \right| p_{y,O} > = -i\hbar < p_{x,O} | p_{x,O} > = -i\hbar(1) = -i\hbar \neq 0$$

Therefore, the nonzero value for the one-center term on the carbonyl oxygen atom demonstrates strong spin-orbit coupling between two states of different orbital configurations, and hence, efficient $S(\pi, \pi*) \rightarrow T(n, \pi*)$ intersystem crossing.

APPENDIX B

^{1}H NMR AND ^{13}C NMR SPECTRA OF COMPOUNDS

Figure B-1. bis-dmab

Figure B-2. bis-dmac

Figure B-3. bis-juldmac

Figure B-4. 2dbmxcp

Figure B-5. 1dbzfcp

Figure B-6. Asdimcy1

Figure B-7. Asunsub

Figure B-8. Ashrbor

Figure B-9. dmab

Figure B-10. dmac

Figure B-11. 1pdbcy

Figure B-12. 1pdbmx

Figure B-13. 1pdbun

Figure B-14. 1pdbzf
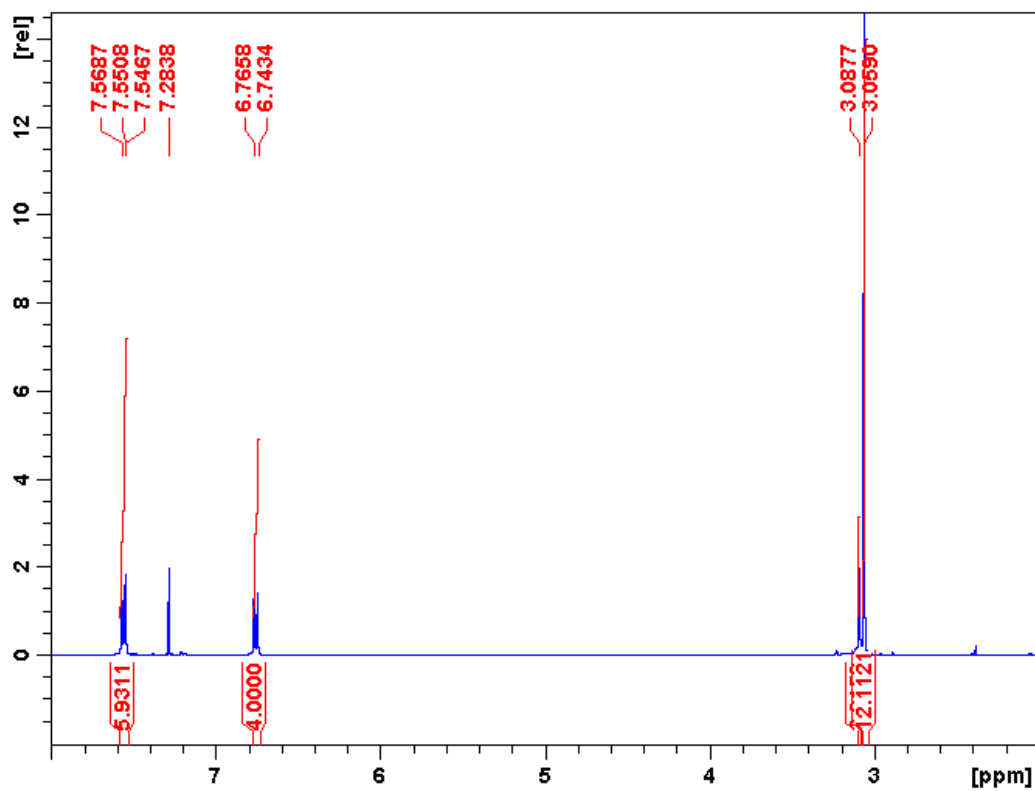
Figure B-1. (a) ^{1}H NMR bis-dmab δ 2.0-8.0 ppm
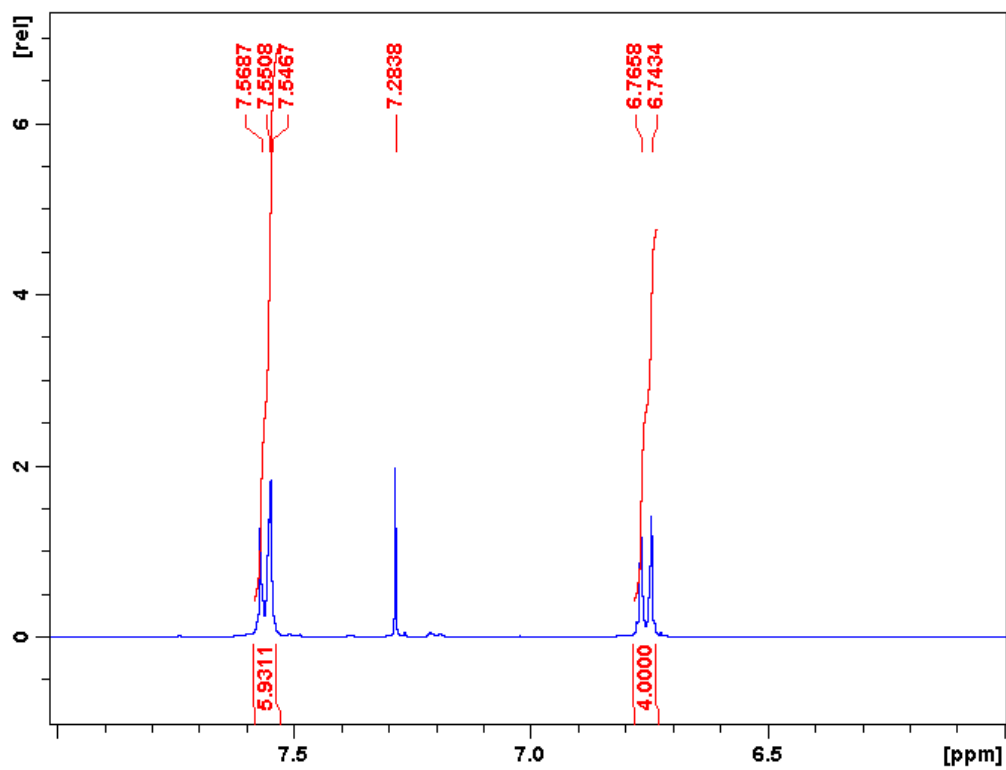
Figure B-1. (b) ^{1}H NMR bis-dmab δ 6.0-8.0 ppm
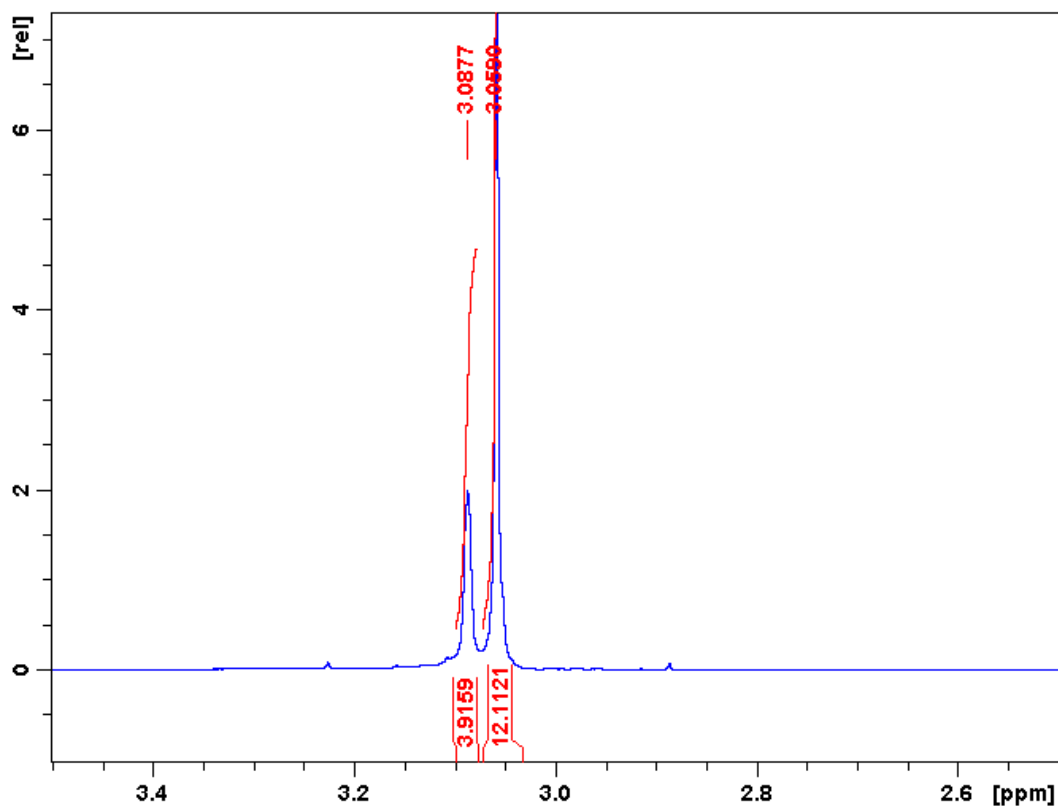
Figure B-1. (c) ^{1}H NMR bis-dmab δ 2.5-3.5 ppm
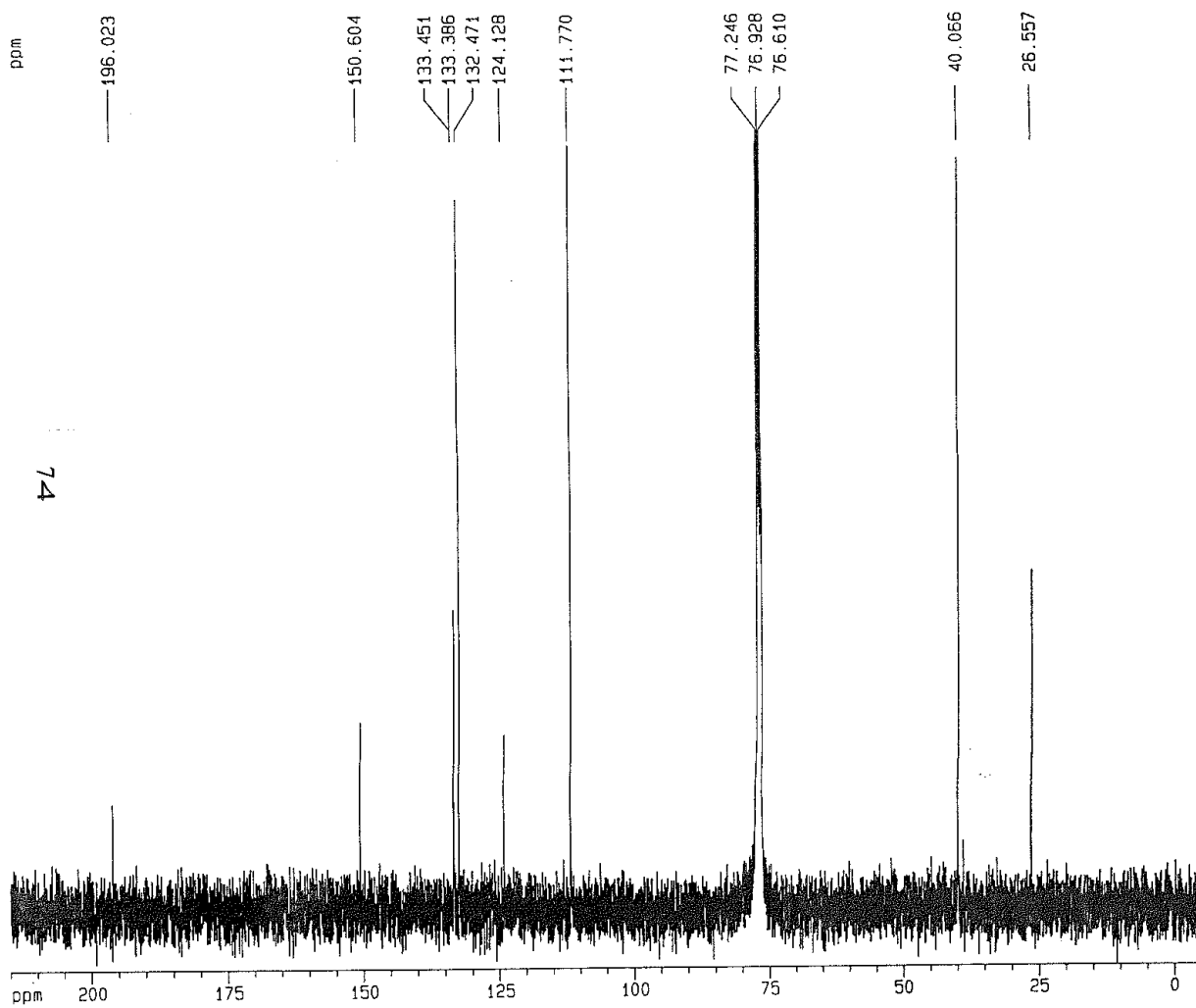
Figure B-1. (d) ^{13}C NMR bis-dmab [53]
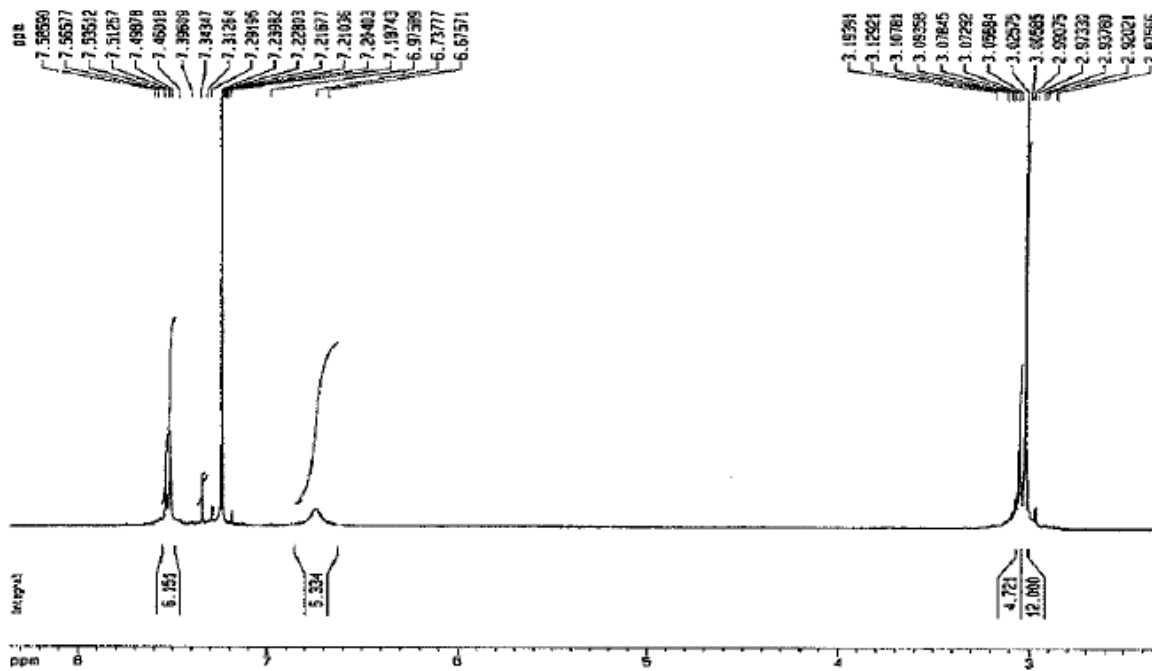
Figure B-2. (a) ^{1}H NMR bis-dmac [12]
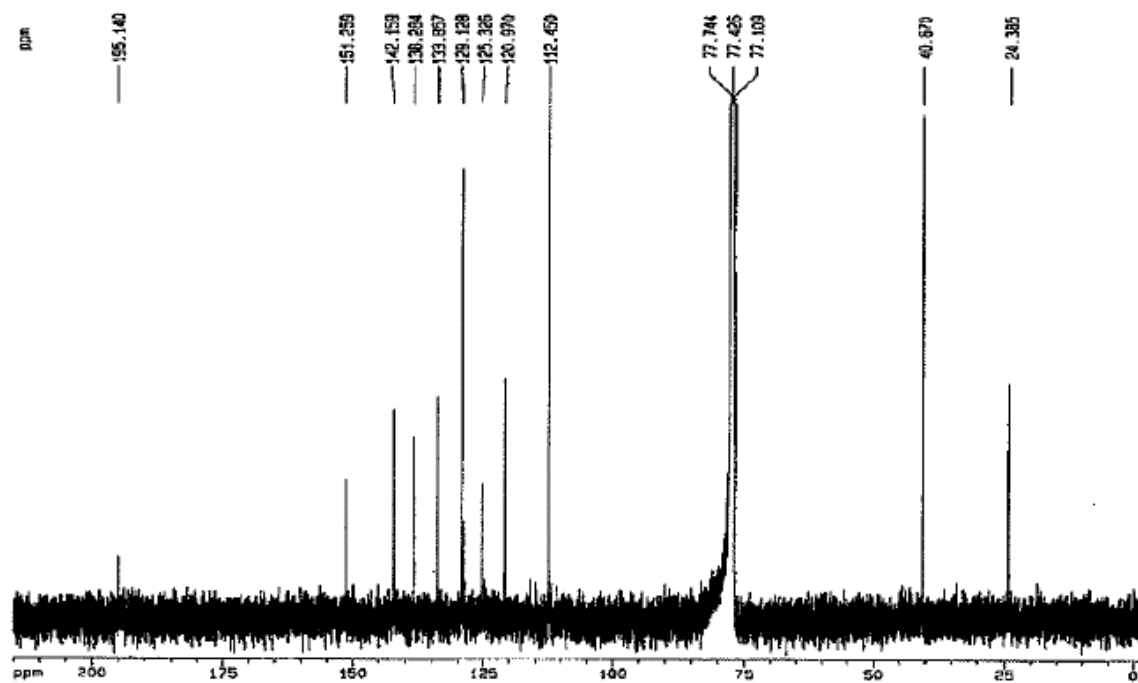
Figure B-2. (b) ^{13}C NMR bis-dmac [12]
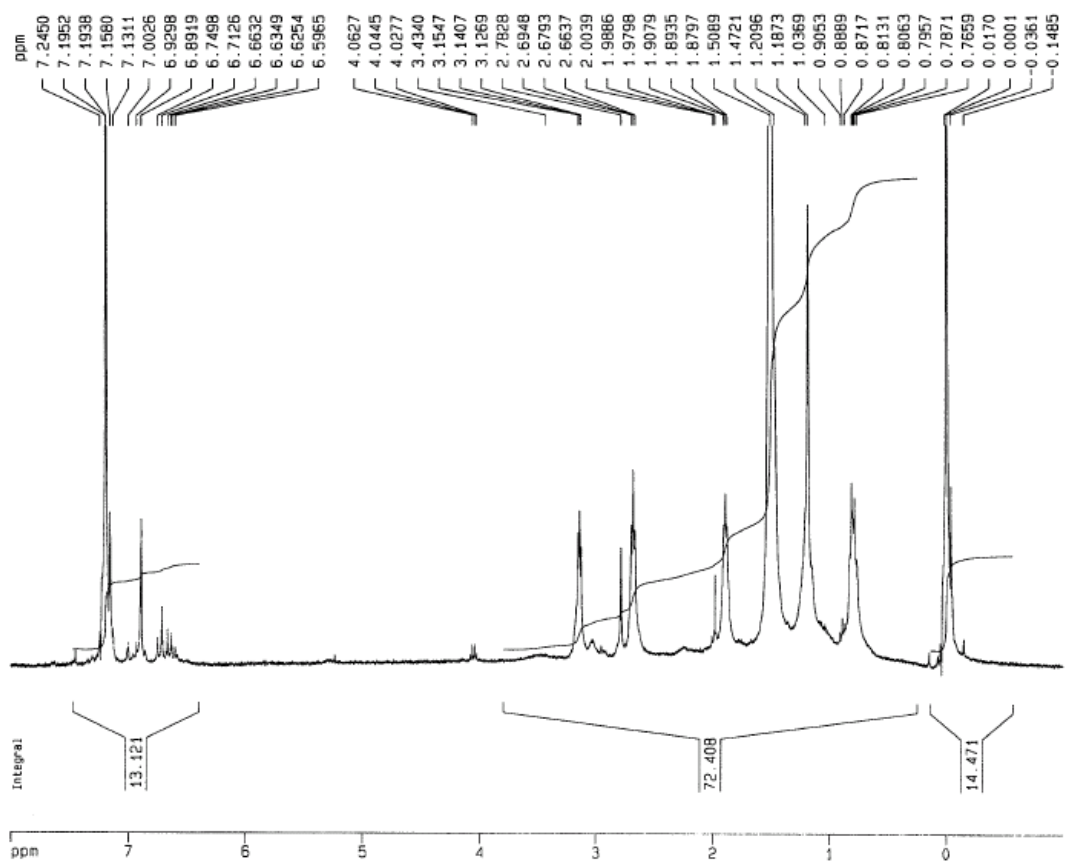
Figure B-3. ^{1}H NMR bis-juldmac
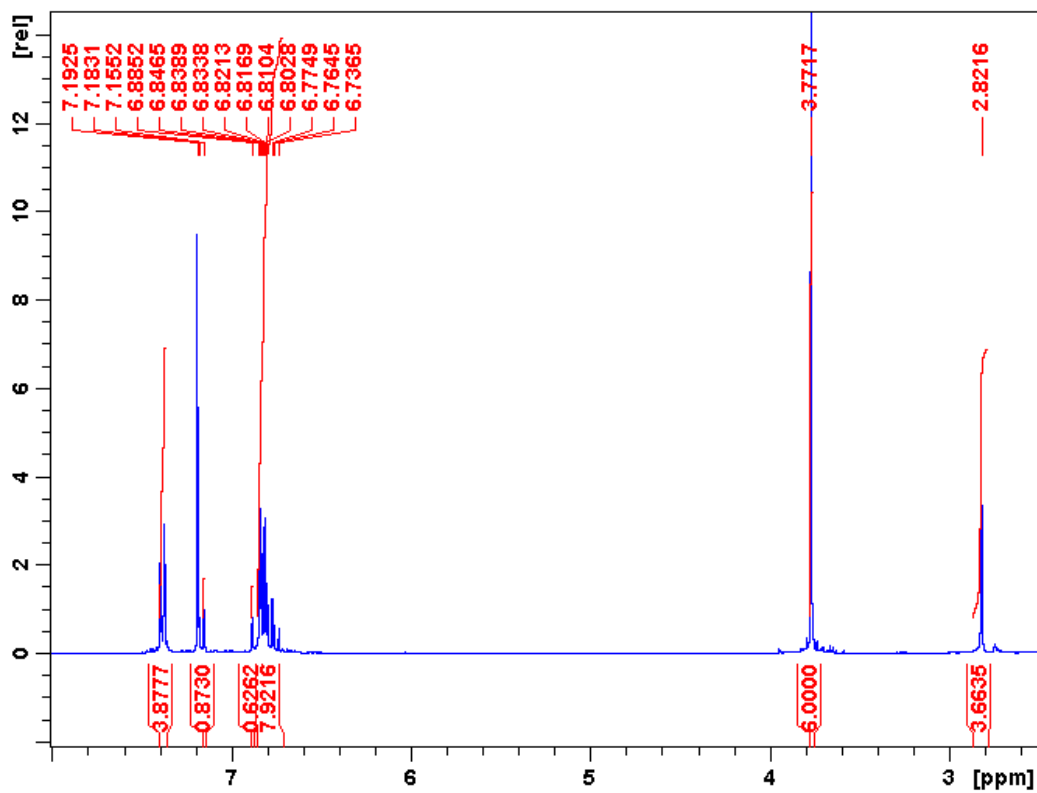
Figure B-4. (a) ^{1}H NMR 2dbmxcp δ 2.5-8.0 ppm
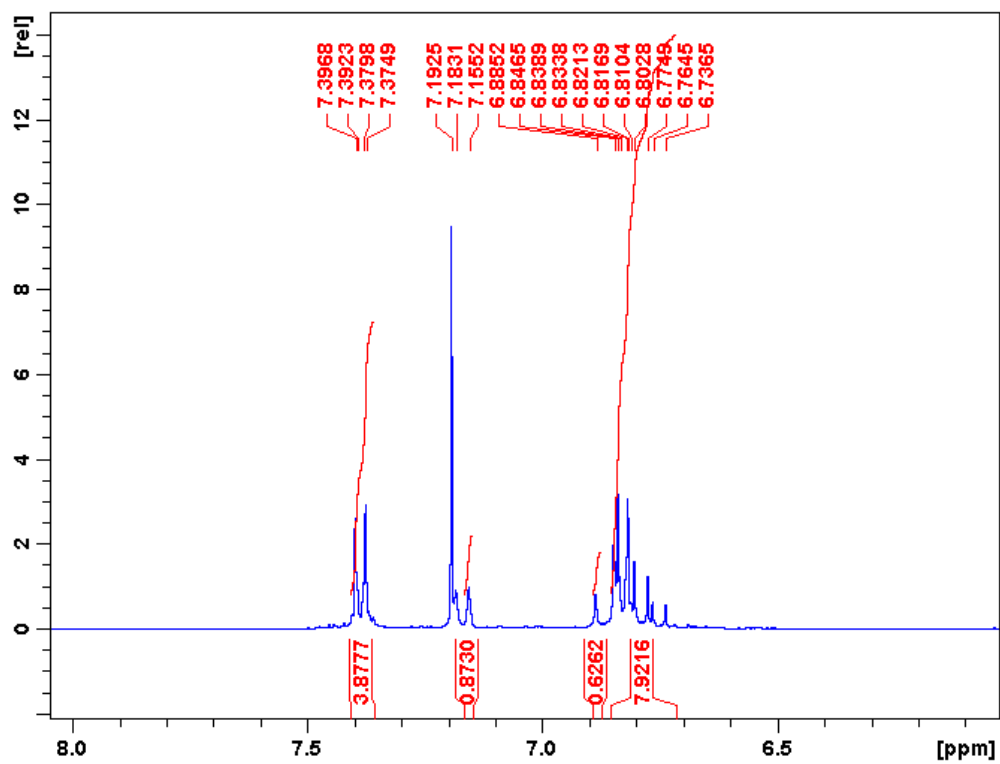
Figure B-4. (b) ^{1}H NMR 2dbmxcp δ 6.0-8.05 ppm
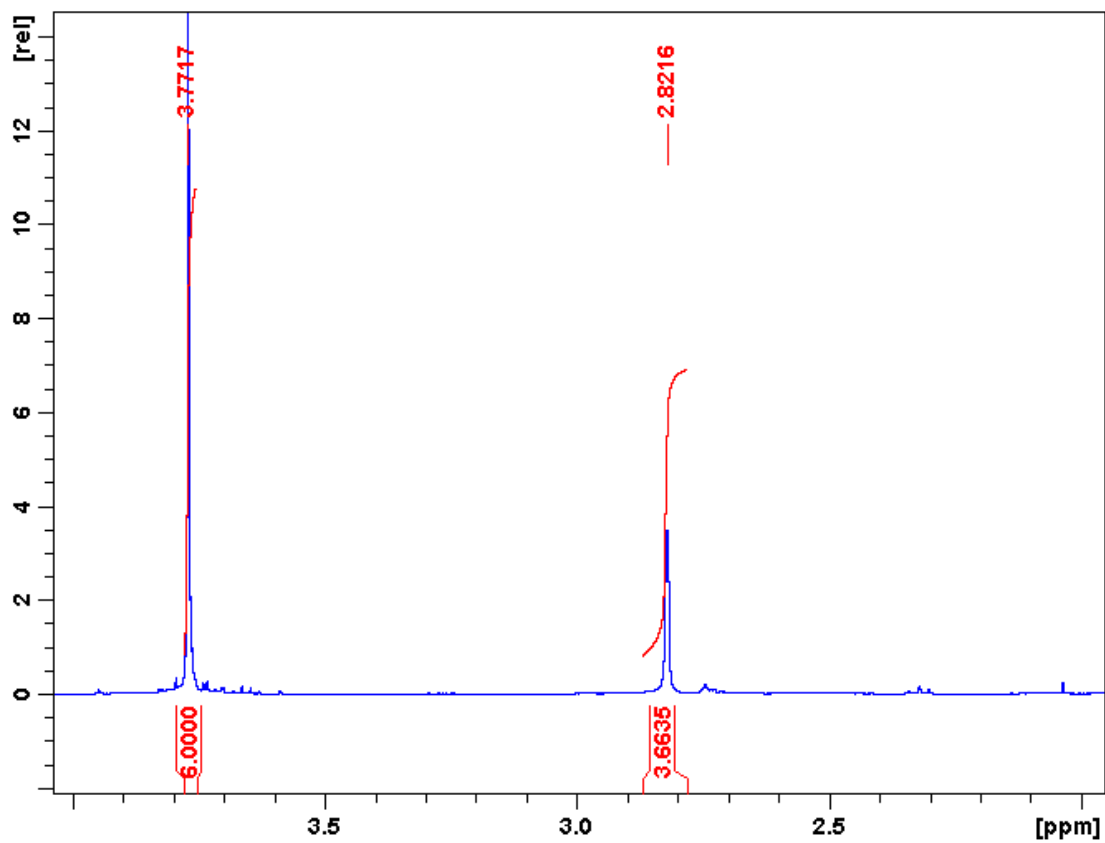
Figure B-4. (c) ^{1}H NMR 2dbmxcp δ 1.95-4.05 ppm
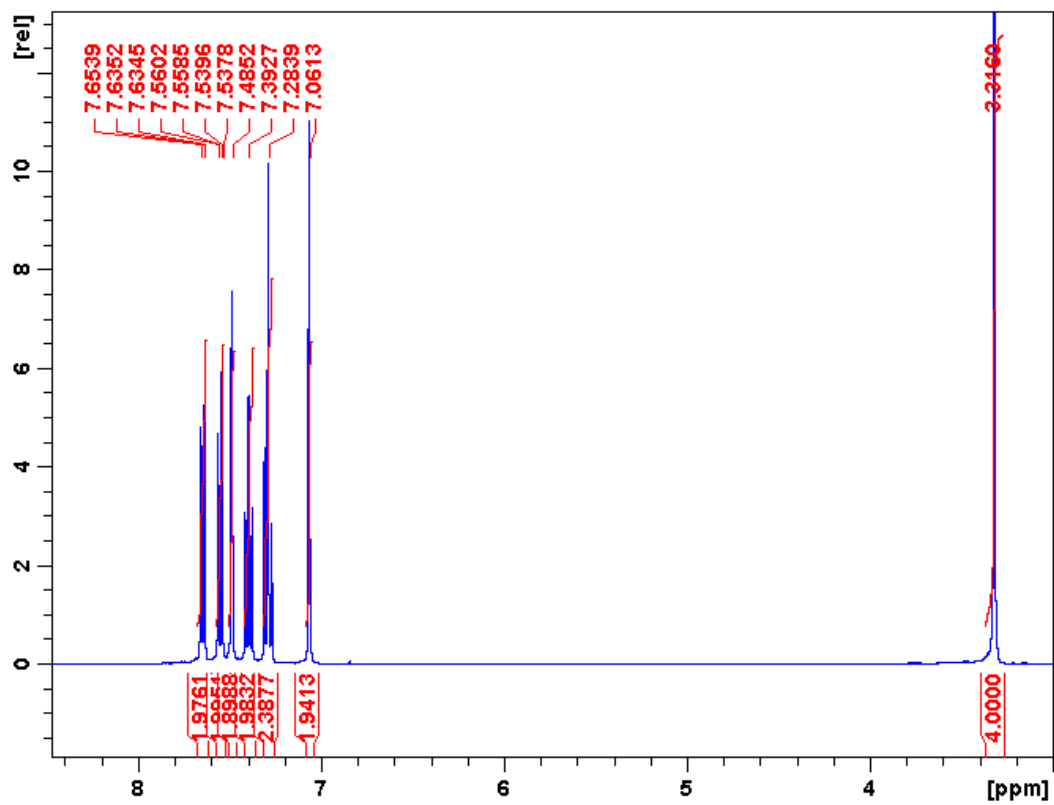
Figure B-5. (a) ^{1}H NMR 1dbzfcp δ 3-8.5 ppm
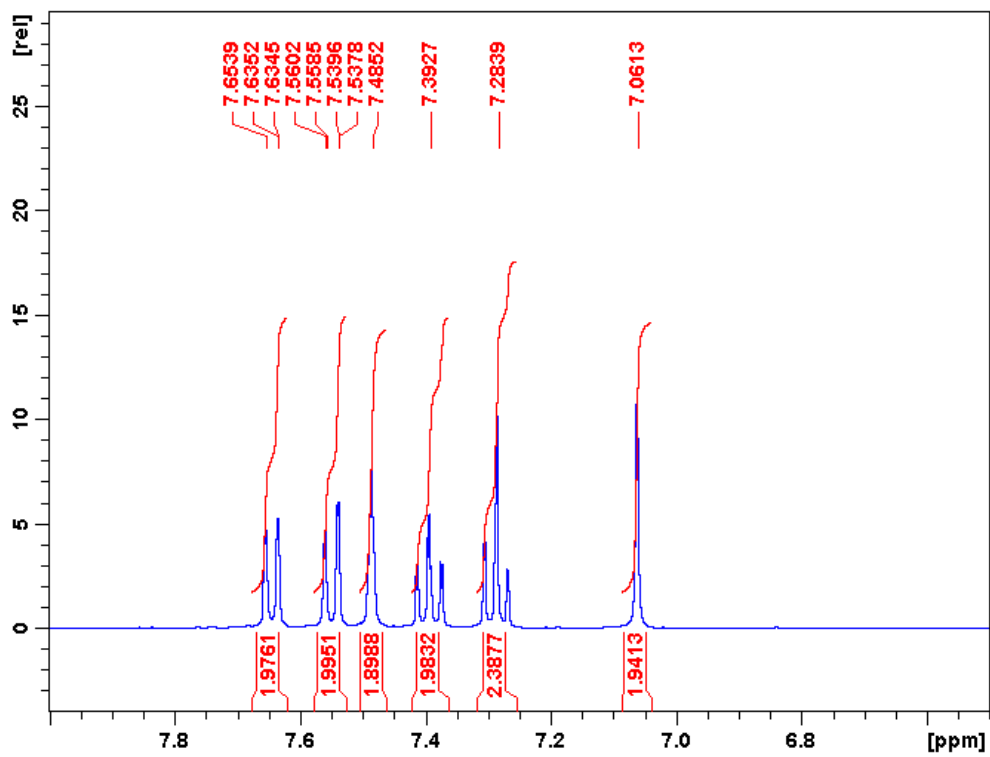
Figure B-5. (b) ^{1}H NMR 1dbzfcp δ 6.5-8 ppm
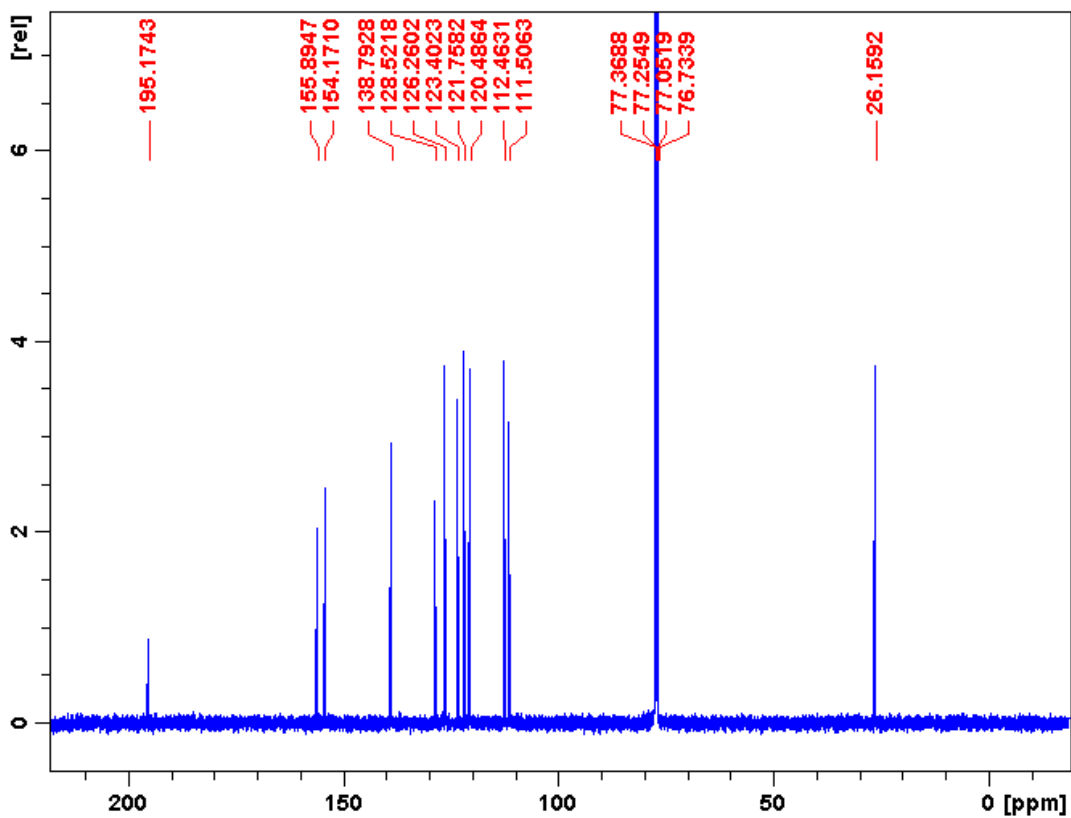
Figure B-5. (c) ^{13}C NMR 1dbzfcp
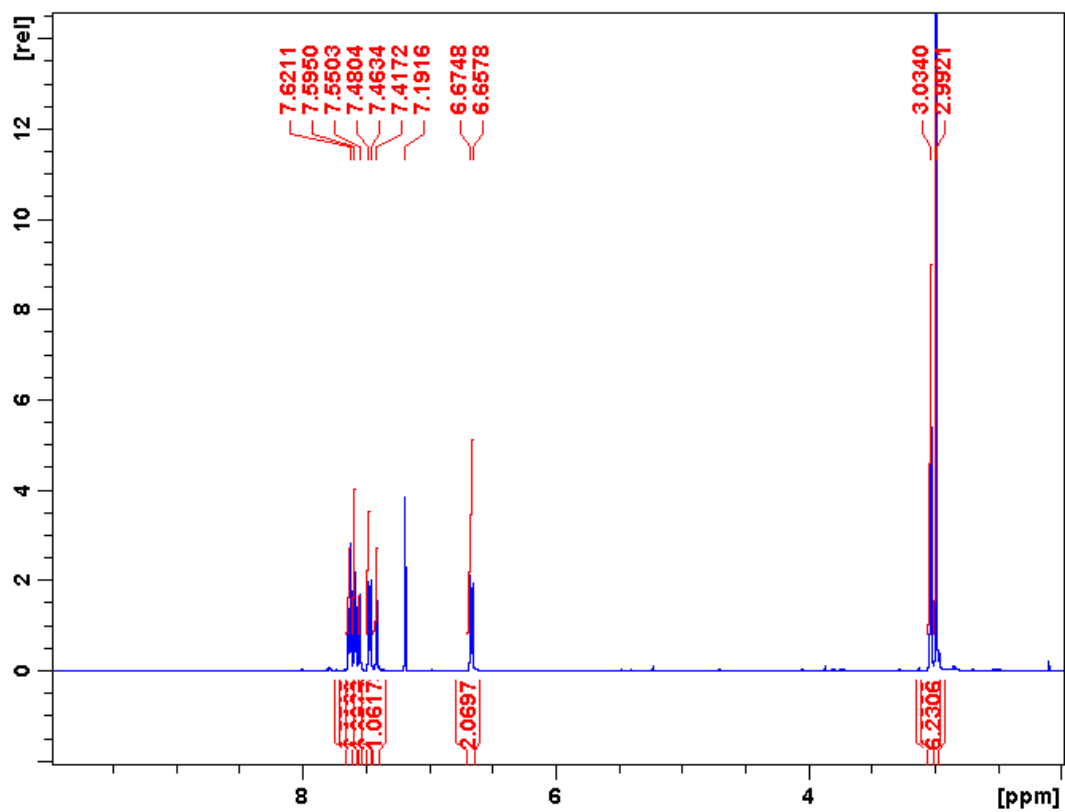
Figure B-6. (a) ^{1}H NMR Asdimcy1 δ 2-10 ppm
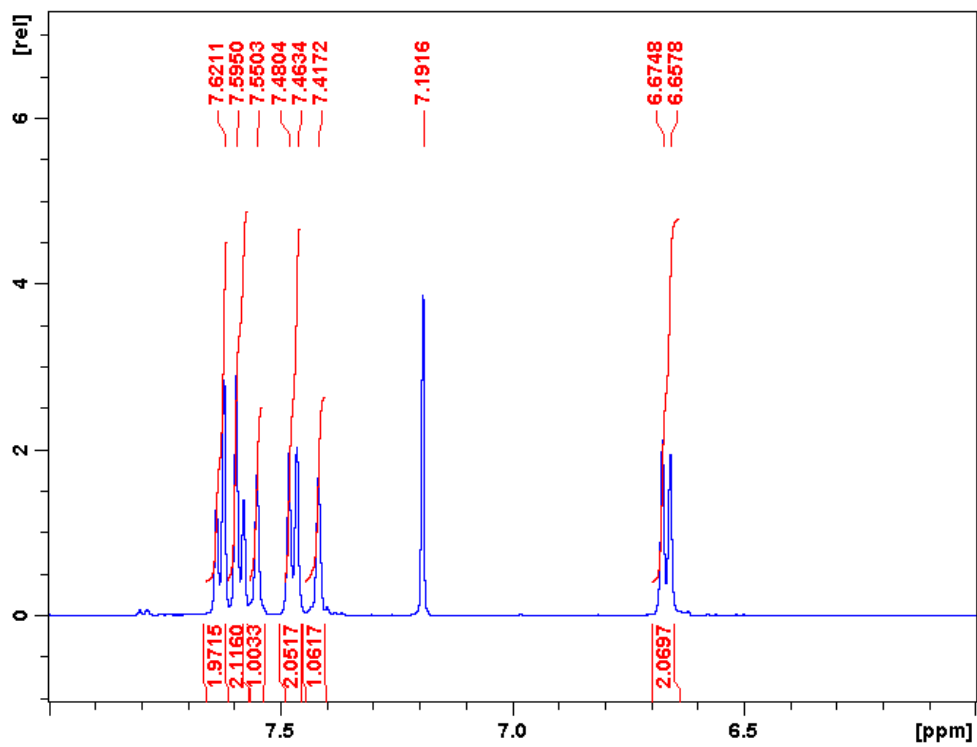
Figure B-6. (b) ^{1}H NMR Asdimcy1 δ 6-8 ppm
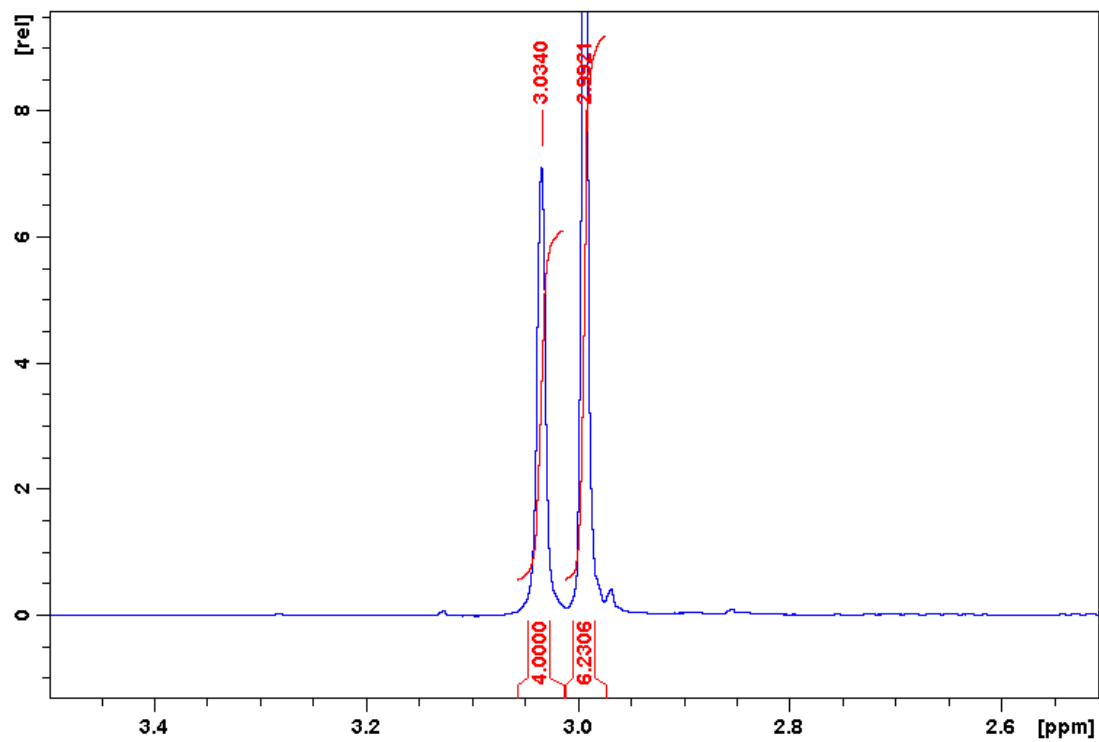
Figure B-6. (c) ^{1}H NMR Asdimcy1 δ 2.5-3.5 ppm
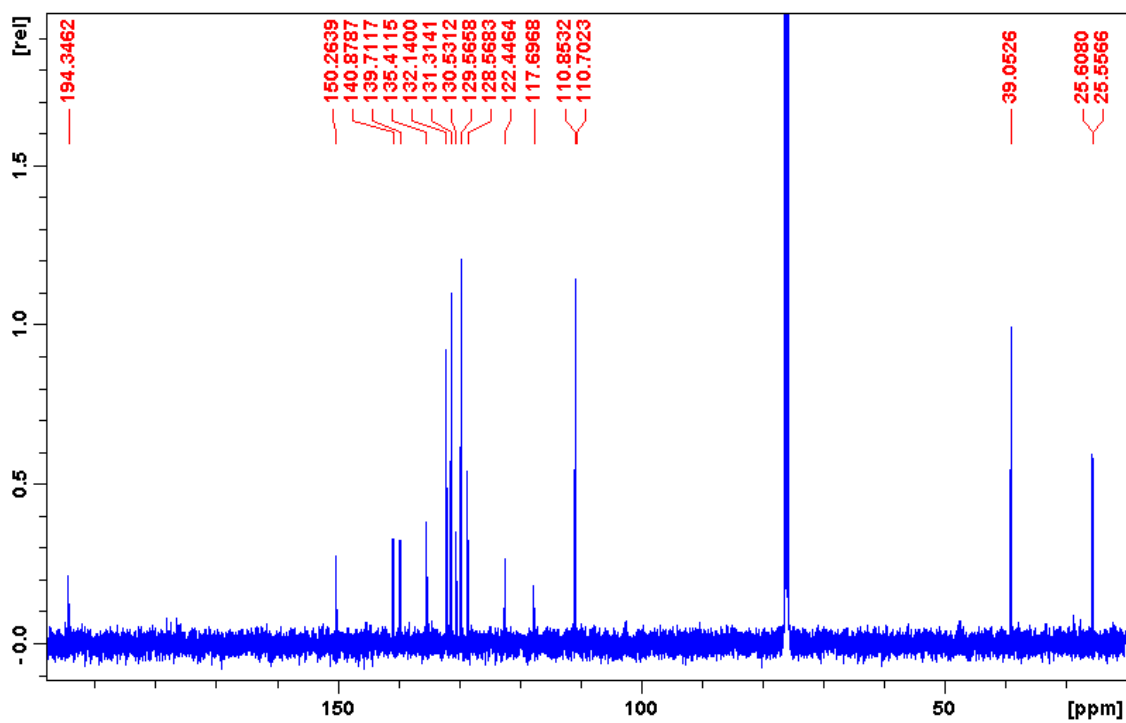
Figure B-6. (d) ^{13}C NMR Asdimcy1
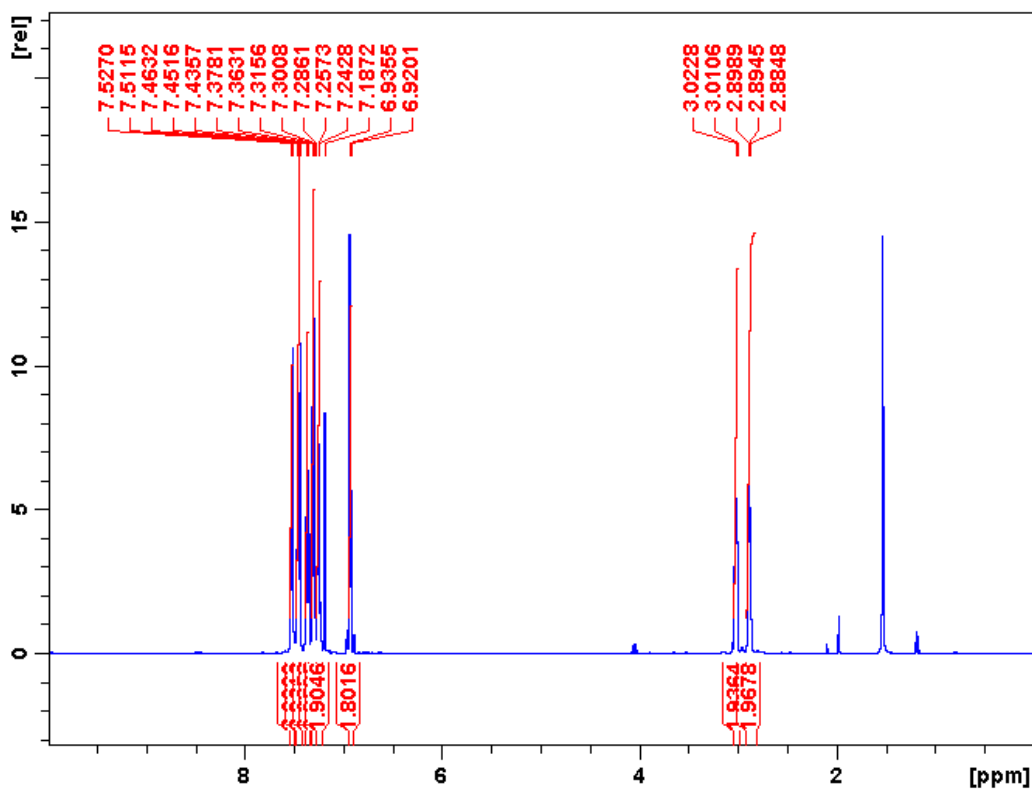
Figure B-7. (a) ^{1}H NMR Asunsub δ 0-10 ppm
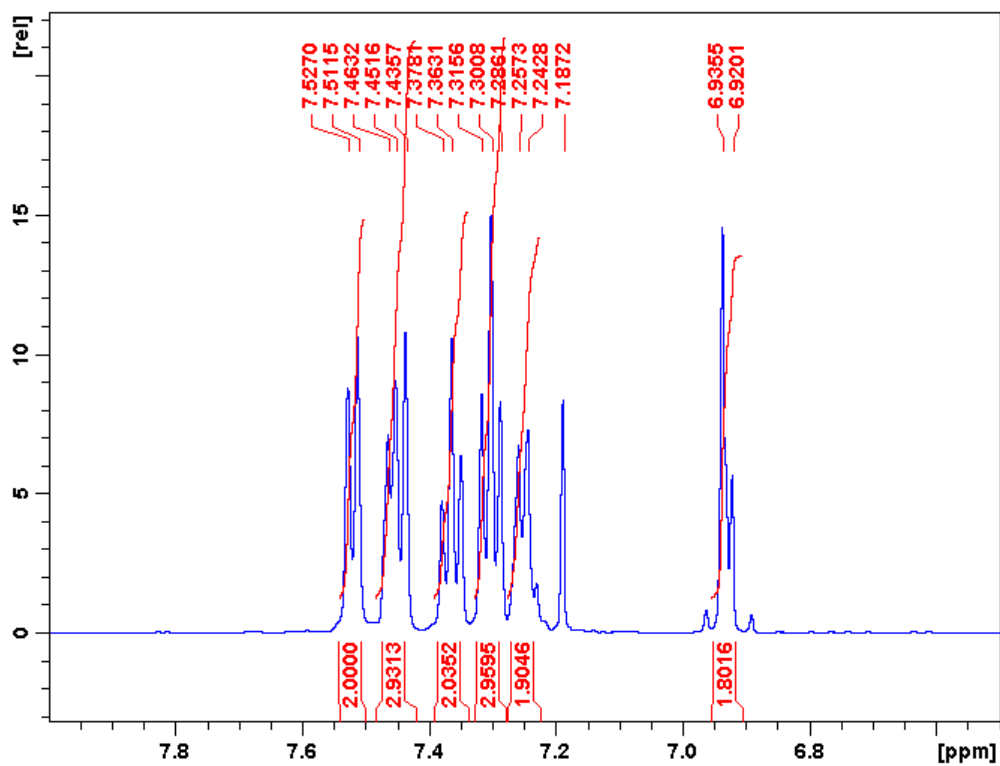
Figure B-7. (b) ^{1}H NMR Asunsub δ 6.5-8.0 ppm
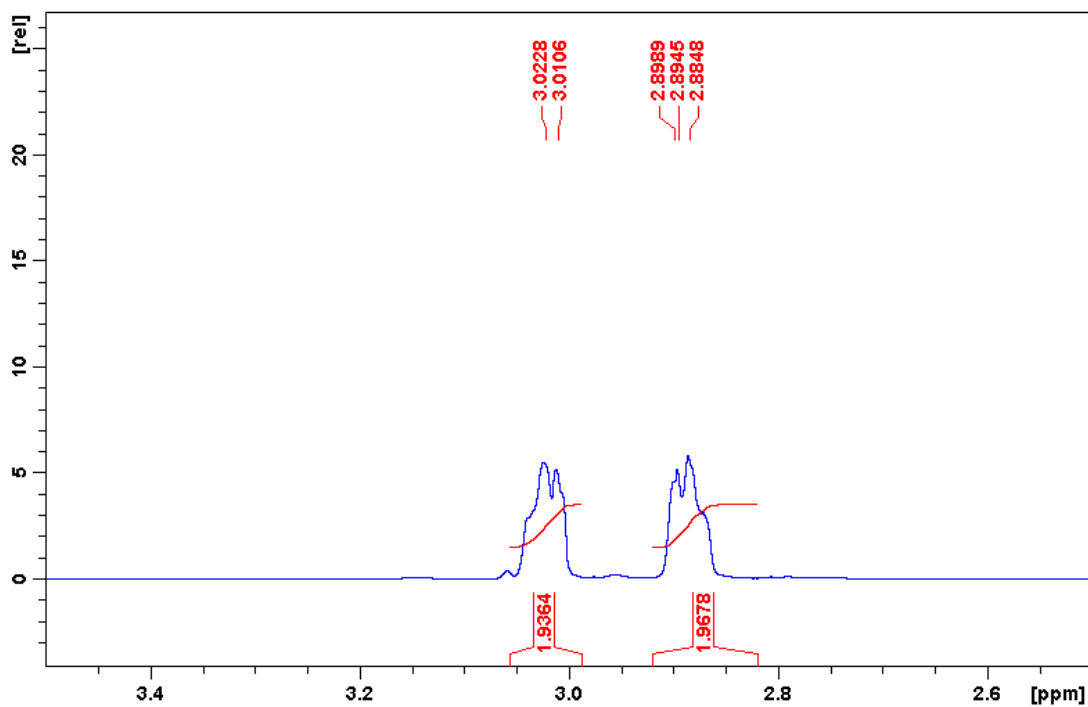
Figure B-7. (c) ^{1}H NMR Asunsub δ 2.5-3.5 ppm
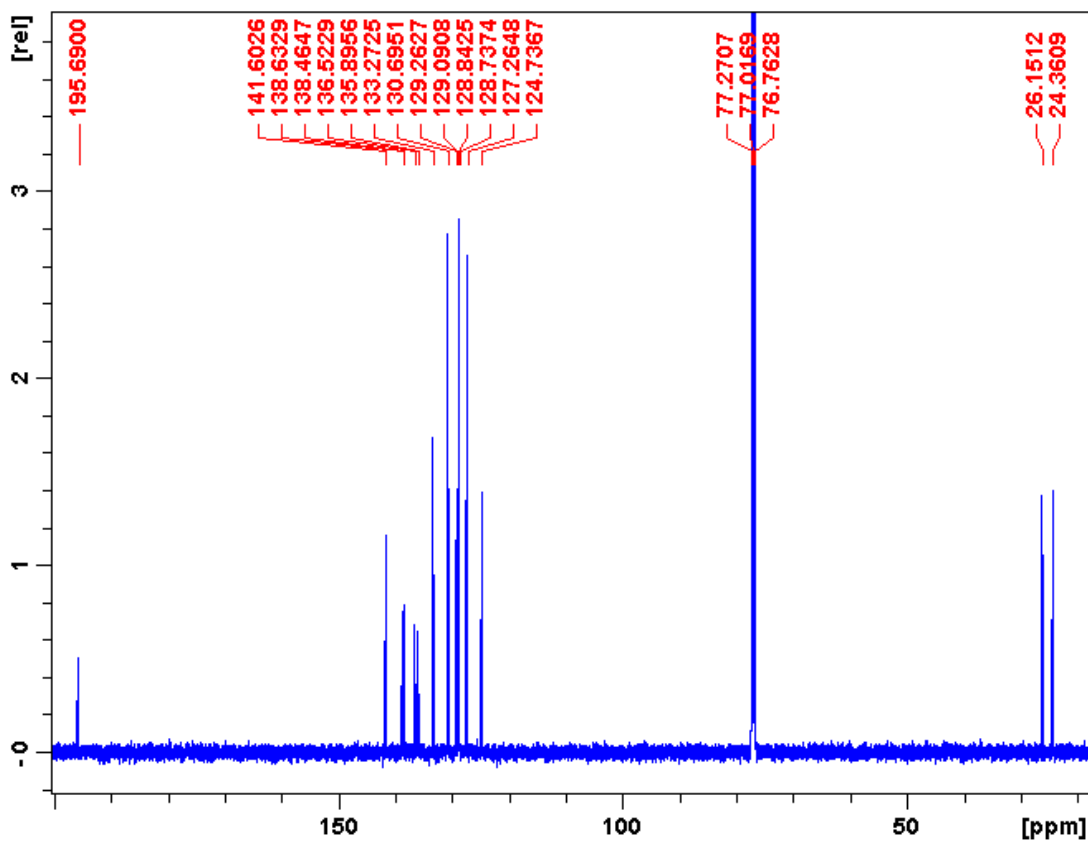
Figure B-7. (d) ^{13}C NMR Asunsub
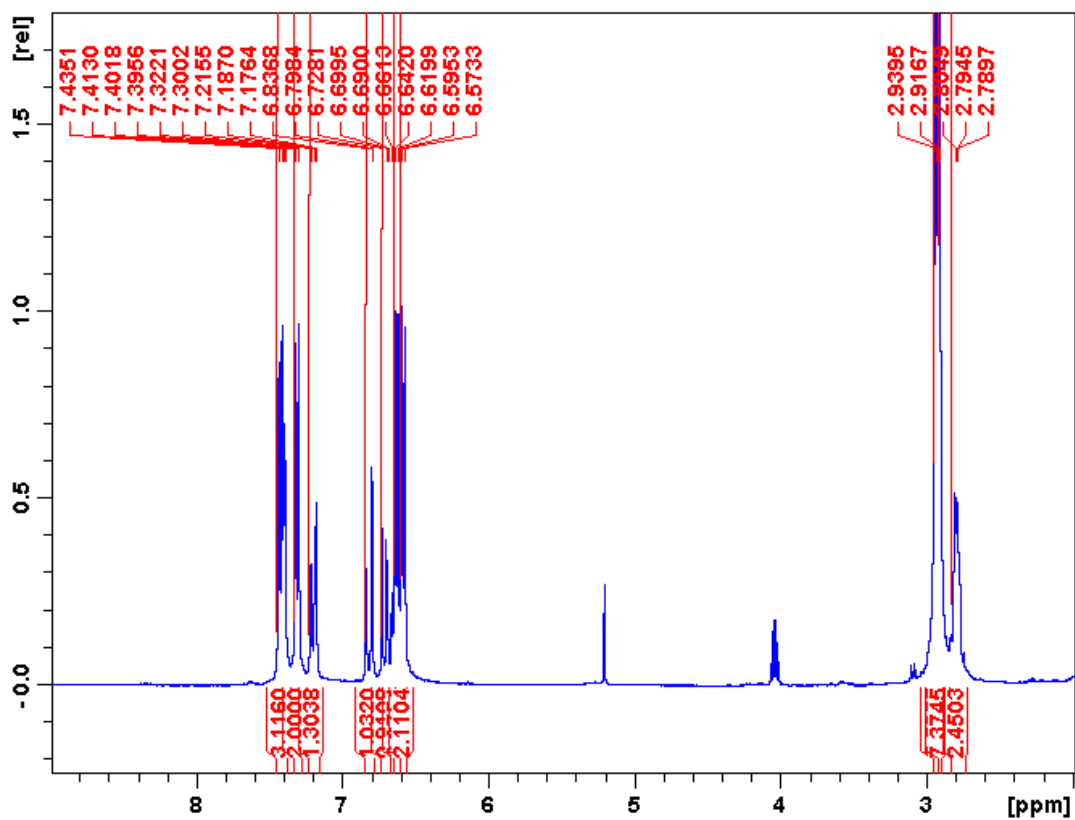
Figure B-8. (a) ^{1}H NMR Ashrbor δ 2-9 ppm
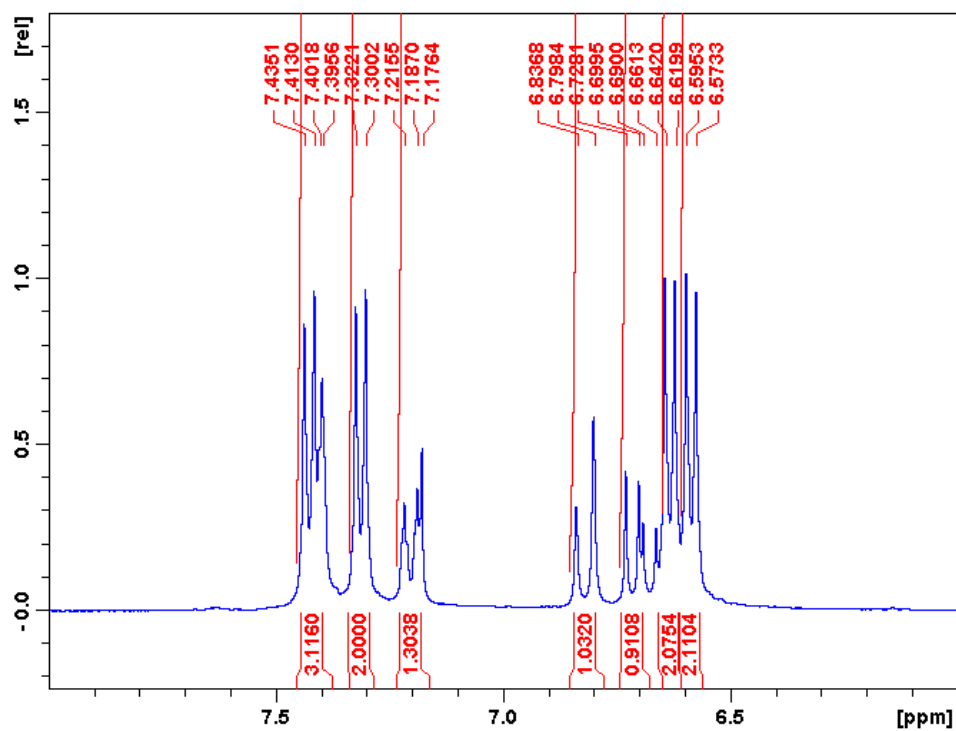
Figure B-8. (b) ^{1}H NMR Ashrbor δ 6.0-8.0 ppm

375
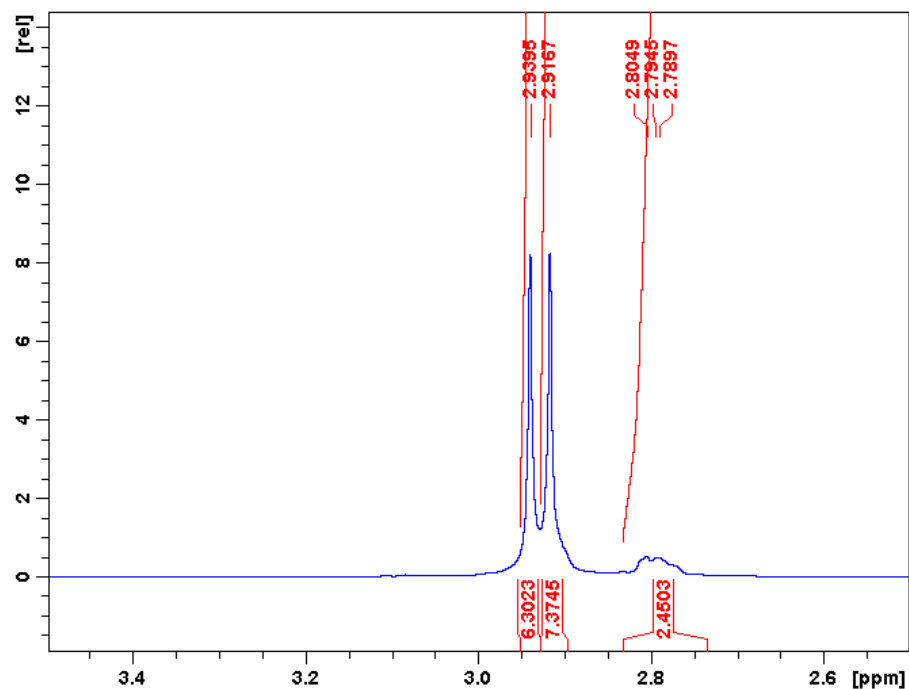
Figure B-8. (c) ^{1}H NMR Ashrbor δ 2.5-3.5 ppm
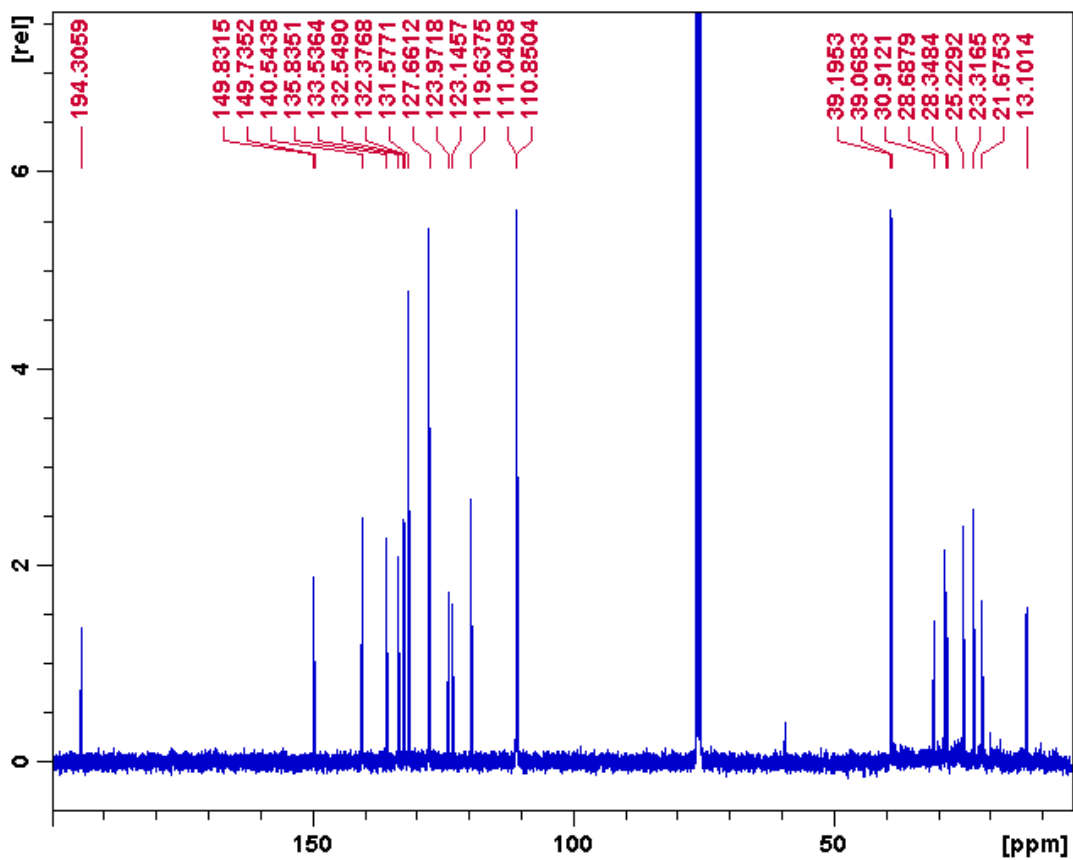
Figure B-8. (d) ^{13}C NMR Ashrbor
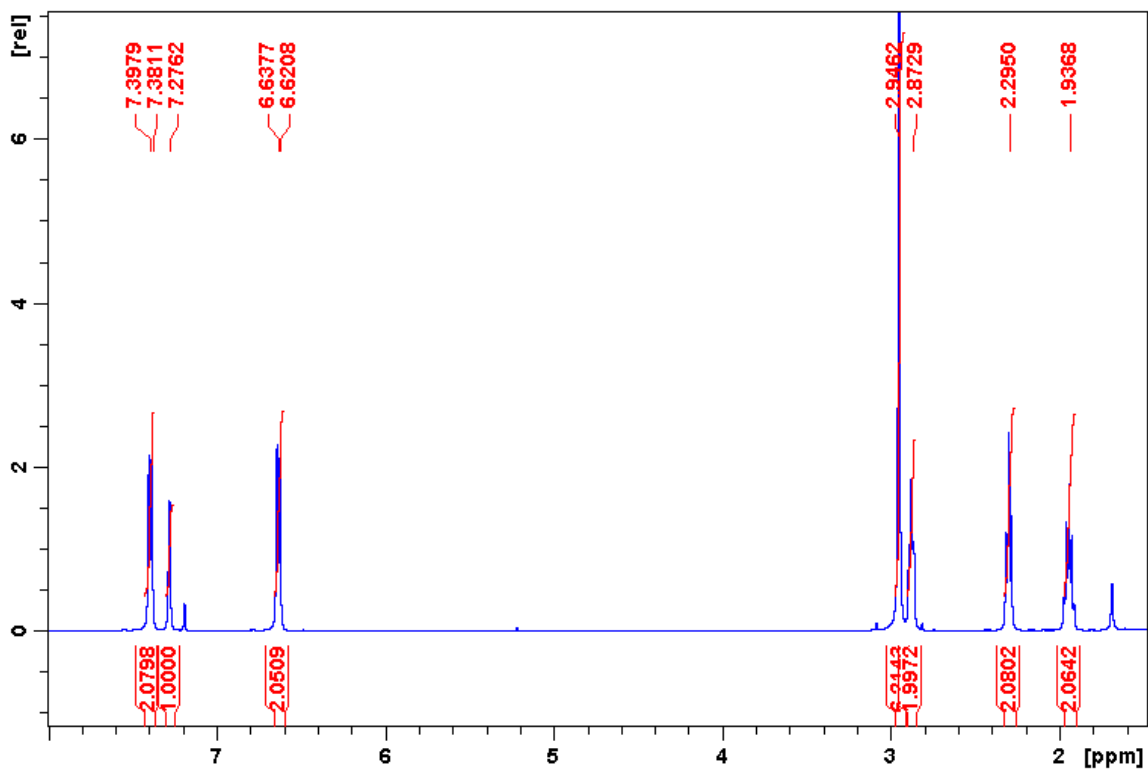
Figure B-9. (a) ^{1}H NMR dmab δ 1.5-8.0 ppm
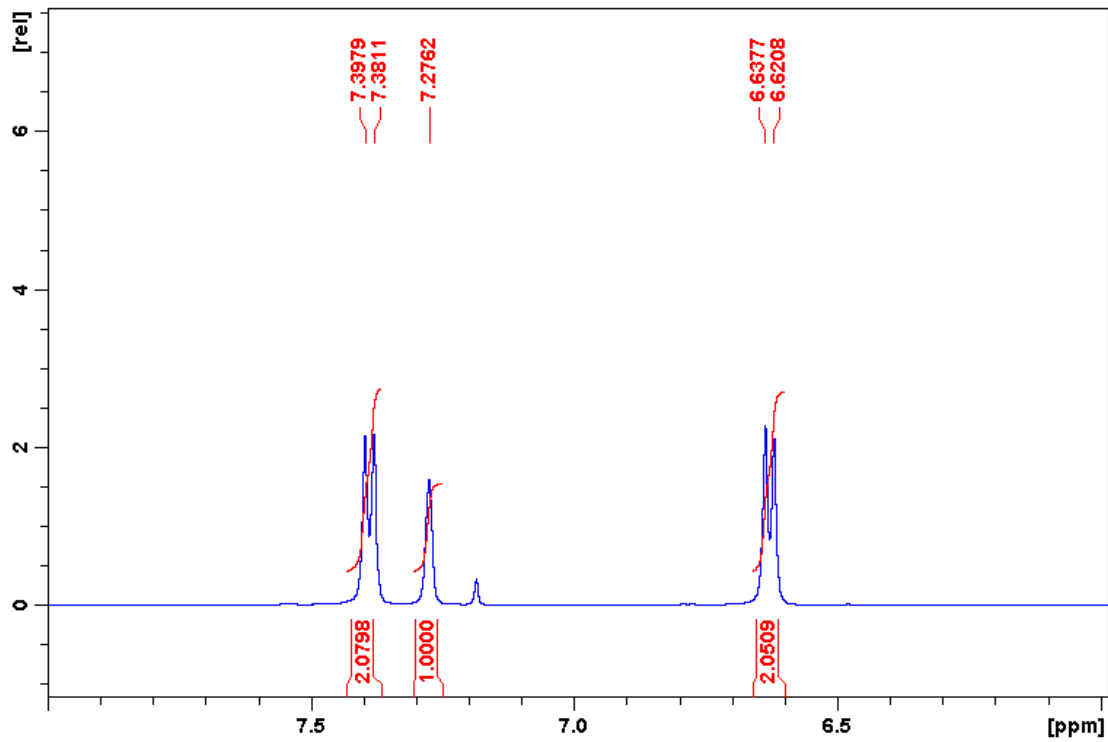
Figure B-9. (b) ^{1}H NMR dmab δ 6.0-8.0 ppm
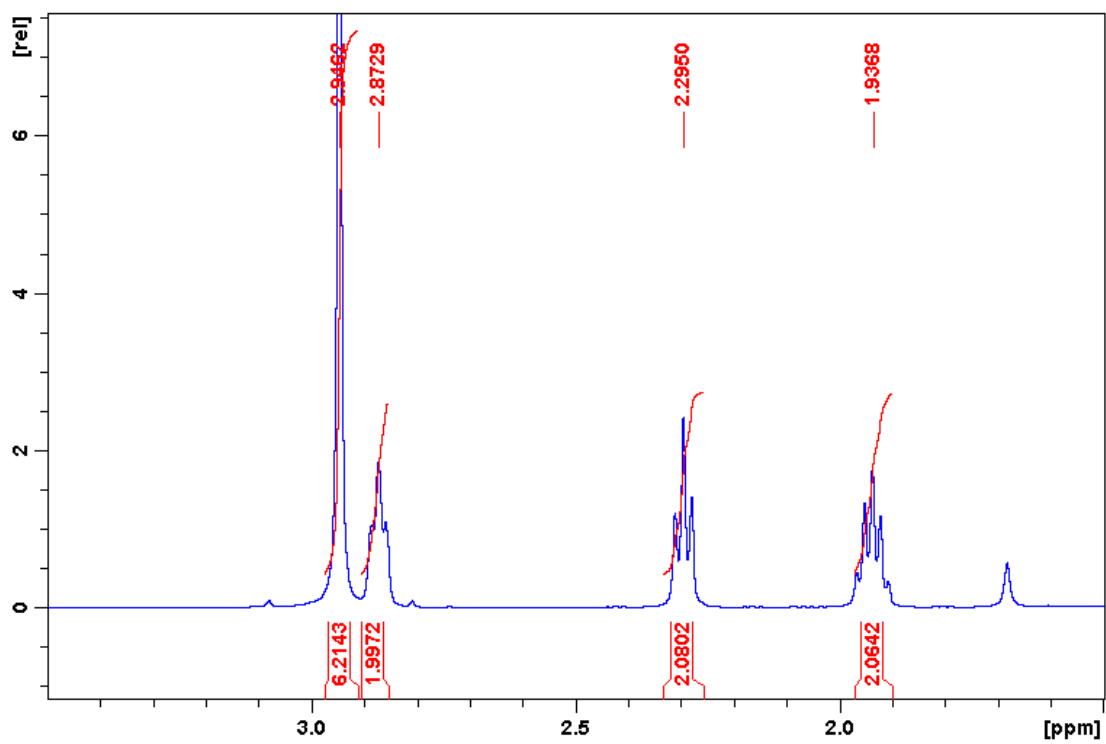
Figure B-9. (c) ^{1}H NMR dmab δ 1.5-3.5 ppm
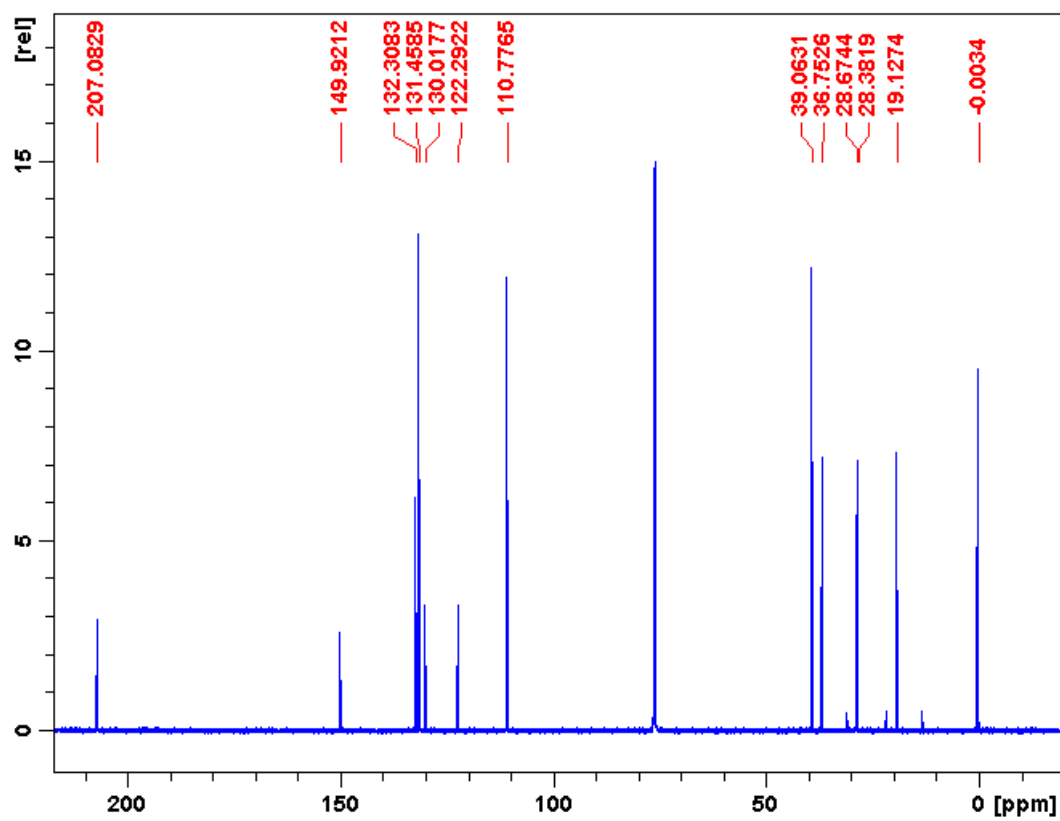
Figure B-9. (d) ^{13}C NMR dmab
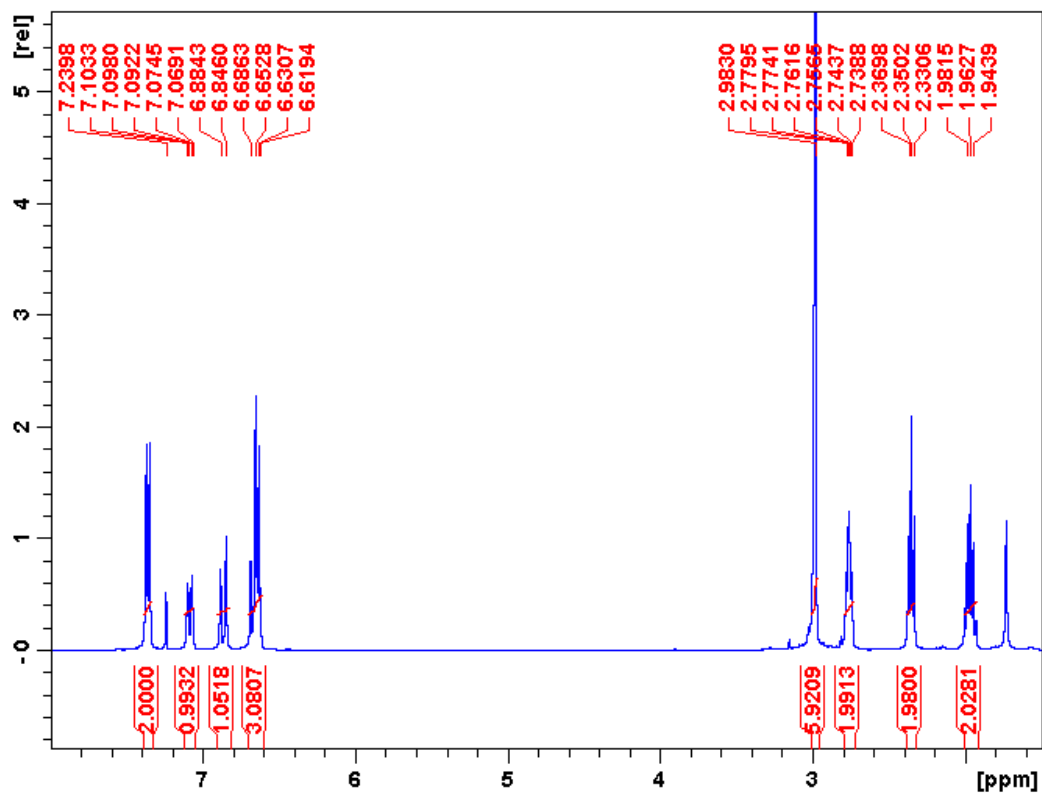
Figure B-10. (a) ^{1}H NMR dmac δ 1.5-8.0 ppm
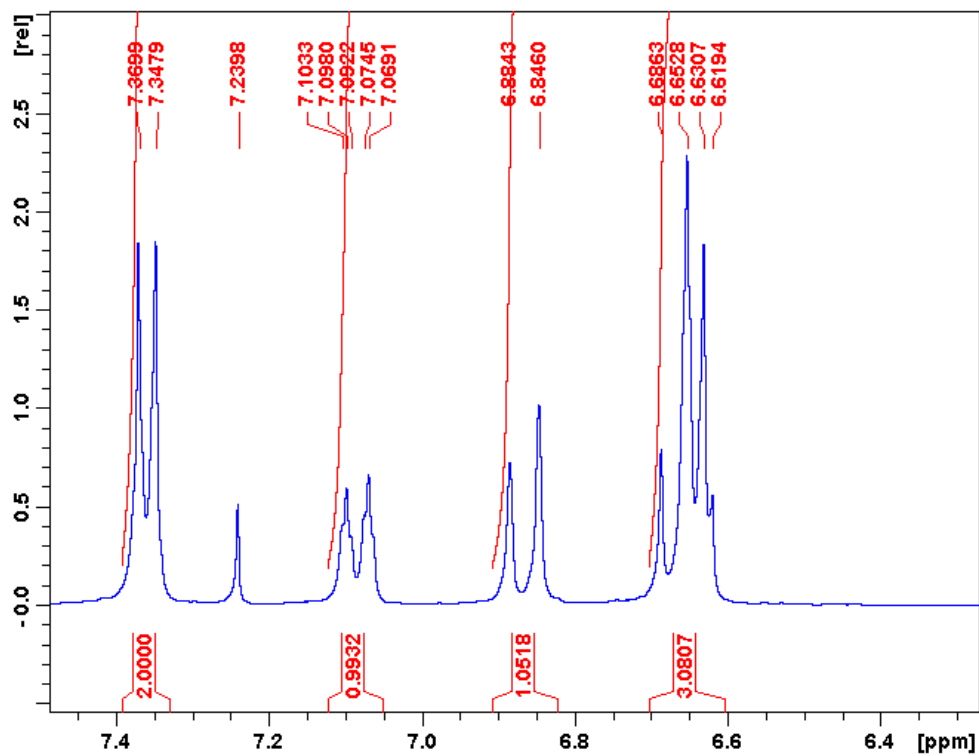
Figure B-10. (b) ^{1}H NMR dmac δ 6.25-7.5 ppm
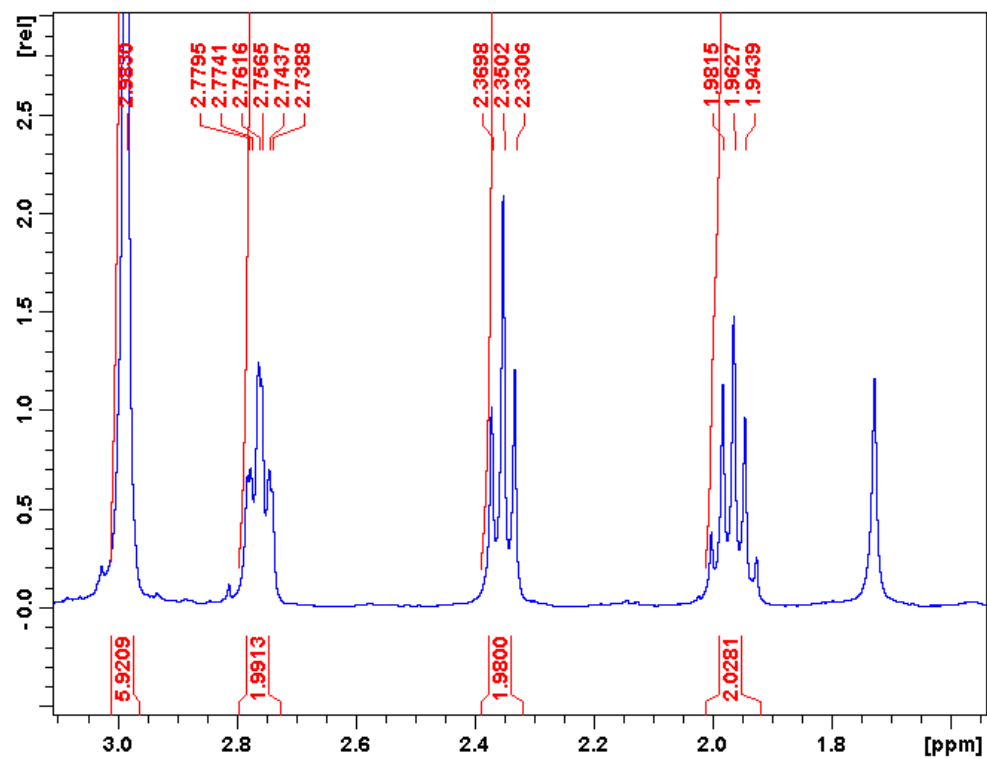
Figure B-10. (c) ^{1}H NMR dmac δ 1.55-3.1 ppm
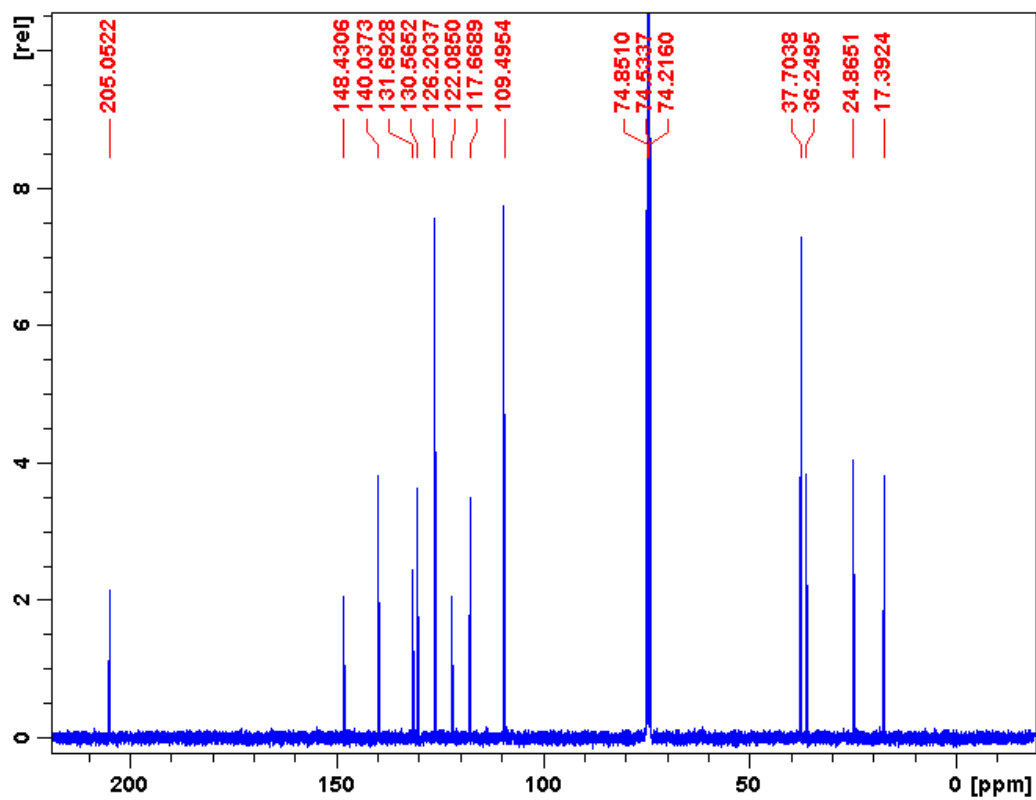
Figure B-10. (d) ^{13}C NMR dmac
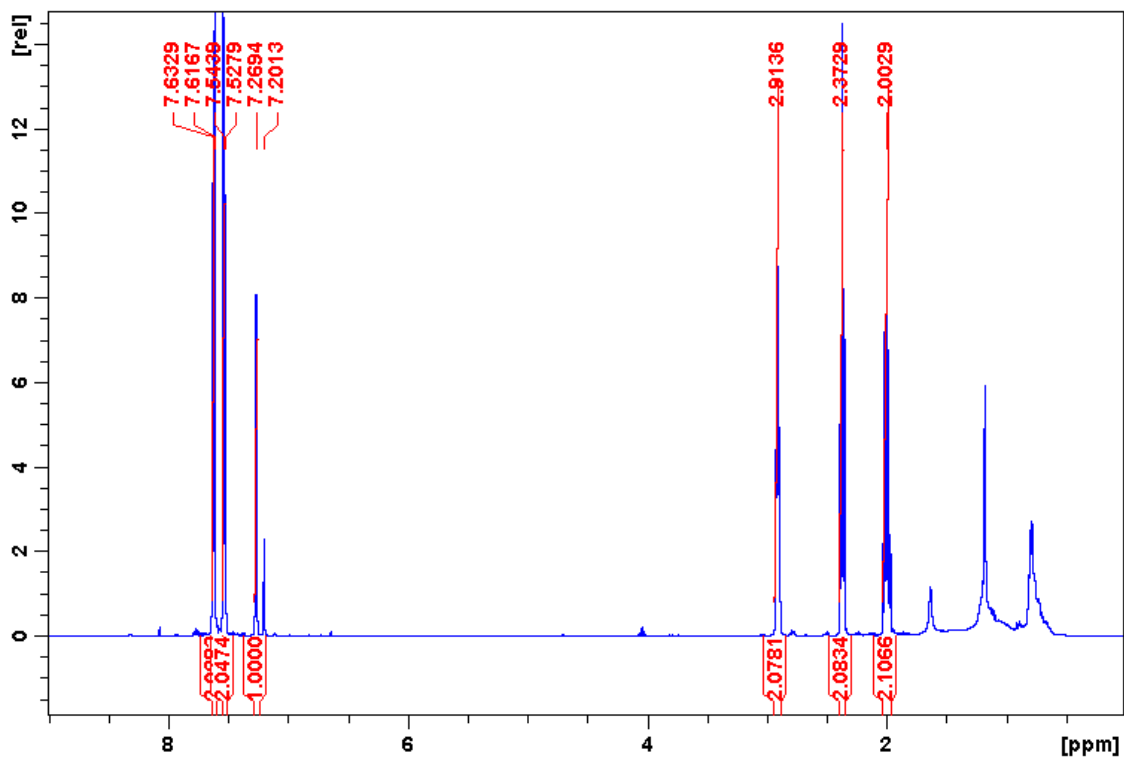
Figure B-11. (a) ^{1}H NMR 1pdbcy δ 0-9 ppm
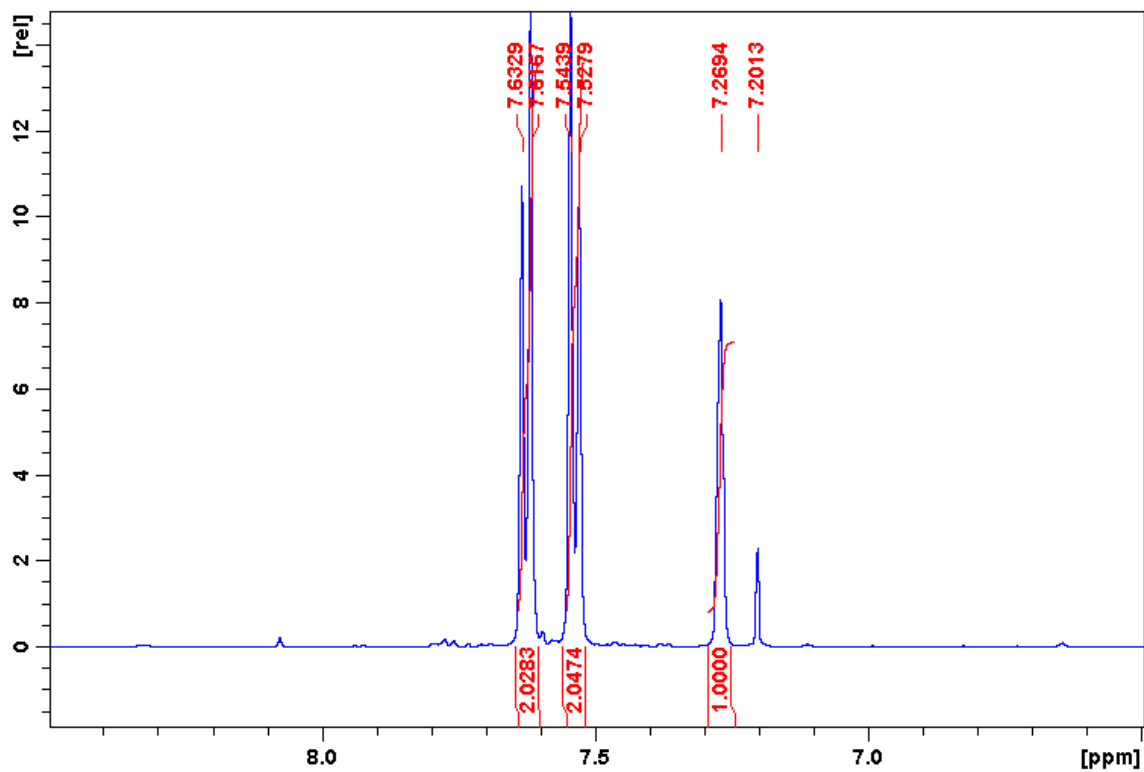
Figure B-11. (b) ^{1}H NMR 1pdbcy δ 6.5-8.5 ppm
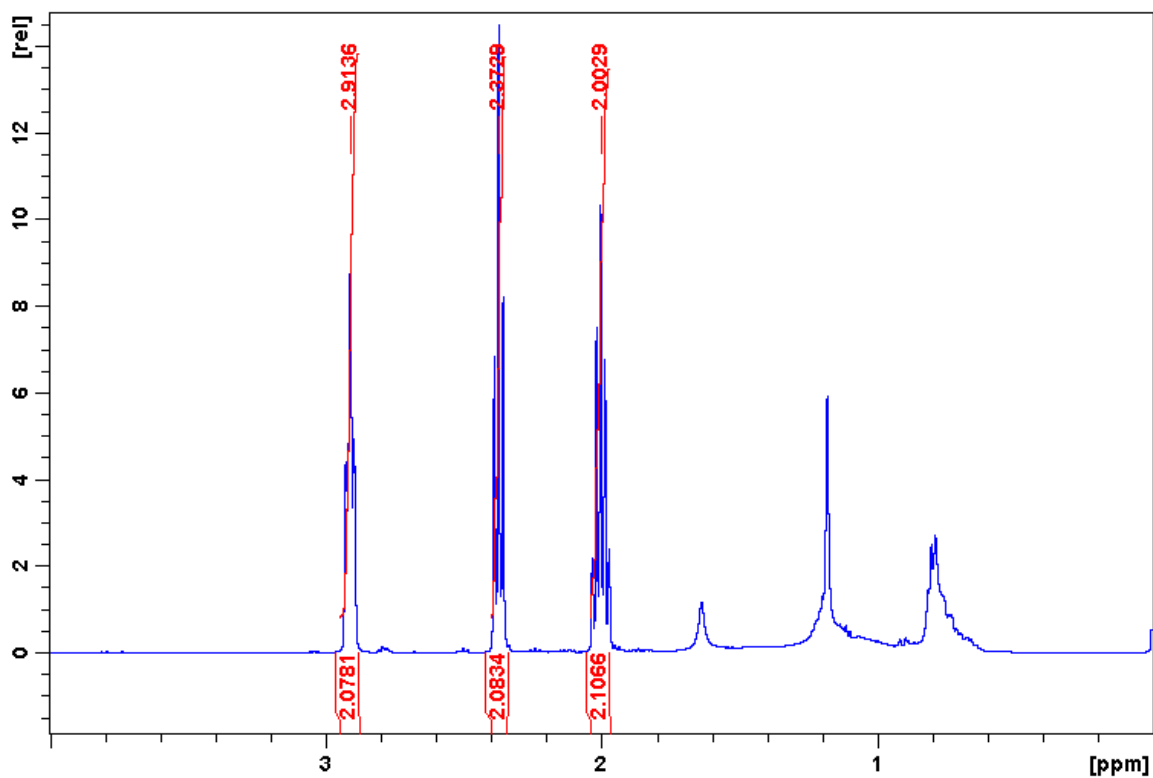
Figure B-11. (c) ^{1}H NMR 1pdbcy δ 0-4 ppm
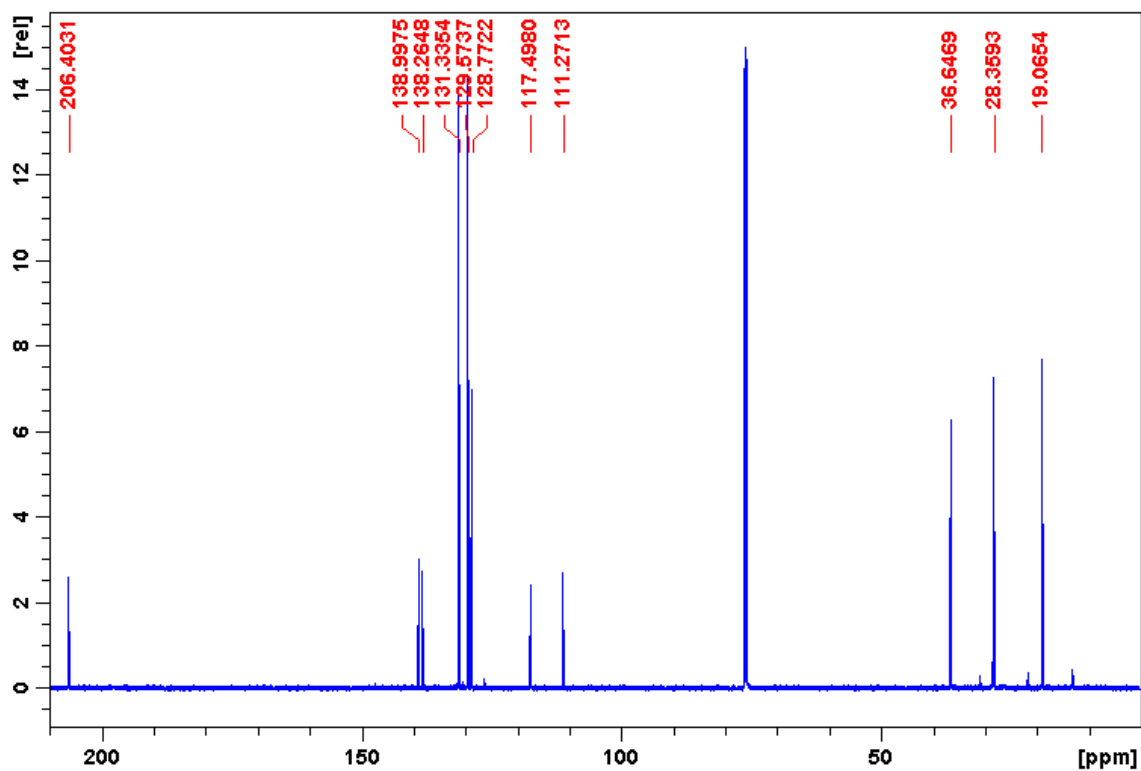
Figure B-11. (d) ^{13}C NMR 1pdbcy
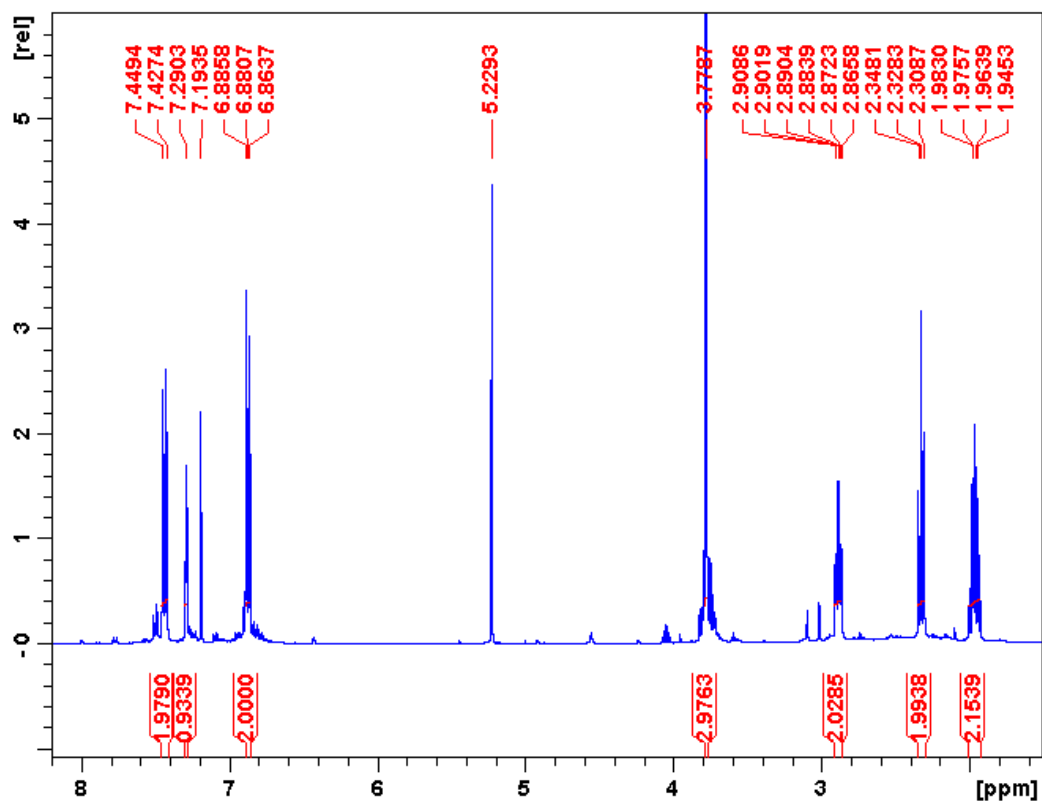
Figure B-12. (a) ^{1}H NMR 1pdbmx δ 1.75-8.2 ppm
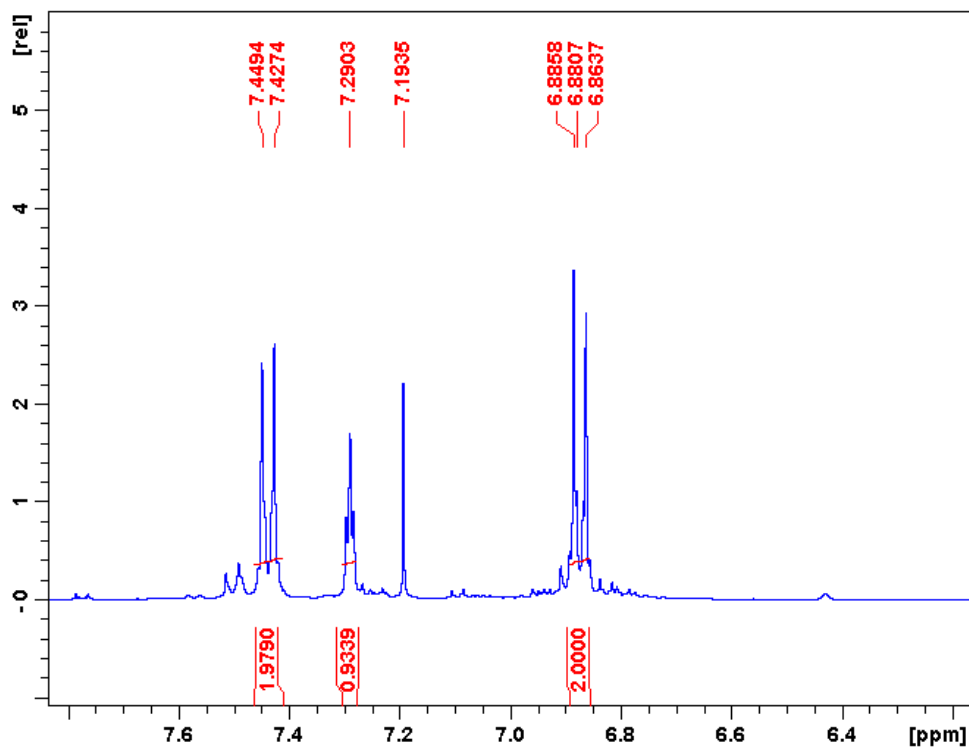
Figure B-12. (b) ^{1}H NMR 1pdbmx δ 6.15-7.85 ppm
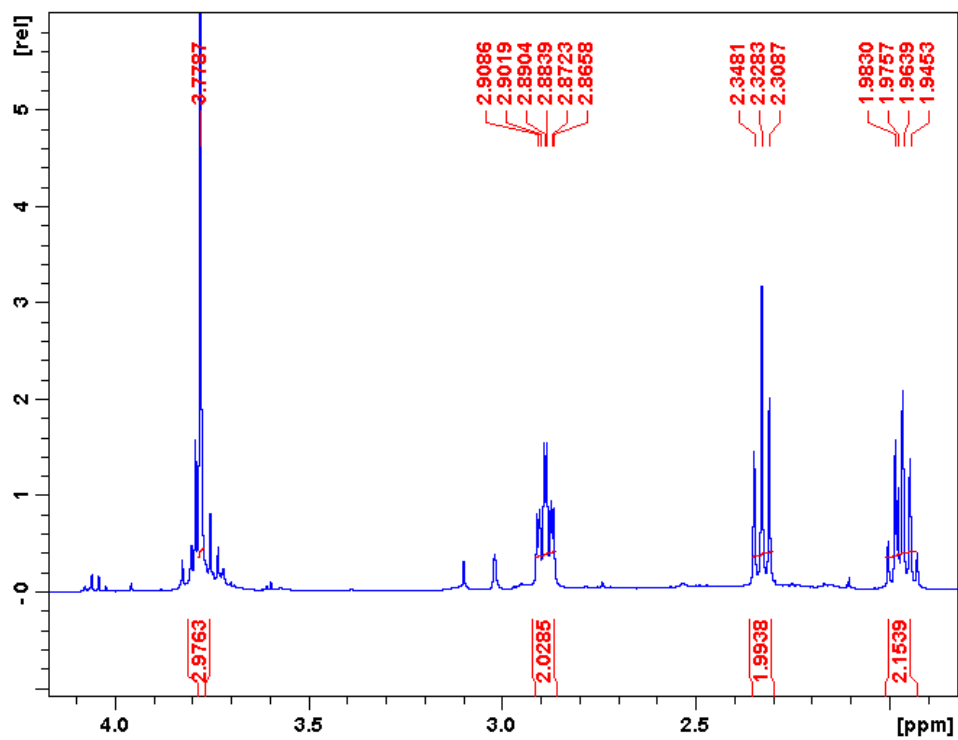
Figure B-12. (c) ^{1}H NMR 1pdbmx δ 1.8-4.2 ppm
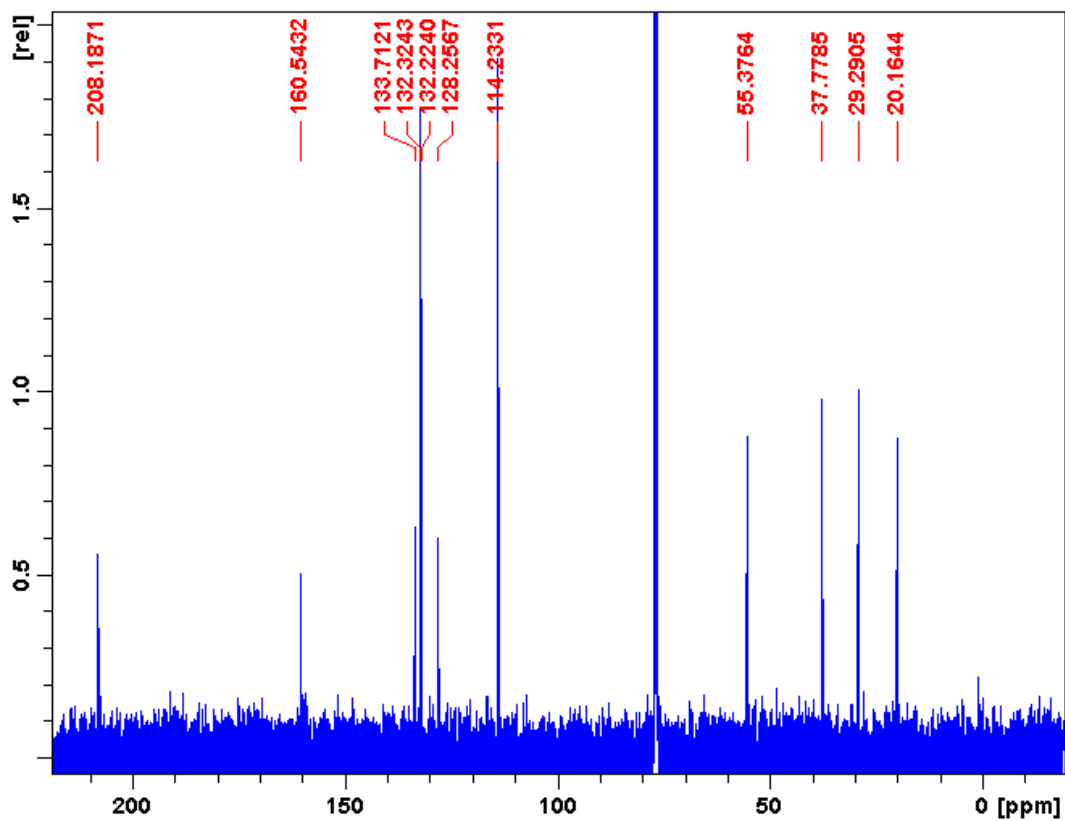
Figure B-12. (d) ^{13}C NMR 1pdbmx
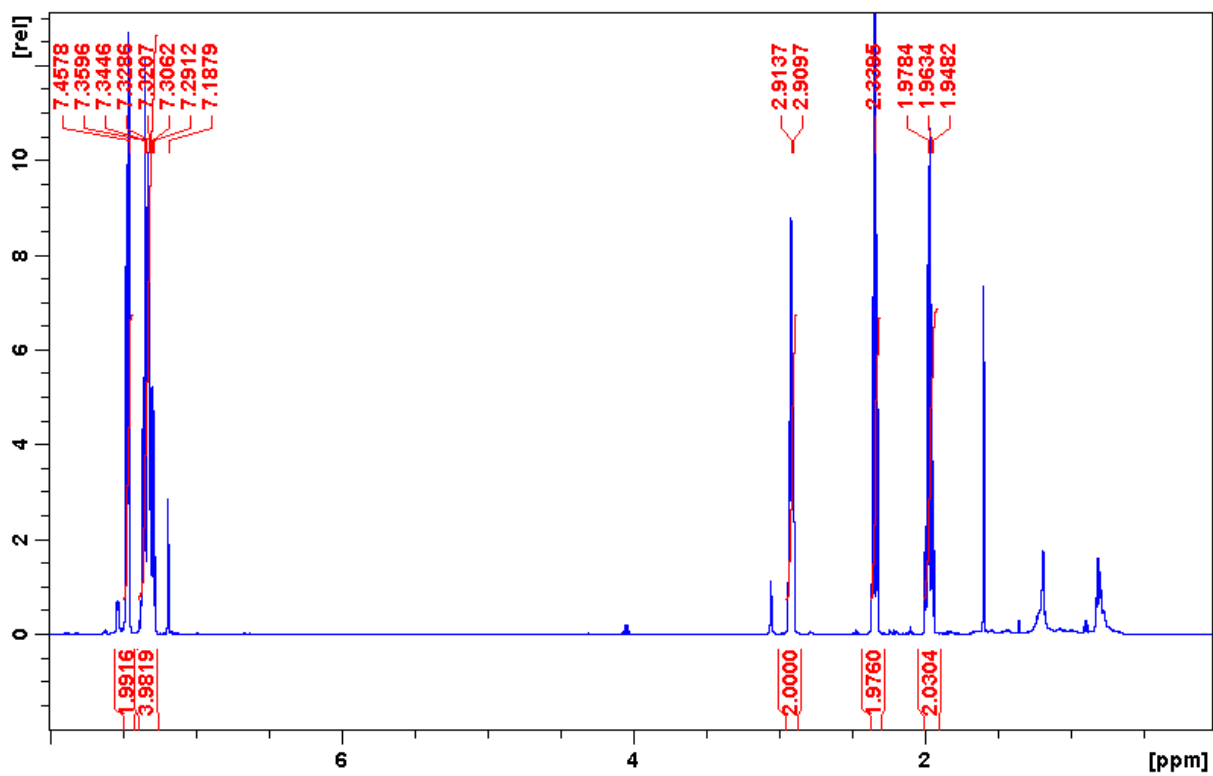
Figure B-13. (a) ^{1}H NMR 1pdbun δ 0.0-8.0 ppm
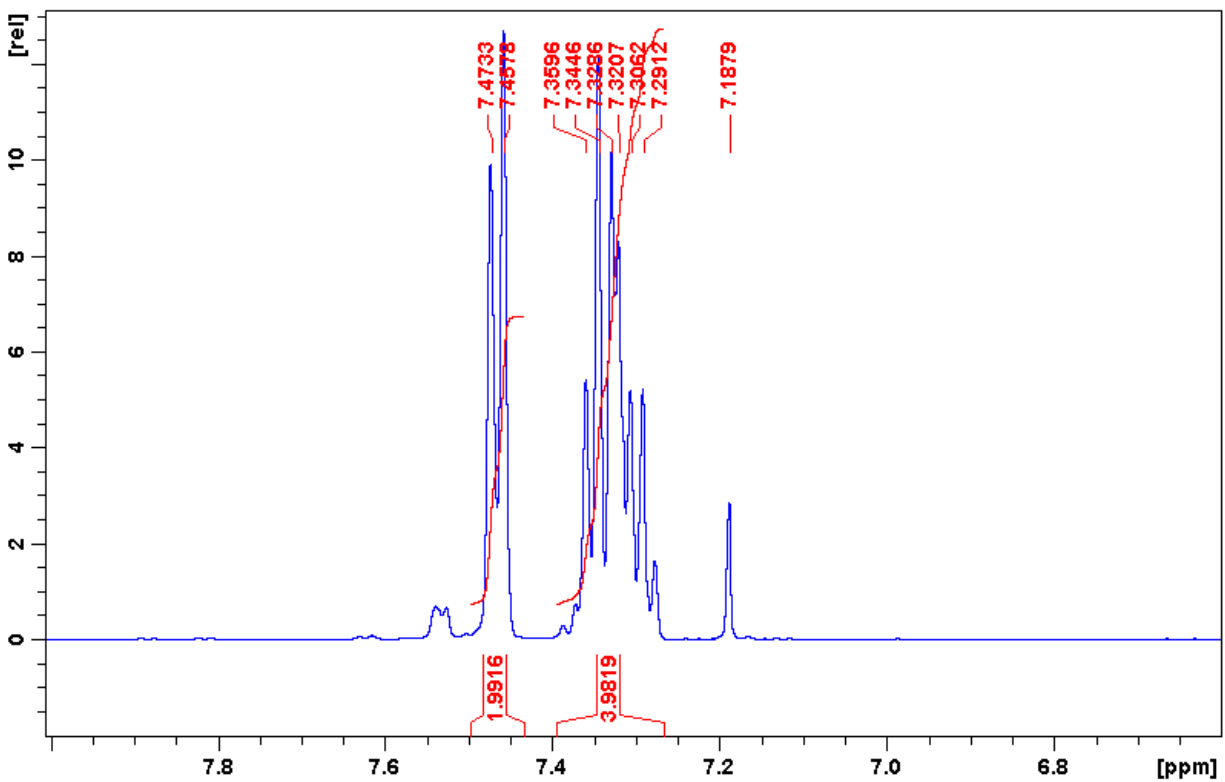
Figure B-13. (b) ^{1}H NMR 1pdbun δ 6.6-8.0 ppm

385
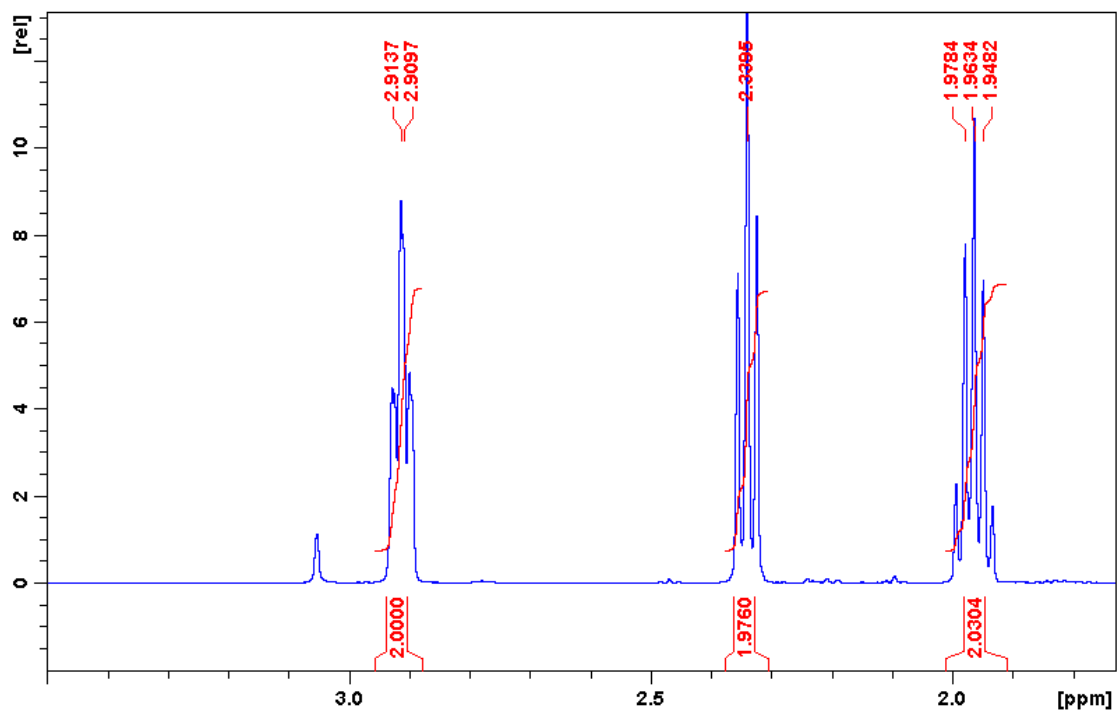
Figure B-13. (c) ^{1}H NMR 1pdbun δ 1.7-3.5 ppm
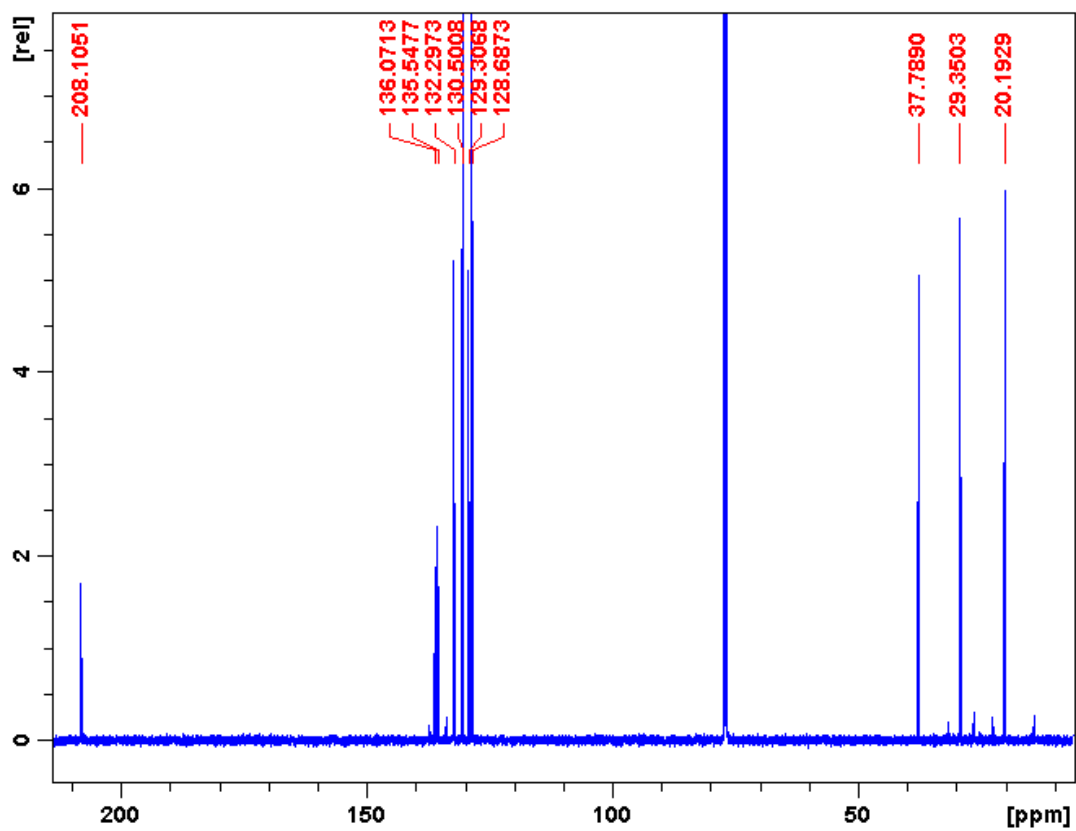
Figure B-13. (d) ^{13}C NMR 1pdbun
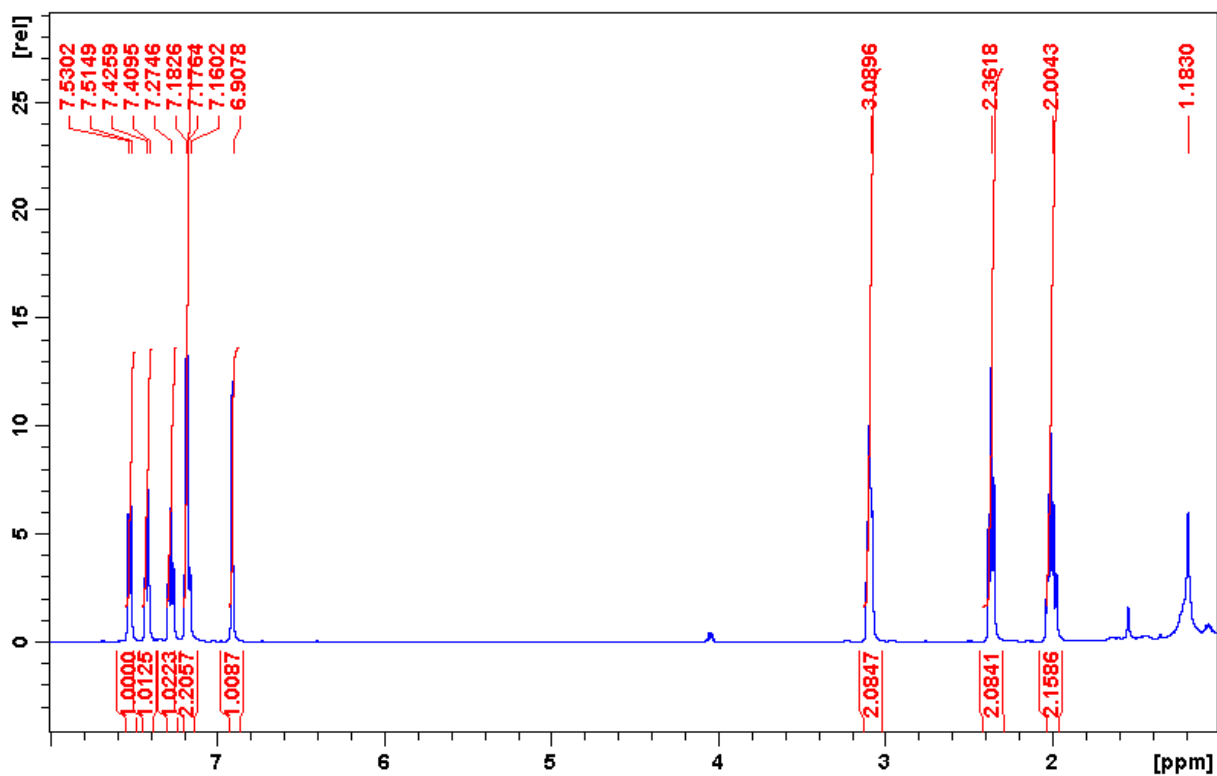
Figure B-14. (a) ^{1}H NMR 1pdbzf δ 1-8 ppm
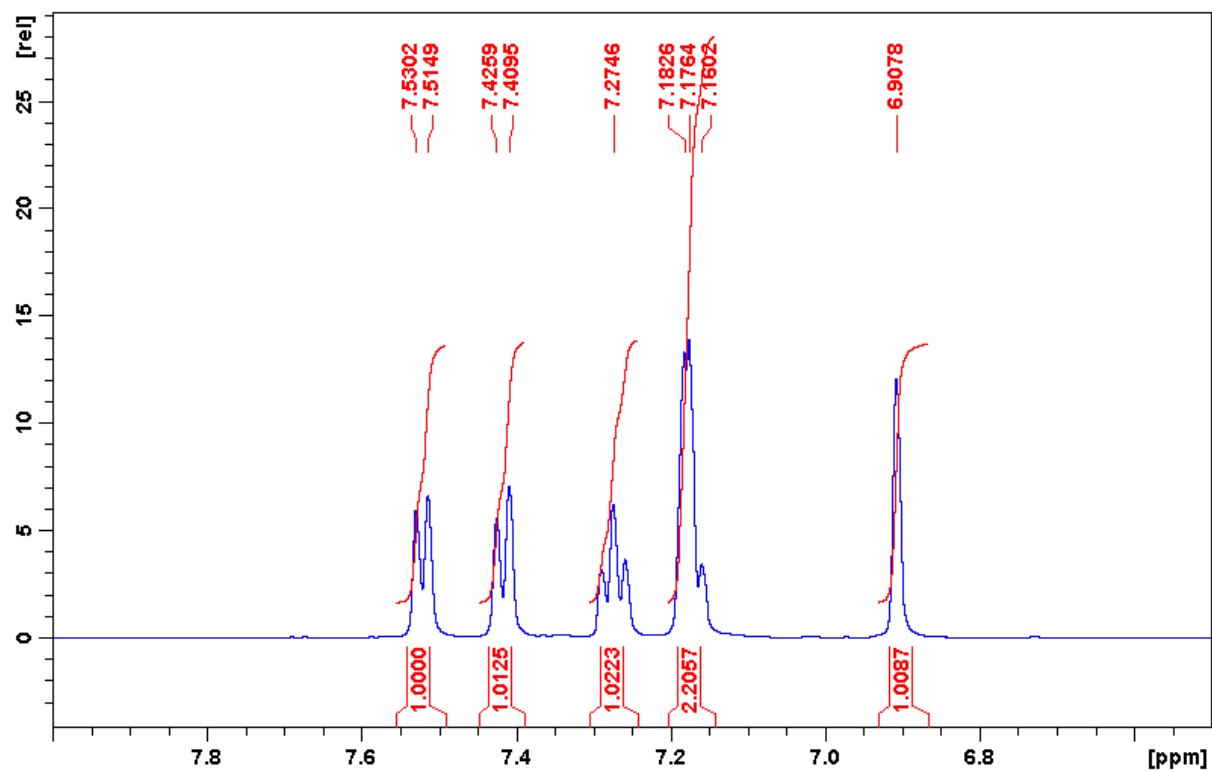
Figure B-14. (b) ^{1}H NMR 1pdbzf δ 6.5-8.0 ppm

387
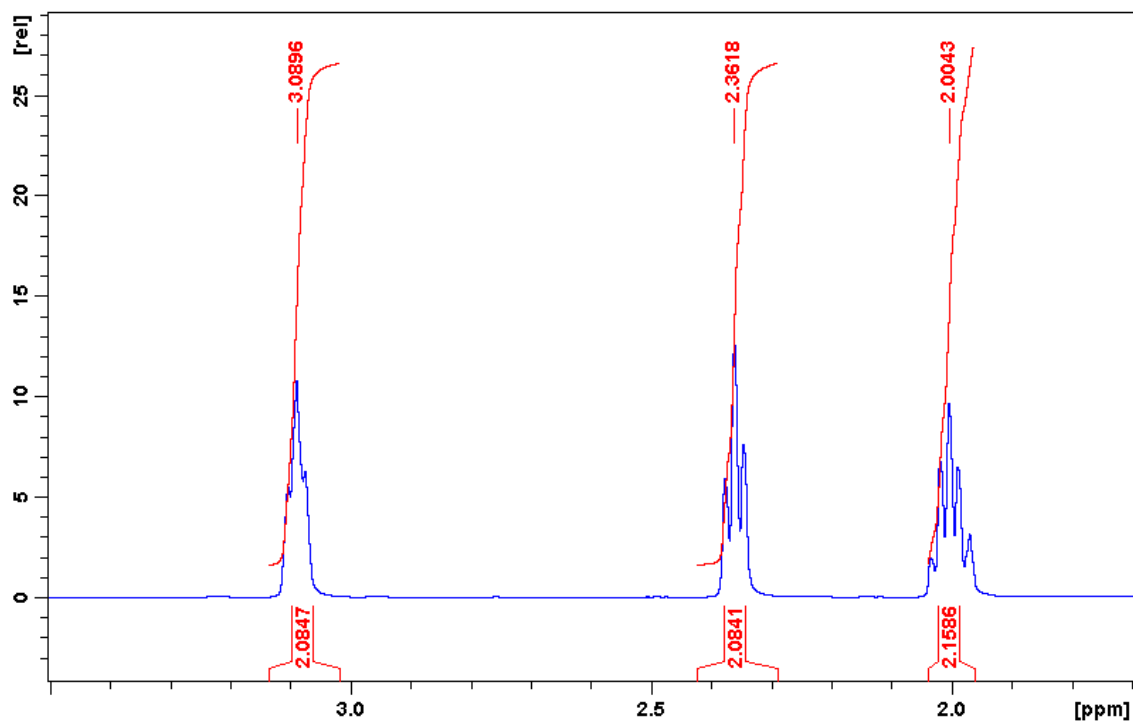
Figure B-14. (c) ^{1}H NMR 1pdbzf δ 1.7-3.5 ppm
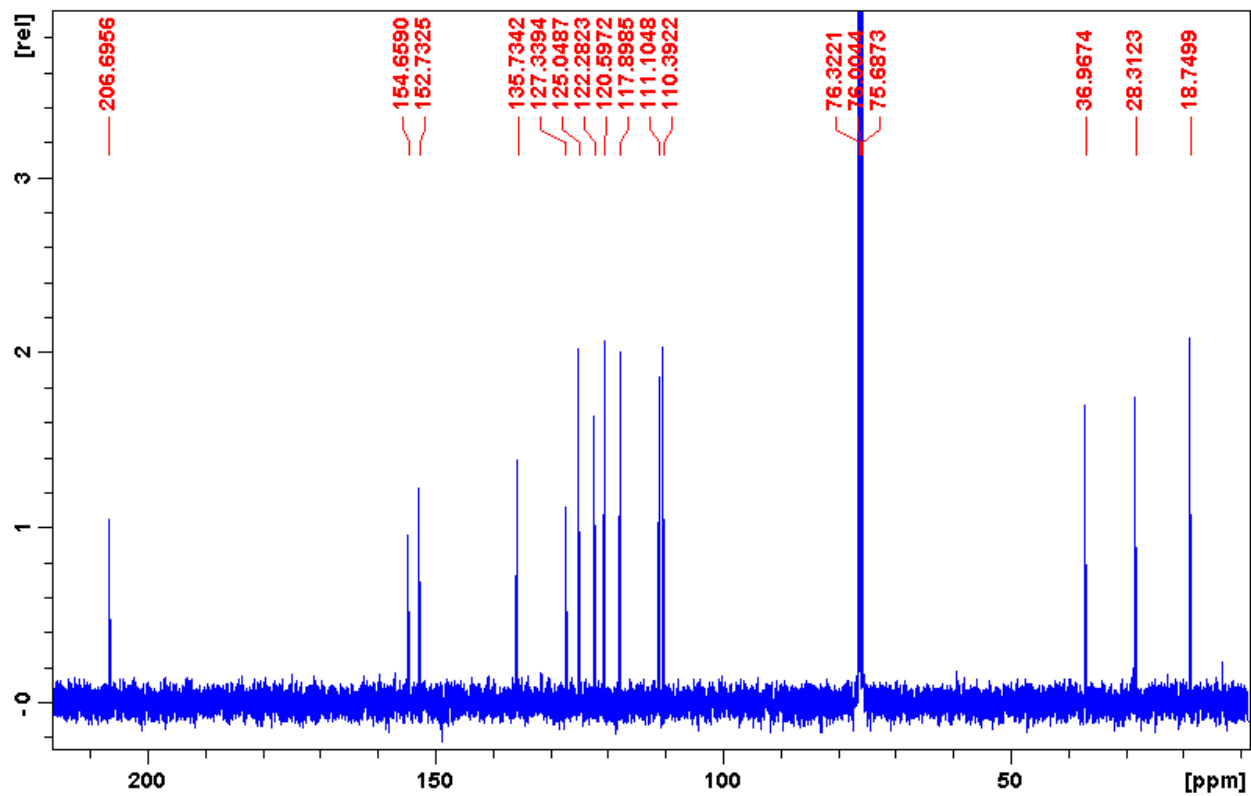
Figure B-14. (d) ^{13}C NMR 1pdbzf

APPENDIX C

INFRARED SPECTRA OF COMPOUNDS

Figure C-1. bis-dmab

Figure C-2. bis-dmac
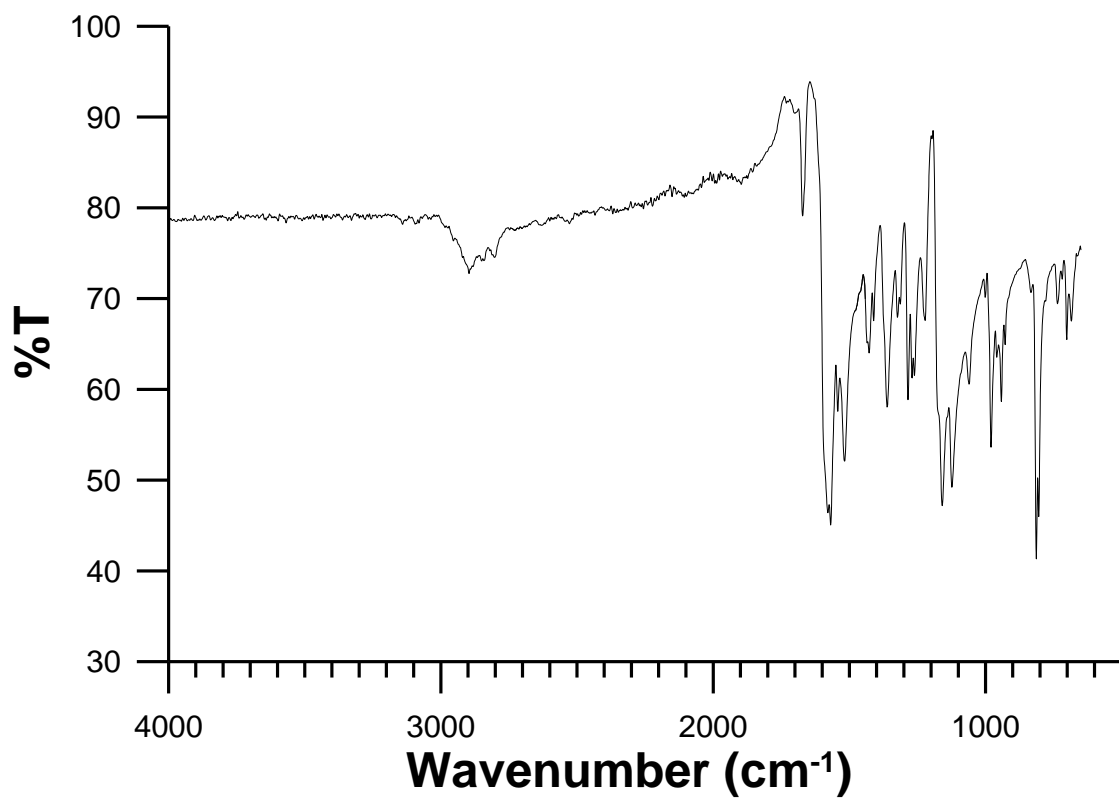
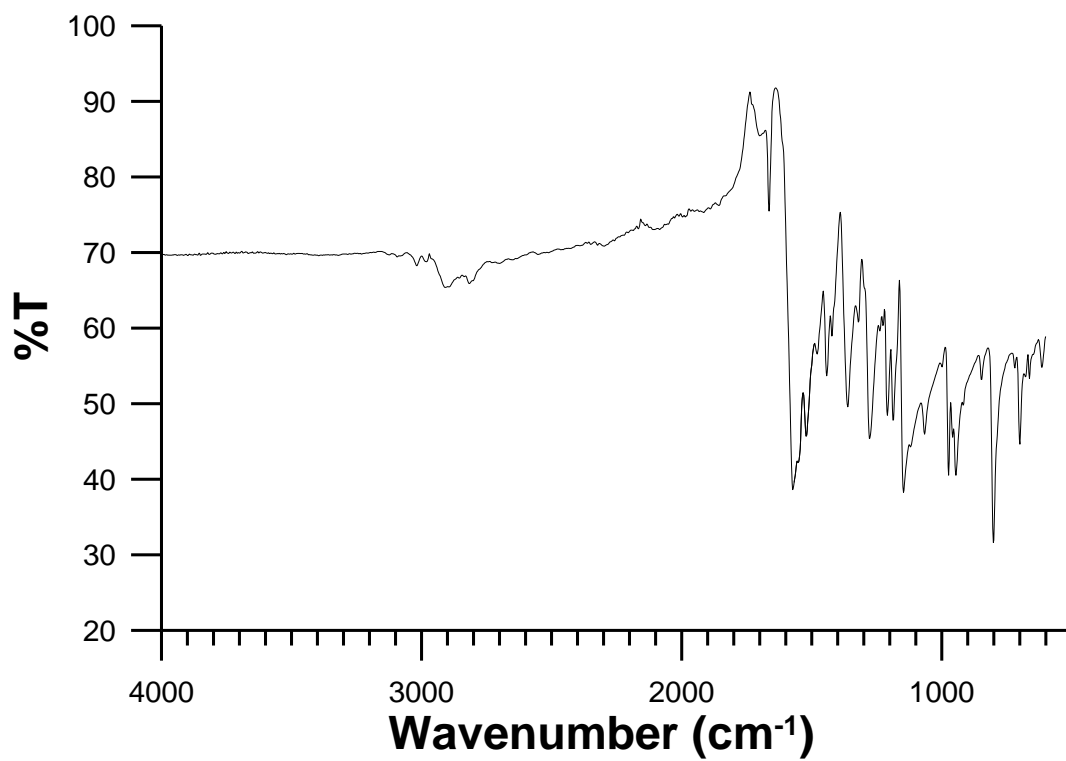Figure C-3. bis-juldmac

Figure C-4. Ashrbor

Figure C-5. Asdimcy1

Figure C-6. Asunsub

Figure C-7. 1dbzfcp

Figure C-8. 2dbmxcp

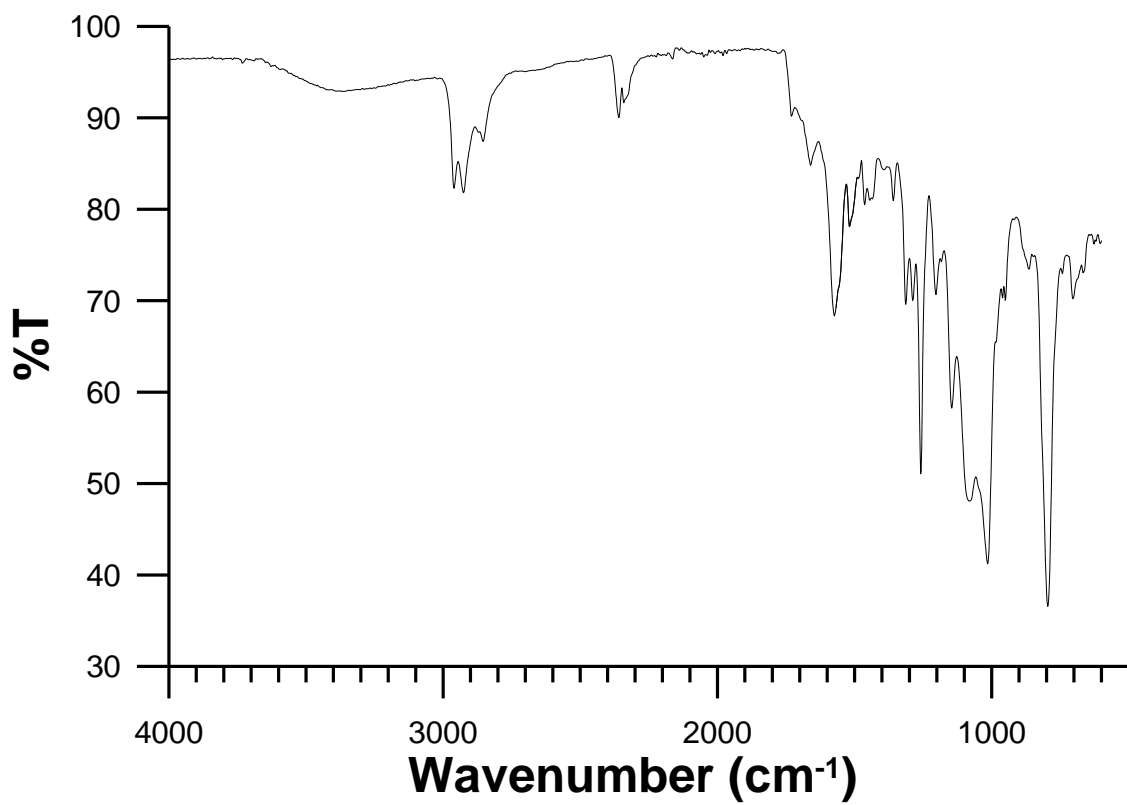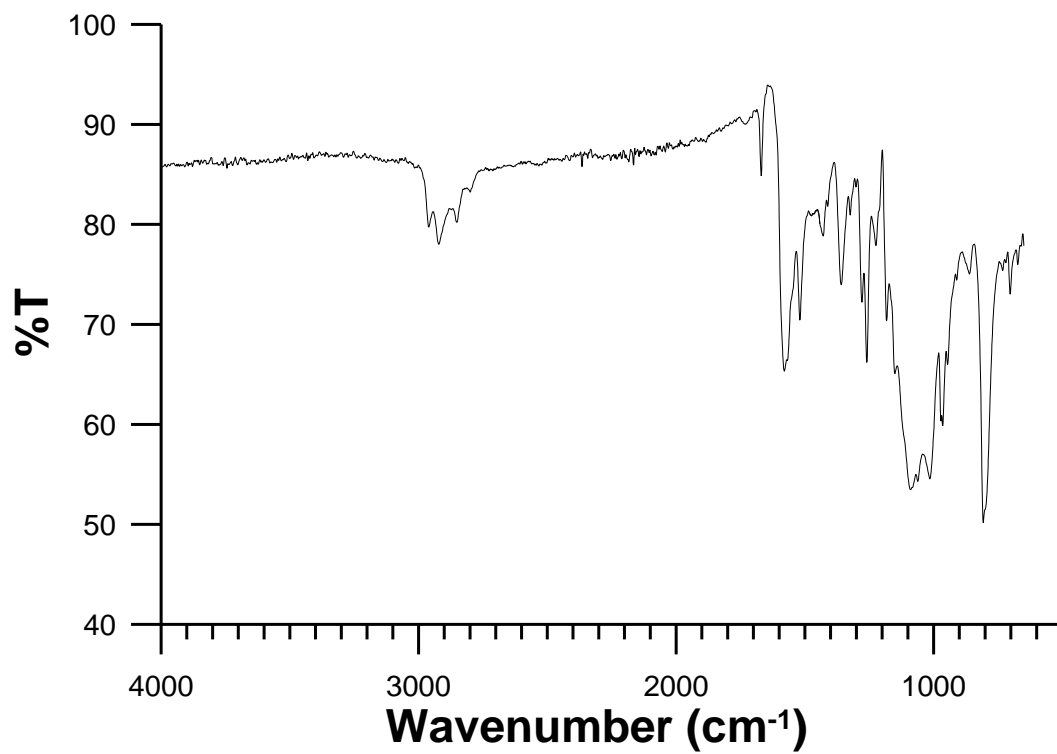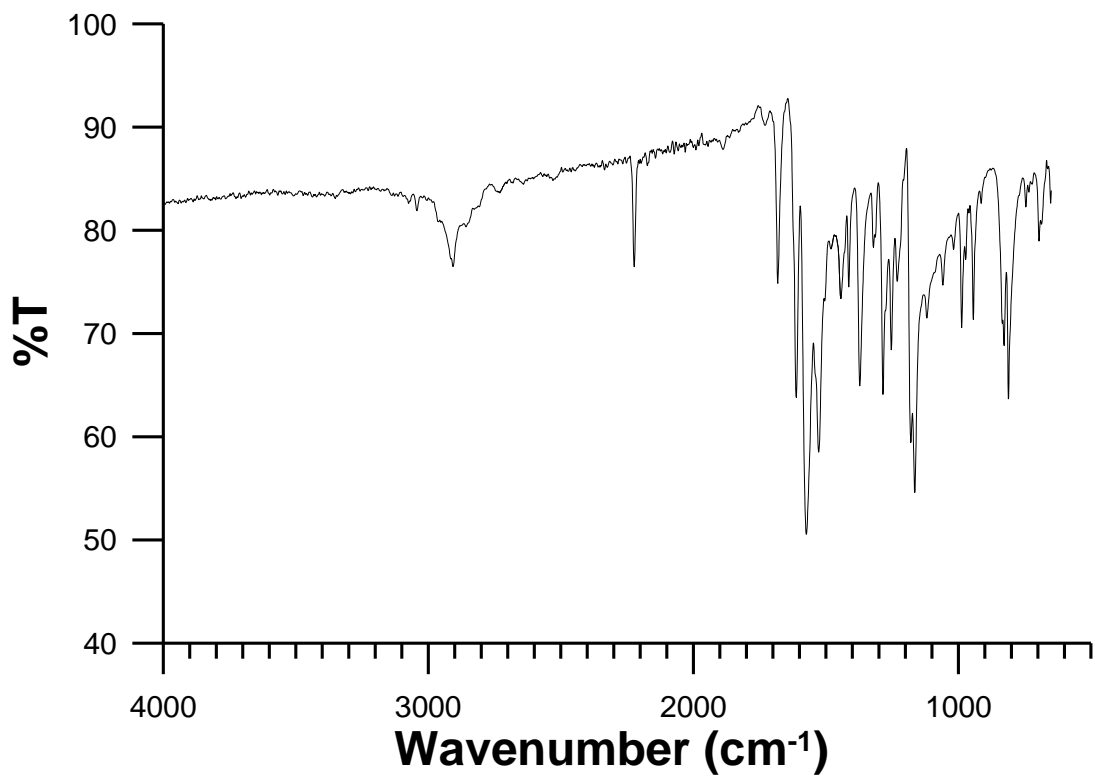**Figure C-1**. bis-dmab

Figure C-2. bis-dmac

Figure C-3. bis-juldmac

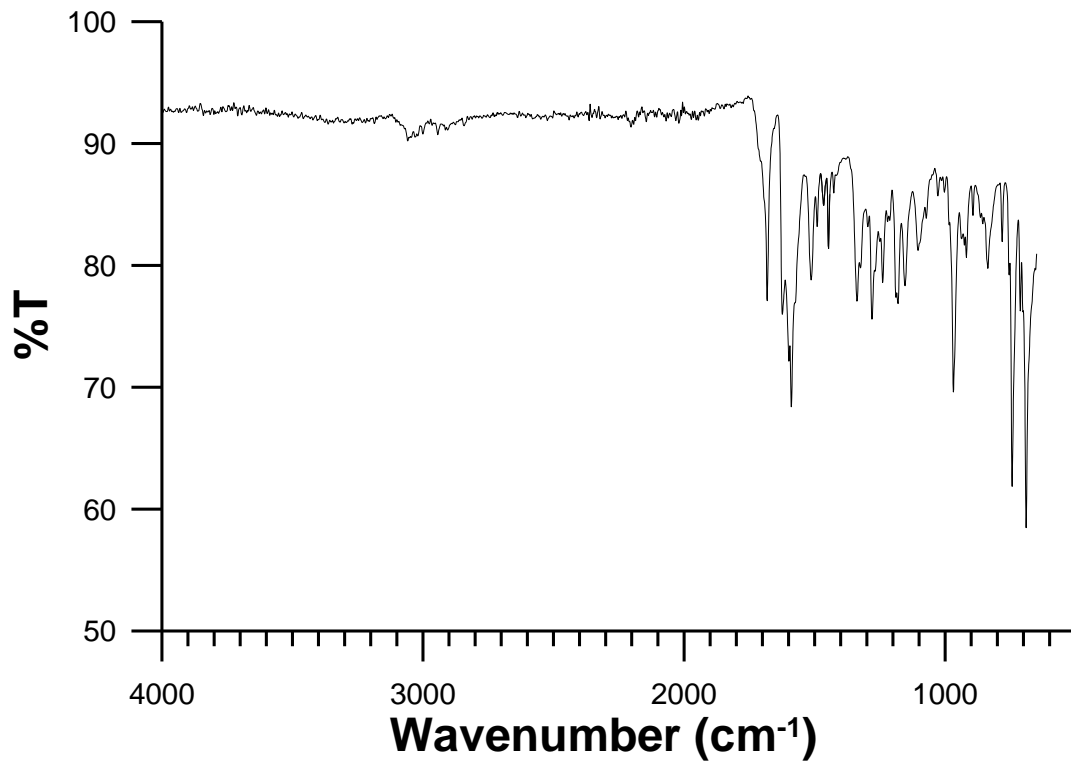**Figure C-4**. Ashrbor

Figure C-5. Asdimcy1

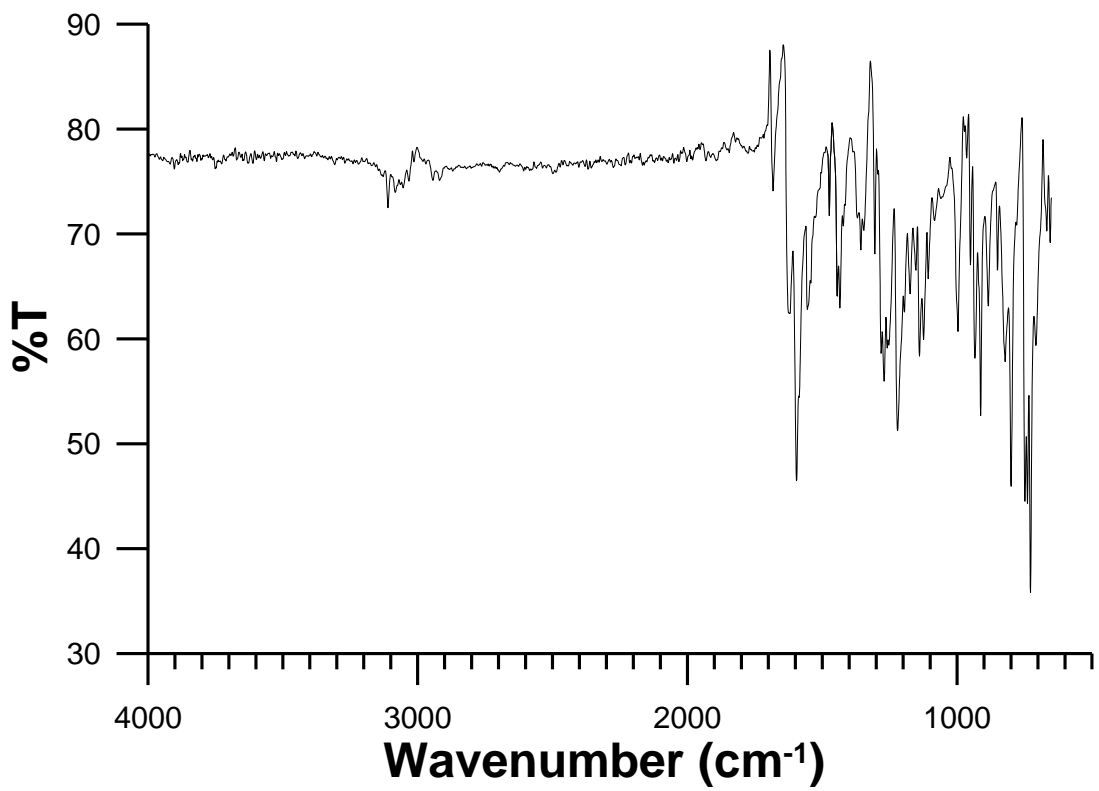**Figure C-6**. Asunsub

392

Figure C-7. 1dbzfcp
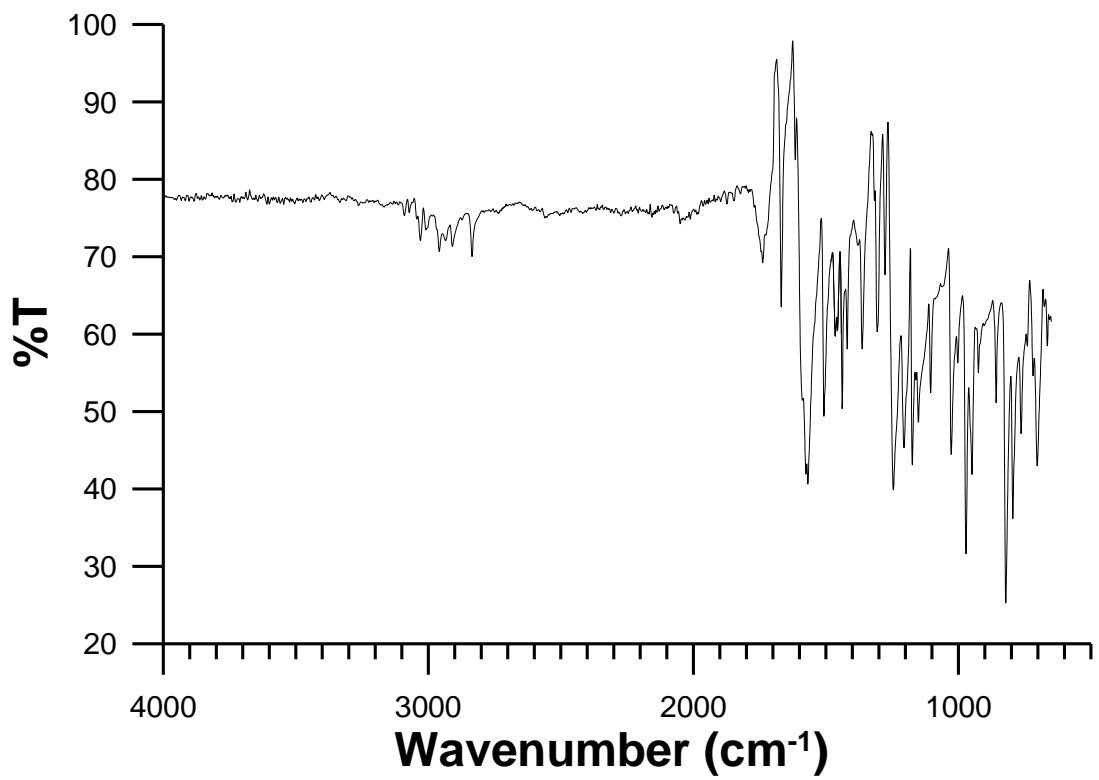
Figure C-8. 2dbmxcp

APPENDIX D

ADDITIONAL ABSORPTION AND FLUORESCENCE SPECTRA
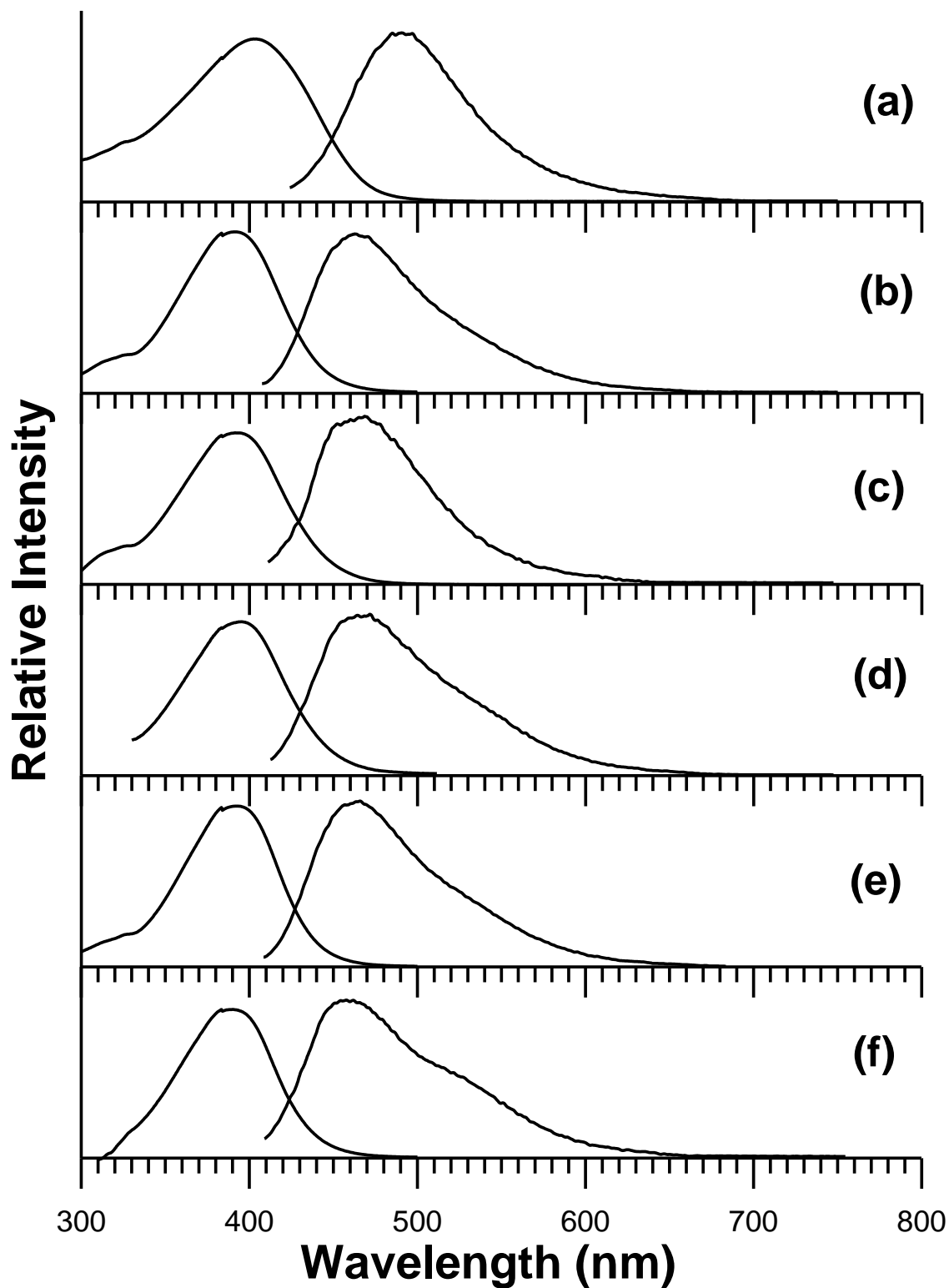
Figure D-1(a). Absorption and fluorescence emission spectra of dmab in (a) 2,2,2-trifluoroethanol (TFE), (b) methanol, (c) ethanol, (d) 1-propanol, (e) 1-butanol, and (f) 2-propanol.
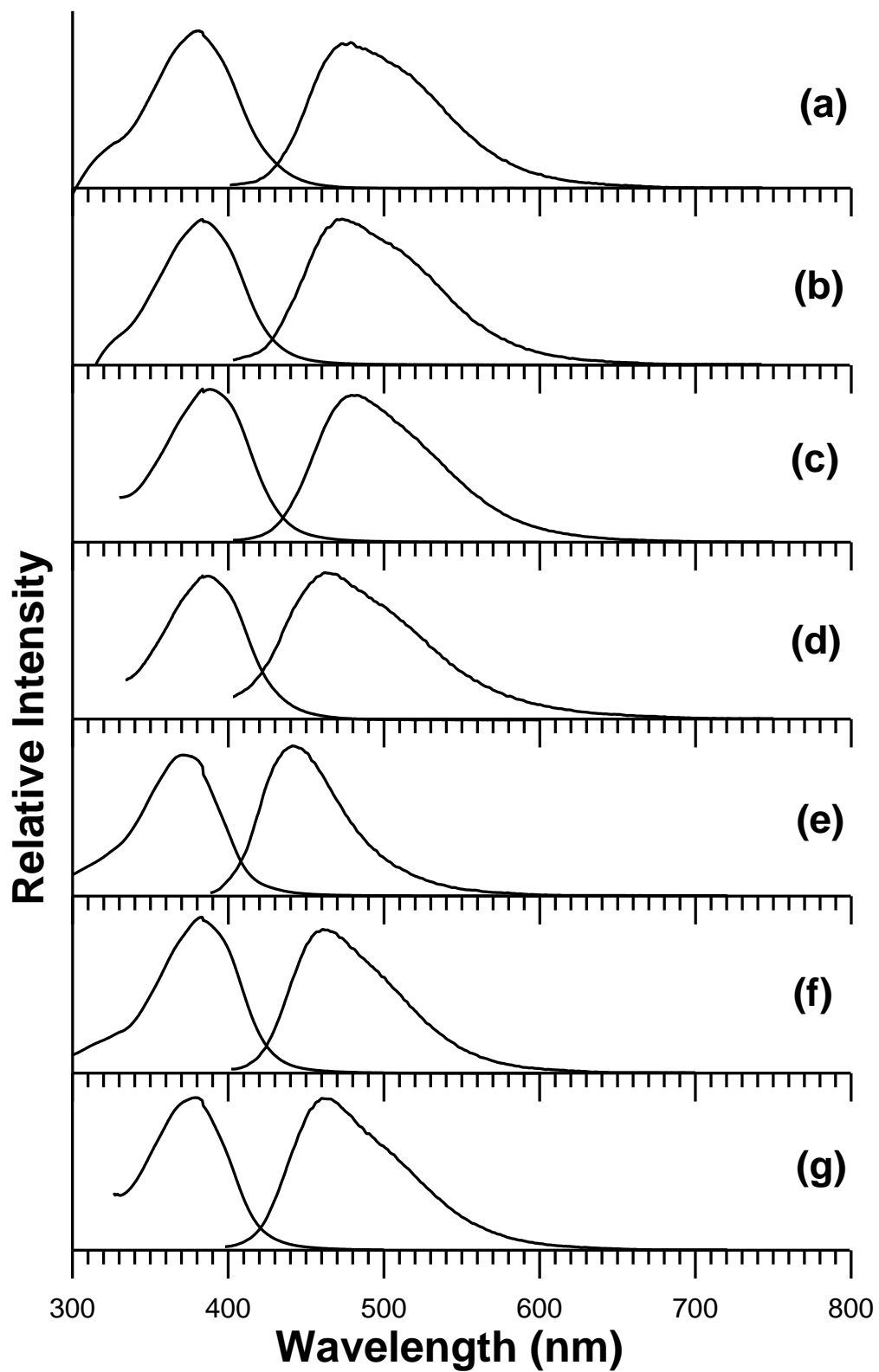
Figure D-1(b). Absorption and fluorescence emission spectra of dmab in (a) acetonitrile, (b) N,N-dimethylformamide, (c) dimethyl sulfoxide, (d) pyridine, (e) ethyl acetate, (f) dichloromethane, and (g) acetone.
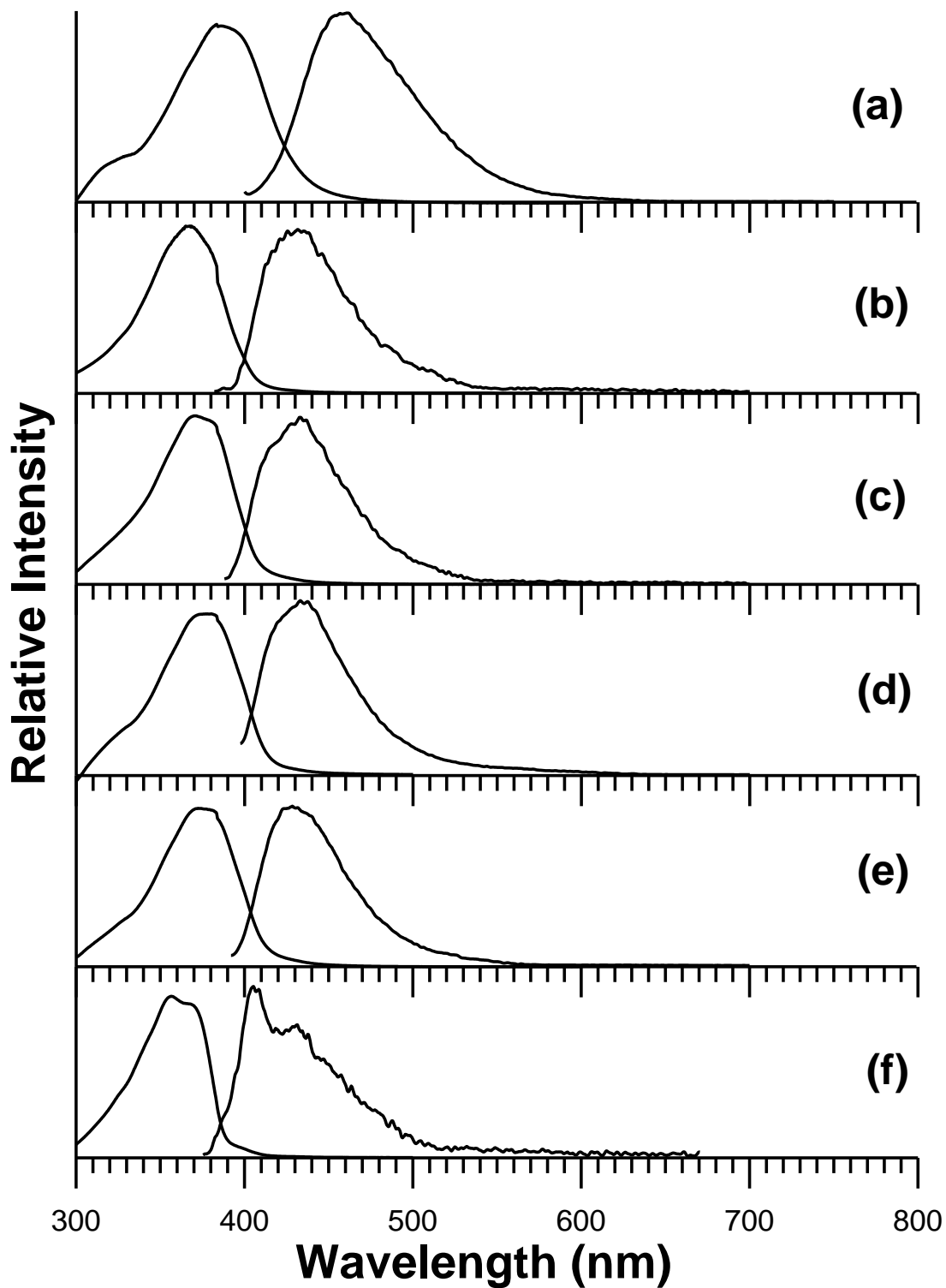
Figure D-1(c). Absorption and fluorescence emission spectra of dmab in (a) chloroform, (b) diethyl ether, (c) carbon tetrachloride, (d) benzene, (e) toluene, and (f) n-hexane.
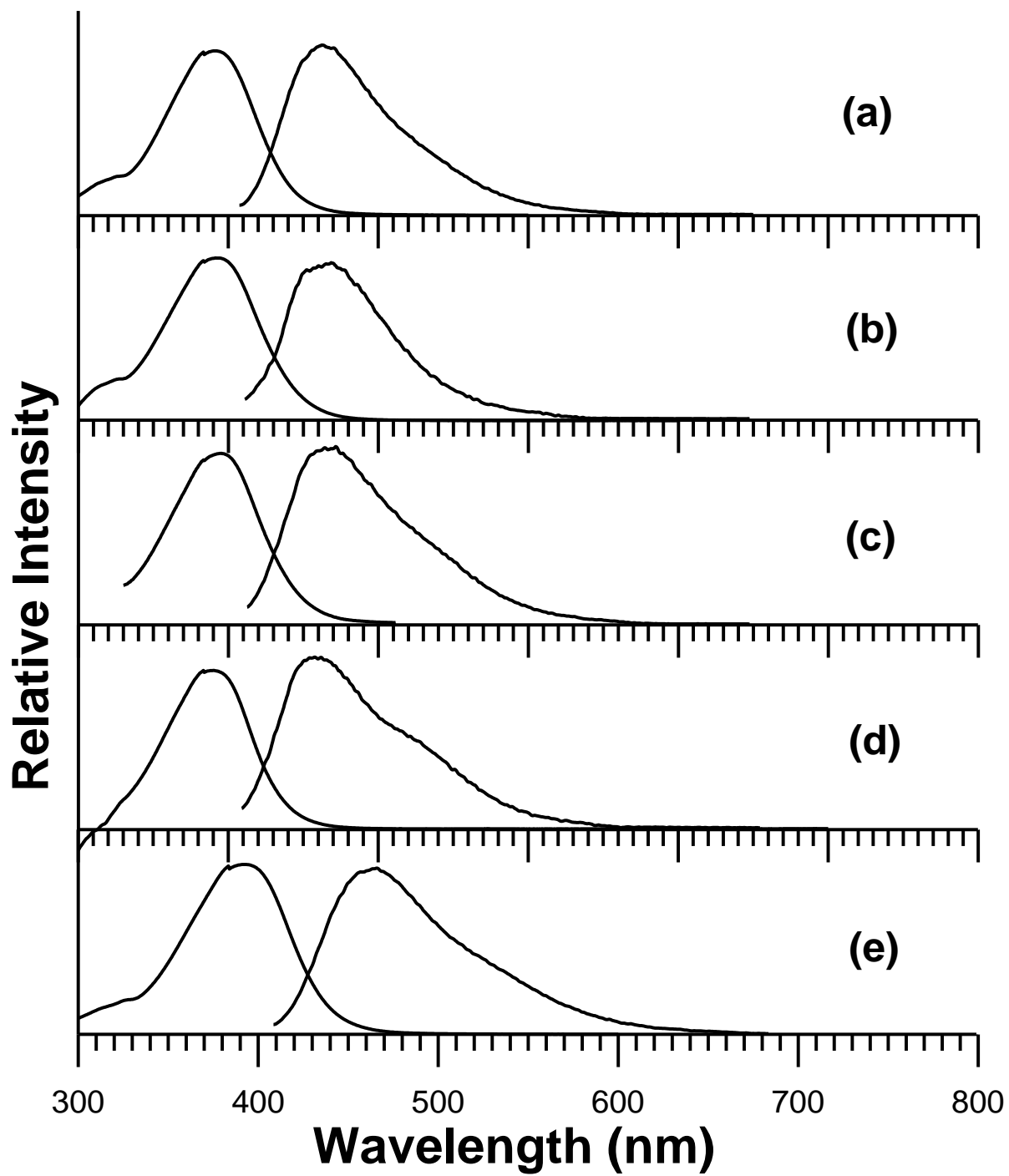
Figure D-2(a). Absorption and fluorescence emission spectra of dmac in (a) methanol, (b) ethanol, (c) 1-propanol, (d) 2-propanol, and (e) 1-butanol.
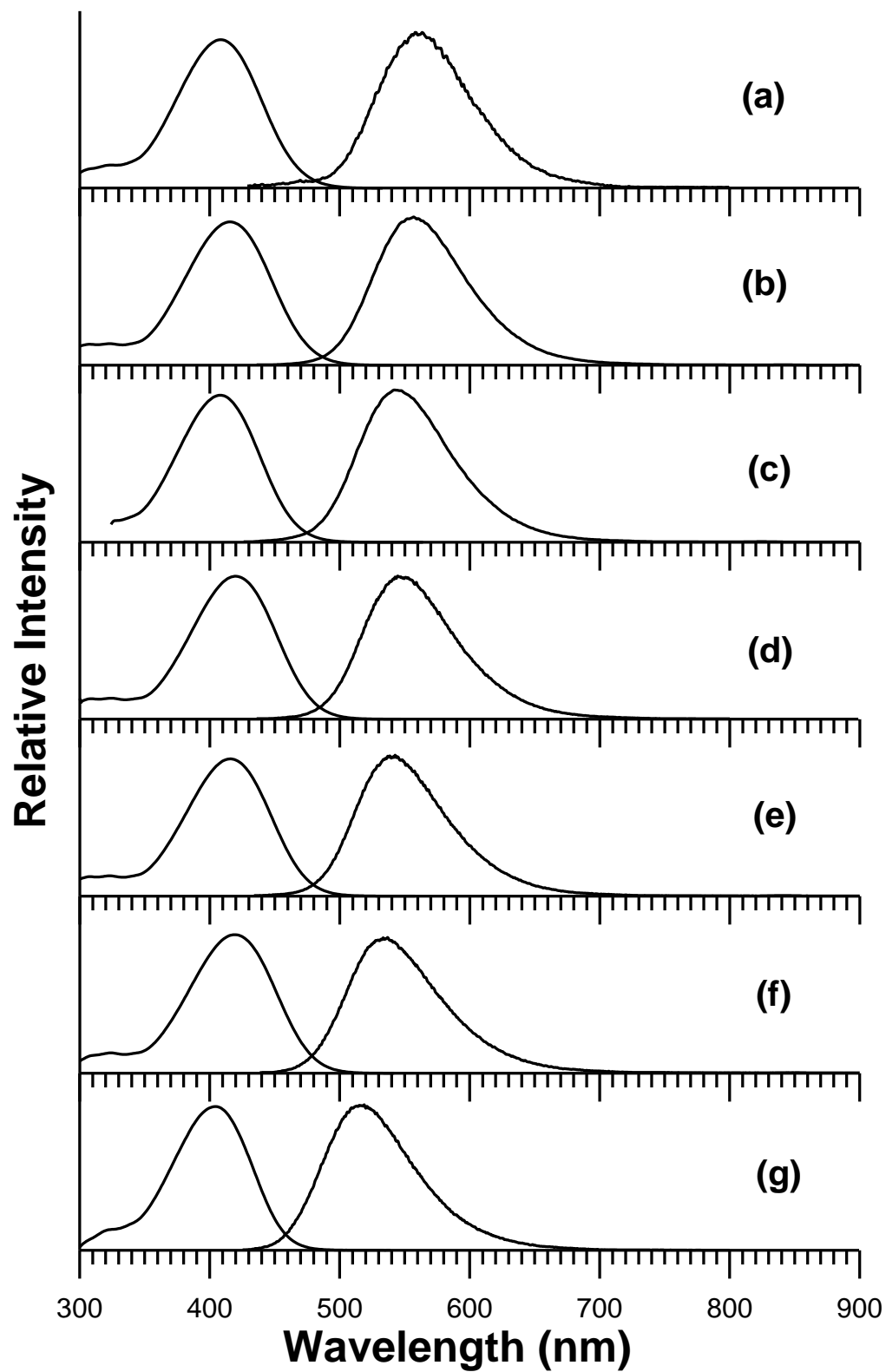
Figure D-2(b). Absorption and fluorescence emission spectra of dmac in (a) acetonitrile, (b) N,N-dimethylformamide, (c) acetone, (d) pyridine, (e) dichloromethane, (f) chloroform, and (g) ethyl acetate.
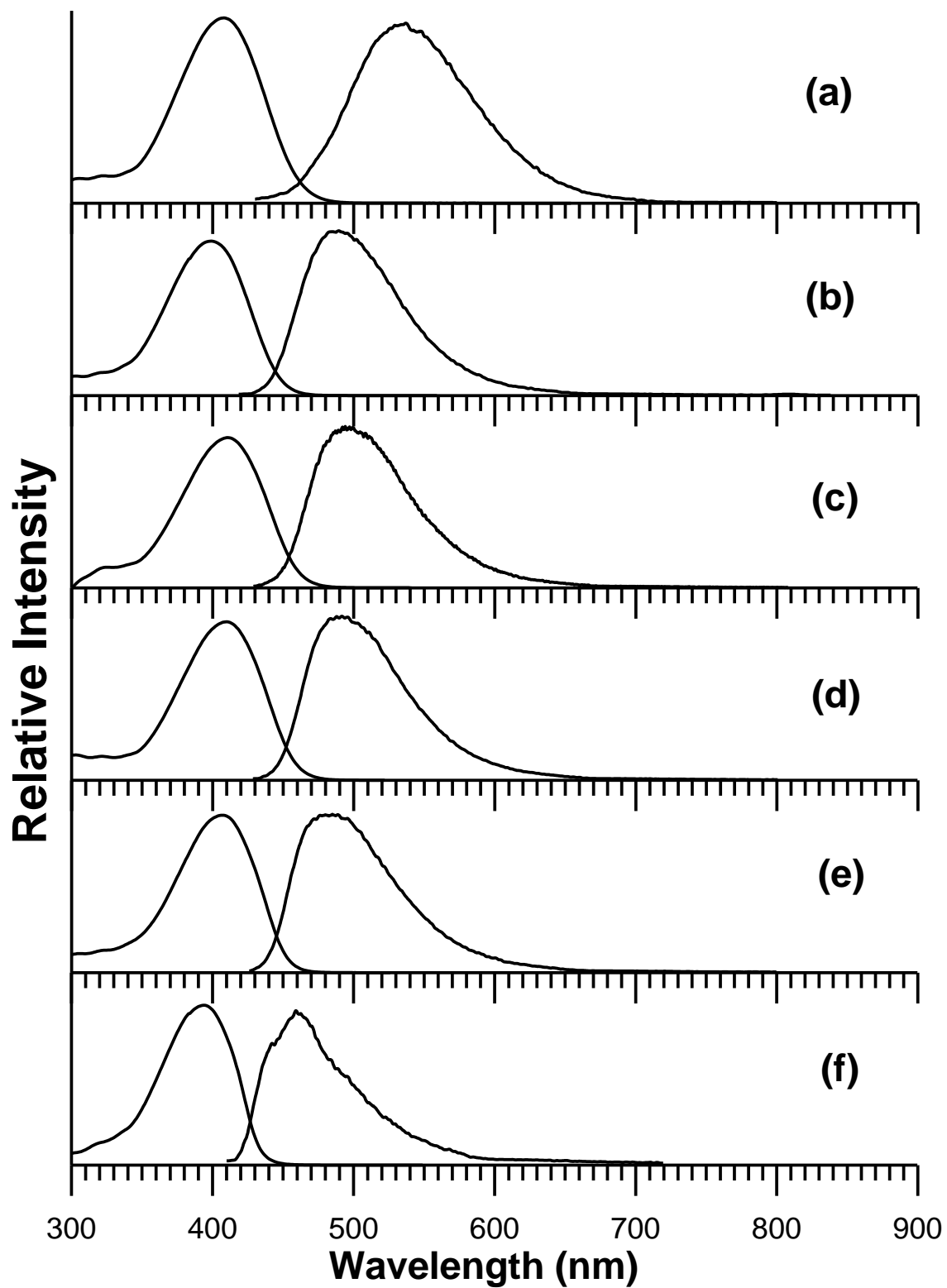
Figure D-2(c). Absorption and fluorescence emission spectra of dmac in (a) tetrahydrofuran, (b) diethyl ether, (c) benzene, (d) toluene, (e) carbon tetrachloride and (f) n-hexane.

Figure D-3(a). Absorption and fluorescence emission spectra of bis-dmab in (a) methanol, (b) ethanol, (c) 2-propanol, (d) dimethyl sulfoxide, (e) acetonitrile, (f) N,N-dimethylformamide, and (g) acetone.
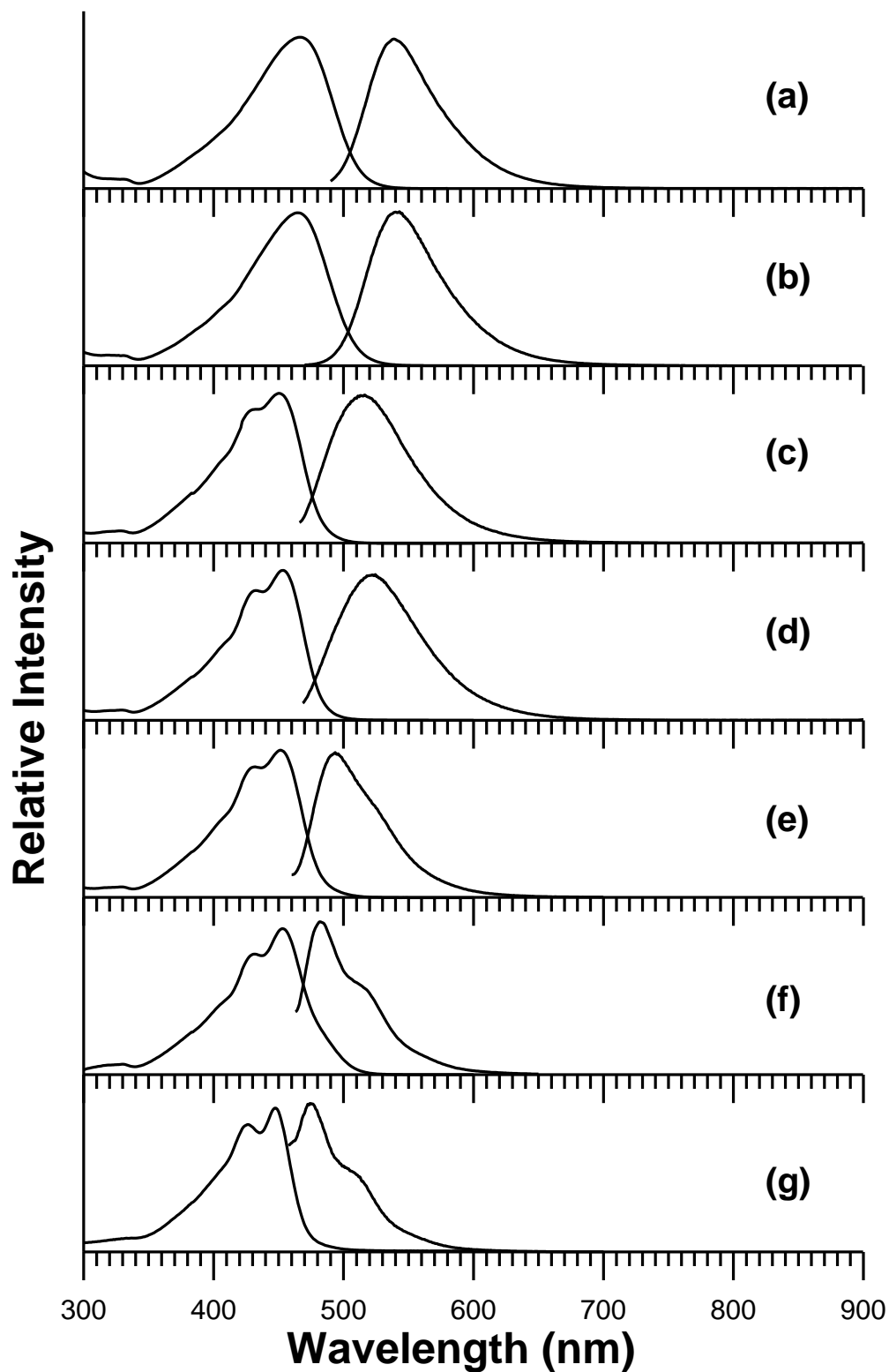
Figure D-3(b). Absorption and fluorescence emission spectra of bis-dmab in (a) chloroform, (b) dichloromethane, (c) ethyl acetate, (d) tetrahydrofuran, (e) 1,4-dioxane, (f) toluene, and (g) carbon tetrachloride.

Figure D-4(a). Absorption and fluorescence emission spectra of Ashrbor in (a) methanol, (b) ethanol, (c) 1-propanol, (d) 2-propanol, and (e) 1-butanol.

Figure D-4(b). Absorption and fluorescence emission spectra of Ashrbor in (a) acetonitrile; (b) dimethyl sulfoxide; (c) dichloromethane; (d) N,N-dimethylformamide; (e) acetone; (f) pyridine; and (g) chloroform.

Figure D-4(c). Absorption and fluorescence emission spectra of Ashrbor in (a) n-butyl acetate, (b) ethyl acetate, (c) ethyl benzoate, (d) 1,2-dichlorobenzene, (e) tetrahydrofuran, and (f) diethyl ether.
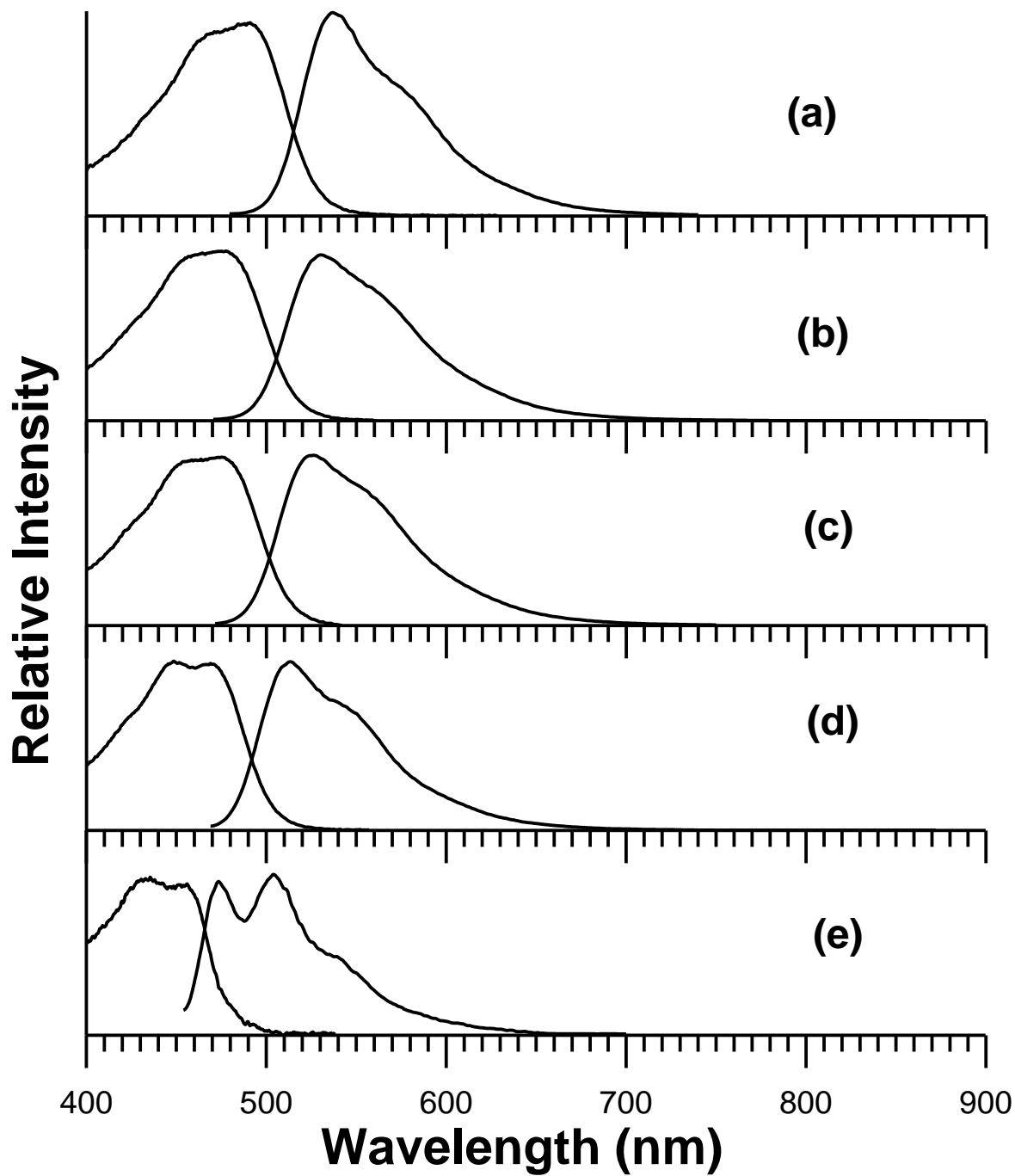
Figure D-4(d). Absorption and fluorescence emission spectra of Ashrbor in (a) carbon disulfide; (b) benzene; (c) toluene; (d) carbon tetrachloride; and (e) n_hexane.
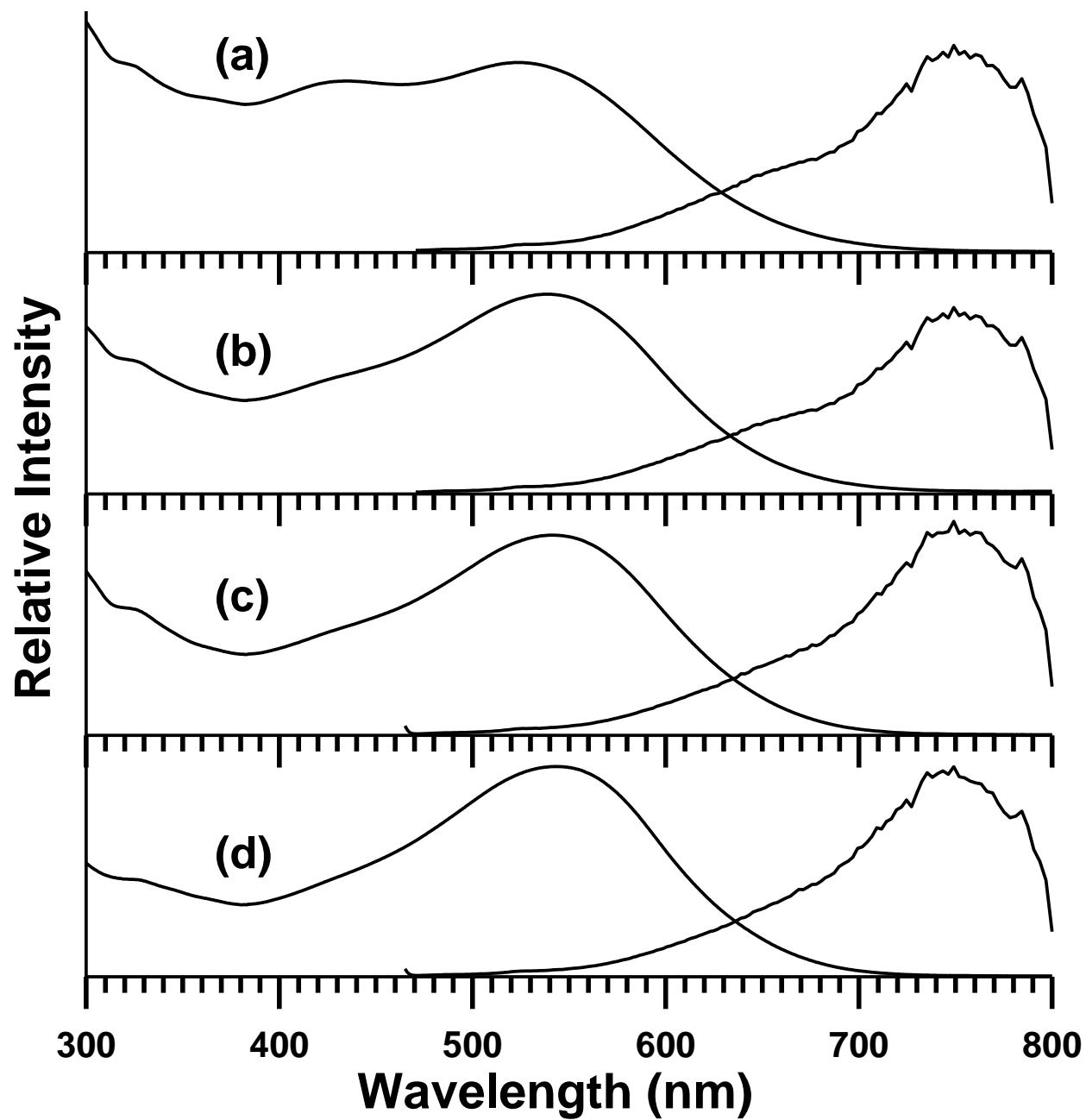
Figure D-5(a). Absorption and corrected fluorescence emission spectra of bis-juldmac in (a) methanol; (b) ethanol; (c) 1-propanol; and (d) 1-butanol.
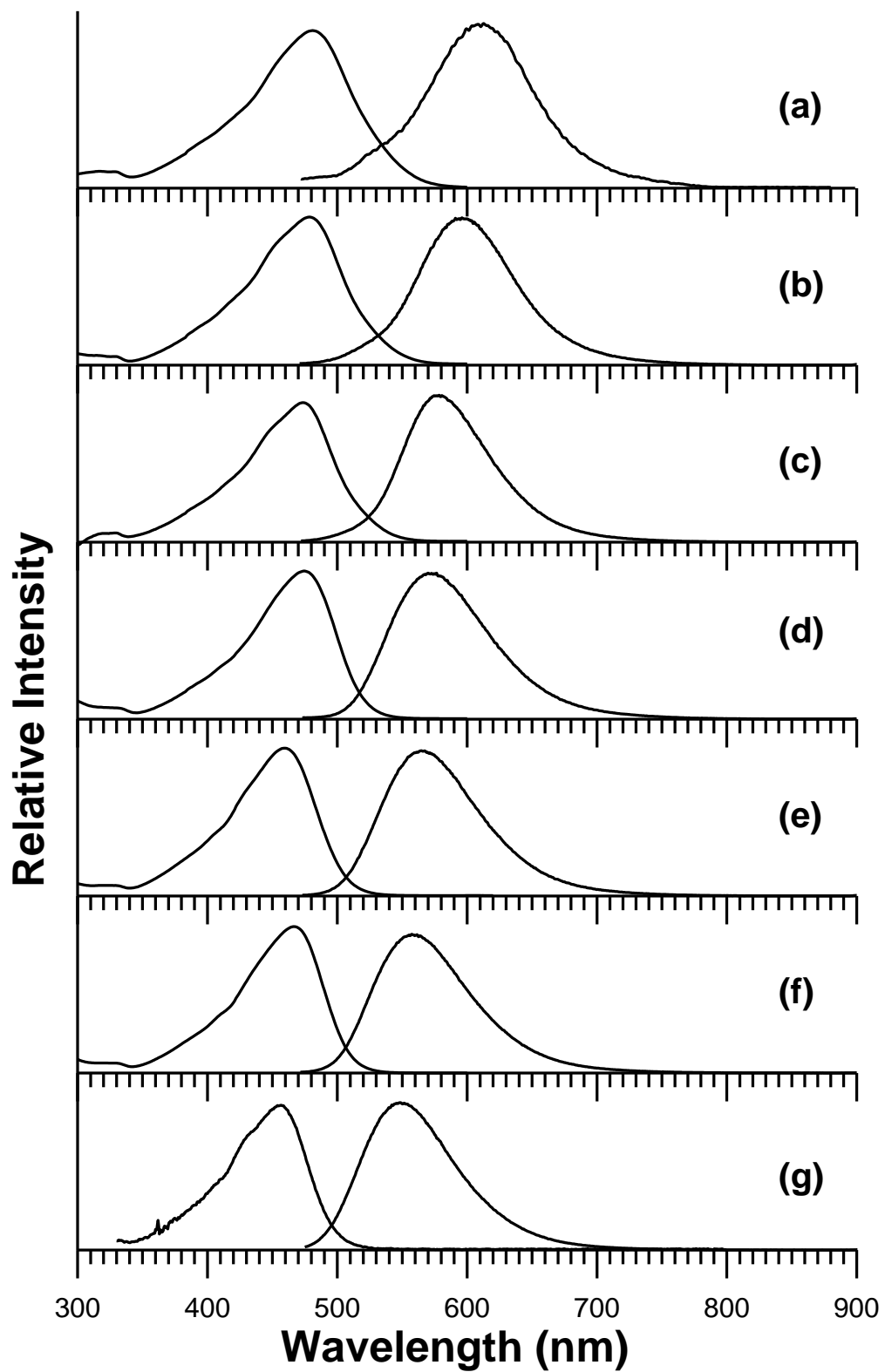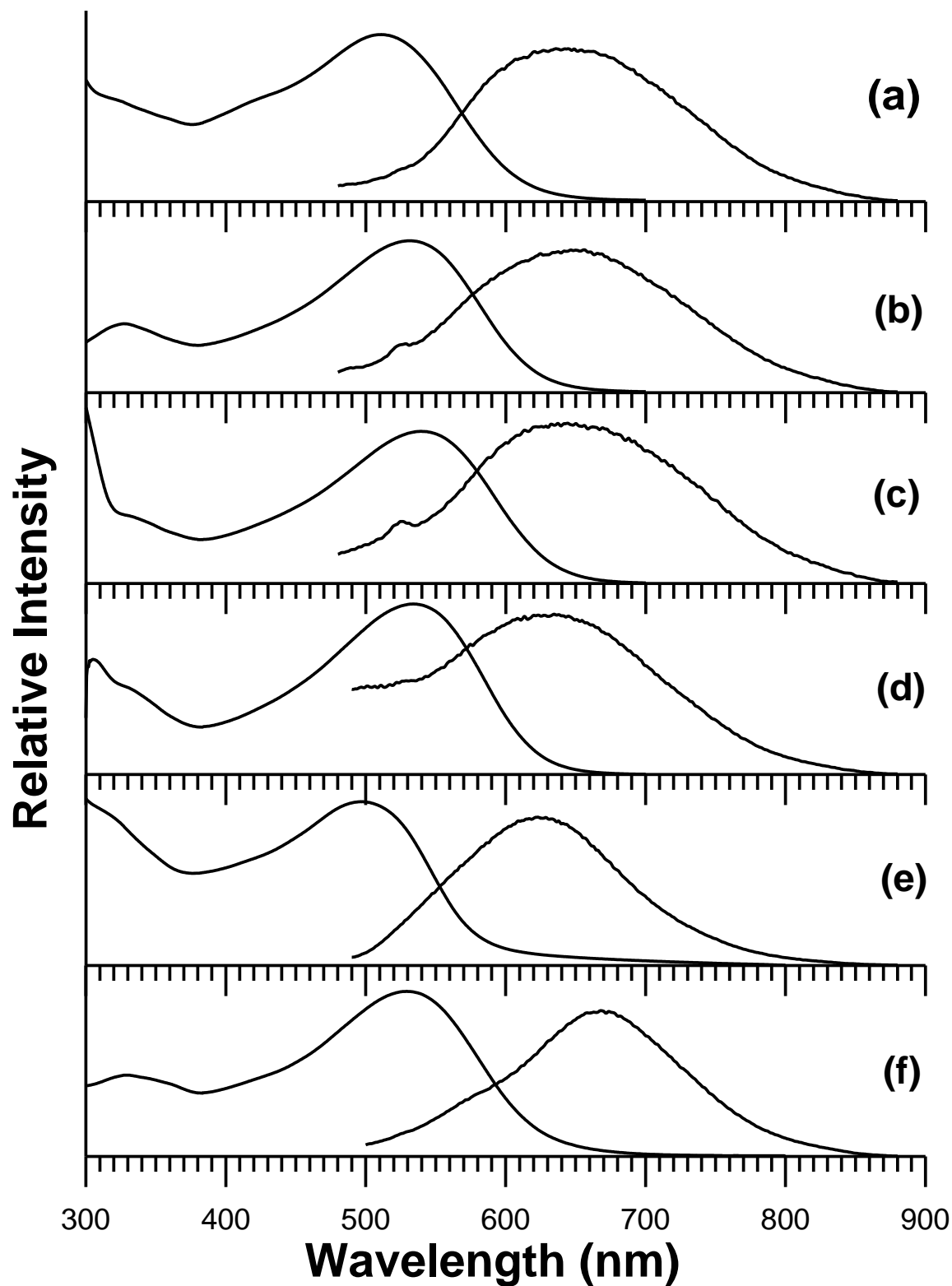
Figure D-5(b). Absorption and fluorescence emission spectra of bis-juldmac in (a) acetonitrile, (b) N,N-dimethylformamide, (c) dimethyl sulfoxide, (d) pyridine, (e) ethyl acetate, and (f) dichloromethane.
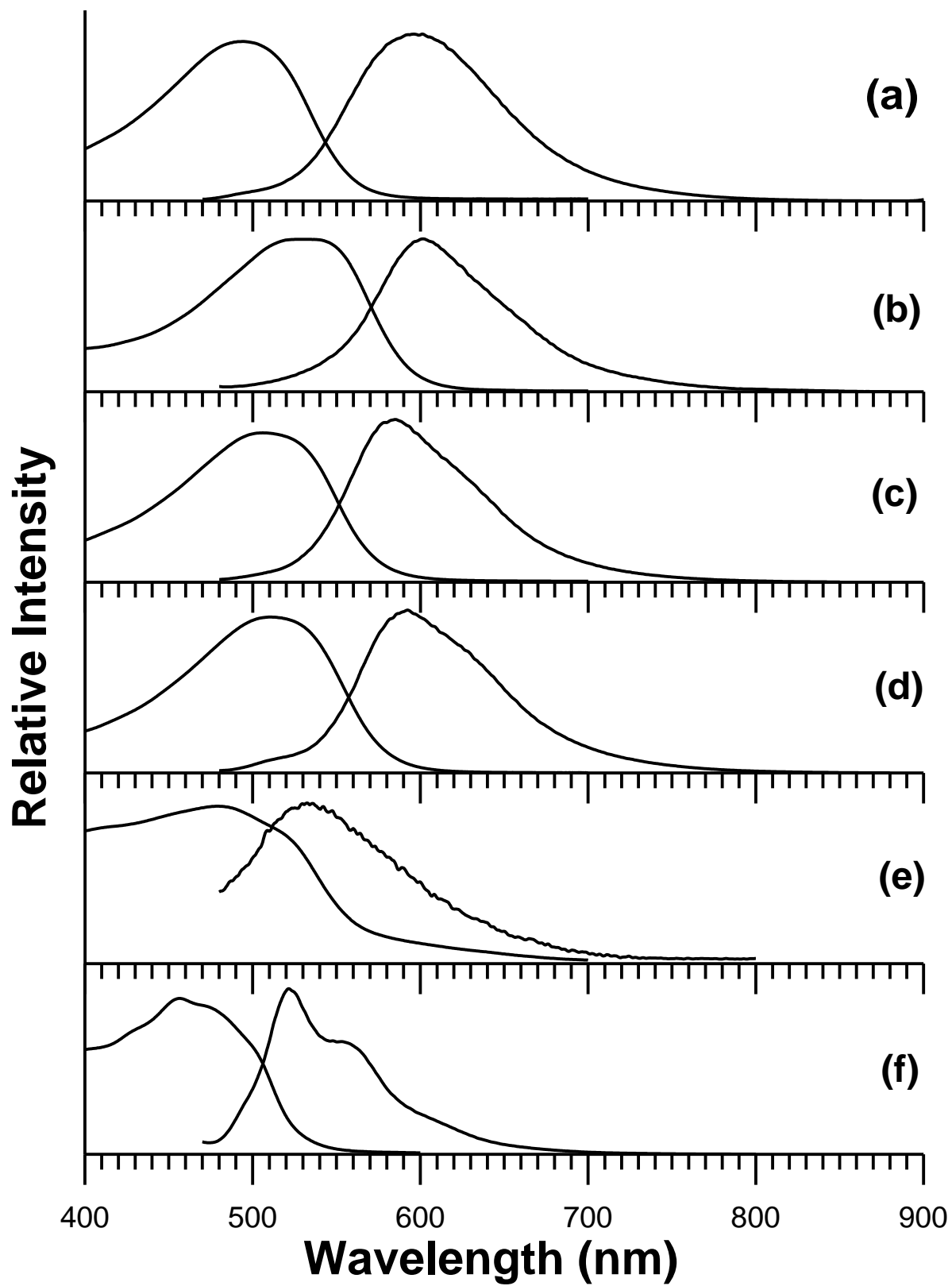
Figure D-5(c). Absorption and fluorescence emission spectra of bis-juldmac in (a) diethyl ether, (b) carbon disulfide, (c) toluene, (d) benzene, (e) carbon tetrachloride, and (f) n-hexane.
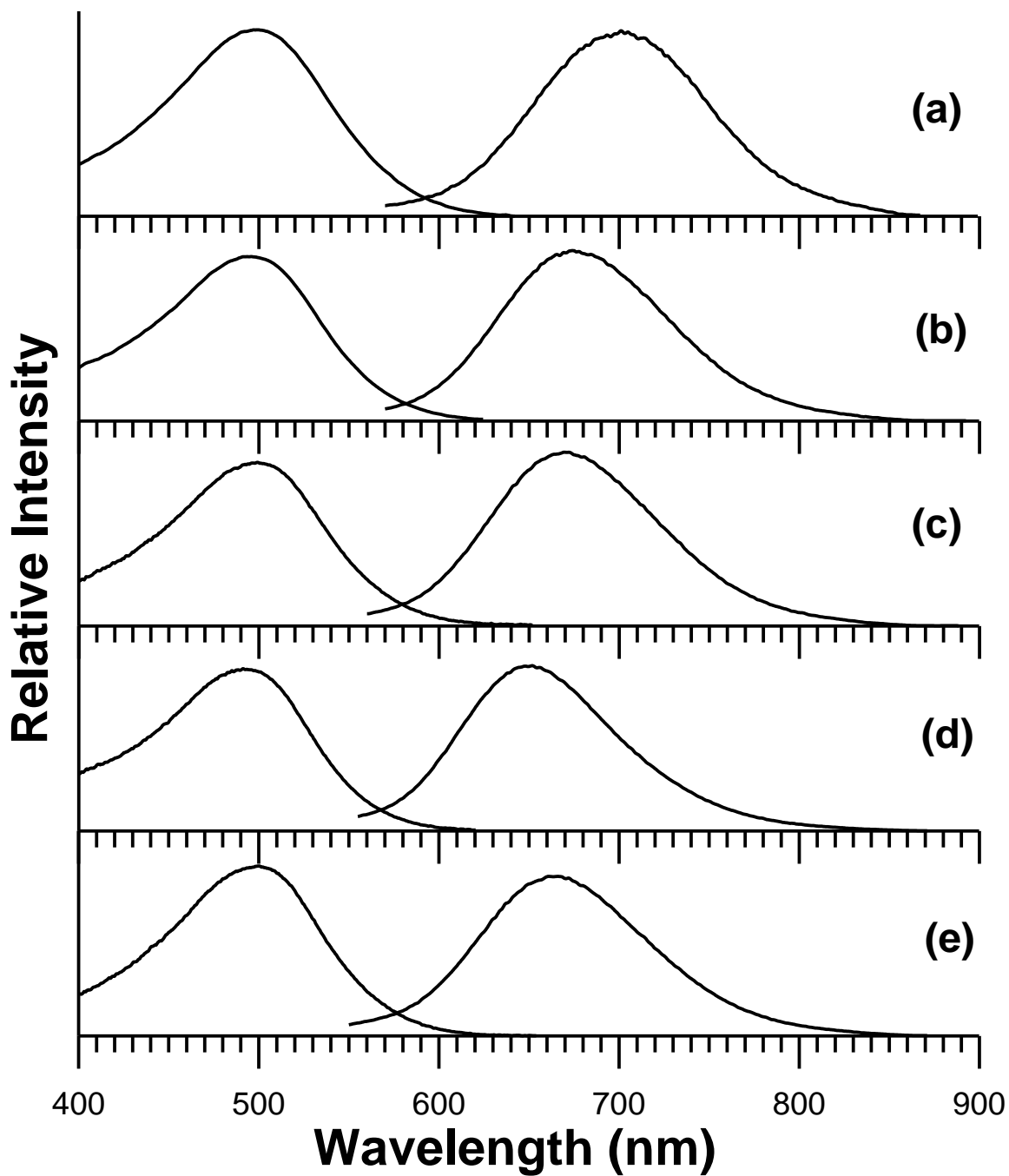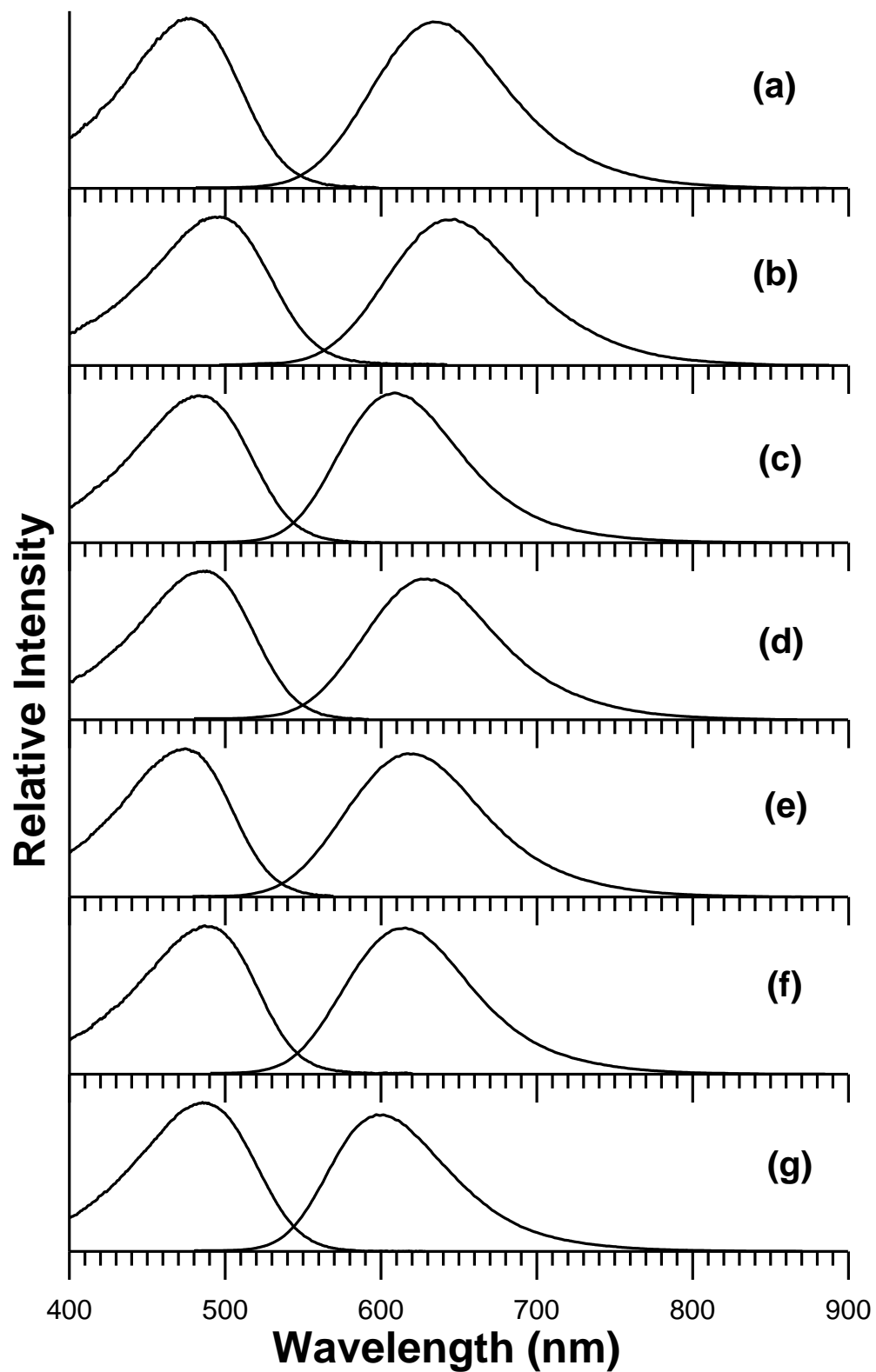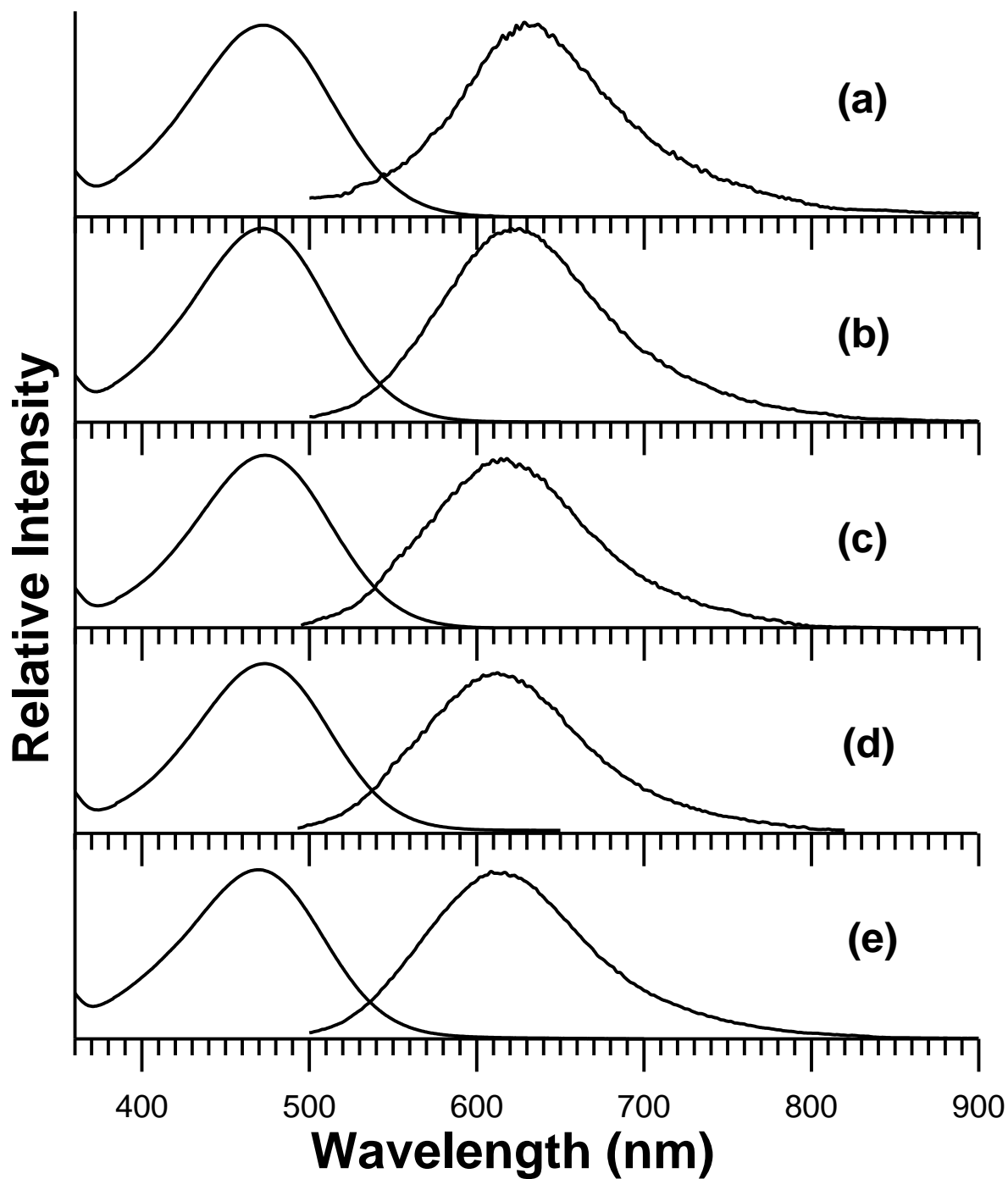
Figure D-6(a). Absorption and fluorescence emission spectra of Asdimcy1 in (a) methanol, (b) ethanol, (c) 1-propanol, (d) 1-butanol, and (e) 2-propanol.
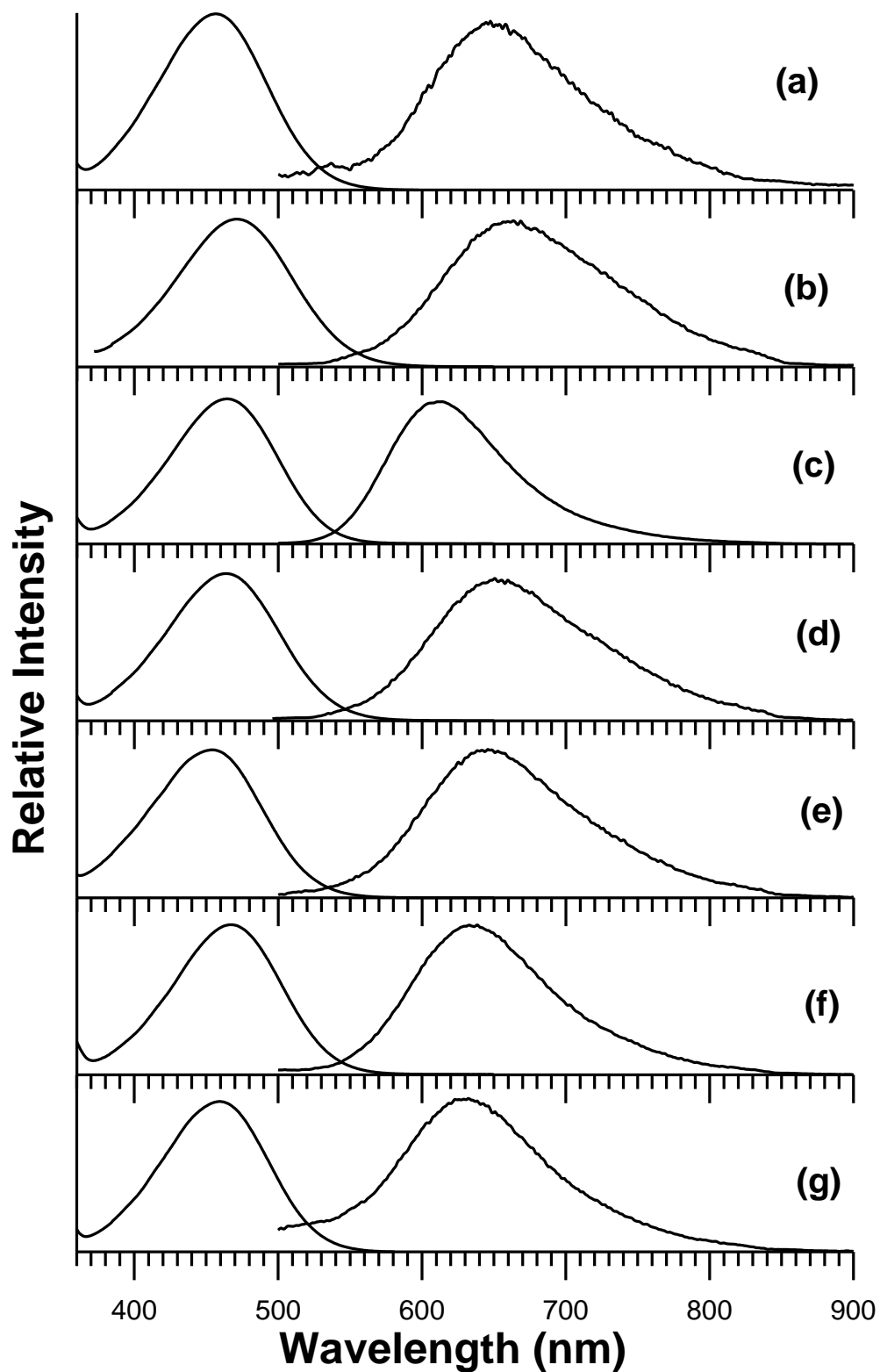
Figure D-6(b). Absorption and fluorescence emission spectra of Asdimcy1 in (a) acetonitrile, (b) dimethyl sulfoxide, (c) dichloromethane, (d) N_N-dimethylformamide, (e) acetone, (f) pyridine, and (g) cyclopentanone.
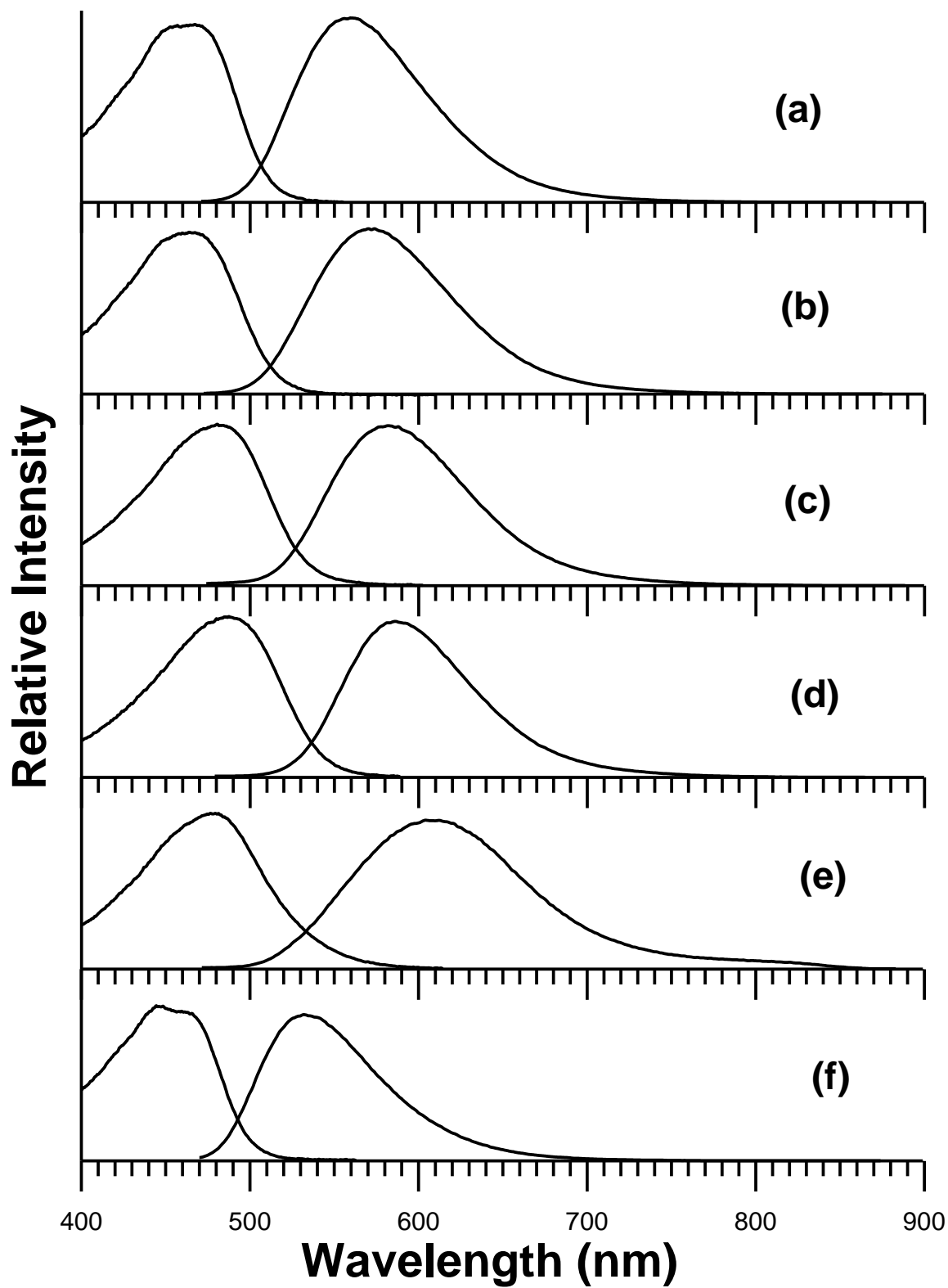
411
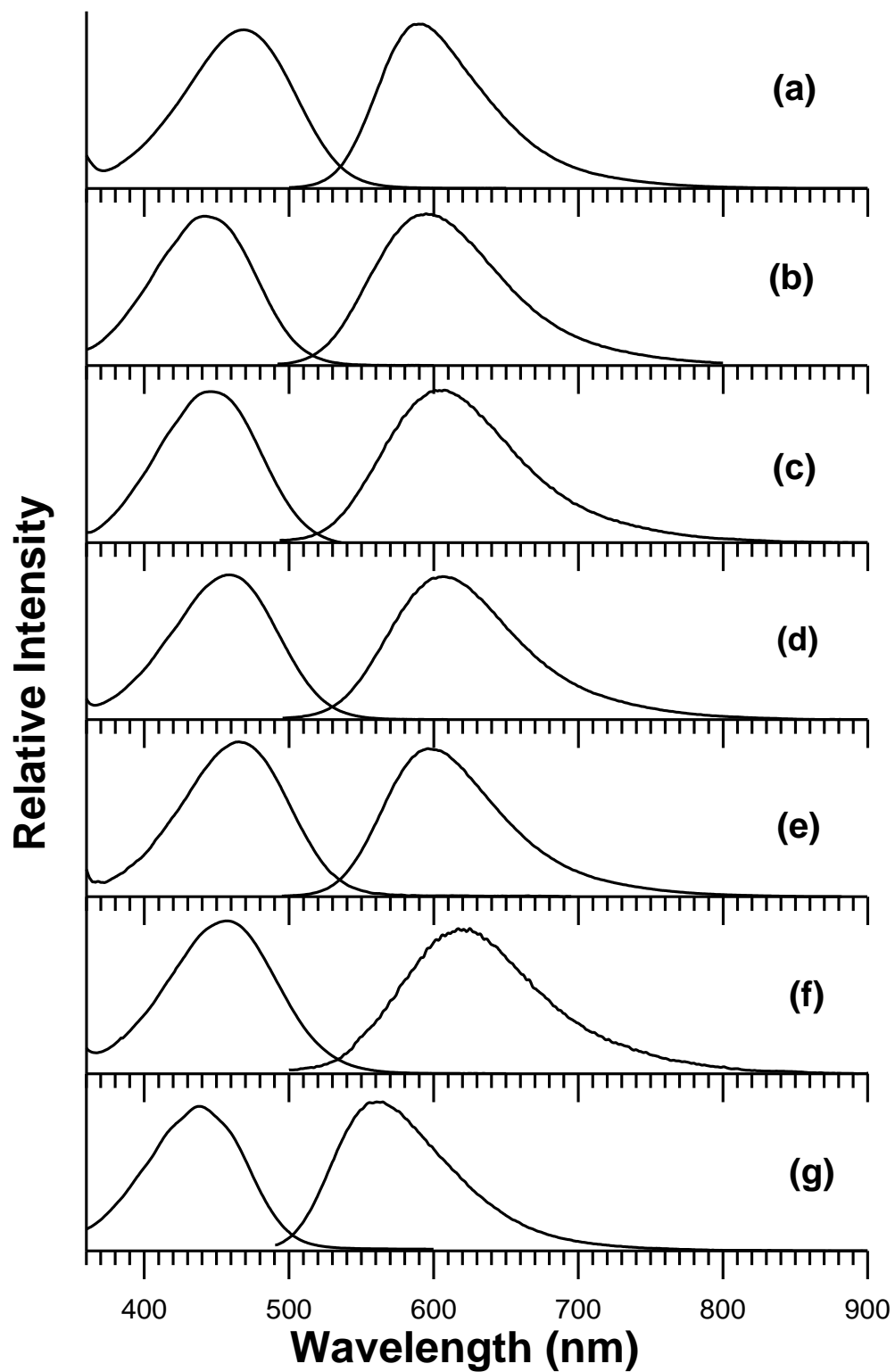
Figure D-6(c). Absorption and fluorescence emission spectra of Asdimcy1 in (a) chloroform, (b) n_butyl acetate, (c) ethyl acetate, (d) ethyl benzoate, (e) 1,2-dichlorobenzene, (f) tetrahydrofuran, and (g) diethyl ether.
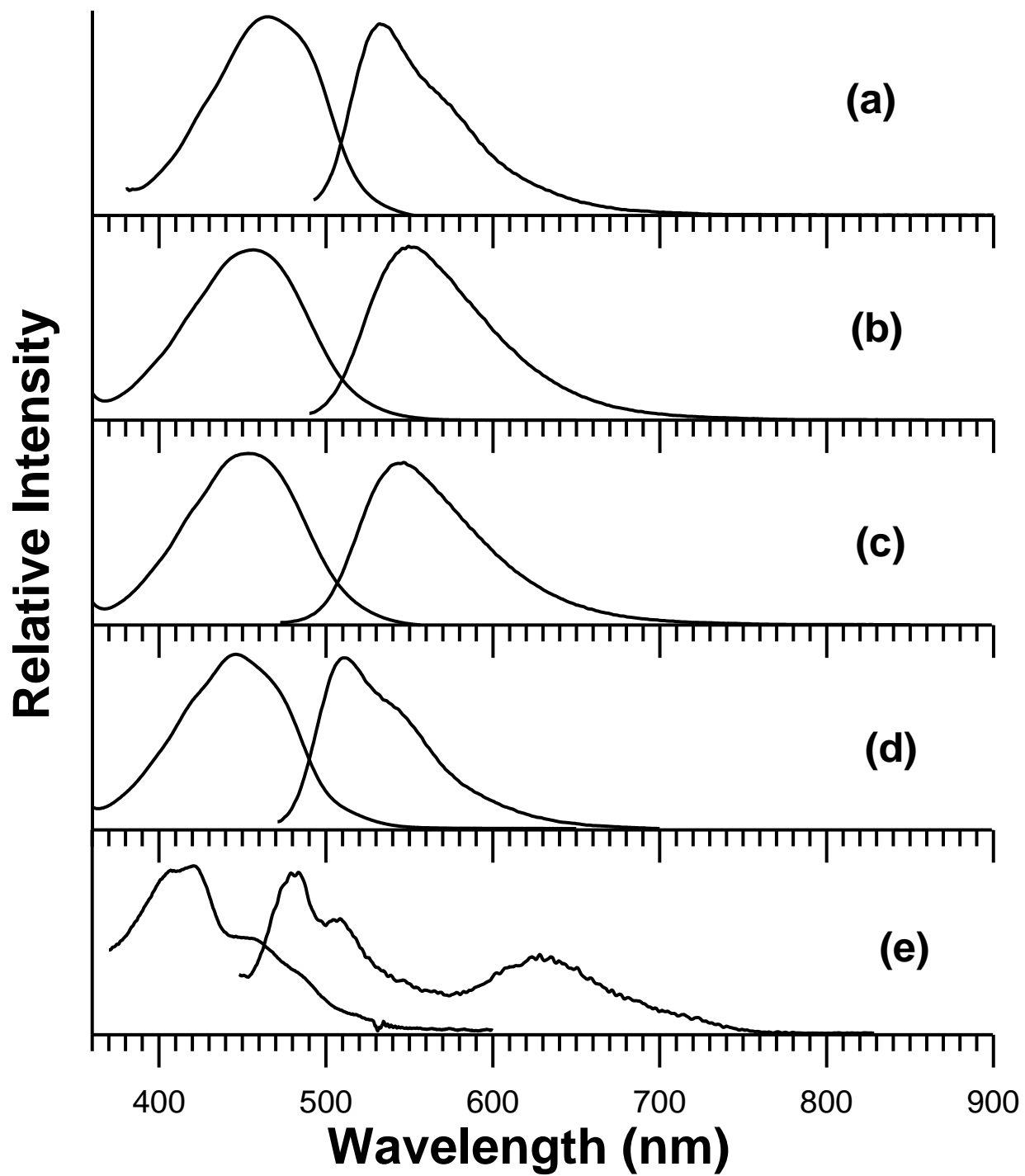
Figure D-6(d). Absorption and fluorescence emission spectra of Asdimcy1 in (a) carbon disulfide, (b) benzene, (c) toluene, (d) carbon tetrachloride and (e) n-hexane.
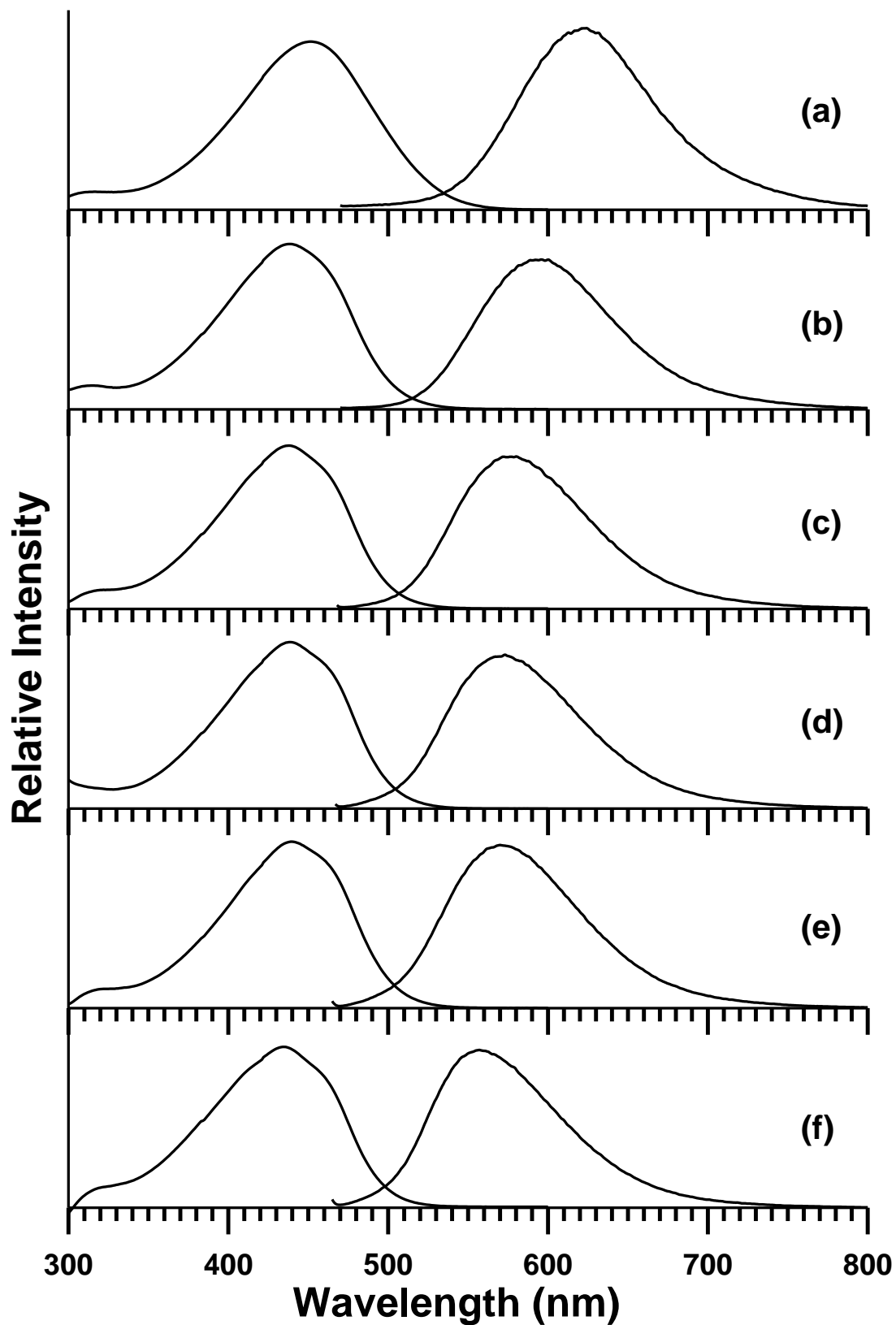
Figure D-7(a). Absorption and fluorescence emission spectra of 2dbmxcp in (a) 2,2,2-trifluoroethanol, (b) methanol, (c) ethanol, (d) 1-propanol, (e) 1-butanol, and (f) 2-propanol.

414
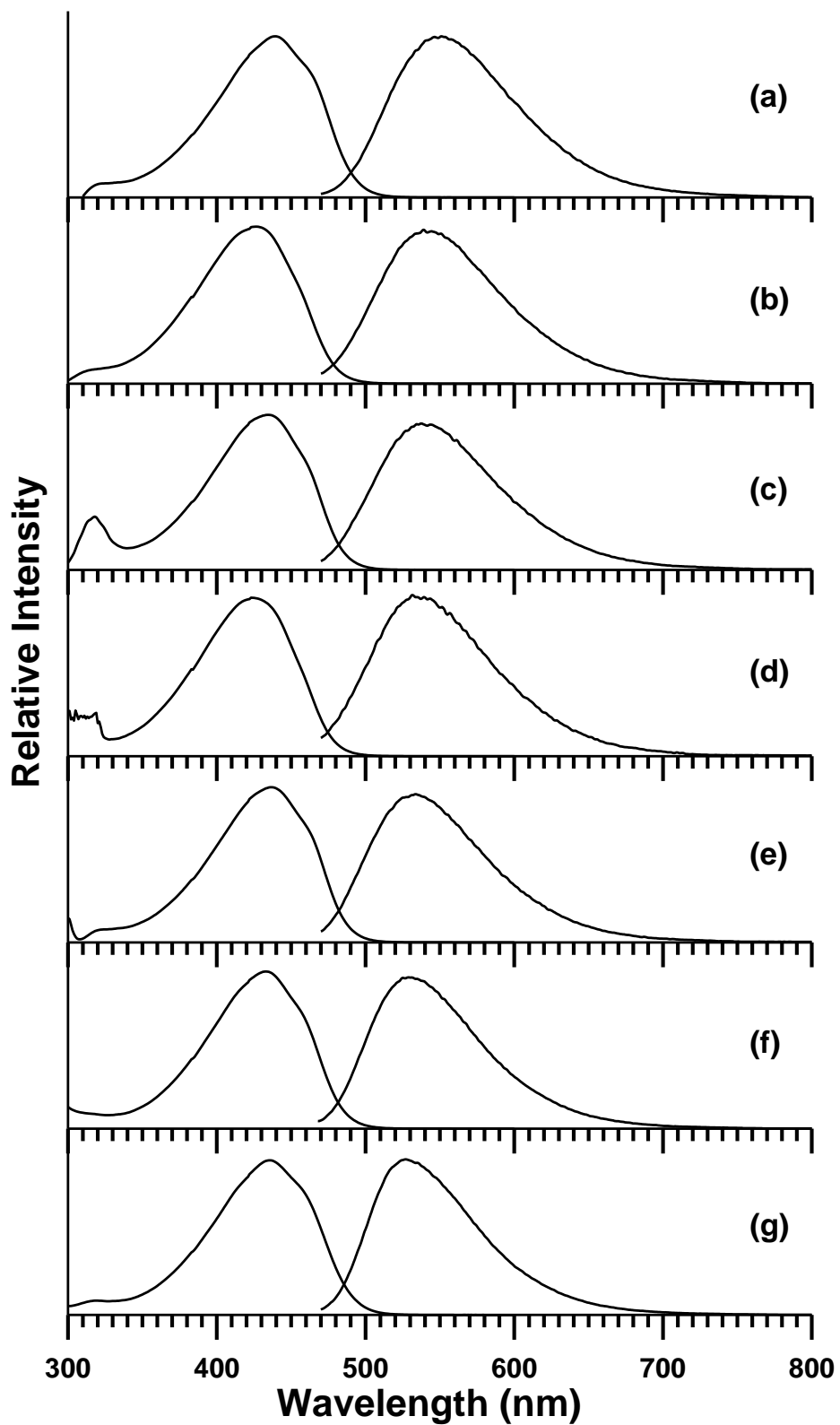
Figure D-7(b). Absorption and fluorescence emission spectra of 2dbmxcp in (a) dimethyl sulfoxide, (b) acetonitrile, (c) N,N-dimethylformamide, (d) acetone, (e) pyridine, (f) dichloromethane, and (g) chloroform.

APPENDIX E
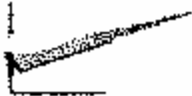
FLUORESCENCE SPECTRA CORRECTION FACTOR CALCULATIONS

Figure E-1. N,N-dimethylamino-m-nitrobenzene (N,N-DMANB) in 30% benzene/70% n-hexane

Figure E-2. Quinine sulfate in 0.1 N H_2SO_4

DATA ANALYSIS

Cubic Spline Interpolation

N,N'-DMANB Corrected Fluorescence Standard
For LS50B with RED Sensitive Phototube

This QuickSheet demonstrates Mathcad's **cspline**
and **interp** functions for connecting X-Y data.

Enter a matrix of X-Y data to be interpolated:

Corrected emission spectrum for N,N'-DMANB taken from J.R. Lakowicz, <u>Principles of</u>
<u>Fluorescence Spectroscopy</u> 2nd Ed.

data :=

22502.25	1.49
22251.89	2.01
22002 2	2.98

Click on the **Input Table** above until you see the handles, and
enlarge it to see the matrix **data** used in this example.

$$data := csort(data, 0) \qquad X := data^{\langle 0 \rangle} \qquad Y := data^{\langle 1 \rangle}$$

Spline coefficients:

$$S := cspline(X, Y)$$

Fitting function:

$$fit(x) := interp(S, X, Y, x)$$

Sample interpolated values: fit(14000) = 23.455 fit(13) = -1.117

fit(18400) = 99.781

$j := 12500, 12550 .. 22200$

Corrected spectrum of N,N-DMANB

Intensity

$1 \cdot 10^4 \ 1.23 \cdot 10^4 \ 1.47 \cdot 10^4 \ 1.7 \cdot 10^4 \ 1.93 \cdot 10^4 \ 2.17 \cdot 10^4 \ 2.4 \cdot 10^4$
Wavenumbers

+++ X-Y data
—— Cubic spline interpolation
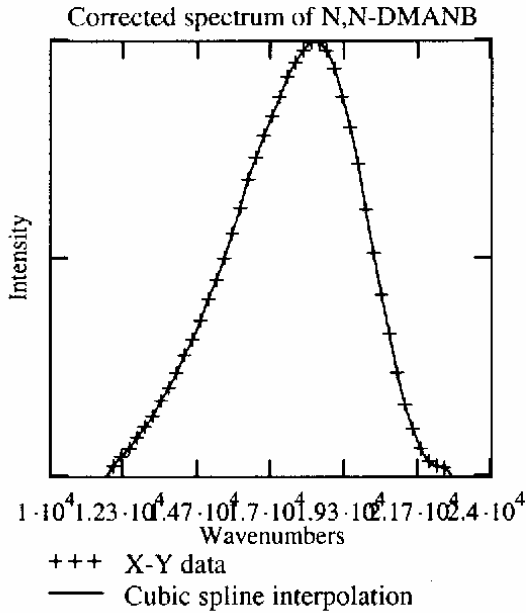
j =
$1.25 \cdot 10^4$
$1.255 \cdot 10^4$
$1.26 \cdot 10^4$
$1.265 \cdot 10^4$
$1.27 \cdot 10^4$
$1.275 \cdot 10^4$
$1.28 \cdot 10^4$
$1.285 \cdot 10^4$
$1.29 \cdot 10^4$
$1.295 \cdot 10^4$
$1.3 \cdot 10^4$
$1.305 \cdot 10^4$
$1.31 \cdot 10^4$
$1.315 \cdot 10^4$
$1.32 \cdot 10^4$
$1.325 \cdot 10^4$

fit(j) =
5.927
6.374
6.861
7.375
7.904
8.437
8.963
9.479
9.984
10.476
10.954
11.419
11.887
12.374
12.898
13.476

$$\int_{12500}^{22000} fit(x)\, dx = 4.972 \times 10^5$$

Fluorescence data for N,N-DMANB from LS50B corrected for bandbass by multiplying intensities by λ^2 and normalized to 100. RED sensitive phototube. Data copied from excel and insert>component>input table.. paste table from excel

xdata :=

	0	1
0	23529.41	1.05
1	23501.76	1.05

$xdata := csort(xdata, 0)$ $A := xdata^{\langle 0 \rangle}$ $B := xdata^{\langle 1 \rangle}$

Spline coefficients:

$S := cspline(A, B)$

418

Fitting function:

$$xfit(x) := interp(S, A, B, x)$$

Corrected and LS50 / cubic spline fit.
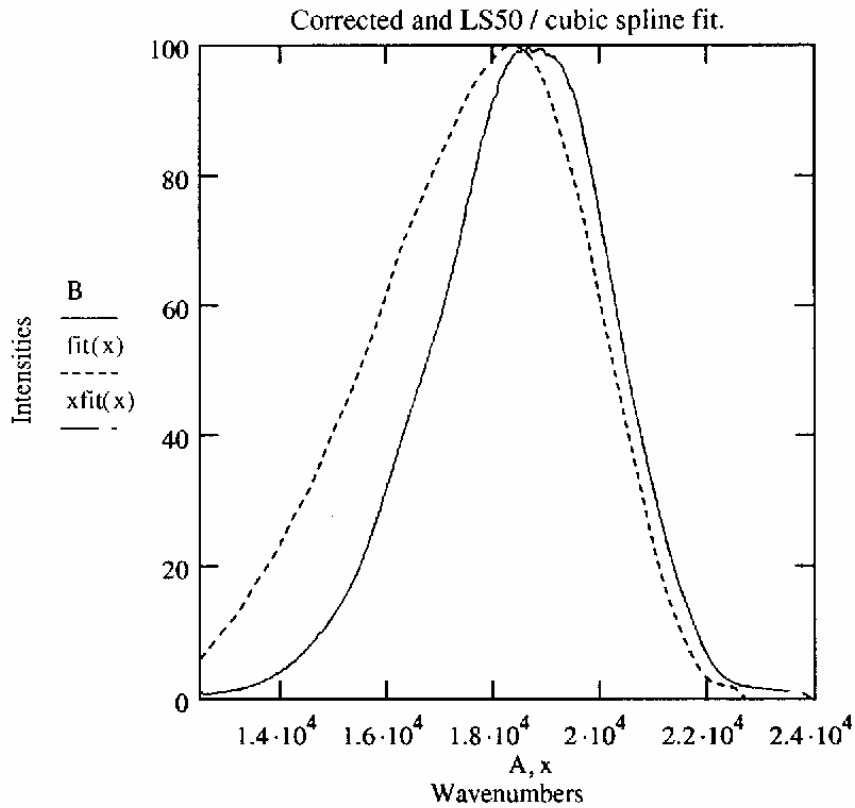
Determining correction factors at regular wavenumber intervals by dividing corrected spectral data by uncorrected spectral data.

$$l := 13000, 13050 .. 22200$$

$l =$

$1.3 \cdot 10^4$
$1.305 \cdot 10^4$
$1.31 \cdot 10^4$
$1.315 \cdot 10^4$
$1.32 \cdot 10^4$

$xfit(l) =$

1.03
1.097
1.142
1.207

$$\left[\frac{(fit(l))}{(xfit(l))} \right] =$$

10.64
10.411
10.41
10.254
9.699

419
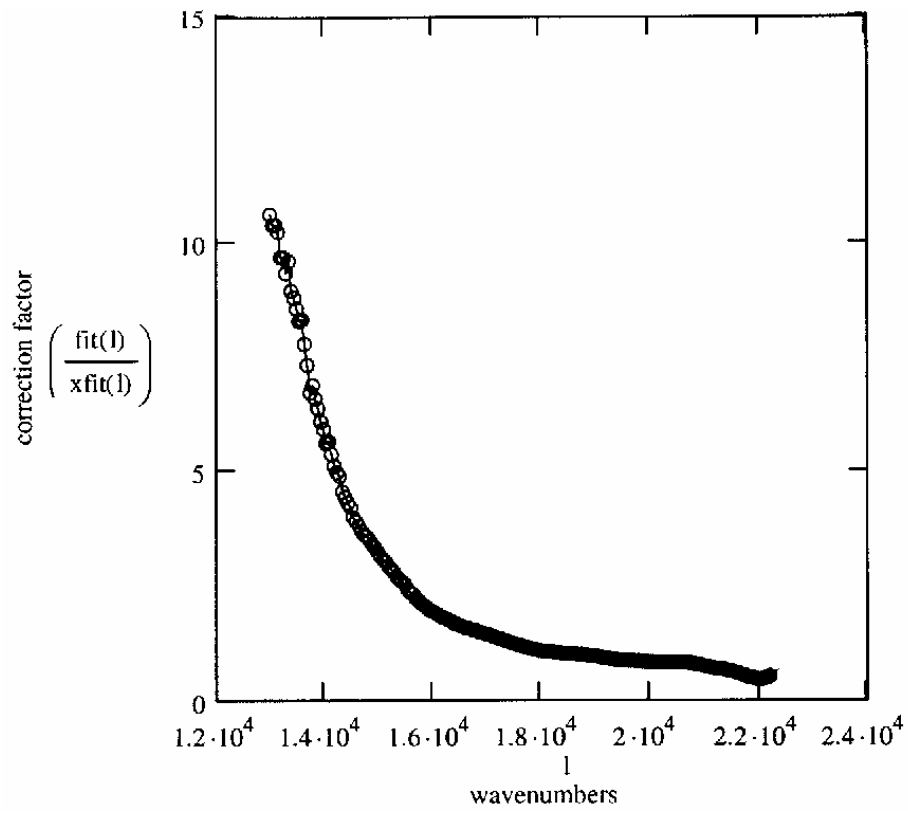
Figure E-2

DATA ANALYSIS

Cubic Spline Interpolation

Quinine Sulfate Corrected Fluorescence Standard For LS50B with Blue Sensitive Phototube

This QuickSheet demonstrates Mathcad's **cspline** and **interp** functions for connecting X-Y data.

Enter a matrix of X-Y data to be interpolated:

Corrected emission spectrum for Quinine Sulfate taken from J.R. Lakowicz, Principles of Fluorescence Spectroscopy 2nd Ed.

data :=

26001.04	0.98
25753.28	2.5
25497.2	...

Click on the **Input Table** above until you see the handles, and enlarge it to see the matrix **data** used in this example.

$$\text{data} := \text{csort}(\text{data}, 0) \qquad X := \text{data}^{\langle 0 \rangle} \qquad Y := \text{data}^{\langle 1 \rangle}$$

Spline coefficients:

$$S := \text{cspline}(X, Y)$$

Fitting function:

$$\text{fit}(x) := \text{interp}(S, X, Y, x)$$

Sample interpolated values: fit(15800) = 4.867   fit(18000) = 24.026   fit(18400) = 31.936

$j := 15750, 15800 .. 26000$

Corrected spectrum of Quinine Sulfate

Wavenumbers

+++ X-Y data
——— Cubic spline interpolation

j =	fit(j) =
$1.575 \cdot 10^4$	4.584
$1.58 \cdot 10^4$	4.867
$1.585 \cdot 10^4$	5.136
$1.59 \cdot 10^4$	5.397
$1.595 \cdot 10^4$	5.658
$1.6 \cdot 10^4$	5.927
$1.605 \cdot 10^4$	6.209
$1.61 \cdot 10^4$	6.51
$1.615 \cdot 10^4$	6.83
$1.62 \cdot 10^4$	7.174
$1.625 \cdot 10^4$	7.545
$1.63 \cdot 10^4$	7.942
$1.635 \cdot 10^4$	8.356
$1.64 \cdot 10^4$	8.776
$1.645 \cdot 10^4$	9.191
...	...
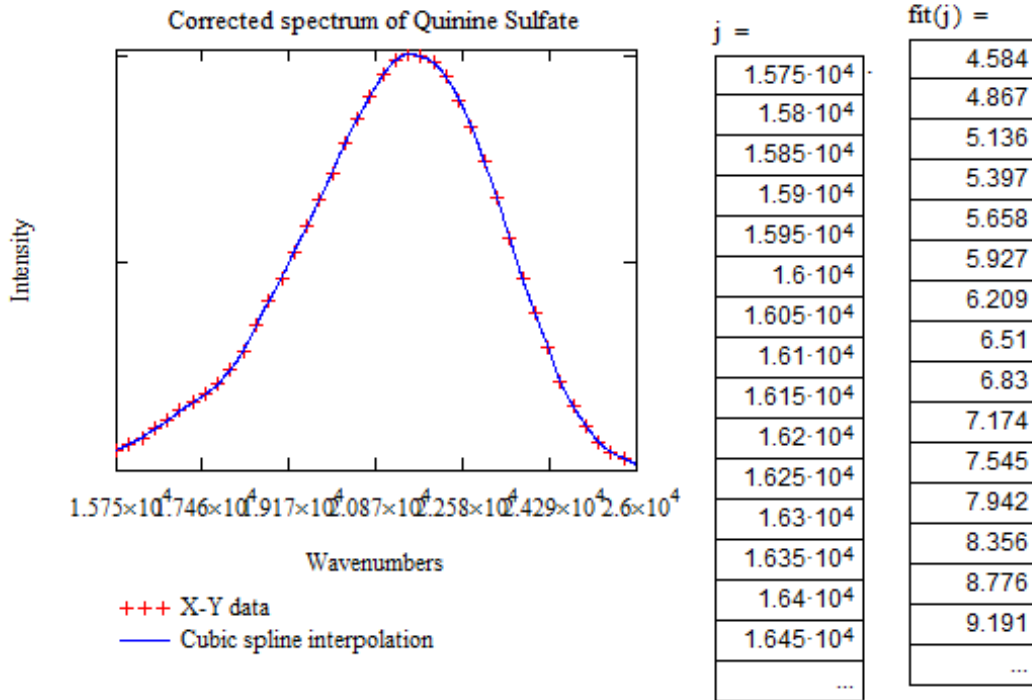
$$\int_{15750}^{26000} fit(x)\, dx = 4.758 \cdot 10^5$$

Fluorescence data for Quinine Sulfate from LS50B corrected for bandbass by multiplying intensities by λ^2 and normalized to 100. Blue sensitive phototube. Data copied from excel and insert>component>input table.. then copy and paste from Excel

xdata :=

	0	1
0	28571.43	4.48
1	28530.67	...

$xdata := csort(xdata, 0)$ $A := xdata^{\langle 0 \rangle}$ $B := xdata^{\langle 1 \rangle}$

Spline coefficients:

$S := cspline(A, B)$

422

Fitting function:

$$xfit(x) := interp(S, A, B, x)$$

Corrected and LS50 / cubic spline fit.

Determining correction factors at regular wavenumber intervals by dividing corrected spectral data by uncorrected spectral data.

$$l := 15750, 15800 .. 26000$$

$$l =$$

$1.575 \cdot 10^4$ ·
$1.58 \cdot 10^4$
$1.585 \cdot 10^4$
...

$$xfit(l) =$$

1.388 ·
1.468
1.566
...

$$\left(\frac{fit(l)}{xfit(l)} \right) =$$

3.303 ·
3.315
3.28
3.276
3.281
3.387
3.307
3.281
3.223
3.248
3.216
3.222
3.236
3.281
3.226
...

423
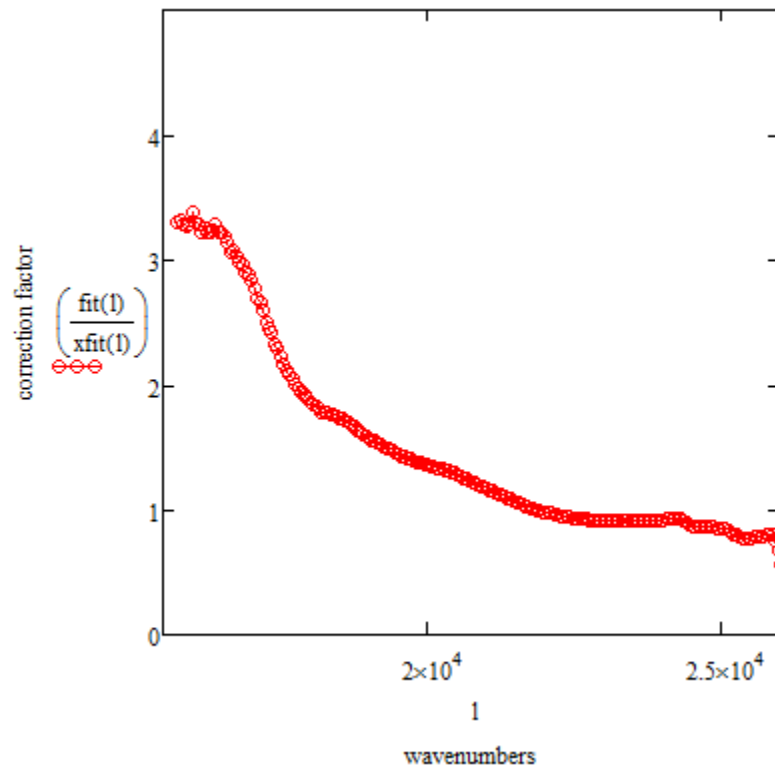
APPENDIX F

FLUORESCENCE QUANTUM YIELD SAMPLE CALCULATION

Connors

Quantum yield determination for 2bjulcp in undegassed
Benzene with red sensitive tube.
experiment 1

This QuickSheet demonstrates Mathcad's **cspline** and
interp functions for connecting X-Y data.

Enter a matrix of X-Y data to be interpolated:
Enter spectral data for compound after converting to wavenumbers, multiplying intensity by
lambda squared DO NOT normalize intensity. Insert data from Excel -right key, paste table.

data1 :=

21978.02	$5.75 \cdot 10^6$
21953.9	$5.64 \cdot 10^6$
21929.82	$5.48 \cdot 10^6$
21905.81	...

Click on the **Input Table** above until you see the handles, and
enlarge it to see the matrix **data** used in this example.

$$\text{data1} := \text{csort}(\text{data1}, 0)$$

$$X := \text{data1}^{\langle 0 \rangle} \qquad Y := \text{data1}^{\langle 1 \rangle}$$

Spline coefficients:

$$S1 := \text{cspline}(X, Y)$$

Fitting function:

$$\text{fit}(x) := \text{interp}(S1, X, Y, x)$$

425

Sample interpolated values:

$$\text{fit}(21000) = 7.816 \times 10^4$$

$$\text{fit}(18800) = 1.007 \times 10^6$$

2bjulcp in benzene

××× X-Y data
—— Cubic spline interpolation
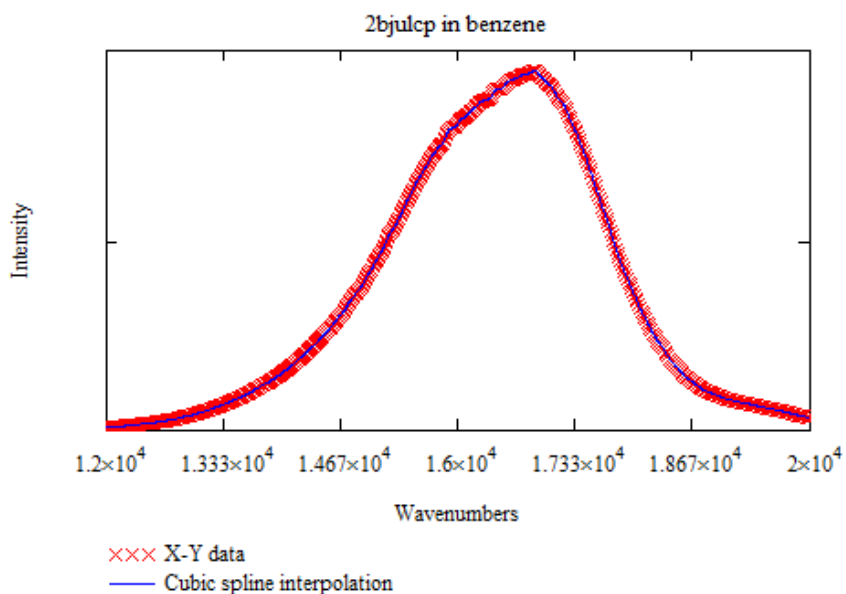
Correction factors for LS50B with red sensitive tube

DATA Limits 12,500-22,200 Wavenumbers

corrdata :=

	0	1
0	12500	4.43
1	12550	...

$$\text{xdata} := \text{csort}(\text{corrdata}, 0)$$

$$A := \text{corrdata}^{\langle 0 \rangle} \qquad B := \text{corrdata}^{\langle 1 \rangle}$$

Spline coefficients:

$$S := \text{cspline}(A, B)$$

Fitting function:
Fitting function:

$$\text{corrfit}(x) := \text{interp}(S, A, B, x)$$

426

$$\text{corrspec}(x) := \text{corrfit}(x) \cdot \text{fit}(x)$$

$$\underset{\sim}{1} := 12500, 12550 .. 22200$$

$$1 =$$

$1.25 \cdot 10^4$
$1.255 \cdot 10^4$
$1.26 \cdot 10^4$
...

corrspec(x)
━━━

fit(x)
┄┄┄

$$\text{corrspec}(1) =$$

$8.201 \cdot 10^5$
$1.867 \cdot 10^6$
$2.271 \cdot 10^6$
$2.533 \cdot 10^6$
...
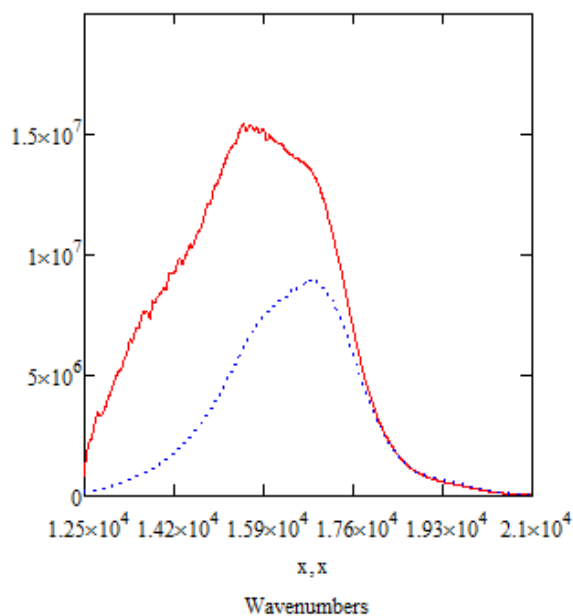
Wavenumbers

$$\int_{12500}^{21000} \text{fit}(x)\, dx = 2.682 \times 10^{10}$$

$$\int_{12500}^{21000} \text{corrspec}(x)\, dx = 5.788 \times 10^{10}$$

Enter a matrix of X-Y data to be interpolated:

Enter spectral data for standard (fluorescein) after converting to wavenumbers, multiplying intensity by lambda squared DO NOT normalize intensities. Insert data from Excel -right key, paste table.

$$\text{stdata} :=$$

21978.02	$9.6 \cdot 10^6$
21953.9	$9.46 \cdot 10^6$
21929.82	...

Click on the **Input Table** above until you see the handles, and enlarge it to see the matrix **data** used in this example.

$\text{stdata} := \text{csort}(\text{stdata}, 0)$

$$C := \text{stdata}^{\langle 0 \rangle} \qquad D := \text{stdata}^{\langle 1 \rangle}$$

Spline coefficients:

$$S := \text{cspline}(C, D)$$

Fitting function:

$$\text{sfit}(x) := \text{interp}(S, C, D, x)$$

$$\text{sfit}(18000) = 1.817 \times 10^7$$
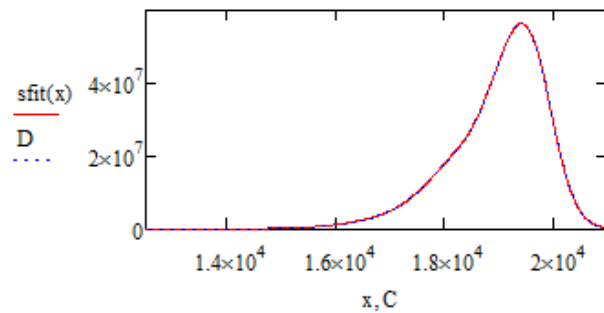
$$\text{scorrspec}(x) := \text{corrfit}(x) \cdot (\text{sfit}(x))$$
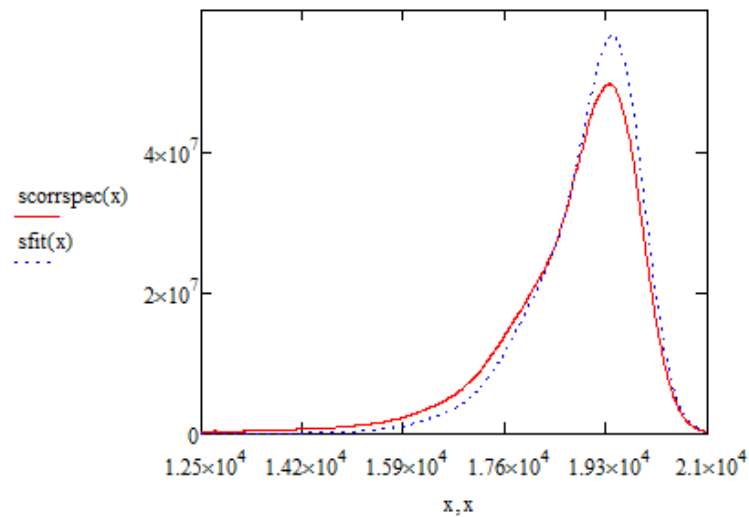
Compound

Standard

$$\int_{12500}^{21000} \text{corrspec}(x)\,dx = 5.788 \times 10^{10}$$

$$\int_{12500}^{21000} \text{scorrspec}(x)\,dx = 9.965 \times 10^{10}$$

Area under corrected compound curve

Area under corrected standard curve

$$Dc := \int_{12500}^{21000} \text{corrspec}(x)\,dx$$

$$Ds := \int_{12500}^{21000} \text{scorrspec}(x)\,dx$$

$$Dc = 5.788 \times 10^{10}$$

$$Ds = 9.965 \times 10^{10}$$

	Compound	Standard
Absorbance at λ(ex)	Ac := 0.02481	As := 0.0107460
Index of refraction	Benzene	NaOH
	nc := 1.501	ns := 1.334

quantum yield of standard

$$QYs := 0.95$$

$$QYc := QYs \cdot \left(\frac{As}{Ac}\right) \cdot \left(nc \cdot \frac{nc}{ns \cdot ns}\right) \cdot \left(\frac{Dc}{Ds}\right)$$

$$QYc = 0.303$$

APPENDIX G

FLUORESCENCE LIFETIME SAMPLE CALCULATION

Fluorescence Lifetime Determination of 2bjulcp in Pyridine

Single Exponential Lifetime

```
*************************************************
Analysis Function :          Wed Jul 25 2007 at 16:03

    ****** one-to-four exponentials ******

    ***** Input Values *****


Decay curve    : A1 534.8:625
IRF curve      : A1 534.8:534.8


Start Time     : 42.5
End Time       : 90

Offset fixed at -25
Shift  fixed at  0.5

Pre-exp. 1     : 1
Lifetime 1     : 1


    ***** Statistics *****

Job done after 5 iterations in  0.047 sec.


Fitted curve    : FLD Fit (12)
Residuals       : FLD Residuals (12)
Autocorrelation : FLD Autocorrelation (12)
Deconvolved Fit          : FLD Deconvoluted (12)

Chi2           : 2.092
Durbin Watson  : 0.8608
Z              : 0

Pre-exp. 1     : 2.132      ± 9.454e-002   ( 100     ± 4.434%)
Lifetime 1     : 0.9299     ± 4.196e-002

F1             : 1


Tau-av1        : 0.9299
Tau-av2        : 0.9299

Offset         : -25
Shift          : 0.5

*************************************************
```
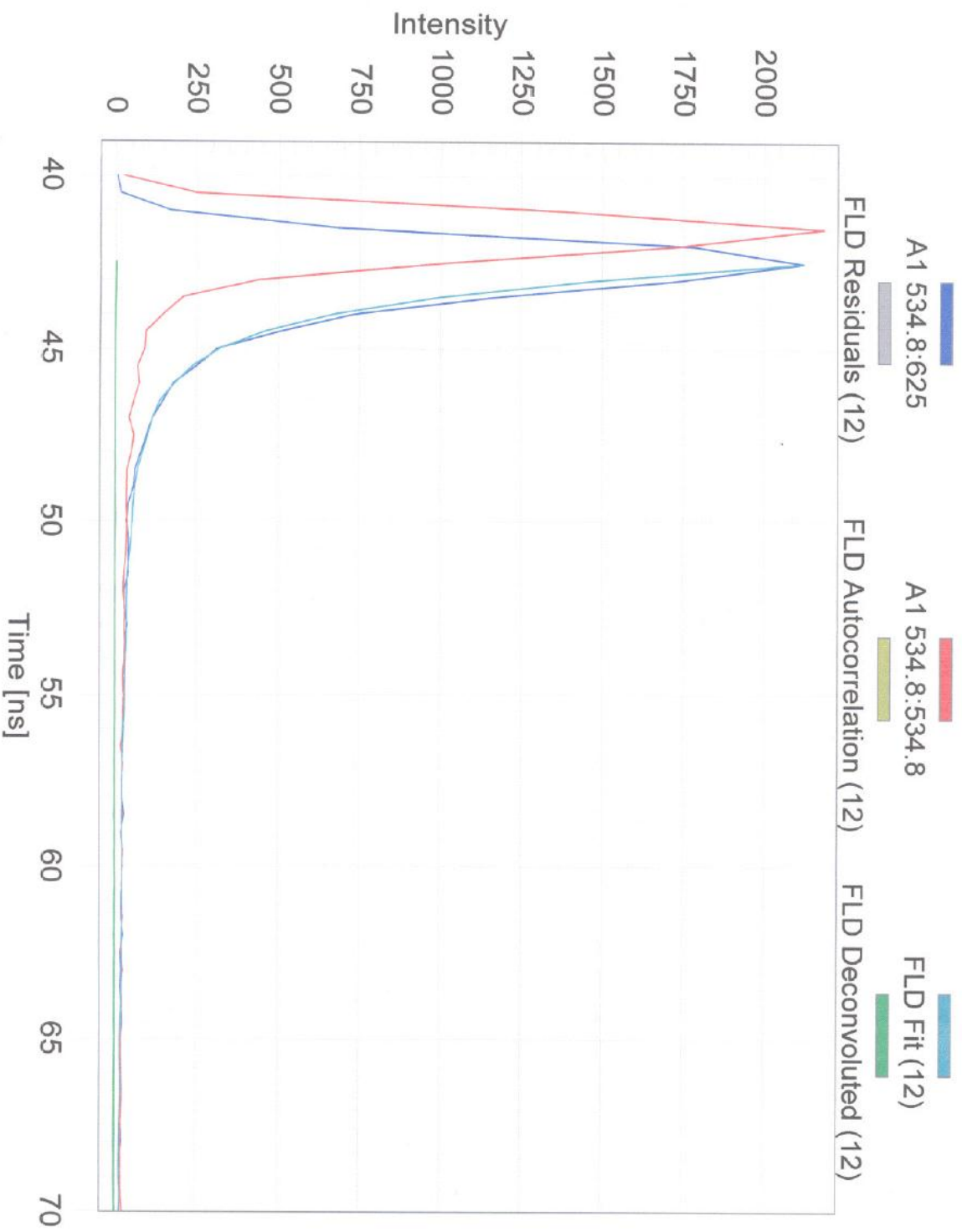
2bjulcp in Pyridine

APPENDIX H

CHARACTER AND PRODUCT TABLES FOR THE C_{2v} POINT GROUP

C_{2v} Point Group

Abelian, 4 irreducible representations

Subgroups of C_{2v} point group: C_s, C_2

Character table for C_{2v} point group

	E	C_2 (z)	$\sigma_v(xz)$	$\sigma_v(yz)$	linear, rotations	quadratic
A_1	1	1	1	1	z	x^2, y^2, z^2
A_2	1	1	-1	-1	R_z	xy
B_1	1	-1	1	-1	x, R_y	xz
B_2	1	-1	-1	1	y, R_x	yz

Product table for C_{2v} point group

	A_1	A_2	B_1	B_2
A_1	A_1	A_2	B_1	B_2
A_2	A_2	A_1	B_2	B_1
B_1	B_1	B_2	A_1	A_2
B_2	B_2	B_1	A_2	A_1

APPENDIX I

BASIS SETS

Density functional theory (DFT) and *ab initio* quantum mechanical modeling methods are used to study the electronic structure of many-body systems. In DFT and *ab initio* methods, basis functions, χ, are used, which are combined to give the molecular orbital wavefunction, Ψ_{MO}.

$$\Psi_{MO} = \sum_{i=1}^{n} c_i \, \chi_i \qquad (\text{I-1})$$

Semi-empirical methods use Slater type orbitals (STO), which are similar to hydrogen and hydrogen-like atomic orbitals

$$\chi_{n,l,m} = A \exp(-\xi r) \qquad (\text{I-2})$$

where A is a normalization constant. It is common practice in DFT and *ab initio* methods to employ Gaussian functions to construct basis functions

$$g_{n,l,m} = A \exp(-\alpha r^2) \qquad (\text{I-3})$$

The value of Gaussian wavefunctions is that they simplify the mathematics, such as the evaluation of multicenter integrals. Instead of using a single Gaussian function to represent a basis function, the current practice is to take a linear combination of a small number of Gaussian functions (primitive Gaussians) to represent a basis function. To exemplify, for the addition of three primitive Gaussians, g_1, g_2, and g_3,

$$\chi_r = \sum_{i=1}^{3} c_i\, g_i = c_1 g_1 + c_2 g_2 + c_3 g_3 =$$

$$c_1 \exp(-\alpha_1 r^2) + c_2 \exp(-\alpha_2 r^2) + c_3 \exp(-\alpha_3 r^2)$$

(I-4)

where χ_r is referred to as a contracted Gaussian function and the coefficents (c_i) are held

constant. The above equation represents a Slater type orbital (STO) approximated as a linear

combination of three primitive Gaussian functions, referred to as STO-3G, a minimal basis set.

A minimal basis set consists of one contracted Gaussian function for each inner (core)

shell orbital and each outer (valence) atomic orbital. For row 1 elements (H, He), 1s is the only

atomic orbital; thus, there is one contracted Gaussian function. For row 2 elements (Li – Ne),

there are a total of 5 core and valence atomic orbitals (1s, 2s, $2p_x$, $2p_y$, and $2p_z$); thus, there are

five contracted Gaussian functions. For row 3 elements (Na – Ar), there are a total of 9 core and

valence atomic orbitals (1s, 2s, $2p_x$, $2p_y$, $2p_z$, 3s, $3p_x$, $3p_y$, $3p_z$); thus, there are a total of nine

contracted Gaussian functions.

A split valence (SV) basis set uses two STOs for each valence atomic orbital (one

contracted and one diffuse), but only one STO for each inner core atomic orbital. Take for

example the row 2 elements (Li – Ne):

<div align="center">

1s 2s' $2p_x$' $2p_y$' $2p_z$' (contracted)

$2s$" $2p_x$" $2p_y$" $2p_z$" (diffuse)

</div>
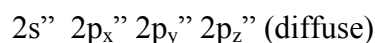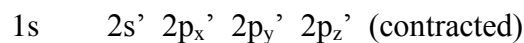
The SV basis set allows electron density on a particular atom to expand or contract,

depending on the molecular environment.

Common SV basis sets are listed and described below.

3-21G: The inner shell orbitals are constructed from a linear combination of **3** primitive Gaussian functions, and the valence orbitals are constructed of **2** contracted primitive Gaussian functions and **1** diffuse primitive Gaussian function.

6-31G: The inner shell orbitals are constructed from a linear combination of **6** primitive Gaussian functions, and the valence orbitals are constructed of **3** contracted primitive Gaussian functions and **1** diffuse primitive Gaussian function.

6-311G: The inner shell orbitals are constructed from a linear combination of **6** primitive Gaussian functions, and the valence orbitals are constructed of **3** contracted primitive Gaussian functions and 2 diffuse primitive Gaussian functions (triply split valence orbitals).

The description of some systems (e.g. small rings) requires that there be a nonuniform displacement of charge away from the atomic nuclei. One approach is to include functions of higher angular momentum quantum number in the basis set (e.g. p-type functions on first row elements and d-type functions on second row elements of the periodic table). A basis function that incorporates functions of higher angular momentum quantum number than are needed by the atom of interest in its ground state is called a polarization basis set. Examples of polarization basis sets are listed and described below.

6-31G* or 6-31G(d): Add 6 primitive d-type Gaussian functions to the 6-31G(d) basis set.

6-31G** or 6-31G(d,p): Add 6 primitive d-type Gaussian functions to heavy atoms and 6 primitive p-type Gaussian functions to hydrogen and helium atoms to the 6-31G(d) basis set.

Diffuse functions are larger sized versions of s- and p-type functions that allow orbitals to occupy a larger region of space. The use of diffuse functions is important for molecules with lone pairs, anions, and excited states. Examples of diffuse functions are listed and described below.

6-31+G: 6-31G basis set with diffuse functions added to heavy atoms.

6-31++G: 6-31G basis set with diffuse functions added to heavy atoms and hydrogen atoms.

6-311+G(d,p): This basis set is a large basis set, which includes the addition of d-type functions to heavy atoms, p-type functions to hydrogen and helium atoms, and diffuse functions added to heavy atoms to the 6-311G basis set. Large basis sets tend to give superior results.

Furthermore, the larger the basis set, the longer the calculation time because of the increased number of functions involved in the computations.